

THIS WEEK

EDITORIALS

WORLD VIEW What Earth can learn from sci-fi classic *Dune* **p.601**

DISCOVERY Meet the multi-limbed squidworm **p.602**

OIL Robust report rules on Deepwater Horizon spill **p.604**



An end to gridlock?

Europe says it is embarking on an unprecedented overhaul of its electricity system. But it must do more to convince the private sector that it is serious.

Few people care how their electricity is generated, as long as the lights come on when they press the switch. Even fewer care how it is delivered, which is why the growing problem of ageing energy infrastructure across Europe and the United States rarely gets the attention it deserves. A welcome exception to this attitude is the agreement to develop a new subsea electricity grid in the North Sea, which is due to be signed on 3 December by the energy ministers of ten European nations, including France, Germany and the United Kingdom.

Such an offshore grid would be a world first and would bring many benefits. These would include far greater integration, and hence price competition, between the electricity markets in northern Europe, wider access to extensive short-term hydropower storage in Norway, and crucial links to bring to land the energy generated by offshore wind, wave and tidal power. The grid is just one of half-a-dozen energy-infrastructure priorities for Europe that the European Commission announced last month. Together, they will require €200 billion (US\$264 billion) of investment over the next decade according to the commission, half of it from public sources. The quoted price for the North Sea grid is about €20 billion.

Other parts of the world face similar infrastructure challenges: in the United States, for example, a consortium led by Google has proposed a \$5-billion offshore grid to access offshore wind power and shore up the creaking electricity grid of the US eastern seaboard. A report from the American Physical Society last month pointed out that most US states don't yet have the necessary grid in place to handle the renewable capacity that they have committed to build.

Tomorrow's expected agreement, a memorandum of understanding on the North Sea grid, is only a small step towards its actual construction. In Europe as elsewhere, the high financial stakes associated with different energy projects can leave the real agendas unspoken, which makes energy policy a difficult political game to read.

In this case, the sustenance and development of nuclear energy may be a higher priority, to varying extents, for the centre-right governments led by David Cameron in Britain, Angela Merkel in Germany and Nicolas Sarkozy in France, than the rapid development of the renewable energy sources associated with the North Sea grid — although all three governments would be reluctant to say so in public.

In signing the memorandum, the European governments involved at least acknowledge that market forces alone cannot be expected to gain the infrastructure investments that Europe needs if it is to secure its electricity supplies and meet its carbon-emissions targets. Until quite recently, many political leaders continued to insist that all that was really needed to build energy infrastructure was the efficient distribution of private finance. They argued, fatuously, that 'markets would decide' which energy sources were appropriate and what infrastructure was needed. The reason that argument breaks down is that private investment in the energy sector depends heavily on rules and expectations set by governments. Decisions about where to build power lines, especially

international ones, are ultimately political. And the availability of grid capacity will determine, to a considerable degree, which power sources are best placed to generate economically viable electricity. If Europe had relied entirely on the private sector to plan, build and finance existing electricity grids half a century ago, it would not have a functioning grid at all. If Europe relies on private finance for its future grid development, it will end up with something more like the blackout-prone electricity grid of the United States, which has been starved of public investment for decades.

"Market forces alone cannot be expected to secure the infrastructure investments that Europe needs."

Future grid development also requires research and development, much of it in areas that have received little attention in recent decades (see page 624). To lower costs and increase efficiency, subsea grids will need technologies such as high-voltage d.c. converters and control systems. Research institutions such as the University of Strathclyde in Glasgow, UK, which is planning a £100-million (US\$157-million) centre devoted to innovation and renewable energy, can help to provide the knowledge needed to underpin these technologies.

To raise private money for new energy infrastructure and so control public costs, governments must send strong and consistent signals about their intentions. A deadline for countries involved in this project to revise their regulatory regimes to allow them to trade electricity would be a good start. The end result will be lower emissions, lower electricity costs for consumers, and the lights staying on as Europe embarks on an unprecedented overhaul of its power system. ■

A long way to go

Overpriced and underused, the International Space Station could still be a research asset.

Handed US\$100 billion to spend on research, few scientists would invest in a cramped laboratory in constant need of maintenance with few facilities and one hell of a commute. So it is worth stating the obvious up front: the International Space Station (ISS) is an expensive, wasteful and probably unnecessary way to conduct science. The value of research carried out on the station will almost certainly never justify its ludicrous price tag. The money could surely have been put to better use on Earth.

But would it have been? Construction of the space station was never really about science, and researchers should think twice before continuing to use the project's epic cost as a stick with which to beat it. In

a time of austerity, they have been handed the ultimate luxury: a new frontier for research that is limited only by their imagination.

Conceived during the cold war, the ISS was born of global politics, and remains a showpiece of international collaboration. An engineering marvel, the orbiting laboratory came within a whisker of cancellation in 1993, yet is expected to remain a bright fixture of the night sky for at least the next decade. It is time for the ISS to show what it can do. So what can it do? “Grow crystals,” shout the critics. It is true that the image of research on the space station, and space science more generally, suffers from the limited scope of early experiments. Much of the research carried out on the ISS so far can, perhaps unfairly, be lampooned in a similar way. The impact of the lack of gravity on an experiment often seems to be investigated purely because it can be, rather than because the question has genuine scientific value. The other popular function of the space station’s facilities — to probe the effects of weightlessness on its occupants — is based on the circular logic that demands such information as essential for continued human presence in space.

To their credit, those running research on the ISS seem determined to push those boundaries. Last month, the European Space Agency appealed for ideas and ‘vision’ from scientists to shape its next ISS research programme, due to be presented to member states in 2012. And next week, NASA will hold a public meeting to help throw open the airlock of the ISS to sister government agencies, chemical firms and pharmaceutical companies, among others (see page 610).

NASA is the biggest funder of the ISS and its biggest stakeholder, yet it would be a sensible step for the agency to hand over its control of ISS science to an independent body. Acting as a buffer between

NASA managers and the broader research community who could use the ISS facilities, such a body was first proposed last year in the Augustine committee’s review of US human spaceflight plans and was mandated by the NASA authorization bill passed this September. The Space Telescope Science Institute in Baltimore, Maryland, which oversees research on space telescopes such as Hubble, shows how such an operation can work well. If set up properly, a similar body could offer a useful arms-length approach to space science that could boost both the profile and quality of orbiting experiments.

“Flagship shiny projects help to stir wider public interest in science and so loosen political purse strings.”

This could help to counter continuing accusations that expanded space-station research will merely throw into orbit good money after bad. But for such a strategy to succeed, the scientific demand to drive competition for expensive time aboard the ISS must be there — a condition that is by no means certain. But scientists, whatever their views on its cost effectiveness, should not glibly dismiss the research credentials of the space station and its possible contribution to science. Those with even a passing interest should take the officials in charge at their word and give serious thought to how the facility could be used.

Flagship shiny projects help to stir wider public interest in science and so loosen political purse strings to release funds that might otherwise not flow to research. And basic, blue-skies research, scientists often say, is the bedrock of useful creativity. Decades in the making, the overpriced and underused marvel that is the International Space Station offers bluer skies than most. ■

Undue obstruction

Republican opposition to the US–Russia arms-control treaty is based on politics, not science.

When US President Barack Obama signed the latest arms-control treaty with Russia in April 2010, he called it “an important first step”. But the administration has been tripped up by Republican opposition to the New Strategic Arms Reduction Treaty (New START), which would reduce both nations’ arsenals by roughly one-third. The Republicans are blocking the treaty with pseudoscientific arguments about the state of the country’s weapons complex. Yet it is politics, not science, that is behind their move.

Earlier this week, Arizona senator Jon Kyl, the number-two Republican in the Senate, said he believed that the treaty could not be ratified by the end of the year. Debate over its merits would take “at least two weeks”, and Senate Democrats had not provisioned enough time for the discussion, Kyl said on US network NBC’s *Meet the Press* talk show.

Pushing a vote on the treaty into 2011 would present it to a new Senate — containing more Republicans — potentially making it less likely to pass. Such a delay would also increase the chances of Kyl, no fan of arms control, giving the Obama administration a bloody nose.

The debate Kyl hungers for is less about the treaty itself than it is about the state of the US nuclear complex. In a 24 November memo to Senate Republicans, Kyl and Bob Corker (Republican, Tennessee) characterized nuclear-weapons scientists as mechanics working in a decrepit garage on a fleet of 30-year-old Ferraris. The scientists are “responsible for assuring that, at any given moment, each of the eight finely tuned cars will respond to the key turn”, they wrote.

Implicit in this analogy is that there is some uncertainty over how the country’s decades-old nuclear weapons will behave if they are ever used. Moreover, Kyl implies that weapons scientists are ill-equipped to analyse and diagnose problems associated with the arsenal.

There is little in the open scientific literature to support these positions. The chief concern surrounding ageing nuclear weapons has been that their plutonium triggers will be damaged by self-irradiation. Yet a 2006 review of weapons-lab data by the independent JASON scientific advisory group found that the triggers are heartier than expected and will last for at least 85 years.

Similarly, the image of a rickety garage is hardly appropriate. Weapons scientists have a slew of modern tools to ensure that their weapons continue to work effectively. Last year saw the start-up of the US\$3.5-billion National Ignition Facility, a giant laser at Lawrence Livermore National Laboratory in California that aims to replicate the forces inside an exploding warhead. Livermore’s sister lab, Los Alamos National Laboratory in New Mexico, is home to a radiographic facility that can create three-dimensional X-rays of dummy bombs as they explode. And scattered across the weapons complex are powerful supercomputers that can simulate full nuclear explosions based on data from these experiments and from past tests.

The weapons labs want more, and have found an ally in Kyl. Over the summer, the senator conducted tours of the labs, and came away with strengthened demands for funds, including money for modern uranium and plutonium manufacturing facilities. Many of the arguments he uses have been used by some within the weapons complex for years to call for a return to underground testing, as well as the development of new kinds of ‘reliable’ weapons.

The Obama administration had offered Kyl a decade-long funding commitment worth more than \$85 billion to the weapons complex in exchange for agreement on the treaty, but the senator has continued to advance his flimsy political arguments over the fitness of the country’s complex. As *Nature* went to press, Obama was due to host a bipartisan meeting to try to resolve the dispute.

There is certainly a need to debate the future shape and size of the US weapons complex, but there is no need to do so before ratifying New START. The facts speak for themselves: the weapons will work, and the scientists watching them have the tools to make sure that they do. ■

➔ **NATURE.COM**
To comment online,
click on Editorials at:
go.nature.com/xhunjq



A sustainable planet needs scientists to think ahead

Globalization means that Earth's life-support system can no longer be treated as separate from the socio-economic system, says Sybil Seitzinger.

In Frank Herbert's 1965 science-fiction classic *Dune*, the number-one position on the planet is held not by a politician, but by a planetary ecologist. His job is to oversee the long-term conversion of the desert planet to a lush biosphere — a role demanding formidable far-sightedness.

On Earth, the human population is set to top 9 billion within two generations. Meanwhile, we are altering, in profound and uncontrolled ways, key biological, physical and chemical processes of ecosystems on which this growing population will depend. Gordon Conway, former head of the Rockefeller Foundation, once suggested that Earth should appoint a planetary ecologist of its own. Given that today's policy-makers have consistently demonstrated an inability to take more than a short-term view of life on Earth, perhaps it is time to take the idea seriously.

The number-one position on Earth at present is arguably that of head of the United Nations (UN). Ban Ki-moon, the current UN secretary-general, seems to understand the scale and nature of the problem much better than his predecessors. This is welcome, but is still not enough. Indeed, it is doubtful whether a UN system shackled by national self-interest can ever set out a vision for a sustainable planet, or a sensible plan to realize it.

Policy-makers must take on board that Earth's ecology acts as a complex and non-linear system, and is in a constant state of change. And they must recognize that to fully understand this system, they need to take a long-term view. Is this so different from acknowledging the complexity and timescales of the world economy?

Politicians do accept that the global economic meltdown was caused by relatively small changes in parts of the financial system. The response of global markets to US toxic debt and sub-prime mortgages was nonlinear and far-reaching. The effects tumbled through other social systems and rippled through the global carbon cycle by way of reduced emissions. The crash exposed the way in which a jumbled mass of connections can cause a colossal and abrupt decline that the full might of human ingenuity struggles to stem. We should note, given the frequent warnings from scientists about our fragile natural systems, that many economists saw the financial crash coming.

For a decade or more, scientists have built up a picture of Earth as a similarly complex, interconnected system — resilient in places but vulnerable in others. Progress has been slower than many hoped, but planetary models now go beyond simple atmospheric chemistry and the carbon cycle to include cryosphere, ocean and land processes. The basics of the nitrogen cycle are being included, as are elementary descriptions of social and economic systems such as energy and agriculture. As a result, there

has been an explosion in our knowledge of Earth as a complex system. One conclusion is clear: our behaviour will shape our future.

Despite these advances, the UN still doesn't seem to see that Earth's restless and powerful social system operates within a complex and intricately linked ecological system — let alone manage it. The UN system currently includes more than 500 international treaties and agreements related to the environment. Although the current climate talks in Cancún, Mexico, are being held under the UN's Framework Convention on Climate Change, its related Millennium Development Goals, Convention on Biological Diversity and Millennium Ecosystem Assessment are all managed separately. And the UN's iconic Human Development Index takes no account of sustainable development.

Some reasons for this are apparent. The UN's 192 member states are primarily governed by narrow perspectives, self-interest and short time horizons. Nations prefer to deal with environmental issues separately because such an approach gives them more leverage in negotiations.

Given what we now know about the long-term planetary impact of human activities, this piecemeal and short-term management of individual environmental issues leaves us exposed should one part of the system fail and send shockwaves through the rest.

In August, Ban Ki-moon called for fresh ideas as he announced the creation of an independent high-level panel to direct the world towards sustainability. The panel, due to report ahead of the UN's 2012 Conference on Sustainable Development in Rio de Janeiro, is made up largely of senior politicians and business people. Although the business community can inject dynamic thinking to counter what they view as immediate threats,

there must also be strong input to this debate from scientists with a long view and an understanding of how Earth operates as a complex social-ecological system.

Just six weeks before the UN's 2012 Rio conference, scientists from around the world will gather to set out such a long-term vision of planetary stewardship. The London-based Planet Under Pressure conference aims to attract 2,500 natural and social scientists along with policy-makers, industry and others. It will offer a timely update on what we know about the Earth system, including the impact of its economic, political and social sub-systems. The results will be offered to the Rio meeting and the wider world as sorely needed long-term thinking and leadership from the scientific community. For, as Herbert wrote, "The highest function of ecology is the understanding of consequences." ■

Sybil Seitzinger is Executive Director of the International Geosphere-Biosphere Programme, based in Stockholm.
Sybil.seitzinger@igbp.kva.se

**THERE MUST BE
STRONG INPUT
FROM SCIENTISTS WITH A
LONG VIEW
AND AN UNDERSTANDING
OF HOW EARTH
OPERATES.**

➔ **NATURE.COM**
Discuss this article
online at:
go.nature.com/9zig7m

RESEARCH HIGHLIGHTS

Selections from the
scientific literature

GEOSCIENCE

How plants check global warming

Plants' response to a twofold increase in atmospheric carbon dioxide could put a much stronger brake on global warming than expected.

Greater vegetation growth in hotter, wetter climates leads to more evaporation and transpiration from leaves, and therefore more heat loss from land. Other studies have noted this effect, but Lahouari Bounoua at the Goddard Space Flight Center in Greenbelt, Maryland, and his colleagues built into their modelling study additional feedback effects — such as alterations in plants' photosynthetic activity — that further boost vegetation growth.

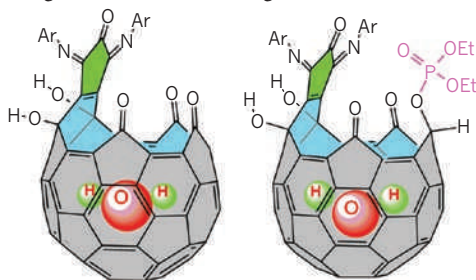
They predict that the effects on plants of growing in 700 parts per million of carbon dioxide would reduce expected 30-year temperature rises by around 13% globally. *Geophys. Res. Lett.* doi:10.1029/2010GL045338 (2010)

CHEMISTRY

Tiny molecular 'water bottle'

A 'buckyball' — a spherical molecule made up of 60 carbon atoms — has been turned into a vial just big enough to hold a single water molecule, complete with its own removable stopper.

Liangbing Gan of Peking University, Wim Klopper of the Karlsruhe Institute of Technology in Germany and their team created a 60-carbon fullerene sphere with an orifice big enough for water to pass through.



They show that a phosphate group can be easily attached and removed from the edge of the orifice, where it acts as a plug for the fullerene vial. With this 'stopper' removed (pictured left), water is incorporated into the vial 230 times faster than with it attached (right).

The authors say that uses for the vial could include acting as a carrier for drugs in the body. *Angew. Chem. Int. Edn* doi:10.1002/anie.201004879 (2010)

OPTICAL PHYSICS

A peek at a molecule's guts

Advanced microscopy techniques have provided researchers with an unprecedented glimpse into a molecule. Researchers used the electron beam of a scanning tunnelling microscope (STM) to excite

different parts of the molecule, causing it to emit light.

Wilson Ho and his colleagues at the University of California, Irvine, used an STM and photon detector to image molecules of magnesium porphine. The images reveal a structure with twofold symmetry, which the authors say is due to an approximately planar molecule distorting into a saddle shape. This distortion warps molecular orbitals and so changes the spectra of the emitted photons, revealing the inner structure.

Previously, optical techniques have been able to detect individual molecules



ZOOLOGY

Showcasing the sea's strange secrets

A bizarre worm with ten 'arms' has been discovered almost 3,000 metres below the ocean surface near Indonesia. *Teuthidodrilus samae* (pictured) is a newly identified genus and species of free-swimming annelid worm. Karen Osborn, currently at the University of California, Santa Cruz, and her colleagues report that it seems to be common deep in the Celebes Sea.

The 'squidworms' can reach 94 millimetres

in length, and their appendages can be even longer. The worms have probably avoided detection for so long because of their ability to swim away from sampling gear and the difficulties of exploring the vast ocean depths. The strange creature shows how little we know about even common members of the sea's deep-water communities, say the authors.

Biol. Lett. doi:10.1098/rsbl.2010.0923 (2010)

but not to resolve details of their interiors.

Phys. Rev. Lett. 105, 217402 (2010)

MEDICINE

Profiling for blood pressure

Whether the powerful high-blood pressure medicine rostafuroxin will be effective for a particular patient can be predicted from a set of gene variants.

Giuseppe Bianchi at the Prassis sigma-tau Research Institute in Milan, Italy, and his colleagues show how the drug works. It normalizes sodium transport in the kidneys that is disrupted by two specific mechanisms: a mutated version of a protein called adducin and a boost in levels of a hormone called ouabain. The researchers identify several gene variants heralding the faulty mechanisms and, in a second paper, show that patients with certain combinations of variants in five specific genes respond well to rostafuroxin, but not necessarily to two other blood-pressure medicines.

The key combination of variants is present in about 25% of patients. *Science Transl. Med.* 2, 59ra86; 59ra87 (2010)

STEM CELLS

Platelets get a boost

The reprogramming of adult cells to produce induced pluripotent stem (iPS) cells shows promise for tissue repair. c-MYC is one of the proteins used to reprogram cells, but at high levels it also hinders the transformation of iPS cells into platelets, a blood cell important in clotting and wound healing.

Some iPS cells do turn into platelets, however, and Koji Eto at the University of Tokyo, and his colleagues have now found out how. The team created numerous human iPS cell lines by delivering a cocktail of proteins, including c-MYC, to skin

cells, and then differentiated these into platelets. The iPS cells that became platelets most efficiently were those that rapidly muffled the expression of c-MYC. In mice, these platelets homed in on damaged blood vessels just like natural platelets.

J. Exp. Med. doi:10.1084/jem.20100844 (2010)

MATERIALS

Controlling water on synthetic silk

Tiny water droplets have been made to move in a controlled direction along threads of synthetic spider webs.

Lei Jiang at the Chinese Academy of Sciences in Beijing, Yongmei Zheng of the Beijing University of Aeronautics and Astronautics and their colleagues constructed webs from different polymers and observed the spontaneous movement of micrometre-sized water droplets on their strands. On polymers with a rough surface, drops always migrate towards and coalesce at knots in the silk, regardless of its hydrophobicity. But if the surface is smoother they move away from the knots if the polymer is hydrophobic, and towards them if it is hydrophilic.

These results should allow the design of devices that can drive water droplets in a controllable manner.

Adv. Mater. doi:10.1002/adma.201003169 (2010)

DEVELOPMENTAL BIOLOGY

Placenta key to fetal growth rate

Gestation period varies widely in the mammalian world, with some species developing twice as fast as others in the womb. This is largely because of differences in the arrangement of fetal and maternal tissues in the placenta.

Isabella Capellini at Durham University, UK, and her team analysed data from previous studies on neonatal brain mass, body and litter size, and

COMMUNITY CHOICE

The most viewed papers in science

CELL BIOLOGY

Genes that make cells move

HIGHLY READ
on genesdev.
cshlp.org the
week beginning
15 November

The movement of cells in the body is important for normal development, but can also be deadly — in metastatic cancer. Researchers have teased out 31 genes whose products belong to various pathways that seem to regulate human cell migration. The pathways converge on a key signalling enzyme called RSK, suggesting that this could be a target for new cancer drugs.

Daniel Haber at the Massachusetts General Hospital in Boston and his co-workers screened roughly 11,000 genes in human cells using 55,000 small RNA molecules that silence specific genes. They used a chamber with a perforated membrane to identify which cells retained their roving abilities.

The authors found that many of the 31 genes they identified had not previously been linked to cell motility. Furthermore, when the researchers blocked RSK with a small-molecule inhibitor, single cells moved much more sluggishly.

Genes Dev. doi:10.1101/gad.1989110 (2010)

maternal placental morphology from 109 mammalian species. They discovered that animals with placentas where fetal and maternal tissues interlock the most — creating a greater surface area over which nutrients can flow — gestate in less than half the time taken by animals that have placentas with a minimal surface area for nutrient exchange.

Am. Nat. doi:10.1086/657435 (2010)

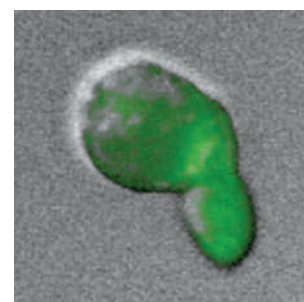
NEUROBIOLOGY

The source of sour taste

The five basic tastes are sensed on the tongue by different sets of cells, but the acidic taste of sour has long defied molecular analysis. Now researchers have genetically engineered mice in which they can fluorescently tag sour-taste cells (pictured), and have pinpointed the changes that acid triggers in the cells.

Isolating the cellular mechanisms associated with sour-taste recognition has been challenging because many ion channels in cell membranes

respond to acid, whether or not they are involved in sour sensing. Emily Liman and her team at the University of Southern California in Los Angeles tagged not only the sour-taste cells but also those for bitter, sweet and umami, and compared the responses of these cells to acid. They found that the sour-taste cells fired alone when protons were transported across the membrane — but all cells reacted to sodium ions, which were previously thought to mediate sour sensing. *Proc. Natl Acad. Sci. USA* doi:10.1073/pnas.1013664107 (2010)



NATL ACAD. SCI.

NATURE.COM

For the latest research published by Nature visit:

www.nature.com/latestresearch

SEVEN DAYS

The news in brief

POLICY

German GM crops

The highest court in Germany has upheld a law that makes planters of genetically modified (GM) crops liable for any contamination of their neighbours' non-GM fields. The Federal Constitutional Court said on 24 November that the 2004 (amended in 2008) legislation, which also requires minimum 150-metre buffer zones between GM and conventional crops and a public register for the location of GM plantings, was justified because the long-term consequences of GM technology are still unclear. The law had been first challenged by the state of Saxony-Anhalt.

Patient protection

US President Barack Obama has asked his bioethics commission to review the recent discovery that US government-funded scientists intentionally infected subjects with syphilis in a study in Guatemala in the 1940s (see *Nature* 467, 645; 2010). In a 24 November memorandum, he also asked the commission to launch a panel in January to examine whether current rules, domestically and internationally, adequately protect those taking part in federally funded scientific research from harm.

UK immigration

UK government quotas on immigration, announced in outline last week, may leave young scientists from outside the European Union (EU) unable to secure visas to the country. Overall, 21,700 skilled non-EU migrants will be allowed in annually (down from 28,000 in 2009); most will come in through a points-based visa system that could squeeze out young PhD scientists on typical academic

salaries, according to the advocacy group Campaign for Science and Engineering. Some scientists might be able to enter through the 1,000 places set aside for those of 'exceptional talent' — although qualifications for this route are unclear.

Q-fever delay

A report has found that the Dutch government took too long to respond to an outbreak of Q fever, which since 2007 has killed 14 people and made almost 4,000 ill in the Netherlands. The disease, caused by the bacterium *Coxiella burnetii*, can trigger abortions in goats and sheep and cause flu-like symptoms and sometimes pneumonia in humans. The seven-man panel, whose evaluation was released

last week, found that the health and agriculture ministries coordinated their efforts poorly before they ordered a cull of more than 50,000 dairy goats in 2009, which seems to have quashed the disease.

US energy boost

The United States needs to triple its annual federal funding — from US\$5 billion to \$16 billion — for energy 'research, development, demonstration and deployment', and adopt a strategic, coordinated energy policy, a report from the President's Council of Advisors on Science and Technology (PCAST) recommends. The report, released on 29 November, urges that the government aid coherent planning by

producing, from 2015, a 'Quadrennial Energy Review', modelled on an existing defence review.

Oil-spill budget

Scientists have welcomed a long-awaited peer-reviewed US government report on the short-term fate of the oil from the Deepwater Horizon spill in the Gulf of Mexico this summer. Released on 23 November, the report supersedes an 'oil budget calculator' published in August, which was not peer reviewed and was criticized for its lack of information about how calculations were carried out, uncertainties in estimates and overly optimistic press presentation. The new report comes to similar conclusions to those of the August report,



D. CHOWDHURY/AFP/GETTY IMAGES

Nations pledge to double tiger numbers

Thirteen countries that are home to the world's last wild tigers have pledged to try to double the animal's numbers to about 7,000, and to "significantly expand" its habitat by 2022 (the next Chinese year of the tiger). The agreement, at a conference in St Petersburg, Russia, last

week, saw nations including Russia and India put up US\$127 million in new funding and a loan package from the World Bank for some tiger-range countries. One of the challenges will be to prevent poaching and trade in tiger skins (pictured — a seized skin in Kolkata, India).

although oil experts note a paucity of solid data on which to base estimates. See go.nature.com/j3ixm6 for more.

Bisphenol A ban

The European Commission has agreed to ban the common chemical bisphenol A from baby bottles across the European Union by mid-2011. The decision, announced on 25 November, follows similar precautionary bans by France, Denmark, Canada and some US states. Studies in animals suggest that exposure to bisphenol A, a hormone-disrupting plasticizer used in food-can linings and bottles, may affect development and immune responses, and poses cancer risks.

Tuna quotas

Fisheries regulators are showing little mercy to the Atlantic bluefin tuna (*Thunnus thynnus*), which is in danger of being wiped out by commercial fishing. On 27 November at a meeting in Paris, members of the Madrid-based International Commission for the Conservation of Atlantic Tunas, which manages tuna fishing, voted for 2011 catch quotas in the Mediterranean Sea to be set at 12,900 tonnes, only slightly lower than this year's 13,500 tonnes. Susan Lieberman, director of international policy for the Pew Environment Group



in Washington DC, says the agreement showed that management of high seas fisheries was "flawed and inadequate".

Polar-bear pad

The US Fish and Wildlife Service has set aside roughly 484,000 square kilometres in Alaska and the surrounding seas as a 'critical habitat' for the polar bear (*Ursus maritimus*), more than two years after the species was given a protection status of 'threatened' by the US Endangered Species Act. Almost all of the protected area is sea ice off Alaska's northern and western coasts. Oil and gas companies can still drill in the area, but federal agencies have to ensure that proposed activities don't jeopardize polar bears and their habitat.

BUSINESS

Orphan drugs

European spending on research and development (R&D) of 'orphan' drugs for rare diseases jumped from

€158 million (US\$207 million) in 2000 to nearly €500 million in 2008 — doubling from 1% to 2.2% of total European pharmaceutical R&D spending, a report has found. In that same period, global R&D spending on orphan drugs grew from €305 million to €1.9 billion, or from 1.1% to more than 4% of the global total. The report, released on 29 November, was commissioned by two trade associations based in Brussels: the European Association for Bioindustries and European Biopharmaceutical Enterprises.

PEOPLE

Murder in Iran

Majid Shahriari, an Iranian nuclear physicist, was killed and his wife injured in a bomb attack on 29 November in Tehran. Another nuclear scientist, Fereydoon Abbasi-Davani, and his wife, survived an identical simultaneous attack. See page 607 for more.

Scientist threatened

Animal-rights activists mailed razor blades and a 'threatening note' to neuroscientist David Jentsch at the University of California, Los Angeles, in November, the university said last week. Jentsch, who often speaks out about the importance of animal research and maintains a dialogue with some animal-rights groups,

COMING UP

2 DECEMBER

Heads of East African states hold a meeting to formulate a policy on agricultural innovation and food security in response to climate change in the region. go.nature.com/b4gqxb

7 DECEMBER

Commercial space-flight company SpaceX, of Hawthorne, California, is scheduled to make its first attempt to launch a spacecraft into orbit on its Falcon 9 rocket and return the craft to Earth. Such a round-trip has only ever been performed by government agencies.

had his car torched last year. "I will not feel fear in response to your increasingly desperate and puerile attempts to frighten," he wrote in a letter, posted online, to the group who claimed responsibility for sending the package. See go.nature.com/iy9xbq for more.

RESEARCH

Temperature hike

The figure of 0.05–0.13 °C for the world's warming during the past decade has been underestimated by around 0.03 °C, the UK Met Office said on 26 November. Drifting buoys — increasingly used since 2000 — tend to report a cooler temperature relative to ships' measurements, researchers calculated. A corrected trend would come closer to the long-term warming trend seen since the 1970s, of 0.16 °C per decade. It could also make 2010 the world's hottest year; the World Meteorological Organization is expected to pronounce its verdict on 2 December.

► **NATURE.COM**

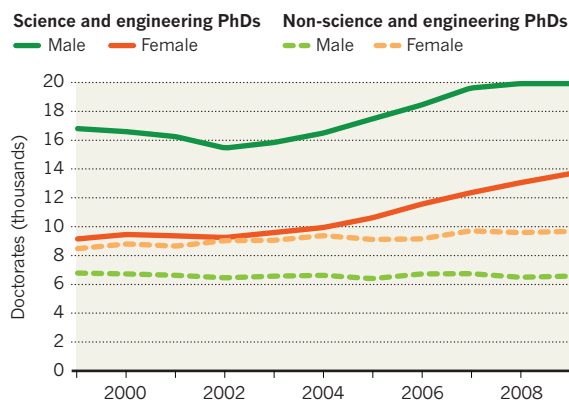
For daily news updates see: www.nature.com/news

TREND WATCH

A 1.6% jump in doctorates awarded in the United States last year was almost entirely the result of more women gaining science and engineering PhDs — up 4.3% (since 2008) to 13,593 (see chart). Ethnic minorities earning PhDs were up 6.4% from 2008 and 34.3% from 2004, to 4,719. But job prospects for these new doctorate holders are less rosy. In some fields, science and engineering PhDs were slightly less likely to have a postdoc or other job lined up, compared with 2008.

US SCIENCE DOCTORATES HIT RECORD

Female scientists are driving a boom in science and engineering PhDs in the United States.



NEWS IN FOCUS

DRUG DEVELOPMENT Chemists mimic a sponge's molecular artistry **p.608**

SPACE A \$100-billion national lab is open for business — in orbit **p.610**

ARCHAEOLOGY Lab scientists dig into biblical history **p.614**



FUNDING The man who made California a stem-cell power **p.620**

PRESS TV; INSET: BOTTOM RIGHT: MASHREGH NEWS



Majid Shahriari (above) was killed, and Fereydoun Abbasi-Davani (below) injured, in bomb blasts.

NUCLEAR PHYSICS

Iranian nuclear scientists attacked

Murder and cyber-assault target nuclear programme.

BY DECLAN BUTLER

The killing of an Iranian physicist and injury of another in separate bomb attacks earlier this week in Tehran are fuelling speculation about the implications for Iran's nuclear programme. The news follows hard on the heels of an admission by the Iranian regime that a computer worm had interfered with uranium enrichment at its nuclear facility in Natanz. Iran claims the enrichment is to provide fuel for civilian nuclear power stations, but the once-secret programme — which has repeatedly violated the nuclear safeguard obligations of the International Atomic Energy Agency — is widely seen as an effort to furnish the country with nuclear weapons.

The bombings have had a chilling effect on Iran's physicists. "I am shocked, really deeply shocked," says one, who wished to remain anonymous, given the repressive regime.

Majid Shahriari was killed, and his wife injured, on his way to work at the Shahid Beheshti University in Tehran when attackers on motorcycles attached a bomb to his car on 29 November. Another nuclear scientist, Fereydoun Abbasi-Davani, and his wife, survived an identical simultaneous attack.

Mahmoud Ahmadinejad, who hung onto power as president after a disputed election in June 2009, immediately laid blame on the West and Israel. "The Western governments and the Zionist regime have a hand in the assassination of the two Iranian university professors," he asserted at a press conference in Tehran hours after the attacks. "They will not be able to stop the Iranian nation's activities by such acts."

Abbasi-Davani, whose handful of publications on neutron physics are mainly in Iranian journals, is a key figure in Iran's nuclear programme. He is reported to be a scientist at the country's defence ministry, and a member

of Iran's revolutionary guards since the 1979 Islamic Revolution. He was also named as being among "Persons involved in nuclear or ballistic missile activities" in the 2007 UN Security Council Resolution 1747, which imposed sanctions on Iran over its refusal to stop enrichment of uranium.

Nature has been unable to establish whether Shahriari — who published several papers on nuclear reactor physics and nuclear medicine in international peer-reviewed journals — had any links to the enrichment programme. Shahriari was part of the Iranian delegation on the board of a 'science for peace' project, the non-nuclear SESAME (Synchrotron-light for Experimental Science and Applications in the Middle East) facility, in Alaa, Jordan. SESAME, which opened in 2008 and is the Middle East's first synchrotron, is intended to promote peace through cooperation among member countries in the region, including Israel. But physicist Christopher Llewellyn Smith, president of SESAME's council, says that he has little recollection of Shahriari, and records show he attended only one board meeting, at the opening of the SESAME building.

Although Shahriari's murder is unlikely to be connected with his involvement in SESAME, he is the second member of the project's council to be assassinated. In January 2009, Masoud Ali-mohammadi, a particle physicist at the University of Tehran and one of Iran's representatives on the board, was also killed by a bomb as he got into his car (see *Nature* **463**, 279; 2010). His work on theoretical particle physics was far removed from nuclear matters, leading researchers to speculate that he had been killed by hardliners in the Ahmadinejad regime in response to Ali-mohammadi's support for the reformist movement. This week's attacks, in contrast, bear the hallmarks of a hit by foreign powers, speculates one Iranian expatriate researcher.

Meanwhile, Iran acknowledged for the first time in late November that the sophisticated computer worm Stuxnet was deployed in the Natanz attack. The worm seems to have been designed specifically to damage the centrifuges used for enrichment, potentially causing them to run or brake too quickly. A 23 November report by the International Atomic Energy Agency on Iran's nuclear activities at Natanz noted a temporary shutdown of the plant earlier this month. While conceding the attack, Ahmadinejad claimed on 29 November that any impact had been limited. ■

Complex synthesis yields breast-cancer therapy

Drug approval marks culmination of a marathon trek from sea sponges to clinic.

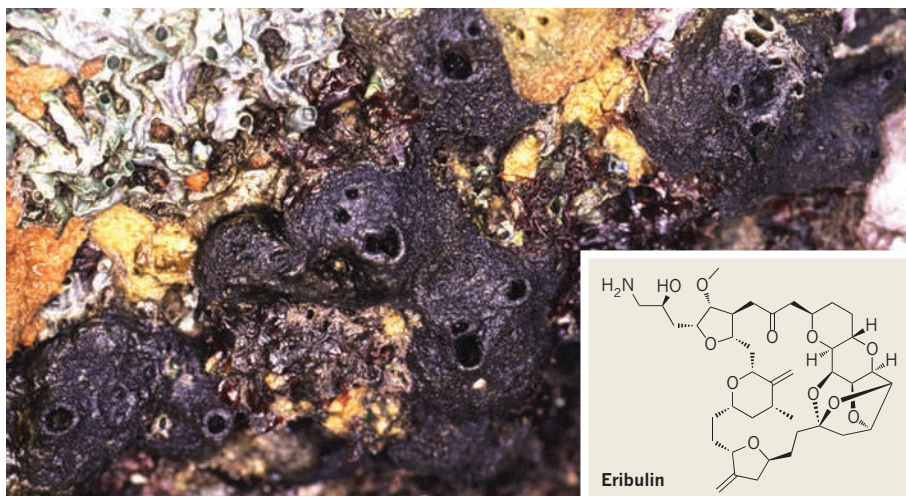
BY HEIDI LEDFORD

The latest breast-cancer chemotherapy to hit the market is more than just a triumph for patients in desperate need of treatment. Approved by the US Food and Drug Administration on 15 November, the highly complex molecule Halaven (eribulin mesylate) is the product of nearly 25 years of struggle in the lab. It represents a hard-won victory for the total synthesis of natural products, a field of chemistry that, although still popular in academia, had gone out of fashion for many in the pharmaceutical industry.

Eribulin is a synthetic compound that mimics part of the structure of halichondrin B, a molecule found in the sea sponge *Halichondria okadai*. Researchers learned that halichondrin B has potent tumour-fighting activity shortly after its discovery in 1986. But it is present in very low concentrations, making it difficult to isolate. The compound also has a fiendishly complicated structure — at the time of its discovery, producing it from scratch was well beyond the abilities of chemists.

A few years later, however, organic chemist Yoshito Kishi of Harvard University in Cambridge, Massachusetts, eyed the halichondrin B structure and decided to take a crack at it. His team had little interest in its anticancer properties, he says. They were simply looking for a project to test a chemical reaction — the Nozaki-Hiyama-Kishi reaction — that could be used to build bonds between carbon atoms.

Kishi's team had set themselves an enormous challenge with halichondrin B. Natural products often contain carbon stereocentres, in which surrounding atoms can be arranged in two mirror-image configurations. "If you don't get the stereocentres set up perfectly, it generates a mixture" of different molecules that can



The drug eribulin (inset) was inspired by a compound from the sea sponge *Halichondria okadai*.

be extremely troublesome to separate, says Ian Paterson, a chemist at the University of Cambridge, UK, who works on natural-product synthesis. Although two mirror-image forms of a molecule are indistinguishable for most chemical reactions, they can produce completely different biological effects.

Halichondrin B has a staggering 32 stereocentres, meaning that there are 2^{32} — more than 4 billion — possible forms, or isomers, of the molecule. "It's just ridiculous," says Robert Salomon, an organic chemist at Case Western Reserve University in Cleveland, Ohio, whose lab spent four years unsuccessfully trying to synthesize the compound in the early 1990s.

Nevertheless, Kishi's team succeeded. By the time he published a method for synthesizing the compound in 1992 (T. D. Aicher *et al.* *J. Am. Chem. Soc.* **114**, 3162–3164; 1992), researchers at the Natural Products Branch of the US National Cancer Institute (NCI)

in Frederick, Maryland, had discovered that halichondrin B fights cancer cells by inhibiting a protein component of the cytoskeleton — the internal latticework of rods and filaments that gives a cell its shape. That protein, called tubulin, is needed to support the rapid growth of cancer cells and is the target of several other cancer chemotherapies, including Taxol (paclitaxel).

DEEP-SEA DRUG

But Kishi's synthesis was practical for generating only small quantities of halichondrin B, unlikely to be enough to usher the compound through preclinical and then clinical testing, says David Newman, now chief of the NCI's Natural Products Branch. Newman decided that he would simply isolate the compound from natural samples. So he headed for the sea to hunt for the prized compound.

Newman and his team collected more than one tonne of *Lissodendoryx*, another type of

YASUNORI SAITO



**MORE
ONLINE**

CLIMATEGATE



All our coverage of the affair in one online collection
go.nature.com/a2eebt

LATEST NEWS

Premature ageing reversed in mice
go.nature.com/rxepdo
Cuts threaten UK archaeology
go.nature.com/bzyt8a
Bespoke genetic circuits rewire human cells
go.nature.com/s56pln
Protein factory mapped
go.nature.com/nxngpd

ON THE BLOG



Reporter Jane Qiu's updates from a research vessel bound for the Antarctic Peninsula
go.nature.com/wspgih

C. HUSH/NSF

sponge containing halichondrin B, from the deep waters off New Zealand. He also teamed up with researchers to grow more of the sponges, flying seaplanes out to remote aquatic farms where the sponges grew attached to lines dangling 40 metres beneath buoys. The reward for his efforts: just 300 milligrams of halichondrin B, the equivalent of a few grains of rice. “My hair turned white as a result of halichondrin B,” he jokes.

Meanwhile, Tokyo’s Eisai Pharmaceuticals had licensed the patent on Kishi’s method and began synthesizing hundreds of analogues of the compound. Newman’s haul from New Zealand was just enough to conduct comparative studies with some of these analogues. One of them, eribulin, is more potent than halichondrin B yet also substantially smaller and easier to make. But it still has 19 stereocentres (see structure, inset), and production of eribulin on a commercial scale seemed unfathomable.

Eisai says that eribulin takes 62 steps to synthesize — a remarkably long process for a marketable drug. The company was initially apprehensive about the project, says Kishi. But once the phase I study results had shown that the drug was safe — and revealed hints of clinical efficacy — “all the reservations disappeared,” he says.

Further clinical trials showed that eribulin extends the lifespan of patients with late-stage breast cancer by an average of 2.5 months in those who are not benefiting from other chemotherapies such as Taxol, also a natural-product derivative. Analysts suggest that eribulin could command a US\$1-billion market if it is approved for treatment of other cancers.

Few other pharmaceutical companies have been willing to bet on complex natural products. During the 1990s, many largely abandoned natural-product chemistry, focusing more on screening large libraries of synthetic chemicals for drug candidates, says Michael Jirousek, who once worked on halichondrin B synthesis and is now chief scientific officer and co-founder of Catabasis, a biotechnology company in Cambridge, Massachusetts. “Screening natural products and isolating the active ingredients is becoming a lost art,” he says.

Proponents of total synthesis point to eribulin as proof that their approach, albeit arduous, can be highly successful. Phil Baran, a synthetic chemist at the Scripps Research Institute in La Jolla, California, says that more young investigators are entering the field and that improvements in chemical techniques are making it possible to synthesize additional complex molecules by commercially viable routes. “As advances in organic chemistry become greater and greater,” he says, “I think we’re going to see a lot more complex compounds being pursued by companies.” ■



Canada’s Perimeter Institute boasts a freewheeling intellectual environment — and a gourmet bistro.

RESEARCH

Physics centre plans rapid growth

Perimeter Institute steps up drive to attract top talent.

BY IVAN SEMENIUK

Newton, Maxwell, Einstein, Bohr, Dirac — the list reads like the ultimate physics dream team. That the Perimeter Institute for Theoretical Physics in Waterloo, Canada, has chosen to name five new research chairs after some of the greatest physicists in history is a sign of its lofty aspirations.

“We’re scouring the world for exceptional talent,” says director Neil Turok, who took the helm at the Perimeter in 2008. The institute began attracting up-and-coming researchers soon after its creation, but it has had a harder time building into its ranks the experience and scientific prowess to rival more established theoretical centres, such as the Institute for Advanced Study (IAS) in Princeton, New Jersey. The new chairs, announced on 29 November, are designed to attract top theorists in “a gathering of critical mass around the most fundamental questions”, Turok says. “Our mission is to make breakthroughs.”

This is not the first time a physics institute has announced such an ambitious goal, but the Perimeter’s resources give it a better chance than most of achieving it. The institute was founded in 1999 with a hefty personal gift from entrepreneur Mike Lazaridis, whose company, Research in Motion, makes the popular BlackBerry products, and it has grown quickly since then through additional public and private funds.

The faculty now numbers 14 full-time posts and 12 part-time associate posts, with more hirings expected in 2011. Largely spared the commitments that come with an academic appointment at a university, researchers at the Perimeter enjoy an unfettered and freewheeling intellectual environment, together with less cerebral indulgences, including a gourmet

bistro and a squash court. The institute has begun to make significant contributions in areas such as quantum field theory.

“The chair holders will be free to engage in investigator-driven research, without limits or mandates,” according to a description of the new positions. An Can\$8-million (US\$7.8-million) endowment has been secured for the first chair, named after Isaac Newton, with half the money provided by the Perimeter’s existing endowment and the rest by BMO Financial Group, one of Canada’s largest banks. The institute is now seeking partners to fund the remaining chairs.

“The place is really flourishing now,” says Nima Arkani-Hamed, a theoretical physicist at the IAS. Despite initial reservations when the Perimeter first opened, Arkani-Hamed now collaborates frequently with colleagues there and has seen growing numbers of IAS students and postdocs choosing job offers from the Perimeter over those from more established institutions. IAS researcher Davide Gaiotto, who will take up a faculty position at the Perimeter next year, agrees that there is no shortage of physics talent to fill the new positions. Others say that privately endowed institutions such as the Perimeter and the Simons Center for Geometry and Physics at Stony Brook University, New York, are helping to keep theoretical physics active while the economic downturn hits public universities in the United States and Europe.

Even a few strategic hirings can have a powerful effect on a field, notes Michael Douglas, a string theorist at the Simons Center. Douglas recalls his time as a postdoc at Rutgers University in Piscataway, New Jersey, when four key faculty appointments in 1989 — the ‘string quartet’ — led to a collaboration that transformed string theory. “If you choose right,” he says, “then things can really take off.” ■

Partners wanted to run research lab in space

NASA seeks wider research–community involvement in the International Space Station.

BY ADAM MANN

Few births involve as much labour as that of the International Space Station (ISS). After 34 shuttle flights, 24 Soyuz missions, 43 visits by unmanned capsules, and well over US\$100 billion invested by the United States, Russia, Japan, Canada and Europe, the station is now nearing completion. The final bits of hardware, including the Alpha Magnetic Spectrometer, a long-delayed cosmic-ray experiment, will arrive as early as February 2011, on the last space-shuttle flight currently budgeted for. Now, decades after the station was first proposed and more than a dozen years after construction began, NASA must find a way to make its part of the effort — by far the largest — worthwhile.

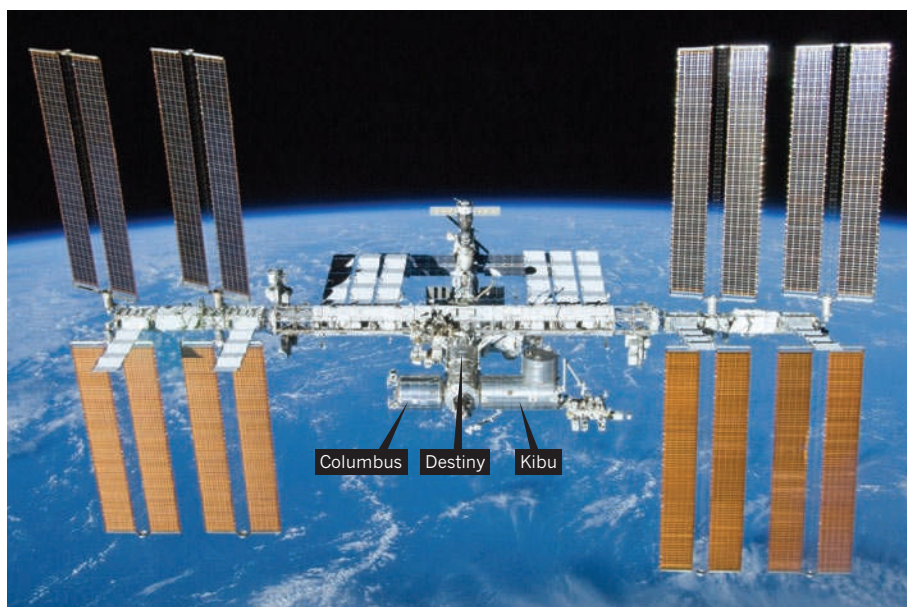
On 10 December, NASA will hold a public meeting in Washington DC to discuss the future of the US portion of the space station as a science facility. Congress declared the US share a national laboratory in 2005, thereby opening it up to public and private research. This year's NASA authorization bill, passed in September, requires the agency to establish an independent, non-profit entity to manage the lab. The upcoming meeting is meant to draw in prospective partners for the venture.

"The ISS is a completely unique asset," says Jeanne DiFrancesco, a principal at ProOrbis, a management consultancy based in Malvern, Pennsylvania, which was hired by NASA to create a 'reference model' for the administration of the lab. "Managed well, it could facilitate the development of new categories of research."

GETTING IT TOGETHER

For much of its long assembly phase, the ISS has been an active science facility. A 2009 NASA report lists more than 100 experiments on the station between 2000 and 2008, in technology development, physical and materials sciences, biological sciences, Earth observation and human research, including ways to counter the effects of 'low-g' on the body.

Today the United States' share of the ISS includes the Destiny pressurized lab as well as access to the Japanese-built Kibo and European-built Columbus modules. In addition to the microgravity environment, the ISS offers exposure to the vacuum of space, to radiation, atomic oxygen and extremes of temperature.



The International Space Station's three main laboratory modules seen from the space shuttle *Atlantis*.

The station's exterior is studded with sites for the attachment of instruments that can observe Earth or space. They provide anywhere from 100 to 300 possible experiment locations, says Mark Uhman, NASA's assistant associate administrator for the ISS.

But while interviewing researchers about the potential of the ISS, DiFrancesco says that she encountered some scepticism about whether the station could serve the scientific community in a meaningful way. To counter such criticism, she says, any new organization that manages science on the station must begin with a concentrated outreach campaign that demonstrates a clear commitment to the research community's needs, interests and concerns. According to the reference model, it would smooth the road for scientists and also foster an impartial approach to choosing what science ends up in space. The idea of creating such an organization was floated in the 2009 Augustine report, a critical review of the US human space-flight programme commissioned by President Barack

Obama. The ProOrbis reference model, which was publicly presented on 16 November at a meeting of the American Astronautical Society

in Cape Canaveral, Florida, reaches the same conclusion: an independent entity is needed to act as a buffer between NASA's operations managers and the broader community that could put the ISS to use.

Its role might resemble that of the Space Telescope Science Institute in Baltimore, Maryland, which helps to oversee research on Hubble and other space telescopes. Among its responsibilities would be building an awareness of the research possibilities on the station, matching prospective projects with funding and helping primary investigators to navigate the space agency's bureaucracy, says DiFrancesco. But unlike the basic research done on the Hubble telescope, ISS projects could come from many sectors, including other government agencies, public universities, pharmaceutical companies, private labs and chemical and materials manufacturing firms, she adds.

"The ultimate hope is that something new will be discovered in the microgravity environment aboard the ISS that can lead to useful insights on the ground," says Uhman.

In theory, such a possibility has been open to US researchers for years, but a completed ISS with a six-person crew can support longer-term studies that require more care and attention than would have been practical in the past.

➔ **NATURE.COM**
For more on the high cost of science in space see:
go.nature.com/zjanow

CREW OF STS-132/NASA

This increased scope is “amazing” says Jeanne Becker, chief science officer at the biotechnology company Astrogenetix in Austin, Texas, and a faculty member at Baylor College of Medicine in Houston. Becker has already cultivated tumour cells in rotating bioreactors aboard the ISS to investigate changes in the cells’ growth and functioning.

If set up properly, management of research on the ISS by a private non-profit entity could make the process of selecting experiments more transparently based on genuine applicability to life on Earth, says Jeff Jonas, senior vice-president of research and development at Shire Pharmaceuticals in Philadelphia, Pennsylvania. “It would open up the station to the marketplace of ideas,” he says, adding that having more researchers and companies involved could create competition for better experiments.

BAD VIBES

NASA has started making moves in this direction. Earlier this year, the agency opened the ISS to biological research funded by the National Institutes of Health, which awarded the first round of grants in September. With an independent body overseeing research, the ISS could also host experiments from other agencies, such

as the US Forest Service, the National Oceanic and Atmospheric Administration and the US Geological Survey, says Erika Wagner, an aerospace biomedical engineer and executive director of the X Prize Lab at the Massachusetts Institute of Technology in Cambridge.

Yet plenty of challenges remain that could prejudice the success of the ISS as a national laboratory. Among these are concerns over the quality of the research environment aboard

Every month that the station is not being fully used by researchers, it loses value.

the ISS. For example, vibrations on the station (known as g-jitter) caused by machinery and human movement can affect some experiments. NASA has installed a special rack for the most sensitive experiments that actively counteracts vibrations, and provided damping material for other research, says Uhran.

A more fundamental obstacle is the question of how to access the ISS in a cost-effective way. In November 2009, the US Government Accountability Office released a report identifying the high cost of launching a payload as one of the biggest challenges the lab faces. Although the nascent commercial space-flight industry

is expected eventually to make the ISS more accessible, it will be years before commercial transport can fully meet researchers’ needs (see ‘Station to rely on private space flight’).

Yet, as DiFrancesco’s model points out, every month that the station is not being fully used by researchers, it loses value. Once a non-profit organization is established, NASA expects to begin research and development, but it will take a few years before the enterprise is running at full throttle, says Uhran. In the meantime, the agency and its international partners are continuing research into human exploration in space. In October, the European Space Agency (ESA) issued a call for proposals in technology and biomedical research that would help to prepare for the next steps of human exploration beyond low-Earth orbit, says Martin Zell, ESA’s head of research operations in human space flight, microgravity and exploration.

Ultimately, to take advantage of what the ISS offers, it will be crucial to get the science management right, says Alan Stern, a planetary scientist at the Southwest Research Institute in San Antonio, Texas, and NASA’s former associate administrator for science. “Like a baby, the ISS has lots of potential,” he says. “NASA is working to turn that potential into a great outcome for the ISS.” ■ [SEE EDITORIAL P.599](#)

AFTER THE SHUTTLE

Station to rely on private space flight

As it works to turn the International Space Station (ISS) into a national laboratory, NASA will have to deal with a major bottleneck: transporting crew and equipment to the facility and back. The existing fleet of space shuttles, each with a carrying capacity of 22,700 kilograms per launch, is set to retire next year, leaving the agency to rely on the unmanned Russian Progress spacecraft, which has a cargo capacity of only 1,700 kg, and the Soyuz spacecraft to transport crew members. To fill the gap, NASA hopes to rely on private space flight.

“The developing commercial industry can open the floodgates for NASA to do more research and get more people up to the ISS,” says John Gedmark, executive director of the Commercial Spaceflight Federation in Washington DC, a space-flight industry group.

NASA currently has contracts with two companies — Orbital Sciences Corporation in Dulles,



Virginia, and Space Exploration Technologies Corporation (SpaceX) in Hawthorne, California — to transport supplies to the ISS once the shuttle stops flying. As well as providing capacity, multiple providers can drive down costs through competition, allowing more experiments to be done, says Gedmark.

Commercial companies

are nearly ready to accept the hand-over from NASA. SpaceX hopes to make the first launch of its reusable Dragon spacecraft (pictured), which can carry 6,000 kg, into orbit on 7 December. The company has two further flights scheduled for next year, the second of which will dock with the ISS and deliver cargo.

But during an address at the

Marshall Space Flight Center in Huntsville, Alabama, on 16 November, NASA administrator Charles Bolden spoke about the risks in this strategy. “If there’s any delay in delivery of commercial capability to take cargo to the station, we could find ourselves in a situation as bad as having to de-man the station or take it down to three people,” he said. Minor delays with Orbital’s Cygnus spacecraft, which will carry supplies and research experiments to the station, have already postponed a demonstration flight from late 2010 to spring 2011.

Bolden advocates an additional shuttle flight to preserve access to the ISS until private space companies are ready to take over, a move currently mandated in the 2010 NASA authorization bill. But the US\$500-million launch remains unfunded and could be on the chopping block as Congress seeks to reduce spending. **A.M.**

SPACEX

NUCLEAR PROLIFERATION

India blocks nuclear meeting

Fission group is 'hostile to India', government claims.

BY GEOFF BRUMFIELD

The Indian government has barred a group of nuclear scientists from meeting in New Delhi, where they planned to challenge key elements of the nation's nuclear programme, *Nature* has learned.

The International Panel on Fissile Materials (IPFM) is an independent group of two dozen scientists and policy analysts devoted to stirring debate on issues related to nuclear materials. The group was formed in 2006 and is funded by the MacArthur Foundation, a philanthropic organization based in Chicago, Illinois. The panel's draft version of the Fissile Material Cutoff Treaty, a proposal that would ban production of weapons-grade nuclear material worldwide, has received backing from Japan, Canada and the Netherlands in United Nations disarmament discussions.

The IPFM had hoped to convene on 9 December to discuss technical and political issues associated with India's nuclear strategy. But the Indian Ministry of External Affairs, which must approve such meetings, has denied it the permission it needs. As *Nature* went to press, the ministry had not responded to e-mails about the incident, but R. Rajaraman, an emeritus professor of physics at Jawaharlal Nehru University in New Delhi and co-chairman of the IPFM, says that an official in the ministry blocked the group because individuals on the panel were supposedly "hostile to India". Rajaraman concedes that some of the views held by panel members clash with those of the government, but he says that the denial is at odds with India's democratic principles. "I'm hopping mad," he says.

The IPFM also works to reduce and safeguard civilian and military stocks of fissile materials, and is considered a reputable source for global inventories of uranium and plutonium. "They're providing data out there on the web, and it's solid stuff," says Sharon Squassoni, a non-proliferation expert at the Center for Strategic and International Studies in Washington DC.

But panel members take a provocative stance against technologies that create more fissile material. They openly oppose nuclear reprocessing, in which fuel is chemically separated and reused in either power reactors or nuclear weapons, and breeder reactors, which generate new nuclear fuel in addition to producing power. Many panel members believe that such technologies are not economically viable and

increase the risk of nuclear war or terrorism.

India's nuclear ambitions are at odds with those views. The nation has refused to sign the Nuclear Non-Proliferation Treaty, which is designed to slow the spread of nuclear weapons. It is actively pursuing nuclear reprocessing, both for weapons and for power, and is near completion of a 500-megawatt plutonium breeder reactor in Kalpakkam, Tamil Nadu. That reactor will pave the way for future breeder reactors capable of converting the nation's vast thorium reserves into uranium-233 fuel.

The decision to bar the IPFM comes at a sensitive

time for India as it looks for acceptance from other nuclear states after decades of isolation because of its weapons programme. In 2008, it signed a nuclear cooperation agreement with the United States, and is seeking entry into the Nuclear Suppliers Group, an international body that sets non-proliferation guidelines for exports of nuclear equipment and material. The IPFM affair should give other nations pause, says Squassoni. "Is this the kind of behaviour that you want in a nuclear supplier?" she asks.

Rajaraman says that the panel hoped to debate India's nuclear policies with scientists from the nation's government and nuclear establishment. Similar debates organized by the IPFM in the United Kingdom, China and the United States have often led to thought-provoking discussions, he says. But even if the Indian government relents now, Rajaraman doubts there will be a truly open meeting with the nation's nuclear leaders: "The spirit in which I wanted to have the discussion has been ruined." ■



India's plutonium breeder reactor in Kalpakkam is nearly complete.

REUTERS/BABU



Was Tel Megiddo in Israel a regional centre of power in the fabled kingdom of David and Solomon?

ARCHAEOLOGY

Chemists help archaeologists to probe biblical history

Collaboration establishes a new approach for teasing out clues hidden in the soil.

BY HAIM WATZMAN IN TEL MEGIDDO

Fabled as a site of biblical battles and spectacular palaces, Tel Megiddo today is a dusty mound overlooking Israel's Jezreel valley. It is also host to one of the hottest debates in archaeology — a controversy over the historical truth of the Bible's account of the first united Kingdom of Israel.

Ancient Megiddo is said to have been a key administrative and military centre in the kingdom ruled by King David and his son Solomon during the eleventh and tenth centuries BC. But the biblical narrative is challenged by archaeologists such as Israel Finkelstein of Tel Aviv University, who believe that David and Solomon did not rule over an Iron Age empire. Instead, they suggest, David and Solomon commanded a small and not terribly influential kingdom, and Megiddo's peak came nearly a century after the united kingdom had divided.

Important evidence relating to this debate is being unearthed by a unique collaboration between archaeologists and natural scientists,

working shoulder-to-shoulder at Tel Megiddo and several other important Israeli sites. "In the past, all too often, archaeologists and scientists worked together, but it was two parallel lines," says archaeologist Aren Maeir of Bar-Ilan University in Ramat Gan, Israel. It could take months or even years before finds were sent away to the lab, he says, with results taking just as long to come back. "On top of that, sometimes the samples weren't taken correctly."

The Tel Megiddo dig is different. Chemists make up half of the two dozen excavators on the team, which is being led by Finkelstein and Steve Weiner, a structural biologist specializing in mineralized tissues who is director of the Kimmel Center for Archaeological Science at the Weizmann Institute in Rehovot, Israel. Funded by a European Research Council grant worth €3 million (US\$4 million) over

NATURE.COM
For more stories on
archaeology see:
go.nature.com/8sigiq

five years, the pair hope that their work at Tel Megiddo and elsewhere will show that this model of close collaboration

should become the norm for archaeology.

"It's definitely where archaeology is headed," says Ran Boytner of the University of California, Los Angeles, an archaeologist who works in South America. "This is partly to do with the miniaturization of analytical tools and the lowering of costs, as well as a revival of interest in archaeology, especially among senior scientists who are eager to get out of the lab."

CHEMICAL CLUES

Archaeologists are trained to use their eyes to identify a stratum — a buried layer representing a particular period of habitation. A black stripe, for example, might be a burn layer — evidence of a hearth, or of the ransacking of a city, depending on its size. Artefacts and pottery embedded in strata can also serve as markers for defining and dating them. But chemical analysis can add many more details to the picture.

When *Nature* visited Tel Megiddo in October, excavators were working with brushes, tweezers and teaspoons to gather sediment samples into small plastic vials before taking them to an

infrared spectrometer set up on a folding table at the edge of the site. The chemical clues yielded by the spectrometer gave immediate feedback to the diggers as they collected further samples.

Chemical analysis can distinguish between soil layers that look identical to the naked eye, explains Weiner. In a paper published this month, for example, he and his colleagues show how infrared spectrometry can reveal the distinctive origins of seemingly identical layers of calcite, a form of calcium carbonate (L. Regev *et al. J. Archaeol. Sci.* 37, 3022–3029; 2010). Wood burnt at above 500°C produces calcite, although the mineral can also come from limestone slaked to make lime for construction, and is found in the soil used to make mud bricks. Each type of calcite has a distinctive infrared signature, providing information that helps archaeologists to distinguish between a floor, a wall or a kiln.

In another part of Tel Megiddo, Weiner points out a layer rich in a form of silica (SiO₂) that accreted in and around the cells of plants. These ‘phytolith’ layers mark locations where vegetation grew or was stored. Weiner and his team have calculated that the layer, now just 3–5 centimetres thick, was originally a metre or so deep. Their first assumption, based on similar findings in other locations, was that the area had been used as an animal enclosure. But an analysis of the phytoliths showed that they all came from domesticated grasses. Because the dung of grazing animals would be expected to contain a high proportion of wild plants, it seems possible that the phytoliths are evidence that animal fodder or grains were stockpiled at the site.

Experts in radiocarbon dating, who usually stick close to their laboratories, are also getting their hands dirty. Elisabetta Boaretto, a nuclear physicist at the Weizmann Institute, is a regular participant in digs, where she can be seen on her hands and knees scraping up samples with the rest of the team. “I’m one of the few, if not the only one, in my field who’s down in the pits digging,” she says. “But it’s essential.”

While digging in the southeastern area of Tel Megiddo, Boaretto’s PhD student Michael Toffolo unearthed a pottery storage jar full of

grains of wheat. After carefully photographing and noting the context of the find, he collected kernels in a vial so that they could be sent abroad to a particle-accelerator facility for dating. Boaretto is currently shopping for a particle accelerator for her lab at Weizmann. The machine, expected to cost about \$2 million, should be ready for radiocarbon dating work in 12–18 months. Having an accelerator near to local excavation sites will help to yield results much more quickly, says Boaretto, and her team will be able to supervise samples at every stage from the dig to the accelerator, preventing contamination that could otherwise cast doubt on the analysis.

Boaretto explains that she is on site because an understanding of precisely where samples came from is key to getting the most accurate dating. For instance, wheat grains and pieces

Chemical analysis can distinguish between soil layers that look identical to the naked eye.

of charcoal are often used to date pottery shards found in the same spot. But without seeing the stratigraphy, it is all too easy to miss evidence that the grains or chunks of burnt wood found

in a particular layer actually originated elsewhere, making them useless for dating neighbouring samples. And if the carbon sample removed for analysis actually contains material from more than one source, it can throw the dating off completely.

Having scientists on site can help archaeologists to make faster decisions about where to excavate and what samples to collect, and, ultimately, yield more useful analyses. “Scientists in the field may come up with different questions than archaeologists,” says archaeologist Joseph Maran at the University of Heidelberg, Germany, who specializes in ancient Greek sites. “It’s different from having an archaeologist define the question and then call in a scientist to address that specific issue.”

Maran says that the practice of having scientists actually excavating with archaeologists is, to the best of his knowledge, a uniquely Israeli phenomenon. As a small country rich in archaeological sites and with a strong science base, it may be much easier for Israel’s scientists to spend extended periods at excavations than for those in other countries, he says.

But Weiner hopes that the collaborative approach will catch on elsewhere. Earlier this year, he published a book, *Microarchaeology: Beyond the Visible Archaeological Record*, about the union of archaeology and analytical science, which he hopes will inspire other digs.

In the past, few scientists have been willing to spend a large amount of time in the field, Weiner says. The key to making the collaboration work, he says, is “matching the right analytical tool to the challenge of revealing the microscopic record without slowing the excavation down enormously”. ■

H. WATZMAN



A portable spectrometer allows researchers to get a fuller picture of their samples during a dig.

The impatient ADVOCATE

Bob Klein founded the California Institute for Regenerative Medicine, the biggest state-run research project in US history. What legacy will he leave behind?

BY ELIE DOLGIN

James Harrison had just stepped out to grab a sandwich when his mobile phone rang. Bob Klein, chairman of the California Institute for Regenerative Medicine (CIRM), was on the line telling Harrison, the agency's legal counsel, to skip lunch and come back to the office right away. It was 23 August, and a district court judge in Washington DC had just issued an injunction barring the use of federal grant money for human embryonic stem-cell research. At that instant, CIRM became the world's largest funder of such research, and needed to issue a public statement.

At CIRM headquarters in San Francisco's Mission Bay neighbourhood, executives from legal and communications branches soon gathered around the long, white board table in Klein's corner office. Klein sat at the head. The mood in the room was bittersweet, he says — a mixture of concern about the setbacks to stem-cell science and to CIRM-funded researchers who also received federal money, and vindication that at least Californian research dollars would continue to flow. The injunction — coming six years after Klein first convinced voters in California to fund embryonic stem-cell research despite major political and religious opposition — “became a huge reinforcer of the conclusion that [CIRM] is a critical safeguard for science”, Klein says.

As always, Klein took charge. He listened attentively to the advice of his colleagues and then delegated tasks. He asked the legal team to draw up an analysis of the decision's impact on CIRM grant recipients while he worked with the agency's press officer to issue a public statement that captured the nuanced emotion in the room. The agency “deplores the decision”, the statement read, although the injunction “points to the importance of CIRM's California model of sustained funding”.

“It illustrated to me what Bob does best,” recalls Harrison, “which is to bring people together and respond to crisis in a very thoughtful and intelligent way.”

On 17 December, however, Klein is stepping down as chairman of

the board — a position he has held since CIRM's inception. He leaves behind an agency with a long list of accomplishments, including more than US\$1.15 billion in grants, six new facilities dotted across the state and close to 700 scientific papers (see “Top earners”).

Yet many critics say that Klein and CIRM have failed to fully deliver. Despite promises that money borrowed from the state — at least \$6 billion over ten years, when interest is factored in — would be returned through commercial spin-offs and savings to health care, the first marketable therapies have yet to materialize. Only two CIRM-funded projects have made it to early-stage clinical trials, and neither of these involves embryonic stem cells — the main impetus for launching the agency in the first place. The embryonic stem-cell clinical trials that have recently been approved in the United States are the product of privately funded research.

Klein's critics say his promotion of stem cells' therapeutic promise was zealous and oversimplified. He “left voters with the impression that people will be jumping out of their wheelchairs and not being diabetic within a year”, says John Simpson, a long-time observer and critic of the agency's governance, who is at the consumer-advocacy group Consumer Watchdog based in Santa Monica, California. “There's been this constant compulsion for [Klein] to say, ‘See, we're delivering, we're delivering’, and that's something that's haunted him throughout the whole thing.”

Throughout CIRM's existence, Klein has pulled the strings, maintaining control over nearly every aspect of its structure and science, often to the chagrin of its other leaders. Still, many observers say that no one else could have weathered CIRM's early storms. “With Bob, there's always this indefatigableness,” says Douglas Wick, a movie producer and diabetes advocate who worked with Klein to get CIRM funded.

Bob Klein in front of the recently dedicated Lorry I. Lokey Stem Cell Research Building at the Stanford University School of Medicine in California.

D. JOURNALS/NATURE



"His personal energy and charisma are so strong, and he has this ability to get punched, stand up and go at it again."

Klein was a Stanford-educated lawyer who had made millions in real-estate development when, in September 2001, a week after the terrorist attacks on the Twin Towers and the Pentagon, his youngest son Jordan was diagnosed with type 1, or juvenile-onset, diabetes. Klein was devastated. "It's a life-changing shock when you know your child's life is in danger," he says.

THE THREE FAMILIES

Klein wanted to speed the search for cures. "I thought, 'we've got to get some broader-based research funding.'" He soon approached the Juvenile Diabetes Research Foundation International (JDRF) in New York to ask how he could help. Klein had some political experience from working with the state and with the national Democratic Party on housing issues. And in 2002, he put it to use, leading the JDRF's efforts in lobbying Congress to pass a \$1.5-billion federal funding measure to support diabetes research. The experience of getting that bill approved, Klein says, "demonstrated to me that dedicated, well-informed, focused patient advocacy could be very effective".

By that time, US President George W. Bush had imposed tough restrictions on federal funding for human embryonic stem-cell research. Convinced that such research offered the best hope for reversing his son's disease, Klein turned his attention to an idea then percolating in California: that the state directly fund biomedical research that federal money couldn't support. "Getting a Bush override was not feasible," Klein recalls. "So the question then was: what can I do back home?"

Klein teamed up with several other affluent and politically savvy parents of diabetic children — including movie director Jerry Zucker and his wife Janet, and home developer Tom Coleman and his wife Polly — and the 'three families', as they called themselves, together with political consultants and lawyers, devised a ballot initiative that would ask California taxpayers to support stem-cell science to the tune of around \$300 million per year for ten years.

The measure — which became known as the California Stem Cell Research and Cures Bond Act of 2004, or simply Proposition 71 — did not require approval or regular appropriations from the legislature. Instead, the proposed initiative relied on long-term state-issued bonds, effectively shielding the endowment from the whims of lawmakers.

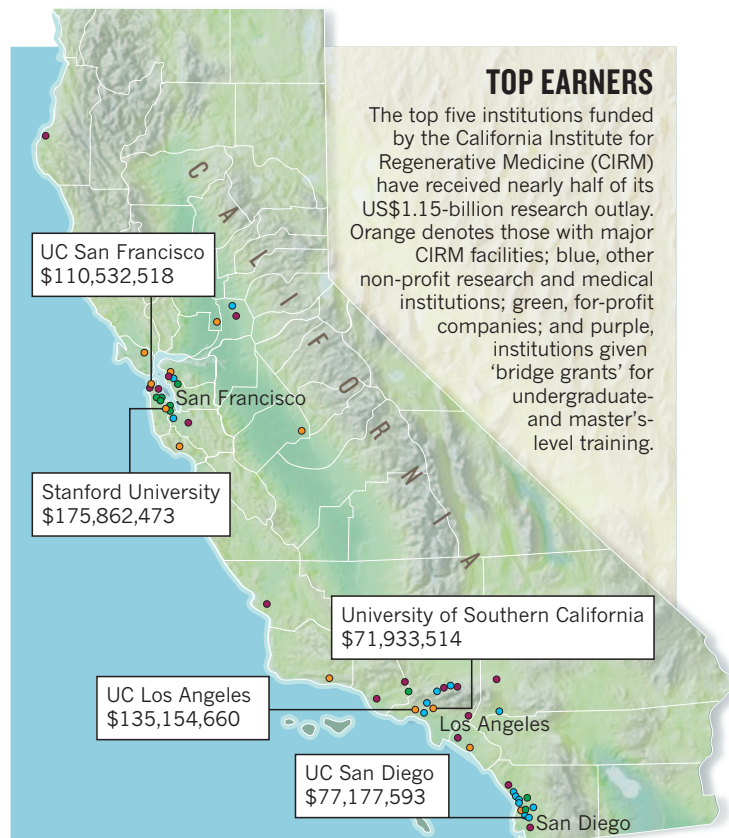
Klein had experience in bond financing for housing development and quickly took control of the campaign. He personally donated around \$1.2 million to get the initiative off the ground, later adding another \$3.1 million out of his pocket and raising \$30 million more in non-tax-deductible campaign contributions from others.

After a star-studded campaign endorsed by the likes of Brad Pitt, Christopher Reeve, Michael J. Fox and state governor Arnold Schwarzenegger, the campaigners gathered at the Millennium Biltmore hotel in Los Angeles on election night, in November 2004, to watch as the votes came in. The proposition passed with 59% approval. That night, says Wick, "I remember saying to the celebratory gathering that if our daughter is cured of her diabetes, the person who will be more responsible than any living human will be Bob Klein".

But not all the early organizers of Proposition 71 remain enthusiastic about the way Klein led the charge. "It became Bob's show almost entirely, and there was some friction about that," recalls Peter Van Etten, former JDRF president and chief executive. Coleman has not spoken to Klein since the initiative passed, following disagreements over what Coleman viewed as Klein's self-promotional approach. Zucker remains on better terms with Klein, but still feels some lingering resentment.

"If I had to do it over again I'd make the same call to Bob Klein because I don't think the rest of us would have got it done without him," Zucker

"I REALIZED THAT KLEIN WROTE THE INITIATIVE FOR HIM TO BE CHAIRMAN. IT'S SHAMELESS ALMOST."



says. But, he adds, "what I was most unhappy about was the realization after a while that [Klein] wrote the initiative for him to be the chairman. That was something I was too naive to realize. It's shameless almost."

Under the terms of Proposition 71, the 29-member governing board must include appointees with experience in academia, research, disease advocacy and biotechnology. The chair of the board, meanwhile, must meet a laundry list of mandatory criteria. These include a history of patient advocacy, leadership experience with a government agency, legal experience passing medical legislation and a direct knowledge of bond financing. Scientific expertise is not a requirement.

Sound familiar? "Look at the qualifications. They don't fit a lot of people," notes board member David Serrano Sewell, a lawyer with the San Francisco city attorney's office.

Klein defends the job qualifications that he wrote into the statute. "I wrote the job description based on what I thought would be the challenges. I'm trained as a lawyer, so I'm going to think that legal is an important criterion. I'm trained in finance, and I'm going to think that finance during the projected period of economic distress for the state is going to be very important. So I wrote those requirements in knowing that if no one else could qualify, I could meet those. But someone had to meet those criteria."

Many people maintain that Klein was simply the best person for the job. "He lived and breathed the mission," says Jeannie Fontana, executive director of patient advocacy at the Sanford-Burnham Medical Research Institute in La Jolla, California, who has often acted as a stand-in on the CIRM board. Bernard Siegel, director of the non-profit Genetics Policy Institute in Palm Beach Gardens, Florida, adds: "He was able to blend in his passion with his networking skills, which are formidable, with this knowledge of bonds. When you put all this together he was able to create a state agency with unprecedented resilience that has been extraordinary successful."

That resilience would be tested almost immediately after Proposition 71 passed. Critics of embryonic stem-cell science mounted legal challenges against the agency; as a result, bond sales were frozen until the court cases were settled. Klein, thinking ahead, had written a workaround into the bylaws. He was able to take out loans from elsewhere on the basis

that the bonds would eventually be paid — a little-known instrument called a 'bond anticipation note'. Buoyed by these and other loans from the state's general fund, Klein managed to keep administrative operations going and fund the agency's first training and research grants even before the lawsuits were eventually thrown out, in May 2007.

In the first two years of legal and financial setbacks, the board was struggling to find a president to lead the day-to-day operations of the agency. Zach Hall, then an associate dean at the University of Southern California School of Medicine in Los Angeles, was brought in as an interim president. He had the administrative chops, having previously directed the US National Institute of Neurological Disorders and Stroke. And as the lawsuits dragged on, Klein asked Hall to stay on full time.

Hall agreed. But it wasn't long before he and Klein butted heads. One of the main points of contention revolved around the agency's scientific strategic plan — a policy measure adopted in December 2006. Some maintained that the president's office alone should set the agency's scientific agenda, yet Klein made sure that he and several board members had a seat on the subcommittee that crafted the plan. As a result, many people felt that the original strategic plan, as well as last year's update approved by Hall's successor, the Australian assisted-reproduction pioneer Alan Trounson, focuses too heavily on clinical applications at the expense of more fundamental basic science. For example, the strategic plan allocates 16% of CIRM's \$2.4 billion projected research budget to what it calls "innovation science", exploratory open-ended research, and more than half is allocated to "mission-directed science", which is focused on developing therapies.

Joel Adelson, a health-policy researcher at the University of California, San Francisco, who interviewed 17 of CIRM's key stakeholders and co-wrote an independent review of the agency earlier this year¹, says that Klein's disagreements with Hall, and to a lesser extent with Trounson, stemmed from Klein's insistence on being involved in every aspect of CIRM's operations, including the scientific decisions.

"Klein has in effect acted like the chief operating officer beside Trounson and beside Hall, and I can only say that this looks like it must have been very uncomfortable for these guys," Adelson says. "It's an unusual situation," says Trounson. "And if you ask me what I prefer, I prefer the simple situation where the president is in charge of all management and reporting to a board on policies. But it's bifurcated, and it was set up that way, so you don't have a choice." (Hall declined to comment for this story.)

STICK TO THE VISION

Klein defends his march to the clinic as adhering to the vision he presented to voters on the campaign trail. And although some basic scientists take issue with CIRM's funding allocations, most have come to embrace the translational emphasis. For example, Jeanne Loring, a CIRM-funded stem-cell researcher at the Scripps Research Institute in La Jolla, says that Klein "has taken purely academic scientists who didn't give a damn about the clinical applications of their work, and turned them into scientists who will now talk, without a trace of embarrassment, about the benefit of their research to patients".

Patient advocates praise Klein as well. "He's an historic figure with real genius in terms of moving biomedicine forward," says Jeff Sheehy, a CIRM board member and director for communications at the University of California, San Francisco's AIDS Research Institute. "He's as good as they get if not better."

Developments in both science and politics have challenged CIRM's original rationale. In November 2007, researchers in Japan and Wisconsin reported that human skin cells could be coaxed in the laboratory to form embryonic-like pluripotent stem cells^{2,3}. This discovery provided a new path to patient-specific stem cells without the need for embryos. Then, a year and a half later, US President Barack Obama issued an executive order widening the scope of federal funding for embryonic stem-cell research, easing the need for state and private initiatives.

But Klein says CIRM's mission goes beyond simply serving as a stop-gap for embryonic stem-cell research during Bush-era restrictions, stressing that its focus on translational medicine distinguishes the California agency from the National Institutes of Health (NIH). For instance, he points to the disease team grants, launched last year, that require recipients to have a strategy for landing an investigational new drug application within four years.

"The purpose of CIRM is not science for science's sake," Klein says. "The purpose of CIRM is medical science with a plan to drive that science all the way through to therapies."

"KLEIN IS AN HISTORIC FIGURE WITH REAL GENIUS IN TERMS OF MOVING BIOMEDICINE FORWARD."

Marie Csete, a former chief scientific officer at CIRM, says that Klein embraced the new 'induced pluripotent' stem cells. "There was a transient moment where hanging on to embryonic stem cells was important, but he very quickly grasped that they were only one tool in the toolbox of regenerative medicine," she says.

After dedicating nine years and millions of dollars to the agency, Klein says

it's time to step aside and focus on family issues — his son is still battling diabetes, he lost his mother to Alzheimer's disease last year and his wife is currently undergoing chemotherapy for breast cancer. Agency insiders are sad to see him go. "The joke is to clone Bob Klein," says Lynn Harwell, CIRM's deputy to the chair for finance, policy and outreach. She pauses before quickly adding: "Although of course we don't condone cloning."

Geoffrey Lomax, CIRM's senior officer for medical and ethical standards, commends Klein's many accomplishments, but thinks that fresh leadership might help to clarify boundaries between the board and the staff. "As Mr Prop 71, Bob's relationship to the organization is unique," Lomax says. "I would suspect that there might be cleaner lines with someone coming in who doesn't bring that intimacy with the proposition."

Depending on who replaces him — nominations were made earlier this week by state officials including Schwarzenegger, and the new chair will be elected by the board on 15 December — Klein's departure might also trigger the president to leave, thereby causing a complete overhaul of CIRM's leadership. Trounson says he told Schwarzenegger that he would like that next chairperson to be "somebody who's in the delivery end of the spectrum — that is, somebody who has worked with the biotech or pharmaceutical industry".

But as this issue was going to press, the leading internal candidate to replace Klein, many say, is vice-chair Art Torres, a former state senator and chairman of the California Democratic Party. Torres and Trounson reportedly cannot stand each other. Trounson notes that Torres is "a politician, so he's in that end of the spectrum". Torres, for his part, declined to comment on his relationship with the president.

Whoever takes the reins will continue to deal with the fallout from the federal injunction. But Klein leaves the agency in strong legal and scientific positions, with several projects — including a few that rely on embryonic stem cells — likely to enter early clinical development in the next few years.

Gerald Levey, an ex-board member and former dean of the David Geffen School of Medicine at the University of California, Los Angeles, says that Klein's record at CIRM stands for itself. "If he did nothing else with his life, he did a wonderful thing."

But Klein vows to return to the agency's service in 2014 to help CIRM secure another \$3 billion commitment from California's taxpayers. "I have four years to put my life back into a position where I can commit myself to another campaign," says Klein. He has no plans to retire or stop the search for a cure for his son's diabetes: "You're either learning and growing or you're dying, and I want to continue to learn and grow." ■

Elie Dolgin is a news editor with *Nature Medicine* in New York.

1. Adelson, J. W. & Weinberg, J. K. *Am. J. Public Health* **100**, 446–451 (2010).
2. Takahashi, K. *et al. Cell* **131**, 861–872 (2007).
3. Yu, J. *et al. Science* **318**, 1917–1920 (2007).

➔ NATURE.COM
For an interactive graphic of CIRM grant recipients see: go.nature.com/38ew9w

SUPERGRID

Is a vast undersea grid bringing wind-generated electricity from the North Sea to Europe a feasible proposition or an overpriced fantasy?

BY COLIN MACILWAIN

North Sea energy used to mean oil and gas. Today, production of both is waning, and the rough weather that challenged the drillers has itself become a resource. In a speech last September, Alex Salmond, Scotland's first minister, estimated that the winds and waves lashing the Scottish coast could generate seven times more energy than Scotland consumes. Other countries around the North Sea hold similar potential. The problem is getting all that power from the windy edge of Europe to its populous, energy-hungry heart — the region roughly bounded by London, Berlin and Milan. "What we need above all is an efficient transmission system," Salmond says. "And the most efficient one would be a grid built across the North Sea."

On 3 December, ten northern European nations are expected to sign a memorandum of understanding spelling out how they'll build an undersea electricity 'supergrid'. The project is a major engineering and political challenge, comparable in scope, scale and ambition to the rush for oil and gas in the same waters 40 years ago. Thousands of kilometres of undersea cable would be laid, at a cost of at least €1 million (US\$1.4 million) per kilometre. Unlike onshore grids, which operate on alternating current (a.c.), the subsea grid would use direct current (d.c.) and would therefore require new types of offshore and onshore substations, control systems, converters and circuit breakers in a set of projects costing billions of dollars (see 'Wiring up Europe'). The whole project has an estimated €20-billion price tag.

An even more ambitious project, called Desertec, is planned to bestride the Mediterranean Sea and North Africa, pumping electricity generated by wind and solar power from the Sahara to Europe's cities. And a group of US investors led by Google released plans in October for an undersea grid in the North Atlantic that would ship power from offshore wind farms to the eastern seaboard of the United States. But the North Sea supergrid is closest of the three to becoming reality.

Momentum for the project comes from two main sources. A 2003 European directive, updated last year, demands that European Union (EU) states open up their electricity markets to competition with each other, which will require stronger connections between their national grids. And the EU has pledged to cut carbon emissions by 20% from 1990 levels by 2020, which will require a 35% cut in emissions from electricity generation and a vast expansion of renewables. "Without these grids, there will be no meeting of emissions targets in Europe," says Georg Adamowitsch, the EU coordinator for offshore grids in northern Europe.

Wind energy is already a mainstay of clean power generation in Europe, with 74 gigawatts of capacity installed so far, and another

136 GW anticipated by 2020, according to projections released by the European Commission (EC) in August. (By comparison, just 14 GW of new nuclear generating capacity is likely to be added by then.) Analysts expect much of this capacity to be installed offshore, because it is windier and easier to get planning permission. The need to connect up those offshore farms — and future wave- and tidal-power farms — to the mainland is the first reason that a North Sea grid is inevitable, analysts say.

Without these grids, there will be no meeting of emissions targets in Europe.

The second is that it would permit the large-scale storage of electricity in the only type of 'battery' so far developed for that purpose: pumped-storage hydroelectric dams, mostly located in Norway. Wind and other renewable energy sources are intermittent, but by using the energy to pump water uphill and recapturing power as the water flows down again, these dams can store electricity at more than 85% efficiency, evening out fluctuations in supply.

The attractiveness of such storage helped to spur the completion in 2009 of a 'point-to-point' high-voltage direct-current (HVDC) link between Norway and the Netherlands, which allows surplus power from the low-lying Netherlands to be stored in the Norwegian fjords, and brought back when needed. But on their own, such links cannot tap into offshore power sources, and cannot integrate the multiple electricity markets bordering the North Sea: only an undersea grid would do that. Last December, nine EU nations (the United Kingdom, Ireland, Sweden, Denmark, France, Germany, the Netherlands, Belgium and Luxembourg), joined later by Norway, agreed to start an initiative to get such a grid built, resulting in this week's memorandum. At the same time, the EC is supporting researchers who are looking in detail at the costs and benefits of different grid configurations — and at the technical challenges of taking a power grid offshore.

EDISON RULES

A crank called Thomas Edison once expected that most electricity would move around as d.c. But almost all transmission has turned out to use a.c. instead, chiefly because it can easily be transformed from high-voltage transmission lines down to the safe 120 volts or the somewhat less safe 240 volts in the home. It is also easy to isolate parts of an a.c. grid, to deal with faults and do routine maintenance, using massive mechanical circuit breakers that slam open just as the sine wave of the alternating current hits zero.

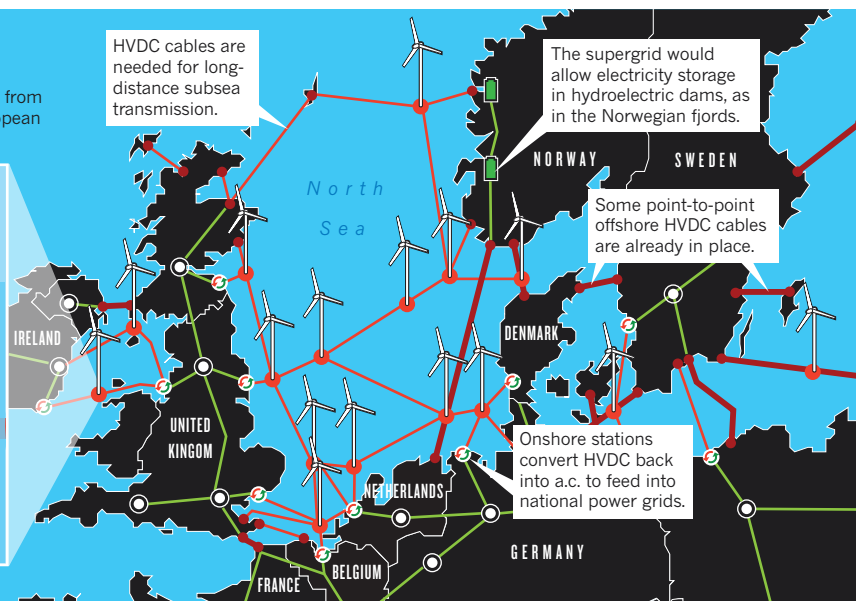
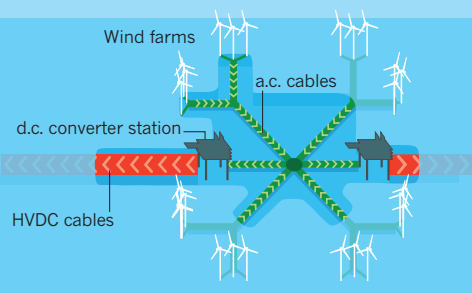
➔ NATURE.COM
For more on
energy.
go.nature.com/jyfb2l

WIRING UP EUROPE

A vast electricity grid under the North Sea would tap energy from future offshore wind farms and connect up the grids of European nations. The map shows one possible configuration.

Offshore nodes

A cluster of wind farms transmits a.c. to offshore converter stations, where it is stepped up to high-voltage direct current (HVDC) for transmission to shore.



Alternating current is no good for underground or subsea transmission over more than about 80 kilometres, however, because of heavy reactive losses which arise when the aluminium or copper conductor is buried. In effect, the cable and the surrounding earth form a capacitor, draining power from the a.c. lines, and rendering them useless over long distances. So a subsea grid has to be d.c. — posing a challenge for electrical engineers who lack the technological tools they have developed for a.c. power. “There’s no such thing currently as circuit breakers for high-voltage d.c.,” says Paul Neilson, transmission development manager at Scottish and Southern Energy in Perth, UK. “If there was a fault in the grid, all the energy would pour straight to it, a bit like decompression in an aeroplane. You need to be able to isolate it, automatically, in milliseconds.”

BREAKING THE CIRCUIT

Electrical engineers in industry and academia are addressing this and other challenges through a three-year €60-million programme called TWENTIES, a consortium of 26 academic and industrial partners supported by the EC. One TWENTIES project, led by Energinet, an agency of the Danish Climate and Energy Ministry, is seeking to design a control system that would react when storms approach. Electrical grids are designed to cope with some degree of perturbation — but a storm could make it necessary to rapidly shut down a whole cluster of wind farms. “This may develop into a system security problem, if we don’t improve the present storm control algorithms,” says Poul Sørensen, an electrical engineer and project partner at the Risø National Laboratory in Roskilde. “One of the solutions we’re looking at is to control the turbines more, and ramp them down slowly.”

Another TWENTIES project, led by transmission company RTE in France, will study the optimal configuration for a d.c. grid and test a prototype d.c. circuit breaker. Major electrical-engineering suppliers, including ABB, based in Zurich, Switzerland, and Siemens, based in Erlangen, Germany, are developing such circuit breakers, although they are not revealing details of their designs.

Dragan Jovicic, an electrical engineer at the University of Aberdeen, says that existing approaches are unlikely to yield appropriate d.c. circuit breakers, being either too slow in responding to faults, or “very high cost”. Jovicic has developed and patented a new type of d.c.–d.c. converter, which involves a set of inductors and capacitors linked in

a resonant circuit to step up d.c. voltage. This type of converter also doubles as a d.c. circuit breaker and, says Jovicic, could weigh five times less than some other designs that rely on conversion to a.c. and back again, because it lacks the heavy iron core transformers. Extra weight is expensive because the connection points will be mounted on platforms offshore, for maintenance access (see D. Jovicic and B. T. Ooi *IEEE Trans. Power Deliv.* **25**, 2535–2543; 2010).

In October, Jovicic won an award from the European Research Council to design new models for high-voltage d.c. converters. These have to work on microsecond timescales, rather than the millisecond timescales at which a.c. oscillates. The new model will also be able to deal with the complicated configurations in a substation that connects four or five high-voltage d.c. lines together.

But solving the technical problems will only go part-way to getting a North Sea supergrid built. The capital costs of laying grids offshore are immense. A report published in July by the EU-funded research project OffshoreGrid, based in Brussels (see go.nature.com/cssy3s), envisages, for example, that €32 billion will be invested in offshore interconnectors in northern Europe by 2020 and a further €58 billion by 2030, if wind farms are connected up individually. It suggests that €15 billion could be shaved from this if wind farms were clustered. On top of this, the opening up of electricity markets will require wholesale legal and regulatory change: at present, for example, generating companies that receive subsidies for feeding renewable energy into a German grid receive nothing if they supply power elsewhere.

Not all European countries are equally enthusiastic about the North Sea supergrid. The United Kingdom has embraced the project because it needs offshore wind capacity to meet its carbon-emissions targets. Ireland, Norway and Scotland are especially keen, because they want to build new industries that manufacture and service offshore wind and wave farms. But despite their stated intention to sign the memorandum of understanding, the French and German governments have been lukewarm, admit grid advocates, with Germany pushing instead for Desertec, which is led by German companies.

The North Sea supergrid is technically more radical than this and other proposals, and could prove almost as politically taxing — despite the theoretical commitment of EU states to get it built. And however much high-level planning goes on, the supergrid’s evolution is likely to be messy, much like that of a national highway system. “Things will happen incrementally,” says Neilson. “It’s not practical to roll out a pre-designed grid like a roll of linoleum.” ■ [SEE EDITORIAL P.599](#)

Colin Macilwain is a freelance writer based in Edinburgh, UK.

It’s not practical to roll out a pre-designed grid like a roll of linoleum.

COMMENT

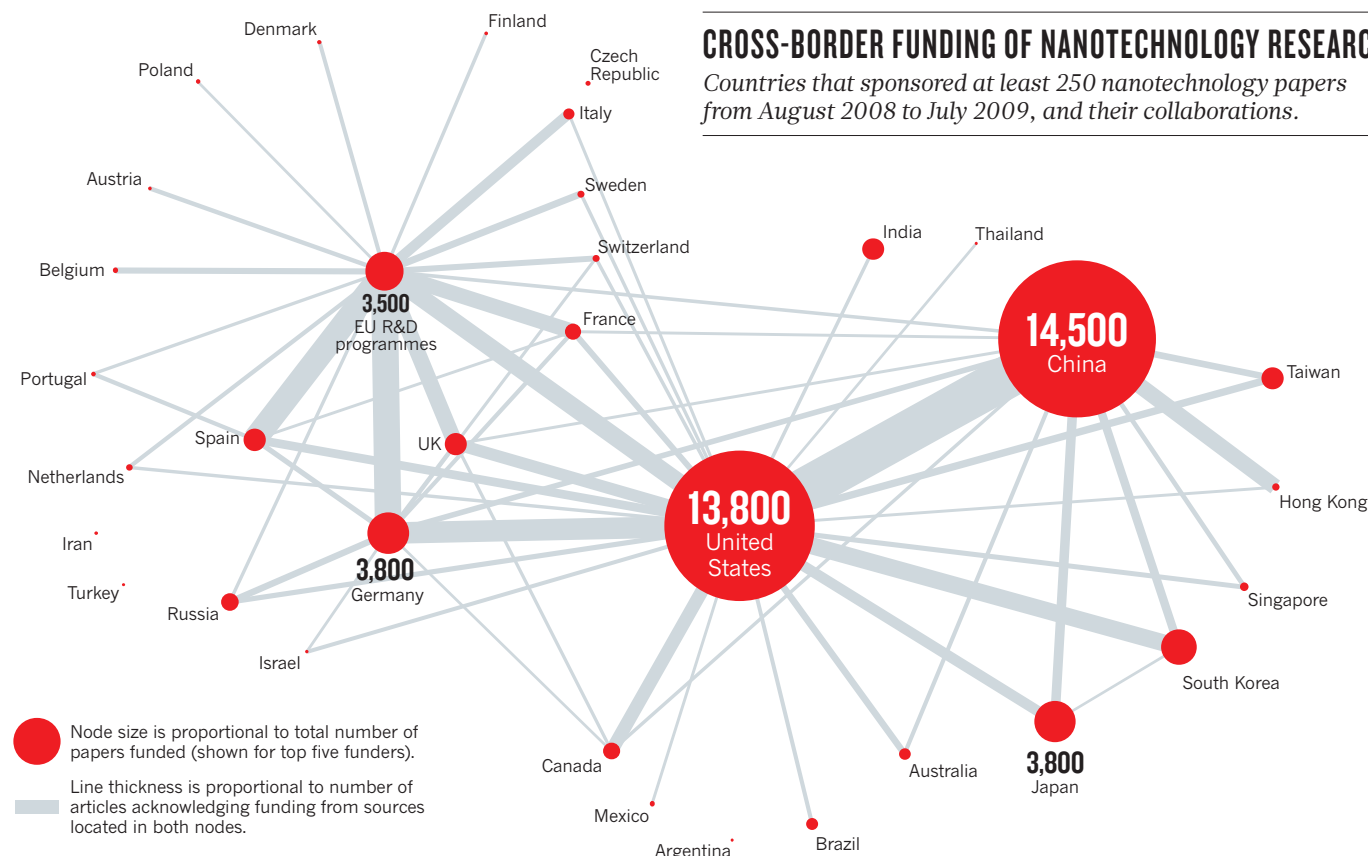
BIOGRAPHY The many contradictions of Edward Teller **p.629**



MATHEMATICS Primer on theoretical foundations of neuroscience **p.630**

HISTORY Exhibition of early ideas on how to behave beyond the grave **p.632**

FORESTS Joined-up thinking to make tropics more resilient to climate change **p.xxx**



Follow the money

What was the impact of the nanotechnology funding boom of the past ten years?
Philip Shapira and Jue Wang have scrutinized the literature to find out.

Nanotechnology research spending worldwide expanded rapidly during the past decade. The US National Nanotechnology Initiative (NNI), announced in 2000, kicked off the funding boom: federal spending jumped from US\$464 million in 2001 to nearly \$1.8 billion in 2010¹. China, Germany, Japan and Korea soon followed in setting up national nanotechnology programmes, and the European Union (EU) designated nanotechnology as a research priority in 2002. More than 60 countries now have national nanotechnology programmes². Global public

investment in research and development (R&D) in nanotechnology reached \$8.4 billion in 2008, with a further \$8.6 billion of corporate funding³.

More spending naturally leads to more publications. But how do these funding outcomes vary in scale, productivity, disciplinary focus, collaboration patterns and impact? Using data-mining techniques, one can now make comparisons across countries for large numbers of organizations. We have analysed funding acknowledgments in nanotechnology papers to link research output to funders (P. Shapira and J. Wang, manuscript

in preparation). We find that despite the initial focus on national initiatives, patterns of nanotechnology funding and collaboration transcend country boundaries (see 'Cross-border funding of nanotechnology research'). Importantly, the concentration of funds — whereby research sponsors support relatively fewer institutions — seems to yield lower-quality research.

Using a broad-based definition of nanotechnology⁴, we identified more than 91,500 articles published worldwide between August 2008 and July 2009 (almost four times more publications than in 1998)⁵. Although the ►

► sample featured researchers in 152 countries, researchers in just 15 authored almost 90% of the papers. (An internationally co-authored paper is assigned to more than one country.) The top four countries by author affiliation are the United States (23%), China (22%), Germany (8%) and Japan (8%). The US share is not surprising given its dominance in funding. China's share has been rising rapidly, although it still spends less on nanotechnology R&D than the United States, particularly in the corporate sector. China's high output of publications reflects much lower personnel costs and national policies that have built up academic nanotechnology research⁶.

Since 2008, the Thomson Reuters bibliographic and citation database has also included funding-acknowledgement data. About 67% of the 2008–09 nanotechnology publications include such acknowledgements, mostly to public research agencies, but also to foundations and corporations. We denote these 'grant-supported publications'. Although this category does not capture all the results of funding — public or otherwise — our data set of more than 61,300 grant-supported nanotechnology publications (some supported by multiple sponsors) tells us much about global funding patterns and their outcomes.

LITERATURE ANALYSIS

From this data set we identified a cluster of major research sponsors (see 'Nanotech's top ten funders'). The top ten by publication output fund 69% of all grant-supported publications, and are led by the National Natural Science Foundation of China, the US National Science Foundation (NSF), the Ministry of Science and Technology of China and the R&D programmes of the European Union (EU). Although the United States and China dominate, 13 other countries are represented among the top 25. Israel, the Netherlands and Switzerland are some of the small advanced economies with high-quality nanotechnology research.

China is close to the United States in number of publications, but still lags behind the United States and Europe in publication quality⁵. We looked at one quality measure — the number of early citations — for the top 25 research sponsors. Eight sponsors saw at least 10% of their grant-supported papers garner five or more citations within a year of publication. This group is led by four US agencies — the National Institutes of Health, the Department of Energy, the Department of Defense, and the NSF — followed by the UK Engineering and Physical Sciences Research Council (which ranks 16th in numbers of sponsored papers), the EU research programmes and the German Research Foundation. The Chinese Academy of Sciences takes the eighth slot, even

NANOTECH'S TOP TEN FUNDERS

Funding data and early-impact data for more than 61,000 grant-supported nanotechnology research publications were analysed to identify key research sponsors.

Organization	Sponsored papers (and % of total)	Early-impact papers (% of sponsor's papers)
National Natural Science Foundation of China	10,200 (16.7)	4.7
US National Science Foundation	6,700 (10.8)	11.4
Ministry of Science and Technology of China	4,700 (7.7)	5.2
European Union (R&D programmes)	3,500 (5.8)	10.4
US Department of Health & Human Services (including National Institutes of Health)	3,100 (5.1)	15.0
Ministry of Education of China	3,100 (5.1)	4.6
US Department of Energy	3,000 (4.9)	12.5
US Department of Defense	2,600 (4.2)	12.3
German Research Foundation	2,600 (4.2)	10.2
Ministry of Education, Culture, Sports, Science and Technology of Japan	2,400 (3.9)	6.2

though it is outside the top ten by volume. Other large Chinese sponsors have much lower early-citation figures.

In general, we find that sponsors who concentrate funds in fewer institutions have lower research impact as measured by early-citation counts. It may well be that when groups from multiple institutions vie for funding, competition increases, review processes become less partial and more promising projects are selected.

Most nanotechnology funding is nationally oriented, but science crosses borders. In our data set, 23% of the papers have co-authors in more than one nation. Authors in China exhibit the lowest levels of international co-authorship (17% of all Chinese papers) and international funding acknowledgement (also 17%), whereas Germany, France and Britain report the highest levels of both. Some of this is mandated by the sponsor: EU R&D programmes typically require teamwork by researchers from different countries. In other cases, the multinational funding arises independently as researchers collaborate.

The United States remains at the centre of the international nanotechnology map. US researchers partner most often with colleagues in China, although the actual number of collaborative articles is still low relative to national totals. China is the hub for co-funded nanotechnology research with other Asian countries (including Japan). Another cluster is evident in Europe, where there are major lines of co-funding between the EU and its member states. In these clusters, scientific capability, proximity, shared cultural norms, research policy

and researcher mobility seem to facilitate the exchange of ideas.

Today, ten years after the launch of the NNI, a handful of countries and research agencies still sponsor much of the world's nanotechnology output. But despite all the international crosstalk, nanotechnology is not yet a truly global activity: most of the developing world is missing.

Nanotechnology has had a decade of growth. Flat public spending and competition from other emerging technologies suggest that nanotechnology funding, in the United States and Europe at least, is unlikely to rise at the same pace in the next few years. So how should stakeholders continue to increase the quality and industrial applications of nanotechnology research? One way would be to foster more high-quality international collaborations, perhaps by opening funding competitions to international researchers and by offering travel and mobility awards for domestic researchers to increase alliances with colleagues in other countries. ■

Philip Shapira is at the University of Manchester, Manchester M15 9PL, UK and Georgia Institute of Technology, Atlanta, Georgia 30332-0345, USA. **Jue Wang** is at Florida International University, Miami, Florida 33199, USA.
e-mail: pshapira@gmail.com.

1. National Nanotechnology Initiative. available at go.nature.com/pwppwf.
2. Sargent, J. F. *Nanotechnology and U.S. Competitiveness: Issues and Options*. (Congressional Research Service, 2008).
3. Lux Research. *Ireland's Nanotechnology Commercialization Framework 2010–2014*. (Forfas, 2010).
4. Porter, A. L. et al. *J. Nanopart. Res.* **10**, 715–728 (2008).
5. Youtie, J. et al. *J. Nanopart. Res.* **10**, 981–986 (2008).
6. Shapira, P. & Wang, J. *Asian Business Mgmt* **8**, 461–489 (2009).



Physicist Edward Teller insisted on building the hydrogen bomb, and opposed nuclear test-ban treaties.

BIOGRAPHY

Envy and power

A balanced biography brings out the many contradictions of nuclear physicist Edward Teller, finds **Robert P. Crease**.

The Hungarian-born US physicist Edward Teller (1908–2003) is remembered less for his scientific achievements than for his political crusades. These include spearheading the development of the hydrogen bomb, demolishing the influence of atomic physicist J. Robert Oppenheimer in government circles, opposing nuclear test-ban treaties, and championing the flawed US Strategic Defense Initiative.

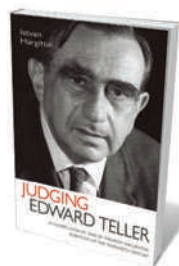
Although Teller's motivations were patriotic, he left turmoil and bitterness in his wake. *Judging Edward Teller* provides a much needed, complex personal portrait of an influential scientist, even if it does not set him fully on the world stage.

Teller saw the world in black and white. He evokes a similarly polarized reaction, making it difficult to evaluate his legacy fairly. Biographer and chemist István Hargittai has an advantage in coming from a Jewish Hungarian background similar to that of his subject. Hargittai notes that he aimed "to be appreciative of [Teller's] virtues and to be conscious of his flaws". Teller had both in abundance.

Teller's early life was dramatic. He spent his first 18 years in Hungary during a tumultuous era that included the 'happy peacetime' of the Austro-Hungarian monarchy, the devastation of the First World War, the country's

humiliating dismemberment, democracy, communism, right-wing terror and anti-Semitism. In 1920, Hungary enacted a law called *numerus clausus* ('closed number'), which restricted the number of Jewish students allowed in higher education. This law, Hargittai says, had the "dubious distinction of being the first anti-Jewish legislation after World War I in Europe".

Hargittai describes Teller's adult life as a series of three exiles. The first began in 1926, when he left Hungary for Germany. Calling this an exile seems forced, however — Teller's outstanding academic performance exempted him from the *numerus clausus*. Furthermore, his departure was anticipated: his family, like those of many other Hungarian Jews, prepared their children linguistically and culturally for emigration to Germany, where the culture was livelier



Judging Edward Teller: A Closer Look at One of the Most Influential Scientists of the Twentieth Century
ISTVÁN HARGITTAI
Prometheus Books:
2010. 575 pp. \$32,
£29.95

and where educational and job prospects were superior.

Teller was fortunate: Germany was a scientific superpower and German was seen as the "language of science". He studied chemical engineering in Karlsruhe, physics in Munich, received a PhD in physics under Werner Heisenberg in 1930 at Leipzig, and from 1931–3 worked in Göttingen with physical chemist Arnold Eucken. While in Munich in 1928, a tram wheel severed his right foot and he wore a prosthesis for the rest of his life. This left him determined to overcome adversity, and with the need to carry a trademark cane that he would pound on the floor for emphasis when speaking.

Soon after the Nazis assumed power in 1933, Teller fled Germany. This was a genuine exile: sudden and with no clear destination, thrusting him into unfamiliar territory. Aided by a British programme to rescue Jewish scientists, Teller spent time in Copenhagen and London, and moved to the United States in 1935. When the Second World War broke out, his friendship with fellow Hungarian physicist Leo Szilard got him a position on the US atomic bomb project. He quickly went from being a ringside viewer to an active participant of the theoretical group at the Los Alamos laboratory in New Mexico. Teller could be exuberant and generous, but also envious and self-important. At Los Alamos, these negative traits began to disrupt relationships with colleagues, leading him to bear grudges against lab director Oppenheimer and others.

After the war, Teller pursued a series of causes that prompted nuclear physicist Enrico Fermi to label him "a monomaniac with many manias". One was Teller's insistence on developing, and getting credit for, the hydrogen bomb. Hargittai diligently traces Teller's changing stories of the bomb's history, describing at least five versions Teller gave with different names, dates and deeds. Hargittai quips that if the changes were plotted as a graph, they would show that "what should have been a fairly constant set of attributes appear to be fast-moving variables".

In April 1954, Teller testified against Oppenheimer at a hearing convened by the US Atomic Energy Commission in Washington DC, which considered Oppenheimer's appeal of the revocation of the security clearance needed for him to continue to be an adviser on atomic policy. Teller stated: "I would prefer to see the vital interests of this country in hands that I understand better and therefore trust more." In his autobiography *Memoirs* (Perseus Books, 2001) and else-

where, Teller said that he had planned to testify that Oppenheimer should be cleared, but changed his mind after seeing parts ▶

➤ **NATURE.COM**
For a review of
an Oppenheimer
biography, see:
go.nature.com/16m7nw

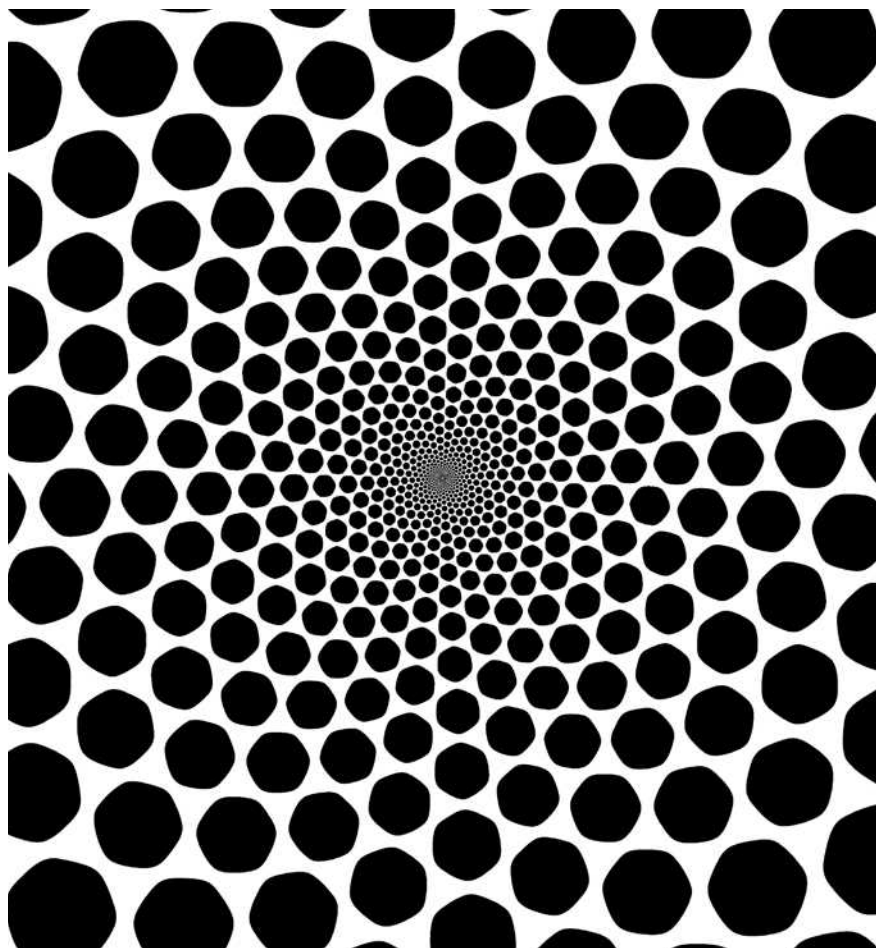
► of Oppenheimer's trial testimony. This recollection has been shown by historians to be incorrect: Teller had already significantly contributed to the anti-Oppenheimer case.

Teller's testimony was not the decisive point of the hearing — the inevitable outcome of which was to deny Oppenheimer's appeal and thus exclude him from government circles — but it was the psychological *coup de grâce*. Those who knew Oppenheimer found Teller's remarks preposterous. From then on, many refused to acknowledge him, isolating him from the mainstream physics community. Thus began what Hargittai calls Teller's third exile; again, a description that is a stretch, because it was self-inflicted and because Teller blossomed into an influential and canny insider in US political and military circles. "Edward understood power," remarked George Keyworth, science adviser to President Ronald Reagan. "He could have written [Machiavelli's] *The Prince*."

Hargittai is an acute observer of Teller's personal interactions. He gives an astute reading, for instance, of Teller's letters to the German-American physicist Maria Goeppert Mayer, which ranged from physics to personal matters. Hargittai exposes Teller's half-truths and falsehoods, including his erroneous suggestion that he opposed dropping the atomic bomb on Hiroshima. Such revisionist statements might be described as 'truthy' in the sense applied by US comedian Stephen Colbert to the remarks of certain politicians — as portraying the truth they want to exist. Hargittai also points out exaggerations by Teller's critics, such as unjustified comparisons with Trofim Lysenko, the biologist who destroyed Soviet genetics by sending it on a politically thrilling but scientifically questionable crusade.

Hargittai sometimes acts too much like an umpire, evaluating claims about Teller rather than appraising him as a moral and political agent. It would have been intriguing to investigate the psychological factors at work in a person whose idea of protecting his adopted country was to damage its science base by undermining eminent people whose views were less extreme than his own. How did such an envious and petulant individual become a point person for the US military? Answering such issues would require more background knowledge than Hargittai provides about the US weapons establishment, which itself used Teller as much as he used it. It would also require an understanding of the pernicious US preoccupation with security that often moves its leaders to damage their country in order to save it. ■

Robert P. Crease is professor of philosophy at Stony Brook University, New York 11794, USA, and author of *The Great Equations*. e-mail: rcrease@notes.cc.sunysb.edu



M. RULE

The visual disturbances seen by some people with migraines can be modelled mathematically.

NEUROSCIENCE

Patterns from the brain

Vincent A. Billock recommends an introduction to the mathematics of geometric hallucinations.

Until recently, biologists treated theory as a reward, claimed after a lifetime of labour in experiment and observation. Yet, within just a few generations, theorists in neuroscience have begun to resemble their cousins in physics, choosing to specialize in theory early in their careers. The focus of theoretical neuroscience has shifted in that time towards complexity: from models of nerve conduction to an emphasis on the dynamics of nonlinear neural interactions. Bard Ermentrout, a biophysicist, had much to do with that transformation, which is highlighted in his and mathematician David Terman's textbook, *Mathematical Foundations of Neuroscience*.

Terman and Ermentrout share an interest in the failure modes of neural systems. Nonlinear dynamic aspects are often only

revealed when neural systems are pushed to the edges of their performance abilities. Migraines, strobe lights and drug intoxication can all cause geometric hallucinations: Ermentrout studies these as well as the illusions produced by viewing moving images during electric retinal stimulation.

"Should maths be conveyed separately to students who show theoretical aptitude, or mixed in as digressions to a lecture series?"

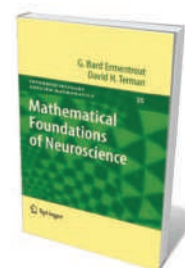
Terman's model of image segmentation fragments noisy images (such as television static) in a manner that is reminiscent of these visual effects. However, aside from geometric hallucinations, the wilder

sides of Ermentrout and Terman's research interests are not emphasized in the book, which is directed at a broad interdisciplinary audience.

The traditional material on membrane biophysics, cable theory and neural-spike generation models is presented first. The latter part of the book — covering the nonlinear dynamics of neural interactions — takes a balanced approach, describing models in which the correct timing of individual neural spikes

is crucial, and population models based on the firing rates of an ensemble of neurons. Rapidly evolving topics such as neural synchronization and spatially extended models are included.

Ermentrout and Terman go deeper into the mathematics of neural activity than say, Hugh Wilson's 1999 textbook *Spikes, Decisions and Actions* (Oxford University Press). But, unlike



Mathematical Foundations of Neuroscience
G. BARD
ERMENTROUT AND
DAVID H. TERMAN
Springer: 2010.
422 pp. \$74.95

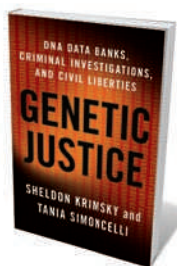
Wilson, they pass up most opportunities to connect the mathematics to its cognitive and perceptual consequences.

They emphasize the mathematical basics even over exciting developments in theory. For example, a strong chapter on neural noise neglects stochastic resonance — a phenomenon of nonlinear systems in which a weak signal can be amplified and optimized by noise — and its role in promoting neural pattern formation. Similarly, Terman omits his own model when describing oscillatory neural synchronization, a process that may perceptually bind together the disparate parts of a stimulus.

This tight focus raises the question of how mathematical skills should be taught across science subjects. Should they be conveyed separately to students who show theoretical aptitude, or mixed in as digressions to a science-based lecture series? *Mathematical Foundations of Neuroscience* falls somewhere in between: it is a good substitute for a lengthy regime of abstract maths classes, but it is also well integrated into the field of neuroscience. Ermentrout and Terman's book conveys much of the advanced mathematics used in theoretical neuroscience today. ■

Vincent A. Billock is a visiting senior fellow with the US National Research Council at the US Air Force Research Laboratory, Building 248, Wright-Patterson Air Force Base, Ohio 45433, USA.
e-mail: vincent.billock.ctr@wpafb.af.mil

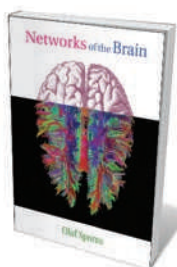
Books in brief



Genetic Justice: DNA Data Banks, Criminal Investigations, and Civil Liberties

Sheldon Krinsky and Tania Simoncelli COLUMBIA UNIVERSITY PRESS
448 pp. \$29.95 (2010)

Governments worldwide are increasingly storing the DNA profiles of their populations. Medical ethics advisers Sheldon Krinsky and Tania Simoncelli describe the US situation, placing those trends in context with precedents in other nations. They examine ethical issues such as holding DNA from juveniles and broadening searches to include a suspect's family members. The fallibility of DNA profiling, they suggest, has major implications for criminal justice.



Networks of the Brain

Olaf Sporns THE MIT PRESS 375 pp. \$40 (2010)

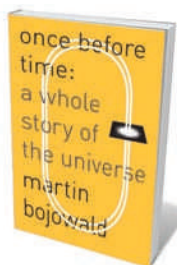
The study of brain connectivity increasingly borrows from theories of complex systems. Points of contact between these disciplines are explored in this wide-ranging book by neuroscientist Olaf Sporns. From individual cells and synapses to whole cognitive systems, he explains how networks connect levels of organization in the brain and how their structures link to brain function. As well as documenting the latest developments — using an informal approach that does not rely on mathematics — he traces the historical roots of the field.



The Cuban Cure: Reason and Resistance in Global Science

Simon M. Reid-Henry UNIVERSITY OF CHICAGO PRESS 216 pp.
\$39 (2010)

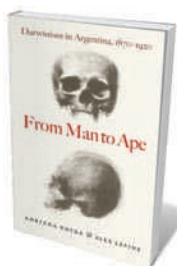
Since Fidel Castro took over the nation in 1959, Cuba has taken science seriously. Its biotechnology programme is especially advanced — it has produced a meningitis B vaccine and cutting-edge cancer therapies despite poverty and a trade embargo. Geographer Simon M. Reid-Henry examines the culture clashes that arise when biomedical scientists from Cuba work on the international stage and compete with big pharma. He asks what lessons Cuba holds for the science bases of other developing countries.



Once Before Time: A Whole Story of the Universe

Martin Bojowald KNOPF 320 pp. \$27.95 (2010)

The origin of the Universe before the Big Bang is difficult to model mathematically. Physicist Martin Bojowald describes his own work to overcome this problem using loop quantum cosmology — a model he developed a decade ago based on the theory of loop quantum gravity, which merges general relativity and quantum mechanics. He explains his search for testable hypotheses. If verified, these might show that the Big Bang was not a one-off event, but one of many recyclings of a Universe that alternately swells and contracts.



From Man to Ape: Darwinism in Argentina, 1870-1920

Adriana Novoa and Alex Levine UNIVERSITY OF CHICAGO PRESS 328 pp.
\$49 (2010)

Charles Darwin's ideas about evolution were received differently in Latin America than elsewhere. Focusing on Darwin's use of analogies, science philosophers Adriana Novoa and Alex Levine explore how Argentina's culture influenced interpretations of evolution in the nineteenth century. Darwin's 'tree of life' became a 'tree of death' in the hands of one local scientist. Argentina's diverse peoples and unusual fossils also contributed alternative views of nature.



TRUSTEES OF THE BRITISH MUSEUM

Ancient Egyptians believed that their lives would be judged by the gods when they died — as shown in the papyrus of Ani, part of a Book of the Dead from 1275 BC.

HISTORY

How to behave beyond the grave

Instructions for the afterlife from Ancient Egypt reveal a step change in moral psychology, discovers **Andrew Robinson**.

In 1819, the English physician and polymath Thomas Young — known for his discovery of the interference of light — published a pioneering article on ancient Egypt in the *Encyclopaedia Britannica*. It offered a partially correct translation of the Rosetta Stone's hieroglyphic and demotic texts and outlined the new science of Egyptology. Young persevered in trying to understand the scripts, expressing impatience with the “monstrously complicated Egyptian superstitions”. But he was overtaken. His reluctance to engage with the bewildering pantheon of animal-headed Egyptian gods and priestly mumbo-jumbo was a key factor in the ascendancy of his French rival, the philologist Jean-François Champollion, who deciphered the Egyptian hieroglyphic script fully in 1822–23.

Visitors to *Journey Through the Afterlife*, the British Museum's elegant exhibition on the ancient Egyptian Book of the Dead, may initially sympathize with Young. The displayed texts — not a single book but various compilations of instructions for the afterlife, in

hieroglyphic, hieratic and demotic scripts — describe a bizarre universe of belief. They were first interpreted as a funerary ritual by Champollion working from papyrus scrolls in the 1820s.

Yet the intricately painted vignettes — featuring the deities, animals, chimeras, kings and scribes of Egypt more than 3,000 years ago — have a disconcerting power. However fantastical the ideas depicted, the Book's pages document the shift in human thought towards judgements based on moral behaviour. Ethical precepts were written down in Egypt as early as 3000 BC. They were followed more than a thousand years later by the Babylonian King Hammurabi's famous law code.

The Book of the Dead, which appeared before the beginning of the New Kingdom around 1550 BC and was commonly used until the Graeco-Roman era in Egypt in the first century BC, shows for the first time the

Journey Through the Afterlife: Ancient Egyptian Book of the Dead
British Museum,
London.
Until 6 March 2011.

idea that the benefits of eternal life depend on an individual's adherence to correct behaviour on Earth. The law of ancient Israel, and the Ten Commandments in the Bible, were influenced by ancient Egyptian ethics.

Inscribed on stone sarcophagi, wooden coffins and stone amulets, but mainly painted and drawn on long papyrus scrolls placed close to a mummified corpse, Books of the Dead collected up to 200 spells. They were intended to reanimate and protect the corpse of an Egyptian in the afterlife, in a civilization where the average lifespan was 35 years. Neither the number of spells nor their order and content were fixed, so there is no definitive version of the Book; nor does it have a simple narrative, although the exhibition does its best to provide one.

The dominant idea is that the *ba* (soul) of the deceased should fly during the daylight hours from the grave of its mummified

NATURE.COM
For an exhibition on ancient Egyptian body image, see:
go.nature.com/1ebtdb

corpse and continue to enjoy earthly pleasures beside the fertile Nile, returning at nightfall — much as the Sun god Ra endlessly cycles through the sky. Indeed, the ancient Egyptians called these compilations the ‘book of coming forth by day’; the modern name ‘book of the dead’ was coined by the German Egyptologist Richard Lepsius in the 1840s, probably from the term used by Egyptian workers on excavations when they discovered such manuscripts.

There are major collections of Books of the Dead in museums in Egypt, Europe and the United States. The British Museum’s holding is among the finest, and this exhibition is drawn almost exclusively from it. Many of the papyri have not been exhibited before, mainly because of the extreme sensitivity to daylight of the paints used in illustrating them. Tests by British Museum conservationists on the pigments, such as realgar (red arsenic) and orpiment (yellow arsenic), show that fading begins within days of exposure to natural light. “Choosing items which could be exhibited safely has been a lengthy process”, writes the exhibition’s curator John H. Taylor in the magnificent catalogue. Moreover, sensitivity of the paints to vibration means that the museum will have to modify its original plan of taking the exhibition on tour.

The best-known vignette in the Book of the Dead, rightly given pride of place near the end of the exhibition, is the judgement of the deceased before he or she is permitted to enter the afterlife. In the papyrus of Ani (pictured), a scribe who probably died around 1275 BC during the reign of Ramesses II, Ani and his wife bow respectfully towards the gods, as Ani’s heart (regarded as the seat of intelligence) is weighed in the balance scales by the jackal-headed Anubis against the feather of Maat (truth). The procedure is watched greedily by Ammit the Devourer, a monstrous combination of crocodile, lion and hippopotamus.

Ani speaks to his heart, telling it not to testify against him like a bad conscience. “The Egyptians devised ways to escape punishment by the gods, but the fact that they felt a need to do so is revealing of a new stage in human psychology, a new notion of just behaviour,” notes Neil MacGregor, director of the British Museum. On studying this compelling vignette, even visitors as dismissive of Egyptian mysticism as Young would have to agree. ■

Andrew Robinson is a writer based in London. He is writing a biography of Jean-François Champollion.
e-mail: ar471@cam.ac.uk

TECHNOLOGY

Libraries of the future

A hands-on exhibition shows how online tools are shaping the way we use knowledge, says **Aleks Krotoski**.

The changing role of the library in scientific enquiry is explored in *Growing Knowledge*, an interactive exhibition at the British Library in London. Through hands-on demonstrations of the latest digital technologies — including the European premiere of Sony’s 360° autostereoscopic (three-dimensional) display — the curators hope to stimulate scientists to pursue new questions, techniques and forms of collaboration.

Visitors can try out immersive video and input technologies and interact with online research tools on multiscreen workstations. Touch screens demonstrate ways in which high-resolution images of scientific phenomena, ancient texts or sculptures can be stored, shared and manipulated by collaborators worldwide. Topics of debate are emphasised on displays and video panels, through interviews with devel-

opers, academics and information scientists.

The exhibition also highlights the recent shift towards open data sets. Databases are increasingly being made freely available to the

research community as a means of maximizing efforts and inspiring more creative analyses. Public release of scientific data is often demanded by research-funding bodies, but concerns remain about data ownership and misrepresentation. To alleviate such fears, the curators display a range of examples of such data sets, including the website that collects public information from the UK government (<http://data.gov.uk>), orchestrated by Tim Berners-Lee, inventor of the World Wide Web, and computer scientist Nigel Shadbolt of the University of Southampton, UK.

Issues around data sharing are explored in related workshops. Questions to be investigated include how the academic community ensures that author contributions are acknowledged; how shared data are secured and protected in a way that does not conflict with accessibility goals; and how the information is archived. Others look at how researchers with access to different technology platforms can work

Growing Knowledge: The Evolution of Research
British Library, London.
Until 16 July 2011.

with the same data reliably.

The British Library is scheduled to host a public debate to consider how research will be reported as

authors seek to distribute findings to as wide an audience as possible. Funding bodies increasingly require digital dissemination of results to maximize public impact, and some researchers rush to reveal results on blogs to claim priority. Articles openly released on the Internet garner more citations than those in subscription journals, but many scientists are concerned that publicly posted content that has not been peer reviewed could be used out of context. Traditional forms of academic publication are still favoured, although other open-access models are being explored by publishers.

The exhibition also probes advances in searching for information. Future readers might require ‘intelligent’ personalized searches that deliver quality content based on previous patterns of search activity. Library users are also likely to participate in knowledge generation through shared resources such as Wikipedia or crowd-sourced research projects such as Galaxy Zoo, which asks the public to help classify millions of galaxies. The challenge for libraries is to handle the data deluge — which is expected to increase exponentially — by exploiting remote, Internet-based ‘cloud computing’ storage.

Although solutions to managing information in the Internet era are still evolving, one thing is certain: library visitors of the future will be demanding. They will expect interactive catalogues to contain every permutation of possible data, and for it to be accessible on multiple devices at any time. Research libraries will define and maintain standards, host and disseminate archives and provide flexible user support. Library buildings will encourage collaboration and discussion as well as quiet study. *Growing Knowledge* exposes these changes at the core of research practice. ■

Aleks Krotoski is Researcher-in-Residence of the Growing Knowledge exhibition at the British Library, London.
e-mail: aleks@alekskrotoski.com

CORRESPONDENCE

Archiving lessons from radiobiology

Rescuing endangered primary data is important (*Nature* 468, 17; 2010). Even more crucial is to archive it at the time it is generated. This lesson has been learned by the radiobiology community, who took on that challenge 25 years ago.

The past 60 years have seen many large-scale studies of radiation effects on animals. The scale, cost (estimated at US\$2 billion today) and ethical aspects of these experiments make them unlikely to be repeated. However, the data could usefully be reanalysed in the light of new paradigms in radiobiology.

These endangered data were deposited between 1985 and 1999 in the International Radiobiology Archives (IRA): they include results collected during 1960–98 on more than 460,000 animals in Europe, the United States and Japan. The IRA is now integrated into a legacy database, the European Radiobiology Archive (ERA), a project funded by the European Commission (see go.nature.com/evbdFv).

Development of the ERA taught us that integrating legacy data into a standard format is difficult. But the data must be searchable and usable to prevent the database becoming an information graveyard.

Sustainability is also a problem. It is hard to find agencies and institutions that are prepared to fund long-term archives. Fortunately, Germany's Federal Office for Radiation Protection has committed to maintaining the ERA database — an important asset for the radiobiology community.

The European Commission's STORE project will act as a data warehouse and radiobiological resource directory. Its importance is recognized by

the Multidisciplinary European Low-Dose Initiative (www.melodi-online.eu), which coordinates policy on low-dose radiation research.

Paul N. Schofield *University of Cambridge, UK.*

ps@mole.bio.cam.ac.uk

Soile Tapio *Helmholtz Zentrum München, Institute of Radiation Biology (ISB), Germany.*

Bernd Grosche *Federal Office for Radiation Protection, Germany.*

The politics of climate (dis)belief

The most telling feature of the climate-sceptic movement (aside from the large amount of money behind it) is that it is organized along the left–right political axis, with the left generally being sympathetic to climate science and the right far less so.

Liberals usually view science as a force for change that could benefit society. For conservatives, science typically serves to reinforce the status quo by making society more efficient and more powerful. This is not to brand the right as anti-science (see *Nature* 468, 508; 2010): as an objective truth, science is an appealing bulwark against the relativism of liberals.

Scepticism about global warming illustrates the right's difficulty in conceptualizing the group (rather than the individual) as a political actor. Conservatives traditionally believe that the course of history is decided by a few heroic figures — Churchill, Napoleon, and so on. The left tends to sideline such figures in favour of the mass movements they spearheaded. The right's popular argument that global warming is a hoax neatly demonstrates this. After all, a hoax demands a hoaxer, a 'heroic villain' who is faking data and distributing bribes behind the scenes.

If one believes in mass

movements, it is easy to imagine a mass movement of waste — a kind of rotten plebiscite cast against our planet. If one does not, global warming cannot help but seem unlikely, no matter how strong the evidence.

Francis Nicholson *Coventry, UK.*
francisnicholson@gmail.com

How to conserve the tropics as they warm

To make tropical forests more resilient to climate change, we need a coordinated effort to refocus conservation tools at regional and international levels.

The tools include expansion of protected areas, control of fires, and application of REDD policy ('reduced emissions from deforestation and forest degradation'). The latter is intended to protect forest carbon but lacks explicit mechanisms for increasing forest resilience.

These conservation instruments should be focused on two goals. First, they should be deployed to increase the large-scale connectivity of tropical forests, especially across latitudinal and elevational gradients, to facilitate range shifts by tropical species in response to future climate change. Second, they should be coordinated to reduce or halt agricultural expansion in areas of rapid deforestation, especially when such areas are also susceptible to drying, as in the Amazon's arc of deforestation.

The biodiversity benefits of REDD projects and new protected areas would be augmented by strategically locating them to protect connectivity between major ecozones — for example, between the Amazon lowlands and the uplands of the Brazilian and Guiana shields — or to span large-scale moisture gradients, as in the Central Amazonian Conservation Corridor.

In tropical Asia, the strategic use of REDD projects could help to link existing protected areas into large-scale conservation networks in central Borneo, in the forests along the border of Thailand and Myanmar and in the Annamite Mountains of Laos and Vietnam.

Similarly, a more strategic approach is needed for fire-control education and regulation. Although they will always be important in southeast Asia, we can predict when these measures will be crucial: after El Niño events, for example, which can dry out Indonesia's and Malaysia's tropical forests and increase the risk of huge fires.

Jedediah Brodie *University of Montana, USA.*

jedediah.brodie@gmail.com

Eric Post *Pennsylvania State University, USA.*

William Laurance *James Cook University, Australia.*

Faraday on the fiscal benefits of science

In considering Daniel Sarewitz's view of the value of scientific research in today's difficult economic times (*Nature* 468, 135; 2010), it is worth recalling physicist Michael Faraday's reply in the 1850s to William Gladstone, then British chancellor of the exchequer. Questioned about the practical value of electricity, Faraday answered: "One day, sir, you may tax it."

Michael Polymenis *Texas A&M University, USA.*
polymenis@tamu.edu

CONTRIBUTIONS

Items for Correspondence may be submitted to **correspondence@nature.com** after consulting the author guidelines at <http://go.nature.com/cMCHno>.

A cloudy view of exoplanets

The lack of absorption features in the transmission spectrum of exoplanet GJ 1214b rules out a hydrogen-rich atmosphere for the planet. It is consistent with an atmosphere rich in water vapour or abundant in clouds. [SEE LETTER P.669](#)

DRAKE DEMING

Sometimes the most telling evidence comes not from what is observed but from what is not observed. On page 669 of this issue, Bean and colleagues¹ report results of the latter type for the transiting 'super-Earth' exoplanet GJ 1214b.

This nearby world² (it is only about 13 parsecs away from Earth) belongs to the special category of transiting planets. When a planet transits — passes in front of its star as seen from the vantage point of Earth — we can measure its radius from the amount of stellar light that it blocks. By adding precision spectroscopic data, we can also determine its mass from the Doppler 'wobble' that it induces in the parent star's motion. Knowing the mass and radius of an exoplanet is a major step towards characterizing its nature. The mass and radius of GJ 1214b imply that it almost certainly has a massive atmosphere³.

In their study, Bean *et al.*¹ have pushed the methodology even farther than measuring the mass and radius of GJ 1214b. Their measurements offer the first direct probe of the atmosphere of an extrasolar super-Earth. Super-Earths are planets two to ten times more massive than Earth, and GJ 1214b weighs in at 6.5 Earth masses. Specifically, the authors measured the amplitude of the transit — the amount of starlight that the planet blocks — as a function of wavelength. Molecules such as water vapour in the planet's atmosphere can absorb starlight during the transit, and can do so more strongly at some wavelengths than at others, making the amplitude of the transit wavelength-dependent. The pattern of absorption potentially allows specific molecules to be identified.

Using data of exquisite sensitivity, Bean *et al.* show that the transmission spectrum of GJ 1214b is a smooth function of wavelength, with no bumps or wiggles that can be attributed to absorption by atmospheric molecules. It is this absence of specific spectral features that makes the results so intriguing. The simplest molecule, molecular hydrogen, is the easiest to measure, albeit indirectly. Molecular hydrogen produces no absorption features of its own at readily measured wavelengths, but its low molecular mass allows the putative atmosphere

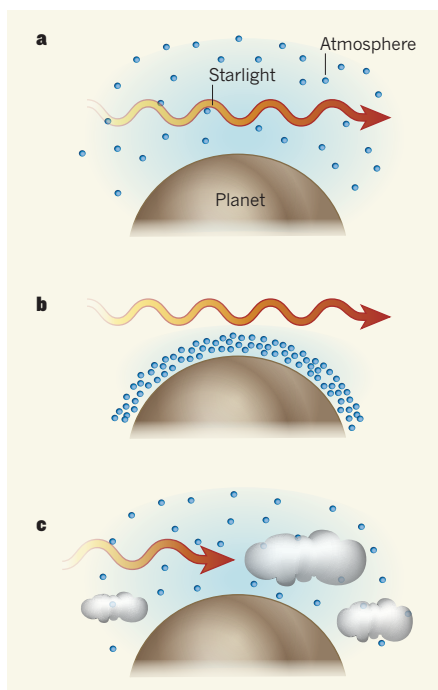


Figure 1 | Possible exoplanet atmospheres.

a, Hydrogen-rich atmospheres are extended in height, allowing starlight to interact with many absorbing molecules, and producing absorption signatures in the planet's transmission spectrum during transit. **b**, Hydrogen-poor atmospheres have high average molecular mass, and are concentrated at low levels, where most starlight misses the potentially absorbing molecules. **c**, Clouds in the atmospheres of transiting planets can block starlight, so that no — or very weak — absorption features are seen in the transmission spectrum. Bean *et al.*¹ find that the transmission spectrum of exoplanet GJ 1214b rules out a hydrogen-rich atmosphere and is consistent with either a hydrogen-poor atmosphere rich in water vapour or an atmosphere abundant in clouds and haze.

to extend to high altitudes. This spreads all of the constituents of the atmosphere over a greater height range, and allows transmitted starlight to interact with many absorbing atoms and molecules (Fig. 1a). Transmission spectra of gas-giant exoplanets^{4,5} show detectable spectral features largely for this reason. One signature of a hydrogen-rich atmosphere surrounding a transiting super-Earth will therefore be the ease with which the absorption features are detected.

Bean and colleagues' high-precision spectral data¹ rule out a hydrogen-rich atmosphere for GJ 1214b — a significant advance in the field of exoplanetary atmospheric science.

An irony of transit spectroscopy is that atmospheres rich in strongly absorbing complex molecules but poor in weakly absorbing hydrogen will not necessarily lead to a strong absorption signal. Paradoxically, they will tend to produce an absence of spectral absorption features. Hydrogen-poor atmospheres, having greater average molecular masses than hydrogen-rich atmospheres, are pulled by a planet's gravity to lower altitudes, where they intercept relatively few photons from the parent star (Fig. 1b). These low-lying atmospheres, even if they are rich in complex molecules, produce very weak absorption features⁶.

One possible interpretation of Bean and colleagues' results¹ showing a lack of absorption features is that this extrasolar super-Earth has an atmosphere rich in molecules heavier than hydrogen. Among molecules heavier than molecular hydrogen, the most cosmically abundant possibility is water. Hence, one particularly intriguing explanation for the authors' results is that the planet is surrounded by an atmosphere rich in water vapour. However, another — and at the moment equally valid — interpretation of their data puts clouds in view for exoplanet transit spectroscopy, both literally and figuratively.

Bean and colleagues' observations are consistent with abundant clouds and haze in the atmosphere of GJ 1214b. Clouds in the atmospheres of giant exoplanets were inferred from the first detection of an exoplanet atmosphere⁴, and other results for giant exoplanets have conclusively demonstrated the existence of hazy atmospheres⁷. Clouds and haze intercept and block starlight as it passes through the atmospheres of transiting planets (Fig. 1c), weakening or totally obscuring absorption features. In addition to real clouds, figurative clouds have recently gathered over exoplanet transit spectroscopy: detections of molecular absorptions in data from the Hubble Space Telescope for several giant exoplanets have recently been challenged, and attributed to uncorrectable instrumental effects⁸.

Fortunately, both the literal and figurative clouds should clear for transit spectroscopy

of exoplanets. Spectroscopy of GJ 1214b in the near infrared has already been scheduled for Hubble's Wide Field Camera 3 (WFC3). WFC3 observations will probe a longer wavelength than was available to Bean *et al.*, and hazy atmospheres can often be clearer at longer wavelengths. As for giant planets, a new and extensive Hubble programme using WFC3 should clarify many questions concerning their molecular absorptions.

On a longer timescale, astronomers await the advent of the James Webb Space Telescope, which will not only provide excellent sensitivity, but also operate at long infrared wavelengths. At sufficiently long infrared

wavelengths, haze and clouds tend to become transparent. Moreover, many molecules have their strongest absorption bands in the long-wavelength infrared region. Sufficiently strong bands can imprint detectable signals on the small portion of the transmitted light that misses the clouds. The James Webb Space Telescope should blow away any remaining clouds surrounding exoplanet spectroscopy, and give us the clearest view yet. ■

Drake Deming is in the Solar System
Exploration Division, NASA Goddard Space
Flight Center, Greenbelt, Maryland 20771, USA.
e-mail: leo.d.deming@nasa.gov

1. Bean, J. L., Kempton, E. M.-R. & Homeier, D. *Nature* **468**, 669–672 (2010).
2. Charbonneau, D. *et al. Nature* **462**, 891–894 (2009).
3. Miller-Ricci, E. & Fortney, J. J. *Astrophys. J.* **716**, L74–L79 (2010).
4. Charbonneau, D., Brown, T. M., Noyes, R. W. & Gilliland, R. W. *Astrophys. J.* **568**, 377–384 (2002).
5. Redfield, S., Endl, M., Cochran, W. D. & Koesterke, L. *Astrophys. J.* **673**, L87–L90 (2008).
6. Miller-Ricci, E., Seager, S. & Sasselov, D. *Astrophys. J.* **690**, 1056–1067 (2009).
7. Pont, F., Knutson, H., Gilliland, R. L., Moutou, C. & Charbonneau, D. *Mon. Not. R. Astron. Soc.* **385**, 109–118 (2008).
8. Gibson, N. P., Pont, F. & Aigrain, S. *Mon. Not. R. Astron. Soc.* (in the press); preprint at <http://arxiv.org/abs/1010.1753> (2010).

CANCER

Chemotherapy counteracted

Resistance of tumour cells to chemotherapy can severely affect the efficacy of this anticancer treatment. The non-tumour cells of the organ in which the tumour resides may aid the emergence of such resistance.

URBAN EMMENEGGER & ROBERT S. KERBEL

Most cancer-related deaths are due to drug resistance and/or metastatic spread of tumour cells. These two properties of cancer cells have often been viewed — and studied — as separate processes. However, increasingly, this is changing. For instance, cancer stem cells have been shown¹ not only to be resistant to diverse anticancer agents, but also to act as the seeds for germinating metastases. In a paper in *Cell*, Gilbert and Hemann² describe another particularly interesting example of this deadly relationship. They demonstrate that cancer therapy can acutely alter a tumour's surrounding tissue and organ environment to promote cancer-cell survival, and so to facilitate metastatic tumour growth and drug resistance. These observations are potentially relevant to enhancing the efficacy of chemotherapy.

Gilbert and Hemann study a mouse model of Burkitt's lymphoma, a cancer of the lymphatic system. They treat the mice with doxorubicin — a DNA-damaging chemotherapeutic agent that is often used to treat human cancers, including lymphomas and breast carcinoma. They note that, as is often the case, tumour cells in most organs respond to this drug, but some cells survive and are eventually detectable, in this case mainly in the thymus gland (Fig. 1). The authors ask why.

They find that doxorubicin induces changes in the expression of several genes in the thymus. Among the genes affected, two seem to be

possible culprits in chemoresistance: the gene encoding the cytokine IL-6 and that encoding a protein called Timp-1. On more detailed studies of IL-6, Gilbert and Hemann find that the source of this protein is thymic blood vessels. This observation adds to previous studies³, which also suggested that endothelial cells (which line blood vessels) contribute to tumour growth by secreting cytokines — or, as they were more aptly called, angiocrines.

A stress-response signalling pathway involving the enzyme p38 MAPK mediates acute IL-6 release by endothelial cells. Gilbert and

Hemann find that IL-6 subsequently acts in a paracrine manner to promote the survival of a small number of doxorubicin-treated tumour cells that lurk in the thymus and can eventually cause extensive metastases (Fig. 1a). IL-6 achieves this by inducing the expression of Bcl-X_L — a protein that inhibits programmed cell death. These results add a fascinating chapter to emerging research on the nature of acute, reactive cytokine responses in host tissues that are induced by cytotoxic anticancer therapies and may subsequently act to blunt the efficacy of the therapy⁴.

Tumour-cell-associated IL-6 secretion has been linked⁵ to chemoresistance in several tumour types, and even the role of tumour-associated endothelial cells in mediating chemoresistance is not completely unexpected. The tumour vasculature provides cancer cells with oxygen and nutrients, is a rich source of growth and survival factors, and regulates the influx of bone-marrow-derived cells with tumour-promoting activities³. Furthermore, the vascular bed is a fertile ground for cancer stem cells, which are particularly chemoresistant^{1,6}.

By showing that endothelial cells mediate

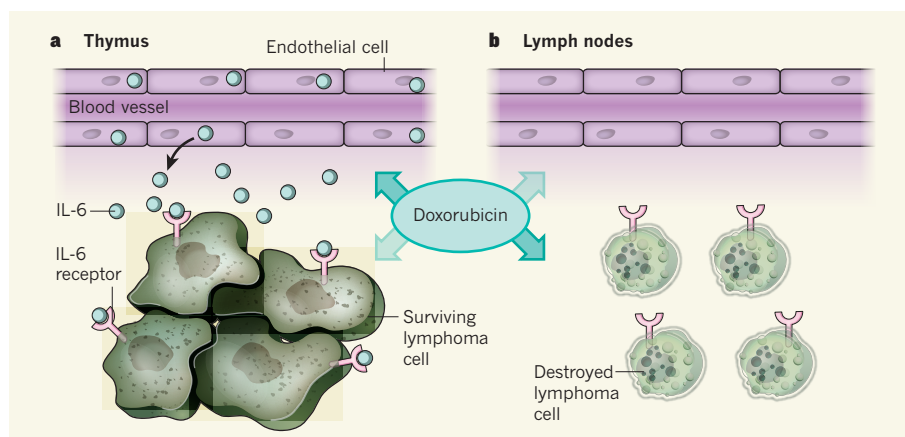


Figure 1 | Endothelial stress response and chemoresistance. a, Gilbert and Hemann² find that the chemotherapeutic drug doxorubicin leads to an acute stress response in the tumour vasculature of the thymus that involves the secretion of IL-6 and other factors. IL-6 then acts in a paracrine fashion to promote the survival of lymphoma cells expressing the IL-6 receptor. b, In the absence of such an endothelial-cell stress response in lymph nodes, doxorubicin can destroy lymphoma cells.

the chemotherapy-associated stress response, and that this may reinforce chemoresistance and the tumour-promoting properties of this vascular niche, Gilbert and Hemann extend the previous findings. For reasons that are not yet known, the nature of the stress response seems to vary depending on the anatomical location of the vascular bed²: in the authors' model, the lymphoma cells preferentially proliferated in the thymus gland but not in lymph nodes (Fig. 1). These results may help to explain the phenomenon of 'mixed responses' — the response of tumours to systemic chemotherapy in one organ site but not in another.

As for the implications of Gilbert and Hemann's data for treating cancer, the results suggest that the outcome of chemotherapy could be improved by blunting the endothelial-cell-mediated stress response associated with treatment. First, however, several issues must be considered.

Treatment-induced IL-6 secretion is not unique to the administration of doxorubicin or to Burkitt's lymphoma. Other anticancer treatments such as the chemotherapeutic agent paclitaxel and radiation therapy also facilitate IL-6 release by tumour cells^{2,7}. But is IL-6 secretion in response to other cytotoxic agents the same in terms of extent and temporal and spatial patterning as that following doxorubicin administration? Does this phenomenon also apply to metronomic chemotherapy — an emerging form of chemotherapy administration characterized by frequent, often daily, extended administration of small doses of conventional chemotherapeutic drugs without major breaks, which is thought to operate primarily through antiangiogenic effects⁸? And how crucial is the role of factors other than IL-6 — for example, Timp-1?

In Gilbert and Hemann's Burkitt's lymphoma model, the doxorubicin-associated acute IL-6 release apparently contributes to inducing senescence in the tumour's underlying support tissue (stroma). In turn, sustained senescence-associated cytokine secretion may provide long-term chemoresistance cues to tumour cells⁹. It will therefore be necessary to study whether impairing the acute phase of this stress response is sufficient to overcome chemoresistance.

Gilbert and Hemann could partially decrease doxorubicin-induced secretion of IL-6 — and possibly other cytokines — by treating the mice with a VEGF-receptor antagonist, thus blocking VEGF function, which is to mediate blood-vessel growth. Is this more proximal approach of blunting the endothelial-cell stress response superior to selective anti-IL-6 therapy? And could adding anti-IL-6 therapy further improve the results achieved with combination regimens using chemotherapy and antiangiogenic agents?

So far, the ongoing clinical trials — mainly involving single agents — on several inhibitors of the IL-6 signalling pathways have produced

mixed results¹⁰. But although most tumours may not respond to single-agent anti-IL-6 treatment, simultaneous chemotherapy may make tumours vulnerable to such a therapy. Moreover, testing for the expression of IL-6 receptors on a patient's tumour cells should help to predict whether a patient would benefit from using IL-6-inducing chemotherapy combined with anti-IL-6 therapy. ■

Urban Emmenegger and Robert S. Kerbel are at the Sunnybrook Research Institute and Odette Cancer Centre, Sunnybrook Health Sciences Centre, Toronto, Ontario M4N 3M5, Canada. They are also at the University of Toronto.

e-mails: robert.kerbel@sri.utoronto.ca; urban.emmenegger@sri.utoronto.ca

1. Pang, R. et al. *Cell Stem Cell* **6**, 603–615 (2010).
2. Gilbert, L. A. & Hemann, M. T. *Cell* **143**, 355–366 (2010).
3. Butler, J. M., Kobayashi, H. & Rafii, S. *Nature Rev. Cancer* **10**, 138–146 (2010).
4. Kerbel, R. S. & Ebos, J. M. L. *Nature Med.* **16**, 1084–1085 (2010).
5. Wang, Y. et al. *Cancer Lett.* **295**, 110–123 (2010).
6. Nie, D. *Front. Biosci. (Schol. Edn)* **2**, 184–193 (2010).
7. Puzsai, L. et al. *Cytokine* **25**, 94–102 (2004).
8. Pasquier, E., Kavallaris, M. & André, N. *Nature Rev. Clin. Oncol.* **7**, 455–465 (2010).
9. Rodier, F. et al. *Nature Cell Biol.* **11**, 973–979 (2009).
10. Dorff, T. B. et al. *Clin. Cancer Res.* **16**, 3028–3034 (2010).

R.S.K. declares competing financial interests; see online article for details.

NEUROSCIENCE

Sexy circuits

As in humans, the actions and reactions of male and female fruitflies during courtship are quite distinct. The differences seem to lie in gender-specific neural interpretations of the same sensory signals. SEE LETTER P.686

RICHARD BENTON

The self-help relationship guide *Men are from Mars, Women are from Venus*¹ stresses the differences in how men and women convey and interpret feelings through words and actions. During courtship, male and female *Drosophila* fruitflies also communicate distinct messages using several sensory stimuli (visual, chemical and acoustic) to evoke very different behaviours². Three papers^{3–5}, including one by Ruta et al.³ on page 686 of this issue,

probe deeply into the neural circuits underlying fruitfly courtship and find that these gender-specific responses may be due not to differences in how external signals are initially sensed, but rather — perhaps similarly to ourselves — in how they are interpreted by the brain.

The mating ground for fruitflies is reminiscent of a Roman orgy: typically a crowded, overripe fruit where these animals feed. Males take the lead in deciding who to court, and assess other flies on the basis of their

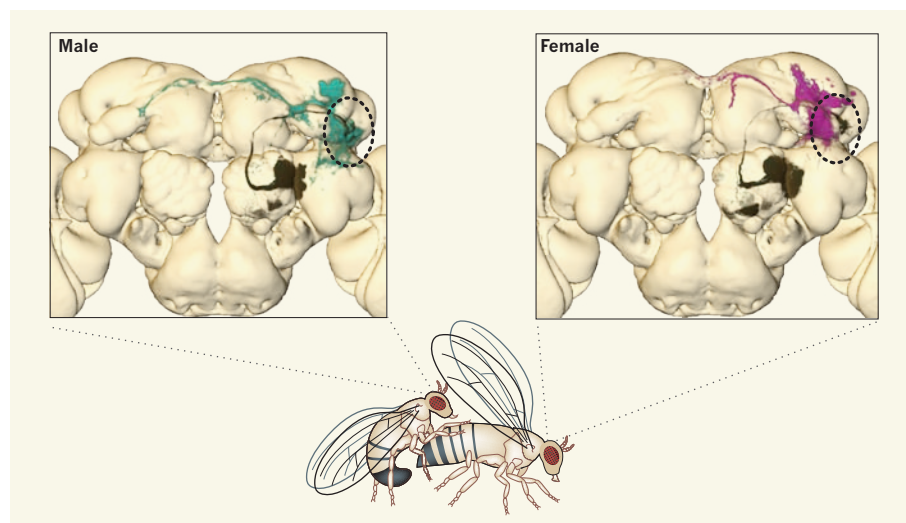


Figure 1 | Sexual dimorphisms in the fly brain⁵. Sex-specific organization of male (blue) and female (pink) neurons in higher olfactory centres may determine the interpretation of pheromone signals transmitted from the fly 'nose' by neurons that are largely similar in both sexes (black). The dashed oval marks a region of putative male-specific connections, absent in females, between these central and more peripheral populations of neurons. (Brain images by Gregory Jefferis from data in ref. 5.)

appearance, smell and taste². On identifying a suitable partner — female, young (preferably virgin) and of the same species — the suitor serenades her with a love song produced by the vibration of one of his wings⁶. The behaviour of the female seems more passive, or at least too subtle for human voyeurs to detect easily; but it is she who ultimately decides whether to allow the male to initiate copulation.

These gender-specific differences in courtship behaviour are largely determined by a male-specific transcription factor called *Fru^M*, which is expressed in 1–2% of the more than 100,000 neurons in the fly nervous system⁷. Neurons expressing this factor (*Fru^M* neurons) include sensory cells for odours, tastes, sounds and sights; central neurons in the brain; and motor neurons that control wing and leg movements^{7,8}. This hints that *Fru^M* neurons form an interconnected circuit^{7,8}. Although *Fru^M* is expressed and essential only in males, female flies contain similar classes of neurons that are required for reproductive behaviours such as egg-laying⁹.

Surprisingly, initial work⁷ reported no dramatic sexual dimorphisms of these neural pathways — apart from differences in *Fru^M* expression — that could account for the distinct male and female courtship behaviours. More recent investigations^{10–12}, however, found that small subpopulations of these neurons have gender-specific properties. The three new studies^{3–5} take a closer look at *Fru^M* neurons in males and their counterparts in females to address two fundamental questions: do they really form an interconnected circuit; and how widespread are sexual dimorphisms? To scrutinize these neural pathways, each team used a distinct approach — a worthy reminder of the power of fly genetics for dissecting brain structure and function.

Yu *et al.*⁴ devised an ‘intersectional’ genetic strategy to express reporter proteins in small, consistent subsets of *Fru^M* neurons in individual brains, which allowed them to visualize the projections of these neurons with greater clarity than before. Cachero *et al.*⁵ used a clonal marking method, in which subpopulations of *Fru^M* neurons that derive from the same neural stem cell were labelled.

The authors^{4,5} applied each approach exhaustively, to identify more than 100 distinct groups of *Fru^M* neurons throughout the nervous system. Moreover, they reconstructed *in silico* a comprehensive (although hypothetical) ‘wiring diagram’ of the *Fru^M* neural circuits, by digitally reconstructing the morphology of these neurons’ projections — dendrites and axons, which receive and transmit neural signals, respectively — and by integrating the mapped neurons into a common reference brain (Fig. 1). This allowed them to predict the flow of information from one set of neurons to another, as well as to locate brain regions essential for integrating the diverse types of sensory message that pass between males and females during courtship.

In contrast to these ‘global’ analyses, Ruta *et al.*³ focused on a single olfactory pathway that is responsive to *cis*-vaccenyl acetate (cVA) — a male-specific pheromone that promotes sexual receptivity in females but inhibits courtship in males¹³. To visualize the neural components of this pathway, the authors expressed in all *Fru^M* neurons a photoactivatable reporter protein, PA-GFP, that can be converted from a low to a high fluorescence state with a pulse of high-energy light¹². They then activated PA-GFP in precisely the brain area that is innervated by the axons of cVA-responsive olfactory sensory neurons. As this region also contains the dendrites of neurons to which these sensory cells connect, PA-GFP was simultaneously activated in this second population of neurons, and its diffusion revealed the neurons’ axonal projections in higher brain centres.

Through this elegant, iterative photolabelling approach, Ruta *et al.* could thus move stepwise through the brain to the output neurons that are likely to link directly with motor pathways. Although the circuit they define corresponds to just a small piece of the wiring diagram defined in the larger-scale anatomical studies^{4,5}, Ruta *et al.*³ go one crucial step further by confirming that these cells are functionally connected. They accomplish this by recording cVA-evoked activity in each of the identified neurons — an impressive achievement deep in the tiny fly brain — and by demonstrating that this activity depends on the presence of intact circuit components upstream.

What do these findings reveal about the neural control of courtship? First, they offer a draft roadmap of a circuit underlying a complex animal behaviour. Although relatively simple neural circuits for reflexes (such as gill withdrawal in the marine slug *Aplysia*¹⁴ or the escape response in the fruitfly¹⁵) have been delineated, the *Fru^M* circuit is the most sophisticated to be mapped so thoroughly, sometimes down to single-neuron resolution. As the male courts his target female, these neurons must integrate diverse sensory information. Yet, as Ruta and co-workers show for the cVA response pathway, the circuit can be surprisingly shallow, with as few as four neurons potentially linking sensory input to motor output. The techniques and tools these studies^{3–5} introduce also make it feasible to test the functional contributions of individual subpopulations of *Fru^M* neurons to these behaviours in males and females.

In addition, these studies identify an unexpected number of new sexual dimorphisms in *Fru^M* neurons, including several cases in which certain groups of these cells are present only in the male or the female brain. They also detect hundreds of putatively distinct connections between the axons and dendrites of *Fru^M* neurons that are common to both sexes (Fig. 1). Although these anatomical (and physiological) observations do not establish a causal relationship between dimorphic wiring and behaviour, they indicate that widely distributed, although



50 Years Ago

Serengeti Shall Not Die by Dr. Bernhard and Michael Grzimek — This is the book of the film. Despite the many fine illustrations, the book cannot compete with the film in showing the space of the Serengeti National Park and the beauty of its animals in motion ... It is a true adventure story. After the success of their first film “No Room for Wild Animals”, the Grzimeks offered part of its revenues for purchase of land to increase the Serengeti National Park, but were persuaded instead to study the animal populations there; that study entailed learning to fly, and that entailed getting permission from their wives.

From *Nature* 3 December 1960

100 Years Ago

We geologists who were privileged to take part in the journey to Spitsbergen before the meeting of the Geological Congress in Stockholm had good reason to count ourselves fortunate ... Not many hours after sinking Bear Island in the southward ... we began to meet ice-floe; which soon thickened, so that we had to slow down and eventually to turn southward and westward for more open water. Again and again during the day was this experience repeated, a chilly ice-blink always paling the hazy sky to the north and east as we threaded our zigzag course amid the floes, on which inquisitive seals shifted uneasily, doubtful whether to regard us as dangerous or not ... Soon, very gently, the haze thinned away; the northern sun shimmered again over the smooth olive sea, burnishing the floes into silver; and then, gradually, an exquisite panorama of peaks and glaciers was unveiled in front of us ... and we knew that this was Spits-bergen, and worthy of its name.

From *Nature* 1 December 1910

often subtle, gender-specific neural connectivity may account for the different behaviour of males and females. How Fru^M specifies the 'male' properties of this circuit during development remains a fascinating unanswered question.

Finally, it is notable that nearly all of these dimorphisms reside in central brain neurons. This suggests that males and females detect many of the same external signals but interpret them differently to produce distinct behavioural responses. Intriguingly, earlier work⁶ showed that courtship circuitry in the thorax of female flies also contains motor-neuron output pathways that can produce wing-evoked

love songs when artificially stimulated. Thus, in fruitflies at least, the principal determinants underlying the distinct behaviour of males and females seem to reside in the mind. ■

Richard Benton is in the Center for Integrative Genomics, Faculty of Biology and Medicine, University of Lausanne, CH-1015 Lausanne, Switzerland.
e-mail: richard.benton@unil.ch

1. Gray, J. *Men are From Mars, Women are From Venus* (HarperCollins, 1992).
2. Dickson, B. J. *Science* **322**, 904–909 (2008).
3. Ruta, V. *et al. Nature* **468**, 686–690 (2010).
4. Yu, J. Y. *et al. Curr. Biol.* **20**, 1602–1614 (2010).

5. Cachero, S., Ostrovsky, A. D., Yu, J. Y., Dickson, B. J. & Jefferis, G. S. *Curr. Biol.* **20**, 1589–1601 (2010).
6. Clyne, J. D. & Miesenböck, G. *Cell* **133**, 354–363 (2008).
7. Stockinger, P., Kvitsiani, D., Rotkopf, S., Tirián, L. & Dickson, B. J. *Cell* **121**, 795–807 (2005).
8. Manoli, D. S. *et al. Nature* **436**, 395–400 (2005).
9. Kvitsiani, D. & Dickson, B. J. *Curr. Biol.* **16**, R355–R356 (2006).
10. Kimura, K. *et al. Neuron* **59**, 759–769 (2008).
11. Kimura, K., Ote, M., Tazawa, T. & Yamamoto, D. *Nature* **438**, 229–233 (2005).
12. Datta, S. R. *et al. Nature* **452**, 473–477 (2008).
13. Kurtovic, A., Widmer, A. & Dickson, B. J. *Nature* **446**, 542–546 (2007).
14. Glanzman, D. L. *Neurobiol. Learn. Mem.* **92**, 147–154 (2009).
15. Allen, M. J., Godenschwege, T. A., Tanouye, M. A. & Phelan, P. *Semin. Cell Dev. Biol.* **17**, 31–41 (2006).

millisecond timescale, and can thus visualize the movements of proteins that fold in microseconds as they repeatedly fold and unfold³. This opens up the prospect of refining the force fields used in molecular dynamics simulations, so that the simulations can be made valid over even longer timescales. It also offers the hope of being able to correctly predict the biologically active structure of a protein starting from the unfolded state. More experimental data about fast-folding proteins are essential to realize these desirable goals. Fast-folding proteins are also of interest because they are predicted to undergo 'downhill' folding, in which no significant energy barrier is encountered. Further experimental confirmation of downhill folding would provide crucial evidence in support of an important mechanistic model of protein folding — the energy-landscape theory⁴.

Since the mid-1990s, resistive heating⁵ (in which a sample is warmed up by passing an electric current through it) and nanosecond laser T-jumps⁶ have been used in studies to initiate the refolding of proteins from their cold denatured states. Cold denaturation occurs at low temperatures when water molecules bind to hydrophobic amino acids that are normally buried inside proteins. The method generally

ANALYTICAL BIOCHEMISTRY

Weighing up protein folding

Labelling molecules by fast oxidation allows mass spectrometry to study protein folding at submillisecond time resolution. The method also brings a wealth of structural information about protein folding within reach.

MARTIN GRUEBELE

When it comes to protein-folding studies, mass spectrometry can provide much structural information. But its time resolution has been insufficient to detect the fastest folding events, which occur on the microsecond timescale¹. Chen *et al.*² now report a solution to this problem in their study of the submillisecond folding of the barstar protein, published in the *Journal of the American Chemical Society*. They have married two techniques that could potentially reach microsecond resolution: laser temperature jumping

(T-jumping), which initiates protein-folding reactions, and fast photochemical oxidation of the protein (FPOP), which allows mass spectrometry to monitor how far folding has progressed. Their technique should enable more structural information to be obtained from studies of protein-folding kinetics — crucial for developing the next generation of computational methods for simulating protein dynamics, and to allow more complex proteins and protein complexes to be studied experimentally.

There is currently great interest in fast-folding proteins. Computational simulations of protein folding have extended into the

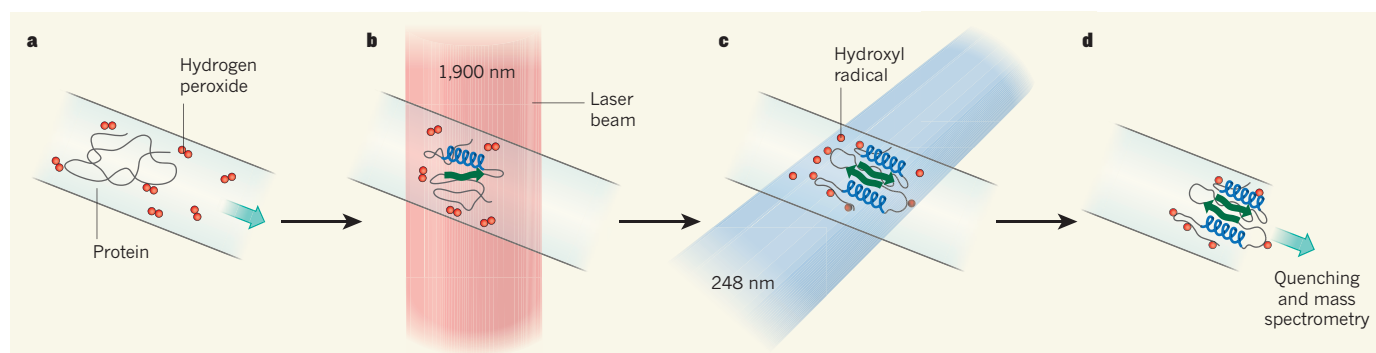


Figure 1 | Improving the time resolution of mass spectrometry in protein-folding studies. Chen *et al.*² report a method that allows fast protein folding to be monitored using mass spectrometry. **a**, A solution of unfolded protein and hydrogen peroxide flows through a capillary tube into the reaction region. **b**, There, a T-jump — a laser pulse of wavelength 1,900 nanometres — initiates refolding of the protein. **c**, After a time delay, an ultraviolet laser pulse (wavelength 248 nm) breaks the peroxide into hydroxyl radicals. The radicals

rapidly oxidize solvent-exposed amino acids in the protein (red dots become attached to the protein), increasing the protein's mass. The longer the delay, the more the protein is folded (exposing fewer amino acids to solvent), and so less mass is added. **d**, Finally, the protein sample is flushed out of the capillary, excess peroxide is removed and mass spectrometry is used to determine the extent of protein oxidation (and so of protein folding). (Figure based on an idea by Jiawei Chen.)

appearance, smell and taste². On identifying a suitable partner — female, young (preferably virgin) and of the same species — the suitor serenades her with a love song produced by the vibration of one of his wings⁶. The behaviour of the female seems more passive, or at least too subtle for human voyeurs to detect easily; but it is she who ultimately decides whether to allow the male to initiate copulation.

These gender-specific differences in courtship behaviour are largely determined by a male-specific transcription factor called *Fru^M*, which is expressed in 1–2% of the more than 100,000 neurons in the fly nervous system⁷. Neurons expressing this factor (*Fru^M* neurons) include sensory cells for odours, tastes, sounds and sights; central neurons in the brain; and motor neurons that control wing and leg movements^{7,8}. This hints that *Fru^M* neurons form an interconnected circuit^{7,8}. Although *Fru^M* is expressed and essential only in males, female flies contain similar classes of neurons that are required for reproductive behaviours such as egg-laying⁹.

Surprisingly, initial work⁷ reported no dramatic sexual dimorphisms of these neural pathways — apart from differences in *Fru^M* expression — that could account for the distinct male and female courtship behaviours. More recent investigations^{10–12}, however, found that small subpopulations of these neurons have gender-specific properties. The three new studies^{3–5} take a closer look at *Fru^M* neurons in males and their counterparts in females to address two fundamental questions: do they really form an interconnected circuit; and how widespread are sexual dimorphisms? To scrutinize these neural pathways, each team used a distinct approach — a worthy reminder of the power of fly genetics for dissecting brain structure and function.

Yu *et al.*⁴ devised an ‘intersectional’ genetic strategy to express reporter proteins in small, consistent subsets of *Fru^M* neurons in individual brains, which allowed them to visualize the projections of these neurons with greater clarity than before. Cachero *et al.*⁵ used a clonal marking method, in which subpopulations of *Fru^M* neurons that derive from the same neural stem cell were labelled.

The authors^{4,5} applied each approach exhaustively, to identify more than 100 distinct groups of *Fru^M* neurons throughout the nervous system. Moreover, they reconstructed *in silico* a comprehensive (although hypothetical) ‘wiring diagram’ of the *Fru^M* neural circuits, by digitally reconstructing the morphology of these neurons’ projections — dendrites and axons, which receive and transmit neural signals, respectively — and by integrating the mapped neurons into a common reference brain (Fig. 1). This allowed them to predict the flow of information from one set of neurons to another, as well as to locate brain regions essential for integrating the diverse types of sensory message that pass between males and females during courtship.

In contrast to these ‘global’ analyses, Ruta *et al.*³ focused on a single olfactory pathway that is responsive to *cis*-vacenyl acetate (cVA) — a male-specific pheromone that promotes sexual receptivity in females but inhibits courtship in males¹³. To visualize the neural components of this pathway, the authors expressed in all *Fru^M* neurons a photoactivatable reporter protein, PA-GFP, that can be converted from a low to a high fluorescence state with a pulse of high-energy light¹². They then activated PA-GFP in precisely the brain area that is innervated by the axons of cVA-responsive olfactory sensory neurons. As this region also contains the dendrites of neurons to which these sensory cells connect, PA-GFP was simultaneously activated in this second population of neurons, and its diffusion revealed the neurons’ axonal projections in higher brain centres.

Through this elegant, iterative photolabelling approach, Ruta *et al.* could thus move stepwise through the brain to the output neurons that are likely to link directly with motor pathways. Although the circuit they define corresponds to just a small piece of the wiring diagram defined in the larger-scale anatomical studies^{4,5}, Ruta *et al.*³ go one crucial step further by confirming that these cells are functionally connected. They accomplish this by recording cVA-evoked activity in each of the identified neurons — an impressive achievement deep in the tiny fly brain — and by demonstrating that this activity depends on the presence of intact circuit components upstream.

What do these findings reveal about the neural control of courtship? First, they offer a draft roadmap of a circuit underlying a complex animal behaviour. Although relatively simple neural circuits for reflexes (such as gill withdrawal in the marine slug *Aplysia*¹⁴ or the escape response in the fruitfly¹⁵) have been delineated, the *Fru^M* circuit is the most sophisticated to be mapped so thoroughly, sometimes down to single-neuron resolution. As the male courts his target female, these neurons must integrate diverse sensory information. Yet, as Ruta and co-workers show for the cVA response pathway, the circuit can be surprisingly shallow, with as few as four neurons potentially linking sensory input to motor output. The techniques and tools these studies^{3–5} introduce also make it feasible to test the functional contributions of individual subpopulations of *Fru^M* neurons to these behaviours in males and females.

In addition, these studies identify an unexpected number of new sexual dimorphisms in *Fru^M* neurons, including several cases in which certain groups of these cells are present only in the male or the female brain. They also detect hundreds of putatively distinct connections between the axons and dendrites of *Fru^M* neurons that are common to both sexes (Fig. 1). Although these anatomical (and physiological) observations do not establish a causal relationship between dimorphic wiring and behaviour, they indicate that widely distributed, although



50 Years Ago

Serengeti Shall Not Die by Dr. Bernhard and Michael Grzimek — This is the book of the film. Despite the many fine illustrations, the book cannot compete with the film in showing the space of the Serengeti National Park and the beauty of its animals in motion ... It is a true adventure story. After the success of their first film “No Room for Wild Animals”, the Grzimeks offered part of its revenues for purchase of land to increase the Serengeti National Park, but were persuaded instead to study the animal populations there; that study entailed learning to fly, and that entailed getting permission from their wives.

From *Nature* 3 December 1960

100 Years Ago

We geologists who were privileged to take part in the journey to Spitsbergen before the meeting of the Geological Congress in Stockholm had good reason to count ourselves fortunate ... Not many hours after sinking Bear Island in the southward ... we began to meet ice-floe; which soon thickened, so that we had to slow down and eventually to turn southward and westward for more open water. Again and again during the day was this experience repeated, a chilly ice-blink always paling the hazy sky to the north and east as we threaded our zigzag course amid the floes, on which inquisitive seals shifted uneasily, doubtful whether to regard us as dangerous or not ... Soon, very gently, the haze thinned away; the northern sun shimmered again over the smooth olive sea, burnishing the floes into silver; and then, gradually, an exquisite panorama of peaks and glaciers was unveiled in front of us ... and we knew that this was Spits-bergen, and worthy of its name.

From *Nature* 1 December 1910

used to rapidly probe refolding is to measure the fluorescence of tryptophan amino-acid residues in a protein. Tryptophan residues buried inside the protein fluoresce differently from those exposed to water, so that fluorescence serves as a global probe of folding. By contrast, detection techniques such as infrared spectroscopy show promise for acquiring localized structural information from proteins, and are fast enough to be combined with the laser T-jump method for initiating folding reactions.

Chen *et al.*² now show that mass spectrometry could join the ranks of fast, structure-sensitive techniques for studying protein folding. The first step of their technique is to add hydrogen peroxide to a cold solution of a denatured protein (Fig. 1). By using a low concentration of peroxide at low temperature, the authors ensure that the protein does not rapidly react with the oxidizing agent. Next, a nanosecond laser T-jump is used to initiate refolding of the protein. After a set time delay, the sample is then irradiated with a nanosecond ultraviolet laser pulse, which breaks up some of the peroxide into hydroxyl radicals. These radicals exist for about a microsecond and efficiently oxidize solvent-exposed protein segments, changing the protein's mass. This is the FPOP step of the process⁷.

An increasingly large fraction of proteins becomes folded as time passes after the T-jump, which means that more of the amino acids become buried within the proteins' interiors. Progressively fewer amino acids are therefore exposed to solvent as folding proceeds, and so less mass is added to the protein by FPOP as the time delay between the T-jump and the FPOP step increases. By performing a series of experiments in which the time delay is varied, and then measuring the mass of the resulting protein samples using mass spectrometry, protein folding can be tracked. In practice, the protein solution flowed through the laser set-up in a capillary tube. Chen *et al.* collected the oxidized samples, quenched any remaining peroxide using a chemical scavenger, and then performed mass spectrometry on the quenched samples in a separate step.

The authors² used their T-jump–FPOP (TJFPOP) technique to study the refolding kinetics of denatured barstar as it adopts an intermediate conformation en route to the fully folded protein. The formation of the intermediate takes hundreds of microseconds, and had never before been observed using mass spectrometry techniques. The resulting spectra contained hundreds of peaks, and so the authors analysed only the centroid of the spectra. This simple approach limited the structural information that could be obtained, but the technique offers potentially much better time and structural resolution than was achieved in this proof-of-principle study. The ultimate time resolution of the FPOP step is about 1 microsecond, limited by the hydroxyl

radicals' diffusion rate and lifetime. And as the authors point out², if the oxidized protein samples were enzymatically degraded before mass spectrometry⁸, then analysis of the resulting fragments could pinpoint where oxidation had actually occurred. The TJFPOP technique could thus follow how amino acids in different parts of a protein become buried with time. Such a technique would be complementary to hydrogen-exchange mass-spectrometry methods, which track the formation of secondary structures in proteins by measuring how easily protons (H^+ ions) are exchanged between water and amino acids in the proteins⁹.

The TJFPOP approach has some drawbacks in its current implementation. The method requires a T-jump for every kinetic data point, whereas fluorescence and infrared-detection methods collect data continuously after a single T-jump. The TJFPOP method thus introduces additional noise compared with the other techniques, and requires larger amounts of sample. Chen and colleagues' approach is also less suitable for studies at high temperatures, because the radical precursor (hydrogen peroxide) would itself react with the protein sample. But precursors more benign than peroxide can be developed.

On the plus side, a strong advantage of TJFPOP is that the whole experiment could

easily be automated. But the real key to the utility of TJFPOP will be the development of suitable data-analysis techniques, to deconvolute the statistical mass distributions observed in the spectra and to analyse oxidation patterns of fragments. If these hurdles can be overcome, then the technique could provide truly massive amounts of detail about fast protein folding. ■

Martin Gruebele is in the Departments of Chemistry and of Physics, the Center for Biophysics and Computational Biology, and at the Beckman Institute, University of Illinois, 600 South Mathews Avenue, Urbana, Illinois 61801, USA.
e-mail: mgruebel@illinois.edu

1. Kubelka, J., Hofrichter, J. & Eaton, W. A. *Curr. Opin. Struct. Biol.* **14**, 76–88 (2004).
2. Chen, J., Rempel, D. L. & Gross, M. L. *J. Am. Chem. Soc.* **132**, 15502–15504 (2010).
3. Shaw, D. E. *et al. Science* **330**, 341–346 (2010).
4. Gruebele, M. *C.R. Biol.* **328**, 701–712 (2005).
5. Nölting, B., Golbik, R. & Fersht, A. R. *Proc. Natl Acad. Sci. USA* **92**, 10668–10672 (1995).
6. Ballew, R. M., Sabelko, J. & Gruebele, M. *Proc. Natl Acad. Sci. USA* **93**, 5759–5764 (1996).
7. Gau, B. C., Sharp, J. S., Rempel, D. L. & Gross, M. L. *Anal. Chem.* **81**, 6563–6571 (2009).
8. de Laureto, P. P., De Filippis, V., Di Bello, M., Zamboni, M. & Fontana, A. *Biochemistry* **34**, 12596–12604 (1995).
9. Tsui, V. *et al. Protein Sci.* **8**, 45–49 (1999).

PARASITOLOGY

Nematode debt to bacteria

The transition by certain nematode worms to plant parasitism, and possibly more generally to herbivory, is illuminated by an investigation into how nematodes acquired the protein weapons to penetrate the plant cell wall.

NOAH K. WHITEMAN & ANDREW D. GLOSS

In the *Iliad*¹, Homer chronicles how the Achaeans, after invading Trojan territory, built a mighty wall around their encampment to protect themselves. The Trojans retaliated with a multi-pronged assault, and with heavenly intercession the wall was breached.

According to remarkable findings published in *Proceedings of the National Academy of Sciences* by Danchin *et al.*², a similar multi-pronged attack is deployed by nematode worms that parasitize plant roots. Danchin *et al.* studied two lineages of nematode that are obligate plant endoparasites; that is, as an essential part of their life cycle they must breach the plant cell wall and enter living cells. The authors show that, over deep evolutionary time, these nematodes have incorporated into their genomes at least six distinct types

of bacterial genes encoding proteins that can modify the plant cell wall. These genes have subsequently undergone extensive gene duplication in the nematode lineages. A clear hypothesis emerging from this study is that the proteins encoded by these genes facilitated the invasion of the plant root, and perhaps herbivory in nematodes more generally.

Nematodes are important ecologically and hyperdiverse evolutionarily; most are parasitic³. Among the plant-parasitic nematodes that cause serious crop losses are the two lineages of root nematodes within a group (clade IV) of the Tylenchina, in which endoparasitism in plants evolved independently at least ten times⁴. These lineages — root-knot nematodes (RKN) and cyst nematodes (CN) — each have free-living stages that, as juveniles, invade root tissue, enter individual cells and then migrate within the roots to complete their

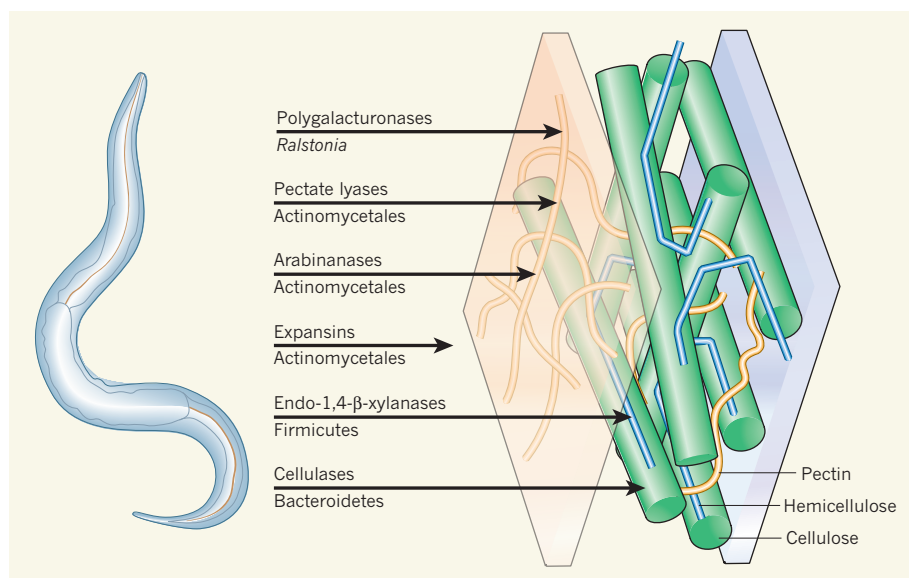


Figure 1 | A multi-pronged assault. Plant-parasitic nematodes possess a diverse suite of proteins capable of degrading plant cell walls. On the basis of phylogenetic analyses of genomic sequence data from nematode lineages, Danchin *et al.*² suggest that the distribution of genes encoding six families of cell-wall-modifying proteins is the result of multiple lateral gene transfers from bacteria to ancestral nematodes. The protein families are noted above the arrows, and the likely source bacteria below. The cell-wall targets of attack are pectin (orange), hemicellulose (blue) and cellulose (green).

development. This life history is distinct from that of other plant-parasitic nematodes, which insert structures called stylets into plant cells, but do not invade them.

The primary plant cell wall consists largely of polysaccharides, principally cellulose (a polymer of glucose), hemicellulose and branched polysaccharides including pectins and glycans. Bacteria and fungi are adept at overcoming these barriers and gaining entry to exploit the resources within cells. By contrast, animals are not typically well equipped for breaking down cell walls; to do so, various species — ranging from cows to termites and nematodes — have turned to bacterial genomes for assistance. Some of these arrangements rely on host–symbiont relationships. But a more subtle form of mutualism can occur as a result of lateral gene transfer (LGT), the movement of a gene from one species' genome to another, with subsequent vertical transmission in the new genome⁵.

Danchin *et al.*² searched whole-genome sequences of RKN and CN for genes encoding proteins that degrade or modify plant cell walls, and subjected them to phylogenetic analysis. The authors identified a diverse array of six families of genes with distinct functional roles in the invasion of plant cell walls (Fig. 1). Although cell-wall-modifying proteins of bacterial origin have been reported previously from plant-parasitic nematodes, the whole-genome data allowed Danchin *et al.* to identify six, probably independent, transfer events and subsequent gene duplications, resulting in the presence of more than 60 loci peppered throughout nematode genomes.

The authors infer that the timing of these events is ancient because the genes have certain

features that are not typical of bacteria, indicating a long period of divergence since the original transfer. Their phylogenetic analyses in nearly every case do not support hypotheses other than those indicating a bacterial origin for each gene family within the plant-parasitic nematode lineages.

Remarkably, the closest relatives of the nematode members for all six gene families include genes in soil bacteria, some of which are known plant symbionts or pathogens. This is evidence that potential bacterial donors and nematodes occur together in the same habitat, providing the ecological opportunity for LGT to occur. The sequencing of further plant-parasitic nematode genomes will allow more precise identification of the origin and elaboration of each gene family in relation to the ten or more independent evolutions of plant endoparasitism across the Tylenchina evolutionary tree. There is also the possibility that these genes occur in other, non-endoparasitic, nematode species.

To understand the full implications of these gene transfers, future studies should focus on identifying the functional and ecological role of each protein in model nematode species. Through antibody staining of proteins bearing a laterally acquired cellulose-binding module (CBM2), Danchin *et al.* demonstrate that some of these acquired proteins, in addition to being secreted into surrounding plant tissue, localize to the shells of eggs developing within nematodes. The experimental silencing of laterally acquired cell-wall-modifying proteins has, importantly, been shown to reduce nematode virulence in plants⁶. Whether any of the proteins are also required for successful egg laying remains unclear. Their localization to eggshells

suggests that one or more of them may have secondarily evolved roles in egg development, perhaps through an interaction with chitin — a glucose-based polymer found in nematode eggshells that is structurally very similar to cellulose. Interestingly, mechanisms conferring binding specificity for chitin have been identified in a CBM2 domain from an archaeal microorganism⁷. Screening for mutant worms showing abnormal egg development, following the silencing of CBM2-encoding genes, could reveal whether proteins that interact with the cell wall have been co-opted by nematodes to perform novel biochemical roles.

Plant-parasitic nematodes display the most extensive diversifications of functionally related, laterally acquired genes to have been identified in complex eukaryotes (organisms, such as animals, plants and fungi, with a membrane-bound nucleus, in contrast to bacteria and archaea). But ecologically significant LGT events have been discovered in other eukaryotes as well. Convergent strategies to parasitize plants are correlated with LGT from fungi to oomycetes, with a subset of these transferred genes representing secondary transfers from bacteria⁸. Similarly, the acquisition of bacterial genes for anaerobic metabolism has been extensively documented in protozoan parasites^{9–11}. Although LGT has been observed in non-parasitic eukaryotes, the cell-wall-modifying proteins in plant-parasitic nematodes represent yet another example of LGT that potentially prompted a major transition to an endoparasitic or herbivorous lifestyle.

The recent explosion of eukaryotic genome sequencing projects will facilitate further discovery of LGT events that could have enabled ecological transitions in environmentally and economically important parasites. Such studies will also offer unique opportunities to determine how laterally acquired genes evolve at both the single-gene and genome-wide scales. ■

Noah K. Whiteman and Andrew D. Gloss are in the Department of Ecology and Evolutionary Biology, University of Arizona, Tucson, Arizona 85721, USA.
e-mail: whiteman@email.arizona.edu

1. Lattimore, R. (transl.) *The Iliad of Homer* (Univ. Chicago Press, 1951).
2. Danchin, E. G. J. *et al.* *Proc. Natl Acad. Sci. USA* **107**, 17651–17656 (2010).
3. Hugot, J.-P., Baujard, P. & Morand, S. *Nematology* **3**, 199–208 (2001).
4. Holterman, H. *et al.* *Phytopathology* **99**, 227–235 (2009).
5. Keeling, P. J. & Palmer, J. D. *Nature Rev. Genet.* **9**, 605–618 (2008).
6. Lilley, C. J., Bakhetia, M., Charlton, W. L. & Urwin, P. E. *Mol. Plant Pathol.* **8**, 701–711 (2007).
7. Nakamura, T. *et al.* *J. Mol. Biol.* **381**, 670–680 (2008).
8. Richards, T. A. *et al.* *Curr. Biol.* **16**, 1857–1864 (2006).
9. Loftus, B. *et al.* *Nature* **433**, 865–868 (2005).
10. Carlton, J. M. *et al.* *Science* **315**, 207–212 (2007).
11. Morrison, H. G. *et al.* *Science* **317**, 1921–1926 (2007).

HIGH-TEMPERATURE SUPERCONDUCTIVITY

How the cuprates hid their stripes

Extensive mapping of local electronic structure in copper oxide superconductors reveals fluctuating stripe-like electron patterns that appear as a high-temperature precursor to superconductivity. [SEE LETTER P.677](#)

KATHRYN A. MOLER

Copper oxide compounds, known as the cuprates, may be most famous for their high-temperature superconducting state. But aficionados are fascinated by a phenomenon called the pseudogap, which appears at yet higher temperatures. The pseudogap's basic nature, as well as its relationship to superconductivity and to a menagerie of other possible related states of matter, is poorly understood. On page 677 of this issue, Parker *et al.*¹ report the observation in one family of cuprate superconductors of a fluctuating stripe-like electron arrangement that is ubiquitous throughout the pseudogap region of the materials' phase diagram and seems to engulf the superconducting region.

Their discovery relied not only on extensive and precise collection of data with an apparatus known as a scanning tunnelling microscope, but also on detailed modelling, which allowed the fluctuating stripes (Fig. 1) to be separated from other stripy features that are formed by a phenomenon called quasiparticle interference. This finding gives a substantial boost to previous theoretical work hypothesizing that superconductivity arises from fluctuating stripes of electronic order.

Ordinary superconductivity can be achieved by cooling a simple metal, such as lead or tin, to a few degrees above absolute zero. Cuprate superconductivity is much more complicated, and caught the world by surprise by appearing at well over a hundred degrees kelvin above absolute zero. The cuprates' defining structural feature is copper oxide planes. Each cuprate family has a different set of atoms between the layers and is defined by a particular formula such as $\text{Bi}_2\text{Sr}_2\text{CaCu}_2\text{O}_{8+x}$, affectionately known as BSCCO (pronounced 'bisco') and the subject of Parker and colleagues' investigation¹.

In the parent compound of a cuprate family, each copper site has a single unpaired electron and the copper oxide planes are insulating. In addition to having a charge, all electrons have a spin and therefore a tiny magnetic moment, which is widely believed to be pivotal to understanding high-temperature superconductivity. The parent compounds all have antiferromagnetic order, meaning that the spin orientation of each electron is opposite to

those of its neighbours. This well-understood state is known as a half-filled Mott insulator. Changing the material's stoichiometry to either add electrons to the planes (electron doping) or remove electrons from the planes (hole doping) leads to dramatic effects. In all the hole-doped materials, increased doping levels lead to the disappearance of the antiferromagnetic order and eventually to superconductivity, with the pseudogap region covering a wide range of doping.

To understand what Parker *et al.*¹ have achieved, we must consider what happens to the Mott insulator as it is doped with holes. Several theoretical models have shown that the insulator's electrons tend to form one-dimensional 'stripes' of spin and charge order. In general terms, this tendency comes from the competition between the kinetic energy of the electrons, which is lowered if they are free to move; the energy of interactions between their spins, which is lowered if neighbouring spins are anti-aligned as in an antiferromagnet; and their electrostatic Coulomb repulsion, which pushes them away from each other. Such stripes are likely to occur most strongly at 1/8 doping, in which every eighth electron has been

removed from the system, and are expected to have a period of four lattice unit cells. The spin part of the stripe orders antiferromagnetically and looks like a narrow ribbon of Mott insulator, whereas the part with more charge can conduct along its length and is often described as a river, even though it is only a unit cell or so wide (Fig. 2, overleaf). Although static stripes seem to compete with superconductivity, it has been proposed² that fluctuating stripes might actually give rise to superconductivity.

Of course, if fluctuating stripes are not present, they cannot be the mechanism of superconductivity. Static stripe-like order has clearly been seen in some cuprate compounds^{3–5} by means of neutron scattering and X-ray scattering, and other materials have shown some indications of static or fluctuating stripe order. But the lack of a clear signature of fluctuating stripe order throughout most compounds and dopings where superconductivity is seen has been one reason to doubt that fluctuating stripe order may cause superconductivity.

In scanning tunnelling microscopy (STM), a sharp metal tip is scanned across the sample a tiny and precise distance above the surface. Electrons quantum-mechanically tunnel across the gap between the sample and the tip, and a map of the electron current reveals the underlying electronic structure with atomic resolution. By varying the voltage between the tip and the sample, it is even possible to make separate images of the electronic order at different energies. It therefore seems the perfect tool to address the question: how common are stripes?

For many years, however, STM did not weigh in on this question, perhaps because of difficulties in preparing suitable surfaces and the presence of disorder. But over the past decade,



Figure 1 | Of zebras and cuprates. Just as a zebra's stripes disappear behind the stripes of the African bush, until now the fluctuating electronic stripes reported by Parker *et al.*¹ in a family of cuprate superconductors have been difficult to distinguish from a superficially similar feature called quasiparticle interference.

REUTERS/ALAMY

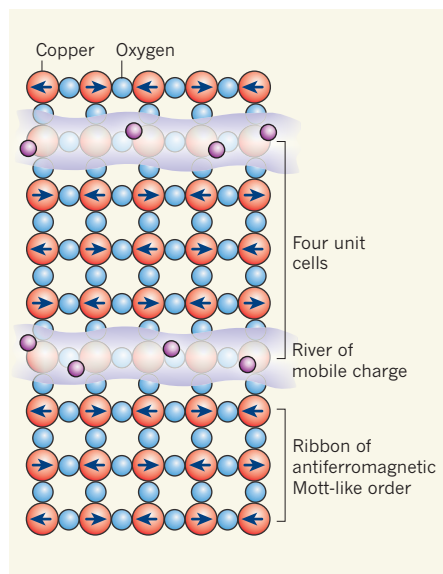


Figure 2 | Stripe-like electronic order in the cuprates. In this form of electronic order, the material's copper oxide planes have ribbons of antiferromagnetic Mott-like order — the spin of each electron (arrowed) is in the opposite direction to those of its neighbours — separated by narrow rivers of mobile charge (purple spheres). The periodicity of the arrangement is four lattice unit cells. Parker and colleagues' results¹ support the hypothesis that fluctuating stripes (more disordered than those shown here) promote superconductivity.

advances in STM technology have enabled the discovery⁶ of chequerboard patterns in a magnetic field similar to what would be expected for stripes, and a stripe-like pattern⁷ in zero field. However, the main features of these patterns were argued^{8,9} to be consistent with a completely different explanation: quasiparticle interference, in which particle-like entities scatter from defects in the material, creating standing waves. Since then, a debate has raged as to whether the features observed in the STM data are fully explainable as quasiparticle interference, or whether stripe-like order must also be present^{10,11}. Quantitative tests have been proposed¹² to distinguish between the two classes of effect, and more experiments have been carried out.

Parker *et al.*¹ analysed STM maps at many values of doping and temperature. In addition to the quasiparticle-interference patterns, the authors clearly demonstrated, using tests proposed earlier¹², the existence of a fluctuating stripe order — strongest at 1/8 doping and with a periodicity of four unit cells — at temperature and doping values that are associated with the pseudogap regime. This observation is consistent with the picture of fluctuating microscopic phase separation into ribbons of Mott insulator separated by rivers of charge. They find that the fluctuating stripe order weakens at dopings lower than 1/8, whereas the pseudogap is known to remain strong into

the antiferromagnetic phase. This indicates that the pseudogap is necessary for the stripe formation but that the pseudogap and stripe formation are not the same phenomena.

Much more work is needed before the mechanism of superconductivity will be solved or the cuprates have a full microscopic theory, if they ever do. Other points of view and related topics, such as the role of a quantum critical point and the question of whether the pseudogap is a well-defined phase, continue to both incite and inspire. Nevertheless, Parker and colleagues' new data and analysis¹, which show the existence of fluctuating stripe order throughout the pseudogap region of BSCCO, make a convincing case that fluctuating stripes are much more common than previously thought. Although they detect only the charge order and not the spin, and other measurements are needed to create a complete picture, these results increase the plausibility of the hypothesis that fluctuating stripes indeed aid the superconductivity, and will give pause to those who have considered stripes a mere distraction. ■

STEM CELLS

The blood balance

Blood cells are generated from haematopoietic stem cells on demand. The protein *Lkb1*, which lies at the crossroad of energy metabolism and cell growth, seems to regulate these stem cells' dynamics. SEE ARTICLES P.653, P.659 & LETTER P.701

ELLEN M. DURAND & LEONARD I. ZON

The haematopoietic stem cells (HSCs) give rise to all mature blood cells through the process of haematopoiesis. This rare cell population also maintains the balance of blood cells in response to stress, by fluctuating between quiescent and actively cycling states depending on physiological conditions. Transplantation of HSCs is an effective treatment for cancers, such as lymphoma and leukaemia, as well as for autoimmune diseases and other blood-related conditions¹. But despite much information about the function and clinical relevance of HSCs, little is known about the energetics and metabolic control of HSC dynamics. Three papers^{2–4} in this issue describe a role for the protein *Lkb1* in the metabolic regulation of HSCs.

Best known for its functions as a tumour suppressor, *Lkb1* is a kinase enzyme that regulates the activity of AMP-activated protein kinase (AMPK) — a master regulator of energetics — and several other AMPK-related enzymes through phosphorylation. When energy and nutrient levels are low, *Lkb1* activates AMPK, which in turn causes repression of mTORC (a protein complex that mediates protein synthesis) and

Kathryn A. Moler is in the Departments of Applied Physics and of Physics, and the Stanford Institute for Materials and Energy Science, Stanford University, Stanford, California 94305, USA.
e-mail: kmoler@stanford.edu

1. Parker, C. V. *et al.* *Nature* **468**, 677–680 (2010).
2. Emery, V. J., Kivelson, S. A. & Zachar, O. *Phys. Rev. B* **56**, 6120–6147 (1997).
3. Tranquada, J. M., Sternlieb, B. J., Axe, J. D., Nakamura, Y. & Uchida, S. *Nature* **375**, 561–563 (1995).
4. Fujita, M., Goka, H., Yamada, K. & Matsuda, M. *Phys. Rev. Lett.* **88**, 167008 (2002).
5. Abbamonte, P. *et al.* *Nature Phys.* **1**, 155–158 (2005).
6. Hoffman, J. E. *et al.* *Science* **295**, 466–469 (2002).
7. Howald, C., Eisaki, H., Kaneko, N., Greven, M. & Kapitulnik, A. *Phys. Rev. B* **67**, 014533 (2003).
8. Hoffman, J. E. *et al.* *Science* **297**, 1148–1151 (2002).
9. McElroy, K. *et al.* *Nature* **422**, 592–596 (2003).
10. Fang, A., Howald, C., Kaneko, N., Greven, M. & Kapitulnik, A. *Phys. Rev. B* **70**, 214514 (2004).
11. Vershinin, M. *et al.* *Science* **303**, 1995–1998 (2004).
12. Kivelson, S. A. *et al.* *Rev. Mod. Phys.* **75**, 1201–1241 (2003).

a decline in cell proliferation⁵ (Fig. 1).

Nakada *et al.*² (page 653) set out to determine whether *Lkb1* regulates HSC dynamics and function. They used genetically engineered mice (*Mx1-Cre; LKB1^{fl/fl}*), which can be manipulated using a polynucleotide, polyinosine–polycytosine (pIpC), to delete the *Lkb1* gene whenever desired. The authors could thus study the effect of *Lkb1* on haematopoiesis, and on the cell-cycle dynamics of not only HSCs, but also the multipotent blood-cell progenitors that arise from HSCs, and whole-bone-marrow (WBM) cells, which include a collection of cells of the haematopoietic system — ranging from HSCs to completely differentiated cells.

Deletion of *Lkb1* resulted in an initial expansion of HSCs and multipotent progenitor cells. With time, however, a depletion of these cell populations and eventually a depletion of all blood cell types (pancytopenia) occurred. *Lkb1* deficiency also led to increased turnover of HSCs and multipotent progenitor cells, but not of WBM cells. This hints that *Lkb1* has a role in regulating the cell-cycle dynamics of HSCs and multipotent progenitor cells but not of fully differentiated cells.

Transplantation assays are the gold standard for testing the function of HSCs, as only HSCs can completely restore the haematopoietic

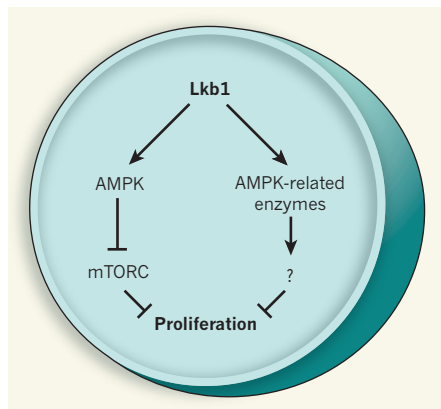


Figure 1 | The regulatory role of Lkb1. Normally, Lkb1 is inactive and so cells can divide. In response to physiological stress, however, Lkb1 signals through the kinase AMPK to suppress mTORC and so decrease cell proliferation. New work^{2–4} shows that Lkb1 regulates the function and dynamics of haematopoietic stem cells (HSCs), although these regulatory roles of Lkb1 are not mediated by the AMPK–mTORC pathway. Whether Lkb1 exerts its effects on HSCs through AMPK-related kinases and their as-yet-unknown downstream pathways, remains unclear.

system of the recipient. Nakada *et al.* report that in mice irradiated to deplete their HSCs, Lkb1-deficient WBM cells could not reconstitute the haematopoietic system — an indication that Lkb1 also regulates HSC function. The authors therefore conclude that, compared with more differentiated cells (multipotent progenitor cells and some WBM cells), the survival of HSCs depends more acutely on Lkb1.

Gurumurthy *et al.*³ (page 659) and Gan *et al.*⁴ (page 701) use a different mouse model (*RosaCreERT2; Lkb1^{L/L}*) to study the effects of *Lkb1* deletion on the haematopoietic system. These authors^{3,4} also observe decreased levels of HSCs and multipotent progenitor cells, as well as pancytopenia, albeit at earlier time points following *Lkb1* deletion. Their data are also consistent with those of Nakada *et al.* in showing that, compared with the more differentiated haematopoietic cell types, *Lkb1* deletion particularly affects HSC dynamics, leading to both increased proliferation of these cells and their increased programmed death by the process of apoptosis.

As well as the function and dynamics of HSCs, Lkb1 seems to regulate the function of mitochondria (the cellular powerhouses) in these cells. In cell populations enriched for HSCs, depletion of Lkb1 protein led to a decrease in the expression of PGC-1 α and PGC-1 β — two transcriptional regulators of mitochondrial biogenesis⁴. Lkb1 depletion also caused a reduction in mitochondrial membrane potential in HSCs^{2,3} — a sign of decreased mitochondrial function and integrity. Finally, an increase in mitochondrial mass was associated with the lack of this protein, possibly to compensate

for decreased ATP levels in these cells.

Intriguingly, the mechanism by which Lkb1 regulates HSC homeostasis seems to be largely independent of its downstream effectors AMPK and mTORC. Not only was mTORC not activated in Lkb1-deficient HSCs, but the addition of the mTORC inhibitor rapamycin did not overcome HSC defects². Similarly, treatment with the AMPK activators metformin or A-769662 did not reverse any of the cellular or functional defects associated with Lkb1 deletion in HSCs^{3,4}. What's more, AMPK-deficient mice did not show a depletion of HSCs — as was seen following Lkb1 depletion — and transplantation of HSCs from these animals into irradiated normal mice allowed long-term multi-lineage reconstitution of blood cells².

These findings clearly establish an essential role for Lkb1 in HSC homeostasis, and show that, among blood-lineage cells, the HSC population is particularly sensitive to depletion of this protein. The relatively minor differences in the results of experiments in *Mx1-Cre; Lkb1^{fl/fl}* mice from those in *RosaCreERT2; Lkb1^{L/L}* mice could probably be explained by the dose and the source of the plpC used to trigger *Lkb1* deletion (these factors can cause great variation in the efficiency of conditional gene deletion).

For instance, such differences might account for Gurumurthy and colleagues' observation of an earlier onset of pancytopenia — compared with the findings of Nakada *et al.*² — and an increased activity of the enzyme caspase,

which mediates apoptosis. As the *RosaCreERT2* system is a more reliable and consistent method for targeted gene deletion, the *RosaCreERT2; Lkb1^{L/L}* mice may be a more useful model to investigate the extent of defects caused by Lkb1 deficiency, and to ascertain that these effects are truly HSC specific.

Nonetheless, the collective data of all three papers^{2–4} provide a framework for understanding the role of Lkb1 in the homeostasis of blood-cell formation and suggest a novel metabolic checkpoint that is active during this process. Whether the AMPK-related kinases mediate the effects of Lkb1 depletion on HSC homeostasis, or whether the mechanism is entirely AMPK independent, remains an intriguing outstanding question. ■

Ellen M. Durand and Leonard I. Zon are at the Children's Hospital Boston, Division of Hematology/Oncology, Boston, Massachusetts 02115, USA.

e-mails: edurand@fas.harvard.edu; zon@enders.tch.harvard.edu

1. Shizuru, J. A., Negrin, R. S. & Weissman, I. L. *Annu. Rev. Med.* **56**, 509–538 (2005).
2. Nakada, D., Saunders, T. L. & Morrison, S. J. *Nature* **468**, 653–658 (2010).
3. Gurumurthy, S. *et al. Nature* **468**, 659–663 (2010).
4. Gan, B. *et al. Nature* **468**, 701–704 (2010).
5. Shaw, R. J. *Acta Physiol.* **196**, 65–80 (2009).

L.I.Z. declares competing financial interests; see online article for details.

STRUCTURAL BIOLOGY

An alphavirus puzzle solved

Alphaviruses infect their host by binding to cellular receptors and fusing with cell membranes. New studies define the receptor-binding protein of these viruses and its regulation of the membrane-fusion reaction. SEE LETTERS P.705 & P.709

MARGARET KIELIAN

Many viruses are enclosed in an envelope — a membrane that is derived from the infected host cell during virus exit. To infect a new host cell, specialized membrane-fusion proteins on the virus envelope fuse it with a membrane of the host cell, delivering the viral genome into the cell. This fusion activity must be deployed at precisely the right time during virus entry, and must also be silenced during viral assembly and exit. In this issue, Li *et al.*¹ and Voss *et al.*² provide structural insights into the regulation of the membrane-fusion proteins of enveloped alphaviruses during the viruses' entry into and exit from the host cell.

Many alphaviruses are medically relevant; chikungunya virus, for example, is an emerging human pathogen responsible for major recent epidemics³. There are currently no treatments for alphavirus infections, and detailed information on the structure and life cycle of these viruses is crucial for developing antiviral strategies and vaccines.

But first, a quick glance at what is already known. The membrane-fusion protein of alphaviruses is E1, and its fusion activity is triggered by the mildly acidic pH of intracellular vesicles⁴. Structural studies have defined the architecture of the E1 molecule^{5,6}, its arrangement on the virus particle^{5–8}, and conformational changes in it that drive membrane fusion⁹. E1 is tightly associated with another

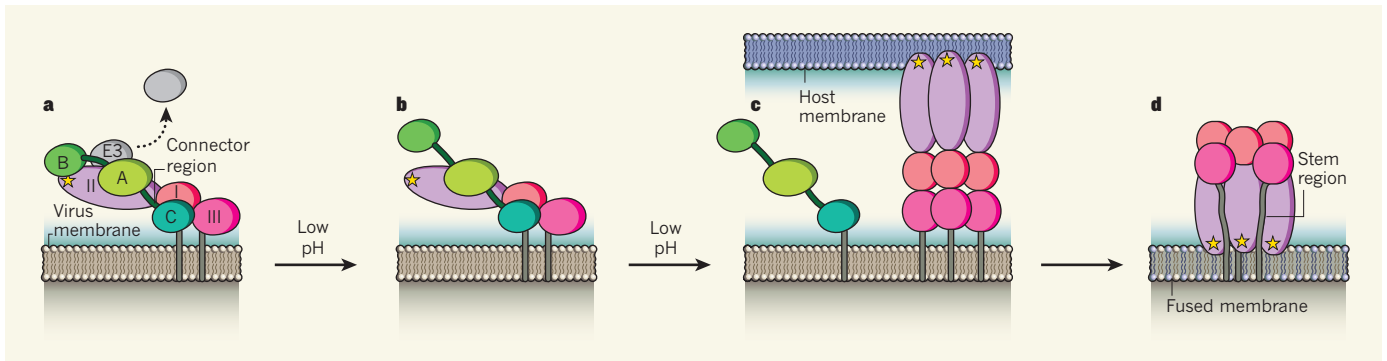


Figure 1 | The alphavirus infection cycle. **a**, The fusion proteins of an alphavirus are connected to the viral membrane and can consist of three components: E1, which contains domains I, II and III, and a fusion loop (star); E2, which contains domains A, B and C, and a ribbon-like connector region; and E3. The alphavirus envelope is peppered with trimers of E2/E1 pairs, although for simplicity only one E2/E1 pair is shown. E3 is a by-product of the cleavage of the E2 precursor protein p62 by the enzyme furin (not

shown), and is released in some alphavirus species. **b**, On exposure to low pH, domain B and the connector region of E2 move, exposing the E1 fusion loop. **c**, E1 can then detach from E2 and insert into the host cell membrane to form an extended trimer. **d**, Finally, to drive membrane fusion, E1 refolds into a hairpin-like structure through the movement of its domain III and the stem region, which lies adjacent to the membrane. For simplicity, only the final fused membrane is shown.

membrane protein, E2, which has been an elusive missing piece of the virus's structural puzzle. The alphavirus envelope is covered by an organized lattice composed of E2/E1 pairs arranged into 80 trimers, or 'spikes'.

The alphavirus infection cycle begins when E2 binds to receptors on the surface of a host cell. This allows the virus to be internalized and transported into the acidic intracellular vesicles. The low pH induces a rearrangement of the E2/E1 pair, unleashing E1's fusion activity¹⁰ (Fig. 1). E1 inserts its hydrophobic fusion loop into the membrane of the host-cell vesicle, forms E1 trimers, and refolds to pull the host-cell and viral membranes together, thereby causing membrane fusion and virus infection⁹.

In addition to binding to host-cell receptors, E2 is an essential component throughout the alphavirus life cycle. During viral replication, this protein is synthesized as a precursor called p62 (or PE2) and acts to chaperone the folding of its E1 partner. Like the vesicular entry pathway, the exit pathway involves transport through cellular compartments that have an acidic pH. The p62/E1 pair is more acid-resistant than the E2/E1 dimer, and this property seems to protect E1 from premature fusion during transport through the exit pathway¹¹. Late in transport, the cellular enzyme furin cleaves p62 to produce the mature E2 protein plus a small peripheral protein, E3 (ref. 12). The virus then exits by budding from the cell surface, with some alphavirus species retaining E3 and others releasing it.

Li *et al.*¹ (page 705) and Voss *et al.*² (page 709) present the molecular structure of the E2/E1 pair and define the mechanisms by which E2 both silences E1 during virus exit and regulates E1's triggering at low pH during virus entry. Focusing respectively on Sindbis virus¹ and chikungunya virus², the authors generated modified versions of p62/E1 proteins that were joined together by flexible linkers and lacked their membrane-anchoring domains; such

modifications were critical for stabilizing E2 for structural studies.

Each team determined the crystal structures of these protein pairs for their virus and fitted them into the molecular outline of the alphavirus particle, previously established^{18,13} by electron microscopy. Voss and colleagues' chikungunya virus structures define the immature p62/E1 pair and the mature E2/E1 complex with the retained E3, whereas the Sindbis virus structures of Li *et al.* reveal the mature E2/E1 pair (without E3), associated in trimeric spikes as on the surface of the virus. The new structures show that the mature E2 protein is an elongated molecule containing three domains with immunoglobulin-like folds: the amino-terminal domain A, located at the centre; domain B at the tip; and the carboxy-terminal domain C, located close to the viral membrane.

The chikungunya E2 covers much of its E1 partner on the virus surface, with the hydrophobic fusion loop of E1 clamped in the groove between domains A and B of E2 (Fig. 1). The Sindbis virus E2/E1 pair was crystallized at acidic pH. Although it closely resembles the chikungunya E2/E1 structure, the E2 domain B that 'caps' the E1 fusion loop is disordered and not visualized. This structure suggests that an early intermediate in the low-pH-triggered fusion process is formed by the release of E2 domain B, exposing the E1 fusion loop. This E2/E1 rearrangement seems to occur through changes in a flexible, ribbon-like connector that links domain B to domains A and C, and packs tightly against the underlying E1 protein.

The immature p62/E1 and mature E3/E2/E1 complexes are very similar apart from the tether region that links E3 to E2 and is the site of cleavage by furin. This suggests that the main difference leading to the increased acid resistance of the immature spike is that the connector ribbon that maintains the domain-B cap in place is stabilized by interactions of the tethered E3.

The new structures^{1,2} illuminate key aspects

of the alphavirus life cycle. In addition, the exposed regions of E2 domains A and B contain several sites to which neutralizing antibodies bind, as well as sites implicated in virus–receptor interaction. The structures of these domains can therefore now be used to clarify the mechanisms of virus receptor binding and neutralization, and to exploit these processes for antiviral and vaccine strategies.

The structures of the p62/E1 and E2/E1 pairs identify specific residues that may control their dissociation at low pH and explain how p62 and E2 regulate virus fusion. Knowing the details of the p62/E1 interaction will also help to determine how much of the requirement for p62 during E1 synthesis is to protect E1 from low pH and how much is to directly assist with E1 folding. The intriguing 'uncapped' structure of the alphavirus spike highlights how little is known about the downstream fusion intermediates, which must involve considerable movements of E2 and E1 on a highly organized virus particle, and which will be an exciting area for future work. ■

Margaret Kielian is in the Department of Cell Biology, Albert Einstein College of Medicine, Bronx, New York 10461, USA.
e-mail: margaret.kielian@einstein.yu.edu

- Li, L., Jose, J., Xiang, Y., Kuhn, R. J. & Rossmann, M. G. *Nature* **468**, 705–708 (2010).
- Voss, J. E. *et al.* *Nature* **468**, 709–712 (2010).
- Schwartz, O. & Albert, M. L. *Nature Rev. Microbiol.* **8**, 491–500 (2010).
- Helenius, A., Kartenbeck, J., Simons, K. & Fries, E. *J. Cell Biol.* **84**, 404–420 (1980).
- Lescar, J. *et al.* *Cell* **105**, 137–148 (2001).
- Roussel, A. *et al.* *Structure* **14**, 75–86 (2006).
- Pletnev, S. V. *et al.* *Cell* **105**, 127–136 (2001).
- Mukhopadhyay, S. *et al.* *Structure* **14**, 63–73 (2006).
- Gibbons, D. L. *et al.* *Nature* **427**, 320–325 (2004).
- Wahlberg, J. M. & Garoff, H. *J. Cell Biol.* **116**, 339–348 (1992).
- Wahlberg, J. M., Boere, W. A. & Garoff, H. *J. Virol.* **63**, 4991–4997 (1989).
- Zhang, X., Fugère, M., Day, R. & Kielian, M. *J. Virol.* **77**, 2981–2989 (2003).
- Mancini, E. J. *et al.* *Mol. Cell* **5**, 255–266 (2000).

Impacts of biodiversity on the emergence and transmission of infectious diseases

Felicia Keesing¹, Lisa K. Belden², Peter Daszak³, Andrew Dobson⁴, C. Drew Harvell⁵, Robert D. Holt⁶, Peter Hudson⁷, Anna Jolles⁸, Kate E. Jones⁹, Charles E. Mitchell¹⁰, Samuel S. Myers¹¹, Tiffany Bogich³ & Richard S. Ostfeld¹²

Current unprecedented declines in biodiversity reduce the ability of ecological communities to provide many fundamental ecosystem services. Here we evaluate evidence that reduced biodiversity affects the transmission of infectious diseases of humans, other animals and plants. In principle, loss of biodiversity could either increase or decrease disease transmission. However, mounting evidence indicates that biodiversity loss frequently increases disease transmission. In contrast, areas of naturally high biodiversity may serve as a source pool for new pathogens. Overall, despite many remaining questions, current evidence indicates that preserving intact ecosystems and their endemic biodiversity should generally reduce the prevalence of infectious diseases.

In June 2010, a new organization, the Intergovernmental Science-Policy Platform on Biodiversity and Ecosystem Services (IPBES)—patterned after the Intergovernmental Panel on Climate Change (IPCC)—was established to assess changes to the diversity of life on the Earth and how these changes will affect human well-being¹. Human well-being would be adversely affected by biodiversity losses if ecosystems with reduced biodiversity are less able to provide the ecosystem services—such as carbon sequestration, nutrient cycling and resistance to drought—on which humans rely. In recent years, a consensus has emerged that ecosystem functions decline as biodiversity is lost². Here we examine how biodiversity affects the transmission and emergence of infectious diseases and evaluate the evidence that reduced disease transmission is an important ecosystem service provided by high biodiversity.

Biodiversity encompasses the diversity of genes, species and ecosystems. Increases in human populations have resulted in an unprecedented and precipitous loss of biodiversity³. Current extinction rates are estimated to be at least 100–1,000 times background extinction rates and future extinction rates (over the next 50 years) are estimated to be 10 to 100 times present extinction rates³. A large proportion of species in all assessed taxa are currently threatened with extinction (12% of birds, 23% of mammals, 32% of amphibians; 31% of gymnosperms; 33% of corals⁴) and the best estimate of population trends of birds, mammals, amphibians, reptiles and fish indicates that since 1970 global population sizes have declined by almost 30% (ref. 5). Global and local extinction rates of some taxa, particularly microbes, have not been well characterized. For the many organisms that are symbionts of other organisms, extinction of their hosts can cause their extinction too⁶. Collectively, these declines and extinctions are caused by changing the Earth's ecosystems to meet growing demands for food, fresh water, fibre, timber and fuel, and by climate change.

Changes in biodiversity have the potential to affect the risk of infectious disease exposure in plants and animals—including humans—because infectious diseases by definition involve interactions among species. At a minimum, these species include a host and a pathogen;

often many more species are involved, including additional hosts, vectors and other organisms with which these species interact. Intriguingly, biodiversity may play a dual role in the emergence and transmission of infectious diseases. On the one hand, high biodiversity may provide a larger potential source of novel pathogens, but on the other hand, biodiversity can reduce further pathogen transmission for both long-established and newly emerging diseases. We first review the effects of biodiversity on the transmission of established diseases and then turn to disease emergence.

Biodiversity and pathogen transmission

Transmission of pathogens between species

Biodiversity loss might affect disease transmission through several mechanisms (Box 1). If the effect of each species on pathogen transmission were entirely idiosyncratic, one would expect that diversity declines would be equally likely to cause a decrease or an increase in disease transmission in the remaining species. However, in recent years, a consistent picture has emerged—biodiversity loss tends to increase pathogen transmission and disease incidence. This pattern occurs across ecological systems that vary in type of pathogen, host, ecosystem and transmission mode (Table 1). As an example, West Nile virus is a mosquito-transmitted virus for which several species of passerine birds act as hosts. Three recent studies detected strong correlations between low bird diversity and increased human risk or incidence of West Nile encephalitis in the United States^{7–9}. Communities with low avian diversity tend to be dominated by species that amplify the virus, inducing high infection prevalence in mosquitoes and people, while communities with high avian diversity contain many species that are less competent hosts. For hantavirus pulmonary syndrome, a directly transmitted zoonotic disease, correlational and experimental studies have shown that a lower diversity of small mammals increases the prevalence of hantaviruses in their hosts, thereby increasing risk to humans (Box 2). Diversity has a similar effect for plant diseases, with species losses increasing the transmission of two fungal rust pathogens that infect perennial rye grass and other plant species¹⁰.

¹Department of Biology, Bard College, Annandale, New York 12504, USA. ²Department of Biological Sciences, Virginia Tech, Blacksburg, Virginia 24061, USA. ³EcoHealth Alliance, New York, New York 10001, USA. ⁴EEB, Eno Hall, Princeton University, Princeton, New Jersey 08544-3417, USA. ⁵Department of Ecology & Evolutionary Biology, Cornell University, Ithaca, New York 14853, USA. ⁶Department of Biology, University of Florida, Gainesville, Florida 32611, USA. ⁷Center for Infectious Disease Dynamics, Pennsylvania State University, College Station, Pennsylvania 16802, USA. ⁸College of Veterinary Medicine, Oregon State University, Corvallis, Oregon 97331-4801, USA. ⁹Institute of Zoology, Zoological Society of London, London, NW1 4RY, UK. ¹⁰Department of Biology, The University of North Carolina at Chapel Hill, Chapel Hill, North Carolina 27599, USA. ¹¹Harvard Medical School, Harvard University, Cambridge, Massachusetts 02138, USA. ¹²Cary Institute of Ecosystem Studies, Millbrook, New York 12545, USA.

BOX 1

Effects of biodiversity on disease transmission

The loss of biodiversity can affect the transmission of infectious diseases⁶⁵ by changing:

(1) The abundance of the host or vector. For plants, seeding experimental fields with plant species that are not hosts for fungal pathogens decreased threefold the pathogen load of species that are hosts, apparently by reducing host density through competition⁶⁶. On the other hand, a greater diversity of host species can sometimes increase pathogen transmission by increasing the abundance of vectors⁶⁷.

(2) The behaviour of the host, vector or parasite. In a more diverse community, one of the parasitic worms that causes schistosomiasis (which infects 200 million people worldwide) is more likely to end up in an unsuitable intermediate host. This can reduce the probability of subsequent infection of humans by 25–99% (ref. 68). For hantavirus in Utah, USA, rodent hosts on more diverse plots are more likely to come in contact with heterospecific mammals and less likely to come in contact with conspecifics, reducing the probability of transmission of the virus⁶⁵. In principle, higher diversity could influence behaviours with a resulting increase in disease transmission⁶⁵ or could alter the evolutionary dynamics of virulence and transmission pathways.

(3) The condition of the host or vector. In experimental rice fields in China, rice plants in genetically diverse mixtures had drier leaves because the mixture changed microclimatic conditions⁶⁹. As a consequence, infection with rice blast fungus was less prevalent in diverse fields. Genetically diverse plantings can also lead to induced resistance in host plants because they are exposed to similar pathogens that are specialists on the other cultivars⁷⁰.

For some disease systems (for example, Lyme disease), multiple mechanisms operate in concert, leading to a compounding effect of biodiversity loss on increased disease transmission (Table 1).

Recent attention has focused on assessing the mechanisms by which reduced biodiversity increases pathogen transmission (Box 1). Biodiversity loss can clearly increase transmission if it reduces predation and competition on reservoir hosts, thereby increasing their density. However, controversy has centred around whether the loss of species can increase transmission in other ways¹¹. This is because field studies like those on West Nile virus, hantaviruses and rye grass have typically not controlled for changes in host density that can result from changes in 'species richness' (the number of species present in a community, which is a measure of taxonomic diversity). As a consequence, it has been difficult to separate the effects of higher density from those of reduced diversity. Recent experiments confirm that increases in disease transmission can occur when

species richness declines even if host density stays constant. One of the best examples comes from a study of *Schistosoma mansoni*, a trematode that causes schistosomiasis in humans. The parasite alternately infects snails and humans via free-living infectious stages. Host snails were placed in tanks at a constant density either alone or with one or two other species of non-host snails and then exposed to the parasite¹². In single-species treatments, host snails were 30% more likely to be infected because parasites in multi-species treatments often ended up in dead-end hosts. Increased parasite–host encounter rates caused by reduced diversity are sufficient to increase disease transmission for *Schistosoma*.

The loss of species can increase encounter rates between pathogens and hosts, as in the *Schistosoma* example, when the lost species are not hosts for the pathogen. But if the lost species are indeed hosts capable of transmission, this declining diversity could also reduce the total number of hosts, thereby decreasing transmission if all else remains equal^{13,14}. Certainly reductions in the number of hosts can reduce the number of vectors¹⁵ and also their infection prevalence^{16,17}, but empirical examples are relatively rare, in part because the issue has been neglected, and also because all else rarely remains equal. For example, the loss of hosts can cause compensatory increases in the abundances of other hosts, such that total host abundance changes little relative to total host abundance in more diverse communities. Even when total host abundance does decline in less diverse systems, differences in host quality among species can alter simple correlations between host abundance and infection risk¹⁸.

Pathogen transmission is not always a function of host density. For example, the number of infectious bites delivered by highly mobile vectors like mosquitoes can be independent of the density of the host population¹⁴. Transmission of directly transmitted pathogens like hantaviruses can also be independent of host density if transmission involves behavioural encounters, for example, aggressive interactions between rodents, and if the frequency of these encounters does not vary much with host density^{14,19}. In systems like these, the loss of host species can actually increase transmission if the lost hosts are suboptimal for parasite development and reproduction; this is because these suboptimal hosts absorb pathogens but are poor at transmitting them.

In sum, reducing biodiversity can increase disease transmission when the lost species are either not hosts for the pathogen or are suboptimal ones. For pathogens for which transmission is a function of host density, loss of diversity is most likely to increase transmission if the loss causes an increase in the density of competent hosts. The number and diversity of examples of pathogens for which species loss leads to increases in total transmission suggests that these conditions are frequently met (Table 1). Additional studies in other disease systems would better establish the generality of these relationships.

Species diversity versus species identity

The loss of particular species in a community clearly has the potential to increase disease transmission. But does reducing diversity itself increase transmission, or is increased transmission the consequence of the removal of particular species? The answer depends on how species composition changes as richness changes^{20,21}. For example, if those host species most responsible for amplifying the pathogen tend to persist or even thrive as biodiversity is lost, then disease risk will consistently increase as biodiversity declines. On the other hand, if amplifying species tend to disappear as biodiversity declines, then biodiversity loss will tend to reduce disease risk. These hypothetical possibilities indicate the importance of understanding both the non-random sequences by which species are lost from communities, and whether the species that tend to occur only in more species-rich communities tend to amplify or buffer pathogen transmission.

In several case studies, the species most likely to be lost from ecological communities as diversity declines are those most likely to reduce pathogen transmission. In the Lyme disease system of eastern North America, for example, the white-footed mouse is simultaneously the most abundant host species, the most competent host for the Lyme bacterium, and the highest-quality host for immature tick vectors¹⁸

Table 1 | Biodiversity loss can increase transmission

Disease	Mechanism	Reference
Amphibian limb malformation	B	12
Bacteriophage of <i>Pseudomonas syringae</i>	B	52
Coral diseases	A	53
Fungal disease of <i>Daphnia</i>	B	54
Hantavirus disease	A, B	23,55–57
Helminthic parasite of fish	A*	58
Lyme disease	A, B	18,22,59
Malaria	A	60
<i>Puccinia</i> rust infection of ryegrass	A*	10
Schistosomiasis	B	12
Trematode diseases of snails and birds	B	61–63
West Nile fever	A*, B*	7–9,64

Disease examples are since 2005. A more complete table, including several counterexamples, is available from the corresponding author. Mechanisms for effects were reported by authors or demonstrated in the text (A = host/vector abundance; B = host/vector/parasite behaviour; see Box 1 for details). Asterisks indicate a suggested mechanism. Other studies have been reviewed elsewhere^{21,65}.

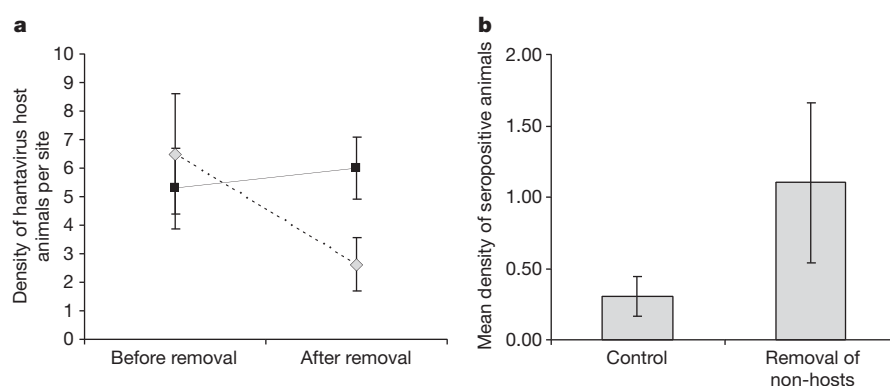
BOX 2

Case study of hantavirus pulmonary syndrome

Hantaviruses are a group of negative-stranded RNA viruses associated with murid rodents. They can cause severe morbidity and mortality in humans, with case-fatality rates near 40% (ref. 71). Infected rodents shed hantavirus in saliva, urine and faeces; transmission to humans occurs through inhalation of aerosolized excreta as well as through rodent bites⁷². The risk of human exposure increases as the density and infection prevalence of rodent reservoirs increase⁷².

In a field study in Oregon, USA, the only variable significantly linked to infection prevalence in deer mouse host populations was mammalian species diversity, with the prevalence of the hantavirus Sin Nombre virus rising from 2% to 14% as diversity declined. Deer mouse population density was not statistically associated with Sin Nombre virus infection prevalence, suggesting that high diversity reduced intraspecific encounters rather than host abundance⁵⁶. A study in Utah, USA⁵⁵, also found a negative correlation between small-mammal diversity and Sin Nombre virus infection prevalence in deer mice. As in Oregon, high diversity reduced infection prevalence apparently by reducing intraspecific encounters rather than by reducing host density, a result supported by experiments¹⁹.

The conclusions of these studies were supported by an experimental study of hantaviruses in small mammal communities of Panamá²³. In replicated plots, small-mammal diversity was reduced by trapping and removing species that are not hosts for the virus; infection prevalence in hosts was compared on manipulated and unmanipulated plots (Box 2 figure). Experimentally reduced small-mammal diversity caused an increase in the density of host species and also in seroconversion rates and seroprevalence within hosts (Box 2 figure).



Box 2 figure | Effects of experimental removal of species. **a**, Mean (\pm standard error) population abundance of hantavirus hosts in Panamá in field plots before and after non-host species had been removed (solid line), and in unmanipulated controls (dashed line). Hosts on control plots underwent a strong seasonal decline in abundance, whereas those on plots

where non-hosts were experimentally removed did not. **b**, Mean (\pm standard error) density of seropositive (currently or previously infected) animals on plots from which non-hosts had been removed and on control plots. Analysed from data provided in ref. 23.

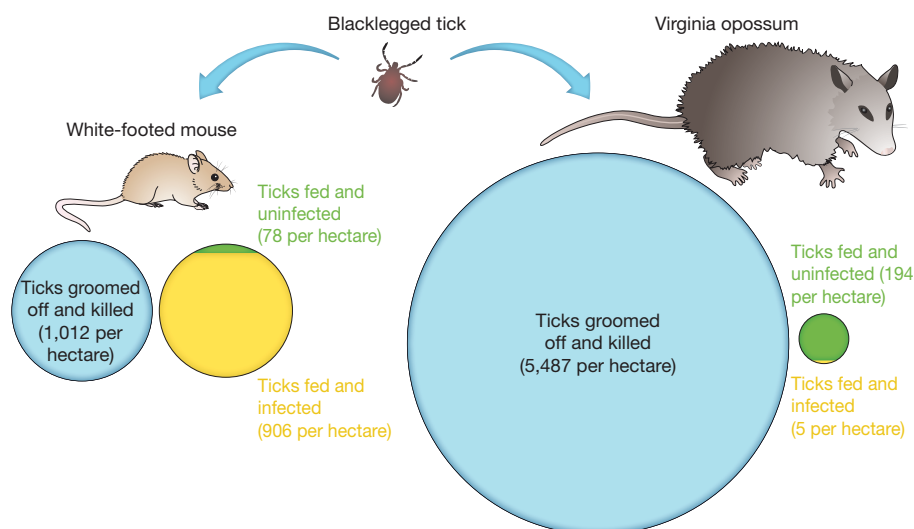


Figure 1 | Roles of host species in the transmission of Lyme disease in the northeastern USA. Lyme disease is transmitted to humans by the bite of an infected blacklegged tick (*Ixodes scapularis*). Immature ticks can acquire the infection if they feed on an infected host and can become infectious to humans if they subsequently survive to the next life stage. White-footed mice are abundant in northeastern forests and feed many ticks¹⁸. Ticks that attempt to

feed on Virginia opossums are likely to be groomed off and killed. Green-and-yellow circles show the mean number of ticks per hectare fed by mice or opossums; yellow shading shows the proportion of ticks infected after feeding. Blue circles show the mean number of ticks per hectare groomed off and killed. Ticks that feed on mice are highly likely to become infected with the bacterium that causes Lyme disease, whereas those that feed on opossums are not.

(Fig. 1). As a consequence, this host species infects a high proportion of the ticks within forest communities. The white-footed mouse is also an ecologically resilient species, present in both species-rich and species-poor communities²². In contrast, Virginia opossums are poor hosts for the pathogen, kill the vast majority of ticks that attempt to feed on them, and are absent from many low-diversity forest fragments and degraded forests where mice are abundant^{18,22}. Therefore, as biodiversity is lost, the host with a strong buffering effect—the opossum—disappears, while the host with a strong amplifying effect—the mouse—remains. The primary hosts for the pathogens that cause West Nile encephalitis, hantavirus pulmonary syndrome, and bartonellosis also appear to be resilient species that increase in abundance as biodiversity is lost^{7,23,24}.

Whether an organism's host competence and its resilience to factors that reduce biodiversity are causally related is an unresolved but critical issue. Traits that make a host resilient to biodiversity loss may also make them susceptible to pathogen infection and transmission. Such a relationship would explain the frequency with which the link between diversity loss and disease transmission has been observed in nature (Table 1). For plants, species that are fast-growing and nutrient-rich with relatively high metabolic rates—characteristics of 'weedy' species—can be more competent hosts for arthropod vectors and plant pathogens than those with less weedy traits²⁵. Plants with these weedy traits are also more likely to become more abundant when plant diversity declines²⁶. Consequently, the very species that have traits permitting persistence in degraded and species-poor ecosystems are also more likely to carry high pathogen and vector burdens. A similar pattern may occur in vertebrates—resilience in the face of disturbances that cause biodiversity loss, such as habitat destruction and fragmentation, is facilitated by life-history features such as high reproductive output and intrinsic rates of increase²⁷. Vertebrates with these features tend to invest minimally in some aspects of adaptive immunity^{28–30}; we hypothesize that this may make them more competent hosts for pathogens and vectors. Understanding the interrelationships among pathogen transmission, biodiversity loss and inter-specific differences in immune function is an important area for future research. Such studies would illuminate how frequently resilient species are also those that increase pathogen transmission, and might provide general rules about the impact of biodiversity loss on disease transmission.

Diversity within individual hosts

Could changes in biodiversity within the bodies of organisms also alter pathogen transmission? Recent improvements in the ability of researchers to detect unculturable microbial species have allowed documentation of the tremendous diversity of microbes upon and within plants and animals. In human bodies, for example, 90% of all cells are microbial³¹. A number of studies have begun to show links between diseases and the diversity of an organism's 'microbiome'.

Changes in the composition of microbiomes are frequently associated with infection and disease. For example, corals suffering from white plague disease have microbial communities distinctly different from those in healthy corals³². In humans, bacterial vaginosis results from changes in the composition of the vaginal microbial community³³, and this in turn increases the risk of HIV infection³⁴. Although changes in microbial species composition associated with infection are well-documented, few studies have investigated the effects of changes in diversity itself. In a recent investigation, patients with recurrent episodes of infection caused by the bacterium *Clostridium difficile* had significantly lower diversity of intestinal microbes than did control patients³⁵. Correlational studies such as these, though intriguing, make it difficult to determine whether changes in microbial communities are the cause or the consequence of infections. But some experimental studies clearly demonstrate that increasing microbial biodiversity can protect against infection. For example, children with a history of ear infections given a mixture of five strains of *Streptococcus* were less likely to develop subsequent infections compared to a control group³⁶. Similarly, reducing microbial diversity within a host can increase transmission. When mice with persistent infections of *C. difficile* were treated with antibiotics that

reduced the diversity of intestinal microbes, they began shedding *C. difficile* spores at high rates³⁷.

In some of these examples, a rich microbial community appears to regulate the abundance of endemic microbial species that can become pathogenic when overly abundant³⁵. In other cases, high microbial species diversity can prevent colonization by invasive pathogenic species. For example, the more diverse the microbiome surrounding the roots of wheat plants, the more protected the plants were against invasion by the pathogenic bacterium *Pseudomonas aeruginosa*³⁸. Similarly, piglets raised in natural environments supporting a high diversity of microbes were more resistant to invasion by pathogenic gut microbes than those raised in more sterile environments³⁹.

The effects of microbial diversity within and upon host bodies show intriguing similarities to the effects of macroscopic species diversity on disease transmission in aquatic and terrestrial ecosystems. Further exploration of these similarities, and particularly the specific mechanisms operating within hosts, is a critical research frontier because changes in microbial diversity might accompany biodiversity loss in their hosts.

Biodiversity and pathogen emergence

For pathogens already established within ecological communities, we have shown that biodiversity loss frequently increases the rate of transmission. But what role, if any, does biodiversity have in the processes by which new pathogens emerge? Between 1940 and 2004, over 300 emerging disease events were identified in humans around the world⁴⁰. Concomitantly, other emerging infectious diseases also appeared in wildlife, domesticated animals, and crop and wild plants. Emerging infectious diseases include those in which the pathogen has evolved into a new strain within the same host species, for example, through the evolution of drug resistance (methicillin-resistant *Staphylococcus aureus* or MRSA) or switched to new host species (for example, human immunodeficiency virus or HIV, severe acute respiratory syndrome or SARS). In some cases, the switch to new host species is accompanied by a change in geographic range (for example, West Nile virus in the Americas).

For pathogens that establish in new species, the emergence process involves multiple steps, including the initial invasion into the new host ('spillover'), the production of transmission stages within the new host, and the establishment of the pathogen in the host population as a whole^{41,42}. The effect of biodiversity may vary for each of these steps. For the initial invasion, biodiversity may act as a source pool. This hypothesis is supported by surveys of emerging diseases of humans: most are zoonotic—jumping to humans from other vertebrate animals⁴³. In one recent analysis, the probability of emergence of pathogens from wildlife to humans was positively correlated with mammalian wildlife species richness when data were corrected for reporting bias⁴⁰. Other environmental and socioeconomic factors that bring humans into closer contact with potentially new pathogens (for example, forest clearing for agriculture, wildlife hunting) may also contribute to this pattern. Indeed, almost half of the zoonotic diseases that have emerged in humans since 1940 resulted from changes in land use, from changes in agricultural or other food production practices, or from wildlife hunting (Fig. 2). These human activities increase rates of contact between humans and animals, which may be a critical factor underlying spillover.

Once spillover of the pathogen into a new host has occurred, high densities of that host species may facilitate pathogen establishment and transmission within the new host⁴¹. For example, Nipah virus spilled over from wild fruit bats to domestic pigs in Malaysia; high densities of pigs in local farms appear to have facilitated establishment of pig-to-pig transmission, and the pathogen then spilled over from pigs to humans⁴⁴. Such high densities of domesticated species are almost always associated with low biodiversity.

In contrast to emergence through host-switching, 20% of emergence events between 1940 and 2004 arose through the evolution of drug resistance⁴⁰. For these cases, biodiversity of microbial communities within hosts may have a protective effect; human use of antibiotics is

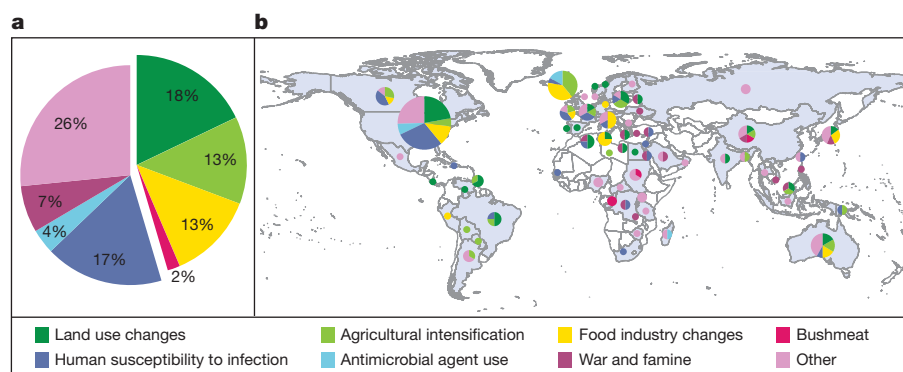


Figure 2 | Drivers and locations of emergence events for zoonotic infectious diseases in humans from 1940–2005. **a**, Worldwide percentage of emergence events caused by each driver; **b**, Countries in which the emergence events took place, and the drivers of emergence. The size of the circle represents the number of emergence events: for scale, the number of events in the United States was 59. Globally, almost half of these diseases resulted from changes in land use, changes

thought to select for resistant microbes by eliminating the great diversity of non-resistant microbial strains and species that suppress resistant strains in the absence of antibiotics. Investigations using recent advances in microbial detection support this idea^{45,46}. Thus, reduced microbial diversity may be an important underlying cause of the emergence of drug-resistant pathogens; this too requires further investigation.

Managing pathogens by managing biodiversity

The addition of particular species—for example, natural enemies or competitors—can reduce the impacts of established pathogens. For example, experimental addition of a naturally occurring bacterium, *Janthinobacterium lividum*, to the skin of the endangered frog *Rana mucosa* eliminated frog mortality from experimental infection with chytridiomycosis, which is devastating amphibian populations worldwide⁴⁷. For corals, application of phages isolated from natural communities can control the spread of bacterial infections⁴⁸. The growing interest in ‘probiotics’ for humans and harvested species provides another example of this approach⁴⁹.

More broadly, biodiversity itself seems to protect organisms, including humans, from transmission of infectious diseases in many cases (Table 1). Preserving biodiversity in these cases, and perhaps generally, may reduce the incidence of established pathogens. To preserve high diversity in nature, conservation scientists have developed robust methods that reflect the key principle that larger areas sustain larger numbers of species⁵⁰. Methods of conserving microbial diversity within and upon bodies or in the environment are less well developed, but avoiding the overuse of antimicrobial compounds is essential. Critically, future research on the relationship between biodiversity and disease must avoid conflating the effects of biogeographic patterns of biodiversity (for example, higher diversity in lower latitudes) with those of anthropogenic reductions in extant biodiversity, because policy and management options can far more readily affect the latter than the former.

For emerging diseases, the observation that a more diverse microbiome within a host suppresses strains that are resistant to antimicrobial compounds suggests that avoiding the over-use of these compounds in medicine and agriculture can prevent the emergence of resistant strains. For pathogens that emerge by switching host species, three management approaches are warranted. First, potential emergence ‘hotspots’ could be predictable on the basis of land-use change and underlying biodiversity patterns; these areas should be targeted for surveillance of endemic wildlife pathogens that have the potential to jump host species^{40,51}. Second, preserving and protecting intact habitats in these hotspots provides a simple, direct way of reducing human–animal contact and reduces the likelihood of emergence of new pathogens, although methods for achieving reduced contact are not always straightforward⁵¹. And third, to reduce the probability that pathogens become established and

in agricultural and other food production practices, or through wildlife hunting, which suggests that contact rates between humans and other animals are an important underlying cause of zoonotic disease emergence. ‘Other’ includes international travel and commerce, changes in human demographics and behaviour, changes in the medical industry, climate and weather, breakdown of public health measures, and unspecified causes. Analysed from data in ref. 40.

transmissible within a new host population once spillover occurs, the husbandry of high-density monocultures of domestic animals, particularly in areas at high risk of spillover, should be subject both to more intensive surveillance and to measures that reduce contact between wildlife and livestock. Managing potential emergence hotspots by attempting to eliminate them is likely to backfire because the species most resilient to habitat destruction and degradation may be those that amplify pathogen transmission.

Despite many recent advances in our understanding of biodiversity and disease, much remains to be learned. First, we must increase the number of disease systems for which we understand the effects of biodiversity loss on disease transmission across a range of spatial and temporal scales. We must also focus on how to implement specific policies informed by this science. Future research, for example, should monitor changes in epidemiology in regions in which conservation measures are imposed compared to reference sites. A major challenge will be to untangle the complex ways in which other global anthropogenic trends—such as climate change, biotic exchange, nutrient pollution, armed conflict and economic collapse—interact with biodiversity loss to influence disease dynamics, and which of these trends have the greatest impacts on human well-being. Despite remaining questions, connections between biodiversity and disease are now sufficiently clear to increase the urgency of local, regional, and global efforts to preserve natural ecosystems and the biodiversity they contain.

- Marris, E. New UN science body to monitor biosphere. *Nature*. doi: 10.1038/news.2010.297 (2010).
- Naeem, S., Bunker, D., Hector, A., Loreau, M. & Perrings, C. *Biodiversity, Ecosystem Functioning, and Human Wellbeing: an Ecological and Economic Perspective* (Oxford University Press, 2009).
- Mace, G. M., Masundire, H. & Baillie, J. E. M. in *Ecosystems and Human Well-Being: Current State and Trends: Findings of the Condition and Trends Working Group Vol. 1*, Ch. 4 (Millennium Ecosystem Assessment Series, Island Press, 2005).
- IUCN. *IUCN Red List of Threatened Species* Version 2010.2. (<http://www.iucnredlist.org>) (downloaded on 29 June 2010).
- Loh, J. *et al.* in *2010 and Beyond: Rising to the Biodiversity Challenge* (ed. Loh, J.) (Living Planet Index, WWF, 2008).
- Dobson, A. P. *et al.* Homage to Linnaeus: How many parasites? How many hosts? *Proc. Natl Acad. Sci. USA* **105**, 11482–11489 (2008).
- Allan, B. F. *et al.* Ecological correlates of risk and incidence of West Nile virus in the United States. *Oecologia* **155**, 699–708 (2009).
- Ezenwa, V. O., Godsey, M. S., King, R. J. & Guptill, S. C. Avian diversity and West Nile virus: testing associations between biodiversity and infectious disease risk. *Proc. R. Soc. Lond. B* **273**, 109–117 (2006).
- Swaddle, J. & Calos, P. Increased avian diversity is associated with lower incidence of human West Nile infection: observation of the dilution effect. *PLoS ONE* **3**, e2488 (2008).
- Roscher, C., Schumacher, J., Foitzik, O. & Schulze, E.-D. Resistance to rust fungi in *Lolium perenne* depends on within-species variation and performance of the host species in grasslands of different plant diversity. *Oecologia* **153**, 173–183 (2007).
- Begon, M. in *Infectious Disease Ecology: Effects of Ecosystems on Disease and of Disease on Ecosystems* (eds Ostfeld, R., Keesing, F. & Eviner, V.) 12–29 (Princeton University Press, 2008).

12. Johnson, P. T. J., Lund, P., Hartson, R. B. & Yoshino, T. Community diversity reduces *Schistosoma mansoni* transmission and human infection risk. *Proc. R. Soc. Lond. B* **276**, 1657–1663 (2009).
- Through careful experimentation, the authors establish that the presence of another species can reduce parasite transmission even if the total density of hosts remains constant.**
13. Rudolf, V. H. & Antonovics, J. Species coexistence and pathogens with frequency-dependent transmission. *Am. Nat.* **166**, 112–118 (2005).
14. Dobson, A. P. Population dynamics of pathogens with multiple host species. *Am. Nat.* **164**, S64–S78 (2004).
15. Cecère, M. C., Gürtler, R. E., Chuit, R. & Cohen, J. Effects of chickens on the prevalence of infestation and population density of *Triatoma infestans* in rural houses of northwest Argentina. *Med. Vet. Entomol.* **11**, 383–388 (1997).
16. Bouma, M. & Rowland, M. Failure of passive zoophylaxis: cattle ownership in Pakistan is associated with a higher prevalence of malaria. *Trans. R. Soc. Trop. Med. Hyg.* **89**, 351–353 (1995).
17. Laurenson, M. K., Norman, R. A., Gilbert, L., Reid, H. W. & Hudson, P. J. Identifying disease reservoirs in complex systems: mountain hares as reservoirs of ticks and louping-ill virus, pathogens of red grouse. *J. Anim. Ecol.* **72**, 177–185 (2003).
18. Keesing, F. *et al.* Hosts as ecological traps for the vector of Lyme disease. *Proc. R. Soc. Lond. B* **276**, 3911–3919 (2009).
- This paper presents a suite of mechanisms by which diversity could reduce disease transmission and reviews the literature for evidence of these mechanisms.**
19. Clay, C. A., Lehmer, E. M., St. Jeor, S. & Dearing, M. D. Testing mechanisms of the dilution effect: deer mice encounter rates, Sin Nombre virus prevalence and species diversity. *EcoHealth* **6**, 250–259 (2009).
20. Ostfeld, R. S. & LoGiudice, K. Community disassembly, biodiversity loss, and the erosion of an ecosystem service. *Ecology* **84**, 1421–1427 (2003).
- The authors use analytical models of Lyme disease to explore the importance of knowing the order in which species are lost as biodiversity declines.**
21. Johnson, P. T. J. & Thielges, D. W. Diversity, decoys and the dilution effect: how ecological communities affect disease risk. *J. Exp. Biol.* **213**, 961–970 (2010).
- This paper reviews how diversity could affect disease transmission with particular attention to the transmission of parasites.**
22. LoGiudice, K. *et al.* Impact of host community composition on Lyme disease risk. *Ecology* **89**, 2841–2849 (2008).
23. Suzán, G. *et al.* Experimental evidence for reduced mammalian diversity causing increased hantavirus prevalence. *PLoS ONE* **4**, e5461 (2009).
24. Kosoy, M. *et al.* Distribution, diversity, and host specificity of *Bartonella* in rodents from the Southeastern United States. *Am. J. Trop. Med. Hyg.* **57**, 578–588 (1997).
25. Cronin, J. P., Welsh, M. E., Dekkers, M. G., Abercrombie, S. T. & Mitchell, C. E. Host physiological phenotype explains pathogen reservoir potential. *Ecol. Lett.* doi: 10.1111/j.1461-0248.2010.01513.x (2010).
26. Pilgrim, E. S., Crawley, M. J. & Dolphin, K. Patterns of rarity in the native British flora. *Conserv. Biol.* **120**, 161–170 (2004).
27. Cardillo, M. *et al.* The predictability of extinction: biological and external correlates of decline in mammals. *Proc. R. Soc. Lond. B* **275**, 1441–1448 (2008).
28. Martin, L. B., Hasselquist, D. & Wikelski, M. Investment in immune defense is linked to pace of life in house sparrows. *Oecologia* **147**, 565–575 (2006).
29. Martin, L. B., Weil, Z. M. & Nelson, R. J. Immune defense and reproductive pace of life in *Peromyscus* mice. *Ecology* **88**, 2516–2528 (2007).
30. Lee, K. A., Wikelski, M., Robinson, W. D., Robinson, T. R. & Klasing, K. C. Constitutive immune defenses correlate with life-history variables in tropical birds. *J. Anim. Ecol.* **77**, 356–363 (2008).
31. Turnbaugh, P. J. *et al.* The human microbiome project. *Nature* **449**, 804–810 (2007).
32. Sunagawa, S. *et al.* Bacterial diversity and White Plague disease-associated community changes in the Caribbean coral *Montastrea faveolata*. *ISME J.* **3**, 512–521 (2009).
33. Holzman, C. *et al.* Factors linked to bacterial vaginosis in nonpregnant women. *Am. J. Public Health* **91**, 1664–1670 (2001).
34. Atashili, J., Poolea, C., Ndumbab, P. M., Adimoraa, A. A. & Smith, J. S. Bacterial vaginosis and HIV acquisition: a meta-analysis of published studies. *AIDS* **22**, 1493–1501 (2008).
35. Chang, J. Y. *et al.* Decreased diversity of the fecal microbiome in recurrent *Clostridium difficile*-associated diarrhea. *J. Infect. Dis.* **197**, 435–438 (2008).
36. Roos, K., Håkansson, E. G. & Holm, S. Effect of recolonisation with “interfering” α streptococci on recurrences of acute and secretory otitis media in children: randomised placebo controlled trial. *Br. Med. J.* **322**, 1–4 (2001).
37. Lawley, T. D. *et al.* Antibiotic treatment of *Clostridium difficile* carrier mice triggers a supershedder state, spore-mediated transmission, and severe disease in immunocompromised hosts. *Infect. Immun.* **77**, 3661–3669 (2009).
38. Matos, A., Kerkhof, L. & Garland, J. Effects of microbial community diversity on the survival of *Pseudomonas aeruginosa* in the wheat rhizosphere. *Microb. Ecol.* **49**, 257–264 (2005).
39. Mulder, I. E. *et al.* Environmentally-acquired bacteria influence microbial diversity and natural innate immune responses at gut surfaces. *BMC Biol.* **7**, doi: 10.1186/1741-7007-7-79 (2009).
40. Jones, K. *et al.* Global trends in emerging infectious diseases. *Nature* **451**, 990–993 (2008).
- This paper explores patterns in emerging infectious diseases of humans during the 20th century and predicts hotspots for future disease emergence events.**
41. Hudson, P., Perkins, S. & Cattadori, I. In *Infectious Disease Ecology: Effects of Ecosystems on Disease and of Disease on Ecosystems* (eds Ostfeld, R., Keesing, F. & Eviner, V.) 347–367 (Princeton University Press, 2008).
42. Wolfe, N., Dunavan, C. P. & Diamond, J. Origins of major human infectious diseases. *Nature* **447**, 279–283 (2007).
43. Woolhouse, M. E. J. & Gowtage-Sequeria, S. Host range and emerging and reemerging pathogens. *Emerg. Infect. Dis.* **11**, 1842–1847 (2005).
44. Epstein, J. H., Field, H. E., Luby, S., Pulliam, J. R. C. & Daszak, P. Nipah virus: Impact, origins, and causes of emergence. *Curr. Infect. Dis. Rep.* **8**, 59–65 (2006).
45. Flanagan, J. L. *et al.* Loss of bacterial diversity during antibiotic treatment of intubated patients colonized with *Pseudomonas aeruginosa*. *J. Clin. Microbiol.* **45**, 1954–1962 (2007).
46. Dethlefsen, L., Huse, S., Sogin, M. L. & Relman, D. A. The pervasive effects of an antibiotic on the human gut microbiota, as revealed by deep 16S rRNA sequencing. *PLoS Biol.* **6**, e280 (2008).
47. Harris, R. *et al.* Skin microbes on frogs prevent morbidity and mortality caused by a lethal skin fungus. *ISME J.* **3**, 818–824 (2009).
48. Efrony, R., Atad, I. & Rosenberg, E. Phage therapy of Coral White Plague disease: properties of phage BA3. *Curr. Microbiol.* **58**, 139–145 (2009).
49. Sleator, R. D. & Hill, C. New frontiers in probiotic research. *Lett. Appl. Microbiol.* **46**, 143–147 (2008).
50. Margules, C. & Sarkar, S. *Systematic Conservation Planning* (Cambridge University Press, 2007).
51. Wolfe, N. D., Daszak, P., Kilpatrick, A. M. & Burke, D. S. Bushmeat hunting, deforestation, and prediction of zoonoses emergence. *Emerg. Infect. Dis.* **11**, 1822–1827 (2005).
52. Dennehy, J. J., Friedenber, N. A., Yang, Y. W. & Turner, P. E. Virus population extinction via ecological traps. *Ecol. Lett.* **10**, 230–240 (2007).
53. Raymundo, L. J., Halford, A. R., Maypab, A. P. & Kerr, A. M. Functionally diverse reef-fish communities ameliorate coral disease. *Proc. Natl Acad. Sci. USA* **106**, 17067–17070 (2009).
54. Hall, S. R. *et al.* Friendly competition: evidence for a dilution effect among competitors in a planktonic host–parasite system. *Ecology* **90**, 791–801 (2009).
55. Clay, C., Lehmer, E. M., St. Jeor, S. & Dearing, M. D. Sin Nombre virus and rodent species diversity: a test of the dilution and amplification hypotheses. *PLoS ONE* **4**, e6467 (2009).
56. Dizney, L. J. & Ruedas, L. A. Increased host species diversity and decreased prevalence of Sin Nombre virus. *Emerg. Infect. Dis.* **15**, 1012–1018 (2009).
57. Tersago, K. *et al.* Population, environmental, and community effects on local bank vole (*Myodes glareolus*) Puumala virus infection in an area with low human incidence. *Vector-Borne Zoonotic Dis.* **8**, 235–244 (2008).
58. Kelly, D. W., Paterson, R. A., Townsend, C. R., Poulin, R. & Tompkins, D. M. Has the introduction of brown trout altered disease patterns in native New Zealand fish? *Freshwat. Biol.* **54**, 1805–1818 (2009).
59. Brunner, J. & Ostfeld, R. S. Multiple causes of variable tick burdens on small-mammal hosts. *Ecology* **89**, 2259–2272 (2008).
60. Carlson, J. C., Dyer, L. A., Omlin, F. X. & Beier, J. C. Diversity cascades and malaria vectors. *J. Med. Entomol.* **46**, 460–464 (2009).
61. Kopp, K. & Jokela, J. Resistant invaders can convey benefits to native species. *Oikos* **116**, 295–301 (2007).
62. Thielges, D. W., Bordalo, M. D., Caballero-Hernandez, A., Prinz, K. & Jensen, K. T. Ambient fauna impairs parasite transmission in a marine parasite–host system. *Parasitology* **135**, 1111–1116 (2008).
63. Thielges, D. W., Reise, K., Prinz, K. & Jensen, K. T. Invaders interfere with native parasite–host interactions. *Biol. Invasions* **11**, 1421–1429 (2009).
64. Koenig, W. D., Hochachka, W. M., Zuckerberg, B. & Dickinson, J. L. Ecological determinants of American crow mortality due to West Nile virus during its North American sweep. *Oecologia* **163**, 903–909 (2010).
65. Keesing, F., Holt, R. D. & Ostfeld, R. S. Effects of species diversity on disease risk. *Ecol. Lett.* **9**, 485–498 (2006).
66. Mitchell, C. E., Mitchell, C. A., Tilman, D. & Groth, J. V. Effects of grassland plant species diversity, abundance, and composition on foliar fungal disease. *Ecology* **83**, 1713–1726 (2002).
67. Saul, A. Zoophylaxis or zoopotentiality: the outcome of introducing animals on vector transmission is highly dependent on the mosquito mortality while searching. *Malar. J.* **2**, 32–50 (2003).
68. Laracuenta, A., Brown, R. A. & Jobin, W. Comparison of four species of snails as potential decoys to intercept schistosome miracidia. *Am. J. Trop. Med. Hyg.* **28**, 99–105 (1979).
69. Zhu, Y.-Y. *et al.* Panicle blast and canopy moisture in rice cultivar mixtures. *Phytopathology* **95**, 433–438 (2005).
70. Mundt, C. Use of multiline cultivars and cultivar mixtures for disease management. *Annu. Rev. Phytopathol.* **40**, 381–410 (2002).
71. CDC. Hantavirus pulmonary syndrome in five pediatric patients—four states, 2009. *Morbidity Mortality Week Rep.* **58**, 1409–1412 (2009).
72. Yates, T. L. *et al.* The ecology and evolutionary history of an emergent disease: hantavirus pulmonary syndrome. *Bioscience* **52**, 989–998 (2002).

Supplementary Information is linked to the online version of the paper at www.nature.com/nature.

Acknowledgements We acknowledge the support of the joint NSF-NIH Ecology of Infectious Disease programme and the EPA Biodiversity and Human Health programme. M. Gillespie provided help in the preparation of the manuscript.

Author Contributions F.K. and R.S.O. conceived the review. F.K., L.K.B., P.D., A.D., C.D.H., R.D.H., P.H., A.J., K.E.J., C.E.M., S.S.M. and R.S.O. wrote and edited the text. T.B. prepared Fig. 2.

Author Information Reprints and permissions information is available at www.nature.com/reprints. The authors declare no competing financial interests. Readers are welcome to comment on the online version of this article at www.nature.com/nature. Correspondence and requests for materials should be addressed to F.K. (keesing@bard.edu).

Lkb1 regulates cell cycle and energy metabolism in haematopoietic stem cells

Daisuke Nakada^{1,2}, Thomas L. Saunders^{2,3} & Sean J. Morrison^{1,2}

Little is known about metabolic regulation in stem cells and how this modulates tissue regeneration or tumour suppression. We studied the *Lkb1* tumour suppressor and its substrate AMP-activated protein kinase (AMPK), kinases that coordinate metabolism with cell growth. Deletion of the *Lkb1* (also called *Stk11*) gene in mice caused increased haematopoietic stem cell (HSC) division, rapid HSC depletion and pancytopenia. HSCs depended more acutely on *Lkb1* for cell-cycle regulation and survival than many other haematopoietic cells. HSC depletion did not depend on mTOR activation or oxidative stress. *Lkb1*-deficient HSCs, but not myeloid progenitors, had reduced mitochondrial membrane potential and ATP levels. HSCs deficient for two catalytic α -subunits of AMPK (AMPK-deficient HSCs) showed similar changes in mitochondrial function but remained able to reconstitute irradiated mice. *Lkb1*-deficient HSCs, but not AMPK-deficient HSCs, exhibited defects in centrosomes and mitotic spindles in culture, and became aneuploid. *Lkb1* is therefore required for HSC maintenance through AMPK-dependent and AMPK-independent mechanisms, revealing differences in metabolic and cell-cycle regulation between HSCs and some other haematopoietic progenitors.

Lkb1 coordinates cell growth with energy metabolism. Energy stress prompts *Lkb1* to activate catabolic processes and mitochondrial biogenesis and to inactivate anabolic processes including mammalian target of rapamycin (mTOR)-mediated protein synthesis¹. *Lkb1* exerts these effects by activating AMPK and AMPK-related kinases². AMPK activates the tuberous sclerosis complex (TSC), which inhibits mTOR complex 1 (mTORC1), reducing protein translation and cell growth^{3,4}. AMPK also inactivates mTORC1 by phosphorylating Raptor⁵. AMPK can promote the function of Foxo family transcription factors^{6,7}, which regulate energy metabolism, cell cycle, apoptosis and oxidative stress⁸.

Lkb1 regulates embryogenesis and the metabolism and polarity of differentiated adult cells. The *Lkb1* homologue in *Caenorhabditis elegans* regulates embryo asymmetry⁹. *Drosophila* *Lkb1* and AMPK regulate cell polarity, asymmetric division and mitotic spindle formation in embryos^{10–12}. Mice deficient for *Lkb1* die at mid-gestation with vascular and neural tube defects^{13,14}. In adult tissues, *Lkb1* regulates the metabolism of muscle^{15,16}, liver¹⁷, pancreas^{18–20} and T cells^{21,22}. Deletion of *Lkb1* in mammalian neurons²³, epithelial cells²⁴ and pancreatic β cells^{18–20} disrupts their polarity or differentiation; however, *Lkb1* is not known to regulate stem-cell maintenance or adult tissue regeneration.

Lkb1-deficiency increases the proliferation of many tissues^{20,25–27} and immortalizes mouse embryonic fibroblasts²⁸. *Lkb1* is mutated in Peutz–Jeghers syndrome patients^{29,30}, who have a high incidence of epithelial cancers¹. These data suggest that the primary function of *Lkb1* in adult tissues is to negatively regulate cell division, preventing tissue overgrowth. To test whether *Lkb1* positively or negatively regulates stem-cell function we conditionally deleted *Lkb1* from haematopoietic cells.

Deletion of *Lkb1* depletes HSCs

Lkb1 messenger RNA was expressed at approximately twofold higher levels in HSCs (CD150⁺CD48⁺CD41⁺ lineage (Lin)[−]Sca-1⁺c-Kit⁺), transiently reconstituting multipotent progenitors (MPPs)

(CD150⁺CD48⁺CD41⁺Lin[−]Sca-1⁺c-Kit⁺)^{31,32} and granulocyte-macrophage progenitors (GMPs; Lin[−]Sca-1⁺c-Kit⁺CD34⁺CD16/32⁺ (ref. 33)) as compared to whole bone marrow (WBM) cells by quantitative real-time PCR (qPCR) (Supplementary Fig. 1d).

We generated a floxed allele of *Lkb1* (*Lkb1*^{fl}) by gene-targeting in Bruce4 embryonic stem (ES) cells³⁴ (Supplementary Fig. 1) then conditionally deleted *Lkb1* from haematopoietic cells in adult *Mx1-cre*; *Lkb1*^{fl/fl} mice by injecting polyinosinic-polycytidylic acid (pIpC)^{35,36} (Supplementary Fig. 1e, f). All control (*Lkb1*^{fl/fl}) mice and mutant (*Mx1-cre*; *Lkb1*^{fl/fl}) mice were treated with three injections of pIpC over 6 days and the time of analysis is indicated in days after the first pIpC injection. We used a low dose of pIpC (0.5 μ g per gram body mass) that was titrated to completely delete *Lkb1* without significantly altering HSC surface marker phenotype or cell cycle kinetics.

Deletion of *Lkb1* had little acute effect on the cellularity or composition of haematopoietic tissues 6–18 days after starting pIpC treatment (Fig. 1a–d and Supplementary Fig. 2a–c). However, pancytopenia was observed by 24–34 days after pIpC treatment (Fig. 1a, e and Supplementary Fig. 2d–l). Two and six days after starting pIpC treatment, HSC frequency significantly increased ($P < 0.0005$) in pIpC-treated *Mx1-cre*; *Lkb1*^{fl/fl} mice compared to littermate controls (Fig. 1f). HSC frequency declined to one-seventh of normal levels in pIpC-treated *Mx1-cre*; *Lkb1*^{fl/fl} mice by 18 days after pIpC treatment ($P < 0.0005$; Fig. 1f). MPPs transiently expanded and then were depleted in parallel with HSCs (Supplementary Fig. 4c, d). The absolute number of HSCs and MPPs followed similar trends (Supplementary Fig. 4). HSCs were therefore profoundly depleted by 18 days after pIpC treatment, before pancytopenia was evident.

Lkb1 deletion acutely increased the division of HSCs and MPPs but not most WBM cells. Five days after starting pIpC, *Mx1-cre*; *Lkb1*^{fl/fl} mice and *Lkb1*^{fl/fl} controls were administered 5-bromodeoxyuridine (BrdU) for 24 h. We observed a significant increase in BrdU incorporation in HSCs ($P < 0.005$) and MPPs ($P < 0.0005$) from *Mx1-cre*; *Lkb1*^{fl/fl} mice (Fig. 1g and Supplementary Fig. 5a). This increase in BrdU incorporation within *Lkb1*-deficient HSCs continued 18 days

¹Howard Hughes Medical Institute, Life Sciences Institute, Center for Stem Cell Biology, University of Michigan, Ann Arbor, Michigan 48109-2216, USA. ²Department of Internal Medicine, University of Michigan, Ann Arbor, Michigan 48109-2216, USA. ³Transgenic Animal Model Core, University of Michigan, Ann Arbor, Michigan 48109-2216, USA.

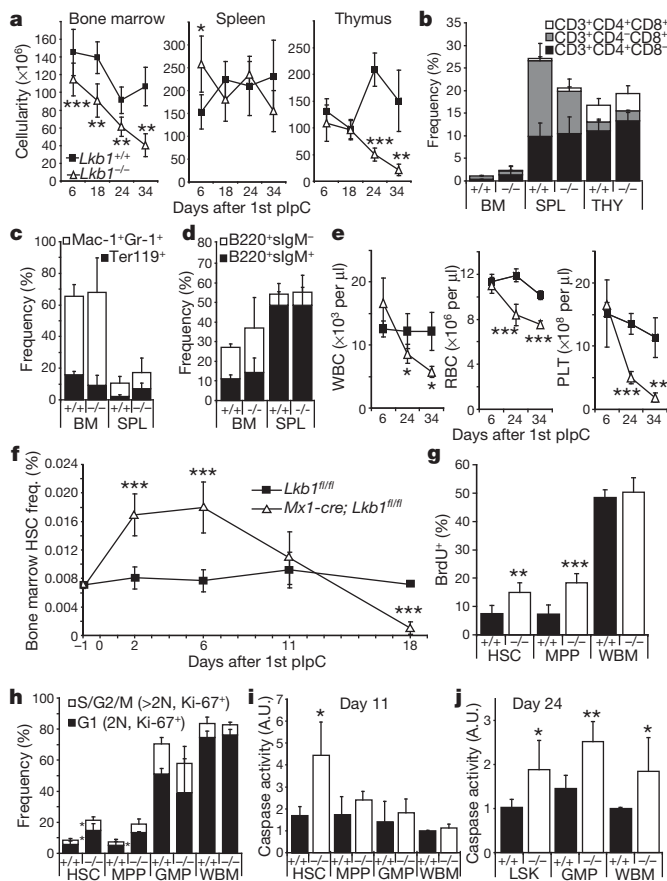


Figure 1 | *Lkb1* deletion causes HSCs to go into cycle before being depleted.

a, *Lkb1* deletion had a limited effect on the cellularity of WBM, spleen or thymus 6–18 days after starting pIpC but WBM and thymus cellularity declined significantly by 24–34 days (all panels show mean \pm standard deviation (s.d.) from at least three independent experiments; * $P < 0.05$; ** $P < 0.005$; *** $P < 0.0005$ by Student's *t*-test). +/+ indicates *Lkb1*^{fl/fl} mice and -/- indicates *Mx1-cre; Lkb1*^{fl/fl} mice. **b–d**, *Lkb1* deletion had little effect on T (**b**), myeloid or erythroid (**c**), or B (**d**) lineage cells 18 days after pIpC treatment. BM, bone marrow; SPL, spleen; THY, thymus. **e**, White blood cells (WBC), red blood cells (RBC) and platelets (PLT) were significantly depleted in the blood of *Lkb1*-deficient mice by 24–34 days after pIpC treatment. **f**, HSC (CD150⁺CD48⁺CD41⁺Lin⁻Sca-1⁺c-Kit⁺) frequency significantly increased 2–6 days and significantly reduced 18 days after pIpC treatment in *Lkb1*-deficient mice. **g**, *Lkb1*-deficient HSCs and MPPs, but not WBM cells, incorporated significantly more BrdU (24-h pulse) 6 days after pIpC treatment. **h**, *Lkb1* deletion drove HSCs and MPPs into cycle, increasing the frequency of these cells in G1 (Ki67⁺ cells with 2N DNA content, 2.5-fold, $P < 0.05$) and S/G2/M phases of the cell cycle (Ki67⁺ cells with >2N DNA content, 2.4-fold, $P < 0.05$) at day 6, but did not affect the cell-cycle distribution of GMPs or WBM cells. **i, j**, *Lkb1*-deficient HSCs had significantly increased caspase activity (**i**, 2.6-fold) at day 11, but other haematopoietic progenitors did not significantly increase caspase activity until day 24 (**j**). A.U., arbitrary units.

after pIpC treatment, when HSC depletion was already evident (Supplementary Fig. 5b). *Lkb1*-deficiency also significantly ($P < 0.05$) increased the frequencies of HSCs and MPPs in G1 and S/G2/M phases of the cell cycle (Fig. 1h and Supplementary Fig. 5c). In contrast, we observed no effect of *Lkb1* deletion on the rate of BrdU incorporation or the frequency of cycling GMPs or WBM cells (Fig. 1g, h and Supplementary Fig. 5a, c).

Lkb1 deletion induced cell death in HSCs. Eleven days after starting pIpC, we observed significant ($P < 0.05$) increases in caspase activity (Fig. 1i) and the frequency of annexin-V⁺4',6-diamidino-2-phenylindole (DAPI)⁺ dead cells (Supplementary Fig. 5d) in *Lkb1*-deficient HSCs but not in MPPs, GMPs or WBM cells. Lin⁻Sca-1⁺c-Kit⁺ (LSK) cells, GMPs and WBM cells from *Lkb1*-deficient mice eventually underwent

cell death, with significantly ($P < 0.05$) increased caspase activity 24 days after pIpC treatment (Fig. 1j). HSCs therefore depend more acutely on *Lkb1* for survival than many other haematopoietic progenitors.

Lkb1-deficient HSCs fail to long-term reconstitute

Lkb1-deficient HSCs failed to long-term multilineage reconstitute irradiated mice. One million donor (CD45.2⁺) WBM cells from *Mx1-cre; Lkb1*^{fl/fl} or *Lkb1*^{fl/fl} mice 6 days after starting pIpC treatment were transplanted into irradiated recipient (CD45.1⁺) mice along with 500,000 recipient cells. *Lkb1*-deficient cells gave significantly lower levels of overall (Fig. 2a), myeloid, B and T (Supplementary Fig. 6a–c) lineage reconstitution.

This reflected an autonomous requirement for *Lkb1* in HSCs. We transplanted one million donor WBM cells from *Mx1-cre; Lkb1*^{fl/fl} mice or *Lkb1*^{fl/fl} controls, without pIpC treatment, along with 500,000 wild-type recipient cells into irradiated recipient mice. Six weeks after transplantation, when donor cells had stably engrafted, we treated all the recipients with pIpC. Reconstitution by *Mx1-cre; Lkb1*^{fl/fl} cells, but not *Lkb1*^{fl/fl} cells, dropped precipitously (Fig. 2b and Supplementary Fig. 6d–f). The low level of residual reconstitution by *Mx1-cre; Lkb1*^{fl/fl} cells was from cells that had not fully deleted *Lkb1* (Supplementary Fig. 7b). Two months after pIpC treatment we recovered donor HSCs from recipients of *Lkb1*^{fl/fl} cells, but not from recipients of *Mx1-cre; Lkb1*^{fl/fl} cells (Fig. 2c).

Lkb1-deficient HSCs were also unable to form normal colonies in culture. Significantly ($P < 0.0005$) fewer *Lkb1*-deficient HSCs formed colonies as compared to control HSCs (Fig. 2d). The *Lkb1*-deficient colonies that did form were often much smaller than control colonies

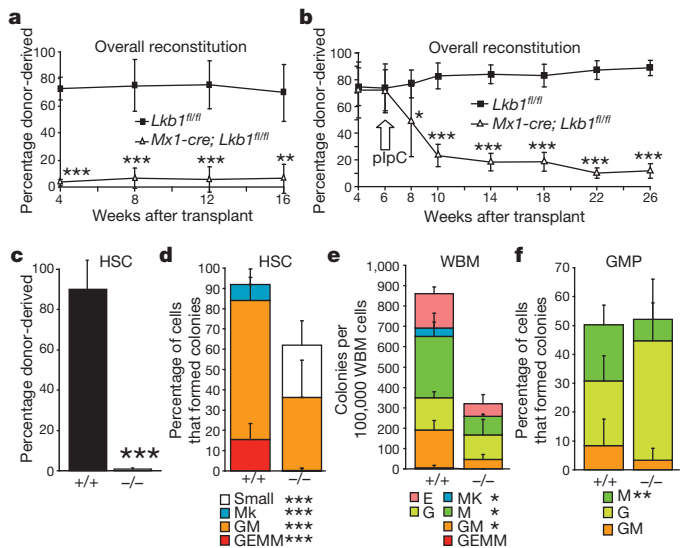


Figure 2 | *Lkb1*-deficient HSCs have a cell-autonomous defect in their ability to reconstitute irradiated mice and to form colonies in culture.

a–c, 1×10^6 donor WBM cells from *Lkb1*^{fl/fl} or *Mx1-cre; Lkb1*^{fl/fl} mice were transplanted into irradiated recipient mice along with 500,000 recipient WBM cells. The transplant was performed 6 days after (**a**) or 6 weeks before (**b**) pIpC treatment. Reconstitution levels were monitored for 16–20 weeks after transplantation (**a**) or after pIpC treatment (**b**). Data (mean \pm s.d.) are from one representative experiment of each type out of three independent experiments of each type. **c**, Donor HSCs (CD150⁺CD48⁺CD41⁺Lin⁻Sca-1⁺c-Kit⁺) were depleted in recipients of *Mx1-cre; Lkb1*^{fl/fl} (*Lkb1*-deficient) cells 2 months after pIpC treatment. Data are from four independent experiments. Six days after pIpC treatment, the frequencies of HSCs (**d**), WBM cells (**e**) and GMPs (**f**) that formed granulocyte, erythroid, macrophage, megakaryocyte (GEMM), granulocyte, macrophage (GM), megakaryocyte (Mk), 'small' colonies with fewer than 100 cells, or single lineage (G, or M, or E) colonies in culture are shown. Data (mean \pm s.d.) are from 3–16 independent experiments per cell type. For all panels: * $P < 0.05$; ** $P < 0.005$; *** $P < 0.0005$ by Student's *t*-test.

(Supplementary Fig. 7a) and failed to form any secondary colonies upon subcloning (Supplementary Fig. 5e). *Lkb1*-deficient WBM cells also formed significantly fewer colonies ($P < 0.005$, Fig. 2e); however, not all colony-forming progenitors required *Lkb1*. Approximately 50% of sorted GMP cells formed colonies irrespective of whether they were wild type or *Lkb1*-deficient (Fig. 2f and Supplementary Fig. 7a). Complete deletion of *Lkb1* was confirmed by western blotting of freshly isolated cells (Fig. 3a).

mTORC1-independent depletion of *Lkb1*-deficient HSCs

To test if AMPK was inactivated by *Lkb1* deletion, we isolated 30,000 $\text{Lin}^- \text{Sca-1}^+ \text{c-Kit}^+ \text{CD48}^-$ (LSK48⁺) cells (highly enriched for HSCs³¹),

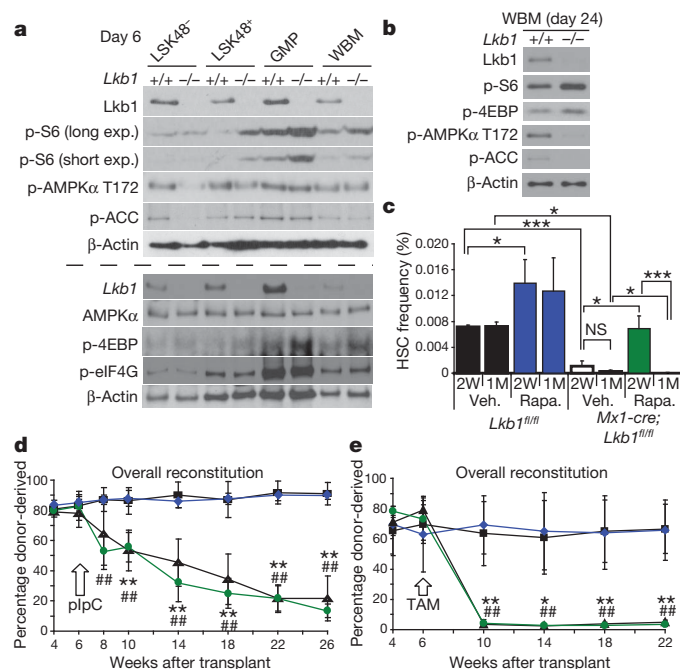


Figure 3 | AMPK signalling requires *Lkb1* in HSCs/MPPs but HSC depletion could not be rescued with rapamycin. **a**, Six days after pIpC treatment, *Lkb1* deletion increased mTORC1 activation (phospho-S6 and phospho-4EBP levels) in restricted progenitors (LSK48⁺ cells, GMPs and WBM cells) but not in LSK48⁺ cells (HSCs/MPPs). Decreased phospho-AMPKα T172 was noted in *Lkb1*-deficient LSK48⁺ and to a lesser extent in LSK48⁺ cells but not in GMPs or WBM cells. Phospho-ACC was decreased in *Lkb1*-deficient LSK48⁺ cells but not in other populations. We did not observe a consistent change in phospho-eIF4G levels after *Lkb1* deletion in any population. Each lane contained protein from 30,000 sorted cells. +/+ indicates *Lkb1*^{fl/fl} cells and -/- indicates *Mx1-cre; Lkb1*^{fl/fl} cells after pIpC treatment. This panel reflects two independent experiments (upper and lower panels separated by the dashed line). **b**, Twenty-four days after pIpC treatment, phospho-AMPKα T172 and phospho-ACC were decreased and phospho-S6 and phospho-4EBP levels were increased in *Lkb1*-deficient WBM cells. **c–e**, Rapamycin failed to rescue the depletion of *Lkb1*-deficient HSCs. Error bars indicate mean \pm s.d. **c**, Mice were treated with rapamycin after pIpC treatment for 2 weeks (2W) or 1 month (1M). Data are from 3–4 independent experiments. NS, not significant. **d–e**, Rapamycin failed to rescue the reconstituting capacity of *Lkb1*-deficient HSCs, irrespective of whether *Lkb1* was deleted using pIpC in *Mx1-cre; Lkb1*^{fl/fl} mice (**d**) or using tamoxifen in *Ubc-cre-ERT2* mice (**e**). In each case, 1×10^6 donor WBM cells from untreated mutant (*Mx1-cre; Lkb1*^{fl/fl} in **d**; *Ubc-cre-ERT2; Lkb1*^{fl/fl} in **e**) or control (*Lkb1*^{fl/fl}) mice were transplanted into irradiated mice along with 500,000 recipient WBM cells. Six weeks after transplantation, all recipients were treated with pIpC (**d**) or tamoxifen (TAM; **e**), then treated with rapamycin or vehicle. One representative experiment is shown out of 2–3 independent experiments for each mode of *Lkb1* deletion (* $P < 0.05$; ** $P < 0.005$ for *Lkb1*^{fl/fl} versus *Mx1-cre; Ubc-cre-ERT2; Lkb1*^{fl/fl} recipients treated with vehicle; ## $P < 0.005$ for *Lkb1*^{fl/fl} versus *Mx1-cre; Ubc-cre-ERT2; Lkb1*^{fl/fl} recipients treated with rapamycin).

LSK48⁺ cells (a mixed population of restricted progenitors), GMPs, or WBM cells from *Lkb1*-deficient and littermate control mice 6 days after pIpC treatment and analysed protein extracts by western blotting. *Lkb1* was expressed by each cell population from control mice but not by cells from mutant mice (Fig. 3a). AMPKα T172 phosphorylation (the site phosphorylated by *Lkb1* (refs 1, 2, 37)) was reduced in *Lkb1*-deficient LSK48⁺ HSCs and to a lesser extent than in LSK48⁺ progenitors, but not in GMPs or WBM cells (Fig. 3a). Phosphorylation of acetyl-CoA carboxylase (ACC), a known substrate of AMPK³⁷, was substantially reduced in *Lkb1*-deficient LSK48⁺ HSCs but not in other cell populations 6 days after pIpC treatment (Fig. 3a). AMPKα T172 and ACC phosphorylation levels were ultimately reduced in *Lkb1*-deficient WBM cells by 24 days after pIpC treatment (Fig. 3b). *Lkb1* therefore regulates AMPK activation in many haematopoietic cells but HSCs depend more acutely upon *Lkb1* for AMPK regulation.

AMPK negatively regulates mTOR activation^{1,2,37} and increased mTOR activation leads to HSC depletion³⁶. We assessed mTORC1 activation based on S6, 4EBP and eIF4G phosphorylation. Phosphorylation of eIF4G did not change significantly after *Lkb1* deletion in any population (Fig. 3a). Phospho-S6 and phospho-4EBP levels increased in *Lkb1*-deficient LSK48⁺ restricted progenitors, GMPs and WBM cells but not in *Lkb1*-deficient LSK48⁺ HSCs (Fig. 3a). *Lkb1*-AMPK signalling is either not required to regulate mTORC1 in HSCs or mTORC1 activity in *Lkb1*-deficient HSCs reflects a complex balance of effects on AMPK/TSC activation versus mitochondrial function/ATP levels³⁸. Either way, *Lkb1* seems to regulate phosphatidylinositol-3-kinase–mTORC1 pathway signalling differently in HSCs as compared to many other haematopoietic progenitors.

To test whether mTOR activation contributes to HSC depletion, we tested whether rapamycin could rescue the depletion of *Lkb1*-deficient HSCs. *Mx1-cre; Lkb1*^{fl/fl} mice and *Lkb1*^{fl/fl} controls were treated with pIpC, then injected daily with rapamycin for 2 weeks or 1 month. Rapamycin treatment increased HSC frequency in both wild-type and *Lkb1*-deficient mice after 2 weeks but rapamycin did not rescue the depletion of HSCs 1 month after *Lkb1* deletion (Fig. 3c). We also transplanted one million *Mx1-cre; Lkb1*^{fl/fl} or *Lkb1*^{fl/fl} WBM cells into irradiated mice along with 500,000 recipient WBM cells. We treated the recipient mice with pIpC 6 weeks later then administered rapamycin daily to half of the recipient mice. In contrast to what we observed after *Pten* deletion³⁶, rapamycin did not significantly affect reconstitution levels by *Lkb1*-deficient cells (Fig. 3d and Supplementary Fig. 6g–i). Our data indicate that increased mTOR activation is not a major mediator of HSC depletion after *Lkb1* deletion.

These results were confirmed using tamoxifen-inducible *Ubc-cre-ERT2; Lkb1*^{fl/fl} mice³⁹. Tamoxifen-induced deletion of *Lkb1* led to a rapid loss of donor cell reconstitution that was not attenuated by rapamycin treatment (Fig. 3e and Supplementary Fig. 6j–l). The depletion of *Lkb1*-deficient HSCs therefore does not require pIpC.

Lkb1 regulates HSC mitochondrial function

Prkaa1 and *Prkaa2*, which encode the two catalytic α -subunits of AMPK, were more highly expressed in various haematopoietic stem/progenitor cell populations than in unfractionated WBM cells (Supplementary Fig. 8a, b). To test whether AMPK regulates HSC function, we generated floxed alleles of both catalytic subunits of AMPK (*Prkaa1*^{fl} and *Prkaa2*^{fl}; Supplementary Fig. 9). pIpC-treated *Mx1-cre; Prkaa1*^{fl/fl}; *Prkaa2*^{fl/fl} mice are hereafter described as AMPK-deficient mice (*Mx1-cre; AMPK α 1/ α 2*^{fl/fl} or AMPK α -/-) for simplicity. After pIpC treatment, AMPK α expression, AMPK T172 phosphorylation and ACC phosphorylation were significantly reduced in all cell populations analysed from *Mx1-cre; AMPK α 1/ α 2*^{fl/fl} mice (Fig. 4a). In contrast to *Lkb1*, AMPK deletion increased phospho-S6 levels in all populations including LSK48⁺ HSCs, LSK48⁺ restricted progenitors, GMPs and WBM cells. These results indicate that AMPK negatively regulates mTORC1 signalling in many haematopoietic stem and progenitor cells.

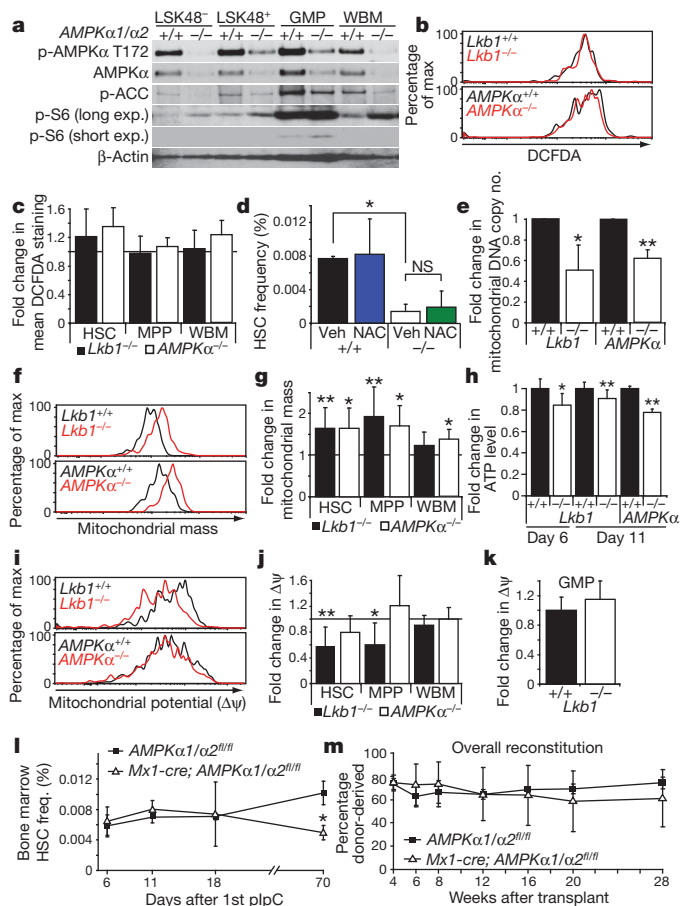


Figure 4 | AMPK deficiency partially phenocopies the mitochondrial defects but not the HSC depletion observed after *Lkb1* deletion. **a**, *AMPKα1/α2* deficiency reduced phospho-AMPKα T172 and phospho-ACC levels and increased phospho-S6 levels, as expected. Each lane contained protein from 30,000 sorted cells. *+/+* indicates *AMPKα1/α2^{fl/fl}* cells and *-/-* indicates *Mx1-cre; AMPKα1/α2^{fl/fl}* cells 6 days after pIpC treatment. **b**, **c**, *Lkb1* or *AMPKα* deletion did not significantly affect 2'-7'-dichlorofluorescein diacetate (DCFDA) staining (ROS levels) in HSCs (**b**, **c**), MPPs or WBM (**c**) cells 11 days after pIpC treatment. **d**, NAC treatment for 2 weeks did not rescue the depletion of *Lkb1*-deficient HSCs (**P* < 0.05 by Student's *t*-test). **e**, Mitochondrial DNA copy number was significantly reduced 6 days after *Lkb1* or *AMPKα* deletion (**P* < 0.05; ***P* < 0.005 in all panels). **f**, **g**, Mitochondrial mass significantly increased 11 days after *Lkb1* deletion in HSCs and MPPs, but not in WBM cells. *AMPKα* deletion significantly increased mitochondrial mass in all populations 11 days after pIpC treatment. A representative histogram shows Mitotracker staining in HSCs after *Lkb1* or *AMPKα* deletion (**f**). **h**, ATP levels were significantly reduced in HSCs after *Lkb1* or *AMPKα* deletion, 6 or 11 days after pIpC treatment. **i**–**k**, Mitochondrial membrane potential ($\Delta\Psi$) was significantly reduced after *Lkb1* deletion in HSCs (**i**, **j**) and MPPs but not in WBM cells (**j**) or GMPs (**k**) 11 days after pIpC treatment. *AMPKα* deletion did not reduce $\Delta\Psi$ in any cell population (**i**, **j**). **l**, *AMPKα* deletion did not cause transient expansion or rapid depletion of HSCs, but did modestly reduce HSC frequency 70 days after pIpC treatment (*P* < 0.05). **m**, *AMPKα*-deficient HSCs were capable of long-term multilineage reconstitution 6 days after pIpC treatment, in contrast to *Lkb1*-deficient HSCs (Fig. 2a, b). All data (mean \pm s.d.) are from 3–7 independent experiments.

Elevated reactive oxygen species (ROS) contribute to HSC depletion in *Foxo*-deficient mice^{40,41}. However, neither *Lkb1* deletion nor *AMPK* deletion significantly affected ROS levels, measured by 2'-7'-dichlorofluorescein diacetate staining 11 days after pIpC treatment (Fig. 4b, c). Oxidative stress contributed little to the depletion of *Lkb1*-deficient HSCs as *N*-acetyl-cysteine (NAC) treatment of *Mx1-cre; Lkb1^{fl/fl}* mice did not rescue HSC depletion (Fig. 4d).

Mitochondria were misregulated in *Lkb1*-deficient and *AMPK*-deficient haematopoietic cells. Eleven days after pIpC treatment,

mitochondrial mass was significantly (*P* < 0.05) increased in both *Lkb1*-deficient and *AMPK*-deficient HSCs (Fig. 4f, g). This could reflect negative regulation of mitochondrial mass by *Lkb1*–*AMPK* or a compensatory expansion of mitochondria in response to mitochondrial dysfunction and ATP depletion, as observed with *Tfam* deficiency⁴². Consistent with the latter possibility, we observed a significant reduction in mitochondrial DNA copy number in both *Lkb1*-deficient and *AMPK*-deficient HSCs 6 days after pIpC treatment (Fig. 4e), as observed in *Tfam*-deficient cells⁴². We also observed a significant (*P* < 0.05) reduction in mitochondrial membrane potential ($\Delta\Psi$) within *Lkb1*-deficient HSCs but not in *AMPK*-deficient HSCs (Fig. 4i, j). This reduction in $\Delta\Psi$ was not observed in *Lkb1*-deficient GMPs or WBM cells (Fig. 4j, k). It is formally possible that the reduction in $\Delta\Psi$ in *Lkb1*-deficient HSCs was caused by the induction of apoptosis. However, we did not observe reduced $\Delta\Psi$ in early apoptotic cells (annexin-V⁺DAPI[−]) compared to cells that showed no sign of initiating cell death (annexin-V[−]DAPI[−]) (Supplementary Fig. 11a). These results indicate that *Lkb1* regulates mitochondrial function by *AMPK*-dependent and *AMPK*-independent mechanisms.

To test ATP levels we sorted live cells from each population to ensure that ATP levels were not confounded by the presence of dead cells or debris, and to normalize ATP levels on a per cell basis. At 6 and 11 days after starting pIpC treatment, we observed a 10–15% reduction in cellular ATP levels in *Lkb1*-deficient HSCs (*P* < 0.05; Fig. 4h) but not in *Lkb1*-deficient MPPs and GMPs (Supplementary Fig. 11b). *AMPK*-deficient HSCs also had significantly reduced levels of ATP 11 days after pIpC treatment (*P* < 0.005) (Fig. 4h). The *Lkb1*–*AMPK* pathway is thus required for mitochondrial function and energy homeostasis in HSCs.

Although *AMPK* deficiency phenocopied some of the effects of *Lkb1* deficiency in HSCs, *AMPK* was not required for HSC maintenance. We did not observe a transient increase (day 6) or a rapid depletion (day 18) of HSCs after pIpC treatment of *Mx1-cre; AMPKα1/α2^{fl/fl}* mice (Fig. 4l). We did, however, observe a twofold reduction in HSC frequency in *AMPK*-deficient mice 70 days after pIpC treatment (*P* < 0.05, Fig. 4l). *AMPK*-deficient HSCs also gave long-term multilineage reconstitution (Fig. 4m and Supplementary Fig. 10). We confirmed that the reconstituting cells in these experiments were *AMPK*-deficient (data not shown). This indicates that *Lkb1* promotes HSC maintenance through mechanisms that are largely *AMPK*-independent.

Lkb1-deficient HSCs become aneuploid

To examine carefully HSC division we sorted HSCs from *Mx1-cre; Lkb1^{fl/fl}* mice and *Lkb1^{fl/fl}* controls into culture after pIpC treatment. Almost all HSCs, regardless of *Lkb1*, divided during the first 3 days of culture (Fig. 5a). However, wild-type HSCs subsequently expanded geometrically, whereas *Lkb1*-deficient HSCs exhibited little further division (Fig. 5b). The limited size of *Lkb1*-deficient HSC colonies was not due to reduced cell-cycle entry as wild-type and *Lkb1*-deficient colonies contained similar frequencies of BrdU⁺ cells after a 1-h pulse on the third day of culture (Fig. 5c). Instead, *Lkb1*-deficient colonies contained significantly (*P* < 0.05) fewer cells that stained positively for the mitosis marker phospho-histone H3 (Fig. 5d). This indicated that *Lkb1*-deficient HSCs were often unable to enter mitosis or they failed to complete mitosis owing to cell death.

Notably, many (32 \pm 9%) of the mitotic cells within *Lkb1*-deficient HSC colonies had supernumerary centrosomes and aberrant mitotic spindles, phenotypes not observed in control HSC colonies (Fig. 5e). We did not observe supernumerary centrosomes or aberrant mitotic spindles in GMPs (data not shown). This raised the possibility that many *Lkb1*-deficient HSCs may die or produce aneuploid progeny. Indeed, *Lkb1*-deficient HSC colonies, but not GMP colonies, contained significantly more annexin-V⁺ cells and dead cells (Fig. 5f, g). Although cells in colonies formed by wild-type (LSK) stem/progenitor cells rarely (6.3 \pm 6.1%) had abnormal chromosome numbers, cells in *Lkb1*-deficient colonies were often (40.5 \pm 19.9%) aneuploid

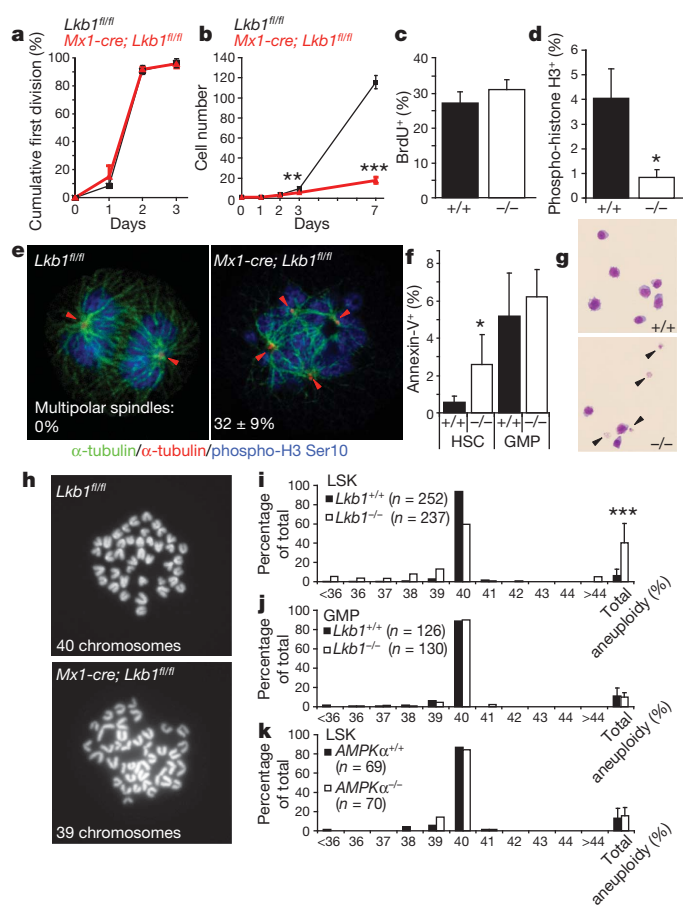


Figure 5 | *Lkb1*-deficient HSCs exhibit defects in mitotic spindles, aneuploidy and cell death. *Lkb1*-deficient HSCs (6 days after pIpC) only underwent a few divisions in culture. **a**, The fraction of cells that divided; **b**, the total number of cells per HSC colony. **c**, **d**, *Lkb1*-deficient HSCs entered S phase normally in culture (**c**) but failed to enter or complete mitosis, perhaps due to cell death (**d**). **e**, *Lkb1*-deficient HSCs, but not GMPs, exhibited supernumerary centrosomes (red arrowheads) and defective mitotic spindles: α-tubulin (green) marks mitotic spindles, γ-tubulin (red) marks centrosomes, and phospho-H3 Ser 10 (blue) marks M phase cells. **f**, **g**, Increased cell death within *Lkb1*-deficient HSC colonies but not GMP colonies based on annexin-V (**f**) or Wright-giemsa (**g**; see the cell fragments, indicated by arrowheads) staining. ×40 magnification images are shown. **h–j**, Cells within *Lkb1*-deficient LSK (Lin⁺ Sca-1⁺ c-Kit⁺) colonies, but not within GMP colonies, became aneuploid within 2 days in culture. Representative chromosome spreads of wild-type and *Lkb1*-deficient LSK cells with 40 and 39 chromosomes, respectively (**h**). **k**, AMPKα-deficient LSK cells did not become aneuploid. All data (mean ± s.d.) are from 3–8 independent experiments, with the indicated numbers of cells scored for chromosome numbers. For all panels: **P* < 0.05; ***P* < 0.005; ****P* < 0.0005 by Student's *t*-test.

(*P* < 0.0005, Fig. 5h, i). *Lkb1*-deficient GMPs from the same mice did not show a significant increase in aneuploidy (Fig. 5j, *P* = 0.75), consistent with their ability to form normal colonies in culture (Fig. 2f). AMPK-deficient LSK cells also did not show increased aneuploidy (Fig. 5k), indicating that *Lkb1* regulates chromosome stability through AMPK-independent pathways.

Discussion

Consistent with our results, two accompanying papers^{43,44} also concluded that *Lkb1* is autonomously required for cell-cycle regulation, survival, mitochondrial function and energy homeostasis in HSCs and that HSCs depend more acutely on *Lkb1* than many other haematopoietic cells. The earlier onset of pancytopenia observed by refs 43 and 44 after *Lkb1* deletion could be explained by the different allele of *Lkb1* (ref. 28) or different genetic background used in those studies,

by the ubiquitous deletion of *Lkb1* with Rosa26-CreER in the study by ref. 43, or by the use of a higher dose of pIpC in the study by ref. 44 (Supplementary Fig. 3).

HSCs were more rapidly depleted after *Lkb1* deletion (Fig. 1f) than after *Pten*³⁶ or *Foxo*⁴¹ deletion. Whereas the mTOR inhibitor rapamycin and/or the anti-oxidant NAC rescued the depletion of *Pten*-deficient HSCs³⁶ and *Foxo*-deficient HSCs⁴¹, they failed to rescue the depletion of *Lkb1*-deficient HSCs (Figs 3c–e and 4d). *Lkb1*-deficient HSCs are therefore depleted by mechanisms that do not depend on increased mTOR activation or ROS levels. *Lkb1* also regulated energy metabolism and mitochondrial function in HSCs through AMPK-dependent and AMPK-independent mechanisms. However, whereas *Lkb1* deficiency and AMPK deficiency both reduced ATP levels in HSCs, AMPK deficiency had much less effect on HSC frequency or function. *Lkb1* also maintained chromosome stability in HSCs through AMPK-independent mechanisms, as AMPK-deficient primitive progenitors did not show increased aneuploidy (Fig. 5k). It is unclear whether *Lkb1* prevents aneuploidy by regulating mitosis or whether the mitotic defects were secondary to other defects, such as in mitotic entry⁴⁵. Our results indicate that in adult mammals, *Lkb1* promotes stem-cell maintenance and tissue regeneration by regulating energy metabolism and by preventing aneuploidy.

METHODS SUMMARY

Mice. Targeting vectors to generate *Stk11^{tm1Sjm}* (*Lkb1^{fl}*), *Prkaa1^{fl}* and *Prkaa2^{fl}* mice were constructed by recombineering⁴⁶ (see Supplementary Figs 1 and 9 for details). Bruce4 ES cells³⁴ were electroporated with the targeting vector and positive clones identified by Southern blotting were injected into blastocysts from C57BL/6-Tyr^{c-2J} mice. The resulting male chimaeric mice were bred to female C57BL/6-Tyr^{c-2J} mice to obtain germline transmission. The FRT-Neo-FRT cassette was removed by crossing with Flp deleter mice⁴⁷, then the mice were backcrossed at least three additional times onto a C57BL/6 background. C57BL/Ka-Thy-1.1 (CD45.2) and C57BL/Ka-Thy-1.2 (CD45.1) mice were used in transplantation experiments. *Mx1-cre* mice³⁵ and *Ubc-cre-ERT2* mice³⁹ were backcrossed onto a C57BL/6 background. All mice were housed in the Unit for Laboratory Animal Medicine at the University of Michigan and treated with procedures approved by the University of Michigan Committee on the Use and Care of Animals.

pIpC, rapamycin, N-acetyl-L-cysteine and tamoxifen administration. pIpC (Amersham) was re-suspended in Dulbecco's PBS at 50 μg ml⁻¹, and mice were injected intraperitoneally (i.p.) with 0.5 μg g⁻¹ of body mass every other day for 6 days. Rapamycin (LC Laboratories) was administered daily by i.p. injection at a dose of 4 mg kg⁻¹ (ref. 36). N-acetyl-L-cysteine (NAC; Sigma) was administered daily by subcutaneous injection at 100 mg kg⁻¹ (pH 7.0)⁴¹. Tamoxifen citrate (Spectrum Chemical) was mixed with regular chow at 400 mg kg⁻¹ with 5% sucrose (Teklad) and given to mice starting at the indicated time point.

Full Methods and any associated references are available in the online version of the paper at www.nature.com/nature.

Received 26 April; accepted 11 October 2010.

- Shackelford, D. B. & Shaw, R. J. The LKB1-AMPK pathway: metabolism and growth control in tumour suppression. *Nature Rev. Cancer* **9**, 563–575 (2009).
- Alessi, D. R., Sakamoto, K. & Bayascas, J. R. LKB1-dependent signaling pathways. *Annu. Rev. Biochem.* **75**, 137–163 (2006).
- Inoki, K., Zhu, T. & Guan, K. L. TSC2 mediates cellular energy response to control cell growth and survival. *Cell* **115**, 577–590 (2003).
- Corradetti, M. N., Inoki, K., Bardeesy, N., DePinho, R. A. & Guan, K. L. Regulation of the TSC pathway by LKB1: evidence of a molecular link between tuberous sclerosis complex and Peutz-Jeghers syndrome. *Genes Dev.* **18**, 1533–1538 (2004).
- Gwinn, D. M. et al. AMPK phosphorylation of raptor mediates a metabolic checkpoint. *Mol. Cell* **30**, 214–226 (2008).
- Greer, E. L. et al. The energy sensor AMP-activated protein kinase directly regulates the mammalian FOXO3 transcription factor. *J. Biol. Chem.* **282**, 30107–30119 (2007).
- Cantó, C. et al. AMPK regulates energy expenditure by modulating NAD⁺ metabolism and SIRT1 activity. *Nature* **458**, 1056–1060 (2009).
- Salih, D. A. & Brunet, A. FoxO transcription factors in the maintenance of cellular homeostasis during aging. *Curr. Opin. Cell Biol.* **20**, 126–136 (2008).
- Watts, J. L., Morton, D. G., Bestman, J. & Kempthorne, K. J. The *C. elegans par-4* gene encodes a putative serine-threonine kinase required for establishing embryonic asymmetry. *Development* **127**, 1467–1475 (2000).
- Lee, J. H. et al. Energy-dependent regulation of cell structure by AMP-activated protein kinase. *Nature* **447**, 1017–1020 (2007).

11. Martin, S. G. & St Johnston, D. A role for *Drosophila* Lkb1 in anterior-posterior axis formation and epithelial polarity. *Nature* **421**, 379–384 (2003).
12. Bonaccorsi, S. *et al.* The *Drosophila* Lkb1 kinase is required for spindle formation and asymmetric neuroblast division. *Development* **134**, 2183–2193 (2007).
13. Ylikorkala, A. *et al.* Vascular abnormalities and deregulation of VEGF in Lkb1-deficient mice. *Science* **293**, 1323–1326 (2001).
14. Jishage, K. *et al.* Role of Lkb1, the causative gene of Peutz-Jegher's syndrome, in embryogenesis and polyposis. *Proc. Natl Acad. Sci. USA* **99**, 8903–8908 (2002).
15. Sakamoto, K. *et al.* Deficiency of LKB1 in skeletal muscle prevents AMPK activation and glucose uptake during contraction. *EMBO J.* **24**, 1810–1820 (2005).
16. Sakamoto, K. *et al.* Deficiency of LKB1 in heart prevents ischemia-mediated activation of AMPK α 2 but not AMPK α 1. *Am. J. Physiol. Endocrinol. Metab.* **290**, E780–E788 (2006).
17. Shaw, R. J. *et al.* The kinase LKB1 mediates glucose homeostasis in liver and therapeutic effects of metformin. *Science* **310**, 1642–1646 (2005).
18. Fu, A. *et al.* Loss of Lkb1 in adult β cells increases β cell mass and enhances glucose tolerance in mice. *Cell Metab.* **10**, 285–295 (2009).
19. Granot, Z. *et al.* LKB1 regulates pancreatic beta cell size, polarity, and function. *Cell Metab.* **10**, 296–308 (2009).
20. Hezel, A. F. *et al.* Pancreatic LKB1 deletion leads to acinar polarity defects and cystic neoplasms. *Mol. Cell. Biol.* **28**, 2414–2425 (2008).
21. Tamás, P. *et al.* LKB1 is essential for the proliferation of T cell progenitors and mature peripheral T cells. *Eur. J. Immunol.* **40**, 242–253 (2010).
22. Cao, Y. *et al.* The serine/threonine kinase LKB1 controls thymocyte survival through regulation of AMPK activation and Bcl-XL expression. *Cell Res.* **20**, 99–108 (2010).
23. Barnes, A. P. *et al.* LKB1 and SAD kinases define a pathway required for the polarization of cortical neurons. *Cell* **129**, 549–563 (2007).
24. Shorning, B. Y. *et al.* Lkb1 deficiency alters goblet and paneth cell differentiation in the small intestine. *PLoS ONE* **4**, e4264 (2009).
25. Contreras, C. M. *et al.* Loss of Lkb1 provokes highly invasive endometrial adenocarcinomas. *Cancer Res.* **68**, 759–766 (2008).
26. Pearson, H. B., McCarthy, A., Collins, C. M., Ashworth, A. & Clarke, A. R. Lkb1 deficiency causes prostate neoplasia in the mouse. *Cancer Res.* **68**, 2223–2232 (2008).
27. Gurumurthy, S. *et al.* LKB1 deficiency sensitizes mice to carcinogen-induced tumorigenesis. *Cancer Res.* **68**, 55–63 (2008).
28. Bardeesy, N. *et al.* Loss of the Lkb1 tumour suppressor provokes intestinal polyposis but resistance to transformation. *Nature* **419**, 162–167 (2002).
29. Jenne, D. E. *et al.* Peutz-Jeghers syndrome is caused by mutations in a novel serine threonine kinase. *Nature Genet.* **18**, 38–43 (1998).
30. Hemminki, A. *et al.* A serine/threonine kinase gene defective in Peutz-Jeghers syndrome. *Nature* **391**, 184–187 (1998).
31. Kiel, M. J., Yilmaz, O. H., Iwashita, T., Terhorst, C. & Morrison, S. J. SLAM family receptors distinguish hematopoietic stem and progenitor cells and reveal endothelial niches for stem cells. *Cell* **121**, 1109–1121 (2005).
32. Kiel, M. J., Yilmaz, O. H. & Morrison, S. J. CD150⁺ cells are transiently reconstituting multipotent progenitors with little or no stem cell activity. *Blood* **111**, 4413–4414 (2008).
33. Akashi, K., Traver, D., Miyamoto, T. & Weissman, I. L. A clonogenic common myeloid progenitor that gives rise to all myeloid lineages. *Nature* **404**, 193–197 (2000).
34. Köntgen, F., Suss, G., Stewart, C., Steinmetz, M. & Bluethmann, H. Targeted disruption of the MHC Class-II A gene in C57BL/6 mice. *Int. Immunol.* **5**, 957–964 (1993).
35. Kuhn, R., Schwenk, F., Aguet, M. & Rajewsky, K. Inducible gene targeting in mice. *Science* **269**, 1427–1429 (1995).
36. Yilmaz, O. H. *et al.* Pten dependence distinguishes haematopoietic stem cells from leukaemia-initiating cells. *Nature* **441**, 475–482 (2006).
37. Hardie, D. G. AMP-activated/SNF1 protein kinases: conserved guardians of cellular energy. *Nature Rev. Mol. Cell Biol.* **8**, 774–785 (2007).
38. Schieke, S. M. *et al.* The mammalian target of rapamycin (mTOR) pathway regulates mitochondrial oxygen consumption and oxidative capacity. *J. Biol. Chem.* **281**, 27643–27652 (2006).
39. Ruzankina, Y. *et al.* Deletion of the developmentally essential gene ATR in adult mice leads to age-related phenotypes and stem cell loss. *Cell Stem Cell* **1**, 113–126 (2007).
40. Miyamoto, K. *et al.* Foxo3a is essential for maintenance of the hematopoietic stem cell pool. *Cell Stem Cell* **1**, 101–112 (2007).
41. Tothova, Z. *et al.* FoxOs are critical mediators of hematopoietic stem cell resistance to physiologic oxidative stress. *Cell* **128**, 325–339 (2007).
42. Larsson, N. G. *et al.* Mitochondrial transcription factor A is necessary for mtDNA maintenance and embryogenesis in mice. *Nature Genet.* **18**, 231–236 (1998).
43. Gan, B. *et al.* Lkb1 regulates quiescence and metabolic homeostasis of haematopoietic stem cells. *Nature* doi:10.1038/nature09595 (this issue).
44. Gurumurthy, S. *et al.* The Lkb1 metabolic sensor maintains haematopoietic stem cell survival. *Nature* doi:10.1038/nature09572 (this issue).
45. Holland, A. J. & Cleveland, D. W. Boveri revisited: chromosomal instability, aneuploidy and tumorigenesis. *Nature Rev. Mol. Cell Biol.* **10**, 478–487 (2009).
46. Liu, P., Jenkins, N. A. & Copeland, N. G. A highly efficient recombineering-based method for generating conditional knockout mutations. *Genome Res.* **13**, 476–484 (2003).
47. Rodriguez, C. I. *et al.* High-efficiency deleter mice show that FLPe is an alternative to Cre-loxP. *Nature Genet.* **25**, 139–140 (2000).

Supplementary Information is linked to the online version of the paper at www.nature.com/nature.

Acknowledgements This work was supported by the Howard Hughes Medical Institute. Flow cytometry was partially supported by the University of Michigan (UM) Comprehensive Cancer National Institutes of Health (NIH) CA46592. D.N. was supported by a postdoctoral fellowship from the Japan Society for the Promotion of Science. We thank A. Prendergast and C. Sifuentes for technical assistance; E. Hughes and the UM Transgenic Animal Model Core for help generating *Lkb1*^{fl} mice; D. Adams and M. White for flow cytometry; E. Smith for antibody production; C. Mountford, S. Grove and R. Coolon for mouse colony management; and L. Cantley and C. Thompson for discussions.

Author Contributions D.N. performed all experiments. T.L.S. helped to design and generate the *Lkb1*^{fl} mice. D.N. and S.J.M. designed and interpreted all experiments and wrote the paper.

Author Information Reprints and permissions information is available at www.nature.com/reprints. The authors declare no competing financial interests. Readers are welcome to comment on the online version of this article at www.nature.com/nature. Correspondence and requests for materials should be addressed to S.J.M. (seanjm@umich.edu).

METHODS

Mice. Targeting vectors to generate *Stk11^{tm1Sjm}* (*Lkb1^{fl}*), *Prkaa1^{fl}* and *Prkaa2^{fl}* mice were constructed by recombineering⁴⁶ (see Supplementary Figs 1 and 9 for details). Bruce4 ES cells³⁴ were electroporated with the targeting vector and positive clones identified by Southern blotting were injected into blastocysts from C57BL/6-*Tyr^{c-2J}* mice. The resulting male chimaeric mice were bred to female C57BL/6-*Tyr^{c-2J}* mice to obtain germline transmission. The FRT-Neo-FRT cassette was removed by crossing with Flp deleter mice⁴⁷, then the mice were backcrossed at least three additional times onto a C57BL/6 background. C57BL/Ka-Thy-1.1 (CD45.2) and C57BL/Ka-Thy-1.2 (CD45.1) mice were used in transplantation experiments. *Mx1-cre* mice³⁵ and *Ubc-cre-ERT2* mice³⁹ were backcrossed onto a C57BL/6 background. All mice were housed in the Unit for Laboratory Animal Medicine at the University of Michigan and treated with procedures approved by the University of Michigan Committee on the Use and Care of Animals.

plpC, rapamycin, N-acetyl-L-cysteine and tamoxifen administration. plpC (Amersham) was re-suspended in Dulbecco's PBS at 50 µg ml⁻¹, and mice were injected intraperitoneally (i.p.) with 0.5 µg g⁻¹ of body mass every other day for 6 days. Rapamycin (LC Laboratories) was administered daily by i.p. injection at a dose of 4 mg kg⁻¹ (ref. 36). N-acetyl-L-cysteine (NAC; Sigma) was administered daily by subcutaneous injection at 100 mg kg⁻¹ (pH 7.0)⁴¹. Tamoxifen citrate (Spectrum Chemical) was mixed with regular chow at 400 mg kg⁻¹ with 5% sucrose (Teklad) and given to mice starting at the indicated time point.

Flow cytometry and isolation of HSCs. Bone marrow cells were either flushed from the long bones (tibiae and femurs) or isolated by crushing the long bones (tibiae and femurs), pelvic bones and vertebrae with mortar and pestle in Hank's buffered salt solution (HBSS) without calcium and magnesium, supplemented with 2% heat-inactivated bovine serum (Gibco). Cells were triturated and filtered through a nylon screen (45 µm, Sefar America) or a 40 µm cell strainer (Fisher Scientific) to obtain a single-cell suspension. For isolation of CD150⁺CD48⁻CD41⁻Lin⁻Sca-1⁺c-Kit⁺ HSCs, bone marrow cells were incubated with PE-conjugated anti-CD150 (TC15-12F12.2; BioLegend), FITC-conjugated anti-CD48 (HM48-1; BioLegend), FITC-conjugated anti-CD41 (MWReg30; BD Biosciences), biotin-, APC- or PerCP-Cy5.5-conjugated anti-Sca-1 (Ly6A/E; E13-6.7), and biotin- or APC-conjugated anti-c-Kit (2B8) antibody, in addition to antibodies against the following FITC-conjugated lineage markers: Ter119, B220 (6B2), Gr-1 (8C5), and CD2 (RM2-5), CD3 (KT31.1) and CD8 (53-6.7). Unless otherwise mentioned, antibodies were obtained from BioLegend, BD Biosciences, or eBioscience. Biotin-conjugated antibodies were visualized using streptavidin-conjugated APC-Cy7. HSCs were sometimes pre-enriched by selecting Sca-1⁺ or c-Kit⁺ cells using paramagnetic microbeads and autoMACS (Miltenyi Biotec). Non-viable cells were excluded from sorts and analyses using the viability dye 4',6-diamidino-2-phenylindole (DAPI) (1 µg ml⁻¹). Apoptotic cells were identified using APC Annexin V (BD Biosciences). Flow cytometry was performed with FACSAria II or FACSCanto II flow-cytometers (BD Biosciences).

For isolation of Lin⁻Sca-1⁺c-Kit⁺ cells (LSKs) and Lin⁻Sca-1⁻c-Kit⁺CD34⁺CD16/CD32⁺ GMPs, whole bone marrow cells were incubated with FITC-conjugated anti-CD34 (RAM34) for 90 min on ice followed by addition of PE-conjugated monoclonal antibodies to lineage markers including B220 (6B2), CD3 (KT31.1), CD4 (GK1.5), CD8 (53-6.7), Gr-1 (8C5), Mac-1 (M1/70) and Ter119 in addition to APC-conjugated anti-Sca-1 (Ly6A/E; E13-6.7), biotin-conjugated anti-c-Kit (2B8) and Alexa Fluor 700 conjugated anti-CD16/32 (93) antibodies. Biotin-conjugated c-Kit staining was visualized using streptavidin APC-Cy7.

B cells were analysed using FITC-conjugated anti-B220, PE-conjugated anti-CD43 (S7) and APC-conjugated anti-sIgM. T cells were analysed using FITC-conjugated anti-CD4, PE-conjugated anti-CD8 and APC-conjugated anti-CD3. Myeloid cells were analysed using FITC-conjugated anti-Ter119, PE-conjugated anti-Gr-1 and APC-conjugated anti-Mac-1.

To measure mitochondrial mass, the HSC stain was modified to make the APC channel available for Mitotracker Deep Red staining (Molecular Probes). After antibody staining cells were incubated with 1 nM Mitotracker Deep red and 50 µM verapamil (Sigma) for 15 min at 37 °C followed by flow cytometry.

To measure ROS levels, the HSC stain was modified to make the FITC channel available for DCFDA staining (2',7'-dichlorofluorescein diacetate, Molecular Probes). To do this, antibodies for HSC isolation were PE/Cy5-conjugated anti-CD150 (TC15-12F12.2; BioLegend), PE-conjugated anti-CD48 (HM48-1; BioLegend), PE-conjugated anti-CD41 (MWReg30; BD Pharmingen), APC-conjugated anti-Sca-1 (Ly6A/E; E13-6.7), biotin-conjugated anti-c-Kit (2B8) antibody, and PE-conjugated antibodies against lineage markers. Biotin-conjugated c-Kit staining was visualized using streptavidin APC-Cy7. After antibody staining cells were incubated with 5 µM DCFDA for 15 min at 37 °C followed by flow cytometry.

To measure mitochondrial membrane potential, the HSC stain was modified to make the PE channel available for tetramethyl rhodamine methyl ester (TMRM; Molecular Probes)³⁹. Antibodies for HSC isolation were PE/Cy5-conjugated anti-CD150 (TC15-12F12.2; BioLegend), FITC-conjugated anti-CD48 (HM48-1; BioLegend), FITC-conjugated anti-CD41 (MWReg30; BD Biosciences), APC-conjugated anti-Sca-1 (Ly6A/E; E13-6.7), and biotin-conjugated anti-c-Kit (2B8) antibody and FITC-conjugated antibodies against lineage markers. Biotin-conjugated c-Kit staining was visualized using streptavidin APC-Cy7. After antibody staining cells were incubated with 25 nM TMRM for 15 min at 37 °C followed by flow-cytometry.

Cell cycle analysis. BrdU incorporation *in vivo* was measured by flow cytometry using the APC BrdU Flow Kit (BD Biosciences). Mice were given an intraperitoneal injection of 1 mg of BrdU (Sigma) per 6 g of body mass in PBS and maintained on 1 mg ml⁻¹ of BrdU in the drinking water for 24 h. Cell cycle analysis *in vitro* was performed as follows. 500 HSCs were sorted into SF-O3 medium containing SCF and TPO (see below) and cultured for 3 days. BrdU (10 µM final concentration) was added for 1 h before cells were cytospun to a slide. Slides were fixed with cold methanol for 5 min at -20 °C, then washed with PBS containing 0.01% NP-40 and treated with 2N HCl for 20 min. Slides were blocked in PBS containing 4% goat serum, 4 mg ml⁻¹ BSA and 0.1% NP-40 followed by staining overnight at 4 °C with antibodies against BrdU (BU1/75, 1:100, Abcam) and phospho-histone H3 Ser 10 (3H10, 1:2500, Millipore) diluted in blocking buffer. Primary antibody staining was developed with secondary antibodies conjugated to Alexa fluor 488 or 594 (Invitrogen) together with DAPI (2 µg ml⁻¹). Slides were analysed on an Olympus microscope equipped with ×40 objective lens.

For Ki-67/propidium iodide staining, HSCs were sorted into 70% ethanol and kept at -20 °C for at least 24 h. Ki-67 staining was performed using a FITC Ki-67 kit (BD Biosciences), followed by staining with 50 µg ml⁻¹ propidium iodide (Molecular Probes) and analysed by flow cytometry.

Long-term competitive repopulation assay. Adult recipient mice (CD45.1) were irradiated with an Orthovoltage X-ray source delivering approximately 300 rad min⁻¹ in two equal doses of 540 rad, delivered at least 2 h apart. Cells were injected into the retro-orbital venous sinus of anaesthetized recipients. Beginning 4 weeks after transplantation and continuing for at least 16 weeks, blood was obtained from the tail veins of recipient mice, subjected to ammonium-chloride potassium red cell lysis, and stained with directly conjugated antibodies to CD45.2 (104), CD45.1 (A20), B220 (6B2), Mac-1 (M1/70), CD3 (KT31.1) and Gr-1 (8C5) to monitor engraftment.

Western blotting. The same number of cells (25,000–35,000) from each population to be analysed were sorted into trichloroacetic acid (TCA) and adjusted to a final concentration of 10% TCA. Extracts were incubated on ice for 15 min and spun down for 10 min at 16,100g at 4 °C. The supernatant was removed and the pellets were washed with acetone twice then dried. The protein pellets were solubilized with solubilization buffer (9 M urea, 2% Triton X-100, 1% DTT) before adding LDS loading buffer (Invitrogen). Proteins were separated on a Bis-Tris polyacrylamide gel (Invitrogen) and transferred to a PVDF membrane (Millipore). Antibodies were anti-Lkb1 (3047), anti-phospho-AMPKα (Thr 172) (2535), anti-AMPKα (2532), anti-phospho-acetyl-CoA carboxylase (Ser 79) (3661), anti-phospho-S6 (2215), anti-phospho-4EBP1 (2855), anti-phospho-eIF4G (2441) (all from Cell Signaling Technology) and anti-β-actin (A1978, Sigma).

Caspase activity and ATP measurement. The same numbers of cells (approximately 5,000 cells, depending on the experiment) were sorted into microcentrifuge tubes containing HBSS with 2% calf serum and pelleted. Cell pellets were lysed using Caspase-Glo2 reagent (Promega) and luminescence was measured using a luminometer. Background luminescence from HBSS plus 2% calf serum was measured and the value was subtracted from sample values, then the values were divided by the cell number used to calculate the caspase activity per cell. Cellular ATP levels were measured using the ATP Bioluminescence Assay Kit CLS II (Roche Applied Science). Cells were sorted in PBS and boiled in the presence of 100 mM Tris, 4 mM EDTA then luciferase reagents were added. Background was measured using buffer without cells and subtracted from the values of each cell sample. ATP level per cell was calculated by dividing the measured value with the cell number used in the assay.

Methylcellulose culture. Methylcellulose culture of bone marrow cells, HSCs and GMPs was performed as described³⁶. Primary colonies were re-suspended and plated in secondary cultures and counted 14 days later.

Cell culture for analysis of mitotic spindles and chromosome numbers. HSCs were sorted into SF-O3 media (Sankyo Junyaku) supplemented with 1% heat-inactivated fetal bovine serum, 1% penicillin-streptomycin-glutamine (Gibco), 50 µM 2-mercaptoethanol, 50 ng ml⁻¹ SCF and 50 ng ml⁻¹ TPO (both from Peprotech). Similar result were obtained by culturing in STIF medium consisting of StemSpan serum-free medium (StemCell Technologies) supplemented with 10 µg ml⁻¹ heparin (Sigma), 10 ng ml⁻¹ mouse SCF, 20 ng ml⁻¹ mouse TPO,

20 ng ml⁻¹ mouse IGF-2 (R&D Systems) and 10 ng ml⁻¹ human FGF-1 (Peprotech). LSKs and GMPs were cultured in STIF supplemented with 10 ng ml⁻¹ IL-3 and IL-6 (both from Peprotech). Single HSCs were sorted into each well and their cell numbers were monitored as indicated. To prepare cytopins for immunostaining, 500 to 1,000 cells were sorted into each well and cultured for 3 days. Annexin-V staining was performed after 3 days of culture.

For chromosome counts, LSK or GMP cells were cultured in STIF medium supplemented with 10 ng ml⁻¹ IL-3 and IL-6 for 2 days then arrested in metaphase by a 2-h incubation with 100 ng ml⁻¹ colcemid (KaryoMAX solution, Gibco). Cells were treated with hypotonic solution (0.56% KCl) for 15 min at 37 °C, then fixed with 3:1 methanol:glacial acetic acid and spread on a slide to prepare metaphase spreads.

Immunostaining. Cytospin slides prepared as above without acid treatment were stained overnight at 4 °C with antibodies against α -tubulin (clone YL1/2, 1:100), γ -tubulin (clone C-11, 1:100, both from Santa Cruz Biotechnology) and phosphohistone H3 Ser 10 (3H10) diluted in blocking buffer. Primary antibody staining was developed with secondary antibodies conjugated to Alexa fluor 488, 555 and 647 together with DAPI (2 μ g ml⁻¹). Slides were analysed on a Leica confocal microscope.

Quantitative real-time (reverse transcription) PCR. HSCs and WBM cells were sorted into Trizol (Invitrogen) and RNA was isolated according to the manufacturer's instructions. cDNA was made with random primers and SuperScript III reverse

transcriptase (Invitrogen). Quantitative PCR was performed using a SYBR green kit and a LightCycler 480 (Roche Applied Science). Each sample was normalized to β -actin. Primers to quantify *Lkb1* cDNA levels were: *Lkb1* F, 5'-CAC ACTTTACAACATCACCA-3', *Lkb1* R, 5'-CTCATACTCCAACATCCCTC-3', *Prkaa1* F, 5'-CACCTCACATCATCAAATG-3', *Prkaa1* R, 5'-CTCCTCCAG AGACATATTCCA-3', *Prkaa2* F, 5'-CTTAAACTCTTTCGTCATCCTC-3', *Prkaa2* R, 5'-AACAATTCACCTCCAGACAC-3', β -actin F, 5'-CGTCGACAACG GCTCCGGCATG-3' and β -actin R, 5'-GGGCCTCGTCACCCACATAGGAG-3'. To quantify mitochondrial DNA copy number, cells were sorted into Trizol and DNA was isolated according to manufacturer's instructions. Quantitative PCR was performed with primers for mtND4 (mtND4 F, 5'-GGAACCAAACCTG AACGCCTA-3' and mtND4 R, 5'-ATGAGGGCAATTAGCAGTGG-3') and β 2 microglobulin intron (B2m F, 5'-TCATTAGGGAGGAGCCAATG-3' and B2m R, 5'-ATCCCCTTTCGTTTTTGCTT-3').

PCR of genomic DNA for genotyping. To assess the degree of *Lkb1* excision in genomic DNA from donor cells after transplantation, approximately 1,000 donor Gr-1⁺ cells were sorted into alkaline lysis buffer (25 mM NaOH, 0.2 mM EDTA) and boiled, then neutralized by addition of an equal volume of neutralizing buffer (40 mM Tris-HCl). The neutralized extract was used for PCR with the following primers: R1 5'-CTGTGCTGCCTAATCTGTGCG-3', F2 5'-TTCACCATCCCTT GTGACTG-3' and F4 5'-ATCGGAATGTGATCCAGCTT-3'. To genotype tail DNA from mice for the presence of the *Lkb1*^f allele, primers R1 and F2 were used.

The Lkb1 metabolic sensor maintains haematopoietic stem cell survival

Sushma Gurumurthy^{1*}, Stephanie Z. Xie^{1,2*}, Brinda Alagesan¹, Judith Kim¹, Rushdia Z. Yusuf^{1,2}, Borja Saez^{1,2}, Alexandros Tzatsos¹, Fatih Ozsolak³, Patrice Milos³, Francesco Ferrari⁴, Peter J. Park⁴, Orian S. Shirihai⁵, David T. Scadden^{1,2} & Nabeel Bardeesy¹

Haematopoietic stem cells (HSCs) can convert between growth states that have marked differences in bioenergetic needs. Although often quiescent in adults, these cells become proliferative upon physiological demand. Balancing HSC energetics in response to nutrient availability and growth state is poorly understood, yet essential for the dynamism of the haematopoietic system. Here we show that the Lkb1 tumour suppressor is critical for the maintenance of energy homeostasis in haematopoietic cells. *Lkb1* inactivation in adult mice causes loss of HSC quiescence followed by rapid depletion of all haematopoietic subpopulations. *Lkb1*-deficient bone marrow cells exhibit mitochondrial defects, alterations in lipid and nucleotide metabolism, and depletion of cellular ATP. The haematopoietic effects are largely independent of Lkb1 regulation of AMP-activated protein kinase (AMPK) and mammalian target of rapamycin (mTOR) signalling. Instead, these data define a central role for *Lkb1* in restricting HSC entry into cell cycle and in broadly maintaining energy homeostasis in haematopoietic cells through a novel metabolic checkpoint.

The metabolic control systems in HSCs are poorly understood although these cells have been shown to be highly sensitive to energetic and oxidative stress and must be able to shift between quiescence and highly proliferative states to maintain the haematopoietic system under varying physiological conditions^{1–5}. The *Lkb1* tumour suppressor encodes an evolutionarily conserved serine/threonine kinase that links metabolism and cell growth⁶. The most clearly defined physiological function of *Lkb1* is to phosphorylate and activate AMPK in response to a decline in the cellular energy charge (ATP/AMP ratio)^{7,8}. AMPK restores cellular ATP levels through phosphorylation of key regulatory proteins involved in protein synthesis, fatty acid and glucose metabolism, and glucose transport⁹. This results in inhibition of energy expending processes and promotes ATP generation. In *Caenorhabditis elegans*, an *Lkb1*–AMPK pathway is critical in inducing quiescence in germline stem cell populations¹⁰. *Lkb1* can also regulate energy homeostasis and cell structure through its capacity to phosphorylate and activate 12 other AMPK-related kinases¹¹. Given the importance of HSC dynamics to the haematopoietic system and the sensitivity of haematopoietic cells to metabolic stress, we sought to investigate the function of *Lkb1* in haematopoiesis.

Lkb1 deletion causes bone marrow failure

Lkb1 mRNA expression is readily detectable in haematopoietic cells in the bone marrow, with highest levels in HSCs¹² and in multipotent and lineage-restricted progenitors compared to committed Lin⁺ cells (Supplementary Fig. 1a). To study *Lkb1* function in haematopoiesis, we bred conditional *Lkb1*^{L/L} mice (ref. 13) with the *Mx1-cre* strain¹⁴ and induced Cre recombinase activity by administration of polyinosinic-polycytidylic acid (pIpC). Experimental *Mx1-cre; Lkb1*^{L/L} mice (designated *Lkb1* mutants) showed a rapid decrease in bone marrow cellularity and 93% died within 30 days after pIpC induction (Fig. 1a, b); *Mx1-cre; Lkb1*^{L/+} and *Mx1-cre; Lkb1*^{+/+} mice showed normal survival

and bone marrow cellularity and were used as controls. Analysis of the bone marrow and individual haematopoietic lineages demonstrated efficient *Lkb1* deletion, marked reductions in *Lkb1* polypeptide levels, reduced AMPK activity without changes in total AMPK α levels, and increased mTOR complex I (mTORC1) activity in the *Lkb1* mutants (Supplementary Fig. 1b–e).

Lkb1 mutant animals displayed progressive pancytopenia as well as rapid loss of bone marrow myeloid, B lymphoid and erythroid cells (Fig. 1c, d and Supplementary Fig. 2a), and markedly decreased cellularity of the thymus and spleen (Supplementary Fig. 2c, d and data not shown). Notably, in the bone marrow and thymus, immature lymphoid cells declined at a faster rate than the more differentiated cells (Supplementary Fig. 2b, c). The *Lkb1* mutants also exhibited a pronounced loss of HSC and multipotent progenitor populations at day 5 after pIpC treatment (Fig. 1e, f and Supplementary Fig. 2f). Furthermore, *Lkb1* mutant bone marrow cells formed fewer and smaller colonies in *in vitro* colony forming assays (Fig. 1g and Supplementary Fig. 2e). Comparable *in vivo* and *in vitro* phenotypes were seen using a second model system in which *Lkb1* was deleted using the tamoxifen-inducible *Rosa26-creERT2* strain (Supplementary Fig. 2g, h, and not shown). These results show that *Lkb1* is critically required for haematopoiesis and for the maintenance of HSCs and progenitor cells.

Lkb1 function in bone marrow is cell intrinsic

Both the *Mx1-cre* and *Rosa26-creERT2* systems induce Cre recombinase activity in many cell types; thus bone marrow transplants were used to determine whether *Lkb1* has a cell-autonomous role in haematopoiesis. We performed non-competitive transplants of CD45.1 whole bone marrow from control or *Mx1-cre; Lkb1*^{L/L} mice into lethally irradiated CD45.2 wild-type congenic recipients, confirmed stable reconstitution, and then administered pIpC (Supplementary Fig. 3a). The results

¹Cancer Center and Center for Regenerative Medicine, Massachusetts General Hospital and Harvard Medical School, Boston, Massachusetts 02114, USA. ²Harvard Stem Cell Institute and Department of Stem Cell and Regenerative Biology, Harvard University, Boston, Massachusetts 02115, USA. ³Helicos BioSciences Corporation, Cambridge, Massachusetts 02139, USA. ⁴Center for Biomedical Informatics and Informatics Program, Children's Hospital, and Harvard Medical School, Boston, Massachusetts 02115, USA. ⁵Department of Medicine, Evans Research Center, Mitochondria ARC, Boston University Medical Center, Boston, Massachusetts 02118, USA.

*These authors contributed equally to this work.

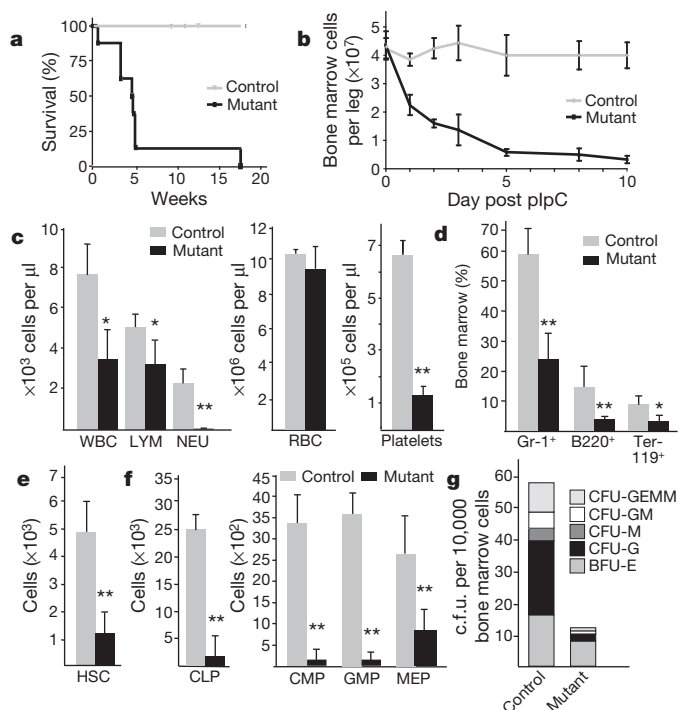


Figure 1 | *Lkb1* is required for haematopoiesis. Mutant (*Mx1-cre; Lkb1^{L/L}*) and control (*Mx1-cre; Lkb1^{L/+}* or *Lkb1^{L/L}*) mice were injected with pIpC every second day over 7 days. **a**, Survival analysis; $n > 10$ mice per genotype; $P < 0.001$. **b**, Mononuclear bone marrow cellularity ($n = 4$). **c–f**, Analysis at day 5 for the indicated subpopulations ($n = 6$ mice per genotype). CLP, common lymphoid progenitors; CMP, common myeloid progenitors; GMP, granulocyte-macrophage progenitors; MEP, megakaryocyte-erythrocyte progenitors; NEU, neutrophil; RBC, red blood cell. **g**, CFU-C assay for myeloid progenitors. * $P < 0.01$; ** $P < 0.001$. Error bars in **b–f** indicate mean \pm s.d.

showed that mice transplanted with *Lkb1* mutant cells died within 12 weeks and exhibited acute pancytopenia and rapid decline of *Lkb1* mutant donor cells in the peripheral blood (Fig. 2a and Supplementary Fig. 3b, c). The effects on bone marrow cells were even more pronounced; there was a marked decrease in cellularity and chimaerism

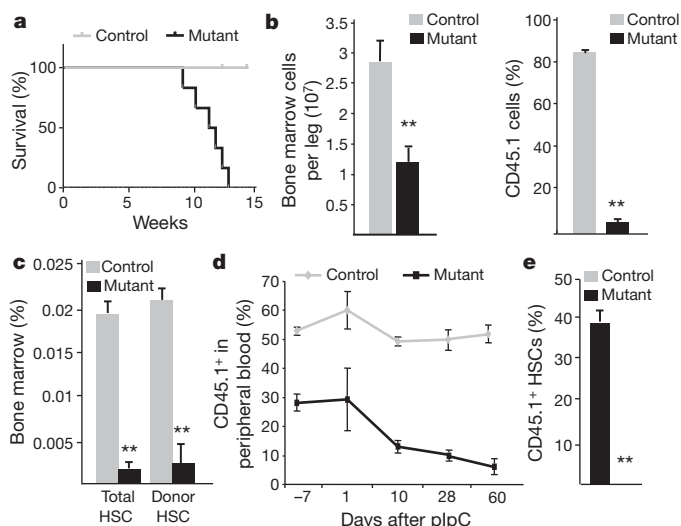


Figure 2 | Cell-autonomous role of *Lkb1* in haematopoiesis. **a–c**, After pIpC induction, transplanted mice were analysed for survival ($P < 0.005$) (**a**), bone marrow cellularity (left) and donor chimaerism (right) on day 5 (**b**), and total HSC numbers and donor contribution at day 18 (**c**). **d, e**, Competitively transplanted mice were induced with pIpC and analysed for CD45.1 status in peripheral blood (**d**), and per cent CD45.1 HSCs at 4 weeks (**e**). $n > 6$ mice per genotype in **a–e**. * $P < 0.05$, ** $P < 0.01$, all error bars indicate mean \pm s.d.

as early as day 5 (Fig. 2b) and the *Lkb1* mutant donor stem cell, progenitor and mature populations were largely depleted by day 18 (Fig. 2c, and not shown). We performed reciprocal transplant experiments in which wild-type donor cells were transplanted into either control or *Lkb1* mutant recipients; treatment with pIpC after stable reconstitution did not result in any alterations in haematopoiesis in the *Lkb1* mutant recipients (Supplementary Fig. 4).

To extend these studies, we transplanted donor CD45.1 control or *Mx1-cre; Lkb1^{L/L}* bone marrow cells with a 1:1 ratio of competitor CD45.2 wild-type bone marrow cells into CD45.2 recipient mice (Supplementary Fig. 3d). After engraftment, the peripheral blood of mice transplanted with *Mx1-cre; Lkb1^{L/L}* bone marrow cells had a lower rate of chimaerism compared to controls (30% versus 53%) (Fig. 2d), an effect probably due to the induction of interferon associated with transplant^{15,16}. Nonetheless, upon pIpC administration, *Mx1-cre; Lkb1^{L/L}* transplanted recipients displayed a sharp decline in CD45.1 cells in the peripheral blood (Fig. 2d and Supplementary Fig. 3e, f). Moreover, there was a complete absence of *Lkb1* mutant CD45.1 HSCs in the bone marrow 4 weeks after induction (Fig. 2e and not shown). Hence, there is an absolute and intrinsic requirement for *Lkb1* in HSCs and in the maintenance of haematopoiesis.

Lkb1 maintains HSC quiescence

Defects in proliferative control can contribute to HSC exhaustion. To study the acute impact of *Lkb1* inactivation on the absolute number and cell cycle profiles of HSCs, we analysed the bone marrow after administering a shorter course of pIpC injections (designated day -3), as well as at a slightly later time point (day $+2$) (Supplementary Fig. 5a). Notably, *Lkb1* mutants showed 2.5-fold increase in HSCs at day -3 , whereas they were markedly reduced at all subsequent time points (Fig. 3a; also see Fig. 1e). A comparable profile was seen in the *Rosa26-creErt2* model (Supplementary Figs 5b and 2h). This early increase in cell number was restricted to HSCs among all the bone marrow subpopulations (not shown).

To assess whether the early, transient increase in HSC number was associated with enhanced proliferation, we performed cell cycle analysis using the proliferation marker Ki-67 and propidium iodide to mark DNA content. pIpC treatment has been previously shown to induce G1 cell-cycle entry in wild-type HSCs¹⁷ and, as expected, we found that this treatment increased the proportion of Ki-67-positive cells (Fig. 3b). Nonetheless, similarly low percentages of proliferating HSCs in S/G2/M were observed in the untreated mice and pIpC-treated controls (6.9% and 7.0% respectively), whereas $>21\%$ of mutant HSCs were cycling in S/G2/M (Supplementary Fig. 5c). Smaller, but still significant, increases in HSC proliferation rates were observed at later time points in the *Lkb1* mutants, despite the decline in HSC numbers (Supplementary Fig. 5c). Comparable results were observed using the *Rosa26-creErt2* system (Supplementary Fig. 5d). *Lkb1* inactivation had a more modest effect on the cell-cycle profiles of differentiated Lin⁺ cells (Fig. 3b, bottom panel). Thus, *Lkb1* is required for the maintenance of HSC quiescence and its loss causes bone marrow failure that is preceded by an increase in the proliferation and absolute number of HSCs.

Lkb1 loss induces apoptosis and autophagy

We subsequently assessed the impact of *Lkb1* loss on cell death pathways in haematopoietic cells. *Lkb1* mutant cells had reduced viability by day 5 after pIpC as documented by 7-amino-actinomycin D (7AAD) staining; stem and progenitor cells exhibited more pronounced sensitivity compared to more differentiated cells (Fig. 3c and Supplementary Fig. 5e, f). Annexin V/7AAD analysis demonstrated that apoptosis was induced in the *Lkb1* mutant HSCs and progenitors starting at day 3 and elevated ~ 5 -fold by day 5; similar profiles were seen in Mac-1⁺ and B220⁺ cells (Supplementary Fig. 5f). Correspondingly, lysates from *Lkb1* mutant bone marrow, spleen and thymus exhibited an elevation in cleaved caspase-3 levels starting at day 3 after pIpC (Fig. 3d).

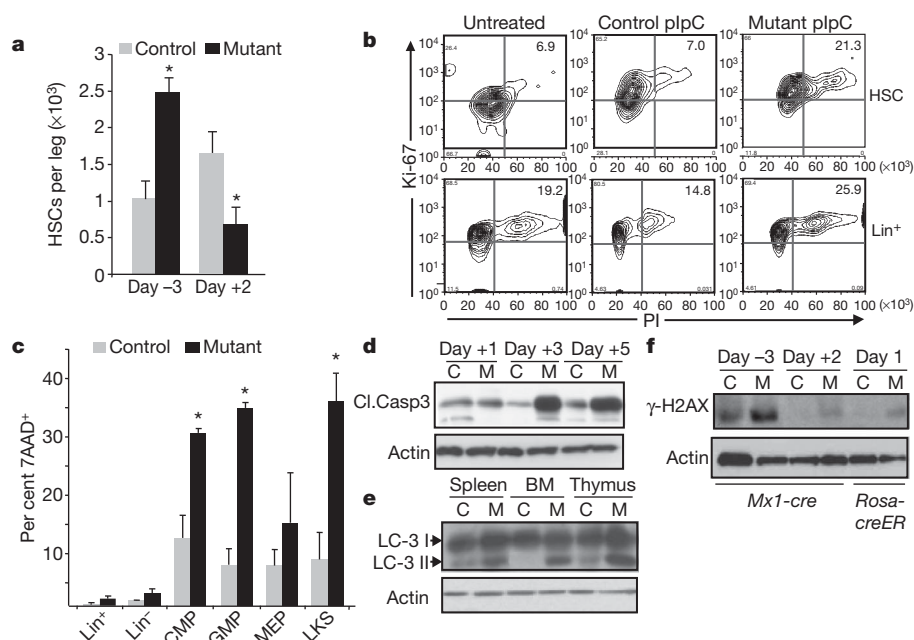


Figure 3 | Impact of *Lkb1* inactivation on proliferation and apoptosis.

a, Quantification of HSCs in the *Mx1-cre* model at day -3 and day +2 after pIpC treatment. $n = 3$ mice per genotype; $P < 0.01$, error bars indicate mean \pm s.d. **b**, Cell-cycle analysis of HSCs (Ki-67/propidium iodide (PI) staining) at day -3 ($n = 3$; $P < 0.01$). **c**, Analysis viability in HSC and

progenitor cells and Lin⁺ cells at day 5 by 7AAD staining ($*P < 0.001$, error bars indicate mean \pm s.d.). **d–f**, Immunoblot of control (C) and *Lkb1* mutant (M) mice for cleaved caspase-3 (Cl.Casp3) in bone marrow (BM) (**d**), LC3 in the indicated tissues at day 5 after pIpC (**e**), and phospho-H2AX levels in bone marrow (**f**).

Next, we investigated the cellular stress responses that may underlie the cell death phenotypes. Macroautophagy (autophagy) is a process of organelle and long-lived protein degradation that is activated in response to nutrient deprivation or oxidative stress and can either serve as a survival mechanism or promote cell death depending on cellular context¹⁸. The lipidated form of the LC3 protein, LC3-II, serves as a marker for active autophagy¹⁹. Notably, immunoblot analysis at day 1 after pIpC treatment showed that LC3-II levels were elevated in *Lkb1* mutant bone marrow, thymus and spleen (Fig. 3e). In support of these findings, immunofluorescence staining demonstrated a fivefold increase in the proportion of bone marrow cells showing LC3 puncta in the *Lkb1* mutants (Supplementary Fig. 5g). Treatment of mice with chloroquine, which inhibits autophagy by blocking lysosomal acidification and autophagosome degradation, accelerated the death of the *Lkb1* mutants while not affecting control mice (not shown), indicating that autophagy induction served as a survival response in these cells. *Lkb1* mutant bone marrow also exhibited increased expression of phospho(Ser 139)-histone H2AX (phospho-H2AX), and a threefold increase in phospho-H2AX foci, indicating the presence of ongoing DNA damage (Fig. 3f and Supplementary Fig. 5h). Hence, apoptotic cell death is markedly increased in *Lkb1* mutant haematopoietic cells and may be associated with nutrient and genotoxic stress.

Lkb1 function is AMPK/mTORC1-independent

Inactivation of mTORC1 is a major component of the *Lkb1*–AMPK energy stress response in primary fibroblasts and cancer cell lines^{20,21}. In addition, knockout of the mTORC1 regulator, *Tsc1*, results in bone marrow failure due to mTORC1 activation and induction of reactive oxygen species (ROS)⁵. *Lkb1* inactivation led to an increase in mTORC1 activity in whole bone marrow as reflected by phospho (serine-235/236)-ribosomal protein S6 levels; yet analysis of bone marrow subpopulations revealed that this increase was entirely due to changes in myeloid cells (Fig. 4a and Supplementary 6a)—a finding in contrast to *Tsc1* and *Tsc2* deficiency, which results in mTORC1 activation in all haematopoietic cells^{2,5}. Correspondingly, inhibition of mTORC1 by administration of rapamycin failed to restore bone

marrow cellularity or the declines in individual populations in the *Lkb1* mutants despite suppressing S6 phosphorylation (Fig. 4b, c and Supplementary Fig. 6b–d). Administration of the anti-oxidant *N*-acetyl-cysteine (NAC) also had no effect on lifespan or bone marrow cellularity (Supplementary Fig. 6e, f and data not shown). Therefore, deregulation of the mTORC1 pathway does not underlie the haematopoietic defects in these mice.

AMPK regulates cell metabolism through multiple pathways in addition to mTORC1. Because AMPK activity is eliminated upon

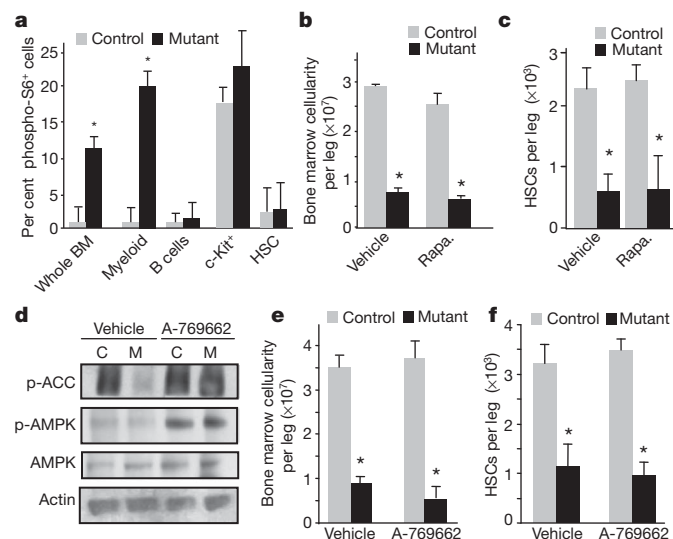


Figure 4 | mTORC1 inhibition and AMPK activation do not rescue bone marrow failure in *Lkb1* mutants. **a**, Phospho(Ser 235/236)-S6 expression in bone marrow subpopulations at day 5 after pIpC treatment. **b**, **c**, Rapamycin (Rapa.) treatment does not rescue the drop in bone marrow cellularity (**b**) or HSCs (**c**) in *Lkb1* mutants at day 5 ($n = 4$ mice per genotype). **d–f**, The AMPK activator A-769662 restores phospho(Ser 79)-ACC levels in *Lkb1* mutant bone marrow cells (**d**), yet does not rescue loss of bone marrow cellularity (**e**), or HSCs (**f**) at day 5 ($n = 4$). $*P < 0.001$, all error bars indicate mean \pm s.d.

Lkb1 deletion in the bone marrow (Supplementary Fig. 1d, e), we sought to test whether the allosteric AMPK activator, A-769662, rescues the haematopoietic defects in these mice. A-769662 induced (Ser 79)-acetyl-CoA carboxylase (ACC) phosphorylation in primary fibroblasts in an AMPK α 1/ α 2-dependent, but *Lkb1*-independent, manner (Supplementary Fig. 6g). When administered before and throughout the course of the pIpC treatment in the *Mx1-cre* model, this compound also effectively restored AMPK activity in *Lkb1*-deficient bone marrow; however, there was no rescue of any bone marrow subpopulations or of overall survival (Fig. 4d–f and Supplementary Fig. 6h and not shown). Hence AMPK may not be a critical effector of *Lkb1* in the maintenance of haematopoiesis.

Lkb1 maintains bone marrow energy homeostasis

Lkb1 deficiency in liver and muscle leads to broad alterations in energy usage, lipid and carbohydrate metabolism and mitochondrial mass. These effects are only partially AMPK dependent, and probably also reflect roles of additional AMPK-related kinases^{22–24}. Therefore, we assessed whether the *Lkb1* mutant bone marrow exhibited metabolic defects, as indicated by our LC3 and chloroquine data. Notably, there was a marked decline in mitochondrial membrane potential in the *Lkb1* mutant common myeloid progenitors (CMPs), common lymphoid progenitors (CLPs) and HSCs at day 3 after pIpC treatment (Fig. 5a). These alterations were associated with defects in bioenergetics, as basal mitochondrial oxygen consumption and total mitochondrial oxidative capacity were reduced in the *Lkb1* mutants at day 1 after induction in both models (Fig. 5b); the use of a shortened induction scheme confirmed that these changes occurred rapidly upon *Lkb1* deletion (Supplementary Fig. 7a). Consistent with a broad inability to maintain energy homeostasis, lineage-negative bone marrow cells had a significant decline in basal ATP levels by day 5, despite showing increased glucose uptake (Fig. 5c, d and Supplementary 7b). Mitochondrial content was significantly decreased upon initial *Lkb1* inactivation whereas it was elevated at later time points (>5 days after pIpC) (Fig. 5e and Supplementary Fig. 7b); this biphasic effect seems to reflect a compensatory response to the metabolic alterations in these cells. Collectively, these data indicate that *Lkb1* mutant haematopoietic cells are unable to sustain the cellular energy charge and have defects in mitochondrial function.

To define the metabolic alterations in *Lkb1*-deficient cells further, we evaluated the global metabolic profiles of both differentiated (Lin⁺)

and lineage negative (Lin[−]) populations at day 1 after pIpC using a combination of liquid/gas chromatography and mass spectrometry (GC/MS and LC/MS/MS) platforms. This analysis showed that the *Lkb1* mutants had statistically significant alterations in lipid metabolism in the Lin⁺ and Lin[−] populations (specifically increases in most detectable long-chain fatty acids and in several essential fatty acids and elevations in nucleotide metabolites (only in *Lkb1* mutant Lin[−] cells); Supplementary Figs 8 and 9). Individual amino acids, dipeptides and some glycolysis and citric acid cycle components showed differences; although, when considered as groups, these metabolites were not altered in our analysis (Supplementary Fig. 10 and not shown). The diminished mitochondrial function and elevations in fatty acid levels are consistent with a model whereby *Lkb1* serves as a rheostat that sets the appropriate balance of anabolic and catabolic activities in haematopoietic cells.

Discussion

The extreme sensitivity of haematopoietic cells to *Lkb1* inactivation is remarkable when compared to the impact of *Lkb1* deficiency in other cell types. In particular, *Lkb1* deficiency results in the development of solid tumours of multiple tissue types and in the immortalization of primary fibroblasts *in vitro*^{13,25–28}. *Lkb1* inactivation does confer increased sensitivity to several stress states including nutrient deprivation, oxidative stress and hypoxia^{7,29}. Here we show that in the haematopoietic system, where stem cell modulation between quiescence and proliferation is necessary to withstand acute physiological stress while preserving long-term regenerative capacity, *Lkb1* has an unanticipated and critical role. *Lkb1* is needed to maintain haematopoietic cells broadly, with *Lkb1* deletion leading to the death of multiple subpopulations. The processes involved seem to be defects in metabolic homeostasis associated with mitochondrial dysfunction, ATP depletion, a compensatory autophagic response, and rapid apoptotic cell death. Given the speed of the cell death response, it remains important to establish which of the metabolic alterations are direct consequences of *Lkb1* inactivation and which are secondary to the induction of apoptosis; the mitochondrial defects in particular could be associated with early stages of an apoptotic program.

HSCs respond to *Lkb1* deficiency with cell-cycle entry, an effect not seen in other haematopoietic subsets. Whereas *Lkb1* function may have a general role in integrating energy sensing and growth control, its unique role in enforcing quiescence of HSCs raises interesting

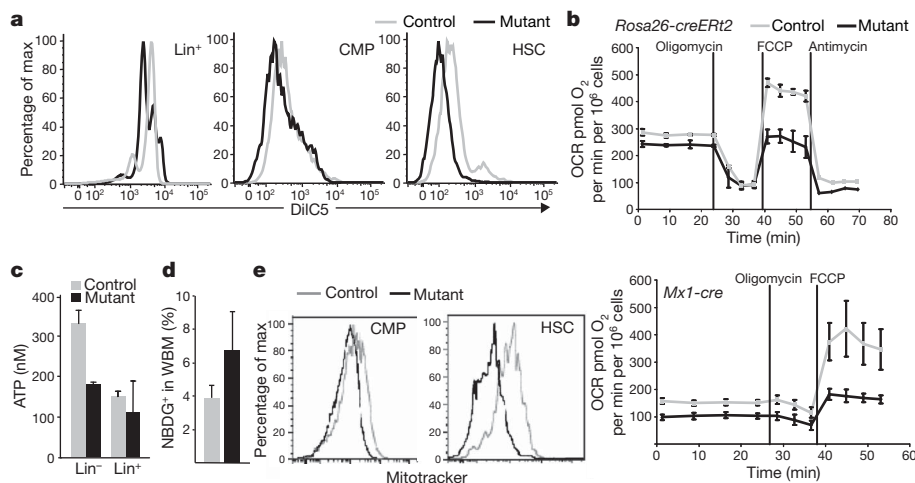


Figure 5 | Inactivation of *Lkb1* alters mitochondrial function of bone marrow cells. **a**, Mitochondrial membrane potential of control and mutant cells at day 3 after pIpC assayed by DiIC5 staining. **b**, Oxygen consumption rates (OCR) in control and mutant bone marrow cells under basal conditions and in response to 0.25 μ M oligomycin, 5 μ M fluoro-carbonyl cyanide phenylhydrazine (FCCP) or 1 μ M antimycin + rotenone at day 1 in the

Rosa26-creERT2 (top) and *Mx1-cre* (bottom) models. **c**, ATP levels of bone marrow cells at day 5 after pIpC. **d**, Glucose uptake in bone marrow at day 1. NBDG, fluorescent D-glucose analogue. **e**, Quantification of relative mitochondrial mass by Mitotracker staining (*Mx1-cre* model). $n = 3$ mice per genotype; $P < 0.001$; all error bars indicate mean \pm s.d.

issues of how this population may be particularly responsive to its metabolic environment. Whether this is due to a primary low-energy state in HSCs that activates Lkb1 signalling or the distinct regulation of Lkb1 in these cells is a subject of further study. Notably, Lkb1 seems to act in the haematopoietic system primarily through pathways independent of AMPK. The data therefore point to a novel metabolic checkpoint active in haematopoiesis. In this regard, direct RNA sequencing³⁰ of LKS (Lin[−]c-Kit⁺Sca-1⁺) and granulocyte-macrophage progenitor (GMP) cells showed that the transcripts encoding a number of AMPK-related kinases are present at comparable or higher amounts than *AMPKα1* (also called *Prkaa1*) and *AMPKα2* (also called *Prkaa2*) (Supplementary Fig. 11). Several of these candidate Lkb1 effectors have overlapping roles in the regulation of metabolism, polarity and mitosis, indicating that they may serve to coordinate energetic states with alterations in cell structure and growth³¹. Our data and two accompanying studies^{32,33} suggest that Lkb1 controls such processes in haematopoiesis and in HSCs in particular. They reveal that Lkb1 function is central to the preservation of a regenerative tissue that is critical for survival.

METHODS SUMMARY

Lkb1^{L/L} mice¹³ were crossed to *Mx1-cre* mice¹⁴ and backcrossed for six generations onto a C57BL/6 background. pIpC (Amersham) was administered intraperitoneally (i.p.) four times every other day with 8.04 g kg^{−1} body weight. *Rosa26-creERT2*; *Lkb1*^{L/L} mice were injected i.p. with 130 mg kg^{−1} body weight tamoxifen (Sigma) daily for 5 days. 100 mg kg^{−1} body weight NAC (Sigma) and 4 mg kg^{−1} body weight rapamycin (LC laboratories) were injected i.p. starting 2 days before pIpC treatment and throughout the course of the experiment. A-769662 (LC laboratories) was administered in drinking water at 30 mg kg^{−1} of body weight per day. For ROS, mitochondrial number, and membrane potential measurements, bone marrow subpopulations were incubated with dichlorofluorescein diacetate (DCFDA), Mitotracker green and DiIc1-5 (Invitrogen), respectively, at 37 °C for 15–30 min before analysis on the LSRII instrument (Becton, Dickinson). ATP was measured from lysates prepared from 20,000 freshly isolated bone marrow cells with the ATP Bioluminescence Assay Kit HS II (Roche). For repopulation experiments, C57BL/6 (CD45.2) mice were lethally irradiated with 9.5 Gy and reconstituted by tail vein injections with 1 million bone marrow cells from *Mx1-cre*; *Lkb1*^{L/L} or control mice. Relative mRNA expression analysis of *Lkb1* and other genes was performed using FastStart SYBR Green Mastermix (Roche) on the MxP3005P real-time PCR system (Stratagene). Analysis of metabolites was performed on Lin⁺ and Lin[−] bone marrow cells by a combination of liquid/gas chromatography combined with mass spectrometry (GC/MS and LC/MS/MS) performed by Metabolon Inc.³⁴.

Full Methods and any associated references are available in the online version of the paper at www.nature.com/nature.

Received 30 April; accepted 11 October 2010.

- Tothova, Z. & Gilliland, D. G. FoxO transcription factors and stem cell homeostasis: insights from the hematopoietic system. *Cell Stem Cell* **1**, 140–152 (2007).
- Gan, B. *et al.* mTORC1-dependent and -independent regulation of stem cell renewal, differentiation, and mobilization. *Proc. Natl Acad. Sci. USA* **105**, 19384–19389 (2008).
- Ito, K. *et al.* Regulation of reactive oxygen species by Atm is essential for proper response to DNA double-strand breaks in lymphocytes. *J. Immunol.* **178**, 103–110 (2007).
- Liu, J. *et al.* Bmi1 regulates mitochondrial function and the DNA damage response pathway. *Nature* **459**, 387–392 (2009).
- Chen, C. *et al.* TSC-mTOR maintains quiescence and function of hematopoietic stem cells by repressing mitochondrial biogenesis and reactive oxygen species. *J. Exp. Med.* **205**, 2397–2408 (2008).
- Shackelford, D. B. & Shaw, R. J. The LKB1-AMPK pathway: metabolism and growth control in tumour suppression. *Nature Rev. Cancer* **9**, 563–575 (2009).
- Shaw, R. J. *et al.* The tumor suppressor LKB1 kinase directly activates AMP-activated kinase and regulates apoptosis in response to energy stress. *Proc. Natl Acad. Sci. USA* **101**, 3329–3335 (2004).
- Hawley, S. A. *et al.* Complexes between the LKB1 tumor suppressor, STRADα/β and MO25α/β are upstream kinases in the AMP-activated protein kinase cascade. *J. Biol.* **2**, 28 (2003).
- Hardie, D. G. AMP-activated/SNF1 protein kinases: conserved guardians of cellular energy. *Nature Rev. Mol. Cell Biol.* **8**, 774–785 (2007).

- Narbonne, P. & Roy, R. *Caenorhabditis elegans* dauers need LKB1/AMPK to ration lipid reserves and ensure long-term survival. *Nature* **457**, 210–214 (2009).
- Lizcano, J. M. *et al.* LKB1 is a master kinase that activates 13 kinases of the AMPK subfamily, including MARK//PAR-1. *EMBO J.* **23**, 833–843 (2004).
- Kiel, M. J. *et al.* SLAM family receptors distinguish hematopoietic stem and progenitor cells and reveal endothelial niches for stem cells. *Cell* **121**, 1109–1121 (2005).
- Bardeesy, N. *et al.* Loss of the Lkb1 tumour suppressor provokes intestinal polyposis but resistance to transformation. *Nature* **419**, 162–167 (2002).
- Kuhn, R., Schwenk, F., Aguet, M. & Rajewsky, K. Inducible gene targeting in mice. *Science* **269**, 1427–1429 (1995).
- Chan, I. T. *et al.* Conditional expression of oncogenic K-ras from its endogenous promoter induces a myeloproliferative disease. *J. Clin. Invest.* **113**, 528–538 (2004).
- Torchia, E. C., Boyd, K., Reh, J. E., Qu, C. & Baker, S. J. EWS/FLI-1 induces rapid onset of myeloid/erythroid leukemia in mice. *Mol. Cell Biol.* **27**, 7918–7934 (2007).
- Essers, M. A. G. *et al.* IFNα activates dormant haematopoietic stem cells *in vivo*. *Nature* **458**, 904–908 (2009).
- Mauri, M. C., Zalcov, E., Kimchi, A. & Kroemer, G. Self-eating and self-killing: crosstalk between autophagy and apoptosis. *Nature Rev. Mol. Cell Biol.* **8**, 741–752 (2007).
- Ichimura, Y. *et al.* A ubiquitin-like system mediates protein lipidation. *Nature* **408**, 488–492 (2000).
- Shaw, R. J. *et al.* The LKB1 tumor suppressor negatively regulates mTOR signaling. *Cancer Cell* **6**, 91–99 (2004).
- Corradetti, M. N., Inoki, K., Bardeesy, N., DePinho, R. A. & Guan, K. L. Regulation of the TSC pathway by LKB1: evidence of a molecular link between tuberous sclerosis complex and Peutz-Jeghers syndrome. *Genes Dev.* **18**, 1533–1538 (2004).
- Shaw, R. J. *et al.* The kinase LKB1 mediates glucose homeostasis in liver and therapeutic effects of metformin. *Science* **310**, 1642–1646 (2005).
- Koh, H. J. *et al.* Skeletal muscle-selective knockout of LKB1 increases insulin sensitivity, improves glucose homeostasis, and decreases TRB3. *Mol. Cell Biol.* **26**, 8217–8227 (2006).
- Koh, H. J. *et al.* Sucrose nonfermenting AMPK-related kinase (SNARK) mediates contraction-stimulated glucose transport in mouse skeletal muscle. *Proc. Natl Acad. Sci. USA*. doi:10.1073/pnas.1008131107 (16 August 2010).
- Gurumurthy, S. *et al.* LKB1 deficiency sensitizes mice to carcinogen-induced tumorigenesis. *Cancer Res.* **68**, 55–63 (2008).
- Contreras, C. M. *et al.* Loss of Lkb1 provokes highly invasive endometrial adenocarcinomas. *Cancer Res.* **68**, 759–766 (2008).
- Hezel, A. F. *et al.* Pancreatic LKB1 deletion leads to acinar polarity defects and cystic neoplasms. *Mol. Cell Biol.* **28**, 2414–2425 (2008).
- Sanchez-Cespedes, M. A role for LKB1 gene in human cancer beyond the Peutz-Jeghers syndrome. *Oncogene* **26**, 7825–7832 (2007).
- Klimova, T. A. *et al.* Hyperoxia-induced premature senescence requires p53 and pRb, but not mitochondrial matrix ROS. *FASEB J.* **23**, 783–794 (2009).
- Ozsolak, F. *et al.* Direct RNA sequencing. *Nature* **461**, 814–818 (2009).
- Hezel, A. F. & Bardeesy, N. LKB1: linking cell structure and tumor suppression. *Oncogene* **27**, 6908–6919 (2008).
- Nakada, D., Saunders, T. L. & Morrison, S. J. Lkb1 regulates cell cycle and energy metabolism in haematopoietic stem cells. *Nature* doi:10.1038/nature09571 (this issue).
- Gan, B. *et al.* Lkb1 regulates quiescence and metabolic homeostasis of haematopoietic stem cells. *Nature* doi:10.1038/nature09595 (this issue).
- Watson, M. *et al.* The small molecule GMX1778 is a potent inhibitor of NAD⁺ biosynthesis: strategy for enhanced therapy in nicotinic acid phosphoribosyltransferase 1-deficient tumors. *Mol. Cell Biol.* **29**, 5872–5888 (2009).

Supplementary Information is linked to the online version of the paper at www.nature.com/nature.

Acknowledgements We would like to thank the Harvard Stem Cell Institute Flow Cytometry Core and D. Brown and the MGH Electron Microscope Imaging Core for expertise and advice. V. Levy and M. Leisa provided technical assistance in the Seahorse measurements. D. Van Buren provided advice and assistance in pilot experiments. We thank A. Camacho for mouse colony assistance. We would also like to thank A. Kimmelman, R. Mostoslavsky, M. Vander Heiden, L. Ellisen, W. Kim and M. Ivan for discussions and critical review of the manuscript. We are grateful to S. Morrison and R. DePinho for sharing unpublished data. N.B. would like to acknowledge support from NIH U01 CA141576-01. D.T.S. would like to acknowledge support from NIH DK050234 and Ellison Medical Foundation. S.G. was supported by a Massachusetts Biotechnology Research Council Tosteson Fellowship. S.Z.X. was supported by an NIH Ruth L. Kirschstein National Research Service Award.

Author Contributions S.G. and S.Z.X. performed the experiments with assistance from B.A., J.K., A.T., B.S. and R.Z.Y. S.G., S.Z.X., D.T.S. and N.B. designed the experiments, analysed and evaluated all data, and wrote the manuscript. F.O. and P.M. performed the RNA sequencing. F.F. and P.J.P. analysed the RNA sequencing data. O.S.S. designed and evaluated the oxygen consumption experiments.

Author Information Reprints and permissions information is available at www.nature.com/reprints. The authors declare no competing financial interests. Readers are welcome to comment on the online version of this article at www.nature.com/nature. Correspondence and requests for materials should be addressed to N.B. (Bardeesy.Nabeel@MGH.harvard.edu) or D.T.S. (Scadden.David@MGH.harvard.edu).

METHODS

Mice. *Lkb1*^{L/L} mice¹³ and *Mx1-cre* mice¹⁴ were described previously. C57BL/6J, B6.SJL-Ptprca Pep3b/BoyJ (B6.SJL) were purchased from the Jackson Laboratory. *Lkb1*^{L/L} mice (FVB background) were crossed with *Mx1-cre* mice (B6.SJL background) to obtain mixed background mice that were used for analysis or further backcrossed to B6.SJL for six generations to express CD45.1 on the C57BL/6 background. *Lkb1*^{L/L} mice were also crossed to the *Rosa26-creERT2* strain³⁵. pIpC, obtained from Amersham and re-suspended in phosphate-buffered saline at 0.67 mg ml⁻¹, was administered to mice by intraperitoneal (i.p.) injection at a dose of 8.04 mg kg⁻¹ every other day for 4 days or as otherwise indicated. *Rosa26-creERT2*; *Lkb1*^{L/L} mice were given tamoxifen (Sigma) injected i.p. at 130 mg kg⁻¹ body weight every day for 5 days. NAC (Sigma) at 100 mg kg⁻¹ body weight and rapamycin (LC laboratories) at 4 mg kg⁻¹ body weight were injected i.p. starting 2 days before pIpC treatment, and continued until the end of the experiment. A-769662 was administered in drinking water at 30 mg kg⁻¹ body weight per day starting 2 days before pIpC and continued through the course of the experiment. The Subcommittee on Research Animal Care of the Massachusetts General Hospital approved all animal work according to federal and institutional policies and regulations.

Transplantation assays. For non-competitive transplantation, 1 million whole bone marrow cells were transplanted into lethally irradiated FVB/C57BL/6 mixed background (CD45.1/CD45.2 double positive) recipients bred in house. pIpC was administered at 8 weeks after transplantation. All experiments were repeated in C57BL/6 CD45.1 mice backcrossed at least six generations into a pure C57BL/6 CD45.2 background for recipient mice. For 1:1 competitive transplantation, 1 million (CD45.1) whole bone marrow cells were mixed with 1 million CD45.2 competitor cells and injected into lethally irradiated C57BL/6 (CD45.2) mice. pIpC injections were initiated at 6 weeks after transplantation. Recipient mice were lethally irradiated with 9.5 Gy 4–24 h before transplantation via lateral tail vein injection. Engraftment was analysed by CD45.1 donor contribution using FACS analysis of peripheral blood samples at multiple time points after transplantation.

Flow cytometry analysis. Slam HSCs, LKS cells and multipotent progenitors were analysed based on their expression of lineage markers and antibodies to the following markers conjugated to fluorochromes: c-Kit-APC, CD34-FITC, CD16/32-PE-Cy7 and CD127-APC-Cy7 (BD Biosciences), CD48-Pacific blue and CD150-PE (BioLegend) and Sca-1-PE-Cy5.5 (Invitrogen)¹². For lineage detection, bone marrow cells were first stained with a cocktail of biotinylated anti-mouse antibodies to Mac-1 α (CD11b), Gr-1 (Ly-6G/C), Ter119 (Ly-76), CD3, CD4, CD8 α (Ly-2) and B220 (CD45R; BD Biosciences) followed by detection with streptavidin conjugated to pacific orange (Invitrogen) or directly to individual fluorochrome-conjugated antibodies. For congenic strain discrimination, anti-CD45.1-FITC and anti-CD45.2 APC antibodies (BD Biosciences) were used. For cell cycle analysis, bone marrow cells were first stained for Slam HSC cell surface markers (Lin⁻, c-Kit⁺, Sca-1⁺, CD48⁻ and CD150⁺ with antibodies described above, except for Sca-1-PE-Cy7 (BD Biosciences)), then were fixed and permeabilized using the BD Cytotfix/Cytoperm Fixation/Permeabilization Solution Kit (BD Biosciences) according to the manufacturer's recommendations, followed by staining with Ki-67-FITC (BD Biosciences) and 50 μ g ml⁻¹ propidium iodide (Invitrogen). For apoptosis, we used 7-AAD and AnnexinV-FITC (BD Biosciences). All data collection was performed on an LSRII or FACS Aria II (Beckon, Dickinson) and data analysis done with FlowJo (Treestar).

Methylcellulose colony assays. 1×10^4 whole bone marrow cells were plated in 1 ml of methocult M3434 (Stem Cell Technologies) on a 6-well plate in duplicate and cultured at 37 °C for 10–14 days before scoring for colony formation.

Immunoblot analysis. Bone marrow cells were obtained by flushing the long bones (tibiae and femurs) with PBS without calcium and magnesium. Freshly isolated bone marrow, spleen and thymus cells were lysed in lysis buffer (20 mM Tris pH 7.5, 150 mM NaCl, 1 mM EDTA, 1% Triton X-100) with protease and phosphatase inhibitors and 25–50 μ g protein loaded on an SDS-PAGE gel. Immunoblots were

probed with antibodies against Lkb1 (Santa Cruz Biotechnologies), p-AMPK T172, p-ACC (S79), p-S6 (S235/236), p-S6 kinase (S371), LC3 (Cell Signaling), phospho-H2AX (S139) (Upstate) and actin (Sigma).

Metabolic and molecular biology assays. ATP was measured from lysates prepared from 20,000 freshly isolated, lineage-depleted or Lin⁺ bone marrow cells with an ATP Bioluminescence Assay Kit HS II (Roche). For ROS, mitochondrial number and membrane potential measurements, bone marrow and thymocytes stained for HSC and progenitor cells were incubated with 5 μ M dichlorofluorescein diacetate (DCFDA), 100 nM Mitotracker green or 50 nM DiIc-5 (Invitrogen), respectively, at 37 °C for 15–30 min and analysed on the LSRII instrument (Becton, Dickinson). For oxygen consumption, 10⁶ freshly isolated bone marrow cells were plated using CellTak and oxygen consumption rate (OCR) was measured using the Seahorse XF24 instrument (Seahorse Biosciences)³⁶. Respiration was measured under basal conditions, in the presence of the mitochondrial inhibitor oligomycin (0.25 μ M), mitochondrial uncoupler FCCP (5 μ M) and respiratory chain inhibitor antimycin and rotenone (1 μ M). For glucose uptake, bone marrow cells were incubated with 100 μ M NBDG at 37 °C for 1 h. Relative mRNA expression analysis of *Lkb1*, mitochondrial and other genes was performed using FastStart SYBR Green Mastermix (Roche) on the MxP3005P real-time PCR system (Stratagene).

Metabolic profiling. Whole bone marrow cells were initially isolated from three control and three *Lkb1* mutant animals by flushing long bones on ice, then separated into Lin⁺ and Lin⁻ cells using MACS separation columns (Miltenyi Biotec) at 4 °C at day 1 after pIpC treatment. Global metabolite analysis of differentiated (Lin⁺) and primitive (Lin⁻) haematopoietic cells was performed by Metabolon, Inc. using a combination of liquid/gas chromatography combined with mass spectrometry (GC/MS). The analysis used 3×10^6 cells for each Lin⁺ sample and 0.5×10^6 cells for the Lin⁻ cells. This analysis identified 150 named biochemicals. After log transformation and imputation with minimum observed values for each compound, Welch's two-sample *t*-tests were used to identify metabolites that differed significantly between control and *Lkb1* mutant cells for both Lin⁺ and Lin⁻ cells.

Helicos direct sequencing and data analysis. For direct RNA sequencing (DRS), the total RNA samples were 3' blocked with the poly(A) tailing kit (Ambion) and 3' deoxyATP (Cordycepin triphosphate, Jena Biosciences), incubating the reaction mixture at 37 °C for 30 min. The blocked total RNA was hybridized to HeliScope flow cell surfaces for sequencing with DRS without additional cleaning steps³⁰. Raw DRS reads were filtered for reads with a minimal length of 25 bases using a suite of Helicos tools available at <http://open.helicosbio.com/mwiki/index.php/Releases> and described at http://open.helicosbio.com/helisphere_user_guide/. Alignments were conducted with indexDPgenomic freely available on the Helicos website (<http://open.helicosbio.com/mwiki/index.php/Releases>). The reads were aligned to the MM9 version of the mouse genome supplemented with the complete ribosomal repeat unit.

RefSeq annotation tables were retrieved from UCSC Genome Browser (MM9 genome version) and read alignments were compared with known locations of RefSeq transcripts for protein coding genes. Each read was counted as associated to a specific transcript if aligned within a ± 2 -kb window around the transcript 3' end. Then per transcript read counts were summarized at gene level, counting only once the reads mapped to multiple transcripts isoforms associated to each specific gene. RPM values were computed using the TMM normalization procedure as described before³⁷ and as implemented in the edgeR Bioconductor package (<http://www.bioconductor.org>).

35. Ventura, A. *et al.* Restoration of p53 function leads to tumour regression *in vivo*. *Nature* **445**, 661–665 (2007).
36. Ferrick, D. A., Neilson, A. & Beeson, C. Advances in measuring cellular bioenergetics using extracellular flux. *Drug Discov. Today* **13**, 268–274 (2008).
37. Robinson, M. D. & Oshlack, A. A scaling normalization method for differential expression analysis of RNA-seq data. *Genome Biol.* **11**, R25 (2010).

U1 snRNP protects pre-mRNAs from premature cleavage and polyadenylation

Daisuke Kaida¹, Michael G. Berg¹, Ihab Younis¹, Mumtaz Kasim¹, Larry N. Singh¹, Lili Wan¹ & Gideon Dreyfuss¹

In eukaryotes, U1 small nuclear ribonucleoprotein (snRNP) forms spliceosomes in equal stoichiometry with U2, U4, U5 and U6 snRNPs; however, its abundance in human far exceeds that of the other snRNPs. Here we used antisense morpholino oligonucleotide to U1 snRNA to achieve functional U1 snRNP knockdown in HeLa cells, and identified accumulated unspliced pre-mRNAs by genomic tiling microarrays. In addition to inhibiting splicing, U1 snRNP knockdown caused premature cleavage and polyadenylation in numerous pre-mRNAs at cryptic polyadenylation signals, frequently in introns near (<5 kilobases) the start of the transcript. This did not occur when splicing was inhibited with U2 snRNA antisense morpholino oligonucleotide or the U2-snRNP-inactivating drug spliceostatin A unless U1 antisense morpholino oligonucleotide was also included. We further show that U1 snRNA-pre-mRNA base pairing was required to suppress premature cleavage and polyadenylation from nearby cryptic polyadenylation signals located in introns. These findings reveal a critical splicing-independent function for U1 snRNP in protecting the transcriptome, which we propose explains its overabundance.

Messenger RNAs in eukaryotic cells are produced from primary transcripts (pre-mRNAs) by extensive post-transcriptional processing, including 5' end capping, removal of introns by splicing, and 3' end cleavage and polyadenylation^{1–4}. Each splicing reaction is carried out by a spliceosome, a large RNA-protein complex comprised predominantly of snRNPs^{5–8}. The U1, U2, U4, U6 and U5 snRNPs are components of the major (U2-type) spliceosome, whereas a much less abundant (~1%) minor (U12-type) spliceosome is comprised of U11, U12, U4atac, U6atac and U5 snRNPs^{5,9–11}. The snRNPs, aided by specific RNA-binding proteins, recognize by snRNA-pre-mRNA base pairing, canonical sequences within pre-mRNAs that define the major- and minor-class introns, including the intron-exon junctions at the 5' and 3'-splice sites. U1 snRNP has an essential role in defining the 5' splice site by RNA-RNA base pairing via the 5' nine nucleotide sequence of U1 snRNA. To form the catalytic core of the spliceosome, the snRNPs come together in 1:1 stoichiometry as a modular machine⁵. However, the abundance of the various snRNPs in cells does not reflect their equimolarity in the spliceosomes. This is particularly striking for U1 snRNP which, at an estimated copy number of ~10⁶ molecules per human cell (HeLa), is much more abundant than the other snRNPs in higher eukaryotes¹². The potential role of the different amounts of the snRNPs is not known.

Our interest in exploring a potential function for cellular snRNP abundance arose from earlier observations that deficiency in the survival of motor neurons (SMN) protein, a key component in snRNP biogenesis^{13–17}, perturbs the normal abundance of snRNPs in cells (the snRNP repertoire)^{18,19} and causes widespread splicing abnormalities¹⁹. The possible effect of snRNP abundance changes on splicing and the molecular consequences of SMN deficiency in general are of importance because SMN deficiency is the cause of spinal muscular atrophy, an often fatal motor neuron degenerative disease^{20–22}. However, the snRNP repertoire changes that occur in an SMN-deficient spinal muscular atrophy mouse model vary in different tissues and are not uniform for all of the snRNPs^{18,19}, including both downregulation and upregulation in the levels of several snRNPs simultaneously, making them difficult to recapitulate. To circumvent this, we investigated the effect of functional

reduction of individual snRNPs on the transcriptome using antisense morpholino oligonucleotide (AMO). Our experiments revealed an unexpected function for U1 snRNP in protecting pre-mRNAs from premature cleavage and polyadenylation (PCPA), distinct from its role in splicing.

Functional knockdown of U1 snRNP with AMO

To decrease the amount of functional U1 snRNP, we designed an AMO that covers the 5' end of U1 snRNA (U1 AMO) to block its binding to 5' splice sites. To confirm the binding of U1 AMO to U1 snRNP and determine the amount required to inhibit it in cells, we performed an RNase H protection assay. Extracts from cells transfected with a scrambled control AMO^{23,24} or various concentrations of U1 AMO were incubated with RNase H and an antisense DNA oligonucleotide probe also complementary to U1 snRNA's 5' end sequence (Fig. 1a). A dose-dependent decrease in the amount of cleaved U1 snRNA was observed as the amount of transfected U1 AMO was increased (Fig. 1a), indicating that the U1 AMO prevented the antisense DNA oligonucleotide probe from binding and eliciting RNase H digestion. Complete or near-complete interference with U1 snRNA 5' base pairing in cells was observed with 7.5 μ M of U1 AMO (Fig. 1a). In addition, we used *in situ* hybridization with a LNA probe complementary to U1 snRNA's 5' sequence (nucleotides 1–25) to determine if the U1 AMO was bound to the same sequence in cells. The images (Fig. 1b) demonstrate that the U1 AMO indeed shields U1 snRNA's 5' sequence in a dose-dependent manner and that this sequence is completely inaccessible at 7.5 μ M U1 AMO, the concentration that was used in all subsequent U1 AMO transfection experiments. To confirm that the U1 AMO inhibited the activity of U1 snRNP directly, we tested its effect on the *in vitro* splicing. As shown in Fig. 1c, U1 AMO, but not control AMO, strongly decreased the amount of spliced product for Ad2AIVS. Thus, U1 AMO functionally inactivated U1 snRNP both *in vivo* and *in vitro*.

Unspliced pre-mRNA accumulation after splicing inhibition

To obtain a high-resolution global picture of the transcriptome changes that occurred upon U1 snRNP knockdown, including effects

¹Howard Hughes Medical Institute, Department of Biochemistry and Biophysics, University of Pennsylvania School of Medicine, Philadelphia, Pennsylvania 19104-6148, USA.

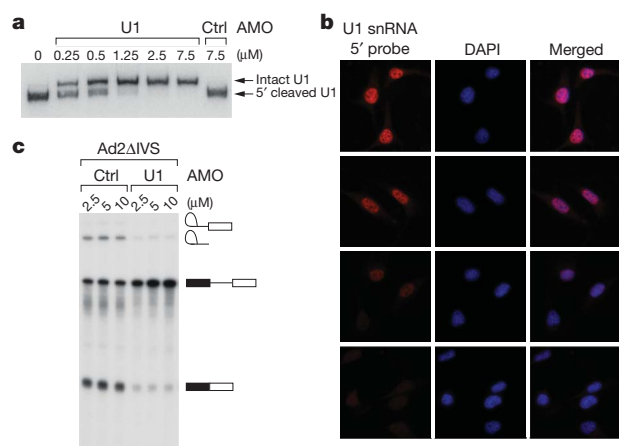


Figure 1 | U1 AMO binds to the 5' sequence of U1 snRNA and inhibits its splicing activity. **a**, HeLa cells were transfected with the indicated concentrations of control and U1 AMO for 8 h. RNase H protection assay was performed using total cell extracts and U1 snRNA was detected by northern blotting. **b**, *In situ* hybridization was performed on HeLa cells transfected with varying concentrations of U1 AMO, as indicated, for 8 h using a biotin-labelled LNA probe to the U1 snRNA (left panels) followed by fluorescent Alexa Fluor 594 streptavidin conjugate detection. Nuclei were visualized with DAPI (middle panels) and merged images are shown (right panels). All images were taken at $\times 40$ magnification. **c**, [α - 32 P]UTP-labelled Ad2ΔIVS pre-mRNA was spliced *in vitro* in the presence of control or U1 AMOs at the indicated concentrations. Splicing product identities are depicted to the right of the gel.

on introns and exons, we analysed total RNA prepared from HeLa cells transfected with either U1 or control AMOs using Affymetrix GeneChip Human Tiling 2.0R E arrays. This high-density genomic tiling array includes tiled probes (25-mer oligonucleotides spaced at 10 nucleotides) covering the entire genomic sequence of chromosomes 5, 7 and 16, which are estimated to contain $\sim 3,600$ genes. All experiments were carried out as separate biological triplicates and treatments were for 8 h to allow transfected cells to recover and for sufficient signals to accumulate above background. As a reference, we treated cells in parallel with the potent and general splicing inhibitor spliceostatin A (SSA), which targets the splicing factor SF3b, a component of U2 snRNP²⁵. As the amount of each pre-mRNA is typically very small and difficult to detect, large increases in intron signals provided the most definitive evidence for the accumulation of unspliced pre-mRNAs, ensuring that the corresponding sequences were actively transcribed and their unspliced transcripts are sufficiently stable to be scored. Statistical analysis was performed to identify significant changes that exceeded the following thresholds: fold-change ≥ 2 , P -value < 0.01 and length of affected region ≥ 100 nucleotides (corresponding to three or more consecutive probes). This identified 319 genes that showed accumulation typically of one or more introns in either U1-AMO-transfected (211 genes) or SSA-treated (216 genes) cells. From the outset we expected two patterns due to splicing inhibition. A general reduction in all signals from a transcript could reflect that unspliced pre-mRNA is less stable and rapidly degraded; however, we did not include them in our analysis as they could also potentially result from transcriptional downregulation. We also expected that U1 AMO and SSA would show similar patterns of intron accumulation throughout the transcript as a result of splicing inhibition in general, but this was observed for only 98 genes (30.7%), as exemplified by *ETF1* (Fig. 2). A small number of genes (41 genes; 12.9%) showed other profiles but did not exhibit any coherent pattern. Unexpectedly, however, most genes (180 genes; 56.4%) showed different patterns for U1 AMO and SSA (*HSPA9*, *SRRM2* and *CBFB* in Fig. 2).

U1 snRNP knockdown causes PCPA

Most notably, the majority of the affected genes in the U1-AMO-transfected cells showed a similar pattern consisting of strong intron

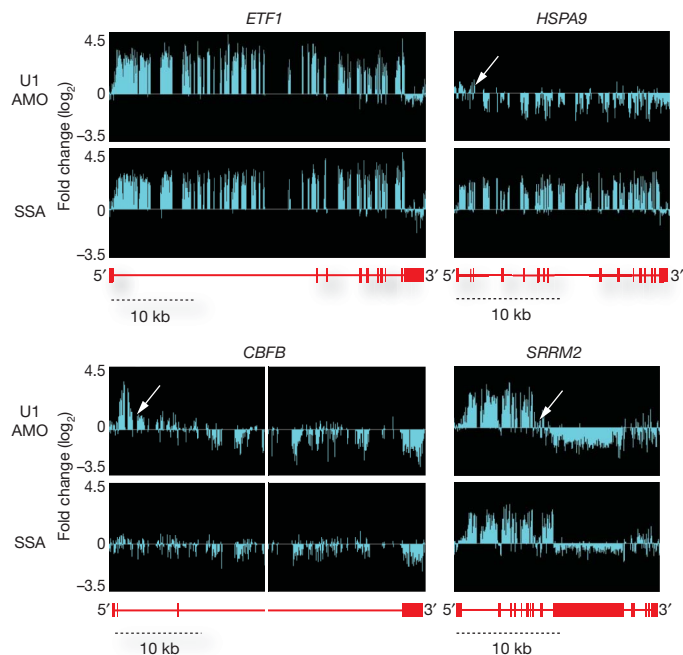


Figure 2 | Genomic tiling arrays identify unspliced pre-mRNAs after U1 AMO and SSA treatment. RNA samples prepared from control or U1-AMO-transfected cells (7.5 μ M, 8 h) or SSA-treated cells (100 ng ml $^{-1}$, 8 h) were analysed using genomic tiling array. Fold changes (\log_2) of signal intensities of U1-AMO-transfected and SSA-treated cells compared to control cells are shown above the corresponding structure of each gene. With a scale shown below, gene structures are depicted in red, with horizontal lines indicating introns and boxes indicating exons. The middle part of the *CBFB* gene (~ 35 kb) was removed. White arrows indicate points showing an abrupt drop of the signal (inflection points).

signals that terminated prematurely relative to SSA, for example in *HSPA9*, *SRRM2* and *CBFB* as indicated by arrows in Fig. 2. This usually occurred in introns in the first quarter of the gene with a strong 5' bias, as shown for several functionally diverse genes in Fig. 3. Notably, in U1-AMO-transfected cells there was an abrupt decrease in unspliced intron signals frequently within 3–5 kb from the start of the transcript. From the point at which a sharp drop in the signals in U1-AMO-treated cells was observed, all downstream signals, including exons, were consistently lower than those of control and the SSA-treated samples. To define the termination point, we characterized cDNA fragments from this region (indicated by arrows in Fig. 3), including 3' rapid amplification of cDNA ends (RACE) products for transcripts of several genes that showed this pattern from U1-AMO-transfected cells, of which *NR3C1* and *STK17A* were sequenced (Fig. 4a). Surprisingly, this revealed that the transcripts had a poly(A) sequence at the 3' end that is not found in the genomic sequence and which was added post-transcriptionally ~ 20 nucleotides downstream of a potential polyadenylation signal (PAS), typically AAUAAA (Fig. 4a). These findings indicate that pre-mRNAs are prematurely cleaved and polyadenylated within an intron when the levels of functional U1 snRNP are reduced.

To determine if these putative PASs are functionally relevant, we constructed a *NR3C1* mini-gene comprising exons 2 and 3 which flank a truncated intron 2 where the cleavage and polyadenylation occurred. An identical plasmid was also constructed with a mutation in the putative PAS in intron 2 inferred from the tiling array results (Fig. 4b). Cells expressing each of these plasmids were then transfected with either control or U1 AMOs. Wild-type plasmid-expressing cells showed PCPA at the cryptic PAS only after U1 AMO treatment (Fig. 4b), consistent with the result of the endogenous *NR3C1* gene. No cleavage and polyadenylation occurred in the transcript containing a mutant PAS in either control or U1-AMO-transfected

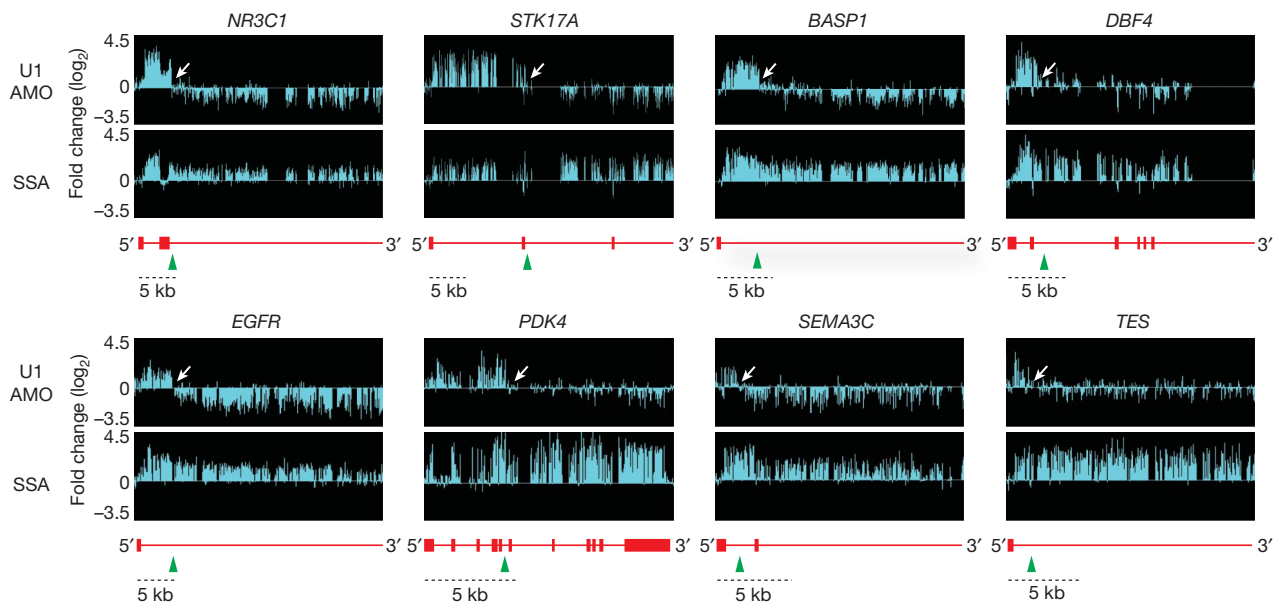


Figure 3 | Premature termination in introns of pre-mRNAs in U1-AMO-transfected cells. Representative examples of genes differentially affected by U1 AMO and SSA are shown. The sudden drop in signals in U1-AMO-

transfected cells is indicated by green arrowheads and white arrows. With a scale shown below, gene structures are depicted in red with horizontal lines indicating introns and boxes indicating exons.

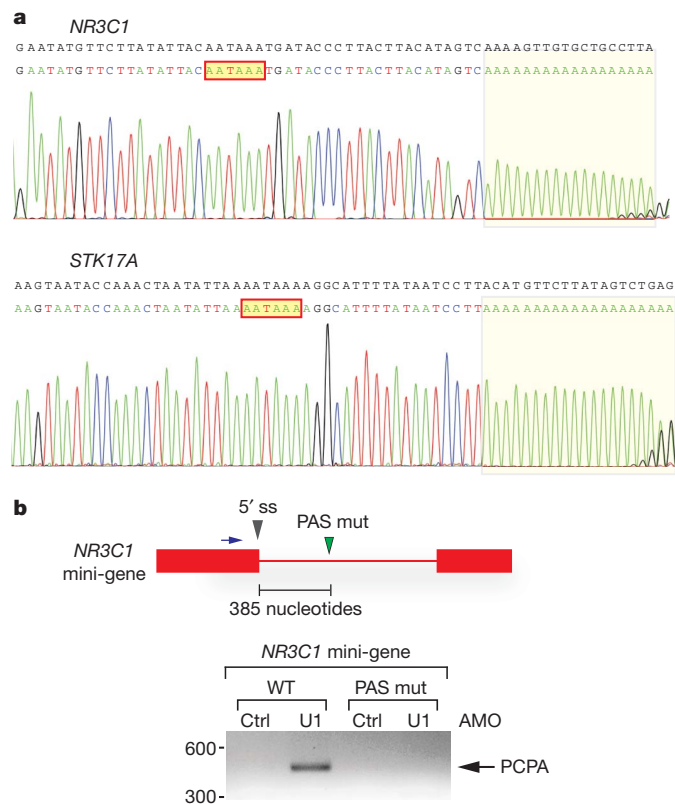


Figure 4 | Prematurely terminated pre-mRNAs are polyadenylated from cryptic PASs in introns. **a**, 3' RACE using nested PCR was performed to detect polyadenylated mRNAs using total RNA from U1-AMO-transfected cells (7.5 μ M, 8 h). Sequencing results of the 3' RACE products for the *NR3C1* and *STK17A* genes are shown with the corresponding genomic sequence in black. The poly(A) tails are shaded and the putative PASs are indicated in red-bordered boxes. **b**, HeLa cells were transfected with the wild-type and PAS mutant (mutated from AAUAAA to GAAUUC) *NR3C1* mini-gene construct followed by either control or U1 AMOs. 3' RACE was performed as described in **a**. The mini-gene structure is depicted above the gel, with a blue arrow indicating the forward primer for 3' RACE. Grey arrowhead, PAS mutation; PCPA, premature cleavage and polyadenylation. Band sizes (bp) are indicated to the left of the gel.

cells (Fig. 4b), demonstrating that this cryptic PAS is functional and that this process is similar to that which occurs normally at the 3' ends of mRNAs.

PCPA suppression is a non-splicing function of U1 snRNP

Unlike U1 AMO, tiling arrays with SSA or U2 AMO (which generally showed a tiling array pattern of splicing inhibition similar to that of SSA; Supplementary Fig. 1) did not show PCPA. To test this directly, we used an oligo(dT) reverse primer to amplify *NR3C1* and *STK17A* transcripts in control, U1 or U2-AMO-treated cells and SSA-treated cells (Fig. 5a). As expected, PCPA was observed for U1 AMO; however, none or very little was seen in U2-AMO- and SSA-treated cells, which could be due to destabilization of U1 snRNP binding upon U2 snRNP inhibition. Notably, PCPA still occurred in cells treated simultaneously with U1 AMO and SSA, indicating that the effect of U1 inhibition is dominant over splicing inhibition (Fig. 5b). We conclude that U1 suppresses cleavage and polyadenylation and that this is not a consequence of the splicing inhibition that it causes, as neither U2 AMO nor SSA showed this effect.

The functional PAS from which cleavage and polyadenylation occurred in the *NR3C1* mini-gene upon U1 snRNP depletion is less than 400 nucleotides downstream of the 5' splice site and it thus seemed likely that U1 snRNP that is base paired to this 5' splice site suppresses utilization of this cryptic PAS. To test this, we mutated the 5' splice site, which inactivated splicing as evidenced by the lack of mRNA (Fig. 5c). Whereas the wild-type mini-gene showed PCPA only upon U1 AMO treatment, in 5' splice site mutant transfected cells, PCPA was observed even with control morpholino treatment. This indicates that U1 snRNP that is base paired to the 5' splice site is able to suppress the cryptic PAS (Fig. 5c). However, treatment of the 5' splice site mutant with U1 AMO resulted in ~4-fold increase in PCPA from the same cryptic PAS and concomitantly ~8-fold decrease in polyadenylation from the normal PAS at the transcript's 3' end (Fig. 5c, d). Therefore, U1 snRNP that is base paired to sequences other than the 5' splice site also suppresses PCPA. The large number of potential U1 snRNP binding sites in introns precluded identification of other sites from which U1 snRNP might suppress premature utilization of this PAS (Supplementary Fig. 2). These findings indicate that the PCPA results from loss of the base pairing of the 5' end of U1 snRNA with the pre-mRNA, indicating a

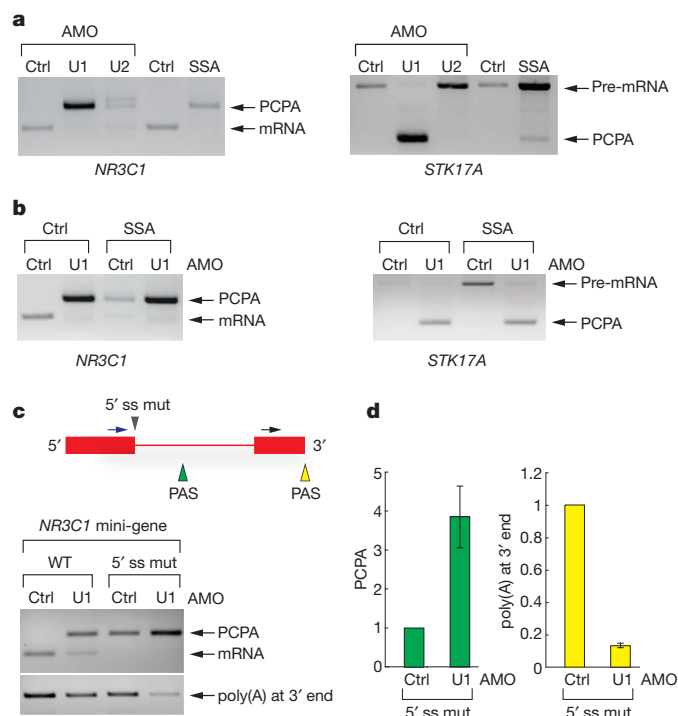


Figure 5 | U1 snRNP suppression of premature cleavage and polyadenylation from a nearby cryptic PAS is splicing independent and requires base pairing. **a**, 3' RACE was carried out as described in Fig. 4a on the endogenous *NR3C1* and *STK17A* genes using RNA samples from HeLa cells transfected with control, U1 (7.5 μ M, 8 h) or U2 AMO (25 μ M, 8 h), or treated with SSA (100 ng ml⁻¹, 8 h). **b**, 3' RACE was carried out as described in Fig. 4a using RNA samples from HeLa cells transfected with control or U1 AMOs (7.5 μ M) with or without SSA (100 ng ml⁻¹) for 8 h. **c**, HeLa cells were transfected with wild-type and 5' splice site mutant *NR3C1* (mutated from AAGGTAAGA to GTCCATTCA) mini-gene. 3' RACE was performed as described in Fig. 4a. The mini-gene structure is depicted. Blue arrow, forward primer to detect PCPA; black arrow, forward primer to detect polyadenylation at 3' end; grey arrowhead, 5' splice site mutation; green and yellow arrowheads, polyadenylation signals in intron and at 3' end, respectively. An unspliced and normally cleaved product was too large to detect. **d**, Quantification of PCPA and normal polyadenylation at the 3' end represented as fold change in control, which was set to one, and U1-AMO-treated cells was performed using real-time PCR. Error bars indicate s.d. ($n = 3$).

U1 snRNP function other than and independent of its known function in splicing.

Discussion

Our experiments here revealed an unexpected function for U1 snRNP in protecting transcripts from PCPA in addition to and independent of its role in splicing. As a reference for U1 AMO, the general splicing inhibitor SSA²⁵, which inactivates the U2 snRNP component SF3b (refs 5, 26), allowed identification of introns that were stable enough and that accumulate to significantly detectable levels when their splicing was inhibited. As expected, the patterns observed for U1 AMO and SSA (which is similar to that of U2 AMO) showed that both efficiently inhibited splicing. However, U1 snRNP functional reduction had an additional and marked effect, resulting in the failure to produce full-length pre-mRNA from the majority of genes in our data set. We showed that this was due to premature cleavage and polyadenylation from a cryptic PAS, typically in an intron and frequently within the first few kilobases (<5 kb) from the start of RNA polymerase II transcripts. A non-splicing role for a snRNP has been previously shown for U2 snRNP in the 3'-end formation of histone mRNAs^{27,28}.

The mechanism by which U1 snRNP suppresses PCPA is not presently known. However, as it occurs from canonical PASs, it is

reminiscent of previous observations on the capacity of tethered U1 snRNP to regulate normal 3'-end cleavage and polyadenylation from the natural PASs in the last exon²⁹, and may have features in common with it. For example, the U1 snRNP protein U1-70K can interact directly with the poly(A) polymerase (PAP)^{30,31} and inhibit polyadenylation. Targeting 5'-mutated U1 snRNAs with complementarity to sequences in the vicinity (within <500 nucleotides) of the natural PAS at the 3'-terminal exon results in degradation of the transcript because cleavage occurs without addition of a poly(A) tail, leaving the transcript vulnerable to 3' exonucleases³². A considerable number of genes that we surveyed, but that were not included in our analysis, showed a decrease in exon signals or in both introns and exons throughout the transcript in U1-AMO-treated cells. It is possible that in these cases cleavage occurred without subsequent polyadenylation, and the transcript was therefore rapidly degraded. Alternatively, cleavage and polyadenylation may have occurred very close to the transcription start site, making these transcripts difficult to detect. These scenarios are nevertheless consistent with a role for U1 snRNP in suppressing cleavage and polyadenylation throughout the entire pre-mRNA by a similar machinery that until now was thought to only process the 3' end of mRNA, in an even larger number of genes than our data set presents.

Stochastically, canonical PASs (most frequently AAUAAA or AUUAAA) occur every 2,000 nucleotides, although in several of the genes we studied, including *NR3C1*, *STK17A* and *BASPI*, cryptic PASs are found every 500–800 nucleotides. The strong 5' bias with which PCPA occurred in these genes upon U1 snRNP functional knockdown indicates that one of the first few cryptic PASs is used. Up to the point at which PCPA occurred, these transcripts also contained many cryptic 5' splice sites (Supplementary Fig. 2). We propose the following model to explain our observations. Pre-mRNA processing factors, including splicing factors, hnRNP proteins, snRNPs and 3'-end cleavage and polyadenylation factors co-transcriptionally associate with nascent transcripts^{33–37}. Direct association of cleavage/polyadenylation factors with the C-terminal domain of RNA polymerase II in the transcription elongation complex has been demonstrated³⁶. U1 snRNP associates with nascent transcripts, by base pairing with cognate sequences on the nascent pre-mRNA, including 5' splice sites and cryptic 5' splice sites, and inhibits the cleavage/polyadenylation machinery from attacking the pre-mRNA at cryptic PASs. We envisage that when U1 snRNP's base pairing is prevented, as is the case in U1-AMO-transfected cells, cleavage and polyadenylation occur co-transcriptionally at the first actionable PAS that the transcription elongation complex encounters. By actionable PAS, we mean one that has the necessary hexanucleotide consensus and is in an RNP context that makes it accessible and susceptible to attack by the cleavage/polyadenylation machinery unless U1 snRNP base-paired in the vicinity is able to protect it. We suggest that under normal circumstances, this encounter happens after the last strong U1 binding site (5' splice site or a cryptic 5' splice site) in the 3' untranslated region of the terminal exon because a sufficient density of U1 snRNP base paired throughout protects the transcript up to that point. The likelihood of normal or premature termination may be enhanced by the presence of pausing sites³⁸.

U1 snRNP bound to 5' splice sites may thus serve a dual purpose—in splicing and suppression of PCPA. The perimeter of U1 snRNP's protective zone is not known, but its binding to 5' splice site alone is unlikely to be able to protect the majority of introns, which in humans average ~3.4 kb in length³⁹. Furthermore, if suppression of actionable PASs was provided only via U1 snRNP bound to 5' splice sites, 5' splice-site mutations would be expected to cause premature termination, as opposed, for example, to exon skipping, which would be extremely deleterious and, to our knowledge, has not been observed. Additional U1 snRNP binding sites, including cryptic 5' splice sites, may function as tethering sites for its activity in suppression of cleavage and polyadenylation in introns. Viewed from this perspective, sequences referred to as cryptic 5' splice sites may serve a non-splicing purpose to recruit U1 snRNP to protect introns. It is also reasonable to

consider that modulating U1 snRNP levels or its binding at sites that protect actionable PASs could be a mechanism for regulating gene expression, including downregulation of the mRNA or switching expression to a different mRNA produced from a prematurely terminated pre-mRNA. We suggest that the vulnerability to PCPA would be expected to increase with increasing intron size if U1 snRNP and cognate base-pairing sites are not available to protect it. We propose that the large excess of U1 snRNP over what is required for splicing in human cells serves an additional critical biological function, to suppress PCPA in introns and protect the integrity of the transcriptome.

METHODS SUMMARY

Antisense morpholino oligonucleotide (AMO) transfection was performed by electroporation. The sequences of the U1 and control AMOs (Gene Tools) are 5'-GGTATCTCCCTGCCAGGTAAGTAT-3' and 5'-CCTCTTACCTCAGTTACAATTTATA-3', respectively^{23,24}. RNase H protection assay was carried out using AMO-transfected cell extracts and antisense DNA oligonucleotide for U1 snRNA (5'-CAGGTAAGTAT-3'). After RNase H treatment, RNA samples were purified and analysed by northern blotting with a U1 snRNA probe (5'-CA AATTATGCGAGTTCCTCCACATTG-3'). *In situ* hybridization of U1 snRNA was performed with a biotin-labelled LNA probe (5'-GGTATCTCCCTGCCAGGTAAGTAT-3'). Nuclei were stained by DAPI. For *in vitro* splicing, [α -³²P]UTP labelled Ad2 Δ IVS pre-mRNA was prepared as previously described⁴⁰. *In vitro* splicing reactions were carried out in 293T whole cell extracts prepared as previously described⁴¹. Splicing products were resolved on denaturing PAGE, and gels were autoradiographed. For tiling array, labelled cDNA targets were prepared and applied to Affymetrix GeneChip human tiling 2.0R E arrays. Arrays were scanned to produce .CEL files. The .CEL files were analysed using the Affymetrix Tiling Analysis Software (TAS) to produce .BED files of signal intensity and *P*-value. Overlapping regions of two data sets were chosen using Galaxy (<http://galaxy.psu.edu/>)⁴². We produced .BAR files from the .CEL files using TAS to visualize on the Integrated Genome Browser (Affymetrix). For 3' RACE, cDNA was synthesized from total RNA using an oligo dT18-XbaKpnBam primer. The first and second (nested) PCR reactions were performed using gene-specific forward primers and the XbaKpnBam reverse primer. For 3' RACE of the *NR3C1* mini-gene, pcDNA3.1-5' primer was used as the first primer to distinguish mini-gene RNA from endogenous *NR3C1* RNA. To construct the *NR3C1* mini-gene, DNA fragments of *NR3C1* intron 1-exon 2-intron 2 and *NR3C1* intron 2-exon 3 were amplified and subcloned into pcDNA3.1 vector. The poly(A) site and 5' splice site were mutated in this construct where indicated. Sequences of all primers are listed in Supplementary Table 1.

Full Methods and any associated references are available in the online version of the paper at www.nature.com/nature.

Received 10 February; accepted 9 September 2010.

Published online 29 September 2010.

- Danckwardt, S., Hentze, M. W. & Kulozik, A. E. 3' end mRNA processing: molecular mechanisms and implications for health and disease. *EMBO J.* **27**, 482–498 (2008).
- Gu, M. & Lima, C. D. Processing the message: structural insights into capping and decapping mRNA. *Curr. Opin. Struct. Biol.* **15**, 99–106 (2005).
- Mandel, C. R., Bai, Y. & Tong, L. Protein factors in pre-mRNA 3'-end processing. *Cell. Mol. Life Sci.* **65**, 1099–1122 (2008).
- Moore, M. J. & Proudfoot, N. J. Pre-mRNA processing reaches back to transcription and ahead to translation. *Cell* **136**, 688–700 (2009).
- Wahl, M. C., Will, C. L. & Luhrmann, R. The spliceosome: design principles of a dynamic RNP machine. *Cell* **136**, 701–718 (2009).
- Kambach, C., Walke, S. & Nagai, K. Structure and assembly of the spliceosomal small nuclear ribonucleoprotein particles. *Curr. Opin. Struct. Biol.* **9**, 222–230 (1999).
- Nilsen, T. W. The spliceosome: the most complex macromolecular machine in the cell? *Bioessays* **25**, 1147–1149 (2003).
- Staley, J. P. & Guthrie, C. Mechanical devices of the spliceosome: motors, clocks, springs, and things. *Cell* **92**, 315–326 (1998).
- Hall, S. L. & Padgett, R. A. Requirement of U12 snRNA for *in vivo* splicing of a minor class of eukaryotic nuclear pre-mRNA introns. *Science* **271**, 1716–1718 (1996).
- Patel, A. A. & Steitz, J. A. Splicing double: insights from the second spliceosome. *Nature Rev. Mol. Cell Biol.* **4**, 960–970 (2003).
- Tarn, W. Y. & Steitz, J. A. A novel spliceosome containing U11, U12, and U5 snRNPs excises a minor class (AT-AC) intron *in vitro*. *Cell* **84**, 801–811 (1996).
- Baserga, S. J. & Steitz, J. A. In *The RNA World* (eds Gesteland, R. F. & Atkins, J. F.) 359–381 (Cold Spring Harbor Laboratory Press, 1993).
- Fischer, U., Liu, Q. & Dreyfuss, G. The SMN-SIP1 complex has an essential role in spliceosomal snRNP biogenesis. *Cell* **90**, 1023–1029 (1997).
- Liu, Q., Fischer, U., Wang, F. & Dreyfuss, G. The spinal muscular atrophy disease gene product, SMN, and its associated protein SIP1 are in a complex with spliceosomal snRNP proteins. *Cell* **90**, 1013–1021 (1997).

- Meister, G., Buhler, D., Pillai, R., Lottspeich, F. & Fischer, U. A multiprotein complex mediates the ATP-dependent assembly of spliceosomal U snRNPs. *Nature Cell Biol.* **3**, 945–949 (2001).
- Pellizzoni, L., Yong, J. & Dreyfuss, G. Essential role for the SMN complex in the specificity of snRNP assembly. *Science* **298**, 1775–1779 (2002).
- Wan, L. *et al.* The survival of motor neurons protein determines the capacity for snRNP assembly: biochemical deficiency in spinal muscular atrophy. *Mol. Cell Biol.* **25**, 5543–5551 (2005).
- Gabanella, F. *et al.* Ribonucleoprotein assembly defects correlate with spinal muscular atrophy severity and preferentially affect a subset of spliceosomal snRNPs. *PLoS ONE* **2**, e921 (2007).
- Zhang, Z. *et al.* SMN deficiency causes tissue-specific perturbations in the repertoire of snRNAs and widespread defects in splicing. *Cell* **133**, 585–600 (2008).
- Cifuentes-Diaz, C., Frugier, T. & Melki, J. Spinal muscular atrophy. *Semin. Pediatr. Neurol.* **9**, 145–150 (2002).
- Iannaccone, S. T., Smith, S. A. & Simard, L. R. Spinal muscular atrophy. *Curr. Neurol. Neurosci. Rep.* **4**, 74–80 (2004).
- Lefebvre, S. *et al.* Identification and characterization of a spinal muscular atrophy-determining gene. *Cell* **80**, 155–165 (1995).
- König, H., Matter, N., Bader, R., Thiele, W. & Müller, F. Splicing segregation: the minor spliceosome acts outside the nucleus and controls cell proliferation. *Cell* **131**, 718–729 (2007).
- Matter, N. & König, H. Targeted 'knockdown' of spliceosome function in mammalian cells. *Nucleic Acids Res.* **33**, e41 (2005).
- Kaida, D. *et al.* Spliceostatin A targets SF3b and inhibits both splicing and nuclear retention of pre-mRNA. *Nature Chem. Biol.* **3**, 576–583 (2007).
- Krämer, A. *et al.* Structure-function analysis of the U2 snRNP-associated splicing factor SF3a. *Biochem. Soc. Trans.* **33**, 439–442 (2005).
- Friend, K., Lovejoy, A. F. & Steitz, J. A. U2 snRNP binds intronless histone pre-mRNAs to facilitate U7-snRNP-dependent 3' end formation. *Mol. Cell* **28**, 240–252 (2007).
- Kyburz, A., Friedlein, A., Langen, H. & Keller, W. Direct interactions between subunits of CPSF and the U2 snRNP contribute to the coupling of pre-mRNA 3' end processing and splicing. *Mol. Cell* **23**, 195–205 (2006).
- Millevoi, S. & Vagner, S. Molecular mechanisms of eukaryotic pre-mRNA 3' end processing regulation. *Nucleic Acids Res.* **38**, 2757–2774 (2010).
- Vagner, S., Rueggsegger, U., Gunderson, S. I., Keller, W. & Mattaj, I. W. Position-dependent inhibition of the cleavage step of pre-mRNA 3'-end processing by U1 snRNP. *RNA* **6**, 178–188 (2000).
- Gunderson, S. I., Polycarpou-Schwarz, M. & Mattaj, I. W. U1 snRNP inhibits pre-mRNA polyadenylation through a direct interaction between U1 70K and poly(A) polymerase. *Mol. Cell* **1**, 255–264 (1998).
- Fortes, P. *et al.* Inhibiting expression of specific genes in mammalian cells with 5' end-mutated U1 small nuclear RNAs targeted to terminal exons of pre-mRNA. *Proc. Natl Acad. Sci. USA* **100**, 8264–8269 (2003).
- Calvo, O. & Manley, J. L. Strange bedfellows: polyadenylation factors at the promoter. *Genes Dev.* **17**, 1321–1327 (2003).
- Dreyfuss, G., Kim, V. N. & Kataoka, N. Messenger-RNA-binding proteins and the messages they carry. *Nature Rev. Mol. Cell Biol.* **3**, 195–205 (2002).
- Kornblihtt, A. R., de la Mata, M., Fededa, J. P., Munoz, M. J. & Nogues, G. Multiple links between transcription and splicing. *RNA* **10**, 1489–1498 (2004).
- Perales, R. & Bentley, D. "Cotranscriptionality": the transcription elongation complex as a nexus for nuclear transactions. *Mol. Cell* **36**, 178–191 (2009).
- Proudfoot, N. New perspectives on connecting messenger RNA 3' end formation to transcription. *Curr. Opin. Cell Biol.* **16**, 272–278 (2004).
- Gromak, N., West, S. & Proudfoot, N. L. Pause sites promote transcriptional termination of mammalian RNA polymerase II. *Mol. Cell Biol.* **26**, 3986–3996 (2006).
- Lander, E. S. *et al.* Initial sequencing and analysis of the human genome. *Nature* **409**, 860–921 (2001).
- Pellizzoni, L., Kataoka, N., Charroux, B. & Dreyfuss, G. A novel function for SMN, the spinal muscular atrophy disease gene product, in pre-mRNA splicing. *Cell* **95**, 615–624 (1998).
- Kataoka, N. & Dreyfuss, G. A simple whole cell lysate system for *in vitro* splicing reveals a stepwise assembly of the exon-exon junction complex. *J. Biol. Chem.* **279**, 7009–7013 (2004).
- Giardine, B. *et al.* Galaxy: a platform for interactive large-scale genome analysis. *Genome Res.* **15**, 1451–1455 (2005).

Supplementary Information is linked to the online version of the paper at www.nature.com/nature.

Acknowledgements We are grateful to the members of our laboratory, especially J. Yong and J. Bachorik, for discussions and comments on this manuscript. We thank M. Yoshida for providing spliceostatin A. We also thank D. A. Baldwin and H. Rodriguez at the Microarray Core Facility at the University of Pennsylvania School of Medicine for help with the tiling array. This work was supported by the Association Française Contre les Myopathies (AFM). G.D. is an Investigator of the Howard Hughes Medical Institute.

Author Contributions D.K., M.G.B., I.Y., M.K., L.N.S. and L.W. designed and performed experiments and contributed to data analysis. G.D. is responsible for the project planning and experimental design. All authors contributed to writing the paper.

Author Information The tiling array data have been submitted to the GEO database under the accession number GSE24179. Reprints and permissions information is available at www.nature.com/reprints. The authors declare no competing financial interests. Readers are welcome to comment on the online version of this article at www.nature.com/nature. Correspondence and requests for materials should be addressed to G.D. (gdreyfuss@hhmi.upenn.edu).

METHODS

Cell culture and antisense morpholino oligonucleotide transfection. HeLa cells were cultured as previously described. HeLa cells ($\sim 10^7$ cells per transfection) were trypsinized, washed twice with PBS and re-suspended in 400 μ l of DMEM without serum. After mixing cells with morpholino oligonucleotide, they were transferred to a 0.4-cm gap cuvette (Bio-rad). Electroporation was performed using a Bio-Rad Gene pulser at 960 μ F and 280 V. After electroporation, cells were cultured for 8 h in 6-well plates with 2 ml DMEM. The sequence of the 25-mer U1 AMO is 5'-GGTATCTCCCCTGCCAGGTAAGTAT-3', which is complementary to nucleotides 1–25 in human U1 snRNA. The sequence of the 25-mer U2 AMO is 5'-TGATAAGAACAGATACTACACTTGA-3', which is complementary to nucleotides 27–51 in human U2 snRNA. The 25-mer scrambled sequence control AMO is 5'-CCTCTTACCTCAGTTACAATTATA-3', as previously described^{23,24}. AMOs were obtained from Gene Tools, LLC.

RNA preparation and 3' RACE. Total RNA was extracted from cultured cells using TRIzol (Invitrogen). cDNA was synthesized using SuperScript III reverse transcriptase (Invitrogen) using oligo dT18-XbaKpnBam primer for 3' RACE according to the manufacturer's directions. 3' RACE was carried out using the first and second (nested) forward primers and XbaKpnBam reverse primer.

For 3' RACE of the *NR3C1* mini-gene, pcDNA3.1-5' primer was used as a forward primer to distinguish mini-gene RNA from endogenous *NR3C1* RNA. PCR products were cut with HindIII to distinguish PCR products of prematurely polyadenylated RNA from mRNA spliced and polyadenylated at the canonical PAS at the 3' end. Quantification of PCPA and polyadenylation at the canonical PAS at the 3' end in control and U1-AMO-treated cells (Fig. 5d) was performed using real-time PCR. Primer sequences are listed in Supplementary Table 1.

Tiling array target preparation, hybridization and data analysis. Total RNAs were prepared from HeLa cells transfected with control or U1 AMOs (7.5 μ M), or SSA (100 ng ml⁻¹) or methanol for 8 h. Labelled cDNA targets were prepared using the GeneChip WT amplified Double-Stranded cDNA Synthesis Kit and the GeneChip WT Double-Stranded DNA Terminal Labelling Kit (Affymetrix) according to the manufacturer's directions. The end-labelled cDNA targets were applied to GeneChip human tiling 2.0R E arrays (Affymetrix). Hybridization was performed using F450-001 fluidics wash and stain script on the Affymetrix GeneChip Fluidics Station 450. Arrays were scanned using the Affymetrix GCS 3000 7G GeneChip Operating Software (GCOS) to produce .CEL files.

For tiling array analysis, we used .CEL files and the Affymetrix Tiling Analysis Software (TAS) version 1.1 to produce .BED files of the following signal intensity and *P*-value (bandwidth = 50, Min. Run = 100, Max. Gap = 100, fold change ≥ 2 -fold, *P*-value < 0.01). Overlapping regions of two files of signal intensity and *P*-value were chosen using Galaxy (<http://galaxy.psu.edu/>)⁴². We

produced .BAR files from the .CEL files using TAS to visualize on the Integrated Genome Browser (IGB) (Affymetrix).

In vitro splicing. [α -³²P]UTP-labelled Ad2ΔIVS pre-mRNA was prepared as previously described⁴⁰. *In vitro* splicing reactions were carried out in 293T whole cell splicing extracts prepared as previously described⁴¹. Increasing amounts of control and U1 AMOs were added to reactions that were incubated for 90 min at 30 °C. Splicing products were purified with TRIzol, resolved on denaturing PAGE, and gels were autoradiographed.

RNase H protection assay and northern blotting. HeLa cells were transfected with AMOs and incubated for 8 h. Cells were harvested and total cell extract was prepared using RSB-100 buffer (10 mM Tris-HCl, pH 7.5, 100 mM NaCl, 2.5 mM MgCl₂). The cell extract was incubated with 1.5 U of RNase H (Promega) and 5 μ M antisense DNA oligonucleotide in a 20- μ l reaction for 25 min at 30 °C. Antisense DNA oligonucleotide for U1 snRNA is 5'-CAGGTAAGTAT-3'. After RNase H treatment, RNA samples were purified and analysed by northern blotting with [γ -³²P]ATP-labelled U1 snRNA probe, the sequence of which is 5'-CAAATTATGCAGTCGAGTTTCCCACATTTG-3'.

Plasmid construction. To construct the *NR3C1* mini-gene, DNA fragments of *NR3C1* intron 1-exon 2-intron 2 and *NR3C1* intron 2-exon 3 were amplified from genomic DNA from HEK293T cells using *NR3C1* int1 for and *NR3C1* int2 rev XhoI, and *NR3C1* int2 for XhoI and *NR3C1* Ex3 rev XhoI. The *NR3C1* intron 1-exon 2-intron 2 fragment was digested with XhoI and EcoRI, and the *NR3C1* intron 2-exon 3 fragment was digested with XhoI. These fragments were sub-cloned into pcDNA3.1 vector (Invitrogen). The intron 2 of *NR3C1* was truncated from 80 kb to 2 kb to facilitate cloning, mutagenesis and transfection. To introduce mutations, the QuikChange II Site-Directed Mutagenesis Kits (Stratagene) was used with *NR3C1* poly(A) site mutation forward and *NR3C1* poly(A) site mutation reverse, and *NR3C1* 5' SS mutation forward and *NR3C1* 5' SS mutation reverse primers. Sequences of all primers are listed in Supplementary Table 1.

In situ hybridization. *In situ* hybridization of U1 snRNA in HeLa cells transfected with control or U1 AMO for 8 h was performed with a biotin-labelled LNA probe (5'-GGTATCTCCCCTGCCAGGTAAGTAT-3') obtained from Exiqon. The protocol was essentially as described by the manufacturer (Exiqon). Hybridization was performed in 50% formamide, 2 \times SSC, 50 mM sodium phosphate (pH 7), and 10% dextran sulphate, containing 10 nM LNA probe, at ~ 20 °C below the melting temperature (*T*_m) for 1 h (50 °C) in a humidified chamber. After hybridization, cells were washed in 2 \times SSC + 0.1% Triton X-100, followed by detection with a fluorescent Alexa Fluor 594 streptavidin conjugate. Cells were washed 3 \times 5 min at 37 °C in 4 \times SSC + 0.1% Triton X-100, followed by washes in 2 \times and 1 \times SSC, with a final wash in PBS at 25 °C. Nuclei were stained by DAPI.

A ground-based transmission spectrum of the super-Earth exoplanet GJ 1214b

Jacob L. Bean^{1,2}, Eliza Miller-Ricci Kempton³ & Derek Homeier²

In contrast to planets with masses similar to that of Jupiter and higher, the bulk compositions of planets in the so-called super-Earth regime (masses 2–10 times that of the Earth) cannot be uniquely determined from a measurement of mass and radius alone. For these planets, there is a degeneracy between the mass and composition of both the interior and a possible atmosphere in theoretical models^{1,2}. The recently discovered transiting super-Earth exoplanet GJ 1214b is one example of this problem³. Three distinct models for the planet that are consistent with its mass and radius have been suggested⁴. Breaking the degeneracy between these models requires obtaining constraints on the planet's atmospheric composition^{5,6}. Here we report a ground-based measurement of the transmission spectrum of GJ 1214b between wavelengths of 780 and 1,000 nm. The lack of features in this spectrum rules out (at 4.9 σ confidence) cloud-free atmospheres composed primarily of hydrogen. If the planet's atmosphere is hydrogen-dominated, then it must contain clouds or hazes that are optically thick at the observed wavelengths at pressures less than 200 mbar. Alternatively, the featureless transmission spectrum is also consistent with the presence of a dense, water vapour atmosphere.

We observed transits of the planet GJ 1214b in front of its host star on 29 April and 6 June 2010 UT using the FORS2 instrument on the UT1 telescope of the Very Large Telescope facility. The instrument was configured for multi-object spectroscopy, using a mask with slits positioned on GJ 1214 and six other nearby reference stars of similar brightness. The slits had lengths of 30 arcsec and widths of 12.0 arcsec to eliminate possible differential losses due to variations in the telescope guiding and seeing⁷. Complete spectra from 780 to 1,000 nm with a resolution of approximately 1 nm were obtained for all the stars in each exposure. A total of 197 exposures were obtained during the two observing runs, 88 of which were during a transit.

We extracted both 'white' light curves and 11 spectrophotometric light curves (of 20-nm channel width) for GJ 1214 and the reference stars by summing the obtained spectra over wavelength. We corrected the transit light curves by combining the fluxes for five of the reference stars and dividing them into the flux of GJ 1214. After this reduction, the light curves for GJ 1214 exhibit the expected transit morphology superimposed on a curvature that is well-matched by a second order polynomial as a function of time. We modelled this trend for each time series simultaneously with the transit modelling described below. Normalized and corrected light curves for the spectrophotometric data are shown in Fig. 1. The photon-limited uncertainties in the measurements after reduction and correction are 350–710 parts per million (p.p.m.). We found that these estimates potentially underestimate the true uncertainties in the data, and we therefore revised the uncertainties upward by 25–78% to yield reduced χ^2 values of unity for the light curve model fits. (See Supplementary Information for more details on the observations, data reduction, and reference star corrections.)

We fitted models for the transit⁸ to the spectrophotometric time-series data to measure the apparent radius of GJ 1214b in each channel—this is

the planet's transmission spectrum. We assumed that the planet is on a circular orbit, and we fixed the transit and system parameters to the values we determined from an analysis of the white light curves. The uncertainties in the fixed parameters do not contribute any additional uncertainty in the transmission spectrum, and only the overall level of the transmission spectrum would be influenced by changing these values within their confidence limits.

We detect a marginally significant (1.5 σ) difference in the depths of the white light curves between the two observed transits of $(2.4 \pm 1.6) \times 10^{-4}$. This level of variation is consistent with brightness variations of the unocculted portion of the stellar disk similar to the contemporaneously observed *I*-band variation of 0.65% (Z. Berta, personal communication). We accounted for this variability in our analysis of the spectrophotometric light curves by reducing the planet-to-star radius ratio parameter (R_p/R_*) used to generate the models for the first transit by an amount corresponding to the change in depth in the white light curves ($\Delta R_p/R_* = 0.0010$). We did not apply any additional corrections to the data to attempt to account for a colour bias due to occulted or unocculted spots, because simulations that we had performed indicated that the effects across the small wavelength range studied here would be negligible, given the precision of the data.

The results from our analysis of the white light curves after the stellar activity correction confirm and refine the previous estimates of system parameters. Assuming that the mass of the star is $0.157 \pm 0.019 M_\odot$ (ref. 3), the radius of the star is $0.206 \pm 0.009 R_\odot$ and the average radius of the planet is $2.63 \pm 0.11 R_\oplus$ (here M_\odot , R_\odot and R_\oplus indicate respectively solar mass, solar radius and terrestrial radius). The planet's average central transit time is BJD 2455315.794502 \pm 0.000047 (4 s uncertainty), and its orbital period is 1.58040834 \pm 0.00000034 d. The determined transmission spectrum for GJ 1214b in terms of the planet's radius, assuming the stellar radius from the analysis of the white light curves, is shown in Fig. 2. We obtain similar results for the transmission spectrum when repeating the analysis with different plausible values for the fixed parameters, not adopting a prior on the limb darkening, applying no activity corrections, applying higher-order activity corrections, or using different approaches to correct for the activity.

Previous work has shown that GJ 1214b must have a significant atmosphere because its density is too low for it to be composed only of solid material⁴. However, the composition of the atmosphere cannot be inferred with only the knowledge of the planet's mass and radius, owing to degeneracies between interior structure and atmospheric models. Comparison of our observed transmission spectrum to model spectra for different atmospheric compositions (see Fig. 2) indicates that we would have detected significant variations in the planet's effective radius if the atmosphere was mainly composed of hydrogen. This is because such an atmosphere would have a large scale height, and the resulting absorption of starlight by water vapour in the limb of the planet would lead to variations in effective radius. A hydrogen-dominated atmosphere would be expected if the planet was a scaled down version

¹Harvard-Smithsonian Center for Astrophysics, 60 Garden Street, Cambridge, Massachusetts 02138, USA. ²Institut für Astrophysik, Georg-August-Universität, Friedrich-Hund-Platz 1, 37077 Göttingen, Germany. ³Department of Astronomy and Astrophysics, University of California, Santa Cruz, California 95064, USA.

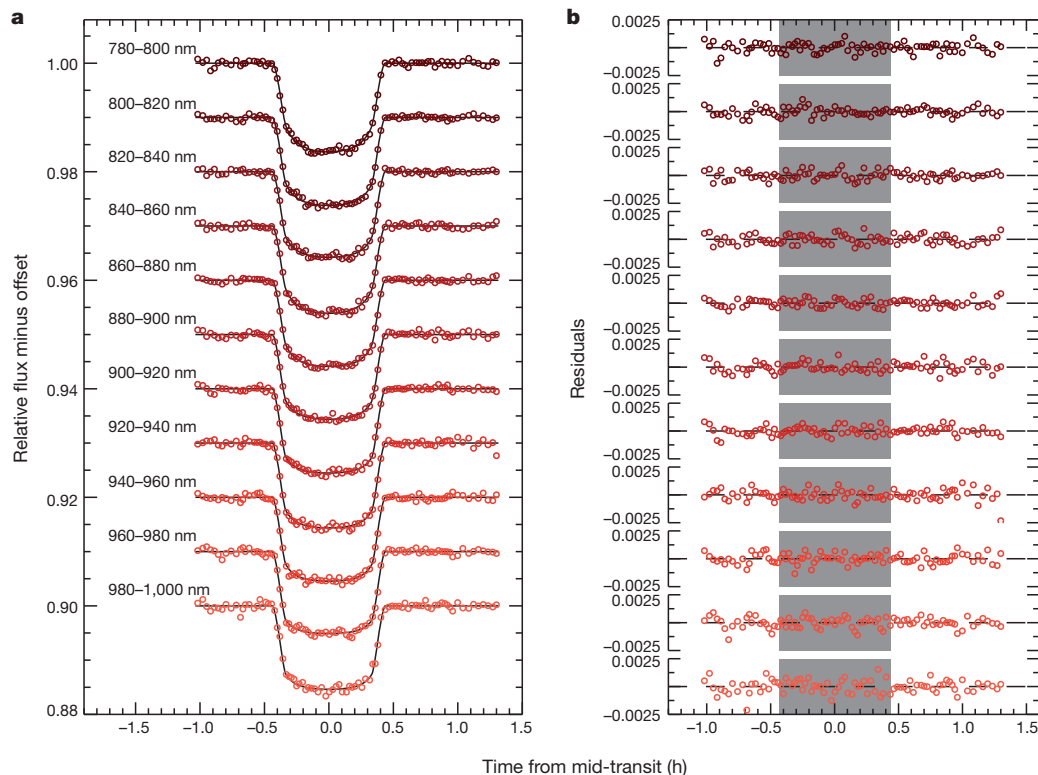


Figure 1 | Spectrophotometric data for transits of GJ 1214b. **a**, Normalized light curves and best-fit models. An offset of 0.01 was subtracted from the data in each successive channel for clarity. The data from the two observed transits were combined after correcting for the variation in the transit depth between the observed transits (the correction factor used was 1.017), and binned at a sampling of 72 s for this figure. Solid lines, best-fit models fitted independently to the data to determine the apparent size of the planet in each channel. **b**, Binned residuals from the best-fit models. Grey boxes, times when the planet is passing in front of the star. The standard deviation of the residuals in the channels ranges from 331 to 580 p.p.m. Model fitting: the free parameters in the model fitted to the data to determine the transmission spectrum were the ratio of the radius of the planet to the radius of the host star, quadratic limb darkening coefficients, and the three terms describing the second order

polynomial as a function of time needed to normalize the data. The ratio of the radii and the limb darkening coefficients were determined for each channel, while the polynomial coefficients for the data normalization were determined for each channel in each transit observation. We estimated limb darkening coefficients that were used as priors with uncertainties for each spectrophotometric channel using a spherically symmetric model atmosphere for the host star calculated with the PHOENIX code²² for parameters $T_{\text{eff}} = 3,026$ K, $[M/H] = 0.0$, $\log g = 5.0$ and $R_* = 0.21 R_{\odot}$. The model intensities were integrated over the bandpass for each channel to account for the variation of the instrument transmission function and the spectral energy distribution of the star. To estimate the uncertainty in these predictions, we repeated the calculations for models with $T_{\text{eff}} = 3,156$ and $2,896$ K.

of the Solar System ice giants Uranus and Neptune with a primordial atmosphere accreted from the protoplanetary nebulae, or if it was a rocky planet that had outgassed large quantities of hydrogen during formation or a period of tectonic activity⁹. Instead, we detect no such variations at high confidence (4.9σ), and we conclude that the planet must possess something other than a simple cloud-free hydrogen-dominated atmosphere.

Of the models proposed for the planet based on constraints from interior modelling^{4,6,10}, only the predicted spectra from cloud-free atmospheres composed predominantly of water vapour (steam) agree with our measured transmission spectrum. Water vapour is present in the planet's limb to absorb the starlight in all the proposed models, but at least 70% water vapour by mass (mean molecular weight $> 5M_{\text{H}}$, where M_{H} is the mass of the hydrogen atom) is needed to result in a transmission spectrum with the relatively small variations required to be consistent with our measurements within 1σ . A predominantly steam atmosphere is a component of the 'water world'^{11–13} bulk composition model of the planet discussed in ref. 4 (their case II), although it has been recently suggested¹⁰ that a water-rich atmosphere is not necessarily indicative of a water-rich interior. In either case, the planet would not harbour any liquid water owing to the high temperatures present throughout its atmosphere^{4,10}. If GJ 1214b contains a significant water abundance, then it probably formed beyond the snow line of its host star's protoplanetary disk, and subsequent orbital evolution brought it inward to its current location. The planet either could have

not accreted as much nebular gas (which would have been composed primarily of hydrogen) as Neptune in the first place, or could have subsequently lost by atmospheric escape any hydrogen-rich gas that it did accrete^{3,4}.

Another possible explanation for the lack of spectral features observed in the transmission spectrum of GJ 1214b is that the planet could have a high layer of clouds or hazes, obscuring the view of lower regions in the planetary atmosphere. The effect of such a cloud deck on the transmission spectrum would be to reduce the strength of predicted spectral features, even for an atmosphere with a low mean molecular weight. We performed a simple test to determine the effect of clouds on the transmission spectrum for the case of a hydrogen-dominated atmosphere by cutting off all transmission of starlight below the height of a hypothetical cloud deck. We find that clouds or hazes located at pressures less than 200 mbar (comparable to cloud/haze layers on Venus and Titan) do flatten out the transmission spectrum of a hydrogen-dominated atmosphere to the point where it is indistinguishable from a steam atmosphere using the current data. Therefore, our observations could be indicative of clouds or hazes in the upper parts of GJ 1214b's atmosphere. Although no candidate has yet been presented for a cloud layer on GJ 1214b, and the planet's proposed temperature–pressure profile does not cross the condensation curves of any known equilibrium condensates that are likely to be present in significant quantities (it does cross the condensation curves of minor species, KCl being the most abundant)¹⁴, hazes resulting from

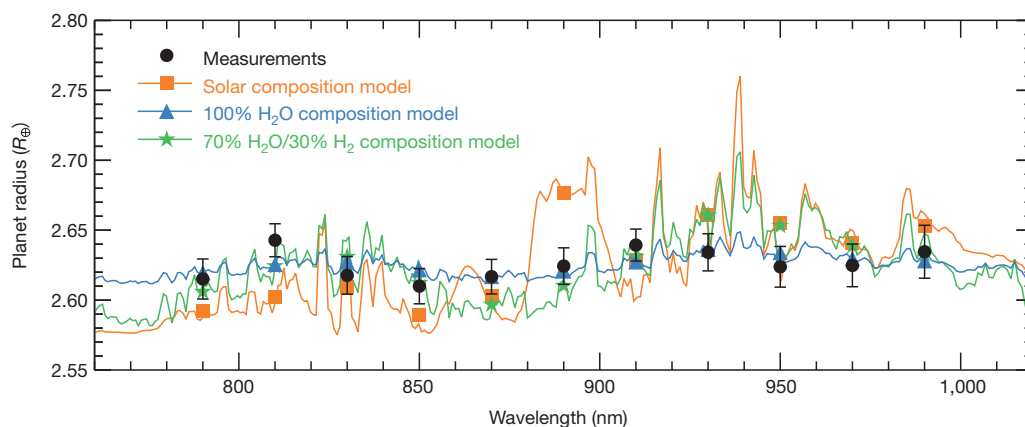


Figure 2 | The transmission spectrum of GJ 1214b compared to models.

Theoretical predictions of the transmission spectrum for GJ 1214b⁶ are shown for atmospheres with a solar composition (that is, hydrogen-dominated; orange line and squares), a 100% water vapour composition (blue line and triangles), and a mixed composition of 70% water vapour and 30% molecular hydrogen by mass (green line and stars). The points for the models give the expected values for the transmission spectrum in each of the spectrophotometric channels. All of the features in the model spectra arise from variations in the water vapour opacity, with the exception of the feature at 890 nm that is due to methane absorption. The measurements and their uncertainties (black circles) were estimated by fitting the spectrophotometric data using five Markov chains with 2.5×10^5 steps. The uncertainties, which are valid for the relative values only, are the 1σ confidence intervals of the resulting posterior distributions, and are

consistent with the estimates we obtained from a residual permutation bootstrap analysis. The uncertainty in the absolute level is $0.11 R_{\oplus}$, and is due mainly to the uncertainty in the host star mass. The data are consistent with the model for the water vapour atmosphere ($\chi^2 = 5.6$ for 10 degrees of freedom) and inconsistent with the model for the solar composition model at 4.9σ confidence ($\chi^2 = 47.3$). The predictions for a solar composition atmosphere with CH_4 removed due to photodissociation (not shown) are equally discrepant with the data. The mixed water vapour and molecular hydrogen atmosphere model contains the most hydrogen possible to still be within 1σ ($\chi^2 = 11.5$) of the measurements. The data are furthermore consistent with a hydrogen-dominated atmosphere with optically thick clouds or hazes located above a height of 200 mbar (not shown). We obtain similar results when comparing the models to measurements obtained using smaller or larger channel sizes.

photochemical processes remain a viable prospect and are currently unconstrained by models. Transit observations of GJ 1214b in the infrared could shed light on the question of clouds and hazes in the planet's atmosphere: scattering from cloud and haze particles is far less efficient at these wavelengths, and radius variations in the planet's transmission spectrum could be more apparent if the atmosphere was actually composed primarily of hydrogen. Indeed, a recent study has suggested there are variations in the planet's transmission spectrum between the near-infrared J and K bands that are qualitatively consistent with the expectations for a hydrogen-dominated atmosphere (B. Croll, personal communication). Further observations are needed to clarify this issue.

The only other known transiting planet in the same mass regime as GJ 1214b, CoRoT-7b^{15,16}, could also harbour an atmosphere despite the extreme level of insolation it receives from its host star¹⁷. However, this planet orbits a much larger star ($R_{\star} = 0.87 R_{\odot}$; ref. 14) than GJ 1214b and, thus, it is unlikely that additional constraints on its atmosphere could be obtained with existing facilities owing to the unfavourable planet-to-star radius ratio. In contrast, our results confirm previous predictions^{18,19} about the excellent prospects for the detailed characterization of transiting exoplanets identified by searches targeting very low-mass stars, like the MEarth project²⁰ and near-infrared radial velocity surveys²¹. Application of the increasingly sophisticated observational techniques of transiting exoplanet spectroscopy to the atmospheres of planets orbiting M dwarfs offers the promise of comparative studies of super-Earths in the near future. Such an approach probably offers the best chance for the eventual first characterization of the atmosphere of a potentially habitable planet.

Received 22 July; accepted 19 October 2010.

- Adams, E. R., Seager, S. & Elkins-Tanton, L. Ocean planet or thick atmosphere: on the mass-radius relationship for solid exoplanets with massive atmospheres. *Astrophys. J.* **673**, 1160–1164 (2008).
- Rogers, L. A. & Seager, S. A framework for quantifying the degeneracies of exoplanet interior compositions. *Astrophys. J.* **712**, 974–991 (2010).
- Charbonneau, D. et al. A super-Earth transiting a nearby low-mass star. *Nature* **462**, 891–894 (2009).
- Rogers, L. A. & Seager, S. Three possible origins for the gas layer on GJ 1214b. *Astrophys. J.* **716**, 1208–1216 (2010).

- Miller-Ricci, E., Seager, S. & Sasselov, D. The atmospheric signatures of super-Earths: how to distinguish between hydrogen-rich and hydrogen-poor atmospheres. *Astrophys. J.* **690**, 1056–1067 (2009).
- Miller-Ricci, E. & Fortney, J. J. The nature of the atmosphere of the transiting super-Earth GJ 1214b. *Astrophys. J.* **716**, L74–L79 (2010).
- Knutson, H. A., Charbonneau, D., Deming, D. & Richardson, L. J. A. Ground-based search for thermal emission from the exoplanet TrES-1. *Publ. Astron. Soc. Pacif.* **119**, 616–622 (2007).
- Mandel, K. & Agol, E. Analytic light curves for planetary transit searches. *Astrophys. J.* **580**, L171–L175 (2002).
- Elkins-Tanton, L. T. & Seager, S. Ranges of atmospheric mass and composition of super-Earth exoplanets. *Astrophys. J.* **685**, 1237–1246 (2008).
- Nettelmann, N., Fortney, J. J., Kramm, U. & Redmer, R. Thermal evolution and interior models of the transiting super-Earth GJ 1214b. Preprint at (<http://arXiv.org/abs/1010.0277>) (2010).
- Kuchner, M. J. Volatile-rich Earth-mass planets in the habitable zone. *Astrophys. J.* **596**, L105–L108 (2003).
- Léger, A. et al. A new family of planets? “Ocean-planets”. *Icarus* **169**, 499–504 (2004).
- Selsis, F. et al. Could we identify hot ocean-planets with CoRoT, Kepler and Doppler velocimetry? *Icarus* **191**, 453–468 (2007).
- Lodders, K. & Fegley, B. Jr. *Chemistry of Low Mass Substellar Objects* 1–28 (Springer, 2006).
- Léger, A. et al. Transiting exoplanets from the CoRoT space mission. VIII. CoRoT-7b: the first super-Earth with measured radius. *Astron. Astrophys.* **506**, 287–302 (2009).
- Queloz, D. et al. The CoRoT-7 planetary system: two orbiting super-Earths. *Astron. Astrophys.* **506**, 303–319 (2009).
- Valencia, D., Ikoma, M., Guillot, T. & Nettelmann, N. Composition and fate of short-period super-Earths. The case of CoRoT-7b. *Astron. Astrophys.* **516**, A20 (2010).
- Deming, D. et al. Discovery and characterization of transiting super-Earths using an all-sky transit survey and follow-up by the James Webb Space Telescope. *Publ. Astron. Soc. Pacif.* **121**, 952–967 (2009).
- Kaltenegger, L. & Traub, W. A. Transits of Earth-like planets. *Astrophys. J.* **698**, 519–527 (2009).
- Nutzman, P. & Charbonneau, D. Design considerations for a ground-based transit search for habitable planets orbiting M dwarfs. *Publ. Astron. Soc. Pacif.* **120**, 317–327 (2008).
- Bean, J. L. et al. The CRISP search for planets around the lowest-mass stars. I. High-precision near-infrared radial velocities with an ammonia gas cell. *Astrophys. J.* **713**, 410–422 (2010).
- Hauschildt, P. H., Allard, F., Ferguson, J., Baron, E. & Alexander, D. R. The NEXTGEN model atmosphere grid. II. Spherically symmetric model atmospheres for giant stars with effective temperatures between 3000 and 6800 K. *Astrophys. J.* **525**, 871–880 (1999).

Supplementary Information is linked to the online version of the paper at www.nature.com/nature.

Acknowledgements We thank D. Charbonneau, J.-M. Desert, J. Fortney, S. Seager, L. Rogers and D. Sasselov for discussions about this work. J.L.B. received funding from the European Commissions Seventh Framework Program as a Marie Curie International Incoming Fellow. J.L.B. and E.M.-R.K. acknowledge funding from NASA through the Sagan Fellowship Program. The results presented are based on observations made with ESO telescopes at the Paranal Observatories under programs 284.C-5042 and 285.C-5019.

Author Contributions J.L.B. performed the observations and data analysis, and led the overall direction of the project. E.M.-R.K. calculated theoretical models for the planetary

atmosphere. D.H. calculated the stellar limb darkening. J.L.B. and E.M.-R.K. wrote the telescope time proposals and the paper. All authors discussed the results and commented on the manuscript.

Author Information The data utilized in this work can be accessed at the ESO/ST-ECF science archive (<http://archive.eso.org/cms/>). Reprints and permissions information is available at www.nature.com/reprints. The authors declare no competing financial interests. Readers are welcome to comment on the online version of this article at www.nature.com/nature. Correspondence and requests for materials should be addressed to J.L.B. (jbean@cfa.harvard.edu).

Trapped antihydrogen

G. B. Andresen¹, M. D. Ashkezari², M. Baquero-Ruiz³, W. Bertsche⁴, P. D. Bowe¹, E. Butler⁴, C. L. Cesar⁵, S. Chapman³, M. Charlton⁴, A. Deller⁴, S. Eriksson⁴, J. Fajans^{3,6}, T. Friesen⁷, M. C. Fujiwara^{8,7}, D. R. Gill⁸, A. Gutierrez⁹, J. S. Hangst¹, W. N. Hardy⁹, M. E. Hayden², A. J. Humphries⁴, R. Hydomako⁷, M. J. Jenkins⁴, S. Jonsell¹⁰, L. V. Jørgensen⁴, L. Kurchaninov⁸, N. Madsen⁴, S. Menary¹¹, P. Nolan¹², K. Olchanski⁸, A. Olin⁸, A. Povilus³, P. Pusa¹², F. Robicheaux¹³, E. Sarid¹⁴, S. Seif el Nasr⁹, D. M. Silveira¹⁵, C. So³, J. W. Storey^{8†}, R. I. Thompson⁷, D. P. van der Werf⁴, J. S. Wurtele^{3,6} & Y. Yamazaki^{15,16}

Antimatter was first predicted¹ in 1931, by Dirac. Work with high-energy antiparticles is now commonplace, and anti-electrons are used regularly in the medical technique of positron emission tomography scanning. Antihydrogen, the bound state of an antiproton and a positron, has been produced^{2,3} at low energies at CERN (the European Organization for Nuclear Research) since 2002. Antihydrogen is of interest for use in a precision test of nature's fundamental symmetries. The charge conjugation/parity/time reversal (CPT) theorem, a crucial part of the foundation of the standard model of elementary particles and interactions, demands that hydrogen and antihydrogen have the same spectrum. Given the current experimental precision of measurements on the hydrogen atom (about two parts in 10^{14} for the frequency of the 1s-to-2s transition⁴), subjecting antihydrogen to rigorous spectroscopic examination would constitute a compelling, model-independent test of CPT. Antihydrogen could also be used to study the gravitational behaviour of antimatter⁵. However, so far experiments have produced antihydrogen that is not confined, precluding detailed study of its structure. Here we demonstrate trapping of antihydrogen atoms. From the interaction of about 10^7 antiprotons and 7×10^8 positrons, we observed 38 annihilation events consistent with the controlled release of trapped antihydrogen from our magnetic trap; the measured background is 1.4 ± 1.4 events. This result opens the door to precision measurements on anti-atoms, which can soon be subjected to the same techniques as developed for hydrogen.

Charged particles of antimatter can be trapped in a high-vacuum environment in Penning–Malmberg traps, which use axial electric fields generated by hollow cylindrical electrodes and a solenoidal magnetic field to provide confinement. The ALPHA apparatus, located at the Antiproton Decelerator⁶ at CERN, uses several such traps to accumulate, cool and mix charged plasmas of antiprotons and positrons to synthesize antihydrogen atoms at cryogenic temperatures. ALPHA evolved from the ATHENA experiment, which demonstrated production and detection of cold antihydrogen at CERN in 2002².

In addition to the charged particle traps necessary to produce antihydrogen, ALPHA features a novel, superconducting magnetic trap⁷ (Fig. 1) designed to confine neutral antihydrogen atoms through interaction with their magnetic moments. The atom trap—a variation on the Ioffe–Pritchard minimum-magnetic-field geometry⁸—comprises a transverse octupole^{9,10} and two solenoidal ‘mirror’ coils, and surrounds the interaction region where antihydrogen atoms are produced. In comparison with a quadrupole field (used in traditional atom traps) producing an equal trap depth, the transverse field of an

octupole has been shown to greatly reduce the perturbations on charged plasmas^{9,10}. The liquid helium cryostat for the magnets also cools the vacuum wall and the Penning trap electrodes; the latter are measured to be at about 9 K. Antihydrogen atoms that are formed with low enough kinetic energy can remain confined in the magnetic trap, rather than annihilating on the Penning electrodes. The ALPHA trap can confine ground-state antihydrogen atoms with a kinetic energy, in

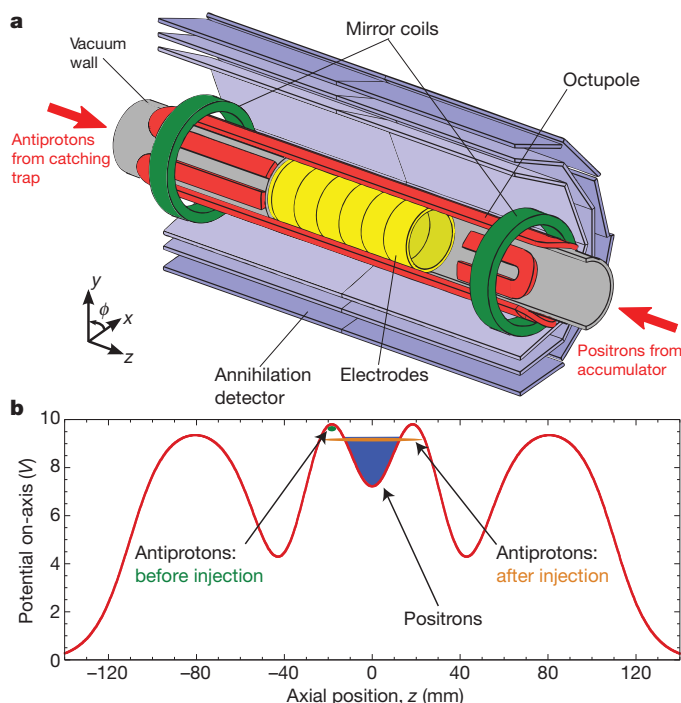


Figure 1 | The ALPHA central apparatus and mixing potential.

a, Antihydrogen synthesis and trapping region of the ALPHA apparatus. The atom-trap magnets, the modular annihilation detector and some of the Penning trap electrodes are shown. An external solenoid (not shown) provides a 1-T magnetic field for the Penning trap. The drawing is not to scale. The inner diameter of the Penning trap electrodes is 44.5 mm and the minimum-magnetic-field trap has an effective length of 274 mm. Each silicon module is a double-sided, segmented silicon wafer with strip pitches of 0.9 mm in the z direction and 0.23 mm in the ϕ direction. **b**, The nested-well potential used to mix positrons and antiprotons. The blue shading represents the approximate space charge potential of the positron cloud. The z position is measured relative to the centre of the atom trap.

¹Department of Physics and Astronomy, Aarhus University, DK-8000 Aarhus C, Denmark. ²Department of Physics, Simon Fraser University, Burnaby, British Columbia V5A 1S6, Canada. ³Department of Physics, University of California, Berkeley, California 94720-7300, USA. ⁴Department of Physics, Swansea University, Swansea SA2 8PP, UK. ⁵Instituto de Física, Universidade Federal do Rio de Janeiro, Rio de Janeiro 21941-972, Brazil. ⁶Lawrence Berkeley National Laboratory, Berkeley, California 94720, USA. ⁷Department of Physics and Astronomy, University of Calgary, Calgary, Alberta T2N 1N4, Canada. ⁸TRIUMF, 4004 Wesbrook Mall, Vancouver, British Columbia V6T 2A3, Canada. ⁹Department of Physics and Astronomy, University of British Columbia, Vancouver, British Columbia V6T 1Z1, Canada. ¹⁰Fysikum, Stockholm University, SE-10691, Stockholm, Sweden. ¹¹Department of Physics and Astronomy, York University, Toronto, Ontario M3J 1P3, Canada. ¹²Department of Physics, University of Liverpool, Liverpool L69 7ZE, UK. ¹³Department of Physics, Auburn University, Auburn, Alabama 36849-5311, USA. ¹⁴Department of Physics, Nuclear Research Center NEGEV, Beer Sheva, IL-84190, Israel. ¹⁵Atomic Physics Laboratory, RIKEN, Saitama 351-0198, Japan. ¹⁶Graduate School of Arts and Sciences, University of Tokyo, Tokyo 153-8902, Japan. †Present address: Physik-Institut, Zürich University, CH-8057 Zürich, Switzerland.

temperature units, of less than about 0.5 K. The extreme experimental challenges are to synthesize such cold atoms from plasmas of charged particles whose electrostatic potential energies can be of order 10 eV—or 10^5 K—and to unequivocally identify rare occurrences of trapped antihydrogen against background processes.

The ALPHA apparatus is designed to demonstrate antihydrogen trapping by releasing the magnetically trapped anti-atoms and detecting their annihilations. A key feature of the device is the ability to turn off the magnetic trapping fields with a time constant of about 9 ms, which is a response several orders of magnitude faster than in typical superconducting systems. Another essential component of ALPHA is an imaging, three-layer, silicon vertex detector¹¹ (Fig. 1), which is used to identify and locate antiproton annihilations from released antihydrogen atoms and to reject background from cosmic rays that happen to arrive during the time window of interest, when the trap is being de-energized. The magnets have a unique, low-density construction⁷ to minimize scattering of annihilation products (pions) so that the positions ('vertices') of antiproton annihilations can be accurately determined.

A trapping attempt involves first preparing clouds of antiprotons and positrons for 'mixing' to produce antihydrogen. The antiproton cloud contains about 30,000 particles obtained from one extracted bunch ($\sim 3 \times 10^7$ particles at 5.3 MeV) from the Antiproton Decelerator. The antiprotons are slowed in a thin foil, dynamically trapped¹² in a 3-T Penning trap (the 'catching' trap, not shown in Fig. 1) with 3.4-keV well depth, cooled using electrons¹³ and then separated from the electrons using pulsed electric fields. The resulting plasma has a radius of 0.8 mm, a temperature of about 200 K and a density of $6.5 \times 10^6 \text{ cm}^{-3}$. The positrons are supplied by a ^{22}Na radioactive source and a Surko-type accumulator^{14,15}. To increase the antihydrogen formation rate and trapping probability, the positrons transferred from the accumulator are evaporatively cooled^{16,17} (Methods) to about 40 K. The resulting positron plasma has 2×10^6 particles, a radius of 0.9 mm and a density of $5.5 \times 10^7 \text{ cm}^{-3}$.

Antiprotons and positrons are made to interact within a nested-well axial potential¹⁸ (Fig. 1b) at the centre of the magnetic atom trap. After the two species are placed in their respective potential wells, the superconducting magnets of the atom trap are ramped up to their maximum fields in 25 s. The antiprotons are then excited into the positron plasma using an oscillating electric field that autoresonantly^{19,20} increases their energy (Methods). This novel technique is essential for introducing the antiprotons into the positron cloud at low relative velocity, so that antihydrogen can be formed with low energy, and to reduce the heating of the positron plasma.

The positrons and antiprotons interact for 1 s to produce antihydrogen before the uncombined charged particles are ejected from the trap volume. During this mixing time, we record $5,000 \pm 400$ triggers in the silicon detector. The detector is triggered when charged particles (principally pions) from an antiproton annihilation deposit energy (above a threshold value) in at least two of the inner silicon modules. Cosmic rays can also trigger the detector and do so at a measured rate of $10.49 \pm 0.03 \text{ Hz}$. Each trigger can initiate a read-out of position information for the entire detector; the maximum read-out rate for such 'events' is 500 Hz. The position information can be analysed to identify pion trajectories (tracks) to locate antiproton annihilation vertices. An antiproton annihilation can usually be distinguished from a cosmic ray by considering their respective track topologies; see examples in Fig. 2. The rate at which we detect cosmic rays that could be misidentified as antiproton annihilations is $(4.6 \pm 0.1) \times 10^{-2} \text{ Hz}$ (Methods). Using the spatial distribution of the reconstructed annihilations during mixing²¹, we infer that about 70% of the mixing events are due to impacts from antihydrogen atoms that are not trapped; the remaining ones are mostly antiprotons from atoms that are sufficiently weakly bound to be field-ionized by Penning trap electric fields before reaching the wall.

The magnetic gradients of the atom trap can also act to trap bare antiprotons. Such 'mirror-trapped' antiprotons could escape and annihilate

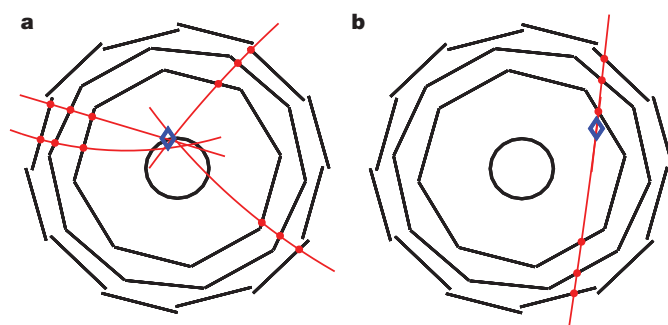


Figure 2 | Detected antiproton annihilation and cosmic ray events.

a, b, Projected end views (x - y plane) of an antiproton annihilation (**a**) and a cosmic-ray event (**b**) detected by the ALPHA detector. The reconstruction algorithm identifies the antiproton vertex (blue diamond) near the Penning trap wall (black circle). The high-energy cosmic ray passes in a near-straight line through the detector, and the vertex-finding algorithm attempts to identify it as a two-track annihilation with an unphysical vertex.

when the magnetic trap is de-energized, mimicking the sought-after signal of trapped antihydrogen atoms being released. After the 1-s mixing period, the charged particles in the mixing trap wells are ejected from the experiment. We then apply four pulses of axial electric 'clearing' fields of up to 500 V m^{-1} to remove mirror-trapped antiprotons. The manipulations after mixing take 172 ms, after which we initiate the trap shutdown. The rapid turn-off causes the superconducting elements to 'quench', or become normally conducting. We look for antiproton annihilations from released antihydrogen in a time window of 30 ms (more than three e-folding times for the confining fields) after the start of the magnet shutdown.

We conducted the above-described search experiment 335 times, in three variations. In one variation, referred to as 'left bias' (101 attempts), we erect a static electric field just before the quench to deflect any remaining antiprotons to the left (negative z direction) of the apparatus as they are released. The second variation, 'right bias' (97 attempts), features a static electric field that should deflect antiprotons to the other side of the device. In the third variation, 'no-bias' (137 attempts), all electrodes are at ground during the magnet quench. The bias electric field has a strength of about 500 V m^{-1} . The use of bias fields allows us to use the annihilation imaging detector to distinguish between the release of trapped antihydrogen—which is neutral and is therefore unaffected by these fields—and that of mirror-trapped antiprotons.

To ensure that any detected events are in fact antihydrogen and to eliminate other sources of background, we repeated the above experiments using heated positrons. Following the method introduced by the ATHENA² collaboration, we heat the positrons (without particle loss) to about 1,100 K by driving their axial motion. The effect in ALPHA is twofold: antihydrogen formation is suppressed because of the temperature dependence of the three-body process that dominates this reaction²², and any antihydrogen formed is unlikely to be trapped because the antiprotons approach thermal equilibrium with the hot positrons through Coulomb collisions. The number of annihilation events during the 1-s mixing time with heated positrons is 97 ± 16 . Apart from the heating of the positrons, the experimental trapping sequence is identical to that described above.

Table 1 summarizes the results of all trapping and background attempts. In the total sample of attempts (335) with cold positrons, we observe 38 annihilations, for a rate of 0.11 events per attempt. For the background sample with heated positrons, we observe one annihilation in 246 attempts, or a rate of 0.0041 events per attempt.

The discrimination provided by the silicon detector and the fast shutdown of our magnetic trap render the cosmic background negligible in comparison with the signal level in the current work. In the integrated observation time ($335 \times 30 \text{ ms}$), we would expect 0.46 ± 0.01 counts to result from misidentified cosmic rays.

Table 1 | Number of annihilations identified in the 30 ms following the trap shutdown

Type of attempt	Number of attempts	Antiproton annihilation events
No bias	137	15
Left bias	101	11
Right bias	97	12
No bias, heated positrons	132	1
Left bias, heated positrons	60	0
Right bias, heated positrons	54	0

We consider the effect of the bias fields in Fig. 3. We plot the event time versus the z coordinate of the reconstructed vertex for all identified annihilations in the 30-ms window. The start of the magnet shutdown corresponds to the zero of time. Figure 3a shows the t - z distribution for the 38 annihilations recorded using cold positrons and the one annihilation from heated positrons. Superimposed is a scatter plot from a dynamical simulation that predicts the behaviour of trapped antihydrogen atoms being released and annihilating on the Penning trap electrodes. (Details of the simulation procedures are given in Methods.) Figure 3b compares the measured annihilation distribution with simulations of mirror-trapped antiprotons released during the magnet shutdown. Predictions for the left-, right- and no-bias variations are shown.

Particles can be mirror-trapped when the ratio of their transverse to longitudinal energies exceeds a threshold determined by the field geometry. Although the phase space distribution of hypothetical mirror-trapped antiprotons is unknown, we illustrate here the prediction for an initial sample of antiprotons that has a uniform spatial distribution and a flat velocity distribution up to a maximum kinetic energy of 75 eV. This choice is quite conservative, as the maximum longitudinal potential well depth during the mixing process is less than 21 eV. We note that the model predicts that only mirror-trapped antiprotons with a transverse kinetic energy of greater than 45 eV could remain trapped after the clearing pulses. We have not been able to identify any mechanism that could create such antiprotons in the course of our experimental procedure, much less one that would then fail to create them when the positrons are heated by only 0.1 eV.

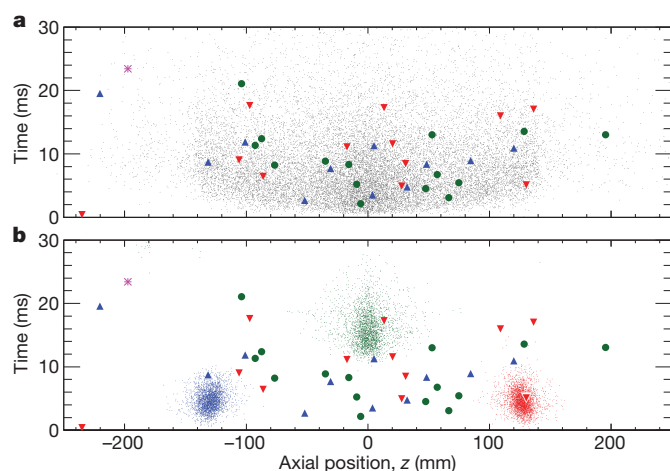


Figure 3 | Distributions of released antihydrogen atoms and antiprotons. **a**, Measured t - z distribution for annihilations obtained with no bias (green circles), left bias (blue triangles), right bias (red triangles) and heated positrons (violet star). The grey dots are from a numerical simulation of antihydrogen atoms released from the trap during the quench. The simulated atoms were initially in the ground state, with a maximum kinetic energy of 0.1 meV. The typical kinetic energy is larger than the depth of the neutral trap, ensuring that all trappable atoms are considered. The 30-ms observation window includes 99% of the 20,000 simulated points. **b**, Experimental t - z distribution, as above, shown along with results of a numerical simulation of mirror-trapped antiprotons being released from the trap. The colour codes are as above and there are 3,000 points in each of the three simulation plots. In both **a** and **b**, the simulated z distributions were convolved with the detector spatial resolution, of ~ 5 mm.

In the unlikely event that there are mirror-trapped antiprotons that survive the clearing pulses, it is clear from Fig. 3b that the measured annihilation distributions for the left- and right-bias trapping attempts are not consistent with the model predictions of the drastic deflection and earlier escape of such particles. Nor is the measured no-bias annihilation distribution consistent with the simulation distribution for antiprotons under no-bias conditions. All measured distributions are, however, consistent with the predicted behaviour of neutral antihydrogen (Fig. 3a). In a separate experiment, we intentionally created mirror-trapped antiprotons using extreme potential manipulations, and demonstrated that those that survive the clearing pulses are clearly deflected by the bias fields during the quench, in accordance with the simulations.

The background comprises 1.4 ± 1.4 events (scaled to 335 attempts) detected when trappable antihydrogen is unlikely to be present owing to heating of the positrons, and includes an expected cosmic background of 0.46 ± 0.01 events. As we have shown that the remaining events could not be mirror-trapped antiprotons, we conclude that we have observed the release of antihydrogen atoms that have been magnetically trapped for at least 172 ms.

The extensive diagnostic capabilities (Methods) of the ALPHA device allow us to make an order-of-magnitude theoretical estimate of the expected number of trapped antihydrogen atoms in our experiments. Following the procedure outlined in an earlier work²³, we estimate that we should detect about 0.4 trapped atoms per attempt, in reasonable agreement with the 0.11 observed here.

We note that although the trapping rate per antihydrogen atom produced is rather low ($\sim 5 \times 10^{-5}$, using the overall detection efficiency of about 50%) in our experiment, there is cause for optimism. The parameter space of positron temperature and density—which are the rate-determining factors for our type of mixing—has only begun to be investigated, and the positrons in ALPHA are still warm in comparison with their cryogenic surroundings. The promising technique of evaporative cooling of antiprotons¹⁷ has yet to be used here. Our work is a crucial step towards precision antihydrogen spectroscopy and anti-atomic tests of fundamental symmetries or gravitation.

METHODS SUMMARY

The ALPHA device has extensive capabilities for characterizing and manipulating charged antimatter plasmas. These include imaging of the plasmas to determine radii and transverse density, temperature measurement by controlled release of the plasma, the rotating-wall technique for control of plasma transverse size and density, evaporative cooling of the positron plasma and autoresonant injection of antiprotons into the positron plasmas.

Extensive simulations of antiproton and antihydrogen motion have been used to inform the experimental programme and to interpret the results of measurements. The simulations track single-particle trajectories using classical force equations.

Event topology is used to distinguish antiproton annihilations from cosmic rays in the silicon detector. The three event characteristics used are the number of reconstructed tracks, the vertex radius, and the deviation from straight-line geometry.

Full Methods and any associated references are available in the online version of the paper at www.nature.com/nature.

Received 8 October; accepted 27 October 2010.

Published online 17 November 2010.

1. Dirac, P. A. M. Quantised singularities in the electromagnetic field. *Proc. R. Soc. Lond. A* **133**, 60–72 (1931).
2. Amoretti, M. *et al.* Production and detection of cold antihydrogen atoms. *Nature* **419**, 456–459 (2002).
3. Gabrielse, G. *et al.* Background-free observation of cold antihydrogen with field-ionization analysis of its states. *Phys. Rev. Lett.* **89**, 213401 (2002).
4. Niering, M. *et al.* Measurement of the hydrogen 1S–2S transition frequency by phase coherent comparison with a microwave cesium fountain clock. *Phys. Rev. Lett.* **84**, 5496–5499 (2000).
5. Drobychev, G. Y. *et al.* Proposal for the AEGIS experiment at the CERN antiproton decelerator (antimatter experiment: gravity, interferometry, spectroscopy). Tech. Report SPSC-P-334; CERN-SPSC-2007-017 (European Organization for Nuclear Research, 2007).
6. Maury, S. The antiproton decelerator: AD. *Hyperfine Interact.* **109**, 43–52 (1997).

7. Bertsche, W. *et al.* A magnetic trap for antihydrogen confinement. *Nucl. Instrum. Methods Phys. Res. A* **566**, 746–756 (2006).
8. Pritchard, D. E. Cooling neutral atoms in a magnetic trap for precision spectroscopy. *Phys. Rev. Lett.* **51**, 1336–1339 (1983).
9. Fajans, J. *et al.* Effects of extreme magnetic quadrupole fields on Penning traps, and the consequences for antihydrogen trapping. *Phys. Rev. Lett.* **95**, 155001 (2005).
10. Andresen, G. *et al.* Antimatter plasmas in a multipole trap for antihydrogen. *Phys. Rev. Lett.* **98**, 023402 (2007).
11. Fujiwara, M. C. *et al.* Particle physics aspects of antihydrogen studies with ALPHA at CERN. *ALP Conf. Proc.* **1078**, 208–220 (2008).
12. Gabrielse, G. *et al.* First capture of antiprotons in a Penning trap: a kiloelectronvolt source. *Phys. Rev. Lett.* **57**, 2504–2507 (1986).
13. Gabrielse, G. *et al.* Cooling and slowing of trapped antiprotons below 100 meV. *Phys. Rev. Lett.* **63**, 1360–1363 (1989).
14. Surko, C. M. & Greaves, R. G. Emerging science and technology of antimatter plasmas and trap-based beams. *Phys. Plasmas* **11**, 2333–2348 (2004).
15. Jørgensen, L. V. *et al.* New source of dense, cryogenic positron plasmas. *Phys. Rev. Lett.* **95**, 025002 (2005).
16. Hess, H. F. Evaporative cooling of magnetically trapped and compressed spin-polarized hydrogen. *Phys. Rev. B* **34**, 3476–3479 (1986).
17. Andresen, G. B. *et al.* Evaporative cooling of antiprotons to cryogenic temperatures. *Phys. Rev. Lett.* **105**, 013003 (2010).
18. Gabrielse, G. *et al.* Antihydrogen production using trapped plasmas. *Phys. Lett. A* **129**, 38–42 (1988).
19. Fajans, J., Gilson, E. & Friedland, L. Autoresonant (nonstationary) excitation of the diocotron mode in non-neutral plasmas. *Phys. Rev. Lett.* **82**, 4444–4447 (1999).
20. Barth, I. *et al.* Autoresonant transition in the presence of noise and self-fields. *Phys. Rev. Lett.* **103**, 155001 (2009).
21. Andresen, G. B. *et al.* Antihydrogen formation dynamics in a multipolar neutral anti-atom trap. *Phys. Lett. B* **685**, 141–145 (2010).
22. Amoretti, M. *et al.* Antihydrogen production temperature dependence. *Phys. Lett. B* **583**, 59–67 (2004).
23. Andresen, G. *et al.* Search for trapped antihydrogen. *Phys. Lett. B*. doi:10.1016/j.physletb.2010.11.004 (in the press).

Acknowledgements This work was supported by CNPq, FINEP/RENAFAE (Brazil); ISF (Israel); MEXT (Japan); FNU (Denmark); VR (Sweden); NSERC, NRC/TRIUMF, AIF, FQRNT (Canada); the DOE and the NSF (USA); and EPSRC, the Royal Society and the Leverhulme Trust (UK). We thank them for their generous support. We are grateful to the Antiproton Decelerator team, T. Eriksson, P. Belochitskii, B. Dupuy, L. Bojtar, C. Oliveira, K. Mikluha and G. Tranquille, for the delivery of a high-quality antiproton beam. The contributions of summer students C. C. Bray, C. Ø. Rasmussen, S. Kemp,

K. K. Andersen, D. Wilding, K. Mikkelsen and L. Bryngemark are acknowledged. We would like to thank the following individuals for help: M. Harrison, J. Escallier, A. Marone, M. Anerella, A. Ghosh, B. Parker, G. Ganetis, J. Thornhill, D. Wells, D. Seddon, K. Dahlerup-Pedersen, J. Mourao, T. Fowler, S. Russenschuck, R. De Oliveira, N. Wauquier, J. Hansen, M. Polini, J. M. Geisser, L. Deparis, P. Frichot, J. M. Malzacker, A. Briswalter, P. Moyret, S. Mathot, G. Favre, J. P. Brachet, P. Mésenge, S. Sgobba, A. Cherif, J. Bremer, J. Casas-Cubillos, N. Vauthier, G. Perinic, O. Pirotte, A. Perin, G. Perinic, B. Vullierme, D. Delkaris, N. Veillet, K. Barth, R. Consentino, S. Guido, L. Stewart, M. Malabaila, A. Mongelluzzo, P. Chiggiato, E. Mahner, A. Froton, C. Lasseur, F. Hahn, E. Søndergaard, F. Mikkelsen, W. Carlisle, A. Charman, J. Keller, P. Amaudruz, D. Bishop, R. Bula, K. Langton, P. Vincent, S. Chan, D. Rowbotham, P. Bennet, B. Evans, J.-P. Martin, P. Kowalski, A. Read, T. Willis, J. Kivell, H. Thomas, W. Lai, L. Wasilenko, C. Kolbeck, H. Malik, P. Genoa, L. Posada and R. Funakoshi.

Author Contributions W.B., P.D.B., J.F., M.C.F., J.S.H., N.M. and D.M.S. conceived, designed and constructed the central ALPHA apparatus and participated in all aspects of the experimental and physics programmes. G.B.A., M.D.A., M.B.-R., E.B., S.C., T.F., A.J.H., R.H., M.J.J., A.P., S.S.e.N. and C.S. participated actively in the experimental runs, data taking, on- and offline analysis, and maintenance and modification of the apparatus. D.R.G., A.O. and J.W.S. contributed to all aspects of the detector systems and participated actively in the experimental and analysis efforts. M.C., D.P.v.d.W. and L.V.J. designed and built the positron accumulator and participated in the experimental programme. F.R. performed the particle simulations reported in this paper, made the theoretical estimate of trapping rate and supported the design and experimental programmes with simulations and calculations. P.N. led the design of the ALPHA silicon detector. P.P. was responsible for implementing the silicon detector at CERN and participated in the experimental and analysis programmes. A.D. and A.G. contributed to the experimental shift work. S.J. and J.S.W. contributed theoretical support in the form of atomic or plasma physics calculations and simulations, and provided guidance in the experimental programme. E.S. contributed to the multichannel plate imaging system and participated in the experimental efforts. C.L.C., W.N.H., M.E.H., S.E., S.M. and R.I.T. participated in the experimental programme and the physics planning effort. Y.Y. provided organizational and financial support and participated in physics discussions. L.K. and K.O. provided off-site support for detector electronics and database management systems, respectively. J.S.H. wrote the initial manuscript, which was edited by J.F., M.C.F., P.D.B., N.M. and E.B. before being improved and approved by the entire collaboration.

Author Information Reprints and permissions information is available at www.nature.com/reprints. The authors declare no competing financial interests. Readers are welcome to comment on the online version of this article at www.nature.com/nature. Correspondence and requests for materials should be addressed to J.S.H. (hangst@phys.au.dk).

METHODS

Plasma diagnostics and control. The rotating-wall technique^{24,25} was used several times in each trapping attempt to control the radius and density of both antiproton and positron clouds. The cloud radii and transverse density profiles were measured by releasing the particles onto an imaging detector^{26,27} using a multichannel plate coupled to a phosphor screen that was imaged by a charge-coupled-device camera. Equilibrium temperatures were determined by ramping down the axial confining potential and measuring the distribution of escaping particles using either the multichannel plate (positrons) or scintillation detectors (antiprotons). The temperature was obtained from a fit to the high-energy tail of the measured distribution²⁸.

We used evaporative cooling¹⁶ to obtain lower positron temperatures. The technique, which we have also recently applied to antiprotons¹⁷, involves reducing one side of the confining potential well to allow the most energetic positrons to escape. Re-equilibration through collisions results in a lower temperature for the remaining particles. For the trapping experiments described here, the applied, on-axis well depth (neglecting space charge) was reduced from 2.5 to 1.1 V in 500 ms, and about 50% of the initial positrons were lost.

The autoresonant injection of antiprotons into the positron cloud makes use of the fact that the confining potential for the antiprotons is anharmonic, which causes the axial oscillation frequency to decrease with increasing oscillation amplitude. We applied a sinusoidal drive that sweeps downwards through the range of axial frequencies defined by the potential. With a proper choice of drive parameters, the antiprotons autoresonantly lock to the drive frequency and their energies increase as the drive frequency is lowered. Using a drive of ~ 55 mV (on-axis) and a frequency sweep of 350–200 kHz, we were able to inject about 70% of the antiprotons into the positrons in 200 μ s. This new method of mixing for antihydrogen production was designed to introduce the antiprotons at low longitudinal kinetic energy with respect to the positrons. The initial transverse energy distribution of the antiprotons should also be minimally perturbed by the rapid and precise energy sweep. We note that extensive searches with ATHENA-type mixing², in which the antiprotons were injected into the positrons with several electronvolts of energy, yielded no trapping signal.

Simulations of antihydrogen and antiproton motion. We used numerical models to simulate the trajectories of both mirror-trapped antiprotons and trapped antihydrogen atoms as the atom trap was de-energized. The simulations propagate the particles using classical force equations: the Lorentz force for antiprotons and the dipole-gradient force for the antihydrogen atoms. The spatially and temporally varying electric and magnetic fields were included from models of the electrode and magnet geometry. Measurements of the time response of the electrode amplifier chain and calculations of magnetically induced eddy currents were used to reproduce the field dynamics accurately. The simulations model the dynamics after the vast majority of charged particles have been expelled from the trap; thus, the density of particles was low, and single-particle dynamics sufficed. The particles were propagated until they struck the surface of the trap electrodes, whereupon they were considered to have annihilated and we recorded their positions.

Selection of annihilation events. Events recorded in the silicon detector can come from cosmic rays and other environmental noise, as well as from the annihilation of antiprotons. Antiproton annihilations on a nucleus produce several charged particles (mostly pions), and they typically produce several tracks in the detector

(Fig. 2a). The radial position, r , of the reconstructed annihilation vertices was distributed about the inner surface of the electrodes (radius of 22.3 mm). However, our event reconstruction algorithm will typically identify cosmic rays as two back-to-back tracks (Fig. 2b), with the radii of the reconstructed vertices randomly distributed. The environmental noise generally does not register a track or a vertex, and is thus effectively rejected by requiring that each event be associated with a vertex.

To distinguish antiproton annihilation events from cosmic rays and noise background, we used three primary pieces of information about the topology of the events for which our reconstruction algorithm finds a vertex²³: the number of tracks, the radial position of the reconstructed annihilation vertex and a measure of the deviation of the event topology from that of a straight line passing through the detector. With the third piece of information, compatibility of the event with a cosmic ray is tested by making a linear fit to the hit positions in the event pattern and calculating the sum of the squared residual distances from the fitted line. The antiproton annihilation events tend to give larger values of this ‘squared residual’ than do the cosmic events, which tend to fit well to a straight line.

To optimize the selection criteria, we collected a data sample of cosmic rays ($\sim 110,000$ events) when there were no antiprotons present in the experiment and we compared this with the sample of antiproton annihilations ($\sim 170,000$ events) recorded during the mixing phase of the trapping experiments. The mixing phase accumulates data at the maximum read-out rate of the detector (~ 500 Hz); this rate is large in comparison with the cosmic trigger rate (~ 10 Hz), so the mixing sample is dominated by annihilations. Following standard practices, we applied ‘cuts’ to the number distributions of the three quantities defined above, to reject cosmic rays while retaining real annihilation vertices. The positions of the cuts were optimized by means of Monte Carlo pseudo-experiments. By performing a large number of pseudo-experiments, we studied the effects of varying the cuts on the resulting significance, averaged over a number of trials. Thus, we derived a set of cuts that would produce, on average, the best statistical significance for cosmic rejection.

The resulting selection criteria for annihilation events were as follows: for two-track events, $r < 4$ cm and the squared residual was greater than 2 cm^2 ; for events with three or more tracks, $r < 4$ cm and the squared residual was greater than 0.05 cm^2 . With the chosen set of cuts, 99.6% of the cosmic events were rejected, enhancing the signal-to-noise ratio by more than two orders of magnitude while maintaining a high overall efficiency, of 47%, for annihilation detection. To avoid experimental bias, the cuts were optimized using mixing and cosmic data only, and applied a posteriori to trapping search data.

24. Huang, X.-P., Anderegg, F., Hollmann, E. M., Driscoll, C. F. & O’Neil, T. M. Steady-state confinement of nonneutral plasmas by rotating electric fields. *Phys. Rev. Lett.* **78**, 875–878 (1997).
25. Danielson, J. R. & Surko, C. M. Radial compression and torque-balanced steady states of single-component plasmas in Penning-Malmberg traps. *Phys. Plasmas* **13**, 055706 (2006).
26. Andresen, G. B. *et al.* Antiproton, positron, and electron imaging with a microchannel plate/phosphor detector. *Rev. Sci. Instrum.* **80**, 123701 (2009).
27. Andresen, G. B. *et al.* Compression of antiproton clouds for antihydrogen trapping. *Phys. Rev. Lett.* **100**, 203401 (2008).
28. Eggleston, D. L., Driscoll, C. F., Beck, B. R., Hyatt, A. W. & Malmberg, J. H. Parallel energy analyzer for pure electron plasma devices. *Phys. Fluids B* **4**, 3432–3439 (1992).

Fluctuating stripes at the onset of the pseudogap in the high- T_c superconductor $\text{Bi}_2\text{Sr}_2\text{CaCu}_2\text{O}_{8+x}$

Colin V. Parker¹, Pegor Aynajian¹, Eduardo H. da Silva Neto¹, Aakash Pushp¹, Shimpei Ono², Jinsheng Wen³, Zhijun Xu³, Genda Gu³ & Ali Yazdani¹

Doped Mott insulators have a strong propensity to form patterns of holes and spins often referred to as stripes^{1–5}. In copper oxides, doping also gives rise to the pseudogap state⁶, which can be transformed into a high-temperature superconducting state with sufficient doping or by reducing the temperature. A long-standing issue has been the interplay between the pseudogap, which is generic to all hole-doped copper oxide superconductors, and stripes, whose static form occurs in only one family of copper oxides over a narrow range of the phase diagram^{2,7}. Here we report observations of the spatial reorganization of electronic states with the onset of the pseudogap state in the high-temperature superconductor $\text{Bi}_2\text{Sr}_2\text{CaCu}_2\text{O}_{8+x}$ using spectroscopic mapping with a scanning tunnelling microscope. We find that the onset of the pseudogap phase coincides with the appearance of electronic patterns that have the predicted characteristics of fluctuating stripes⁸. As expected, the stripe patterns are strongest when the hole concentration in the CuO_2 planes is close to 1/8 (per copper atom)^{2–5,8}. Although they demonstrate that the fluctuating stripes emerge with the onset of the pseudogap state and occur over a large part of the phase diagram, our experiments indicate that the stripes are a consequence of pseudogap behaviour rather than its cause.

Spectroscopic mapping with scanning tunnelling microscopy (STM) probes the spatial structure of electronic states, which reflects band structure effects⁹ as well as the propensity of the system to forming ordering such as stripes or other charge-ordered states^{8,10–15}. Static order manifests itself as bias-independent modulations in the STM conductance maps¹⁶, but detection of fluctuating order is more difficult as it requires the effects of band structure to be disentangled from those associated with proximity to an ordered phase. Previous STM studies of $\text{Bi}_2\text{Sr}_2\text{CaCu}_2\text{O}_{8+x}$ have shown two types of feature: those associated with the interference of quasiparticles from the superconducting state's band structure, caused by scattering from impurities^{9,15,17,18}, and electronic modulations that could be due to charge organization^{10,11,13,14,19}. However, there is a lack of evidence from other experimental probes for any static order in the same compound^{20,21}, but some experiments and theory suggest that fluctuating stripes may be responsible for the formation of the pseudogap^{19,22–24}. Moreover, the relation between the STM features and the pseudogap, whether due to pairing, pairing fluctuations or charge organization has remained unclear because experiments have been limited to temperatures below or just above the superconducting transition temperature, T_c (refs 10–14, 25). Extending these experiments above the region of fluctuating superconductivity^{26,27}, which spans the temperature range between T_c and T_o , to the onset of the pseudogap⁶, at temperature T^* , has been technically challenging.

Figure 1 shows examples of real-space mapping of the low-energy conductance ($G(r, V) = dI/dV(r, V)$; see Supplementary Information, section A) using STM on an underdoped $\text{Bi}_2\text{Sr}_2(\text{Ca}, \text{Dy})\text{Cu}_2\text{O}_{8+x}$ sample (UD35), carried out at three temperatures corresponding to the superconducting state ($T < T_c$), the fluctuating paired state with

weak diamagnetic response^{26,27} ($T_c < T < T_o$) and the pseudogap state ($T_o < T < T^*$). Discrete Fourier transforms (DFTs) of the conductance maps have strong peaks at wavevectors marked Q^* (Fig. 1d–f) along the Cu–O bond direction in all three temperature ranges. Similar strong features appear at a larger wavevector, marked Q^{**} , also along the Cu–O bond direction. At temperatures below T_c , the DFTs of the conductance maps show additional peaks that have been previously associated with the interference of Bogoliubov–de Gennes quasiparticles (BdG-QPI) in the superconducting state^{9,15,17,25}. The contribution to the spatial variation of the density of states with superconducting origin can be further enhanced by the use of a ratio of conductance maps¹⁷ $Z(r, V) = G(r, +V)/G(r, -V)$ (owing to particle–hole symmetry), measured at the same energy, as demonstrated in Figs 1g–i (peaks marked q_2 – q_4 , q_6 and q_7).

All the modulations in the density of states in our measurements, including those corresponding to Q^* and Q^{**} , have energy-dependent wavelengths near the Fermi energy (± 50 mV) throughout the entire temperature range and hence are not due to the formation of static charge ordering (Supplementary Information, section B). However, a distinction between Q^* and Q^{**} and the other wavevectors at which peaks occur owing to impurity-induced interference becomes evident when analysing their properties across a range of energies. It has been proposed that signatures of incipient order appear in STM conductance maps with similar phases across a range of energies, whereas modulations of the density of states due to impurity-induced quasiparticle interference are phase incoherent^{8,12}. To distinguish which features are associated with incipient order, we compute the quantity

$$S(k_x, k_y, V_0) = \frac{\left| \int_{-V_0}^{V_0} G(k_x, k_y, V) dV \right|}{\int_{-V_0}^{V_0} |G(k_x, k_y, V)| dV}$$

where $G(k_x, k_y, V)$ is the DFT of the conductance map measured at energy V and V_0 defines the limits of the energy range over which we examine the phase of the modulations. This quantity measures the phase matching of modulations between different energies, and is independent of whether or not the features are dispersive (Supplementary Information, section C).

Figure 2 shows that integration over a range of energies near the Fermi level results in the suppression of the features at the wavevectors labelled q_2 – q_4 , q_6 and q_7 , indicating that they are due to impurity-induced interference phenomena. In contrast, the features at Q^* and Q^{**} are not suppressed by this integration, even above T_c and T_o (Fig. 2c). In Fig. 2d, we also show the detailed behaviour of all the wavevectors in S with increasing integration window, as measured by V_0 . This analysis establishes the phase-coherent properties of the modulations at Q^* and Q^{**} and shows that their behaviour is consistent with that expected from an incipient charge organization phenomenon. There is the possibility that the Fermi surface of $\text{Bi}_2\text{Sr}_2\text{CaCu}_2\text{O}_{8+x}$ gives rise to impurity-induced bond-oriented interference wavevectors near Q^* and Q^{**} ^{17,28}, but the analysis above establishes that the

¹Joseph Henry Laboratories and Department of Physics, Princeton University, Princeton, New Jersey 08544, USA. ²Central Research Institute of Electric Power Industry, Komae, Tokyo 201-8511, Japan. ³Condensed Matter Physics and Materials Science, Brookhaven National Laboratory, Upton, New York 11973, USA.

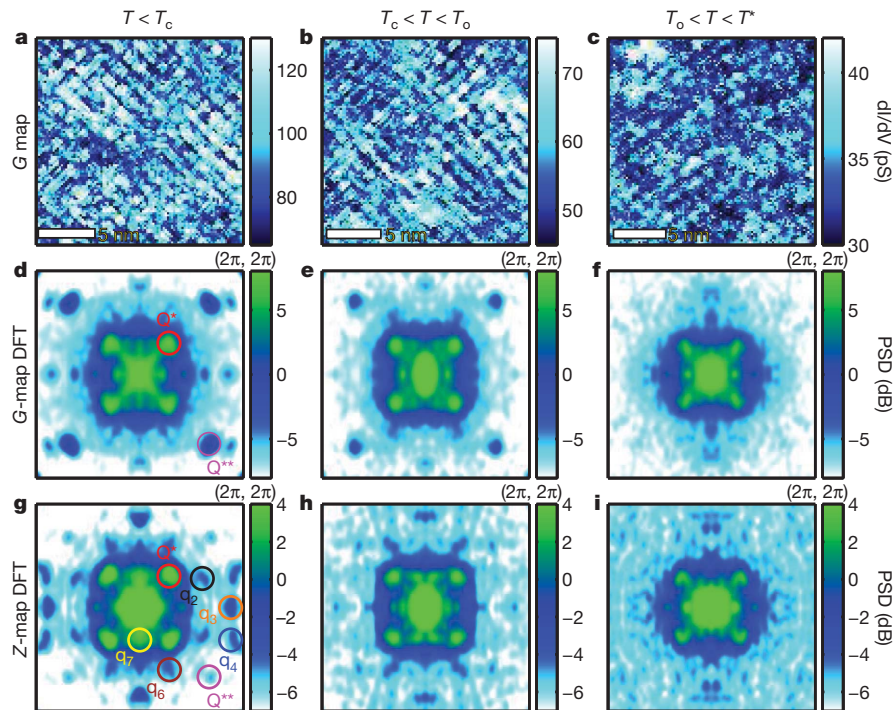


Figure 1 | Electronic modulations in $\text{Bi}_2\text{Sr}_2(\text{Ca,Dy})\text{Cu}_2\text{O}_{8+x}$. **a–c**, Real-space, low-energy conductance maps, $G(r, V)$, at $V = 10$ mV in UD35 ($T_c = 35$ K), carried out at 8 K (**a**), 41 K (**b**) and 122 K (**c**). At all temperatures, strong electronic-bond-oriented modulations are observed. **d–i**, The corresponding DFTs of $G(r, V = 10$ mV) (**d–f**) and $Z(r, V = 10$ mV) (**g–i**), which display strong peaks at the wavevectors marked in **g**. Only the peaks at Q^* and Q^{**} , corresponding to the real-space modulations in **a–c**, survive to temperatures significantly above T_c . The DFTs in **d–i** are normalized to their corresponding standard deviations. PSD, power spectral density.

majority of the contribution to our signal near these wavevectors is associated with an incipient order. As a function of energy, the intensity of the feature at Q^* also shows a strong enhancement near a specific wavevector, which is another predicted feature of incipient order (Supplementary Information, section B). Although there have been indications from previous studies^{8,10,11,14} that the modulations at Q^* and Q^{**} are not simply due to quasiparticle interference phenomena,

the measurements and analysis presented here firmly establish that these modulations are due not to static order but to fluctuating order.

The features at Q^* and Q^{**} behave similarly in the S maps, as shown in Fig. 2b–d; however, their energy dependences are different. The feature at Q^* dominates at lower energies (below 50 mV) whereas that at Q^{**} is strongest at higher energies (Supplementary Information, section D). Because only an incipient order that influences electrons

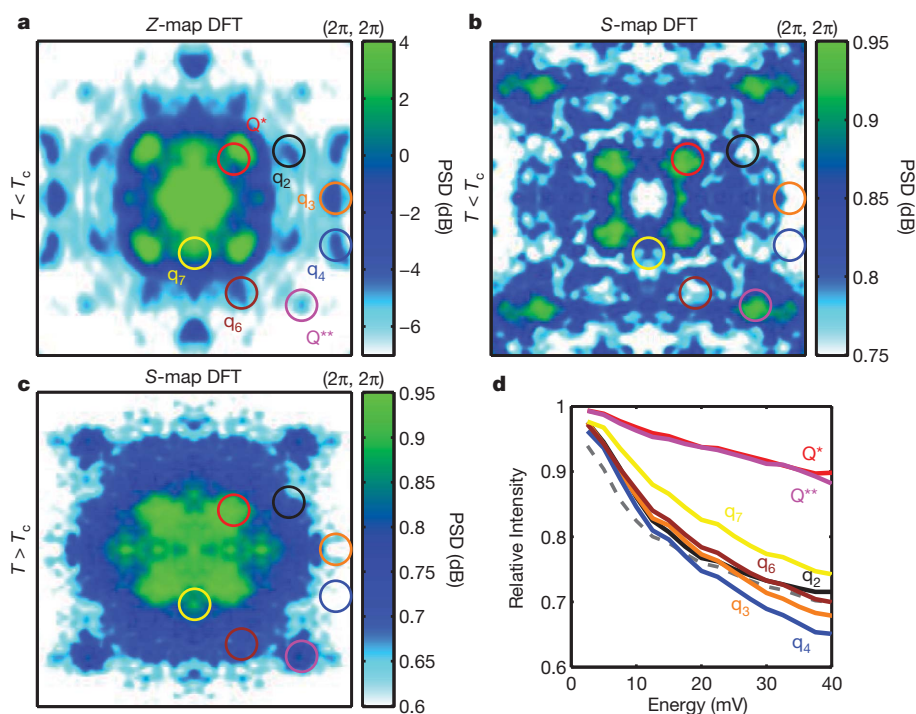


Figure 2 | Impurity-induced interference versus incipient order. **a**, DFT of the Z map at 10 mV in UD35, carried out at 8 K (normalized by its standard deviation, as in Fig. 1). The circles mark the wavevectors (Q^* , Q^{**} , q_2 – q_4 , q_6 and q_7) that show pronounced peaks. **b**, S map of the same data set as in **a**, integrated from $-V_0$ to $+V_0$, where $V_0 = 25$ mV (see text). Only the modulations at Q^* and Q^{**} survive this integration procedure. **c**, Similar measurements to those in **b**, but performed at 70 K, which show similar behaviour at the marked wavevectors. **d**, Relative S-map intensity of the different wavevectors marked in **b**, as functions of the integration-window limit, V_0 . The positions of the different wavevectors are determined by the peak locations in the Z map. The dashed grey line represents the decay profile of the background

near the Fermi level is relevant to the low-energy properties of our system, such as its transport properties, we focus our attention on the modulations at Q^* .

We find further distinction between the fluctuating-order-induced feature at Q^* and the impurity-induced features at other wavevectors, which allows us to establish separate connections to different regions of the copper oxide phase diagram when we study their temperature dependences. As seen in Fig. 1, the features at the BdG-QPI wavevectors (q_2 – q_4 , q_6 and q_7) are strongly suppressed above T_c , whereas that at Q^* remains robust at all temperatures below T^* . By examining conductance maps over the entire phase diagram, we have measured the power spectral density of the feature at Q^* at 10 meV (Supplementary Information, section D) over a wide range of temperatures and dopings. Figure 3a shows that the onset of the feature at Q^* coincides with the onset of pseudogap behaviour, at T^* , the value of which has been determined for our samples by temperature-dependent spectroscopic measurements of pseudogap disappearance²⁹. In strong contrast, the intensity (power spectral density) of superconducting BdG-QPI modulations across the phase diagram, such as that at q_7 (Fig. 3b), is strongly suppressed when the superconducting phase coherence in the sample is lost, above T_c . This behaviour is consistent with recent theoretical modelling of BdG-QPI as a function of temperature³⁰.

In contrast to the pseudogap, we find that the intensity of the feature at Q^* has a non-monotonic doping dependence (Fig. 3a). Plotting the intensity of this feature in DFTs at an intermediate temperature as a function of doping (Fig. 3c), we find a remarkable peak when the nominal hole concentration of the sample is close to 1/8. In contrast, the intensity of the feature at the BdG-QPI wavevector q_7 seems to peak near optimal doping. The hole concentration of 1/8 corresponds to the ideal doping for formation of half-filled stripes, as has been well established by neutron scattering experiments on La-based compounds² and in model calculations of copper oxide properties^{1,4,5,8}. The distinctive doping dependence shown in Fig. 3c suggests that Fermi surface nesting near the anti-node cannot be responsible for the robust feature at Q^* but rather identifies fluctuating half-filled stripes as the origin of these modulations. Moreover, because the $\text{Bi}_2\text{Sr}_2\text{CaCu}_2\text{O}_{8+x}$ system does not undergo a structural distortion near 1/8 doping, we conclude that local Mott and antiferromagnetic correlations, as opposed to structural distortion as in the La-based systems, are stabilizing fluctuating stripe patterns near this hole concentration. Nevertheless, distinguishing whether the observed patterns are strictly one-dimensional (fluctuating stripes) or two-dimensional (chequerboards) is complicated by the presence of doping inhomogeneities that locally pin these modulations³¹.

The connection between the appearance of the incipient fluctuating stripe order and T^* is further corroborated by measurements of the local disappearance of modulations at Q^* . In Fig. 4, we contrast real-space STM conductance maps with spatial maps of the pseudogap energy measured at the same atomic location at a temperature above T_c near optimal doping. At this temperature and above, consistent with our previous studies, we find regions of the sample in which the pseudogap has collapsed²⁹. Such spatially inhomogeneous suppression of the pseudogap is strongly correlated with the disappearance of the feature at Q^* . This behaviour is evident when comparing the conductance map in Fig. 4a with the pseudogap map in Fig. 4b. The regions that show modulations also show the strongest pseudogap. This can also be seen in Fig. 4c, where we plot a local measure of the modulation strength related to smoothed and normalized products of the data and sinusoidal functions, a real-space intensity map of the modulation at Q^* (Supplementary Information, section E). We see that regions where the pseudogap is enhanced nucleate modulations at Q^* at higher temperatures.

Examining the strength of incipient fluctuating stripe order and pseudogap phenomena as a function of doping points to disparate behaviour between these two important phenomena and provides important

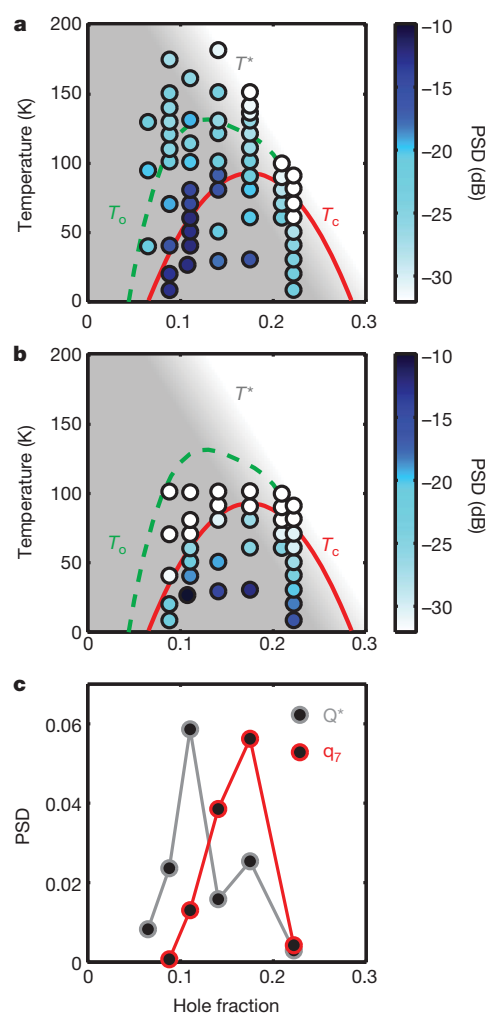


Figure 3 | Phase diagrams. **a**, Intensity (PSD) of the modulation at Q^* over the entire temperature–doping phase diagram for $\text{Bi}_2\text{Sr}_2\text{CaCu}_2\text{O}_{8+x}$. The intensity comes from the amplitude of Gaussian fits to the peak, and is plotted on a logarithmic scale. In many cases, it represents the average taken from multiple measurements on different samples from the same batch of crystals. The shaded grey area, the red solid line and the dashed green line respectively represent the pseudogap phase, bounded by T^* (determined from previously reported spectroscopic measurements of pseudogap disappearance in similar samples²⁹); the boundary, T_c , of the phase of fluctuating superconductivity; and the boundary, T_c , of the superconducting phase. **b**, Intensity of the modulation at q_7 over the same temperature–doping phase diagram. **c**, Intensity of the modulations at Q^* and q_7 near 35 K, showing that the intensity at Q^* is maximal near 1/8 hole doping whereas that at q_7 peaks near optimal doping. The systematic error in the intensity at Q^* is 2 dB.

clues to how they are related. As shown in Fig. 3c, below 1/8 doping the strength of fluctuating stripes is diminished. Furthermore, by examining the local correlation between the modulations at Q^* and the pseudogap, we find that the cross-correlation between these two phenomena switches sign from positive to negative near the nominal doping of 1/8 (Fig. 4d). Approaching the Mott insulating state by lowering the doping results in a stronger pseudogap, whereas propensity to stripe formation is suppressed. Considering these facts together, we conclude that the pseudogap is not caused by stripe correlations, but rather that the pseudogap is required to nucleate fluctuating stripes. Given that stripe formation is believed to occur through phase separation of mobile holes and antiferromagnetically correlated regions, it seems logical that the pseudogap is associated with local spin correlations that make the formation of such spatial patterns possible.

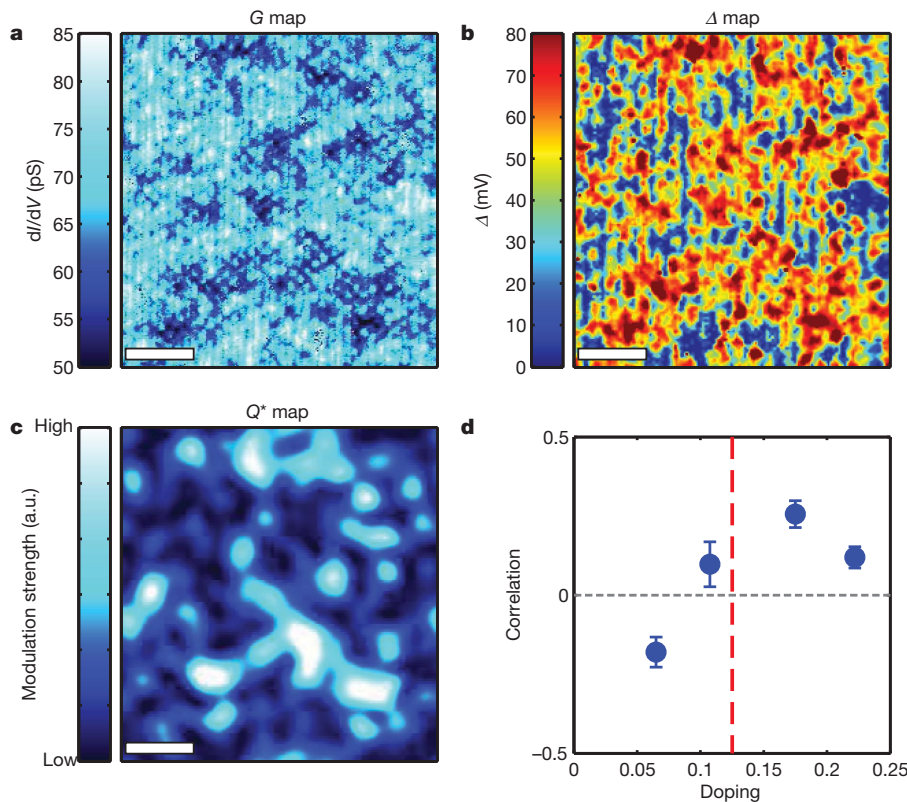


Figure 4 | Spatial correlation of the modulation at Q^* with the pseudogap. **a, b,** Real-space STM conductance map, $G(r, V = 10 \text{ mV})$, of a $T_c = 91 \text{ K}$ sample (OP91) at $T = 102 \text{ K}$ (**a**). The map shows the spatially inhomogeneous disappearance of the modulation at Q^* , mirroring the inhomogeneous suppression of the pseudogap, Δ (**b**). **c,** Local measure of the modulation strength (Supplementary Information, section E), which shows that regions with strong modulations also have large pseudogaps. a.u., arbitrary units. **d,** Measure of the local correlation between the modulation at Q^* and the pseudogap for different dopings, showing that the correlation switches sign near 1/8 doping. The error bars indicate the amount of anomalous correlation that would be expected in data sets of equivalent size. Scale bars, 10 nm.

Received 30 July; accepted 19 October 2010.

- Zaenani, J. & Gunnarsson, O. Charged magnetic domain lines and the magnetism of high- T_c oxides. *Phys. Rev. B* **40**, 7391–7394 (1989).
- Tranquada, J. M., Sternlieb, B. J., Axe, J. D., Nakamura, Y. & Uchida, S. Evidence for stripe correlations of spins and holes in copper oxide superconductors. *Nature* **375**, 561–563 (1995).
- Kivelson, S. A., Fradkin, E. & Emery, V. J. Electronic liquid-crystal phases of a doped Mott insulator. *Nature* **393**, 550–553 (1998).
- White, S. R. & Scalapino, D. J. Density matrix renormalization group study of the striped phase in the 2D t-J model. *Phys. Rev. Lett.* **80**, 1272–1275 (1998).
- Vojta, M. Lattice symmetry breaking in cuprate superconductors: stripes, nematics, and superconductivity. *Adv. Phys.* **58**, 699–820 (2009).
- Timusk, T. & Statt, B. The pseudogap in high-temperature superconductors: an experimental survey. *Rep. Prog. Phys.* **62**, 61–122 (1999).
- Abbamonte, P. et al. Spatially modulated ‘Mottness’ in $\text{La}_{2-x}\text{Ba}_x\text{CuO}_4$. *Nature Phys.* **1**, 155–158 (2005).
- Kivelson, S. A. et al. How to detect fluctuating stripes in the high-temperature superconductors. *Rev. Mod. Phys.* **75**, 1201–1241 (2003).
- Hoffman, J. E. et al. Imaging quasiparticle interference in $\text{Bi}_2\text{Sr}_2\text{CaCu}_2\text{O}_{8+\delta}$. *Science* **297**, 1148–1151 (2002).
- Howald, C., Eisaki, H., Kaneko, N. & Kapitulnik, A. Coexistence of periodic modulation of quasiparticle states and superconductivity in $\text{Bi}_2\text{Sr}_2\text{CaCu}_2\text{O}_{8+\delta}$. *Proc. Natl Acad. Sci. USA* **100**, 9705–9709 (2003).
- Vershinin, M. et al. Local ordering in the pseudogap state of the high- T_c superconductor $\text{Bi}_2\text{Sr}_2\text{CaCu}_2\text{O}_{8+\delta}$. *Science* **303**, 1995–1998 (2004).
- Fang, A., Howald, C., Kaneko, N., Greven, M. & Kapitulnik, A. Periodic coherence-peak height modulations in superconducting $\text{Bi}_2\text{Sr}_2\text{CaCu}_2\text{O}_{8+\delta}$. *Phys. Rev. B* **70**, 214514 (2004).
- Kohsaka, Y. et al. An intrinsic bond-centered electronic glass with unidirectional domains in underdoped cuprates. *Science* **315**, 1380–1385 (2007).
- Wise, W. D. et al. Charge-density-wave origin of cuprate checkerboard visualized by scanning tunnelling microscopy. *Nature Phys.* **4**, 696–699 (2008).
- Kohsaka, Y. et al. How Cooper pairs vanish approaching the Mott insulator in $\text{Bi}_2\text{Sr}_2\text{CaCu}_2\text{O}_{8+\delta}$. *Nature* **454**, 1072–1078 (2008).
- Coleman, R. V., Dai, Z., McNairy, W. W., Slough, C. G. & Wang, C. in *Methods of Experimental Physics* Vol. 27 (eds Strosio, J. A. & Kaiser, W. J.) 349–425 (Academic Press, 1993).
- Hanaguri, T. et al. Quasiparticle interference and superconducting gap in $\text{Ca}_{2-x}\text{Na}_x\text{CuO}_2\text{Cl}_2$. *Nature Phys.* **3**, 865–871 (2007).
- Wise, W. D. et al. Imaging nanoscale Fermi-surface variations in an inhomogeneous superconductor. *Nature Phys.* **5**, 213–216 (2009).
- Lawler, M. J. et al. Intra-unit-cell electronic nematicity of the high- T_c copper-oxide pseudogap states. *Nature* **466**, 347–351 (2010).
- Chatterjee, U. et al. Nondispersive Fermi arcs and the absence of charge ordering in the pseudogap phase of $\text{Bi}_2\text{Sr}_2\text{CaCu}_2\text{O}_{8+\delta}$. *Phys. Rev. Lett.* **96**, 107006 (2006).

- Xu, G. et al. Testing the itinerancy of spin dynamics in superconducting $\text{Bi}_2\text{Sr}_2\text{CaCu}_2\text{O}_{8+\delta}$. *Nature Phys.* **5**, 642–646 (2009).
- Daou, R. et al. Broken rotational symmetry in the pseudogap phase of a high- T_c superconductor. *Nature* **463**, 519–522 (2010).
- Hackl, A., Vojta, M. & Sachdev, S. Quasiparticle Nernst effect in stripe-ordered cuprates. *Phys. Rev. B* **81**, 045102 (2010).
- Hashimoto, M. et al. Particle-hole symmetry breaking in the pseudogap state of $\text{Bi}2201$. *Nature Phys.* **6**, 414–418 (2010).
- Lee, J. et al. Spectroscopic fingerprint of phase-incoherent superconductivity in the underdoped $\text{Bi}_2\text{Sr}_2\text{CaCu}_2\text{O}_{8+\delta}$. *Science* **325**, 1099–1103 (2009).
- Wang, Y., Li, L. & Ong, N. P. Nernst effect in high- T_c superconductors. *Phys. Rev. B* **73**, 024510 (2006).
- Li, L. et al. Diamagnetism and Cooper pairing above T_c in cuprates. *Phys. Rev. B* **81**, 054510 (2010).
- McElroy, K. et al. Relating atomic-scale electronic phenomena to wave-like quasiparticle states in superconducting $\text{Bi}_2\text{Sr}_2\text{CaCu}_2\text{O}_{8+\delta}$. *Nature* **422**, 592–596 (2003).
- Gomes, K. K. et al. Visualizing pair formation on the atomic scale in the high- T_c superconductor $\text{Bi}_2\text{Sr}_2\text{CaCu}_2\text{O}_{8+\delta}$. *Nature* **447**, 569–572 (2007).
- Wulin, D., He, Y., Chien, C.-C., Morr, D. K. & Levin, K. Model for the temperature dependence of the quasiparticle interference pattern in the measured scanning tunneling spectra of underdoped cuprate superconductors. *Phys. Rev. B* **80**, 134504 (2009).
- Robertson, J. A., Kivelson, S. A., Fradkin, E., Fang, A. C. & Kapitulnik, A. Distinguishing patterns of charge order: stripes or checkerboards. *Phys. Rev. B* **74**, 134507 (2006).

Supplementary Information is linked to the online version of the paper at www.nature.com/nature.

Acknowledgements We acknowledge discussions with P. W. Anderson, D. Huse, S. Kivelson, E. Fradkin, N. P. Ong and A. Pasupathy. This work was primarily supported by grant from the DOE-BES. The instrumentation and infrastructure at the Princeton Nanoscale Microscopy Laboratory are also supported by grants from the NSF-DMR, the NSF-MRSEC programme, through the Princeton Centre for Complex Materials, and the W. M. Keck Foundation.

Author Contributions C.V.P., E.H.d.S.N., P.A. and A.P. performed the STM measurements; C.V.P. and P.A. analysed the STM data; S.O., J.W., Z.X. and G.G. prepared the crystals; A.Y. supervised; and A.Y., C.V.P., E.H.d.S.N. and P.A. wrote the manuscript.

Author Information Reprints and permissions information is available at www.nature.com/reprints. The authors declare no competing financial interests. Readers are welcome to comment on the online version of this article at www.nature.com/nature. Correspondence and requests for materials should be addressed to A.Y. (yazdani@princeton.edu).

The redox state of arc mantle using Zn/Fe systematics

Cin-Ty A. Lee¹, Peter Luffi¹, Véronique Le Roux¹, Rajdeep Dasgupta¹, Francis Albarède^{1,2} & William P. Leeman^{1,3}

Many arc lavas are more oxidized than mid-ocean-ridge basalts and subduction introduces oxidized components into the mantle^{1–4}. As a consequence, the sub-arc mantle wedge is widely believed to be oxidized^{3,5}. The Fe oxidation state of sub-arc mantle is, however, difficult to determine directly, and debate persists as to whether this oxidation is intrinsic to the mantle source^{6,7}. Here we show that Zn/Fe_T (where Fe_T = Fe²⁺ + Fe³⁺) is redox-sensitive and retains a memory of the valence state of Fe in primary arc basalts and their mantle sources. During melting of mantle peridotite, Fe²⁺ and Zn behave similarly, but because Fe³⁺ is more incompatible than Fe²⁺, melts generated in oxidized environments have low Zn/Fe_T. Primitive arc magmas have identical Zn/Fe_T to mid-ocean-ridge basalts, suggesting that primary mantle melts in arcs and ridges have similar Fe oxidation states. The constancy of Zn/Fe_T during early differentiation involving olivine requires that Fe³⁺/Fe_T remains low in the magma. Only after progressive fractionation does Fe³⁺/Fe_T increase and stabilize magnetite as a fractionating phase. These results suggest that subduction of oxidized crustal material may not significantly alter the redox state of the mantle wedge. Thus, the higher oxidation states of arc lavas must be in part a consequence of shallow-level differentiation processes, though such processes remain poorly understood.

Oxygen fugacity f_{O_2} is an intensive parameter describing the chemical activity of O₂ in a given system (fugacity represents a corrected partial pressure due to deviation from the ideal gas law)⁸ and is used to describe the electrochemical redox potential between the different valence states of an element. Oxygen fugacity in a rock thus allows one to calculate the valence-state speciation of redox-sensitive metals, such as Fe, and of redox-sensitive species in volcanic gases⁹. In particular, f_{O_2} may have a role in the distinction between tholeiitic and calc-alkalic differentiation series, the two most voluminous magmatic differentiation series on Earth^{5,10}. The calc-alkalic series is characterized by magmas for which Fe content decreases with progressive differentiation. In contrast, the tholeiitic series is characterized by magmas in which Fe progressively increases with differentiation. These differences are most probably due to a relatively oxidized redox state (high f_{O_2} , that is, greater than the f_{O_2} corresponding to the fayalite–quartz–magnetite buffer), which stabilizes Fe³⁺-bearing oxides as fractionating phases in the calc-alkalic series and low redox state (low f_{O_2}), which suppresses Fe-oxide fractionation in the tholeiitic series^{5,10,11}. Given the common association of calc-alkalic series with subduction zones and of tholeiitic series with mid-ocean-ridge environments, it is widely accepted that high f_{O_2} is a general feature of arc magmas⁵. Indeed, arc lavas are in general more oxidized than mid-ocean ridge basalts (MORBs), as evidenced^{1–4} by the higher Fe³⁺/Fe_T ratios of arc lavas (>0.1 and up to 0.5) compared to MORBs (0.1–0.2).

There is, however, no consensus on how arc magmas become more oxidized than MORBs. The prevailing view is that the high f_{O_2} of arc lavas is directly inherited from an oxidized mantle source³. This view is driven by the observation that much of the subducted oceanic crust appears to have been oxidized by hydrothermal seawater alteration¹².

Thus, the mantle wedge becomes oxidized upon infiltration of slab-derived fluids or melts rich in oxidized components, such as Fe³⁺ or dissolved sulphate^{3,9,13}, which in turn may be correlated with slab-derived water contents in arc lavas³. The alternative is that high f_{O_2} is not a source effect but rather the result of shallow-level differentiation processes^{6,7,14}, but if so, outstanding issues remain. First, to what extent can shallow-level differentiation processes, such as degassing, assimilation of oxidized materials, and fractional crystallization of reduced minerals change a magma's oxidation state after it leaves its mantle source¹⁴? Second, although subducted oceanic lithosphere appears to be oxidized overall¹², reduced components in the subducting slab (for example, organic-rich lithologies in hemipelagic sediments and sulphide-rich lithologies in hydrothermal systems¹⁵) also exist. What is their influence, if any, on arc magma compositions? Third, both oxidized and reduced lithologies are represented in sub-arc peridotites^{16–20}. Does this signify a mantle wedge heterogeneous in its redox state and f_{O_2} ? Finally, is the mantle's redox state buffered^{21,22}? If it is buffered, for example by a C-bearing phase, or defined by a significant budget of redox-sensitive elements (for example, Fe or C species), the f_{O_2} of the mantle can only be changed by adding enough oxidized components to overwhelm the existing redox couples.

Resolving the above debate requires that we constrain the f_{O_2} of the mantle source regions of magmas, which is a difficult task. Direct approaches using the valence state of Fe or other redox-sensitive elements in whole-rocks, glasses and mineral phases reflect late equilibration conditions kinetically 'frozen' during magma cooling, and not necessarily the original melting conditions. Determining primary magmatic f_{O_2} requires us to 'see through' the effects of differentiation to retrieve past equilibrium states. Certain redox-sensitive element ratios fit this requirement^{7,23}. Such ratios involve one element, the partitioning behaviour of which during mantle melting is redox-sensitive because of variable oxidation states, and another element that is not redox-sensitive because it has only one valence over the range of f_{O_2} values applicable to the mantle. Then, if the two elements of interest are incompatible in early crystallizing phases (or have similar compatibilities), their ratio will not change during magmatic differentiation, preserving a 'memory' of source f_{O_2} . For example, the ratio of redox-sensitive V to redox-insensitive Sc or Ga, that is, V_T/Sc and V_T/Ga (where V_T denotes the total concentration of V of all valences), is sensitive to the f_{O_2} during mantle melting but insensitive to early fractional crystallization because the two elements are incompatible in olivine^{6,7,23}. For the most part, primitive arc basalts and MORBs have been reported to have similar V_T/Sc ratios, suggesting that MORB and arc source regions have similar f_{O_2} values^{6,7}. Only arc basalts with extreme enrichments in fluid mobile trace elements show higher V_T/Sc ratios and presumably higher f_{O_2} values⁷.

Independent confirmation of the above studies is desirable. Specifically, the Fe oxidation state of the primary magma should be constrained directly, because nearly all f_{O_2} constraints published so far are based on Fe valence state measurements. Recent studies of Fe isotope fractionation, which appears to be redox-sensitive, seem consistent with the V studies²⁴,

¹Department of Earth Sciences, Rice University, Houston, Texas 77005, USA. ²Ecole Normale Supérieure de Lyon, Université Claude Bernard-Lyon I and CNRS, 69007 Lyon, France. ³Earth Science Division, National Science Foundation, Arlington, Virginia 22230, USA.

but still require primary magmas to be measured²⁵. Another approach using Fe is to examine the distribution of Fe_T/Mg between olivine and magma. Deviations of Fe_T/Mg distribution from the expected distribution of Fe^{2+}/Mg , for example:

$$K_D^{\text{Fe}^{2+}/\text{Mg}} = \frac{(\text{Fe}_{\text{ol}}^{2+}/\text{Mg}_{\text{ol}})}{(\text{Fe}_{\text{melt}}^{2+}/\text{Mg}_{\text{melt}})} \approx 0.3$$

may reflect high $\text{Fe}^{3+}/\text{Fe}_T$ (refs 26 and 27). However, because $K_D \ll 1$, Fe_T/Mg fractionates extensively during differentiation, erasing any memory of Fe_T/Mg in the parental magma.

Here, we propose Zn/Fe_T as a redox tracer of magma sources that avoids the above limitations and complications. Over a large f_{O_2} range (from -3 log units to $+4$ log units relative to the fayalite–magnetite–quartz buffer: FMQ–3 to FMQ+4), Fe occurs in two valence states, Fe^{2+} and Fe^{3+} (in mantle peridotites, $\text{Fe}^{3+}/\text{Fe}_T < 0.03$) whereas Zn occurs only as Zn^{2+} . Zn and Fe^{2+} appear to behave similarly because Zn/Fe^{2+} is not fractionated significantly between olivine, orthopyroxene and basaltic melt²⁸, that is, $K_{\text{D}(\text{ol}/\text{opx})}^{\text{Zn}/\text{Fe}^{2+}} \approx 1$ and $K_{\text{D}(\text{ol}/\text{melt})}^{\text{Zn}/\text{Fe}^{2+}} = 0.8\text{--}0.9$. Because olivine and orthopyroxene account for most of the Zn and Fe in peridotites and because clinopyroxene and spinel have compensating

effects (Supplementary Methods), the bulk exchange coefficient for Zn/ Fe^{2+} between peridotite and melt, $K_{\text{D}(\text{perid}/\text{melt})}^{\text{Zn}/\text{Fe}^{2+}}$, is about 1 for all pressures and temperatures relevant to mid-ocean ridge and arc magmatism. In particular, for an olivine-and-orthopyroxene-dominated peridotite, $K_{\text{D}(\text{perid}/\text{melt})}^{\text{Zn}/\text{Fe}^{2+}}$ is largely insensitive to temperature even though individual mineral/melt partition coefficients of Zn and Fe^{2+} are temperature-dependent.

At low f_{O_2} (low $\text{Fe}^{3+}/\text{Fe}_T$), melting of peridotite and olivine crystallization effectively does not fractionate Zn from Fe_T . This describes the state at mid-ocean ridges, where $\text{Fe}^{3+}/\text{Fe}_T$ is low (0.1) and MORBs and peridotites have identical Zn/Fe_T (Fig. 1). In contrast, at higher f_{O_2} (high $\text{Fe}^{3+}/\text{Fe}_T$), Zn/ Fe_T is expected to fractionate because Fe^{3+} is incompatible in crystallizing silicate phases. For example, during partial melting of peridotite or during olivine crystallization, melts evolve towards low Zn/ Fe_T . It follows that the $\text{Fe}^{3+}/\text{Fe}_T$ of a magma can be determined from the deviations of the apparent exchange coefficient involving total Fe—that is, $K_{\text{D}(\text{perid}/\text{melt})}^{\text{Zn}/\text{Fe}_T}$ —from the true exchange coefficient $K_{\text{D}(\text{perid}/\text{melt})}^{\text{Zn}/\text{Fe}^{2+}}$ (Fig. 2). Because peridotites have much lower $\text{Fe}^{3+}/\text{Fe}_T$ than coexisting melts, the following equation can be derived (Supplementary Methods):

$$(\text{Fe}^{3+}/\text{Fe}_T)_{\text{melt}} \approx 1 - \frac{(\text{Zn}/\text{Fe}_T)_{\text{melt}}}{(\text{Zn}/\text{Fe}_T)_{\text{perid}}}$$

The Zn/ Fe_T in peridotites can be taken as a constant $((9.0 \pm 1) \times 10^{-4})$ by weight; Fig. 1 and ref. 28). Because it is insignificantly fractionated by

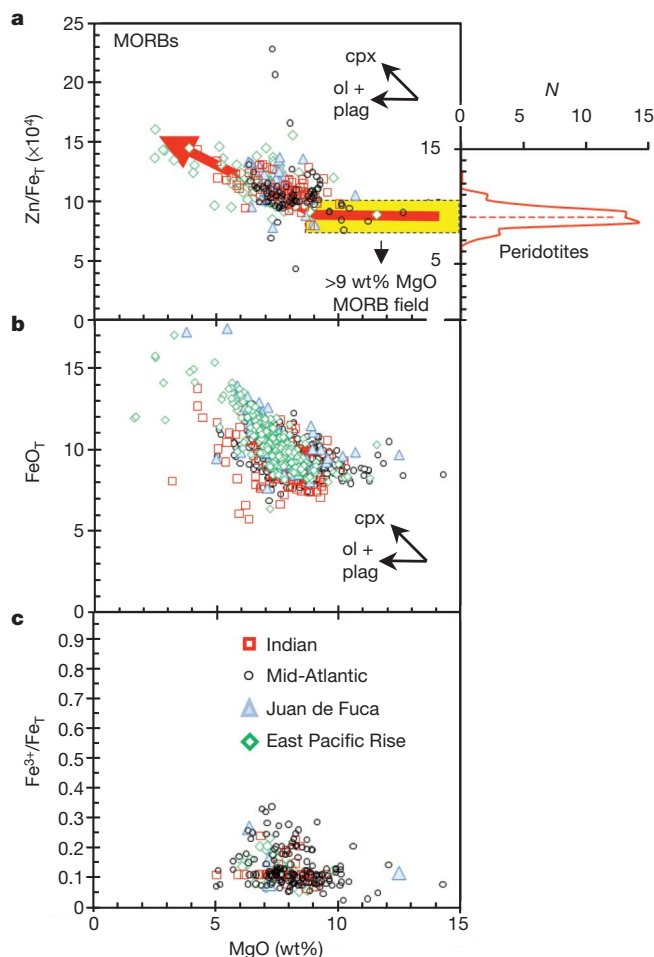


Figure 1 | Literature-compiled MORBs for different ridge systems. Data are taken from the RidgePetDB database. **a**, Zn/Fe_T ($\times 10^4$ by weight) versus MgO (wt%). The histogram on right hand axis is the distribution of peridotite xenoliths²⁸. N is the number of peridotite samples. The dotted red line is the mean. The yellow bar represents the inferred range of Zn/Fe_T for the mantle and primary MORB. The red arrow schematically describes the trajectory over which Zn/Fe_T changes with magmatic differentiation (decreasing MgO). **b**, FeO_T versus MgO . **c**, Wet chemistry determinations of $\text{Fe}^{3+}/\text{Fe}_T$ in whole rocks and glasses versus MgO . Small vectors correspond to olivine (ol), plagioclase (plag) and clinopyroxene (cpx) fractionation.

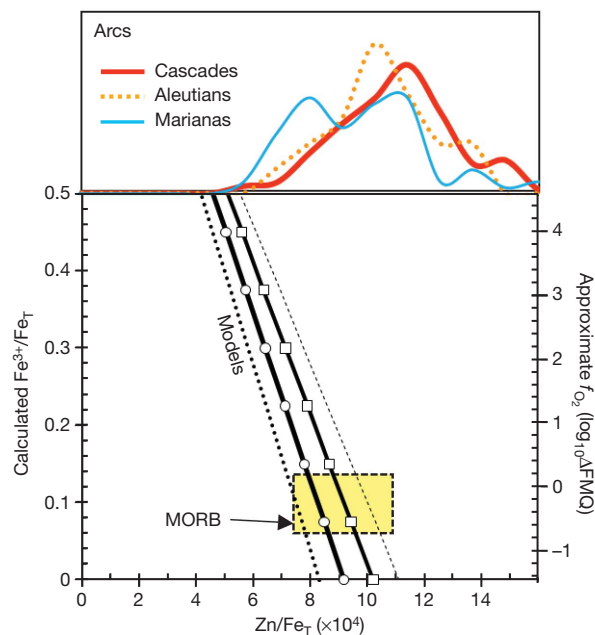


Figure 2 | Calculated $\text{Fe}^{3+}/\text{Fe}_T$ versus Zn/Fe_T in primary basalts. The two thick black model lines were calculated using equation (1). Black line with white circles: $\text{Zn}/\text{Fe}_T = 9 \times 10^{-4}$, $K_{\text{D}(\text{perid}/\text{melt})}^{\text{Zn}/\text{Fe}^{2+}} = 1$, $\text{Fe}^{3+}/\text{Fe}_T(\text{perid}) = 0.02$. Black line with white squares: $\text{Zn}/\text{Fe}_T = 9 \times 10^{-4}$, $K_{\text{D}(\text{perid}/\text{melt})}^{\text{Zn}/\text{Fe}^{2+}} = 0.9$, $\text{Fe}^{3+}/\text{Fe}_T(\text{perid}) = 0.02$. The dashed thin black line is the upper bound for the model predictions: $\text{Zn}/\text{Fe}_T = 10 \times 10^{-4}$, $K_{\text{D}(\text{perid}/\text{melt})}^{\text{Zn}/\text{Fe}^{2+}} = 0.9$, $\text{Fe}^{3+}/\text{Fe}_T(\text{perid}) = 0$. The dotted black line is the lower bound for the model predictions: $\text{Zn}/\text{Fe}_T = 8 \times 10^{-4}$, $K_{\text{D}(\text{perid}/\text{melt})}^{\text{Zn}/\text{Fe}^{2+}} = 1$, $\text{Fe}^{3+}/\text{Fe}_T(\text{perid}) = 0.04$. The coloured curves in the top panel represent normalized histograms of Zn/Fe_T for arc lavas with $\text{MgO} > 8$ wt% from the Cascades ($n = 48$ for this study; $n = 136$ from the literature), the Aleutians ($n = 20$), and the Marianas ($n = 83$); see Figs 3 and 4. The yellow rectangle corresponds to the range of measured $\text{Fe}^{3+}/\text{Fe}_T$ and Zn/Fe_T for MORBs². The right vertical axis represents corresponding f_{O_2} in \log_{10} unit deviations from the fayalite–magnetite–quartz buffer (FMQ) at 1 bar (f_{O_2} is approximate because it depends on melt composition and water content).

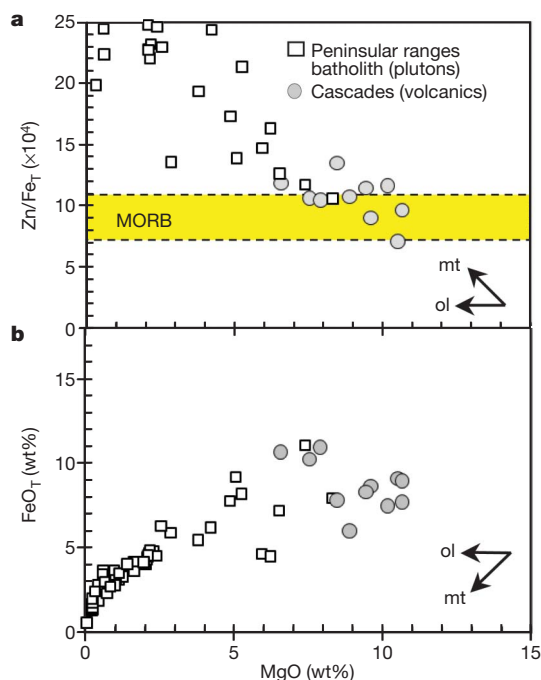


Figure 3 | Internally consistent data for a subset of primitive basalts from the Cascades arc and plutonic rocks from the Cretaceous Peninsular Ranges Batholith. Small vectors correspond to olivine (ol) and magnetite (mt) fractionation. MORB corresponds to mid-ocean basalt.

olivine removal, the Zn/Fe_T of a primitive magma can then be used to estimate the $\text{Fe}^{3+}/\text{Fe}_T$ of the primary magma.

To apply this approach, we present new internally consistent Zn/Fe_T data for primitive arc basalts from the Cascades volcanic arc and plutonic rocks from the Cretaceous Peninsular Ranges Batholith in southern California (Fig. 3). For comparison, we also present literature data for the Cascades along with the Marianas and Aleutian arcs (Fig. 4). Collectively, these case studies cover much of the geophysical variation in subduction zones. The Marianas island arc is associated with cold subduction, the Cascades continental arc with hot subduction, the Aleutians island arc with intermediate-aged subduction, and the Peninsular Ranges are the eroded remnants of a mature continental arc.

Plotting FeO_T and Zn/Fe_T against MgO (which decreases with differentiation) reveals two regimes common to the examined arc magmas, regardless of whether they are extrusive or intrusive. Zn/Fe_T and FeO_T remain largely constant at high MgO (regime I) until the point of magmatic differentiation, where an abrupt increase in Zn/Fe_T and simultaneous decrease in FeO_T (regime II) signals the onset of magnetite precipitation (Fig. 4a–f). Although the transition between the two differentiation regimes occurs at a different MgO in each arc, key conclusions can be drawn. The relatively constant Zn/Fe_T and FeO_T in regime I indicates that Zn and Fe_T behave similarly, which implies olivine fractionation from a low- $\text{Fe}^{3+}/\text{Fe}_T$ magma, but no significant clinopyroxene or hornblende fractionation because these phases cause an increase in Zn/Fe_T and FeO_T given that $K_{\text{D}(\text{cpx}/\text{melt})}^{\text{Zn}/\text{Fe}^{2+}} \approx K_{\text{D}(\text{hb}/\text{melt})}^{\text{Zn}/\text{Fe}^{2+}} \approx 0.6$ and Fe is incompatible (Supplementary Methods). In particular, the Zn/Fe_T of primitive arc magmas ($\text{MgO} > 8 \text{ wt}\%$) converges to $(8\text{--}11) \times 10^{-4}$ (Figs 2–4), yielding primary $\text{Fe}^{3+}/\text{Fe}_T$ ratios

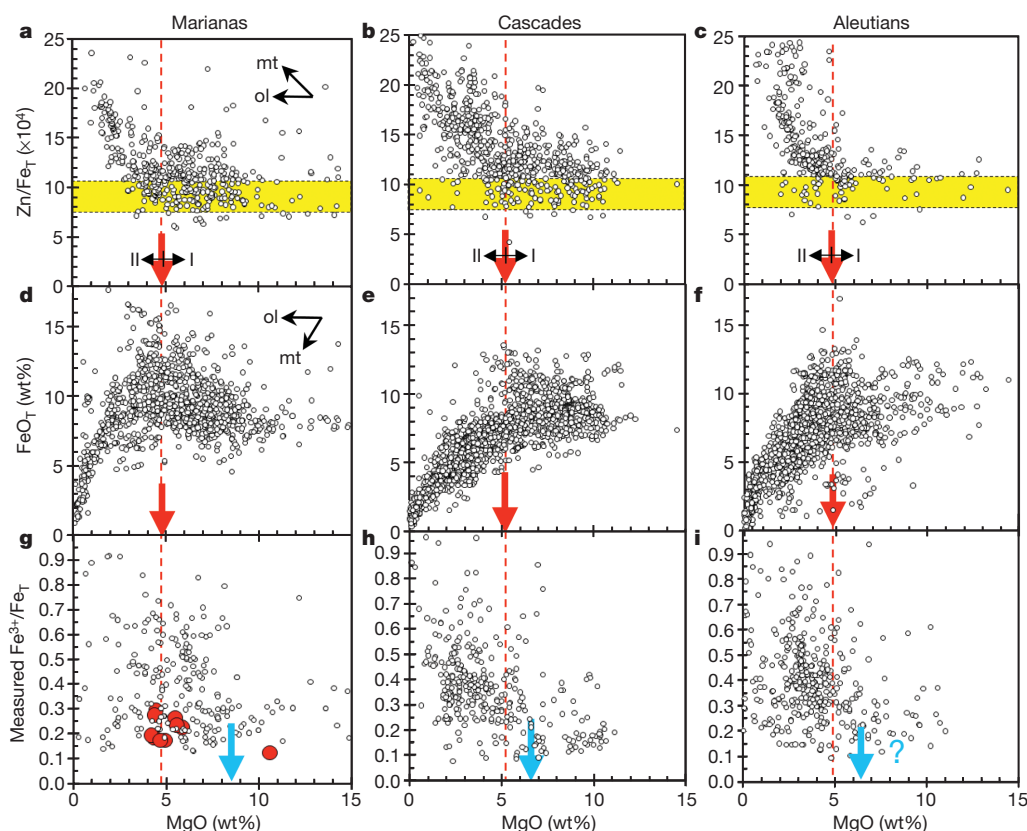


Figure 4 | Literature-compiled Zn/Fe_T , FeO_T and wet chemistry whole-rock $\text{Fe}^{3+}/\text{Fe}_T$ versus MgO in arc lavas from the Marianas, Cascades and Aleutians. The yellow horizontal bar in a–c (the Zn/Fe_T plots) corresponds to MORBs and mantle field from Fig. 1. Vertical red-dashed lines with bold red arrows mark the onset of magnetite fractionation as inferred from the onset of FeO_T depletion and Zn/Fe_T rise. d–f, The FeO_T plots. Blue arrows in g–i (the

$\text{Fe}^{3+}/\text{Fe}_T$ plots) show the MgO content at the estimated $\text{Fe}^{3+}/\text{Fe}_T$ transition from low to high. We note that the increase of Fe oxidation state commences at a higher MgO than in magnetite fractionation. Data from ref. 3 for Marianas arc melt inclusions (using their fractionation-corrected values) are also shown for reference as red-filled circles in g. Small vectors correspond to olivine (ol) and magnetite (mt) fractionation.

between about 0.1 and 0.15, similar to that of MORBs. Although the scatter in the data may allow for calculated $\text{Fe}^{3+}/\text{Fe}_T$ ratios up to about 0.2–0.25, the fact that Zn/Fe_T of primitive arc magmas overlap with mantle peridotite and primitive MORBs is unequivocal (similar overlaps are seen in V_T/Sc and Mn/Fe_T ; Supplementary Fig. 1). Independent of model calculations, this overlap suggests a similar overlap in $\text{Fe}^{3+}/\text{Fe}_T$, and implies f_{O_2} values²⁹ between FMQ–1 and FMQ+1, consistent with the range typical for the uppermost mantle f_{O_2} value^{4,21}. If arc magmas are actually derived from peridotites more oxidized than the MORB source, the overlap between arc basalt and MORB Zn/Fe_T values would require preferential partitioning of Zn into the melt to compensate exactly for the lowering of melt Zn/Fe_T caused by melting an oxidized source. Preferential partitioning of Zn into the melt cannot be achieved by melting of harzburgitic sources because Zn/Fe_T during peridotite melting is insensitive to melting degree at pressures less than 3 GPa (ref. 28). Although partial melting of a non-peridotitic lithology, such as a garnet clinopyroxenite, with bulk $K_{D(\text{rock/melt})} < 1$ (ref. 28), could result in elevated magmatic Zn/Fe_T , there is no evidence so far that pyroxenites are a dominant lithology in the mantle wedge.

The increasing magmatic Zn/Fe_T values in regime II require Zn to fractionate strongly from Fe_T . The onset of such fractionation is plausibly explained by Fe^{3+} becoming compatible in the fractionating minerals while Zn and Fe^{2+} remain moderately incompatible. Magnetite and hornblende are the only phases that are likely to cause simultaneous decrease in Fe_T and increase in Zn/Fe_T . Their formation implies an increase in magmatic $\text{Fe}^{3+}/\text{Fe}_T$ to levels sufficient to saturate Fe^{3+} -bearing minerals as fractionating phases. This inference is supported by literature-compiled wet chemistry measurements of $\text{Fe}^{3+}/\text{Fe}_T$ in whole rocks and glasses in Fig. 4g–i (see Supplementary Methods for discussion of data quality). Much of the variability in $\text{Fe}^{3+}/\text{Fe}_T$ may be due to post-eruptive oxidation processes, such as weathering and alteration, so it is likely that measured $\text{Fe}^{3+}/\text{Fe}_T$ ratios represent maximum bounds. However, a common feature of all the examined arcs is that measured $\text{Fe}^{3+}/\text{Fe}_T$ is low in primitive (high MgO) lavas and that the average $\text{Fe}^{3+}/\text{Fe}_T$ and also its variability increase markedly as MgO decreases. Thus, both measured values and those inferred from Zn/Fe_T for $\text{Fe}^{3+}/\text{Fe}_T$ increase with progressive magmatic differentiation. We also note that, during magmatic differentiation, the increase in $\text{Fe}^{3+}/\text{Fe}_T$ precedes (occurs at a higher MgO) the increase in Zn/Fe_T and decrease in FeO_T (where FeO_T is total Fe taken as FeO), consistent with the above suggestion that saturation of Fe^{3+} -bearing oxides (or Fe^{3+} -bearing silicates, such as amphibole), occur only after f_{O_2} and $\text{Fe}^{3+}/\text{Fe}_T$ of the magma increase to sufficient levels.

Our results suggest that, on average, the f_{O_2} of the uppermost mantle is relatively constant. Thus, subduction of oceanic lithosphere does not systematically oxidize the mantle wedge beneath arcs. Two possibilities are: (1) subducting oceanic lithosphere and sediments are not oxidized in total or (2) the oceanic lithosphere is oxidized but the oxidized components are retained during slab melting or dehydration. A more likely explanation, however, is that the input of oxidized components from the slab into the mantle wedge is not high enough to overwhelm the redox-buffering capacity of the upper mantle. For example, the concentration of buffering phases (such as elemental carbon, carbonate or sulphide) or bulk Fe may be sufficiently elevated in the mantle that its redox state is resistant to perturbations. The abundances of carbon and sulphur in the mantle need to be better constrained to evaluate this suggestion²². In any case, we do not rule out the possibility of locally oxidized regions in the mantle wedge or lithospheric mantle associated with metasomatism. Indeed, the most oxidized magmas tend to be high-potassium types (for example, shoshonites and minettes), which may originate by partial melting of metasomatic veins in the mantle³⁰.

The above observations lead us to predict that arc magmas oxidize during differentiation. One possibility is that because Fe^{3+} is excluded from early crystallizing silicates, such as olivine, $\text{Fe}^{3+}/\text{Fe}_T$ increases in the magma with progressive olivine fractionation (a 50% crystallization

of olivine doubles the $\text{Fe}^{3+}/\text{Fe}_T$ of the magma). However, olivine fractionation alone provides no explanation for the distinction between calc-alkalic and tholeiitic differentiation series. An alternative contributing factor may be auto-oxidation processes involving degassing. It has been suggested that magmatic $\text{Fe}^{3+}/\text{Fe}_T$ may increase owing to the formation of micro-crystalline magnetite by reaction of water with ferrous oxide species in the melt and release of H_2 (ref. 31), but the significance of this effect in arcs is not clear. Any successful alternative to the ‘source’ hypothesis for the oxidation state of arc magmas must explain the observed correlation between high oxidation state and water content in arc lavas³.

METHODS SUMMARY

Zn/Fe^{2+} exchange coefficients between olivine, orthopyroxene, clinopyroxene and spinel were inferred from the Zn/Fe ratios of minerals in natural peridotites²⁸. Bulk peridotite/melt exchange coefficients were inferred by (1) assuming primitive MORB is in equilibrium with peridotite, and (2) tracking Zn/Fe in peridotites as a function of melting degree²⁸. Collectively, these data were used to estimate mineral/melt exchange coefficients. Zn/Fe_T data presented for natural samples were compiled from the literature or represent new, solution-based inductively coupled plasma mass spectrometry analyses. $\text{Fe}^{3+}/\text{Fe}_T$ data represent wet chemistry results of whole-rock data compiled from the literature (following filtering schemes presented in the Supplementary Methods).

Received 10 May; accepted 19 October 2010.

1. Carmichael, I. S. E. The redox states of basic and silicic magmas: a reflection of their source regions? *Contrib. Mineral. Petrol.* **106**, 129–141 (1991).
2. Bezos, A. & Humler, E. The Fe^{3+}/Fe ratios of MORB glasses and their implications for mantle melting. *Geochim. Cosmochim. Acta* **69**, 711–725 (2005).
3. Kelley, K. A. & Cottrell, E. Water and the oxidation state of subduction zone magmas. *Science* **325**, 605–607 (2009).
4. Christie, D. M., Carmichael, I. S. E. & Langmuir, C. H. Oxidation states of mid-ocean ridge basalt glasses. *Earth Planet. Sci. Lett.* **79**, 397–411 (1986).
5. Gill, J. B. *Orogenic Andesites and Plate Tectonics* (Springer, 1981).
6. Mallmann, G. & O'Neill, H. S. C. The crystal/melt partitioning of V during mantle melting as a function of oxygen fugacity compared with some other elements (Al, P, Ca, Sc, Ti, Cr, Fe, Ga, Y, Zr and Nb). *J. Petrol.* **50**, 1765–1794 (2009).
7. Lee, C.-T. A., Leeman, W. P., Canil, D. & Li, Z.-X. A. Similar V/Sc systematics in MORB and arc basalts: implications for the oxygen fugacities of their mantle source regions. *J. Petrol.* **46**, 2313–2336 (2005).
8. Frost, B. R. in *Oxide Minerals: Petrologic and Magnetic Significance* (ed. Lindsley, D. H.) Vol. 25, 1–9 (Mineral. Soc. Am. Rev. Min., 1991).
9. Wood, B. J., Bryndzia, L. T. & Johnson, K. E. Mantle oxidation state and its relationship to tectonic environment and fluid speciation. *Science* **248**, 337–345 (1990).
10. Osborn, E. F. Role of oxygen partial pressure in the crystallization and differentiation of basaltic magma. *Am. J. Sci.* **257**, 609–647 (1959).
11. Arculus, R. J. Use and abuse of the terms calcalkaline and calcalkalic. *J. Petrol.* **44**, 929–935 (2003).
12. Alt, J. C., Honnorez, J., Laverne, C. & Emmermann, R. Hydrothermal alteration of a 1 km section through the upper oceanic crust, Deep Sea Drilling Project Hole 504B: mineralogy, chemistry, and evolution of seawater-basalt interactions. *J. Geophys. Res.* **91**, 10309–10335 (1986).
13. Mungall, J. E. Roasting the mantle: slab melting and the genesis of major Au and Au-rich Cu deposits. *Geology* **30**, 915–918 (2002).
14. Sisson, T. W. & Grove, T. L. Experimental investigations of the role of H_2O in calcalkaline differentiation and subduction zone magmatism. *Contrib. Mineral. Petrol.* **113**, 143–166 (1993).
15. Patino, L. C., Carr, M. J. & Feigenson, M. D. Local and regional variations in Central American arc lavas controlled by variations in subducted sediment input. *Contrib. Mineral. Petrol.* **138**, 265–283 (2000).
16. McInnes, B. I. A., Gregoire, M., Binns, R. A., Herzog, P. M. & Hannington, M. D. Hydrous metasomatism of oceanic sub-arc mantle, Lihir, Papua New Guinea: petrology and geochemistry of fluid-metasomatized mantle wedge xenoliths. *Earth Planet. Sci. Lett.* **188**, 169–183 (2001).
17. Parkinson, I. J. & Arculus, R. J. The redox state of subduction zones: insights from arc-peridotites. *Chem. Geol.* **160**, 409–423 (1999).
18. Ishimaru, S., Arai, S. & Shukuno, H. Metal-saturated peridotite in the mantle wedge inferred from metal-bearing peridotite xenoliths from Avacha volcano, Kamchatka. *Earth Planet. Sci. Lett.* **284**, 352–360 (2009).
19. Malaspina, N., Poli, S. & Fumagalli, P. The oxidation state of metasomatized mantle wedge: insights from C-O-H-bearing garnet peridotite. *J. Petrol.* **50**, 1533–1552 (2009).
20. Wang, J., Hattori, K. H., Kilian, R. & Stern, C. R. Metasomatism of sub-arc mantle peridotites below southernmost South America: reduction of f_{O_2} by slab-melt. *Contrib. Mineral. Petrol.* **153**, 607–624 (2007).
21. Frost, D. J. & McCammon, C. A. The redox state of Earth's mantle. *Annu. Rev. Earth Planet. Sci.* **36**, 389–420 (2008).
22. Canil, D. et al. Ferric iron in peridotites and mantle oxidation states. *Earth Planet. Sci. Lett.* **123**, 205–220 (1994).

23. Canil, D. Vanadium partitioning and the oxidation state of Archaean komatiite magmas. *Nature* **389**, 842–845 (1997).
24. Dauphas, N. *et al.* Iron isotopes may reveal the redox conditions of mantle melting from Archean to present. *Earth Planet. Sci. Lett.* **288**, 255–267 (2009).
25. Teng, F.-Z., Dauphas, N. & Helz, R. T. Iron isotope fractionation during magmatic differentiation in Kilauea Iki lava lake. *Science* **320**, 1620–1622 (2008).
26. Roeder, P. L. & Emslie, R. F. Olivine-liquid equilibrium. *Contrib. Mineral. Petrol.* **29**, 275–289 (1970).
27. Lange, R. A. & Carmichael, I. S. E. The Aurora volcanic field, California-Nevada: oxygen fugacity constraints on the development of andesitic magma. *Contrib. Mineral. Petrol.* **125**, 167–185 (1996).
28. Le Roux, V., Lee, C.-T. A. & Turner, S. J. Zn/Fe systematics in mafic and ultramafic systems: implications for detecting major element heterogeneities in the Earth's mantle. *Geochim. Cosmochim. Acta* **74**, 2779–2796 (2010).
29. Kress, V. C. & Carmichael, I. S. E. The compressibility of silicate liquids containing Fe₂O₃ and the effect of composition, temperature, oxygen fugacity and pressure on their redox states. *Contrib. Mineral. Petrol.* **108**, 82–92 (1991).
30. Rowe, M. C., Kent, A. J. R. & Nielsen, R. L. Subduction influence on oxygen fugacity and trace and volatile elements in basalts across the Cascade Volcanic Arc. *J. Petrol.* **50**, 61–91 (2009).
31. Holloway, J. R. Redox reactions in seafloor basalts: possible insights into silicic hydrothermal systems. *Chem. Geol.* **210**, 225–230 (2004).

Supplementary Information is linked to the online version of the paper at www.nature.com/nature.

Acknowledgements Discussions and debates with D. Canil, R. Lange, E. Cottrell and K. Kelley are appreciated. We especially thank H. O'Neill for insights. This work was facilitated by a Geological Society of America award (to C.-T.A.L.) F.A. was supported by the Keith-Weiss Visiting Professorship at Rice University.

Author Contributions C.-T.A.L. designed the project and wrote the paper, P.L. compiled the ferric iron contents of arc lavas, measurements were done by C.-T.A.L. and V.L.R., and all authors contributed to discussions and data analysis.

Author Information Reprints and permissions information is available at www.nature.com/reprints. The authors declare no competing financial interests. Readers are welcome to comment on the online version of this article at www.nature.com/nature. Correspondence and requests for materials should be addressed to C.-T.A.L. (ctlee@rice.edu).

A dimorphic pheromone circuit in *Drosophila* from sensory input to descending output

Vanessa Ruta¹, Sandeep Robert Datta^{1†}, Maria Luisa Vasconcelos^{1‡}, Jessica Freeland¹, Loren L. Looger² & Richard Axel¹

Drosophila show innate olfactory-driven behaviours that are observed in naive animals without previous learning or experience, suggesting that the neural circuits that mediate these behaviours are genetically programmed. Despite the numerical simplicity of the fly nervous system, features of the anatomical organization of the fly brain often confound the delineation of these circuits. Here we identify a neural circuit responsive to cVA, a pheromone that elicits sexually dimorphic behaviours^{1–4}. We have combined neural tracing using an improved photoactivatable green fluorescent protein (PA-GFP) with electrophysiology, optical imaging and laser-mediated microlesioning to map this circuit from the activation of sensory neurons in the antennae to the excitation of descending neurons in the ventral nerve cord. This circuit is concise and minimally comprises four neurons, connected by three synapses. Three of these neurons are overtly dimorphic and identify a male-specific neuropil that integrates inputs from multiple sensory systems and sends outputs to the ventral nerve cord. This neural pathway suggests a means by which a single pheromone can elicit different behaviours in the two sexes.

The male pheromone 11-*cis*-vaccenyl acetate (cVA) elicits male–male aggression⁴ and suppresses male courtship towards females as well as males^{1–3}. In females, cVA activates the same sensory neurons to promote receptivity to males². cVA-induced aggregation behaviour is shown by both sexes⁵. What neural circuits permit a single pheromone acting through the same set of sensory neurons to elicit several distinct and sexually dimorphic behavioural responses?

The sensory neurons that express the odorant receptor Or67d respond to cVA^{2,6,7}, and these neurons converge on the DA1 glomerulus in the antennal lobe^{8,9}. Projection neurons (PNs) that innervate the DA1 glomerulus terminate in the lateral horn of the protocerebrum^{10–12}. In previous experiments we showed that the DA1 axons are sexually dimorphic and reveal a male-specific ventral axonal arborization in the lateral horn¹³. This dimorphism by itself might explain the sexually dimorphic behaviours or, alternatively, it might presage iterative anatomical dimorphisms at each stage in the circuit to descending output. We therefore characterized a neural circuit that transmits information from the DA1 PNs to the ventral nerve cord. We restricted our analysis to neurons that express the sexually dimorphic transcription factor fruitless (*Fru*^M). *Fru*^M is expressed in both Or67d-expressing sensory neurons and DA1 PNs^{14,15} and governs the development of dimorphic neural circuitry including the male-specific axonal arborization of DA1 PNs^{13,16,17}. In addition *Fru*^M specifies many male-specific behaviours, including those that are mediated by cVA^{14,15,18–22}.

In initial experiments we used PA-GFP²³ to identify *Fru*⁺ third-order neurons whose dendritic processes are closely apposed to DA1 axon termini. We developed a strategy in which two-photon photoactivation is restricted to a small, circumscribed region of a neuron's axonal arborization with the expectation that this would label the postsynaptic cells by photoconversion of PA-GFP in their dendrites. To ensure that this limited activation could produce sufficient signal

from the photoconverted fluorophore to illuminate third-order neurons and their most distal processes, we generated two new enhanced PA-GFPs, namely C3PA-GFP and SPA-GFP²⁴ (Supplementary Fig. 1).

Photoconversion of the DA1 glomerulus in flies expressing C3PA-GFP or SPA-GFP under the control of *fru*^{GAL4} (ref. 14) readily identified the axonal arborizations of the DA1 PNs (Fig. 1a). We then photoactivated the volume of neuropil circumscribing the DA1 axon termini and reproducibly labelled four clusters of presumptive third-order neurons in the lateral horn of male flies ($n = 7$; Fig. 1b and Supplementary Fig. 2). Labelling of the two dorsal clusters, DC1 and DC2, was observed only in males; the clusters were either absent in the female or lacked projections into the ventral lateral horn ($n = 6$; Fig. 1c). The lateral cluster LC1 was present in the two sexes but was dimorphic in both number and projection pattern (males 25.8 ± 3.4 (mean \pm s.d.), $n = 6$; females 15.8 ± 3.0 , $n = 5$). LC2 did not show an apparent numeric or anatomical dimorphism (males 13.0 ± 2.8 , $n = 8$; females 13.3 ± 2.1 , $n = 8$). Photoactivation of DA1 axon terminals in male flies that express C3PA-GFP pan-neuronally labelled few additional neurons and suggests that these four *Fru*⁺ clusters constitute the major potential recipients of DA1 input (Supplementary Fig. 3).

These photoactivation experiments identify clusters of third-order neurons in the lateral horn that are anatomically poised to propagate dimorphic responses to cVA. However, anatomical proximity does not ensure functional connectivity. We therefore developed a method to specifically activate individual glomeruli and simultaneously record from presumptive downstream neurons to determine whether the lateral horn clusters that we identify receive excitatory input from DA1 PNs. We selectively stimulated DA1 PNs by positioning a fine glass electrode in the centre of the DA1 glomerulus and iontophoresing acetylcholine, the neurotransmitter that excites PNs²⁵, into the glomerular neuropil (Fig. 2a). Varying the iontophoretic voltage allowed us to vary the frequency of elicited action potentials systematically in DA1 PNs up to 250 Hz (Fig. 2b), a value close to the upper limit of cVA-elicited responses measured in these PNs^{13,26}. Activation of the DA1 glomerulus over this voltage range excited DA1 PNs specifically and elicited no response in PNs innervating other glomeruli in the antennal lobe (Fig. 2b). Stimulation of the neighbouring glomeruli, VA1d and VA1lm, similarly elicited the specific excitation of their cognate PNs but did not activate DA1 PNs (Fig. 2b).

We then examined whether stimulation of the DA1 glomerulus would result in the excitation of neurons within the four clusters in the lateral horn that we identified, a result indicative of functional synaptic connections with DA1 PNs. We expressed the genetically encoded calcium indicator GCaMP3 (ref. 27) in *Fru*⁺ neurons in male flies and used two-photon imaging to monitor increases in Ca^{2+} concentration in the lateral horn clusters in response to DA1 excitation. Stimulation of the DA1 glomerulus elicited large increases in Ca^{2+} in neurons within the DC1 and LC1 clusters, with a far weaker response being observed in LC2 (Fig. 2c). The small DC2 cluster is difficult to identify reliably because of the low basal fluorescence of GCaMP3; it

¹Department of Biochemistry and Molecular Biophysics and the Howard Hughes Medical Institute, College of Physicians and Surgeons, Columbia University, New York, New York 10032, USA. ²Howard Hughes Medical Institute, Janelia Farm Research Campus, Ashburn, Virginia 20147, USA. [†]Present addresses: Department of Neurobiology, Harvard Medical School, Boston, Massachusetts 02115, USA (S.R.D.); Champalimaud Neuroscience Programme, Instituto Gulbenkian de Ciência, Rua da Quinta Grande, 6, P-2780-156 Oeiras, Portugal (M.L.V.).

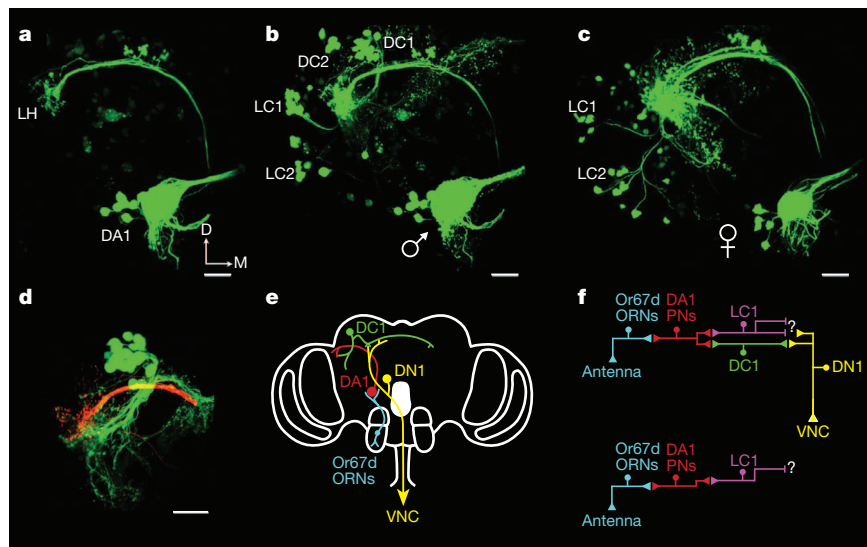


Figure 1 | Photoactivation identifies dimorphic lateral horn neurons.

a, Photoactivation of the DA1 glomerulus in a male fly labels DA1 PNs including their axonal arborization in the lateral horn (LH). **b**, Photoactivation of a volume circumscribing the DA1 axon terminals labels dorsal (DC1 and DC2) and lateral (LC1 and LC2) LH neuronal clusters in the male. **c**, Photoactivation of the DA1 axon terminals analogous to **b** in the female labels only lateral LH clusters. Note that LC1 neurons are more numerous in males and that DC1 and DC2 are absent in females. **d**, DA1 axons and DC1 dendrites interdigitate within the LH. DA1 axons were labelled by electroporation of the DA1 glomerulus with Texas Red dextran, and DC1 neurons were labelled by

direct photoactivation of the fasciculated DC1 dendritic processes. For clarity, the basal fluorescence from non-photoactivated neurons has been masked in **d**. All images are z-projections acquired by two-photon laser scanning microscopy of photoactivated neurons in which *fru*^{GAL4} directs C3PA-GFP or SPA-GFP expression. Scale bars, 20 μ m. Dorsal (D) and medial (M) axes are indicated. All images are oriented similarly to that in **a**. **e**, Diagram of the male fly brain illustrating neurons that constitute the cVA-responsive circuit defined in this study. **f**, Circuit diagrams for identified dimorphic cVA pathways in the male (top) and female (bottom).

was therefore not examined by optical imaging. The Ca^{2+} response in DC1 was specific for DA1 activation and was not observed when the stimulating electrode was repositioned in two neighbouring glomeruli, VA1d and VA1lm ($n = 5$, data not shown). These optical imaging experiments demonstrate that neurons within the DC1 and LC1 clusters extend processes in anatomical proximity to the DA1 axons and receive excitatory input from DA1 PNs (Fig. 1e, f). Immunostaining indicated that neurons within the LC1 cluster produce the inhibitory neurotransmitter GABA (γ -aminobutyric acid; Supplementary Fig. 4). Electrophysiological experiments suggested that DC1 neurons are excitatory (see below) but the neurotransmitter remains unknown.

We focused on the male-specific DC1 neurons to define a cVA-responsive circuit. The DC1 cluster consists of 19.7 ± 2.3 (mean \pm s.d.) cell bodies ($n = 10$) in a spatially stereotyped location in the dorsal aspect of the anterior protocerebrum. Double labelling experiments revealed that the DC1 processes interdigitate richly with DA1 axons (Fig. 1d) in the lateral horn. Photoactivation of single DC1 cell bodies indicated that the cluster is composed of several anatomical classes of neurons characterized by distinct branch patterns within the protocerebrum (Supplementary Fig. 5) that are likely to receive and integrate inputs from both olfactory and non-olfactory brain centres (Supplementary Fig. 6).

We performed electrophysiological recordings to examine the response of DC1 neurons to both DA1 stimulation and cVA exposure. Selective stimulation of the DA1 glomerulus evoked action potentials in 66% of male-specific DC1 neurons ($n = 73$ neurons) recorded in the loose patch configuration (Fig. 2d, g). Among responsive DC1 neurons, we observed that the sensitivity to DA1 stimulation differed. This functional heterogeneity within the DC1 cluster observed by both electrical and optical recording was consistent with the anatomical heterogeneity of dendritic fields in the lateral horn observed for single DC1 neurons (Supplementary Fig. 5).

In accord with the imaging experiments, the electrophysiological response of DC1 neurons is selectively tuned to DA1 input. After recording the response of a DC1 neuron to DA1 stimulation, we repositioned the stimulating electrode into 6–11 other superficial

glomeruli located throughout the antennal lobe ($n = 8$). We observed that DC1 neurons activated by minimal DA1 stimulation (0.3 V) were either weakly excited or unresponsive to strong stimulation (4 V) of other glomeruli (Fig. 2e). Stimulation of the *Fru*⁺ VA1lm glomerulus ($n = 15$) failed to excite DC1 neurons despite the close proximity of DA1 and VA1lm axons¹². These observations demonstrate the specificity of glomerular excitation and reveal that olfactory input to DC1 is mediated largely by the DA1 glomerulus and not by the activation of at least 11 other glomeruli, suggesting that DC1 neurons receive olfactory stimulation only from cVA. We next recorded cVA-evoked responses from DC1 neurons in an intact fly preparation. We observed that 62% of DC1 neurons were responsive to cVA over a range of concentrations (Fig. 2f, g; $n = 71$). The input–output relationship of DC1 neurons was similar whether action potentials were evoked in DA1 PNs through direct glomerular stimulation or by pheromonal excitation of the antenna, suggesting that DC1 neurons are excited primarily by means of DA1 input (Fig. 2g). Both Or67d-expressing sensory neurons and DA1 PNs have been shown to be selectively tuned to cVA^{6,7,26}. DC1 neurons showed similar odorant selectivity (Fig. 2f) and fired only weakly in response to stimulation of the antenna with a cocktail of ten fruit-derived odorants that excite a majority of glomeruli (Supplementary Fig. 7). Thus, DC1 neurons are likely to receive direct excitatory feedforward input from DA1 PNs and respond selectively to cVA.

Photoactivation of PA-GFP in presynaptic DA1 axonal arborizations, in concert with electrophysiology, has identified postsynaptic third-order neurons in the lateral horn that are responsive to cVA. The iterative use of this strategy could allow us to define the complete cVA circuit from sensory input to descending output. Tracing of photoactivated DC1 axons ($n = 15$) revealed that they terminate proximally within a triangular neuropil in the lateral protocerebrum (the lateral triangle) and extend distal processes to a previously uncharacterized tract within the superior medial protocerebrum (the SMP tract; Fig. 3a). The lateral triangle and SMP tract are sexually dimorphic neuropils that are absent in females (Fig. 3c).

Photoactivation of the terminal arborizations of DC1 axons was performed to identify neurons innervating the lateral triangle and

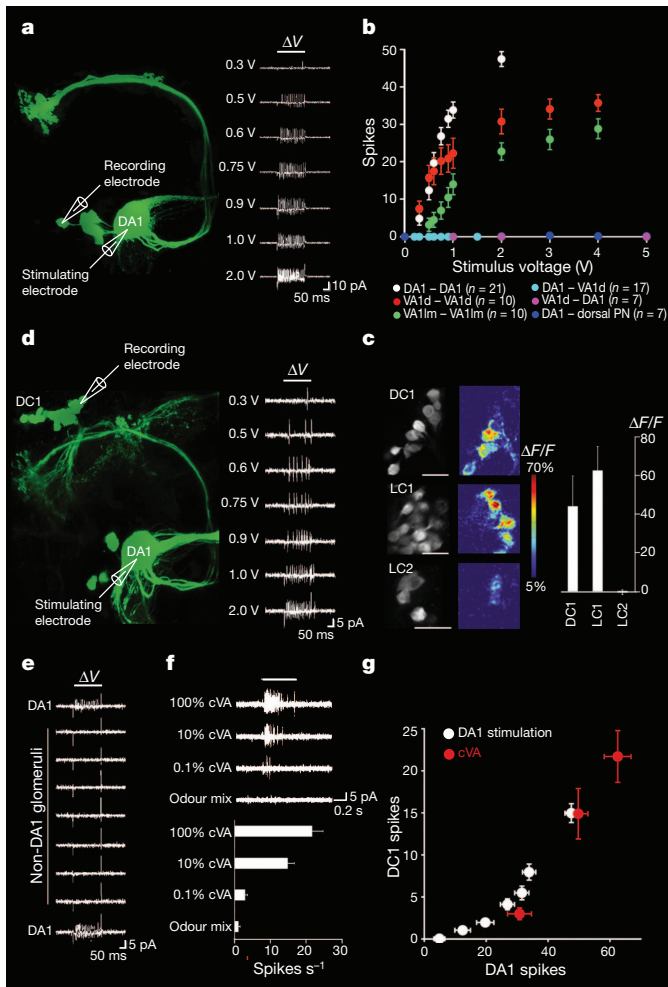


Figure 2 | DC1 neurons synapse with DA1 PNs and are selectively tuned to cVA. **a**, Selective stimulation of single glomeruli through iontophoresis of acetylcholine shown schematically (left). Right: stimulation of the DA1 glomerulus at the indicated voltages evokes graded responses in DA1 PNs recorded in the loose patch configuration. **b**, Spike count recorded in PNs in response to stimulation of a single glomerulus at the indicated voltages. **c**, Optical recordings of Ca^{2+} -mediated changes in fluorescence ($\Delta F/F$) in LH clusters expressing GCaMP3 under the control of *fru*^{GAL4}, evoked by stimulation of the DA1 glomerulus (left). Scale bars, 10 μm . Right: bar graph showing mean and s.e.m. ($n = 5$) normalized fluorescence changes in LH clusters evoked by stimulation of DA1. **d**, Diagram of the recording configuration (left) used to measure the response of a DC1 neuron to stimulation of the DA1 glomerulus at indicated voltages (right). **e**, The response of a DC1 neuron to sequential stimulation of the DA1 glomerulus, seven superficial glomeruli, and then the DA1 glomerulus. Note a residual stimulus artefact at the beginning and end of the 200-ms stimulation. **f**, Spikes evoked in DC1 neurons by exposure of antenna for 1 s to 0.1% cVA ($n = 25$), 10% cVA ($n = 47$), 100% cVA ($n = 27$) or a mix of ten general odorants ($n = 23$). **g**, Input–output relationship of DA1–DC1 neurons observed on stimulation of the DA1 glomerulus for 200 ms at the voltages indicated in **d** ($n = 56$, white) or after an exposure of the antenna for 1 s to different concentrations of cVA (red). All plotted values are means \pm s.e.m. for responsive DC1 neurons.

SMP tract ($n = 6$; Fig. 3b). We observed dense labelling in these structures arising from the rich male-specific projections of multiple classes of Fru⁺ neurons. Dimorphic LC1 neurons that receive direct innervation from DA1 PNs send inhibitory projections to the lateral triangle and SMP tract (Fig. 1e, f and Supplementary Fig. 2). We also observed dimorphic mAL neurons extending from the subesophageal ganglion (SOG) and terminating within these neuropils¹⁶. In addition, these neuropils are innervated by male-specific P1 interneurons implicated in the initiation of male courtship behaviour¹⁷. Thus, the lateral triangle and SMP tract receive dimorphic projections from several brain

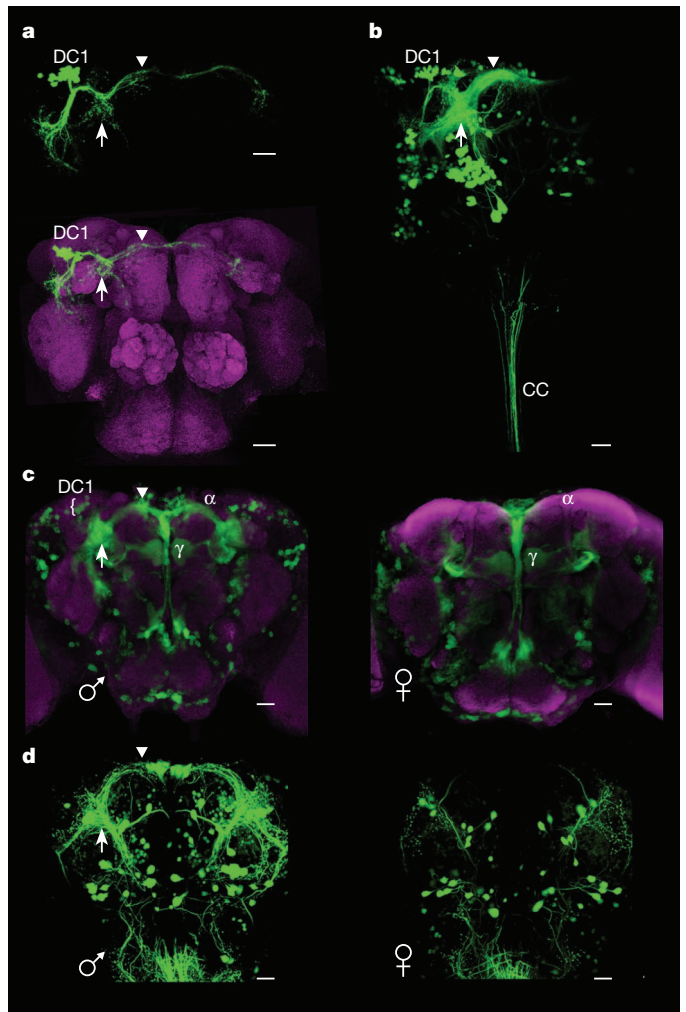


Figure 3 | DC1 and descending neurons innervate Fru⁺ dimorphic neuropil. **a**, Direct photoactivation of the DC1 cluster (green, top) followed by counterstaining of neuropil with the nc82 antibody (magenta, bottom) reveals terminations in the lateral triangle (arrow) and SMP tract (arrowhead) and define a Fru⁺ integrative neuropil. For clarity, background fluorescence from non-photoactivated neurons has been masked in **a**. **b**, Photoactivation of the DC1 axon terminals in the lateral triangle (arrow) labels a large population of Fru⁺ neurons including fibres that project to the SMP tract (arrowhead) and fibres that descend into the cervical connectives (CC). **c**, Images of a male brain (left) and a female brain (right) in which Fru⁺ neurons express CD8-GFP (green). The neuropil is counterstained with the nc82 antibody (magenta). These images highlight dimorphic neural structures including the DC1 cluster, the lateral triangle (arrow) and SMP tract (arrowhead). Equivalent 20- μm confocal z-sections were defined by using the α -lobes and γ -lobes of the mushroom bodies as landmarks. **d**, Photoactivation of the cervical connectives in a male fly (left) and a female fly (right) labels descending neuron cell bodies and reveals dimorphic projections that innervate the lateral triangle (arrow) and SMP tract (arrowhead). Scale bars, 20 μm .

regions including other sensory processing areas, suggesting that these neuropils may integrate sex-specific information from multiple sensory systems.

Several neurons that innervate the lateral triangle and SMP tract also extend processes that descend into the ventral nerve cord, suggesting that these potential fourth-order descending neurons may transmit information from cVA-responsive sensory neurons to the ganglia of the ventral nerve cord. Descending neurons that innervate the lateral triangle and SMP tract were characterized by photoactivation of the cervical connectives conveying neural signals from the brain to the ventral nerve cord (Fig. 3d). In the brain, the processes of these descending neurons showed a marked dimorphism that was apparent in their

extensive innervation of the male-specific SMP tract and lateral triangle (Fig. 3d). A descending neuron, DN1, absent in females, was observed in the ventral posterior aspect of the male brain, at the midline. Labelling of this male-specific cell body revealed short processes terminating within the lateral triangle and SMP tract, and a long descending process entering the ventral nerve cord and terminating within the thoracic and abdominal ganglia (Fig. 4a, b). Electroporation of DN1 with Texas Red dextran, followed by photoactivation of the DC1 cluster, revealed extensive intermingling of the green DC1 axons with the red dendrites of the descending neuron (Fig. 4a). This suggests that this descending

neuron is anatomically poised to make direct synaptic contacts with third-order, cVA-responsive DC1 neurons.

We performed whole-cell patch clamp recordings on DN1 to discern whether it transmits pheromonal information to the ventral nerve cord. We observed that in response to either exposure of the antenna to cVA or direct stimulation of the DA1 glomerulus, DN1 received a barrage of excitatory postsynaptic potentials (EPSPs) bringing its membrane potential close to or past threshold ($n = 6$; Fig. 4c, f). To determine whether this response was mediated by DC1 neurons, we devised a microlesion technique exploiting the spatial precision of a two-photon laser to effectively sever DC1 inputs into the lateral triangle and SMP tract (Fig. 4d). Optical recordings revealed that microlesioning of DC1 dendrites resulted in the immediate and selective loss of DC1 responses to DA1 stimulation without affecting the excitation of neighbouring LC1 dendrites and cell bodies ($n = 5$; Fig. 4e). Severing the connections between DA1 and DC1 resulted in an almost complete loss of the response of DN1 to stimulation of DA1 ($n = 6$; Fig. 4f, g). The response of this descending neuron was far weaker than the response of early neural participants in this circuit. However, the observation that two-photon-mediated microlesions in DC1 resulted in a decrease of more than 70% in the DN1 response to stimulation of DA1 suggests that, despite its weak excitation, DN1 is a component of this circuit. A more potent response may require a more natural setting that integrates pheromonal input with other sensory signals. Taken together, these experiments suggest that male-specific DC1 neurons excite the male-specific DN1 through synaptic connections within the dimorphic lateral triangle and SMP tract. Thus, olfactory information may be processed by as few as three synapses within the brain before descending to initiate motor programs within the ganglia of the ventral nerve cord (Fig. 1e, f). Although we cannot yet define a behaviour elicited by this circuit, we presume that it mediates a component of the innate behavioural repertoire initiated by cVA.

This cVA-responsive circuit provides insights into the mechanism by which sensory information received by the antenna may be translated into motor output. First, the circuit is concise: as few as four neuronal clusters and three synapses bring pheromonal signals from the periphery to the ganglia of the nerve cord. This minimal circuit assumes monosynaptic connections between the neurons that we have identified. This circuit is shallow but seems to include adequate synaptic connections to permit the integration of olfactory and non-olfactory information. Third-order lateral horn neurons reveal a capacity for

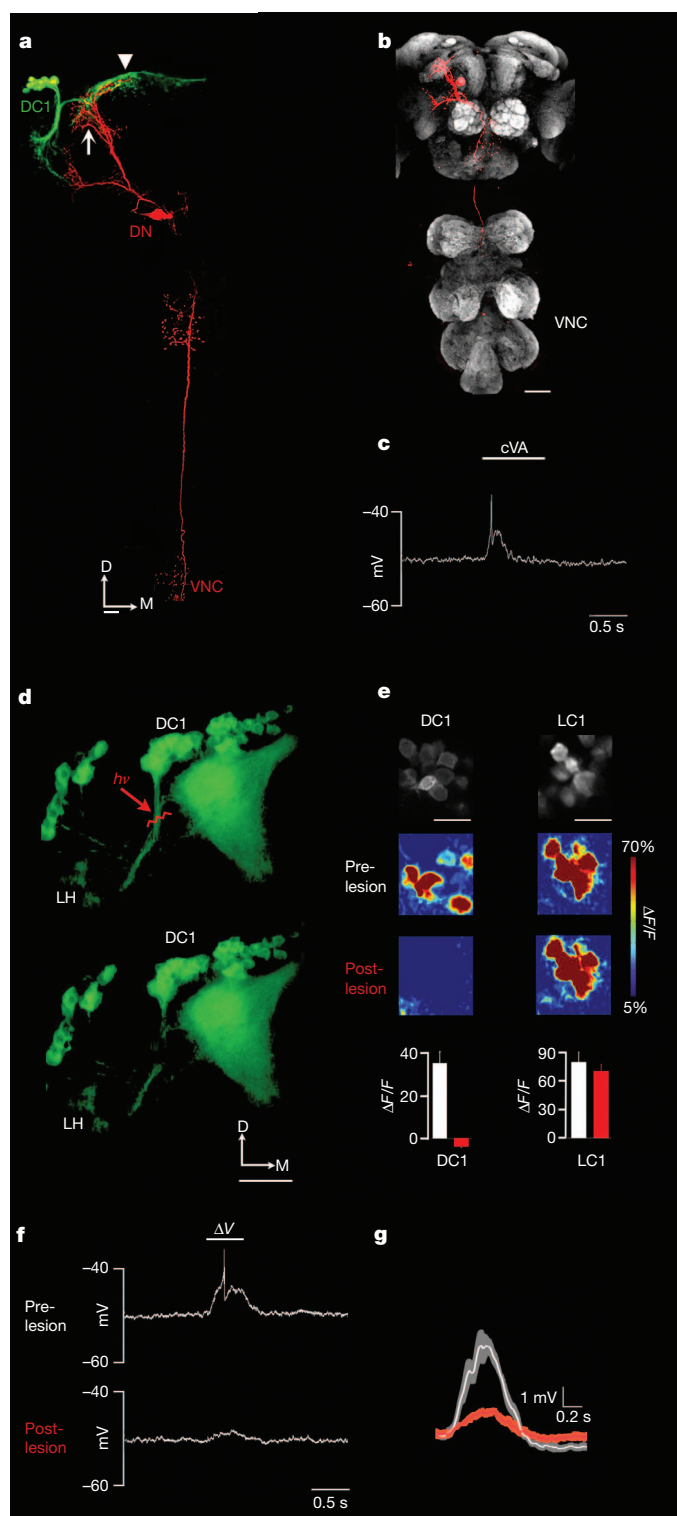


Figure 4 | DC1 neurons excite DN1, a cVA-responsive, male-specific descending neuron. **a**, DC1 axons (labelled green by direct photoactivation) interdigitate with the dendrites of DN1 (labelled by single-cell electroporation of Texas Red dextran) in the lateral triangle (arrow) and SMP tract (arrowhead). Scale bar, 20 μm . Dorsal (D) and medial (M) axes are indicated. **b**, The axon of a dye-filled DN1 (red) terminates within the ventral nerve cord (VNC) in a male fly whose neuropil has been counterstained with the nc82 antibody (grey). Scale bar, 80 μm . **c**, Intracellular recording of DN1 in response to an application of 10% cVA to the antenna for 1 s. **d**, Two-photon laser-mediated microlesioning severs DC1 dendritic processes as they exit from the lateral horn (LH). Images of Fru⁺ neurons expressing CD8-GFP before (top) and after (bottom) microlesioning. The laser was targeted to DC1 neuronal processes at the position indicated by the red arrow (hv). Scale bar, 20 μm . **e**, Microlesioning of DC1 processes results in the loss of Ca^{2+} responses evoked by DA1 stimulation in DC1 but not LC1 cell bodies. Fluorescence changes ($\Delta F/F$) in response to stimulation of the DA1 glomerulus were recorded in DC1 and LC1 neurons expressing GCaMP3 under the control of fru^{GAL4}. The bar graphs (bottom) show normalized changes in fluorescence (means and s.e.m.; $n = 5$ flies) for all DC1 or LC1 cell bodies in the same z plane before (white) and after (red) microlesioning of DC1 processes. **f**, Intracellular recording of DN1 in response to stimulation of the DA1 glomerulus for 500 ms before (top) and after (bottom) microlesioning of DC1 processes. **g**, Average change in synaptic potential recorded in DN1 in response to stimulation of DA1, before (white) and after (red) microlesioning of DC1 processes ($n = 6$, mean \pm s.e.m.). DN1 responses have been digitally low-pass filtered (Butterworth, 10 Hz) to remove action potentials.

multisensory integration with inputs to the DC1 cluster from the SOG and from the optic lobe. The lateral triangle and SMP tract also integrate sensory inputs from DC1 and LC1 as well as inhibitory projections from the SOG¹⁶. This integration provides the opportunity for other sensory signals emanating from a cVA-scented fly to modulate the response to the pheromone.

Second, multiple neural components within the circuit are anatomically dimorphic, and this could explain the different behaviours elicited by cVA in males and females. The initial neural components of the circuit, Or67d-expressing sensory neurons and DA1 PNs, are dedicated to the receipt of a singular olfactory stimulus, cVA, and are equally responsive to the pheromone in the two sexes^{2,13}. However, dimorphisms are observed in the synaptic connections between the PNs and the third-order lateral horn neurons and define a node from which sex-specific neural pathways emanate. The DA1 PNs reveal dimorphic axon arborizations¹³, but this dimorphism is only one component of a highly dimorphic circuit. These dimorphic arborizations synapse with male-specific DC1 neurons that send axons to a male-specific neuropil (the lateral triangle and SMP tract). One output of this neuropil is a male-specific descending neuron, DN1 (Fig. 1e, f). This circuit is likely to participate in the generation of cVA-elicited behaviours observed only in males. The identification of a sex-specific circuit including extensive neuropils present only in males suggests pathways for dimorphic behaviours that differ from earlier proposals that invoke the differential activation of circuits that are common to the two sexes^{28,29}. DA1 PNs also synapse onto the cluster of LC1 neurons that are present in both sexes but are numerically and anatomically dimorphic. The multiple dimorphic targets of a singular olfactory input could explain how a pheromone acting through the same sensory inputs may elicit different behaviours in the two sexes.

METHODS SUMMARY

Optical tracing of neurons was performed on flies that express fru^{GAL4} (ref. 20) driving the expression of C3PA-GFP or SPA-GFP. Photoactivation was performed essentially as described¹³ except that regions of interest for photoconversion were defined manually in three dimensions by using masks generated in Prairie View software (Prairie Technologies). We identified lateral horn neurons receiving functional input from DA1 PNs by first photoactivating the DA1 glomerulus to reveal DA1 axons. We then defined a photoactivation mask circumscribing all DA1 axon terminals in the lateral horn and exposed this masked volume to photoconverting 710-nm light. Direct photoactivation of the DC1 cluster was achieved through irradiation of a small volume (typically about 2–5 µm on each axis) centred on the fasciculated dendritic processes as they exit from the lateral horn. We selectively excited individual glomeruli by positioning glass electrodes (7–8 MΩ) filled with 2 mM acetylcholine in the centre of superficial glomeruli. Voltage pulses (200 or 500 ms) were then applied by means of a Grass stimulator to excite the impaled glomerulus. For microlesioning experiments, we targeted a small area (about 1 µm × 2 µm) centred on the tightly fasciculated DC1 processes proximal to where they bifurcate and innervate the lateral triangle by using a high zoom (×8). We then applied one to four pulses of 800-nm laser light (75–90 mW at the back aperture) until we observed a physical discontinuity.

Full Methods and any associated references are available in the online version of the paper at www.nature.com/nature.

Received 8 July; accepted 29 September 2010.

1. Ejima, A. *et al.* Generalization of courtship learning in *Drosophila* is mediated by *cis*-vaccenyl acetate. *Curr. Biol.* **17**, 599–605 (2007).
2. Kurtovic, A., Widmer, A. & Dickson, B. J. A single class of olfactory neurons mediates behavioural responses to a *Drosophila* sex pheromone. *Nature* **446**, 542–546 (2007).
3. Billeter, J. C., Atallah, J., Krupp, J. J., Millar, J. G. & Levine, J. D. Specialized cells tag sexual and species identity in *Drosophila melanogaster*. *Nature* **461**, 987–991 (2009).

4. Wang, L. & Anderson, D. J. Identification of an aggression-promoting pheromone and its receptor neurons in *Drosophila*. *Nature* **463**, 227–231 (2010).
5. Bartelt, R. J., Schaner, A. M. & Jackson, L. L. *Cis*-vaccenyl acetate as an aggregation pheromone in *Drosophila melanogaster*. *J. Chem. Ecol.* **11**, 1747–1756 (1985).
6. Clyne, P., Grant, A., O'Connell, R. & Carlson, J. R. Odorant response of individual sensilla on the *Drosophila* antenna. *Invert. Neurosci.* **3**, 127–135 (1997).
7. van der Goes van Naters, W. & Carlson, J. R. Receptors and neurons for fly odors in *Drosophila*. *Curr. Biol.* **17**, 606–612 (2007).
8. Couto, A., Alenius, M. & Dickson, B. J. Molecular, anatomical, and functional organization of the *Drosophila* olfactory system. *Curr. Biol.* **15**, 1535–1547 (2005).
9. Fishilevich, E. & Vosshall, L. B. Genetic and functional subdivision of the *Drosophila* antennal lobe. *Curr. Biol.* **15**, 1548–1553 (2005).
10. Marin, E. C., Jefferis, G. S., Komiyama, T., Zhu, H. & Luo, L. Representation of the glomerular olfactory map in the *Drosophila* brain. *Cell* **109**, 243–255 (2002).
11. Wong, A. M., Wang, J. W. & Axel, R. Spatial representation of the glomerular map in the *Drosophila* protocerebrum. *Cell* **109**, 229–241 (2002).
12. Jefferis, G. S. *et al.* Comprehensive maps of *Drosophila* higher olfactory centers: spatially segregated fruit and pheromone representation. *Cell* **128**, 1187–1203 (2007).
13. Datta, S. R. *et al.* The *Drosophila* pheromone cVA activates a sexually dimorphic neural circuit. *Nature* **452**, 473–477 (2008).
14. Stockinger, P., Kvitsiani, D., Rotkopf, S., Tirian, L. & Dickson, B. J. Neural circuitry that governs *Drosophila* male courtship behavior. *Cell* **121**, 795–807 (2005).
15. Manoli, D. S. *et al.* Male-specific *fruitless* specifies the neural substrates of *Drosophila* courtship behaviour. *Nature* **436**, 395–400 (2005).
16. Kimura, K., Ote, M., Tazawa, T. & Yamamoto, D. Fruitless specifies sexually dimorphic neural circuitry in the *Drosophila* brain. *Nature* **438**, 229–233 (2005).
17. Kimura, K., Hachiya, T., Koganezawa, M., Tazawa, T. & Yamamoto, D. Fruitless and doublesex coordinate to generate male-specific neurons that can initiate courtship. *Neuron* **59**, 759–769 (2008).
18. Ryner, L. C. *et al.* Control of male sexual behavior and sexual orientation in *Drosophila* by the *fruitless* gene. *Cell* **87**, 1079–1089 (1996).
19. Demir, E. & Dickson, B. J. *fruitless* specifies male courtship behavior in *Drosophila*. *Cell* **121**, 785–794 (2005).
20. Vrontou, E., Nilsen, S. P., Demir, E., Kravitz, E. A. & Dickson, B. J. *fruitless* regulates aggression and dominance in *Drosophila*. *Nature Neurosci.* **9**, 1469–1471 (2006).
21. Billeter, J. C. *et al.* Isoform-specific control of male neuronal differentiation and behavior in *Drosophila* by the *fruitless* gene. *Curr. Biol.* **16**, 1063–1076 (2006).
22. Chan, Y. B. & Kravitz, E. A. Specific subgroups of FruM neurons control sexually dimorphic patterns of aggression in *Drosophila melanogaster*. *Proc. Natl Acad. Sci. USA* **104**, 19577–19582 (2007).
23. Patterson, G. H. & Lippincott-Schwartz, J. A photoactivatable GFP for selective photolabeling of proteins and cells. *Science* **297**, 1873–1877 (2002).
24. Shaner, N. C., Patterson, G. H. & Davidson, M. W. Advances in fluorescent protein technology. *J. Cell Sci.* **120**, 4247–4260 (2007).
25. Kazama, H. & Wilson, R. I. Homeostatic matching and nonlinear amplification at identified central synapses. *Neuron* **58**, 401–413 (2008).
26. Schlieff, M. L. & Wilson, R. I. Olfactory processing and behavior downstream from highly selective receptor neurons. *Nature Neurosci.* **10**, 623–630 (2007).
27. Tian, L. *et al.* Imaging neural activity in worms, flies and mice with improved GCaMP calcium indicators. *Nature Methods* **6**, 875–881 (2009).
28. Dulac, C. & Kimchi, T. Neural mechanisms underlying sex-specific behaviors in vertebrates. *Curr. Opin. Neurobiol.* **17**, 675–683 (2007).
29. Clyne, J. D. & Miesenböck, G. Sex-specific control and tuning of the pattern generator for courtship song in *Drosophila*. *Cell* **133**, 354–363 (2008).

Supplementary Information is linked to the online version of the paper at www.nature.com/nature.

Acknowledgements We thank T. Jessell, C. Zuker and members of the Axel laboratory for discussion and comments on this manuscript; J. Flores for technical assistance; B. Dickson for reagents; P. Kisloff for assistance in the preparation of this manuscript; and M. Gutierrez and A. Nemes for general laboratory support. This work was funded in part by a grant from the Foundation for the National Institutes of Health through the Grand Challenges in Global Health Initiative. Further financial support was provided by the Helen Hay Whitney Foundation (V.R. and S.R.D.), the Burroughs Wellcome Fund (S.R.D.) and the Howard Hughes Medical Institute (R.A. and L.L.L.).

Author Contributions V.R., S.R.D., M.L.V. and R.A. conceived of the project and contributed to its progression. V.R. performed all the experiments, with the early participation of M.L.V. S.R.D. developed new photoactivatable fluorophores. L.L.L. developed GCaMP3. J.F. performed immunocytochemistry. R.A. provided guidance and wrote the paper with V.R., S.R.D., M.L.V. and L.L.L.

Author Information Reprints and permissions information is available at www.nature.com/reprints. The authors declare no competing financial interests. Readers are welcome to comment on the online version of this article at www.nature.com/nature. Correspondence and requests for materials should be addressed to R.A. (ra27@columbia.edu).

METHODS

Generation of C3PA-GFP and SPA-GFP. The optimized photoconvertible fluorophores C3PA-GFP and SPA-GFP were identified as part of a screen of mutations in the canonical photoconvertible fluorophore PA-GFP²³ with improved diffusional and folding properties. The screen (details of which are available from S.R.D.) included the analysis of previously described mutants of GFP for enhanced photoconversion in our system. C3PA-GFP incorporates three additional mutations (F99S, M153T and V163A) initially identified in the 'Cycle 3' mutant of GFP³⁰. V163A was originally incorporated into the first-generation PA-GFP molecule²³. SPA-GFP incorporates nine mutations (S30R, Y39N, A206V, M153T, Y145F, V163A, I171V, F99S and N105T) identified in the 'Superfolder' mutant of eGFP^{24,31}. The mutations in C3PA-GFP and SPA-GFP do not include the 'eGFP' mutations F64L and S65T, which disrupt the ability of PA-GFP to undergo photoconversion.

Fly stocks. The GH146-Gal4 and MZ19-Gal4 driver lines used to label PNs have been described previously^{10–12,32,33}. fru^{GAL4} (ref. 14) was a gift from B. Dickson. UAS-C3PA-GFP and UAS-SPA-GFP were generated by subcloning into pUAST. UAS-GCaMP3 (ref. 27) was generated by the insertion of *GCaMP3* cDNA into pUAST attB.

Imaging. We performed all imaging experiments on an Ultima two-photon laser scanning microscope (Prairie Technologies) equipped with galvanometers driving either a Coherent Chameleon XR or Chameleon Ultra II Ti:sapphire laser. Fluorescence was detected with either photomultiplier-tube or GaAsP photodiode (Hamamatsu) detectors. Images were acquired with either an Olympus 60× 0.9 numerical aperture or 1.1 numerical aperture objective at 512 pixels × 512 pixels resolution and 1-μm steps.

Labelling neurons through photoactivation. For photoactivation experiments we generated flies bearing fru^{GAL4} and two or three copies of UAS-C3PA-GFP or UAS-SPA-GFP. In some optical tracing experiments we used flies that contained one copy of UAS-C3PA-GFP and two copies of UAS-SPA-GFP. Although the basal fluorescence of C3PA-GFP is higher than that of SPA-GFP (Supplementary Fig. 1), the overall contrast of photoactivated neurons was essentially equivalent when the two fluorophores were used. C3PA-GFP and SPA-GFP were therefore often used interchangeably.

Photoactivation was performed on adult flies aged 12–24 h after eclosion. We initially imaged dissected brains at 925 nm (a wavelength at which photoconversion is relatively inefficient) to define two-dimensional or three-dimensional photoactivation masks of the appropriate neural targets using Prairie View software. We generated three-dimensional masks by defining a two-dimensional mask for each section of a z-series taken every 1–2 μm. Photoactivation of this masked volume was then achieved through two or three cycles of exposure to 710-nm laser light, a wavelength that more efficiently converts the fluorophore. We interposed a 'rest' period between each photoactivation cycle to allow diffusion of the photoconverted fluorophore into more distal neural processes and minimize photodamage. As a result of unavoidable variations in the orientation and optical accessibility of each brain, photoactivation powers and exposure times were determined empirically before each experiment for a single z-section of the masked target neuropil. Powers were typically between 5 and 30 mW (measured at the back aperture of the objective), depending most critically on the depth of the neural target. Exposure times were determined by adjusting the number of averaged images acquired for a given masked region.

We identified lateral horn neurons that receive functional input from DA1 PNs by first photoactivating the DA1 glomerulus as described previously¹³ to reveal the DA1 PN axonal arborization. We then manually defined a three-dimensional mask circumscribing the photoactivated DA1 axon terminals in the lateral horn in Prairie View (Prairie Technologies). The mask included an additional approximately 1 μm around the perimeter of photoactivated axon terminals to ensure more intense exposure of postsynaptic processes to photoconverting light. Photoconversion was achieved by exposing the masked volume in the lateral horn to two or three photoactivation cycles (30-s intervals, 30–60 rounds per cycle).

Direct photoactivation of individual lateral horn clusters, including DC1, was achieved through the irradiation of a small volume (typically about 2–5 μm on each axis) centred on the fasciculated processes that lead to the cell bodies. This masked volume was then subject to two or three photoactivation cycles (5–10-s intervals, 90–120 rounds per cycle). We used the same photoactivation protocol for labelling single neurons except that the photoactivation mask was defined for a single z-plane centred on the cell body.

We identified neurons with processes that interdigitate with DC1 axons by first directly photoactivating the DC1 cluster as described above. This initial photoactivation labelled DC1 axons innervating the lateral triangle and SMP tract. We then defined a photoactivation mask around the DC1 axon terminals in the lateral triangle to label neurons whose processes lie in close anatomical proximity. DC1 boutons are small and spatially distributed within the lateral triangle and SMP tract. We defined this photoactivation mask as the minimum volume encompassing

all the DC1 boutons within the lateral triangle. Consequently, we photoactivated a somewhat larger volume of neuropil than if we had defined separate masks for each individual DC1 bouton. Photoconversion was achieved by exposing the masked volume in the lateral triangle to two or three photoactivation cycles (30-s intervals, 30–60 rounds per cycle). Other photoactivation experiments reveal that most neurons that innervate the SMP tract seem to have terminals in the lateral triangle (data not shown). In accord with this observation, we label a qualitatively similar set of neurons when we restrict our photoactivation to DC1 axon terminals in the SMP tract rather than the lateral triangle.

We labelled all Fru+ descending neurons in a preparation in which we dissected the entire central nervous system of the fly, paying particular attention to preserving the cervical connectives that link the brain to the ventral nerve cord. We then defined a photoactivation mask encompassing the full width and depth of the cervical connectives and about 30–50 μm in length. The masked cervical connectives were then subject to two or three photoactivation cycles (30-s intervals, 60–90 rounds per cycle).

Image processing. Maximum-intensity z-projections of z-stacks were generated in ImageJ (NIH) or Imaris (Bitplane). We masked images of photoactivated single neurons and individual neural clusters in Imaris or Adobe Photoshop to permit a clearer visualization of projection patterns. This procedure removed weak background fluorescence arising primarily from cell bodies and (less frequently) the processes of non-photoactivated neurons that would otherwise obscure photoactivated projection patterns in maximum-intensity z-projections. We emphasize that we did not mask images of photoactivated neuropils (lateral horn and lateral triangle and SMP tract; Figs 1a–c and 3b) and descending neurons (Fig. 3d) in which we examined collections of neurons labelled by virtue of their projections into the photoactivation target. In addition, we did not mask images in which we compared the fluorescent signal of different photoactivatable fluorophores (Supplementary Fig. 1). The contrast between photoactivated and background fluorescence, evident in unmasked images, was generally high, thus minimizing the risk that we lost substantive information in the masking process.

Electrophysiology. Electrophysiological recordings were performed on flies 12–48 h after eclosion. Cell bodies were targeted for patch recording by their fluorescence from CD8-GFP or, in some cases, C3PA-PAGFP that was minimally photoactivated to weakly label soma above the background fluorescence. We obtained similar response profiles for neurons expressing either fluorophore.

The PNs that innervate the DA1 glomerulus reside in two clusters of cell bodies that surround the antennal lobe. The cell bodies of Fru+ cholinergic DA1 PNs are characteristically positioned lateral to the antennal lobe, whereas the cell bodies of Fru– DA1 PNs lie ventral to the antennal lobe. A third cluster of PNs frames the dorsal aspect of the antennal lobe but contains no DA1 PNs. We used the stereotyped position of the PN cell bodies relative to the antennal lobe to target these neurons in Gal4 lines that label more than one glomerulus. DA1 PNs are the only lateral PNs labelled in MZ19-Gal4 and fru^{GAL4} lines. We identified VA1d PNs as soma labelled by MZ19-Gal4 that reside in the dorsal PN cluster. Similarly, we identified VA1lm PNs as soma labelled by fru^{GAL4} that reside in the dorsal PN cluster. GH146-Gal4 labels about 60% of PNs that innervate about 35 glomeruli^{10–12}. We recorded from random PNs that innervate glomeruli other than DA1 by targeting GH146+ PNs in the dorsal PN cluster.

DC1 neurons were targeted for recording in fru^{GAL4} flies. DC1 somata are readily identified even without photactivation by their characteristic position and fasciculated projections in the lateral horn. We did not record from DC1 neurons in flies in which the DC1 cluster was not well separated from neighbouring lateral horn clusters.

The DN1 cell body is positioned at the midline in the ventral portion of the posterior brain. Unfortunately it was not possible to distinguish this neuron unequivocally from a pair of neighbouring Fru+ neurons by anatomy alone. However, we could differentiate DN1 on the basis of intrinsic membrane properties: intracellular recordings reveal that somatic current injection in DN1 elicits action potentials that have a characteristically lower amplitude (about 10–12 mV) than observed for either of the pair of neighbouring neurons (more than 20–30 mV). Nevertheless, after all recordings of DN1 were completed, we filled the neuron (by electroporation of Texas Red dextran) to confirm its distinct projection pattern in the lateral triangle and SMP tract.

We recorded odour-evoked responses from neurons within the cVA circuit in an intact fly preparation performed essentially as described previously¹³. Flies were immobilized beneath a thin acrylic partition. The angle of the head beneath the partition was adjusted to permit access to DA1 PNs and DC1 neurons on the anterior side of the brain or descending neurons on the posterior side of the brain. Either the anterior or posterior side of the brain was exposed by removal of the overlying cuticle with fine forceps; the fly otherwise remained fully intact. The response of neurons to direct stimulation of glomeruli was recorded in an explant preparation in which the brain was dissected from the head capsule, cleaned of

attached tracheal fibres and pinned with fine tungsten wires onto a thin sheet of Sylgard. In both preparations, the perineural sheath was weakened by treatment with 1–2 mg ml⁻¹ collagenase for 1–2 min. The exposed neuropil was then continuously perfused (about 2–3 ml min⁻¹) with external saline (108 mM NaCl, 5 mM KCl, 2 mM CaCl₂, 8.2 mM MgCl₂, 26 mM NaHCO₃, 1 mM NaH₂PO₄, 5 mM trehalose, 5 mM sucrose, 5 mM HEPES, osmolality adjusted to 275 mosM). The external saline was continuously bubbled with 95% O₂/5% CO₂ and reached a final pH of 7.3.

We performed loose patch recordings on PNs and DC1 neurons by using glass electrodes (7–9 MΩ) filled with external saline and connected to a patch-clamp amplifier (Axon MulticlampB; Axon Instruments) in voltage-clamp mode held at the zero-current potential. Loose patch recordings were obtained by gentle suction to form seals of 40–90 MΩ. Data were band-pass filtered at 100–400 Hz and digitized at 10 kHz. Spikes were detected by the application of a threshold function in Clampfit (Molecular Devices) or by applying a continuous wavelet transform to the raw data in a custom program written in MATLAB (Mathworks). Because of the small size of DC1 cell bodies (diameter 3–4 μm), it was not always possible to maintain loose patch seals for multiple trials of each stimulus. Each measurement is therefore the average of one to three trials per cell.

Intracellular recordings of DN1 were performed with patch electrodes (15–18 MΩ) filled with internal saline (130 mM potassium aspartate, 8 mM KCl, 0.2 mM MgCl₂, 5 mM sucrose, 10 mM HEPES pH 7.3, 10 mM EGTA). Recordings were terminated if R_{input} was less than 250 MΩ. In some recordings, we injected hyperpolarizing current (less than 15 pA) to bring the soma to a resting potential of –50 to –55 mV and compensate for leak conductance. Responses of DN1 under these conditions were similar to those observed by loose patch recording. Voltage traces were acquired in current-clamp mode, digitized at 10 kHz and filtered at 5 kHz.

Functional imaging. Optical imaging experiments were performed in flies that contained one copy of *fru*^{GAL4} driving expression from two or three copies of the UAS-GCaMP3 transgene. Fly brains were dissected and imaged in a modified external saline containing 1–2 mM MgCl₂, a condition that we found enhances fluorescence changes reported by GCaMP3 but largely maintains the specificity of glomerular stimulation (data not shown). Images were acquired at 925 nm at 2 Hz. We recorded four trials of fluorescence changes elicited in response to glomerular stimulation for each lateral horn cluster. We averaged these trials and then calculated the normalized changes in fluorescence intensity as $\Delta F/F = 100(F_n - F_0)/F_0$, where F_n is the fluorescence of the n th frame and F_0 is the average baseline fluorescence of the eight frames before stimulation.

Odour stimulation. Odour stimulation was achieved by directing a continuous stream (about 300 ml min⁻¹) of ultrapure-grade air through a 2-mm diameter glass tube directed at the fly's antenna. At a trigger, a solenoid valve controller system (Parker Hannifin Corporation), redirected the air stream from a blank cartridge to one containing various dilutions of cVA or an odorant mix. cVA (Pherobank) or odorants were diluted in paraffin oil (Fluka). The odorant mix consisted of a 1:1,000 dilution of each of ten odorants (benzaldehyde, cyclohexanol, geranyl acetate, 2-heptanone, hexan-1-ol, ethyl 3-hydroxybutyrate, 3-methylbutan-1-yl acetate, octan-3-one, methyl salicylate and propionic acid). Each odour cartridge was made by placing 10 μl of the odour stimulus on filter paper and inserting it into a 10-ml glass vial.

Single glomerular stimulation. Glass stimulating electrodes were pulled to a resistance of 7–8 MΩ when filled with 2 mM acetylcholine (Sigma) in external saline. Stimulating electrodes were positioned into the centre of superficial glomeruli viewed under IR-DIC optics. Although we can observe the boundaries of glomeruli under these conditions, we lack the optical depth and clarity necessary to identify stimulated glomeruli unequivocally in this preparation. This problem is compounded by differences in orientation of the antennal lobe from animal to animal. However, glomeruli marked by *fru*^{GAL4} (DA1, VA1Im and VL2a) or MZ19-Gal4 (DA1 and VA1d) could be identified. We note that the *Fru*⁺ VL2a glomerulus is not sufficiently superficial to be effectively impaled with a stimulating electrode in our preparation; it was therefore not tested. Square current pulses (200 or 500 ms long) generated by a Grass stimulator were applied to excite the impaled glomerulus. PNs are probably depolarized through a combination of electrical and chemical excitation, because stimulation with saline alone elicits action potentials, although at lower frequency than in the presence of neurotransmitter.

We examined the specificity of glomerular stimulation by comparing the responses evoked in cognate and non-cognate PNs (Fig. 2b). We first recorded the response of a genetically marked PN to stimulation of its cognate glomerulus over a range of voltages to establish a baseline response. Without moving the stimulating electrode we then recorded from a non-cognate PN innervating a different

glomerulus. This non-cognate PN was stimulated at increasing voltages until action potentials were evoked. In rare cases, if no response could be elicited by even strong stimulation (10 V) of the non-cognate glomerulus, the recording was terminated. In this way a lack of response could never be ascribed to inadequate formation of a loose patch seal.

We examined the specificity with which DC1 neurons respond to stimulation of different glomeruli by first recording the response of a DC1 neuron to DA1 stimulation over a range of voltages (Fig. 2e). We then repositioned the stimulating electrode into other superficial glomeruli located throughout the antennal lobe, usually beginning with the neighbouring VA1d and VA1Im glomeruli. Given that fewer than about ten DA1 action potentials are required to bring a DC1 neuron to threshold (Fig. 2g), we expect that even weak stimulation of any single glomerulus should be sufficient to elicit a suprathreshold response in a DC1 neuron. Nevertheless, to account for intrinsic differences in the levels of glomerular excitation evoked by iontophoresis of acetylcholine (Fig. 2b), we stimulated other glomeruli at higher voltages (4 V). At the end of all experiments we recorded the response of the DC1 neuron to stimulation of the DA1 glomerulus again, to ensure that there was no loss in responsiveness over time.

Two-photon laser-mediated microlesioning. DC1 processes form a tightly fasciculated bundle as they exit from the lateral horn, allowing us to sever most of these processes with a relatively small lesion. We initially observed DC1 neurons expressing either GCaMP3 of CD8-GFP at 925 nm. We defined a lesion target (about 2 μm × 3 μm) in a single z plane at high zoom (×8) centred on the DC1 processes proximal to where they bifurcate and innervate the lateral triangle. We then applied one to four pulses of intense 800-nm light (75–90 mW at the back aperture) until we first observed the formation of a small transient cavitation bubble. Under these conditions, DC1 processes are acutely and completely severed as revealed by their physical discontinuity and the loss of DC1 cell body responses to DA1 stimulation.

We examined the requirement of the DC1 cluster to mediate the response of DN1 elicited by DA1 stimulation, by initially establishing intracellular recordings of DN1. We then recorded the average membrane potential changes evoked by DA1 stimulation (five trials) with the circuit intact to establish a baseline. We then lesioned the DC1 processes. Microlesioning of DC1 neurons affects neither the input resistance nor the action potential threshold of DN1, suggesting that the microlesioning process does not affect the intrinsic excitability of the neuron. After microlesioning we typically waited for 5–10 min (and up to 25 min) to record the average responses (five trials) of DN1 to DA1 stimulation to ensure that we were not confounded by reversible changes in responsiveness.

Labelling neurons through electroporation of dye. Dye filling of both glomeruli and single neurons was accomplished through electroporation of highly concentrated (100 mg ml⁻¹) 3,000-Da Texas Red dextran (Invitrogen). Pulled glass electrodes were back-filled with the dextran dye and then connected to the output of a stimulator (Grass). We then positioned the dye-filled electrode in the centre of a single glomerulus or adjacent to a single cell body. Voltage pulses (20–30-V pulses, 5 ms, 1 Hz) were applied until the dye became visible in distal neural processes.

Immunocytochemistry and characterization of DC1 neurotransmitter. Brains were fixed in 4% paraformaldehyde for 30 min and then incubated for 24 h at 4 °C in one or more of the following: nc82 antibody (Developmental Studies Hybridoma Bank) at 1:10 dilution, anti-GABA antibody (Sigma) at 1:500 dilution, anti-choline acetyltransferase antibody (Developmental Studies Hybridoma Bank) at 1:100 dilution, anti-vesicular glutamate transporter antibody (a gift from A. DiAntonio) at 1:5,000 dilution, anti-tyrosine hydroxylase antibody (Millipore) at 1:500 dilution or anti-serotonin antibody (Sigma) at 1:500 dilution. Brains were then washed and incubated in secondary antibody (Alexa Fluor 546 or Alexa Fluor 633 anti-mouse or anti-rabbit (Invitrogen) at 1:500 dilution) for 2 h at 22 °C. The samples were mounted in Vectashield (Vector Laboratories) before being imaged on a Zeiss 510 confocal microscope.

- Cramer, A., Whitehorn, E. A., Tate, E. & Stemmer, W. P. Improved green fluorescent protein by molecular evolution using DNA shuffling. *Nature Biotechnol.* **14**, 315–331 (1996).
- Pedelacq, J. D., Cabantous, S., Tran, T., Terwilliger, T. C. & Waldo, G. S. Engineering and characterization of a superfolder green fluorescent protein. *Nature Biotechnol.* **24**, 79–88 (2006).
- Stocker, R. F., Heimbeck, G., Gendre, N. & de Belle, J. S. Neuroblast ablation in *Drosophila* P[GAL4] lines reveals origins of olfactory interneurons. *J. Neurobiol.* **32**, 443–456 (1997).
- Ito, K. *et al.* The organization of extrinsic neurons and their implications in the functional roles of the mushroom bodies in *Drosophila melanogaster* Meigen. *Learn. Mem.* **5**, 52–77 (1998).

Lkb1 regulates quiescence and metabolic homeostasis of haematopoietic stem cells

Boyi Gan^{1,2,3}, Jian Hu^{1,2,3}, Shan Jiang^{1,2,3}, Yingchun Liu^{1,2,3}, Ergün Sahin^{1,2,3}, Li Zhuang^{1,2,3}, Eliot Fletcher-Sananikone^{1,2,3}, Simona Colla^{1,2,3}, Y. Alan Wang^{1,2,3}, Lynda Chin^{1,2,4} & Ronald A. DePinho^{1,2,3}

The capacity to fine-tune cellular bioenergetics with the demands of stem-cell maintenance and regeneration is central to normal development and ageing, and to organismal survival during periods of acute stress. How energy metabolism and stem-cell homeostatic processes are coordinated is not well understood. Lkb1 acts as an evolutionarily conserved regulator of cellular energy metabolism in eukaryotic cells and functions as the major upstream kinase to phosphorylate AMP-activated protein kinase (AMPK) and 12 other AMPK-related kinases^{1–3}. Whether Lkb1 regulates stem-cell maintenance remains unknown. Here we show that Lkb1 has an essential role in haematopoietic stem cell (HSC) homeostasis. We demonstrate that ablation of *Lkb1* in adult mice results in severe pancytopenia and subsequent lethality. Loss of *Lkb1* leads to impaired survival and escape from quiescence of HSCs, resulting in exhaustion of the HSC pool and a marked reduction of HSC repopulating potential *in vivo*. *Lkb1* deletion has an impact on cell proliferation in HSCs, but not on more committed compartments, pointing to context-specific functions for Lkb1 in haematopoiesis. The adverse impact of *Lkb1* deletion on haematopoiesis was predominantly cell-autonomous and mTOR complex 1 (mTORC1)-independent, and involves multiple mechanisms converging on mitochondrial apoptosis and possibly downregulation of PGC-1 coactivators and their transcriptional network, which have critical roles in mitochondrial biogenesis and function. Thus, Lkb1 serves as an essential regulator of HSCs and haematopoiesis, and more generally, points to the critical importance of coupling energy metabolism and stem-cell homeostasis.

HSCs function to replenish the blood system and maintain haematopoietic homeostasis in response to either physiological or imposed stress demands^{4–6}. To explore the role of Lkb1 in various aspects of HSC biology, we assessed the impact of somatic deletion of *Lkb1* in the mouse adult haematopoietic system using *Rosa26-creERT2* deleter mice⁷. In this model, the treatment of adult mice with tamoxifen results in complete deletion of *Lkb1* in haematopoietic organs (Supplementary Fig. 1a) and associated reductions of phosphorylation of AMPK Thr 172 and AMPK substrate acetyl-CoA carboxylase (ACC) Ser 79 (Supplementary Fig. 1b). Notably, within 30 days post completing tamoxifen injection (d.p.i.), all tamoxifen-treated *Lkb1*^{L/L}; *Rosa26-creERT2* mice (hereafter referred to as *Lkb1* knockout) exhibited constitutional signs of weight loss (Supplementary Fig. 2a), lethargy, hunched posture and ultimately death (Fig. 1a); in contrast, tamoxifen-treated *Lkb1*^{+/+}; *Rosa26-creERT2* or *Lkb1*^{L/L} mice (collectively referred to as *Lkb1* wild-type hereafter) remained viable and healthy (Fig. 1a).

Somatic deletion of *Lkb1* led to pancytopenia within 1 week after tamoxifen treatment (7 d.p.i.), as shown by reduced weight of spleen and thymus, and reduction of the absolute cell number of bone marrow, spleen and thymus (Supplementary Fig. 2b–f). *Lkb1* knockout mice also developed acute anaemia as shown by a marked decline in red blood cell, haemoglobin and haematocrit counts (Supplementary Figs 2g–i).

Although anaemic, *Lkb1* knockout mice had increased non-fasting blood glucose levels (Supplementary Fig. 3), making it unlikely that the *Lkb1* knockout anaemia phenotype derives from a profound systemic deficiency in glucose availability. Further analysis revealed severe reductions in *Lkb1* knockout Ter119⁺ cells and erythroid progenitors at all developmental stages (Fig. 1b and Supplementary Fig. 4a, b). Consistent with the pancytopenia phenotype described above, we observed a decline of all haematopoietic lineages examined in the *Lkb1* knockout mice, including platelets (Supplementary Fig. 4c), Gr-1⁺/Mac-1⁺ cells (Fig. 1c and Supplementary Fig. 4d), B cells (Fig. 1d and Supplementary Fig. 4e) and T cells (Supplementary Fig. 4f). To study the underlying mechanism of the multi-lineage defects

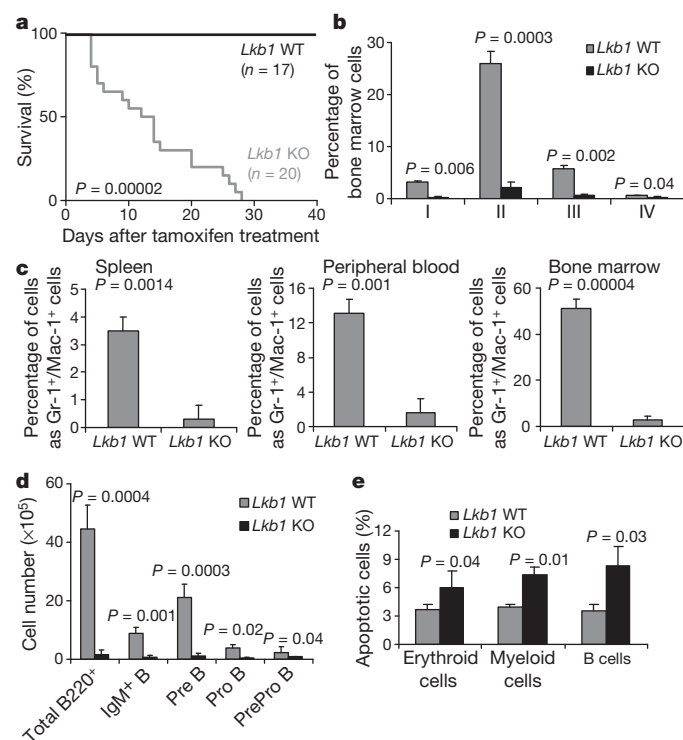


Figure 1 | *Lkb1* deletion leads to a severe pancytopenia phenotype.

a, Kaplan–Meier survival analysis of *Lkb1* wild-type (WT) and knockout (KO) mice. **b**, **c**, The percentage of erythroid lineage from bone marrow (**b**) and Mac-1⁺/Gr-1⁺ cells (**c**) in *Lkb1* wild-type and knockout mice at 5 d.p.i. Erythroid cells at different developmental stages include proerythroblasts (population I, Ter119^{med}CD71^{hi}), basophilic erythroblasts (population II, Ter119^{hi}CD71^{hi}) and late erythroblasts (populations III–IV, Ter119^{hi}CD71^{med} and Ter119^{hi}CD71^{lo}). **d**, The number of bone marrow B-cell lineage at 7 d.p.i. from *Lkb1* wild-type and knockout mice. **e**, The percentage of apoptotic cells in erythroid, myeloid and B cells of *Lkb1* wild-type and knockout bone marrow cells at 3 d.p.i. $n > 3$ (**b**–**e**). Error bars in **b**–**e** represent mean \pm s.d.

¹Belfer Institute for Applied Cancer Science, Dana-Farber Cancer Institute, Boston, Massachusetts 02115, USA. ²Department of Medical Oncology, Dana-Farber Cancer Institute, Boston, Massachusetts 02115, USA. ³Department of Medicine and Genetics, Harvard Medical School, Boston, Massachusetts 02115, USA. ⁴Department of Dermatology, Harvard Medical School, Boston, Massachusetts 02115, USA.

associated with *Lkb1* deletion, we examined the cell survival status of various lineages in *Lkb1* wild-type and knockout mice given the important role of Lkb1 in the maintenance of cell survival under energy stress in other cellular contexts^{8,9}. Indeed, we observed an increase of cleaved caspase-3 in *Lkb1* knockout bone marrow, spleen and thymus samples (Supplementary Fig. 5). Further annexin-V/7-aminoactinomycin D (7AAD) analysis revealed increased apoptosis in myeloid, erythroid and B-cell populations in *Lkb1* knockout bone marrow cells (Fig. 1e). In summary, *Lkb1* deficiency leads to a severe pancytopenia phenotype and impairs the cell survival of multiple lineages.

Next we examined HSC and haematopoietic progenitor populations in *Lkb1* knockout mice. Compared with wild-type controls, serial analysis of *Lkb1* knockout HSC-enriched LSK cells (Lin^- , Sca-1^+ , c-Kit^+) and long-term HSCs (LT-HSCs; $\text{CD34}^-\text{Flt-3}^-$ LSK cells) in bone marrow showed an acute increase at 1 d.p.i., but a subsequent decrease in numbers from 4 d.p.i. and thereafter (Fig. 2a, b). A 5-bromodeoxyuridine (BrdU) labelling experiment revealed a significantly increased percentage of BrdU-positive cells in *Lkb1* knockout LSK cells (Fig. 2c and Supplementary Fig. 6a, b). Notably, *Lkb1* deletion increased cell proliferation only in LSK and LSK CD34^- cells, but not whole bone marrow and mature lineage cells (Fig. 2c), indicating an HSC-specific role for Lkb1 in the regulation of cell quiescence. The more pronounced function of Lkb1 in the HSC compartment also aligns well with its more prominent expression levels in HSCs relative to other more committed compartments (Supplementary Fig. 6c, d). Furthermore, annexin-V/7AAD staining of the LSK population showed increased apoptosis in *Lkb1* knockout LSK cells (Supplementary Fig. 6e, f). Together, our results indicate that Lkb1 functions to maintain HSC quiescence and survival and that *Lkb1* inactivation leads to transient expansion, yet subsequent decline, of bone marrow HSCs.

We next performed competitive and non-competitive transplantation assays to examine the impact of *Lkb1* deficiency on HSC repopulating capability *in vivo* (Supplementary Fig. 7a, b). In the competitive transplantation experiments, we observed that *Lkb1* knockout transplants showed markedly diminished repopulating capability relative to wild-type controls (Fig. 2d and Supplementary Fig. 8a–c). In the non-competitive experiments, all recipient mice reconstituted with *Lkb1*^{L/L}; *Rosa26-creERT2* bone marrow cells died within 60 d.p.i. (Supplementary Fig. 8d) with anaemia, pancytopenia defects (data not shown) and increased HSC cell-cycle entry and subsequent decline (Supplementary Fig. 8e, f). These data collectively indicate that Lkb1 exerts a predominant cell-autonomous impact on haematopoietic repopulating potential and homeostasis.

To understand the mechanisms underlying Lkb1-directed regulation of HSC homeostasis, we assessed the impact of pharmacological inhibition of mTORC1 signalling on the *Lkb1* knockout phenotype, given that mTORC1 serves as a key downstream surrogate of Lkb1–AMPK signalling³ and also has critical roles in the regulation of HSC

homeostasis^{10–14}. Daily rapamycin or vehicle protocols were initiated to *Lkb1* or *Tsc1* wild-type and knockout mice at the time of tamoxifen treatment¹². Rapamycin treatment significantly rescued multi-lineage defects, HSC cycling increase and expansion phenotypes in *Tsc1* knockout mice, but had minimal effect on these phenotypes in *Lkb1* knockout mice (Fig. 3a–c) despite confirmation of abolished S6 phosphorylation in sorted bone marrow B220^+ cells, Mac1^+ cells and CD34^- LSK cells from *Lkb1* knockout mice (Supplementary Fig. 9). Thus, unlike *Tsc1*, Lkb1 regulates haematopoiesis via an mTORC1-independent pathway. Finally, administration of metformin, a known AMPK activator, did not rescue bone marrow/thymus cellularity decline, LSK transient expansion/subsequent depletion phenotype and lineage defects in *Lkb1* knockout mice (Supplementary Fig. 10). These data, together with AMPK activator A-769662 treatment data from ref. 15 and AMPK knockout mice analyses from ref. 16, indicate that either multiple AMPK-related kinases (including AMPK) co-operatively mediate Lkb1 function in HSC homeostasis or that non-AMPK-dependent processes are operative.

The above observations prompted us to carry out transcriptome analysis of sorted LSK cells from *Lkb1* wild-type and knockout bone marrow at 1 d.p.i. to gain further mechanistic insight of Lkb1 regulation of HSC homeostasis (Supplementary Fig. 11a). Ingenuity pathway analysis of 570 significantly differentially expressed genes revealed significant enrichment of genes involved in G1/S cell-cycle checkpoint regulation (Supplementary Fig. 11b and Supplementary Table 1) including upregulation of cyclin D1, cyclin D2, cyclin E1, Cdc25A, E2F1, Cdk4 and Skp2, which would serve to synergistically promote cell cycling of *Lkb1* knockout LSK cells. Most notably, there was prominent representation of LXR/RXR, VDR/RXR and PPAR metabolism pathways (Supplementary Fig. 11b). To identify key networks regulated by Lkb1 in a Tsc–mTORC1-independent manner, we further conducted comparative analysis of *Lkb1* and *Tsc1* (ref. 12) HSC transcriptome data sets (Supplementary Fig. 11a), which revealed that, although G1/S cell-cycle checkpoint was enriched in both data sets, the LXR/RXR, VDR/RXR and PPAR metabolism pathways were distinctively enriched in the *Lkb1* transcriptome data set (Supplementary Fig. 11c). In addition, promoter analysis of the *Lkb1* HSC transcriptome data set identified E2F, nuclear respiratory factor 1 (Nrf1) and PPAR- γ motifs as the most significantly enriched promoter binding elements in the *Lkb1* LSK transcriptome data set (1.4 \times , 2.1 \times and 1.4 \times , respectively). The link to PPAR- γ and Nrf1 is notable given that the peroxisome proliferator-activated receptor-coactivators PGC-1 α and PGC-1 β are the principal transcriptional coactivators for PPAR- γ and Nrf1 (ref. 17), and that the PGC-1s are regulated by Lkb1 (ref. 18).

Prompted by this observation, we next investigated whether deletion of *Lkb1* has an impact on PGC-1—a master transcriptional regulator of mitochondrial biogenesis¹⁹—and its associated biological processes in the haematopoietic system. We found that the expression levels of both PGC-1 α and PGC-1 β were downregulated in *Lkb1*

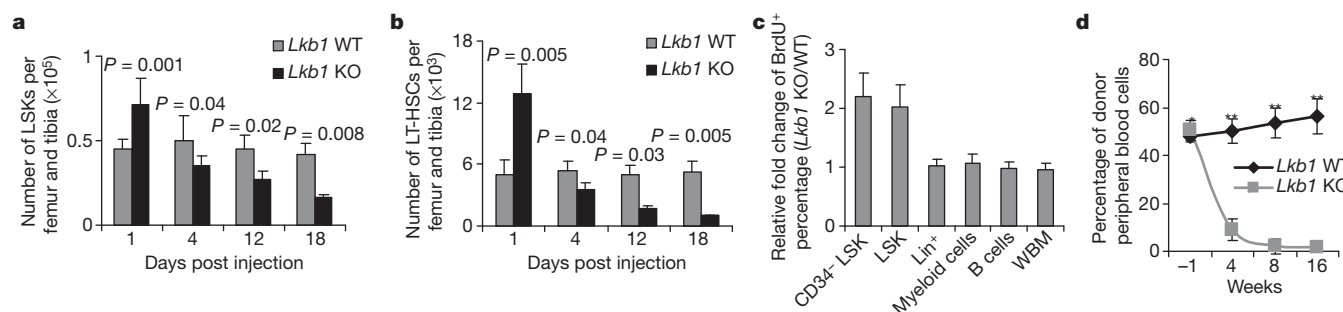


Figure 2 | *Lkb1* ablation results in reduced HSC reserves and decreased repopulating potential. **a, b**, The numbers of LSK cells (**a**) and LT-HSCs (**b**) at various days post infection in *Lkb1* wild-type and knockout bone marrow. **c**, The relative fold change (*Lkb1* knockout/wild type) of the percentage of BrdU⁺ cells from various haematopoietic cell lineages in *Lkb1* wild-type and

knockout bone marrow at 1 d.p.i.; $n \geq 3$ at each time point (**a–c**). **d**, The percentage of donor-derived cells in peripheral blood by CD45 staining in 1:1 competitive transplantation. $n = 15$. * $P > 0.4$; ** $P < 0.01$. All error bars represent mean \pm s.d.

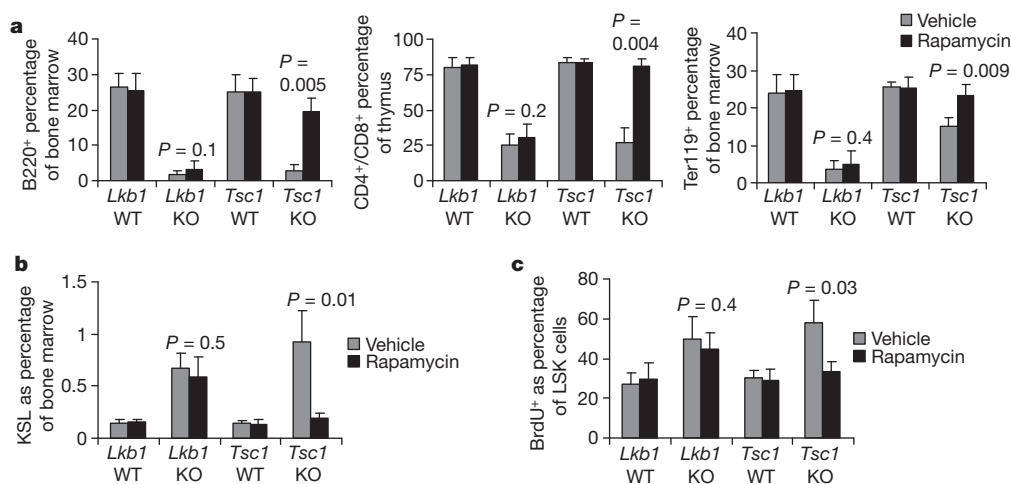


Figure 3 | *Lkb1* regulation of haematopoiesis is Tsc-mTORC1-independent. **a–c**, The percentage of B220⁺ and Ter119⁺ populations in bone marrow and thymic CD4⁺/CD8⁺ cells (**a**), bone marrow LSK cells (**b**) and

knockout LSK cells (Fig. 4a), which coincided with decreased mitochondrial membrane potential and DNA content in *Lkb1* knockout LSK cells at 4 d.p.i. (Fig. 4b, c). Interestingly, we observed increased mitochondrial DNA content in *Lkb1* knockout LSK cells at a later time point (10 d.p.i.), possibly reflecting compensatory (secondary) effects that occur in the wake of mitochondriopathy (Fig. 4c). Finally, we found that the basal ATP levels in spleen and thymus were profoundly decreased in *Lkb1* knockout mice (Fig. 4d). Although our data raise the possibility that *Lkb1* deficiency and associated dysregulation of PGC-1 impair mitochondrial function, the presence of apoptosis in these *Lkb1*^{-/-} HSCs does not allow us to exclude the possibility that mitochondrial dysfunction reflects, in part, an ongoing apoptotic process caused by *Lkb1* deletion.

Our results reveal an essential role of *Lkb1* in the maintenance of HSC homeostasis. Somatic deletion of *Lkb1* in the haematopoietic system impairs HSC quiescence and survival and leads to metabolic catastrophe, resulting in pancytopenia and rapid animal death.

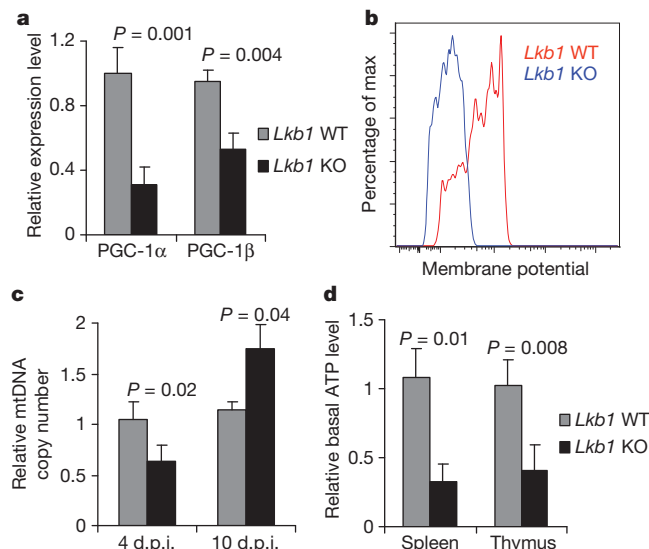


Figure 4 | *Lkb1* deletion diminishes mitochondrial biogenesis and energy production in the haematopoietic system. **a–c**, The relative expression level of PGC-1α/β at 2 d.p.i. (**a**), the mitochondrial membrane potential at 4 d.p.i. (**b**), and the relative mitochondria DNA copy number at 4 and 10 d.p.i. (**c**) of *Lkb1* wild-type and knockout bone marrow LSK cells. **d**, The relative basal ATP levels in spleen and thymus from *Lkb1* wild-type and knockout mice at 4 d.p.i. *n* = 3 (**a–d**). Error bars in **a**, **c**, **d** represent mean + s.d.

BrdU⁺ bone marrow LSK cells (**c**) from the mice indicated. *n* = 3 (**a–c**). All error bars represent mean + s.d.

Mechanistically, we propose that *Lkb1* maintains HSC homeostasis through multiple mechanisms governing mitochondrial function, cell survival and cell-cycle regulation via *Lkb1* regulation of AMPK and other AMPK-related kinases and their downstream effectors (including PGC-1). Our findings align with those of two accompanying papers^{15,16} and provide a broad framework to understand the integration of energy signalling and mitochondrial physiology in the maintenance of HSC homeostasis.

METHODS SUMMARY

The *Lkb1*^{L/L} mice were described previously²⁰. *Rosa26-creERT2* mice were provided by A. Berns⁷. *Lkb1*^{L/+}; *Rosa26-creERT2*⁺ mice were backcrossed six generations into a C57BL/Ka-CD45.2:Thy-1.1 background, which were then intercrossed to generate mice of the desired genotypes. Recipients in transplantation assays were adult C57BL/Ka-CD45.1:Thy-1.2 mice (Jackson Laboratory). Tamoxifen treatment, phenotypic analyses of mice, rapamycin administration, flow cytometric analysis and transplantation assays were performed as previously described¹². All animal manipulations were performed with Harvard/DFCI's Institutional Animal Care and Use Committee (IACUC) approval. For microarray analysis, the RNA from sorted LSK cells (10,000–20,000) was extracted and the cDNA was analysed on the Affymetrix 430 2.0 platform. Quantitative real-time PCR was performed on the Stratagene Mx3000P using the Quantitative SYBR green PCR kit.

Full Methods and any associated references are available in the online version of the paper at www.nature.com/nature.

Received 24 April; accepted 19 October 2010.

- Alessi, D. R., Sakamoto, K. & Bayascas, J. R. LKB1-dependent signaling pathways. *Annu. Rev. Biochem.* **75**, 137–163 (2006).
- Hardie, D. G. AMP-activated/SNF1 protein kinases: conserved guardians of cellular energy. *Nature Rev. Mol. Cell Biol.* **8**, 774–785 (2007).
- Shackelford, D. B. & Shaw, R. J. The LKB1-AMPK pathway: metabolism and growth control in tumour suppression. *Nature Rev. Cancer* **9**, 563–575 (2009).
- Adams, G. B. & Scadden, D. T. The hematopoietic stem cell in its place. *Nature Immunol.* **7**, 333–337 (2006).
- Moore, K. A. & Lemischka, I. R. Stem cells and their niches. *Science* **311**, 1880–1885 (2006).
- Orkin, S. H. & Zon, L. I. Hematopoiesis: an evolving paradigm for stem cell biology. *Cell* **132**, 631–644 (2008).
- Vooijs, M., Jonkers, J. & Berns, A. A highly efficient ligand-regulated Cre recombinase mouse line shows that LoxP recombination is position dependent. *EMBO Rep.* **2**, 292–297 (2001).
- Shaw, R. J. et al. The tumor suppressor LKB1 kinase directly activates AMP-activated kinase and regulates apoptosis in response to energy stress. *Proc. Natl Acad. Sci. USA* **101**, 3329–3335 (2004).
- Corradetti, M. N., Inoki, K., Bardeesy, N., DePinho, R. A. & Guan, K. L. Regulation of the TSC pathway by LKB1: evidence of a molecular link between tuberous sclerosis complex and Peutz-Jeghers syndrome. *Genes Dev.* **18**, 1533–1538 (2004).
- Chen, C. et al. TSC-mTOR maintains quiescence and function of hematopoietic stem cells by repressing mitochondrial biogenesis and reactive oxygen species. *J. Exp. Med.* **205**, 2397–2408 (2008).

11. Gan, B. & DePinho, R. A. mTORC1 signaling governs hematopoietic stem cell quiescence. *Cell Cycle* **8**, 1003–1006 (2009).
12. Gan, B. *et al.* mTORC1-dependent and -independent regulation of stem cell renewal, differentiation, and mobilization. *Proc. Natl Acad. Sci. USA* **105**, 19384–19389 (2008).
13. Ito, K., Bernardi, R. & Pandolfi, P. P. A novel signaling network as a critical rheostat for the biology and maintenance of the normal stem cell and the cancer-initiating cell. *Curr. Opin. Genet. Dev.* **19**, 51–59 (2009).
14. Yilmaz, O. H. *et al.* Pten dependence distinguishes haematopoietic stem cells from leukaemia-initiating cells. *Nature* **441**, 475–482 (2006).
15. Gurumurthy, S. *et al.* The Lkb1 metabolic sensor maintains haematopoietic stem cell survival. *Nature* doi:10.1038/nature09572 (this issue).
16. Nakada, D., Saunders, T. L. & Morrison, S. J. Lkb1 regulates cell cycle and energy metabolism in haematopoietic stem cells. *Nature* doi:10.1038/nature09571 (this issue).
17. Puigserver, P. & Spiegelman, B. M. Peroxisome proliferator-activated receptor- γ coactivator 1 α (PGC-1 α): transcriptional coactivator and metabolic regulator. *Endocr. Rev.* **24**, 78–90 (2003).
18. Shaw, R. J. *et al.* The kinase LKB1 mediates glucose homeostasis in liver and therapeutic effects of metformin. *Science* **310**, 1642–1646 (2005).
19. Kelly, D. P. & Scarpulla, R. C. Transcriptional regulatory circuits controlling mitochondrial biogenesis and function. *Genes Dev.* **18**, 357–368 (2004).
20. Bardeesy, N. *et al.* Loss of the Lkb1 tumour suppressor provokes intestinal polyposis but resistance to transformation. *Nature* **419**, 162–167 (2002).

Supplementary Information is linked to the online version of the paper at www.nature.com/nature.

Acknowledgements We are grateful to A. Berns for providing the *Rosa26-creERT2* mouse strain. We are also grateful to S. Zhou for assistance in the animal facility and C. Lim for assistance with genotyping. We thank S. Lazo-Kallanian, J. Daley and P. Schow for assistance with flow cytometry. We also thank N. Bardeesy and S. Morrison for communicating unpublished information; A. Stegh for comments on apoptosis; and D. Nakada for western blotting protocol from sorted HSCs. This research was supported by U01CA141508 (R.A.D. and L.C.), R21CA135057 (R.A.D. and B.G.) and DOD TSCR Career Transition Award (TS093049) (B.G.). B.G. and J.H. are the Research Fellows of the Leukemia and Lymphoma Society. Y.A.W. is supported by Multiple Myeloma Research Foundation. R.A.D. was supported by an American Cancer Society Research Professorship and the Robert A. and Renee E. Belfer Foundation.

Author Contributions B.G. and R.A.D. designed the experiments, interpreted the data and wrote the manuscript. B.G., S.J., J.H., L.Z. and E.F.-S. performed experiments. Y.L. and L.C. conducted the microarray and promoter analyses. E.S. and S.C. contributed reagents. L.C. and Y.A.W. contributed to the writing of the manuscript.

Author Information Completed microarray data are deposited on the GEO website under super series accession number GSE24765. Reprints and permissions information is available at www.nature.com/reprints. The authors declare no competing financial interests. Readers are welcome to comment on the online version of this article at www.nature.com/nature. Correspondence and requests for materials should be addressed to R.A.D. (ron_depinho@dfci.harvard.edu).

METHODS

Generation and analysis of mice. *Lkb1*^{L/L} mice were crossed with *Rosa26-creERT2* mice to generate *Lkb1*^{L/+}; *Rosa26-creERT2* mice. *Lkb1*^{L/+}; *Rosa26-creERT2*⁺ mice were backcrossed six generations into the C57BL/Ka-CD45.2:Thy-1.1 background, which were then intercrossed to generate mice of the desired genotypes. Recipients in transplantation assays were adult C57BL/Ka-CD45.1:Thy-1.2 mice (Jackson Laboratory). Tamoxifen treatment of mice was done as previously described¹². Briefly, littermates at 4–6 weeks of age were administered daily by intraperitoneal injection of tamoxifen (Sigma) in corn oil (12 µg µl⁻¹ in corn oil) at 132 µg tamoxifen per gram of body weight per day for five consecutive days. Animals were autopsied and all tissues were examined regardless of their pathological status. Tissue samples were fixed in 10% neutral-buffered formalin (Sigma) overnight, and washed once with 1× PBS and then transferred into 70% ethanol and stored at 4 °C. Tissues were processed by ethanol dehydration and embedded in paraffin according to standard protocols. Sections (5 µm) were prepared for antibody detection and haematoxylin and eosin staining. Blood glucose level was measured by Ascensia ELITE Blood Glucose Meter (3873A) following the manufacturer's instruction. All animal manipulations were performed with Harvard/DFCI's Institutional Animal Care and Use Committee (IACUC) approval.

Flow cytometry analysis. Single-cell suspensions were prepared from spleen, thymus and bone marrow (from femoral and tibial bones) by passing cells through a 70-µm cell strainer. Cells were lysed on ice with red blood cell lysis solution (Sigma), washed in PBS +2% FCS, then re-suspended in PBS +2% FCS. Cell numbers were subsequently counted. Cells were incubated with fluorochrome-conjugated (or with biotin-conjugated) antibodies (CD4, CD8, Ter119, Gr-1, Mac-1, B220, Kit, Sca-1, CD34, Flt3, and so on) for 30 min on ice, followed by washing once in PBS +2% FCS. For lineage marker labelling, cells were stained with other fluorochrome-conjugated antibodies and biotin-conjugated lineage markers (CD3, B220, Gr-1, Mac-1, Ter119) (BD Bioscience) for 30 min on ice, followed by incubation with fluorochrome-conjugated Streptavidin (BD Bioscience) for 5 min. For the analysis of bone marrow lymphopoiesis, cells were stained with fluorochrome-conjugated anti-B220, CD19, CD43, IgM and biotin-conjugated lineage markers (CD3, Gr-1, Mac-1, Ter119) (BD Bioscience) for 30 min on ice, followed by incubation with fluorochrome-conjugated Streptavidin for 5 min. LSK and LT-HSC populations were analysed and sorted using FACSaria (Becton Dickinson) as previously reported²¹. For mitochondrial membrane potential measurement, bone marrow cells stained for LSK populations were incubated with 50 mM DiI-C-5 (Invitrogen) at 37 °C for 15–30 min. Apoptosis was determined by staining freshly harvested bone marrow mononuclear cells with lineage, stem and progenitor markers, followed by Annexin-V-FITC and 7AAD staining (BD Bioscience). Cell cycle analysis was carried out as previously reported using the FITC BRDU Flow Kit (BD Bioscience)²². Additional analyses were carried out on a 4-colour FACSCalibur cytometer (Becton Dickinson) with a minimum of 10,000 events acquired. The data were analysed by FlowJo and CellQuest software.

Competitive and non-competitive repopulation assays. In non-competitive repopulation assay, 1 × 10⁶ bone marrow cells from both *Lkb1*^{L/L}; *Rosa26-creERT2* or littermate wild-type (*Lkb1*^{+/+}; *Rosa26-creERT2* or *Lkb1*^{L/L} mice (both CD45.2⁺) were injected into lateral tail veins of lethally irradiated CD45.1⁺ recipient animals. In the competitive repopulation assay, an appropriate amount of bone marrow cells from both *Lkb1*^{L/L}; *Rosa26-creERT2* or littermate wild-type mice (both CD45.2⁺) were mixed with bone marrow cells from CD45.1⁺ wild-type mice (totally 1 × 10⁶), then injected into lateral tail veins of lethally irradiated CD45.1⁺ recipient animals (950 rad in two dosages, 2 h apart). Five to six weeks after transplantation, when these mice showed stable chimaerism, *Lkb1* was deleted by tamoxifen treatment. Peripheral blood was collected at 4, 8 and 16 weeks after tamoxifen treatment, and bone marrow from mice at 16 weeks was analysed for contribution of CD45 congenic and lineage markers by flow cytometry. Tissues from the recipient mice at 16 weeks were collected for further analyses, including cell surface marker staining by flow cytometry, histology characterization, and so on. Both non-competitive and competitive transplants were carried out with three–five donors per genotype with three recipient mice per donor in each experiment.

Administration of rapamycin. At the time of tamoxifen treatment, mice were administered with rapamycin (LC laboratories) by daily intraperitoneal injection at 4 µg per gram of body weight per day. After tamoxifen treatment was finished, mice were treated with rapamycin for another 1–10 days and subjected to various phenotypic analyses. Rapamycin was first reconstituted in absolute ethanol at 25 mg ml⁻¹ and then diluted in 5% Tween-80 and 5% PEG-400 before injection to make 0.5 mg ml⁻¹ solution for injection.

Administration of metformin. At the time of tamoxifen treatment, mice were administered metformin (Sigma) by daily intraperitoneal injection at 250 mg

metformin per kg body weight (mg kg⁻¹) in saline or just saline (vehicle). After tamoxifen treatment was finished, mice were treated with metformin for another 1–10 days and subjected to various phenotypic analyses.

Quantitative real-time PCR analysis. RNA from various tissues was harvested using Trizol (Invitrogen) and the RNeasy kit (Qiagen). RNA was treated with RQ1 RNase-freeDNase (Promega), and cDNA was prepared using Superscript II RNase H-Reverse transcriptase (Invitrogen). RNA from sorted cells was extracted using the PicoPure RNA Isolation kit (Molecular Devices), and cDNA was prepared using Superscript II RNase H-Reverse transcriptase (Invitrogen). Mitochondrial DNA was quantified by determining the ratio of mitochondrial cytochrome c oxidase (Cox) 2 to nuclear intron of β-globin by quantitative real-time PCR (qRT-PCR) of isolated LSK DNA. qRT-PCR was performed on cDNA or genomic DNA samples using the Quantitative SYBR green PCR kit (Qiagen) and was run on the Stratagene Mx3000P. Primer sequences used in this study are: mouse PGC-1α forward (for real-time PCR) 5'-AATCAGACCTGACACAA CGC-3'; mouse PGC-1α reverse (for real-time PCR) 5'-GCATTCCT CAATTTACACAA-3'; mouse PGC-1β forward (for real-time PCR) 5'-CG CTCCAGGAGACTGAATCCAG-3'; mouse PGC-1β reverse (for real-time PCR) 5'-CTTGACTACTGTCTGTGAGGC-3'; mouse Lkb1 forward (for real-time PCR) 5'-GCGGCTGCGGCATCGGAATGTGA-3'; mouse Lkb1 reverse (for real-time PCR) 5'-CTTGGCACACAGGAAGCGCTTCT-3'; mouse Cox2 forward (for mtDNA PCR) 5'-GCCGACTAAATCAAGCAACA-3'; mouse Cox2 reverse (for mtDNA PCR) 5'-CAATGGGCATAAAGCTATGG-3'; mouse β-globin forward (for mtDNA PCR) 5'-GAAGCGATTCTAGGGAGCAG-3'; mouse β-globin reverse (for mtDNA PCR) 5'-GGAGCAGCGATTCT GAGTAGA-3'.

Microarray analysis. Bone marrow LSK cells were sorted from *Lkb1* wild-type and *Lkb1* knockout mice at 1 d.p.i. (15,000–20,000 cells per sample). RNA from sorted LSK cells was extracted using the PicoPure RNA Isolation kit (Molecular Devices), and cDNA was prepared using Superscript II RNase H-Reverse transcriptase (Invitrogen). Gene expression profiling was performed using Affymetrix mouse 430 2.0 chips at Partners Healthcare Center for Genetics and Genomics (HPCGG) at Harvard Medical School. dChip²³ was used to normalize arrays and to compute expression indices as previously described²⁴.

Pathway and promoter analyses. Ingenuity Pathway Analysis was performed at <https://analysis.ingenuity.com/pa/>. For promoter analysis, promoter sequences in the region between –8 kb and +2 kb with respect to the annotated transcription start sites were downloaded from the UCSC Genome Browser (<http://genome.ucsc.edu/>), genome assembly mm8. Transcription factor motifs enriched in the promoters were identified by using the Cisgenome motif analysis algorithm²⁵ against all transcription factor motifs in the TRANSFAC and JASPAR databases. Ten different sets of matched control regions generated by Cisgenome were used to calculate an averaged enrichment for each transcription factor motif.

Western blot analysis. Tissues were lysed with RIPA buffer (20 mM Tris pH 7.5, 150 mM NaCl, 1% Nonidet P-40, 0.5% sodium deoxycholate, 1 mM EDTA, 0.1% SDS) containing complete mini-protease inhibitors (Roche). Western blots were performed using 20–50 µg of lysate protein. Western blotting from sorted HSCs was performed as described in ref. 16. Antibodies used in this study include: S6 (1:1,000), phospho-S6 Ser240/244 (1:2,000), 4E-BP1 (1:1,000), phospho-4E-BP1 Ser65 (1:1,000), eIF4E (1:1,000), AMPK (1:1,000), phospho-AMPK Thr 172 (1:1,000), phospho-ACC Ser 79 (1:1,000), cleaved caspase-3 (1:1,000), Lkb1 (1:1,000) (Cell Signaling Technology) and vinculin (1:5,000) (Sigma).

In vivo ATP measurement from tissues. *In vivo* ATP measurement was performed as previously described²⁶. Briefly, fresh mouse tissues were rapidly harvested and immediately placed in ice-cold ATP buffer (20 mM Tris (pH 7.5), 0.5% Nonidet P-40, 25 mM NaCl, 2.5 mM EDTA) for 5 min. Tissue samples then underwent two 10-s rounds of sonication, centrifuged at 13,000g for 30 min and the supernatant measured for protein concentration. ATP concentration was measured from 1 µg of this protein lysate by using the ATP Determination kit (Molecular Probes). Each ATP sample was measured in triplicate.

Statistical analysis. Animal survival was analysed using Graphpad Prism4. Statistical analyses were performed using a non-parametric Mann–Whitney U-test. Comparisons of cell numbers and gene expression levels were performed using an unpaired Student's *t*-test. For all experiments with error bars, standard deviation was calculated to indicate the variation within each experiment and data, and values represent mean ± s.d.

- Tothova, Z. *et al.* FoxOs are critical mediators of hematopoietic stem cell resistance to physiologic oxidative stress. *Cell* **128**, 325–339 (2007).
- Hock, H. *et al.* Gfi-1 restricts proliferation and preserves functional integrity of haematopoietic stem cells. *Nature* **431**, 1002–1007 (2004).

23. Li, C. & Wong, W. H. DNA-Chip Analyzer (dChip). in *The Analysis of Gene Expression Data: Methods and Software* (eds Parmigiani, G., Garrett, E. S., Irizarry, R. & Zeger, S. L.) (Springer, 2003).
24. Paik, J. H. *et al.* FoxOs are lineage-restricted redundant tumor suppressors and regulate endothelial cell homeostasis. *Cell* **128**, 309–323 (2007).
25. Ji, H., Vokes, S. A. & Wong, W. H. A comparative analysis of genome-wide chromatin immunoprecipitation data for mammalian transcription factors. *Nucleic Acids Res.* **34**, e146 (2006).
26. Ahn, B. H. *et al.* A role for the mitochondrial deacetylase Sirt3 in regulating energy homeostasis. *Proc. Natl Acad. Sci. USA* **105**, 14447–14452 (2008).

Structural changes of envelope proteins during alphavirus fusion

Long Li¹, Joyce Jose¹, Ye Xiang¹, Richard J. Kuhn¹ & Michael G. Rossmann¹

Alphaviruses are enveloped RNA viruses that have a diameter of about 700 Å and can be lethal human pathogens¹. Entry of virus into host cells by endocytosis is controlled by two envelope glycoproteins, E1 and E2. The E2–E1 heterodimers form 80 trimeric spikes on the icosahedral virus surface^{1,2}, 60 with quasi-three-fold symmetry and 20 coincident with the icosahedral three-fold axes arranged with $T = 4$ quasi-symmetry. The E1 glycoprotein has a hydrophobic fusion loop at one end and is responsible for membrane fusion^{3,4}. The E2 protein is responsible for receptor binding^{5,6} and protects the fusion loop at neutral pH. The lower pH in the endosome induces the virions to undergo an irreversible conformational change in which E2 and E1 dissociate and E1 forms homotrimers, triggering fusion of the viral membrane with the endosomal membrane and then releasing the viral genome into the cytoplasm^{3,4}. Here we report the structure of an alphavirus spike, crystallized at low pH, representing an intermediate in the fusion process and clarifying the maturation process. The trimer of E2–E1 in the crystal structure is similar to the spikes in the neutral pH virus except that the E2 middle region is disordered, exposing the fusion loop. The amino- and carboxy-terminal domains of E2 each form immunoglobulin-like folds, consistent with the receptor attachment properties of E2.

The X-ray crystal structure of the ectodomain of the E1 protein (residues 1–383) from Semliki Forest virus (SFV) is homologous to the flavivirus E glycoprotein and consists of three β -barrel domains (domains I, II and III; notated as DI, DII and DIII) with the fusion loop at the distal end of DII⁷. The structure of the E1 ectodomain had been fitted into the 9-Å-resolution cryo-electron microscopy (cryo-EM) reconstruction of Sindbis virus (Fig. 1a), generating a partial structure of the virus^{8,9}. After subtraction of the density representing E1, the E2 density was found to be a long, thin volume that covers the top of each E1 molecule including the fusion loop⁸. However, the crystal structure of E2 has remained unknown until now.

An E2–E1 recombinant protein of Sindbis virus, in which the ectodomains of E2 and E1 were connected by a flexible Strep-tag linker¹⁰ (Fig. 1b and Supplementary Fig. 1), was expressed in *Drosophila* Schneider 2 (S2) cells. Size-exclusion chromatography showed that the purified protein existed in solution as trimers of the E2–E1 heterodimer over a pH range from 5.5 to 9.5. The protein was crystallized at pH 5.6, which is lower than the pH 6.0 fusion threshold for alphaviruses^{4,11,12}. The resultant crystal structure consisted of trimers of E2–E1 heterodimers that were remarkably similar to the trimeric spikes in the virus (Fig. 2 and Supplementary Table 1), demonstrating the biological significance of the crystallized recombinant E2–E1 protein.

The C α backbone of E2 corresponded well with an earlier tracing obtained by connecting known markers such as glycosylation and antibody-binding sites⁸ (Fig. 3). The structure of E2 consists of the N-terminal domain A (residues 1–132), the middle domain B and the C-terminal domain C (residues 264–343). The ~88 residues of domain B are mostly disordered and are connected to domains A and C by long connecting linker peptides (the ‘ β -ribbon connector’). The connecting peptide from domain A to domain B starts at residue

133 and could be traced to residue 166. The connecting peptide from domain B to domain C picks up at residue 255 and continues to residue 263 where it enters domain C (Supplementary Fig. 2). The three domains of E2 are stretched out along the length of E1 in the order C, A, B, with C being closest to the viral membrane and mostly hidden from the viral exterior. Domain B, had it not been disordered, would correspond to the tip of the cryo-EM envelope (Fig. 3b). The glue between the three E1 molecules that constitute a spike is formed by

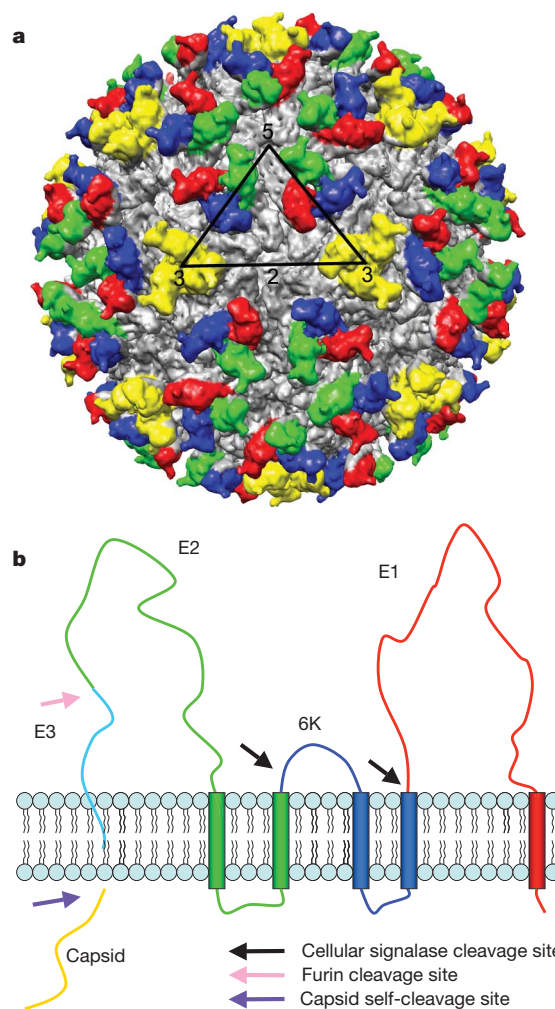


Figure 1 | The structural proteins of an alphavirus. **a**, The cryo-EM density of Sindbis virus showing $T = 4$ symmetry. The four E2 molecules in one asymmetric unit (outlined in black) are coloured red, green, blue and yellow. These give rise to one trimeric spike on each icosahedral three-fold axis and one generally positioned spike. The E1 molecules are coloured grey. **b**, Threading of the Sindbis virus structural polypeptide through an endoplasmic reticulum membrane showing the position of the capsid, E3, E2, 6K and E1 proteins.

¹Department of Biological Sciences, Purdue University, 915 W. State Street, West Lafayette, Indiana 47907-2054, USA.

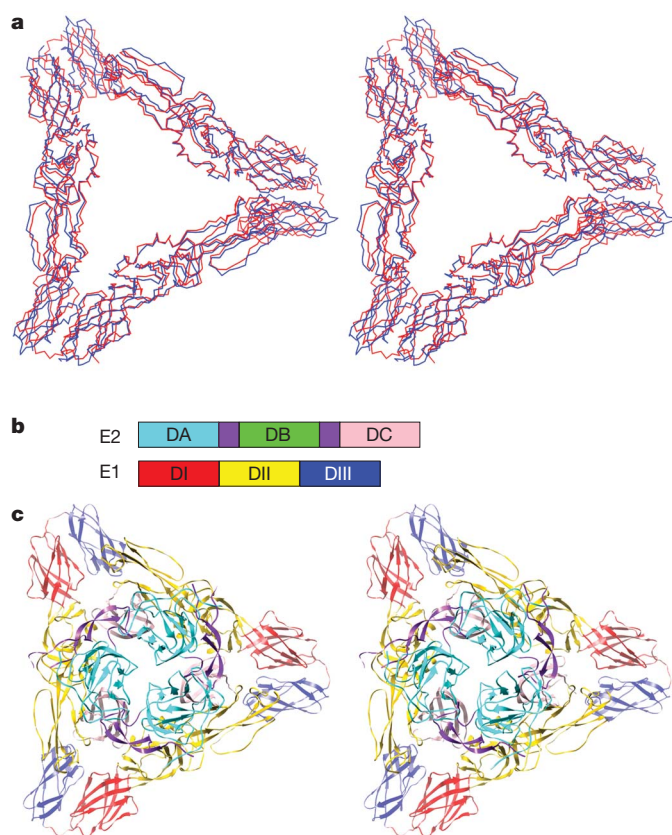


Figure 2 | Stereo diagrams showing the trimeric spike structure. **a**, The E1 molecule in a Sindbis virus spike (blue) compared with the E1 molecules in the crystal structure (red). **b**, Linear representation of polypeptides showing domains A (DA; cyan), B (DB; green), C (DC; pink) and the β -ribbon connector (purple) in E2; as well as DI (red), DII (yellow) and DIII (blue) in E1. **c**, Crystal structure of the trimeric spike at low pH. Domain B is disordered.

E2 domain C, which binds to DII in adjacent E1 molecules within the trimeric spike (Fig. 2c and Supplementary Fig. 3a). The residues in the contact area are primarily hydrophilic making a number of potential hydrogen bonds (Supplementary Table 2.1). In contrast to the low pH, partially disordered structure described here, the fully ordered structure of E2 has been determined at neutral pH for Chikungunya virus in the accompanying paper¹³.

Both domain A and domain C have the topology of an immunoglobulin fold (Fig. 3). This is consistent with E2 functioning as a

cell-receptor-binding protein. Furthermore, residues that had been identified in E2 as being associated with altered receptor binding and tropism are now seen to be in domain A of E2 (Supplementary Table 3 and Supplementary Fig. 4). However, other residues that were associated with cell recognition^{6,14,15} are in the disordered domain B showing that there could be several sites on the virus surface that associate with various cell surface molecules involved in virus attachment and entry.

The A domains of the three E2 molecules within one trimeric spike are situated in the centre of the triangular cavity formed by the three E1 molecules in the spike and make extensive interactions with each other (Supplementary Table 2.2). The presence of histidines, arginines and lysines in the interface, although not conserved among alphaviruses, shows that the interactions will become weak or repulsive as the pH drops below the pK of the histidines. Furthermore, the extensive positive charge on these surfaces indicates that the A domains might be easily separated and then alter their orientation to present their arginines and lysines to the phospholipid headgroups in the membrane.

If the envelope of the E2 density derived from the 9-Å-resolution cryo-EM map⁸ is overlaid onto the E2–E1 trimeric low pH crystal structure by superimposing the E1 molecules, then a large proportion of the tip of the E2 cryo-EM envelope, presumably corresponding to the B domain, overlaps and clashes with a neighbouring trimeric spike assembly in the crystal structure (Supplementary Fig. 5a). This is shown even more markedly by superimposing the neutral pH crystal structure of the Chikungunya virus E2–E1 heterodimer as found in the accompanying paper¹³ (Supplementary Fig. 5b) onto the low pH crystal structure reported in this paper. (The root mean squared deviation (r.m.s.d.) between C α atoms in the ordered part of E2 in these two structures is 4.5 Å, a reasonable result considering that only 36% of the residues are identical in the compared region.) Thus, domain B as found in the virus cannot be in the same position in the crystal structure, partly consistent with previously reported findings¹⁶. The β -ribbon-connector peptides that extend from domains A and C follow the edge of domain A and are within the E2 envelope observed in the cryo-EM map. Thus, the ‘disorder’ of domain B (which is stabilized by two disulphide bonds¹³) might be because the long β -ribbon connector is flexible and allows domain B to detach itself from the tip of E2. The β -ribbon connector is flanked by two completely conserved histidines at Sindbis positions 169 and 256. These might be the acid-sensitive triggers that perhaps control the interaction with E3 (see below) and cause the β -ribbon connector to dissociate itself from the A domain. In summary, whereas the position of domain B in the neutral pH virus covers the fusion loop on E1, protecting the virus from premature fusion with other cellular membranes, acidification of the virus causes

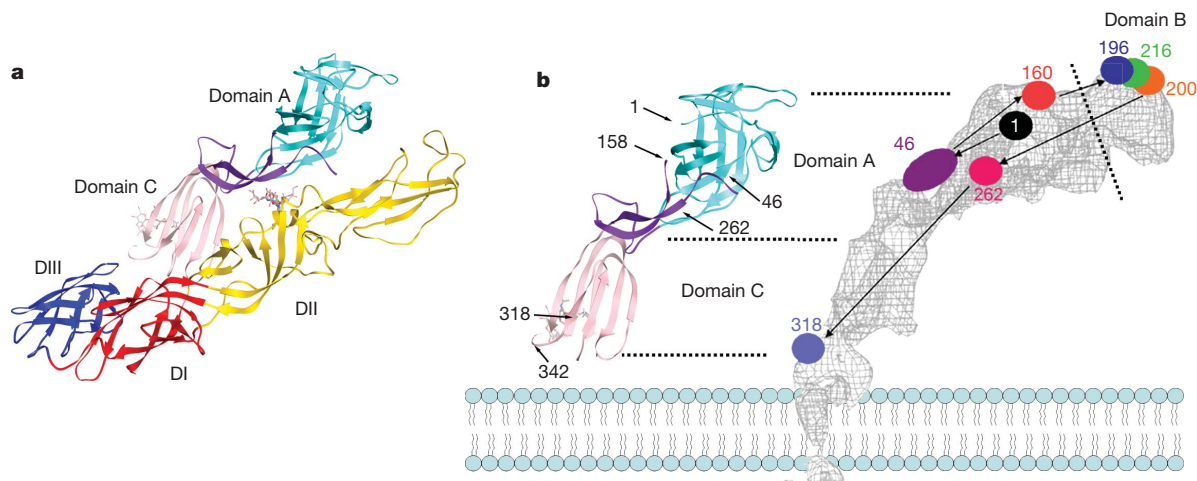


Figure 3 | The E2–E1 heterodimer. **a**, The crystal structure (left) colour coded as in Fig. 2b. **b**, Comparison of the earlier E2 mapping⁸ with the E2 crystal structure. Amino acid sequence numbers are given in strategic positions⁸. The

lipid envelope is shown diagrammatically. Modified from ref. 8 with permission.

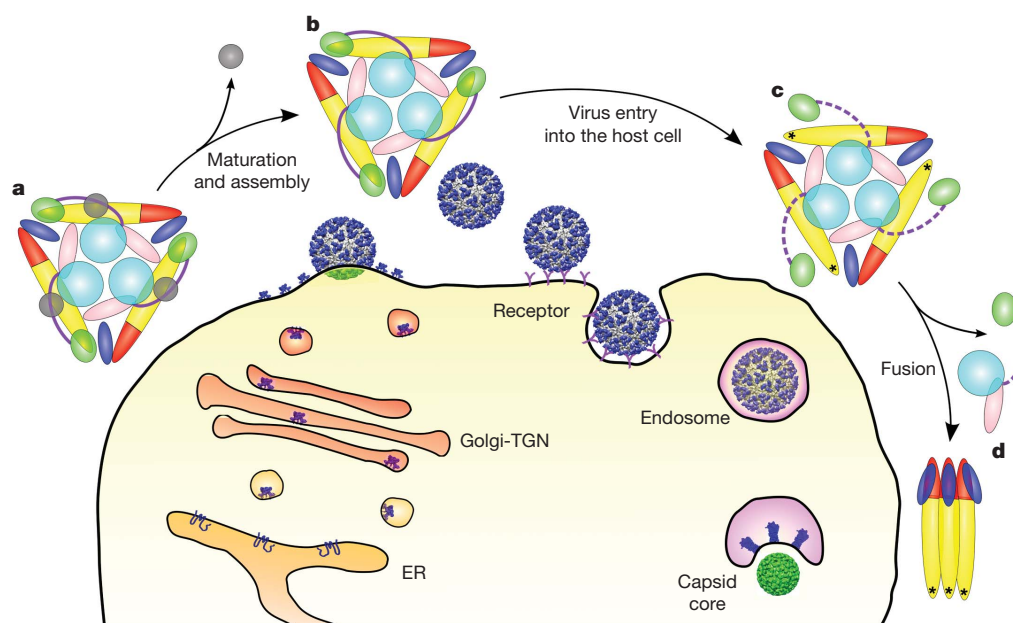


Figure 4 | Cartoon showing maturation and fusion. a–d, Colour coded as in Fig. 2b. a, The viral spike while being transported through the Golgi and trans-Golgi network (TGN). Domain B is attached to DII because E3 (grey) binds the β -ribbon connector to domain A and holds E2 in place at low pH. b, The viral spike on the virus after E3 has been proteolytically cleaved and, in Sindbis virus,

has been jettisoned. c, After the virus has recognized a host cell and entered into a low pH endosomal vesicle, domain B becomes unattached from DII, exposing the fusion loop (marked with an asterisk). The dashed line indicates the disordered β -ribbon connector. d, The trimeric spike disassembles, allowing escape of E2 and formation of E1 homotrimers. ER, endoplasmic reticulum.

domain B to move away from its neutral pH position, thereby exposing the fusion loop and making it accessible to lipid membranes (Fig. 4). Antibodies that bind to epitopes on domain A or B are strong neutralizers¹⁷, perhaps because these antibodies might prevent not only receptor attachment but also prevent disordering of domain B and, hence, inhibit fusion.

During maturation, E1 and PE2 (the precursor to the E3–E2 proteins before cleavage of E3, also referred to as p62) are assembled as heterodimers in the endoplasmic reticulum^{1,18} and processed through the Golgi and trans-Golgi network, where E3 protects the E2–E1 heterodimer from premature fusion with cellular membranes. The resultant E2–E1 heterodimers, or E3–E2–E1 in some viruses¹⁹, are then transported to the plasma membrane²⁰ where budding occurs following association of the glycoproteins with preformed nucleocapsids.

The site of E3 has been mapped by various cryo-EM studies^{21–23} that can now be identified as corresponding to a site where domain A borders onto domain B (Fig. 4 and Supplementary Fig. 3b). This indicates that the function of E3 is to stabilize the β -ribbon connector. As long as the distal end of the β -ribbon connector remains associated with domain A and DII, domain B will continue to protect the fusion loop. This is supported by mutational studies of H169 in Sindbis virus and its equivalent residue in SFV^{24,25}.

Fusion of the viral membrane with the cellular plasma membrane in alphaviruses requires the dissociation of the E1–E2 heterodimer and formation of E1 homotrimers at low pH²⁶ in the presence of a lipid membrane. In the E1 homotrimeric structure the E1 molecules are arranged with their long direction running roughly parallel to a common three-fold axis of rotation, exposing the fusion loops of each monomer at one end of the trimeric complex²⁷. Residues of E1 that were in contact with E2 in the pre-fusion trimeric spike (in part determined from the structure given in the accompanying paper¹³) are located on the surface of the post-fusion E1 homotrimer, facing away from the spike axes, and are predominantly in surface loops⁸ (Supplementary Fig. 6). The conformational changes required to form a post-fusion trimer will require the removal of the E2 molecules from the centre of the trimeric spike to the outside and rotation of the E1 molecules by about 180° about their long axes to face each other across

what was the three-fold axis of the pre-fusion spike. E2 might escape contact with the surrounding E1 molecules by detaching the C domains and slipping to the outside via the gap left by them. Alternatively, two E1 molecules on neighbouring spikes might combine with a third E1 molecule recruited from another unmatched E1 molecule elsewhere on the virus to make the post-fusion trimer (Fig. 4). Similar, huge conformational changes occur in the maturation and fusion of flaviviruses^{28,29}; however, it is still unclear what the pathway is by which these events happen.

METHODS SUMMARY

The recombinant E2–E1 protein was expressed in a *Drosophila* expression system. The protein was purified by His-tag-affinity, ion-exchange and size-exclusion chromatography. A crystallization robot and 96-well sitting-drop plates were used for the initial crystallization screening. The one condition that grew crystals was subsequently optimized using hanging drops with 24-well plates. The crystal diffraction data were collected at the Advanced Photon Source synchrotron. The crystal structure was determined by combining the SeMet multiple wavelength anomalous dispersion (MAD) and molecular replacement methods. The crystal structure was fitted into the electron microscopy image reconstruction density of Sindbis virus using the program EMfit³⁰.

Full Methods and any associated references are available in the online version of the paper at www.nature.com/nature.

Received 21 May; accepted 1 October 2010.

1. Strauss, J. H. & Strauss, E. G. The alphaviruses: gene expression, replication, and evolution. *Microbiol. Rev.* **58**, 491–562 (1994).
2. von Bonsdorff, C. H. & Harrison, S. C. Sindbis virus glycoproteins form a regular icosahedral surface lattice. *J. Virol.* **16**, 141–145 (1975).
3. Kielian, M. Membrane fusion and the alphavirus life cycle. *Adv. Virus Res.* **45**, 113–151 (1995).
4. White, J. & Helenius, A. pH-dependent fusion between the Semliki Forest virus membrane and liposomes. *Proc. Natl Acad. Sci. USA* **77**, 3273–3277 (1980).
5. Dubuisson, J. & Rice, C. M. Sindbis virus attachment: isolation and characterization of mutants with impaired binding to vertebrate cells. *J. Virol.* **67**, 3363–3374 (1993).
6. Strauss, E. G., Stec, D. S., Schmaljohn, A. L. & Strauss, J. H. Identification of antigenically important domains in the glycoproteins of Sindbis virus by analysis of antibody escape variants. *J. Virol.* **65**, 4654–4664 (1991).
7. Lescar, J. *et al.* The fusion glycoprotein shell of Semliki Forest Virus: an icosahedral assembly primed for fusogenic activation at endosomal pH. *Cell* **105**, 137–148 (2001).

8. Mukhopadhyay, S. *et al.* Mapping the structure and function of the E1 and E2 glycoproteins in alphaviruses. *Structure* **14**, 63–73 (2006).
9. Zhang, W. *et al.* Placement of the structural proteins in Sindbis virus. *J. Virol.* **76**, 11645–11658 (2002).
10. Schmidt, T. G. & Skerra, A. The Strep-tag system for one-step purification and high-affinity detection or capturing of proteins. *Nature Protocols* **2**, 1528–1535 (2007).
11. Smit, J. M., Bittman, R. & Wilschut, J. Low-pH-dependent fusion of Sindbis virus with receptor-free cholesterol- and sphingolipid-containing liposomes. *J. Virol.* **73**, 8476–8484 (1999).
12. White, J., Kartenbeck, J. & Helenius, A. Fusion of Semliki Forest virus with the plasma membrane can be induced by low pH. *J. Cell Biol.* **87**, 264–272 (1980).
13. Voss, J. E. *et al.* Glycoprotein organization of Chikungunya virus particles revealed by X-ray crystallography. *Nature* doi:10.1038/nature09555 (this issue).
14. Meyer, W. J. & Johnston, R. E. Structural rearrangement of infecting Sindbis virions at the cell surface: mapping of newly accessible epitopes. *J. Virol.* **67**, 5117–5125 (1993).
15. Zhang, W., Heil, M., Kuhn, R. J. & Baker, T. S. Heparin binding sites on Ross River virus revealed by electron cryo-microscopy. *Virology* **332**, 511–518 (2005).
16. Wu, S.-R. *et al.* The dynamic envelope of a fusion class II virus. Prefusion stages of Semliki Forest virus revealed by electron cryomicroscopy. *J. Biol. Chem.* **282**, 6752–6762 (2007).
17. Griffin, D. E. Roles and reactivities of antibodies to alphaviruses. *Semin. Virol.* **6**, 249–255 (1995).
18. Wahlberg, J. M., Boere, W. A. & Garoff, H. The heterodimeric association between the membrane proteins of Semliki Forest virus changes its sensitivity to low pH during virus maturation. *J. Virol.* **63**, 4991–4997 (1989).
19. Ziemiecki, A. & Garoff, H. Subunit composition of the membrane glycoprotein complex of Semliki Forest virus. *J. Mol. Biol.* **122**, 259–269 (1978).
20. Ziemiecki, A., Garoff, H. & Simons, K. Formation of the Semliki Forest virus membrane glycoprotein complexes in the infected cell. *J. Gen. Virol.* **50**, 111–123 (1980).
21. Ferlenghi, I. *et al.* The first step: activation of the Semliki Forest virus spike protein precursor causes a localized conformational change in the trimeric spike. *J. Mol. Biol.* **283**, 71–81 (1998).
22. Paredes, A. M. *et al.* Structural localization of the E3 glycoprotein in attenuated Sindbis virus mutants. *J. Virol.* **72**, 1534–1541 (1998).
23. Wu, S. R., Haag, L., Sjöberg, M., Garoff, H. & Hammar, L. The dynamic envelope of a fusion class II virus. E3 domain of glycoprotein E2 precursor in Semliki Forest virus provides a unique contact with the fusion protein E1. *J. Biol. Chem.* **283**, 26452–26460 (2008).
24. Zhang, X. & Kielian, M. Mutations that promote furin-independent growth of Semliki Forest virus affect p62–E1 interactions and membrane fusion. *Virology* **327**, 287–296 (2004).
25. Heidner, H. W., McKnight, K. L., Davis, N. L. & Johnston, R. E. Lethality of PE2 incorporation into Sindbis virus can be suppressed by second-site mutations in E3 and E2. *J. Virol.* **68**, 2683–2692 (1994).
26. Wahlberg, J. M. & Garoff, H. Membrane fusion process of Semliki Forest virus. I. Low pH-induced rearrangement in spike protein quaternary structure precedes virus penetration into cells. *J. Cell Biol.* **116**, 339–348 (1992).
27. Gibbons, D. L. *et al.* Conformational change and protein–protein interactions of the fusion protein of Semliki Forest virus. *Nature* **427**, 320–325 (2004).
28. Li, L. *et al.* The flavivirus precursor membrane-envelope protein complex: structure and maturation. *Science* **319**, 1830–1834 (2008).
29. Yu, I. M. *et al.* Structure of the immature dengue virus at low pH primes proteolytic maturation. *Science* **319**, 1834–1837 (2008).
30. Rossmann, M. G., Bernal, R. & Pletnev, S. V. Combining electron microscopic with X-ray crystallographic structures. *J. Struct. Biol.* **136**, 190–200 (2001).

Supplementary Information is linked to the online version of the paper at www.nature.com/nature.

Acknowledgements We wish to thank S. Sun, A. Aksyuk and T. Edwards for discussions. We are also grateful to S. Kelly for help in the preparation of the manuscript. We thank F. Rey for sharing the coordinates of Chikungunya virus E2–E1 to help interpret the Sindbis virus cryo-EM density of the E2 domain B. We would like to thank the staff at the Advanced Photon Source, Argonne National Laboratory, GM/CA sector for their help in data collection. The work was supported by NIH grant P01 AI055672 to R.J.K. and M.G.R.

Author Contributions L.L. designed the expression constructs, J.J. cloned the constructs, and L.L. and J.J. developed the expression system and purified the protein. L.L. crystallized the protein, collected X-ray diffraction data and, with Y.X., determined the structure. L.L., R.J.K. and M.G.R. discussed the results and wrote the paper.

Author Information The atomic coordinates of the E2–E1 heterodimer crystal structures have been deposited with the Protein Data Bank (accession number 3MUU). The fit of the E2–E1 heterodimer into the cryo-EM reconstruction of Sindbis virus has been deposited with the Protein Data Bank (accession number 3MUW). Reprints and permissions information is available at www.nature.com/reprints. The authors declare no competing financial interests. Readers are welcome to comment on the online version of this article at www.nature.com/nature. Correspondence and requests for materials should be addressed to M.G.R. (mr@purdue.edu).

METHODS

Protein production. The coding sequences of E3 (residues 1–64), E2 (residues 1–344) and E1 (residues 1–384) of Sindbis virus (Toto64) were amplified by PCR³¹. The DNA sequence of a peptide linker, STREP, that contains the Strep-tag II¹⁰ (GGGSWSHPQFEKGGGG) was inserted between E2 and E1 by overlapping PCR, thereby omitting the transmembrane and 6K region between E2 and E1. The recombinant gene that codes for E3–E2 (residues 1–344) STREP–E1 (residues 1–384) was inserted between the BglII and XhoI restriction sites in the pMT/BiP/V5-His A vector (Invitrogen). A (His)₆ tag and a stop codon was introduced right after the 3' end of the E1 gene by the 3' PCR primer, so the V5 and His tags from the original vector were omitted from the expression product. Ten micrograms of the resultant plasmid were co-transfected with 0.5 µg of the plasmid pCoHygro (Invitrogen) into 3 ml of *Drosophila* S2 cells at $2\text{--}4 \times 10^6$ cells ml^{−1} by using 30 µl of cellfectin (Invitrogen) in Schneider's *Drosophila* medium (no serum) (Invitrogen). The stable cell line expressing the recombinant protein was selected out after one month in the presence of 300 µg ml^{−1} hygromycin B (EMD Chemicals) in Schneider's *Drosophila* medium supplemented with 10% heat inactivated fetal bovine serum. Stably transfected cells were gradually scaled up and adapted into EX-CELL 420 serum-free medium (Sigma-Aldrich). Protein expression was induced by the addition of 500 µM CuSO₄ after 2 l of the cells, maintained in two 3-l spinner flasks, had grown to a density of $6\text{--}10 \times 10^6$ cells ml^{−1}. The recombinant protein was secreted into the medium as the E2–E1 complex because E3 was cleaved by furin and the furin-like proteases during secretion in the S2 cells. The medium was harvested 3–5 days after induction. The cells were spun down and the supernatant medium was collected and clarified by passing through 0.22-µm cutoff membrane filters (Millipore). The medium was then loaded onto a column packed with 18 ml IMAC sepharose 6 ff resin (GE Healthcare), pre-charged with Ni²⁺ (ref. 32). The protein was eluted with 100 mM and then 500 mM imidazole using a step-elution protocol. The partially purified protein was dialyzed against a phosphate buffer (20 mM NaPO₄, 50 mM NaCl, pH 6.9) at 4 °C overnight. The dialyzed protein solution was loaded onto a 1-ml Hitrap Q and then onto a 1-ml Hitrap SP column (GE Healthcare). The protein was eluted from the SP column with a 50–500 mM NaCl gradient. Solubility of the protein was 1–2 mg ml^{−1} in neutral and low pH buffers. However, the protein could be concentrated to 5–10 mg ml^{−1} when the pH of the buffer was raised to 9.5 or higher. Thus, the protein solution was dialyzed against a CHES (N-cyclohexyl-2-aminoethanesulphonic acid) buffer (20 mM CHES, 200 mM NaCl, pH 9.5) and the protein was purified by passing through a gel filtration column (Superdex 200, GE Healthcare). The purified protein was concentrated to 4–5 mg ml^{−1} in the CHES buffer for crystallization.

To produce the selenomethionine (SeMet)-substituted protein, the medium was replaced with ESF 921 serum-free methionine-free medium (Expression Systems) after 2 l of cells had reached a concentration of $10\text{--}12 \times 10^6$ cells ml^{−1}. The cells were starved for 4–6 h before 400 mg l^{−1} L-SeMet (Acros Organics) and 500 µM CuSO₄ were added. The medium was harvested 2–3 days after induction. The purification was similar to that of the native protein. Amino acid analysis showed that 90% of native methionine in the protein had been substituted by SeMet.

Crystallization and diffraction data collection. Crystals of the native E2–E1 protein grew at 20 °C by using the hanging-drop method. 1.5 µl of the protein solution and 1.5 µl of the mother solution were mixed and hung over 500 µl of the mother solution containing 11% polyethylene glycol (PEG) 8000, 200–275 mM Na/K tartrate, 0.1 M Na/KPO₄ pH 5.6. Crystals of the SeMet protein grew with the mother solution containing 9–10% PEG 8000, 300–375 mM Na/K tartrate, 0.1 M Na/KPO₄ pH 5.6. The crystals appeared in 3 days and grew to full size in 2–4 weeks. The crystals were soaked in the mother liquid plus 20% PEG 400 as a cryo-solvent, followed by flash-freezing in liquid nitrogen. Hundreds of crystals were screened at the Advanced Photon Source (APS, Argonne National Laboratory). The limits of the diffraction were gradually improved from 8-Å to 4-Å resolution. In general, the SeMet protein crystals diffracted better than the native protein crystals. The first complete data set of a native crystal extended to only 4-Å resolution. The best data sets were obtained from the SeMet protein crystals pre-treated with the mother liquid plus 20% PEG 400 and 1% H₂O₂ for 60 s before freezing³³. A multi-wavelength anomalous diffraction (MAD) data set with a resolution limit of 3.3 Å was collected at the APS beamline 23 ID-B (Supplementary Table 1).

Structure determination. The data were processed using the HKL2000 program³⁴. The output intensity files were converted to structure factor files for the CCP4 program package³⁵. For the first native data with the resolution of 4 Å, the space group was determined to be P321 with one E2–E1 heterodimer in an asymmetric unit. The pre- and post-fusion structures of the SFV E1 protein (Protein Data Bank accession numbers 2ALA and 1ERF) were used to generate search models for molecular replacement using the program Phaser³⁶. A solution was found when domains I and II (DI and DII) from the pre-fusion E1 structure were

used as a search model. However, the quality of the resultant electron density map was not good enough to interpret the E2 molecule. A single wavelength anomalous dispersion (SAD) data set of a SeMet crystal was collected with a resolution of 3.7 Å and space group P321. Ten out of the eleven selenium (Se) sites in the protein were found by using the program SHELXD³⁷. Later, a three-wavelength MAD data set was collected with the peak wavelength data having a resolution of 3.3 Å. The space group was determined to be P1 with six E2–E1 heterodimers in an asymmetric unit and cell dimensions similar to the P321 space group. The crystallographic 3, 2 and 2₁ axes present in the P321 space group were now only approximate non-crystallographic symmetry (NCS) axes indicating that the overall molecular packing remained similar to that of the P321 space group. The initial Se sites were generated by using all the Se sites in one unit cell of the SAD data collected for the space group P321. The sites were refined in the program SHARP³⁸. The quality of the resultant map was greatly improved by six-fold NCS averaging and other density improvement methods implemented in the programs DM³⁹ and RESOLVE⁴⁰. DI and DII of E1 and domains A and C of E2 could be traced in the density map. A barrel-shape density was evident for each of the six independent DIII domains of E1, although the individual chains could not be traced. Therefore, the DIII model of SFV was placed in the density using a real space search procedure with the program ESSENS⁴¹, followed by rigid body refinement with the program REFMAC5⁴². The E2–E1 model was built by using the program COOT⁴³ with the guidance from the $(2F_o - F_c)$, $(F_o - F_c)$, omit, and B-factor sharpened $(2F_o - F_c)$ maps. Structure refinement was performed using the programs PHENIX⁴⁴ and REFMAC5⁴² with tight NCS restraints and TLS refinement⁴⁵ (Supplementary Fig. 7 and Supplementary Table 1). The electron density for DIII was recognizable, but the mean B factor of the main chain atoms of DIII was 270 Å² as opposed to 120 Å² for the main chain atoms in DI and DII. The structure of E2, lying roughly parallel to E1, was as expected. Each spike structure consisted of a three-start right-handed helix with a maximum diameter of about 78 Å.

The crystallographic 32 symmetry in the trigonal space group (or quasi-32 symmetry in the triclinic space group) produced two two-fold-related trimers of E2–E1 heterodimers. In the triclinic cell the crystallographic three- and two-fold axes were only approximate because of a slight rotation and displacement of each of the two spikes in the unit cell. Superposition of the crystal structure onto the cryo-EM structure⁸ gave an r.m.s.d. of 3.4 Å between equivalent Cα atoms in DI and D2.

Fitting of the crystal structure into the cryo-EM density. The crystal structure of the E2–E1 heterodimer was fitted into the 9-Å resolution cryo-EM map of Sindbis virus⁸ (Electron Microscopy Data Bank accession number 1121) using the program EMfit³⁰, and gave a fit that was at least as good as the independent fitting of three SFV structures of E1 into the Sindbis virus cryo-EM density⁸. DI, DII and DIII of E1, domain A, the β-ribbon connector and domain C of E2 were fitted as individual rigid bodies for each of the four quasi-equivalent positions (Supplementary Table 4).

The DI–DII component of E1 had behaved as a rigid body in previous structural analyses of alphavirus particles^{8,9}, but the angle between DIII and DI–DII was found to be variable. In the crystal structure reported here the angle between DI–DII and DIII has changed by about 9° relative to the angles observed in the neutral pH cryo-EM structure of Sindbis virus or 18° relative to the crystal structure of SFV E1.

Domain A was found to be rotated (~10°) and translated (~5 Å) slightly relative to the crystal structure in order to obtain the best fit into the cryo-EM density. This small conformational change of the A domain within the trimeric spike may be the result of crystal packing where a carbohydrate moiety associated with Asn 318 in E2 interacts with domain A in a neighbouring spike. As the structure of the B domain has two disulphide bonds¹³, it is likely to be a rigid body. Attempts were made using the computer program EMfit³⁰ to determine alternative positions of the B domain in the uninterpreted regions of density tentatively interpreted as solvent. A number of likely positions were found that had the N and C termini of domain B within 20 Å of the C and N discontinued ends of the β-ribbon connector, respectively. Figures displaying the structure were generated with the program Chimera⁴⁶.

- Owen, K. E. & Kuhn, R. J. Identification of a region in the Sindbis virus nucleocapsid protein that is involved in specificity of RNA encapsidation. *J. Virol.* **70**, 2757–2763 (1996).
- Lehr, R. V., Elefante, L. C., Kiky, K. K., O'Brien, S. P. & Kirkpatrick, R. B. A modified metal-ion affinity chromatography procedure for the purification of histidine-tagged recombinant proteins expressed in *Drosophila* S2 cells. *Protein Expr. Purif.* **19**, 362–368 (2000).
- Sharff, A. J., Koronakis, E., Luisi, B. & Koronakis, V. Oxidation of selenomethionine: some MADness in the method! *Acta Crystallogr. D* **56**, 785–788 (2000).
- Otwinski, Z. & Minor, W. Processing of X-ray diffraction data collected in oscillation mode. *Methods Enzymol.* **276**, 307–326 (1997).
- Collaborative Computational Project Number 4. The CCP4 suite: programs for protein crystallography. *Acta Crystallogr. D* **50**, 760–763 (1994).

36. McCoy, A. J. *et al.* Phaser crystallographic software. *J. Appl. Cryst.* **40**, 658–674 (2007).
37. Sheldrick, G. M. A short history of SHELX. *Acta Crystallogr. A* **64**, 112–122 (2008).
38. de La Fortelle, E. & Bricogne, G. Maximum-likelihood heavy-atom parameter refinement for multiple isomorphous replacement and multiwavelength anomalous diffraction methods. *Methods Enzymol.* **276**, 472–494 (1997).
39. Cowtan, K. D. 'dm': an automated procedure for phase improvement by density modification. *Joint CCP4 ESF-EACBM Newsl. Protein Crystallogr.* **31**, 34–38 (1994).
40. Terwilliger, T. C. Maximum-likelihood density modification. *Acta Crystallogr. D* **56**, 965–972 (2000).
41. Kleywegt, G. J. & Jones, T. A. Template convolution to enhance or detect structural features in macromolecular electron-density maps. *Acta Crystallogr. D* **53**, 179–185 (1997).
42. Murshudov, G. N., Vagin, A. A. & Dodson, E. J. Refinement of macromolecular structures by the maximum-likelihood method. *Acta Crystallogr. D* **53**, 240–255 (1997).
43. Emsley, P. & Cowtan, K. Coot: model-building tools for molecular graphics. *Acta Crystallogr. D* **60**, 2126–2132 (2004).
44. Adams, P. D. *et al.* PHENIX: a comprehensive Python-based system for macromolecular structure solution. *Acta Crystallogr. D* **66**, 213–221 (2010).
45. Winn, M. D., Isupov, M. N. & Murshudov, G. N. Use of TLS parameters to model anisotropic displacements in macromolecular refinement. *Acta Crystallogr. D* **57**, 122–133 (2001).
46. Pettersen, E. F. *et al.* UCSF Chimera—a visualization system for exploratory research and analysis. *J. Comput. Chem.* **25**, 1605–1612 (2004).

Glycoprotein organization of Chikungunya virus particles revealed by X-ray crystallography

James E. Voss^{1,2}, Marie-Christine Vaney^{1,2}, Stéphane Duquerroy^{1,2,3}, Clemens Vornrhein⁴, Christine Girard-Blanc^{5,6}, Elodie Crublet^{5,6}, Andrew Thompson⁷, Gérard Bricogne⁴ & Félix A. Rey^{1,2}

Chikungunya virus (CHIKV) is an emerging mosquito-borne alphavirus that has caused widespread outbreaks of debilitating human disease in the past five years¹. CHIKV invasion of susceptible cells is mediated by two viral glycoproteins, E1 and E2, which carry the main antigenic determinants and form an icosahedral shell at the virion surface. Glycoprotein E2, derived from furin cleavage of the p62 precursor into E3 and E2, is responsible for receptor binding, and E1 for membrane fusion. In the context of a concerted multidisciplinary effort to understand the biology of CHIKV², here we report the crystal structures of the precursor p62–E1 heterodimer and of the mature E3–E2–E1 glycoprotein complexes. The resulting atomic models allow the synthesis of a wealth of genetic, biochemical, immunological and electron microscopy data accumulated over the years on alphaviruses in general. This combination yields a detailed picture of the functional architecture of the 25 MDa alphavirus surface glycoprotein shell. Together with the accompanying report on the structure of the Sindbis virus E2–E1 heterodimer at acidic pH (ref. 3), this work also provides new insight into the acid-triggered conformational change on the virus particle and its inbuilt inhibition mechanism in the immature complex.

Although the symptoms of the disease were first described in the eighteenth century⁴, CHIKV was first isolated only in 1952 during a dengue outbreak in Tanzania⁵. The name Chikungunya means “stooped walk” in the Tanzanian Kimakonde language⁶, an allusion to the persistent arthralgia caused by the disease, which otherwise shares clinical similarities with dengue disease⁷. CHIKV is geographically spread throughout vast regions of Africa and Asia, but remained essentially neglected until an important epidemic outbreak in 2005 in islands of the Indian Ocean⁸ attracted the attention of the western world. This outbreak was the consequence of an adaptation of CHIKV to efficiently infect *Aedes albopictus* mosquitoes in addition to the normal vector *Aedes aegypti*, and important determinants of the new vector adaptation were mapped to the CHIKV envelope proteins^{9,10}. The presence of the new mosquito vector in many areas of Europe and the Americas¹¹ raises concerns of further expansion of the endemic zones.

p62 and E1 are type I membrane proteins that are derived from a structural polyprotein precursor (Supplementary Fig. 1a). Their cotranslational association, in the endoplasmic reticulum of the infected cell, into a p62–E1 heterodimer is required for proper folding. In turn, the heterodimers trimerize to form the viral ‘spikes’. Furin maturation of p62 into E3 and E2 during transport to the cell surface primes the spikes for subsequent fusogenic activation for cell entry. Mature virions bud at the plasma membrane via interactions between E2 and genome-containing viral nucleocapsids present in the cytoplasm. The recently reported cryo-electron microscopy (cryo-EM) reconstruction of CHIKV virion-like particles confirmed that all alphaviruses have a common architecture¹². The particles are organized with icosahedral symmetry of triangulation $T = 4$, containing 80 spikes that

make a glycoprotein shell enclosing the viral membrane and the nucleocapsid. E3, which contains the 64 amino-terminal residues of p62¹³, remains peripherally attached to virions for some alphaviruses¹⁴.

Alphaviruses enter cells via receptor-mediated endocytosis¹⁵. The acidic endosomal environment triggers an irreversible conformational rearrangement of the surface glycoprotein shell of mature virions¹⁶. The E2–E1 heterodimer dissociates and E1 rearranges into fusogenic homotrimers that induce fusion of viral and endosomal membranes^{17,18}, allowing the release of the viral nucleocapsid into the cytosol. The crystal structure of the alphavirus E1 ectodomain has been determined in both pre-¹⁹ and post-fusion²⁰ conformations, showing that it is folded into three β -sheet-rich domains (domains I, II and III; Fig. 1a), with an internal fusion loop at the tip of domain II²¹. The structure of alphavirus E2, in contrast, has remained elusive over the years. We adopted the strategy described in Methods to produce, crystallize and determine the 2.2-Å-resolution structure of recombinant CHIKV p62–E1 and furin-processed, mature E3–E2–E1 glycoprotein complexes.

The structure shows that the p62–E1 heterodimer has the shape of a twisted plate about 150 Å long, 50 Å wide and 25 Å thick (Fig. 1a and Supplementary Fig. 3), with E3 sticking out at one side (Fig. 1a inset, and Supplementary Fig. 3a). The furin site is in an exposed loop at the surface of the spike (Fig. 1a). The mature E3–E2–E1 complex is very similar, the only important difference being in the residues forming the furin loop, which become disordered on cleavage. E3 is an α/β protein, with an N-terminal β -hairpin packing against three α -helices organized into a horseshoe shape (Supplementary Fig. 4c). E2 is an all β protein belonging to the immunoglobulin superfamily, with three immunoglobulin domains labelled A, B and C in amino- to carboxy-terminal order (Fig. 1b). Domain B is at the membrane distal end and domain C is towards the viral membrane, with domain A at the centre. Domain B is presented at the tip of a long β -ribbon connector (Supplementary Fig. 4b), which makes most of the contacts with E3 (Supplementary Fig. 5). A detailed description of the individual domains is provided in Supplementary Information.

In the complex, E1 makes no direct contact with E3, interacting laterally with E2 all along domain II. Furthermore, the segment immediately downstream of domain III makes an additional strand inserted in E2 domain C. E1 is bent compared to its structure in isolation, with the fusion loop unfolded to make a short β -hairpin inserted in a groove between domains A and B (Figs 1a and 2). This conformation is stabilized by a number of E2 histidine side chains (Fig. 2a), some of which hydrogen bond to the main chain of the E1 fusion loop. The area buried from solvent per protomer in the E2–E1 complex is about 2,500 Å² (Supplementary Fig. 3 and Supplementary Table 4a), which is large compared to the 1,100 Å² buried in the flavivirus E homodimer²². The α -helical portion of E3 packs against the E2 β -ribbon, burying 800 Å² of its surface from solvent (Supplementary Table 4b) at the region

¹Institut Pasteur, Département de Virologie, Unité de Virologie Structurale, 25 rue du Dr Roux, 75724 Paris Cedex 15, France. ²CNRS URA 3015, 25 rue du Dr Roux, 75724 Paris Cedex 15, France.

³Université Paris-Sud, Faculté d'Orsay, 91405 Orsay Cedex, France. ⁴Global Phasing Ltd, Sheraton House, Castle Park, Cambridge CB3 0AX, United Kingdom. ⁵Institut Pasteur, Département de Biologie Structurale et Chimie, Plateforme de Production de protéines recombinantes, 25 rue du Dr Roux, 75724 Paris Cedex 15, France. ⁶CNRS URA 2185, 25 rue du Dr Roux, 75724 Paris Cedex 15, France.

⁷Synchrotron SOLEIL, L'Orme de Merisiers, BP 48 St Aubin, 91192 Gif sur Yvette, France.

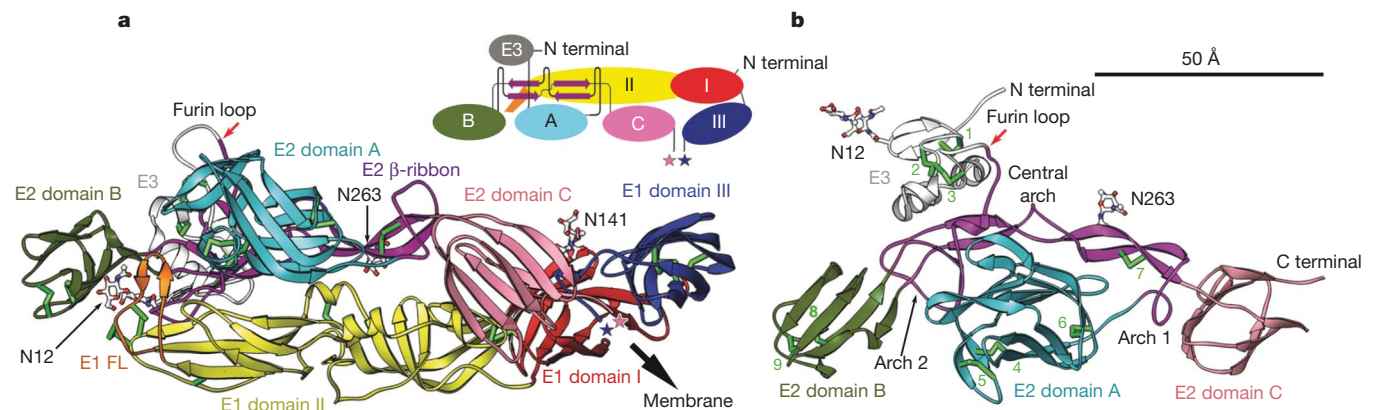


Figure 1 | Structure of the p62–E1 heterodimer. **a**, Ribbon diagram of the p62–E1 heterodimer. E1 domains I, II and III are shown in red, yellow and blue, respectively, and the fusion loop (FL) in orange. E3 is coloured white/grey and E2 domain A is coloured cyan, B dark green, C pink and the β -ribbon dark purple. The N-linked glycans are shown in ball and stick, coloured according to atom type, and labelled. The disulphides are depicted as green sticks. The black

arrow (next to the pink and blue stars indicating the C termini of p62 and E1, respectively) points to the viral membrane. Inset, schematic diagram, with the heterodimer ‘plate’ drawn ‘untwisted’, showing how the domains are positioned with respect to one another and their connectivity. **b**, p62 organization, oriented roughly at 90 degrees from **a** to show E3. Green numbers label the disulphides according to Supplementary Fig. 1b.

behind the groove in which the E1 fusion loop inserts. The structure shows that E3 acts as a brace, maintaining domain B in an orientation with respect to domain A such that it creates the groove accommodating the fusion loop. This is consistent with the observation that recombinant E2 lacking the E3 moiety does not dimerize with E1²³.

We built a model for the whole glycoprotein layer of the alphavirus particle (Fig. 3) by fitting the structure of the CHIKV E2–E1 heterodimer into the available cryo-EM reconstructions of alphavirus particles as explained in Supplementary Information (Supplementary Fig. 6). The result gives the intra- and interspike contact details (Supplementary Table 4c, d), confirming that E2 and E1 make all the intra- and interspike contacts, respectively. Domain A makes three-fold contacts at the spike top, with domain B projecting to the side to give the spike its characteristic propeller shape. Domain C is sandwiched between domain II of two neighbouring E1 molecules, making the walls of a central cavity under domain A, centred on the three-fold axis of the spike.

The inferred atomic model is consistent with the available biological data on alphaviruses, with mutations conferring escape to neutralizing antibodies mostly clustered on domain B, as well as the top of domain A (Supplementary Figs 1b, 7 and Supplementary Table 6). Furthermore, the mutations affecting tissue tropism and host range also map to domains A and B, as described in Supplementary Information and illustrated in Supplementary Fig. 1b and Supplementary Table 7. In particular, a number of determinants for efficient mosquito midgut infectivity of CHIKV²⁴ and other alphaviruses (Supplementary Table 7c) map to the ‘wings’ and the FG loop (see Supplementary Information) at the top of domain A. It is noteworthy that domain A, exposed at the top of the spike, is clearly homologous to domain III of the flavivirus envelope protein E (ref. 22) (Supplementary Fig. 4a and Supplementary

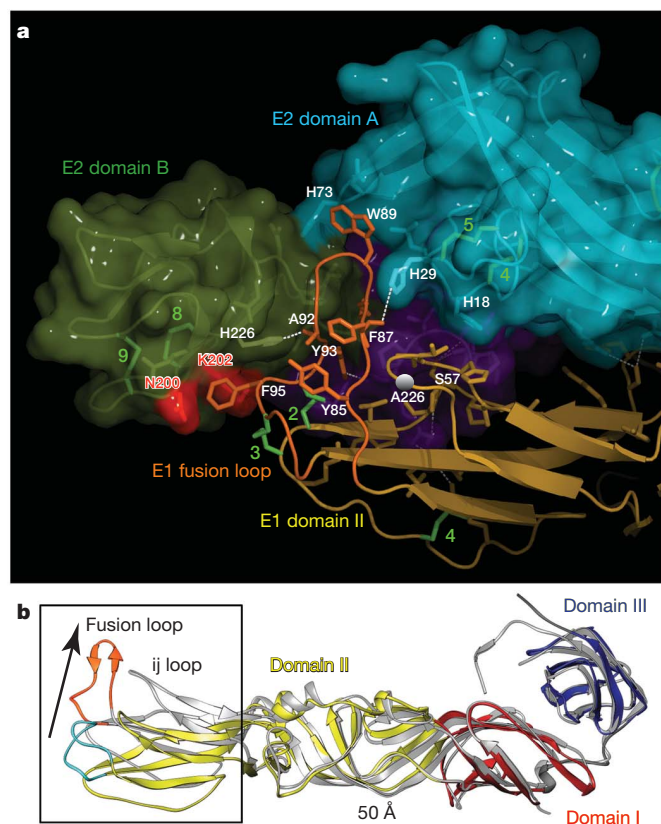


Figure 2 | The E1 fusion loop binding groove in E2. **a**, Fusion loop contacts. E2 (in a transparent surface rendering) and E1 (in ribbons) are in the background and foreground, respectively. Dotted white lines show hydrogen bonds from E2 histidines to the fusion loop main chain. Residues marking the E2 transitional epitope^{26,28} are coloured red and labelled. Green numbers highlight the cluster of disulphide bonds in this part of the complex. The residue Ala 226 is shown as a grey sphere. **b**, E1 conformation. The 3 Å Semliki Forest virus (SFV) E1 model (PDB code 2ALA), coloured by domains with the fusion loop cyan, is shown superposed on E1 from the p62–E1 complex, in grey with the fusion loop orange. The black arrow emphasizes the movement of the fusion loop and the adjacent ij loop, which contains residue Ala 226, mentioned in the text.

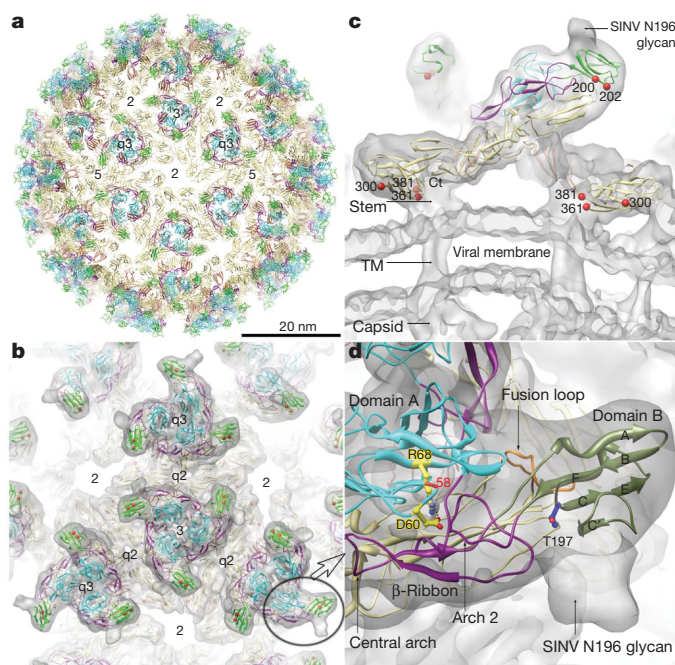


Figure 3 | Combination with cryo-EM data. **a**, The alphavirus $T = 4$ icosahedral surface glycoprotein shell. Atomic model of the 240 chikungunya E2–E1 heterodimers arranged as 80 spikes. E2 is coloured as in Fig. 1 and E1 is sandy brown for clarity. **b**, Top view of the spikes. The 9 Å resolution cryo-EM map of the Sindbis virus (SINV) virion³⁰ is represented as a grey transparent surface. The $T = 4$ icosahedral symmetry and quasi-symmetry axes are indicated. The black circle marks the close-up view of **d**. **c**, Side view of a spike. Red spheres mark the transitional epitopes on E2 domain B and on E1 domain III, in a region buried at interspike contacts. Regions of the map not fitted in this work (stem region, transmembrane (TM) domains, capsid and viral membrane) are indicated. **d**, Close-up of the spike top. The fusion loop (labelled) is capped by E2 domain B. The extra density extending away of domain B corresponds to an N-linked glycan in SINV (attached to N196, corresponding to Thr 197 in CHIKV, labelled). In domain A, the side chains of Asp 60 and the buried Arg 68, shown in yellow sticks and labelled, make a stabilizing salt bridge. Position 58, a virulence determinant (see Supplementary Tables 6 and 7), is marked in red.

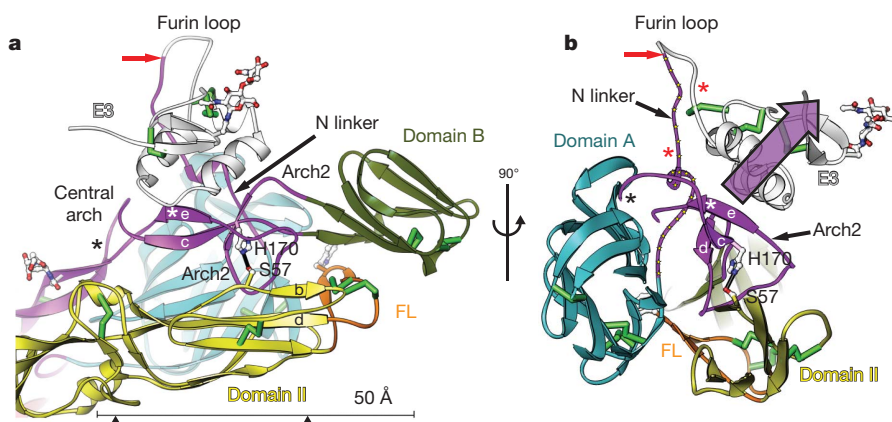


Figure 4 | p62 maturation and low pH conformational transition. **a**, **b**, Interactions of the ASR (see Supplementary Information) of E2 with E1 domain II, centred on the hydrogen bond (thick black line) between E2 His 170 and E1 Ser 57 (labelled). Black and white asterisks indicate the ends of visible density in the low pH structure of SINV E2–E1³. **a**, Side view. The tip of E1 domain II and the fusion loop projecting away from the paper with Trp 89 is in white. Domain A is in the background, behind the N linker. The two solid black

Table 2). A small patch of sequence similarity had indeed been detected²⁵, corresponding to the connection between two homologous β -strands (the EF loop) in the corresponding immunoglobulin β -barrels. Virulence determinants in flavivirus E protein also map to the FG loop of domain III, which has a similar orientation in the flavivirus particle (Supplementary Fig. 4a). The functional data provide further support to propose a common ancestry for these domains, which are inserted within proteins that are otherwise not homologous, confirming the mosaic nature of genes coding for viral envelope proteins in general.

Particularly informative are the locations of transitional epitopes, identified in E2 (residues 200 and 202), and in E1 (residues 300, 361 and 381)²⁶, which were reported to become accessible only on exposure of alphavirus particles to certain treatments, like heat, low pH and others²⁷. Exposure of the virions to susceptible cells was also reported to result in transitional epitope accessibility, which is suggestive of an early conformational change related to cell binding²⁸. The residues in the E1 transitional epitopes map to domain III, in a region that is buried in the particle at the spike interfaces (Fig. 3c). The E2 transitional epitope is in domain B, in a region contacting the E1 fusion loop (Figs 2a and 3c). The fact that this surface becomes exposed indicates that domain B moves out, thereby opening the groove and releasing the fusion loop. This observation is in agreement with the low pH structure reported in the accompanying paper³, in which domain B is out of place and disordered in the crystal. Furthermore, the locations of the E1 transitional epitopes indicate formation of alternative interspike contacts, indicating a possible allosteric transmission of the ‘uncapping’ signal across the particle surface (see Supplementary Movie). A detectable expansion of the alphavirus icosahedral particle on exposure to low pH has indeed been reported²⁹.

The low pH structure of the alphavirus E2–E1 heterodimer³ shows that domain B and half of the β -ribbon connector become disordered, with domains A and C remaining in place. The missing half of the β -ribbon, termed the acid sensitive region (ASR), is a region sandwiched between domain A of E2, E3 and E1 in the CHIKV structures (Supplementary Fig. 5a). The E2–E1 interactions in this region are centred around a hydrogen bond between the side chains of E2 His 170 and E1 Ser 57 (Fig. 4 and Supplementary Fig. 2), which are conserved in all mosquito-borne alphaviruses (Supplementary Fig. 1b, c). In the immature particle, domain A and E3, which are tethered by the N linker (see Supplementary Information), clamp the β -ribbon in place until furin cleaves the tether (Fig. 4b). The CHIKV structures thus explain the resistance of immature alphavirus particles to activation by low pH.

triangles under the scale bar indicate the slab used for **b**. **b**, Clamping by E3 and domain A on the ASR. View at 90 degrees from **a**, as indicated. The N linker is highlighted with yellow dots. Cleavage by furin (red arrow) releases the constraint, allowing the dislodgement of the ASR on low pH destabilization of its contacts with E1 (movement indicated by the purple transparent arrow). Red asterisks delineate the region that becomes disordered on furin cleavage.

This analysis is corroborated by experimental data mapping virus rescue mutations in p62 to the ASR (Supplementary Table 5).

In conclusion, this study reveals the organization of the mature and immature alphavirus surface glycoprotein complexes, the nature of the initial activating transition when exposed to low pH and the inbuilt mechanism to prevent this change from taking place prematurely. Together with the accompanying paper³, the structures show that the first step of the alphavirus fusogenic transition is removal of the domain B cap covering the fusion loop, without full dissociation of the E2–E1 heterodimer. The structures also reveal the organization of the individual immunoglobulin-like domains of E2 that are responsible for receptor interactions, carrying important determinants of virulence and mosquito vector range. These domains also carry the epitopes targeted by neutralizing antibodies, opening the way for vaccine design by immunization against alphaviruses with small recombinant proteins instead of whole particles.

METHODS SUMMARY

Purification, crystallization and X-ray diffraction data collection. The ectodomains of CHIKV-115 p62 and E1 joined with a glycine serine linker were expressed and secreted from stably transfected S2 cells as a strep-tagged (IBA, <http://www.iba-go.com/>) recombinant protein. The protein was purified by affinity chromatography and limited proteolysis was used to cleave the linker. Diffraction data from native and several heavy-atom-derivative crystals were collected at synchrotron sources (Supplementary Table 1a, b).

Structure determination and refinement. The structure was determined using a combination of molecular replacement with the available structure of alphavirus E1, experimental phasing with heavy atoms, density modification, automatic model building and multi-crystal averaging. Atomic models were refined against diffraction data from five crystal forms (Supplementary Table 1c).

EM fitting. E2–E1 heterodimers were fitted in EM maps as described in Supplementary Information. The heterodimer was initially fit as a single rigid body and then was cut into five parts as defined in Supplementary Table 3.

Full Methods and any associated references are available in the online version of the paper at www.nature.com/nature.

Received 24 May; accepted 5 October 2010.

- Her, Z., Kam, Y. W., Lin, R. T. & Ng, L. F. Chikungunya: a bending reality. *Microbes Infect.* **11**, 1165–1176 (2009).
- Schwartz, O. & Albert, M. L. Biology and pathogenesis of chikungunya virus. *Nature Rev. Microbiol.* **8**, 491–500 (2010).
- Li, L., Jose, J., Xiang, Y., Kuhn, R. J. & Rossman, M. G. Structural changes of envelope proteins during alphavirus fusion. *Nature* doi:10.1038/nature09546 (this issue).
- Halstead, S. B. in *Pediatric Infectious Diseases* (eds Feigin, R. & Cherry, J.) 2178–2183 (Saunders, 2004).
- Robinson, M. C. An epidemic of virus disease in southern province, Tanganyika territory, in 1952–1953 I. Clinical features. *Trans. R. Soc. Med. Hyg.* **49**, 28–32 (1955).
- Johnson, F. Notes on Kimakonde. *Bull. Sch. Orient. Studies* **2**, 417–466 (1922).
- Carey, D. E. Chikungunya and dengue: a case of mistaken identity? *J. Hist. Med. Allied Sci.* **26**, 243–262 (1971).
- Schuffenecker, I. *et al.* Genome microevolution of chikungunya viruses causing the Indian Ocean outbreak. *PLoS Med.* **3**, e263 (2006).
- Tsetsarkin, K. A., Vanlandingham, D. L., McGee, C. E. & Higgs, S. A single mutation in chikungunya virus affects vector specificity and epidemic potential. *PLoS Pathog.* **3**, e201 (2007).
- Vazeille, M. *et al.* Two chikungunya isolates from the outbreak of La Reunion (Indian Ocean) exhibit different patterns of infection in the mosquito, *Aedes albopictus*. *PLoS ONE* **2**, e1168 (2007).
- Enserink, M. Entomology: a mosquito goes global. *Science* **320**, 864–866 (2008).
- Akahata, W. *et al.* A virus-like particle vaccine for epidemic chikungunya virus protects nonhuman primates against infection. *Nature Med.* **16**, 334–338 (2010).
- Salminen, A. *et al.* Membrane fusion process of Semliki Forest virus. II. Cleavage-dependent reorganization of the spike protein complex controls virus entry. *J. Cell Biol.* **116**, 349–357 (1992).
- Ziemiacki, A., Garoff, H. & Simons, K. Formation of the Semliki Forest virus membrane glycoprotein complexes in the infected cell. *J. Gen. Virol.* **50**, 111–123 (1980).
- Marsh, M. & Helenius, A. Virus entry into animal cells. *Adv. Virus Res.* **36**, 107–151 (1989).
- Wahlberg, J. M., Boere, W. A. & Garoff, H. The heterodimeric association between the membrane proteins of Semliki Forest virus changes its sensitivity to low pH during virus maturation. *J. Virol.* **63**, 4991–4997 (1989).
- Kielian, M. & Helenius, A. pH-induced alterations in the fusogenic spike protein of Semliki Forest virus. *J. Cell Biol.* **101**, 2284–2291 (1985).
- Wahlberg, J. M., Bron, R., Wilschut, J. & Garoff, H. Membrane fusion of Semliki Forest virus involves homotrimers of the fusion protein. *J. Virol.* **66**, 7309–7318 (1992).
- Lescar, J. *et al.* The fusion glycoprotein shell of Semliki Forest virus: an icosahedral assembly primed for fusogenic activation at endosomal pH. *Cell* **105**, 137–148 (2001).
- Gibbons, D. L. *et al.* Conformational change and protein–protein interactions of the fusion protein of Semliki Forest virus. *Nature* **427**, 320–325 (2004).
- Kielian, M. & Rey, F. A. Virus membrane-fusion proteins: more than one way to make a hairpin. *Nature Rev. Microbiol.* **4**, 67–76 (2006).
- Rey, F. A. *et al.* The envelope glycoprotein from tick-borne encephalitis virus at 2 Å resolution. *Nature* **375**, 291–298 (1995).
- Lobigs, M., Zhao, H. X. & Garoff, H. Function of Semliki Forest virus E3 peptide in virus assembly: replacement of E3 with an artificial signal peptide abolishes spike heterodimerization and surface expression of E1. *J. Virol.* **64**, 4346–4355 (1990).
- Tsetsarkin, K. A. *et al.* Epistatic roles of E2 glycoprotein mutations in adaptation of chikungunya virus to *Aedes albopictus* and *Ae. aegypti* mosquitoes. *PLoS ONE* **4**, e6835 (2009).
- Pierro, D. J., Powers, E. L. & Olson, K. E. Genetic determinants of Sindbis virus mosquito infection are associated with a highly conserved alphavirus and flavivirus envelope sequence. *J. Virol.* **82**, 2966–2974 (2008).
- Meyer, W. J. & Johnston, R. E. Structural rearrangement of infecting Sindbis virions at the cell surface: mapping of newly accessible epitopes. *J. Virol.* **67**, 5117–5125 (1993).
- Meyer, W. J. *et al.* Conformational alteration of Sindbis virion glycoproteins induced by heat, reducing agents, or low pH. *J. Virol.* **66**, 3504–3513 (1992).
- Flynn, D. C., Meyer, W. J., Mackenzie, J. M. Jr & Johnston, R. E. A conformational change in Sindbis virus glycoproteins E1 and E2 is detected at the plasma membrane as a consequence of early virus–cell interaction. *J. Virol.* **64**, 3643–3653 (1990).
- Wu, S. R. *et al.* The dynamic envelope of a fusion class II virus. Prefusion stages of Semliki Forest virus revealed by electron cryomicroscopy. *J. Biol. Chem.* **282**, 6752–6762 (2007).
- Mukhopadhyay, S. *et al.* Mapping the structure and function of the E1 and E2 glycoproteins in alphaviruses. *Structure* **14**, 63–73 (2006).

Supplementary Information is linked to the online version of the paper at www.nature.com/nature.

Acknowledgements We thank the CHIKV task force at Institut Pasteur, in particular the group of F. Tangy and the staff of platform PF8 for the CHIKV complementary DNA; A. Haouz of PF6 for crystallography; the staff of synchrotron beamlines PROXIMA 1 at Soleil, ID23-eh2 at the European Synchrotron Radiation Facility and PX-I at the Swiss Light Source; M. Rossmann and Y. Sun for providing the 16 Å cryo-EM map of CHIKV virion-like particles and for sharing the coordinates and manuscript of the low pH structure of the SINVE1–E2 heterodimer before publication; and members of the F.A.R. laboratory for help during data collection. J.E.V. was supported by a Marie Curie fellowship through the European Union Research Training Network program “Intrapath”. This work was funded in part by the French ‘Agence Nationale de la Recherche’ grant DENTY in the program ‘Microbiologie, Infections et Immunité’, by Merck-Serono, by the Pediatric Dengue Vaccine Initiative and by the Institut Pasteur program PTR201 CHIKV to F.A.R.

Author Contributions J.E.V. made the constructs, produced and purified the protein, grew the crystals and participated in diffraction data collection; analysed the literature and prepared tables and figures. M.-C.V. carried out most of the various crystallographic refinements and prepared the figures, S.D. carried out the fitting into the cryo-EM maps of various alphavirus particles and prepared the figures, C.G.-B. and E.C. participated in optimizing protein production in large scale for crystal trials, C.V. and G.B. participated in data processing and in the structure determination. A.T. carried out specific data collection strategies to improve the signal to noise to extract anomalous signal for phasing; F.A.R. conceived the experiments and wrote the manuscript.

Author Information Structure factors and coordinates for the structures of the p62–E1 (crystal IO), E3–E2–E1_{sp} (crystal MM), E3–E2–E1_t (crystal MO1), E3–E2–E1_t (crystal MO2) and Os2–E3–E2–E1_t (crystal MO3) complexes have been deposited in the Protein Data Bank under accession codes 3N40, 3N41, 3N42, 3N43 and 3N44, respectively. The coordinates of the molecules fitted in the cryo-EM 3D reconstructions of SINVE1 and SFV particles were deposited under accession codes 2XFB and 2XFC, respectively. Reprints and permissions information is available at www.nature.com/reprints. The authors declare no competing financial interests. Readers are welcome to comment on the online version of this article at www.nature.com/nature. Correspondence and requests for materials should be addressed to F.A.R. (rey@pasteur.fr).

METHODS

Recombinant protein production and purification. We produced the recombinant p62–E1 and E3–E2–E1 complexes from the clinical isolate 05-115 (ref. 31) in *Drosophila melanogaster* Schneider 2 (S2) cells with the construct outlined in Fig. 1a, bottom-right panel. A 19-residue linker, with sequence (GGGS)₄ (omitting the last Ser residue) connected the C terminus of the p62 ectodomain to the N terminus of E1, thus bypassing the p62 transmembrane region and the 6K protein (Supplementary Fig. 1a). The actual construct contained amino acids 1–421 of p62 (the last one corresponding to E2 residue 361) and 1–412 of E1 (that is, all of the ectodomain, stopping right at the beginning of the transmembrane segment for both proteins; see Supplementary Fig. 1a, b). We tried a shorter construct in parallel, spanning p62 residues 1–404 (the end corresponding to E2 position 340) and E1 1–392 joined with the same linker, but we did not get diffraction-quality crystals from the resulting protein. For expression in *Drosophila* cells, we used a modified version of the pMRBiP/V5 HisA plasmid (Invitrogen) in which a double strep-tag (IBA, <http://www.iba-go.com/>) replaces the C-terminal His tag³². In addition, the *Drosophila* BiP signal sequence was replaced by the authentic p62 signal sequence, which retracts from the membrane to make part of the E3 domain of p62 during folding (Supplementary Fig. 1a). The secreted protein was the mature E3–E2–E1 complex, resulting from maturation of p62 by *Drosophila* furin. To produce the immature complex we introduced a mutation at the furin site, sequence 61-RQRR↓S-65 (the down arrow indicating the site of cleavage) mutated into 61-RQRES-65 to avoid furin cleavage. In the end, we found it more convenient to use the latter construct, and cleave the immature complex with trypsin at the remaining basic residues of the mutated furin site to obtain the mature E3–E2–E1 complex when needed (both structures, furin-cleaved and trypsin-cleaved, were determined in this work, and they are identical).

Stable transfectant S2 cell lines were generated with these recombinant plasmids. One-litre cultures in logarithmic phase growth (Insect Express Media) were routinely induced with 500 μ M CuSO₄ to secrete protein for 1 week. The supernatants were then collected, concentrated and filtered with 0.2 μ m cutoff membrane and adjusted to pH 8 with Tris buffer containing avidin at 15 μ g ml^{−1}. The protein was purified by affinity chromatography using 4 ml StrepTactin columns (IBA). After loading the protein, the column was washed with 100 mM Tris pH 8.0, 150 mM NaCl, 1 mM EDTA, and the sample was eluted using 2.5 mM desthiobiotin. We adjusted the overall purification protocol after the initial crystallization. Screening results showed that cleavage of the artificial linker introduced in between p62 and E1 was necessary to obtain diffraction quality crystals. We found that the best crystals were obtained with protein digested with chymotrypsin, which cleaved in the region rich in aromatic residues at the end of p62 (around position 425, which corresponds to 360 in E2 numbering; Supplementary Fig. 1b), right before the linker. In our final protocol, the sample eluted from the StrepTactin column was pooled and treated with chymotrypsin (Roche) at a mass ratio of 1:5,000 enzyme:protein overnight at room temperature (20 °C). After stopping the reaction by the addition of phenylmethanesulphonyl fluoride (PMSF), the protein was desalted into 10 mM Tris pH 8.0, 10 mM NaCl (HiTrap Desalting Column 5 ml, GE Healthcare) to perform an ion exchange purification step. For this purpose, the sample was loaded onto a MonoQ 5/50 column (GE Healthcare). A salt gradient from 10 to 200 mM NaCl was applied, and the protein eluted as several overlapping peaks, which were collected in separate fractions, concentrated on a vivaspin 30K cutoff, and applied to a gel filtration Superdex 10/300 column equilibrated in 20 mM Tris pH 8.0, 100 mM NaCl. The gel filtration profile showed that the protein from the various peaks of the ion exchange chromatogram eluted at a similar volume, corresponding to a molecular weight of about 90 kD. The protein from this single peak was concentrated to about 6 mg ml^{−1} for crystallization. Similar crystals were obtained from samples belonging to different peaks in the ion exchange chromatogram. In cases where the mature form was obtained by trypsin treatment of the mutated p62–E1 heterodimer, cleavage of the linker was done first, and after addition of PMSF to stop the chymotrypsin reaction, desalting was done to remove excess PMSF and a second step of proteolysis was carried out with trypsin (Roche) also at a mass ratio of 1:5,000 enzyme:protein overnight at room temperature before the final purification steps by ion exchange and size exclusion chromatography described earlier.

Crystallization and data collection. The crystals were grown by vapour diffusion in hanging drops at 20 °C by mixing 1 μ l of protein at a concentration of 5–7 mg ml^{−1} in 20 mM Tris pH 8.0, 100 mM NaCl with 1 μ l of well solution containing 8–12% PEG4K, 100 mM NaAcetate, 100 mM HEPES pH 7.1–7.5. The original crystals were clusters of plates, and several successive seeding steps were used to obtain single crystals large enough for diffraction data collection (thin plates, 200 × 100 × 5 μ m³). Monoclinic crystals were obtained initially, coded as MM form for ‘mature monoclinic’ form (see Supplementary Table 1). Reproducing these crystals was difficult, until SDS–polyacrylamide gel electrophoresis analysis together with mass spectrometry and N-terminal sequencing of the protein recovered from

these crystals showed that there had been cleavage by an unknown contaminant protease in the region of the linker during the crystallization process (crystal E3–E2–E1_{sp}, where the ‘sp’ subscript stands for ‘spontaneous cleavage’, meaning unintended cleavage). The controlled chymotrypsin treatment outlined earlier was then introduced into the purification protocol, resulting in the growth of orthorhombic crystals. These include both the immature form obtained from the furin site mutant (crystal p62–E1, coded IO for ‘immature orthorhombic’; see Supplementary Table 1) as well as the mature forms; cleaved naturally by furin during expression for the wild type (crystal E3–E2–E1_f, code MO1, for ‘mature orthorhombic form 1’) or by trypsin treatment of the p62–E1 complex as described earlier (crystal E3–E2–E1_t, code MO2). The latter crystals were used to screen for heavy atom derivatives to obtain experimental phases. Useful phase information was recovered from osmate derivatives of the E3–E2–E1_f crystals obtained by soaking in 1 mM or in 10 mM potassium osmate (K₂OsO₄) solutions overnight. Also, a rare-earth derivative was obtained by soaking in a 50 mM holmium chloride (HoCl₃) solution for 2 h. All of the crystals were flash frozen in liquid nitrogen using 25% ethylene glycol as cryoprotectant. Diffraction data were collected at the European synchrotrons listed in Supplementary Table 1, and were processed with autoPROC (version 0.5.3; C. Vonrhein *et al.*, unpublished) using XDS³³, POINTLESS³⁴, SCALA and TRUNCATE from the Collaborative Computational Project, No. 4 (CCP4) suite³⁵. Data collection statistics for native and heavy atom derivative crystals are presented in the Supplementary Table 1a.

Structure determination. Initial phases were obtained by molecular replacement (MR) using AMoRe³⁶ with the structure of monomeric glycoprotein E1 from SFV (PDB code 2ALA)³⁷. The model used successfully for MR was a trimmed version, lacking the regions 52–109 and 217–238 (that is, the tip of domain II). The MR solution did not produce interpretable density for the remaining p62 part. These initial phases, however, were accurate enough to locate several heavy atom sites in anomalous difference Fourier maps for the 10 mM osmate derivative to 3.7 Å (Os1–E3–E2–E1_f) (Supplementary Table 1a). Those sites, together with the phases from the partial molecular replacement model, were refined and used for phasing in SHARP³⁸. The log-likelihood gradient maps were used to complement and correct the heavy atom model.

Density modification with SOLOMON³⁹ produced electron density maps that allowed the interpretation of the missing part of E1. The density in the p62 region could be interpreted in part by BUCCANEER⁴⁰ as polyalanine fragments. This gave a more complete model covering not only most of E1 but also significant portions of p62. The improved phases obtained by combining the phase information from the intermediate partial models with the experimental phases were used to determine the heavy atom sites in the other heavy atom derivative data sets (Os2–E3–E2–E1_f and Ho–E3–E2–E1_f). Because the various data sets were not isomorphous, showing significant variation in cell dimensions (up to 8 Å in the c axis for Os1–E3–E2–E1_f) (Supplementary Table 1a), the phase information from different data sets was combined by using multi-crystal averaging in DMULTI⁴¹. Averaging masks were based on the best partial model available at each step. Multi-crystal averaging was done using the monoclinic crystal form (map calculated with MR phases) with the orthorhombic crystal forms (using SIRAS data and phases based on the Ho–E3–E2–E1_f and p62–E1 data sets, anisotropically corrected within SHARP). The averaged map resulting from this multi-averaging step revealed the missing parts of the structure, which were built manually with the program COOT⁴². After rebuilding the tip of E1 domain II, including the fusion loop, the N-terminal part of E3 and the furin loop, the structure obtained was refined with BUSTER⁴³ against the p62–E1 data at 2.17 Å. The refined p62–E1 structure was then used in PHASER to obtain a molecular replacement solution for the other crystals. All the structures were refined by applying nine ‘TLS’ groups, describing the translation, libration and screw-rotation displacements (TLS⁴⁴) per complex. In the end, five crystal structures were refined: p62–E1 (IO), E3–E2–E1_f (MO1), E3–E2–E1_t (MO2), E3–E2–E1_{sp} (MM) and Os2–E3–E2–E1_f (MO3). The position and interactions in the structure of the heavy atoms used for phasing is listed in Supplementary Table 1b, and refinement statistics for the five structures are presented in Supplementary Table 1c. The superposition of the five refined models shows that there is variability at interdomain contacts (Supplementary Fig. 6a).

Fitting the crystallographic model into the cryo-EM density. The atomic model of the E2–E1 heterodimers was extracted from the p62–E1 and E3–E2–E1_{sp} crystal structures (codes IO and MM, respectively; Supplementary Table 1) and were fitted into the cryo-EM maps of SINV (Electron Microscopy Data Bank (EMDB) code EMD-1121; ref. 45), SFV (EMDB code EMD-1015; ref. 46) and CHIKV⁴⁷ by maximizing the correlation between structure factors calculated from the cryo-EM maps and from the atomic model with the program URO⁴⁸. The CHIKV three-dimensional reconstruction used was a 16 Å cryo-EM map provided by S. Sun and M. Rossmann. The procedure takes into account amplitude and phase information from the map and the $T = 4$ symmetry of the cryo-EM reconstruction. The E2–E1 heterodimers refined in the IO and MM crystals, which

adopt the most extreme conformations among the five refined structures, were fitted. The fits were done first as a single rigid body and were then improved using several rigid bodies (five for SFV and SINV, and three for CHIKV) as defined in Supplementary Table 3. The SFV cryo-EM map was rescaled by a factor of 1.04 after comparison with both CHIKV and SINV maps, to bring the viral membranes to a common radius. This step was done because fitting in the map without rescaling led to small clashes at the interspike contacts, which were released in the expanded version. A sphere of a radius of 260 Å, 250 Å and 255 Å respectively for SINV, SFV (before rescaling) and CHIKV was used to eliminate density belonging to the transmembrane regions and the nucleocapsid from the calculation, leaving only density corresponding to the alphavirus glycoprotein shell of the three different virions. The URO statistics resulting from the fitting are listed in Supplementary Table 3a, whereas Supplementary Table 3b provides the surface area buried in the various contacts in the particle between the fitted atomic models, together with the contacts observed within the E3–E2–E1 heterotrimer in the crystallographic model. The contacts on the spike are the interfaces between heterodimers within a spike and across spikes on the virion (as defined in the key in the bottom-right panel of Supplementary Fig. 1c). Supplementary Table 3c shows the root mean square deviation (r.m.s.d) after superposing the atomic models fitted independently in the four positions of the $T = 4$ icosahedral asymmetric unit of the particles, and on the different viruses. For comparison, the r.m.s.d. after superposition of the model refined in the different crystals is also provided in the same table. Supplementary Table 3d shows the $C\alpha$ – $C\alpha$ distance (normally 3.8 Å) resulting between the C termini and N termini of subsequent segments of the polypeptide chain that were refined in different rigid bodies, to give an idea of the distortion caused to the model (most of the breaks can be reconnected manually without major rearrangement of the polypeptide chain). Finally, Supplementary Fig. 6 shows a comparison of the inter-domain variations, reflecting inherent flexibility of the E2–E1 heterodimer. In all three panels, the $C\alpha$ atoms of the first portion of domain II (closest to domain I) of E1 were superposed and displayed so that the variation in orientation of the adjacent domains of E1 and E2 can be evaluated visually. Supplementary Fig. 6a shows this superposition after refining the atomic E2–E1 atomic models against the various crystals listed in Table 1c. Supplementary Fig. 6b shows this same superposition with the model resulting from fitting the E2–E1 heterodimer as five rigid bodies into the four icosahedrally independent locations of the $T = 4$ surface lattice of the SINV cryo-EM map and superposed in the same way. Superposition of the atomic models resulting from fitting at positions P of the $T = 4$ icosahedral lattice (see definition

in Supplementary Fig. 1c, bottom-right panel) in each of the particles of the three alphaviruses used (SINV, SFV and CHIKV) is shown in Supplementary Fig. 6c. This figure shows that the adjustments between domains are similar to the variations observed in different crystal forms, highlighting a natural flexibility of the E2–E1 heterodimer, which is used to adjust to the quasi-equivalent position in the virus particle.

31. Schuffenecker, I. *et al.* Genome microevolution of chikungunya viruses causing the Indian Ocean outbreak. *PLoS Med.* **3**, e263 (2006).
32. Krey, T. *et al.* The disulfide bonds in glycoprotein E2 of hepatitis C virus reveal the tertiary organization of the molecule. *PLoS Pathog.* **6**, e1000762 (2010).
33. Kabsch, W. Integration, scaling, space-group assignment and post-refinement. *Acta Crystallogr. D* **66**, 133–144 (2010).
34. Evans, P. R. Scaling and assessment of data quality. *Acta Crystallogr. D* **62**, 72–82 (2005).
35. Collaborative Computational Project Number 4. The CCP4 suite: programs for protein crystallography. *Acta Crystallogr. D* **50**, 760–763 (1994).
36. Navaza, J. Implementation of molecular replacement in AMoRe. *Acta Crystallogr. D* **57**, 1367–1372 (2001).
37. Roussel, A. *et al.* Structure and interactions at the viral surface of the envelope protein E1 of Semliki Forest virus. *Structure* **14**, 75–86 (2006).
38. Bricogne, G. *et al.* Generation, representation and flow of phase information in structure determination: recent developments in and around SHARP 2.0. *Acta Crystallogr. D* **59**, 2023–2030 (2003).
39. Abrahams, J. P. & Leslie, A. G. Methods used in the structure determination of bovine mitochondrial F1 ATPase. *Acta Crystallogr. D* **52**, 30–42 (1996).
40. Cowtan, K. The Buccaneer software for automated model building. 1. Tracing protein chains. *Acta Crystallogr. D* **62**, 1002–1011 (2006).
41. Cowtan, K. 'dm': an automated procedure for phase improvement by density modification. *Joint CCP4 ESF-EACBM News. Protein Crystallogr.* **31**, 34–38, (1994).
42. Emsley, P. *et al.* Features and development of Coot. *Acta Crystallogr. D* **66**, 486–501 (2010).
43. Bricogne, G. *et al.* BUSTER version 2.9. (Global Phasing, 2010).
44. Painter, J. & Merritt, E. A. A molecular viewer for the analysis of TLS rigid-body motion in macromolecules. *Acta Crystallogr. D* **61**, 465–471 (2005).
45. Mukhopadhyay, S. *et al.* Mapping the structure and function of the E1 and E2 glycoproteins in alphaviruses. *Structure* **14**, 63–73 (2006).
46. Mancini, E. J. *et al.* Cryo-electron microscopy reveals the functional organization of an enveloped virus, Semliki Forest virus. *Mol. Cell* **5**, 255–266 (2000).
47. Akahata, W. *et al.* A virus-like particle vaccine for epidemic Chikungunya virus protects nonhuman primates against infection. *Nature Med.* **16**, 334–338 (2010).
48. Navaza, J. *et al.* On the fitting of model electron densities into EM reconstructions: a reciprocal-space formulation. *Acta Crystallogr. D* **58**, 1820–1825 (2002).

Head swivel on the ribosome facilitates translocation by means of intra-subunit tRNA hybrid sites

Andreas H. Ratje^{1,2}, Justus Loerke¹, Aleksandra Mikolajka^{3,4}, Matthias Br  nner¹, Peter W. Hildebrand¹, Agata L. Starosta³, Alexandra D  nh  fer³, Sean R. Connell⁵, Paola Fucini⁵, Thorsten Mielke^{1,6}, Paul C. Whitford⁷, Jos   N. Onuchic⁸, Yanan Yu⁹, Karissa Y. Sanbonmatsu⁷, Roland K. Hartmann², Pawel A. Penczek¹⁰, Daniel N. Wilson^{3,4} & Christian M. T. Spahn¹

The elongation cycle of protein synthesis involves the delivery of aminoacyl-transfer RNAs to the aminoacyl-tRNA-binding site (A site) of the ribosome, followed by peptide-bond formation and translocation of the tRNAs through the ribosome to reopen the A site^{1,2}. The translocation reaction is catalysed by elongation factor G (EF-G) in a GTP-dependent manner³. Despite the availability of structures of various EF-G-ribosome complexes, the precise mechanism by which tRNAs move through the ribosome still remains unclear. Here we use multiparticle cryoelectron microscopy analysis to resolve two previously unseen subpopulations within *Thermus thermophilus* EF-G-ribosome complexes at subnanometre resolution, one of them with a partly translocated tRNA. Comparison of these substates reveals that translocation of tRNA on the 30S subunit parallels the swivelling of the 30S head and is coupled to unratcheting of the 30S body. Because the tRNA maintains contact with the peptidyl-tRNA-binding site (P site) on the 30S head and simultaneously establishes interaction with the exit site (E site) on the 30S platform, a novel intra-subunit 'pe/E' hybrid state is formed. This state is stabilized by domain IV of EF-G, which interacts with the swivelled 30S-head conformation. These findings provide direct structural and mechanistic insight into the 'missing link' in terms of tRNA intermediates involved in the universally conserved translocation process.

After peptide-bond formation, pre-translocational (PRE) ribosomes carry a peptidyl-tRNA at the A site and a deacylated tRNA at the P site^{1,3,4}. This is a highly dynamic state of the ribosome, which fluctuates between classical states with A tRNA and P tRNA and hybrid states with A/P tRNAs (A/P denotes that the tRNA is in the A site on the 30S subunit and the P site on the 50S subunit) and P/E tRNAs⁵⁻⁸. Hybrid state formation is coupled to spontaneous rotation of the 30S subunit relative to the 50S subunit⁹⁻¹¹ and is stabilized by the binding of EF-G¹²⁻¹⁴. The ratchet-like subunit rearrangement induced by EF-G and eukaryotic elongation factor 2 (eEF2) also includes a swivel movement of the head that is roughly orthogonal to the inter-subunit rotation of the ribosomal subunits¹⁴⁻¹⁶. EF-G catalyses translocation of the hybrid-state tRNAs on the 30S subunit to form a post-translocational (POST) state ribosome with tRNAs located at classical P and E sites. The translocation process is accelerated by the GTPase activity of EF-G stimulated by the ribosome^{17,18}. However, it is still not known how tRNAs are translocated with respect to the 30S subunit and how the messenger RNA is advanced by one codon.

Structural snapshots of the translocation process come from cryoelectron microscopy and X-ray analysis of EF-G bound to ribosome complexes^{12-14,19}. Despite considerable effort^{12,20-22}, no direct structural information is available for ribosomal PRE complexes simultaneously

containing EF-G and an A tRNA. It seems that this state is too dynamic and transient to be captured, resulting in either a POST state containing EF-G or a PRE state without EF-G bound^{20,22}. Indeed, the stable EF-G-bound POST state determined by X-ray crystallography reveals a non-ratcheted ribosome with tRNAs in classical P/P and E/E sites¹⁹. Therefore, structural insights into intermediate states of translocation—that is, ratcheted ribosomal EF-G complexes—have used complexes without an A-site peptidyl-tRNA¹²⁻¹⁴.

In this study we used the antibiotic fusidic acid (FA) to stall EF-G on the 70S ribosome. FA permits the hydrolysis of GTP by EF-G but prevents the associated changes in EF-G that normally accompany hydrolysis¹⁹. After complex formation and the collection of cryoelectron microscopy data, we employed multiparticle refinement to resolve the heterogeneity of the data (Supplementary Fig. 1). In the first phase of multiparticle refinement a large population of particle images of ribosomes containing EF-G was obtained that yielded a structure in a ratcheted conformation. As refinement progressed to higher resolution, the presence of intrinsic conformational heterogeneity necessitated a second phase of multiparticle refinement, resulting in two final reconstructions of the 70S-EF-G-GDP-FA complex (Fig. 1), at resolutions of 7.6 Å and 7.8 Å (using a 0.5 Fourier shell correlation cut-off criterion), respectively (Supplementary Fig. 2). Both maps have density attributed to EF-G, but they show significant conformational differences (Supplementary Movies 1 and 2): specifically, the substates are distinguished by different degrees of subunit ratcheting and positioning of the L1 protuberance, and also by the swivel movement of the head of the 30S subunit relative to the body/platform (Fig. 1e, f, Supplementary Figs 3 and 4, and Supplementary Table 1). Unlike previous cryoelectron microscopy and X-ray structures of ribosome-EF-G complexes, movement of the head and body/platform of the 30S subunit is uncoupled: in substate I, the 30S subunit is ratcheted by about 7° relative to the 50S subunit, but there is only a modest (roughly 5°) swivelling of the 30S head. In contrast, the 30S in substate II is only ratcheted by about 4°, but there is a very large (roughly 18°) swivel of the head (Supplementary Table 1).

The identification of two different ratcheted substates within the 70S-EF-G-GDP-FA complex prompted us to investigate whether such intrinsic heterogeneity also exists in our previous 70S-EF-G-GMPPNP cryoelectron microscopy data set¹⁴. Additional multiparticle refinement did indeed reveal that the 70S-EF-G-GMPPNP complex could be subdivided into two substates that seemed to be equivalent to those identified in the 70S-EF-G-GDP-FA complex (Supplementary Fig. 5 and Supplementary Table 1). Our findings here provide evidence supporting the emerging energy-landscape model that allows the sampling of several metastable conformations for a defined ribosomal

¹Institut f  r Medizinische Physik und Biophysik, Charit   – Universit  tsmedizin Berlin, Ziegelstrasse 5–9, 10117-Berlin, Germany. ²Institut f  r Pharmazeutische Chemie, Philipps-Universit  t Marburg, 35037 Marburg, Germany. ³Gene Center and Department of Biochemistry, Ludwig-Maximilians-Universit  t, Feodor-Lynenstrasse 25, 81377 M  nchen, Germany. ⁴Center for Integrated Protein Science, Ludwig-Maximilians-Universit  t M  nchen, 81377 M  nchen, Germany. ⁵Frankfurt Institute for Molecular Life Sciences, Institute of Organic Chemistry and Chemical Biology, Goethe University Frankfurt, Max-von-Laue-Strasse 7, D-60438 Frankfurt am Main, Germany. ⁶UltraStrukturNetzwerk, Max Planck Institute for Molecular Genetics, 14195 Berlin, Germany. ⁷Theoretical Biology and Biophysics Group, Theoretical Division, Los Alamos National Laboratory, Los Alamos, New Mexico 87545, USA. ⁸Center for Theoretical Biological Physics and Department of Physics, University of California, San Diego, La Jolla, California 92093, USA. ⁹Florida State University, Department of Computer Science, Tallahassee, Florida 32306, USA. ¹⁰The University of Texas – Houston Medical School, 6431 Fannin, Houston, Texas 77030, USA.

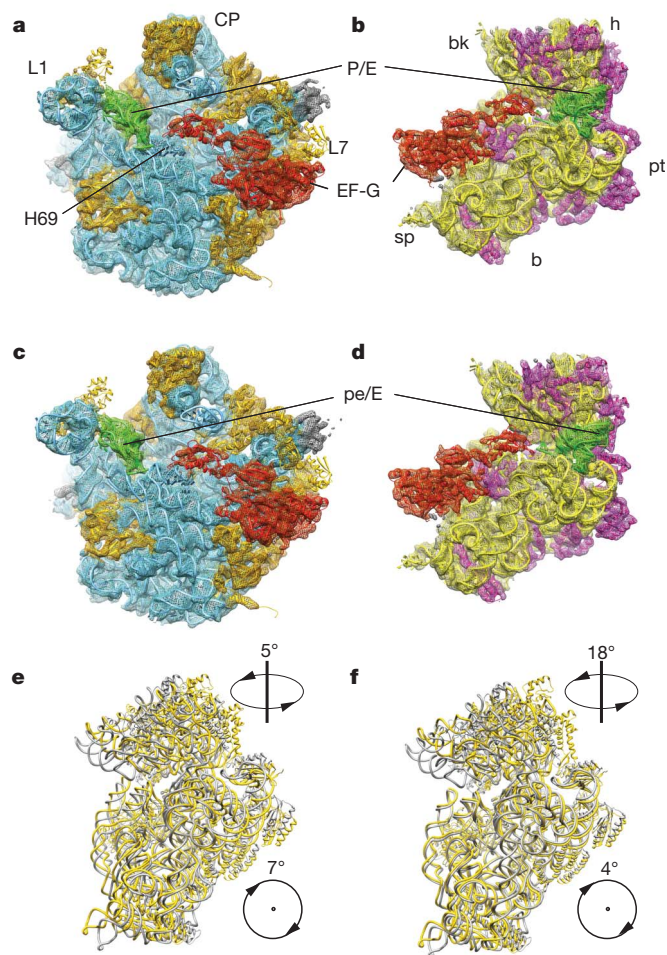


Figure 1 | Substates I (TI^{PRE}) and II (TI^{POST}) of the 70S-EF-G-GDP-FA complex. **a–d**, Cryoelectron microscopy maps of TI^{PRE} (**a**, **b**) and TI^{POST} (**c**, **d**) of the 70S-EF-G-GDP-FA complex are shown in mesh form with docked models in ribbon representation: EF-G (red), tRNA (green), 23S/5S rRNA (blue), 50S ribosomal proteins (orange), 16S rRNA (yellow) and the 30S ribosomal proteins (magenta). The maps are shown from the 30S side with the 30S subunit computationally removed (**a**, **c**) and from the 50S side with the 50S subunit computationally removed (**b**, **d**). CP, central protuberance; bk, beak; sp, spur; pt, platform; h, head; b, back; L1 and L7, ribosomal proteins L1 and L7, respectively; H69, helix 69 of 23S rRNA. **e**, **f**, The 30S subunit of TI^{PRE} (**e**) and TI^{POST} (**f**) (yellow) is compared with the 30S subunit of the POST state¹⁹ (grey) by aligning the respective 50S subunits. Arrows with numbers indicate the direction and magnitude (Supplementary Table 1) of the inter-subunit rotation and the head-swivel from the unrotated state to TI^{PRE} or TI^{POST} , respectively.

complex⁸. The subnanometre resolution of the 70S-EF-G-GDP-FA subpopulations enabled the visualization of secondary structure and thus the generation of molecular models (Fig. 1) by applying our newly developed MDFIT algorithm (see Methods). Comparison with available structures reveals that substate I is similar in conformation to the ratcheted substate of the PRE complex^{9,10} (Supplementary Table 1) and also that the tRNA is bound in a hybrid P/E site (Fig. 2a). We therefore consider substate I to be related to a pre-translocational intermediate (TI^{PRE}).

In contrast, substate II of the 70S-EF-G-GDP-FA complex represents a novel conformational state of the 70S ribosome. The anticodon stem-loop (ASL) of the tRNA has moved by 8–10 Å compared with the P/E position of TI^{PRE} as it maintains strong association with the P-site components of the head and follows the large 18° swivel movement of the head (Fig. 2b and Supplementary Movie 3). Because the tRNA interacts simultaneously with P-site components of the head as well as E-site components of the platform, it can be thought of as a 30S

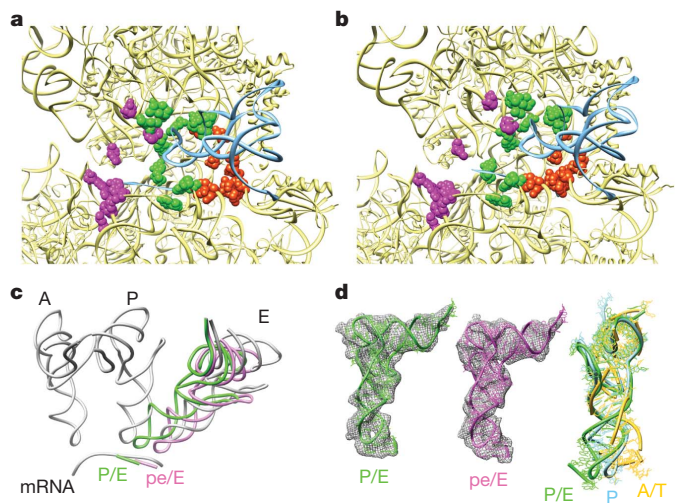


Figure 2 | Localization and conformation of the tRNA of substates I (TI^{PRE}) and II (TI^{POST}). **a**, **b**, Close-up of the tRNA-binding regions of the 30S subunit of TI^{PRE} (**a**) and TI^{POST} (**b**). The 30S subunit and tRNAs are shown as yellow and blue ribbons, respectively; ribosomal residues that contact A, P and E tRNA (magenta, green and orange) are shown as spheres. **c**, In a common 50S alignment, the P/E tRNA (green) of TI^{PRE} and the pe/E tRNA (magenta) of TI^{POST} together with their respective mRNA codons are compared with mRNA and classical A, P and E tRNA positions (grey). **d**, Density for the tRNAs (wire mesh) with molecular models for the P/E tRNA of TI^{PRE} (left, green) and the pe/E tRNA of TI^{POST} (middle, magenta). On the right, the model for P/E tRNA (green), which is essentially the same as that for pe/E-tRNA (root mean squared deviation 1.5 Å), is compared with a classical P tRNA (blue) and an A/T tRNA (yellow) by alignment of the acceptor-stem, D-stem and T-stem loops.

intra-subunit hybrid site (Fig. 2b). Moreover, because the contacts of the CCA end of the tRNA with the E site on the 50S subunit remain unaffected, we extend the previous nomenclature of hybrid sites⁵ and refer to this newly identified state as a pe/E hybrid state (P site on head and E site on platform of the 30S subunit, and E site on the 50S subunit).

The ASL of the pe/E tRNA together with the bound mRNA codon is very close to the position of a fully translocated E/E tRNA (Fig. 2c and Supplementary Movie 4). Apparently, head-swivelling coupled with partial unratcheting of the body/platform of the 30S subunit leads to tRNA translocation, suggesting that substate II of the 70S-EF-G-GDP-FA complex is related to a post-translocational intermediate state (TI^{POST}). We note that although the intermediate states visualized here contain only one tRNA, a second tRNA (ap/P) can be superimposed on the TI^{POST} state without steric interference with the binding position of EF-G (Supplementary Fig. 6). Thus, the structures presented here seem to be valid models for translocation intermediates (see also Supplementary Information for further discussion), but structures of translocation intermediates with two tRNAs will be necessary for the validation of these predictions. The presence of the ratchet-like subunit rearrangement in the yeast 80S-eEF2-sordarin complex¹⁵ hints that translocation in prokaryotes and eukaryotes may use related intermediate conformations. This structure showed a strong head swivel comparable to that of bacterial TI^{POST} combined with a strong inter-subunit rotation of bacterial TI^{PRE} . Thus, the conformation of the 80S-eEF2-sordarin complex¹⁵, although obtained by classical single-particle methods, may present a further intermediate between TI^{PRE} and TI^{POST} .

Whereas the P/E and pe/E tRNAs are in a twisted conformation (Fig. 2d), the overall conformations of EF-G in TI^{PRE} and TI^{POST} are remarkably similar to each other (Fig. 1) and to that observed in the cryoelectron microscopy reconstruction of the 70S-EF-G-GMPPNP¹⁴ as well as in the recent X-ray structure of EF-G-GDP-FA bound to a POST-state ribosome¹⁹ (Fig. 3a). However, one difference between the two EF-G-GDP-FA substates relates to the interaction patterns of domain IV of EF-G: in the TI^{PRE} state, domain IV does not seem to

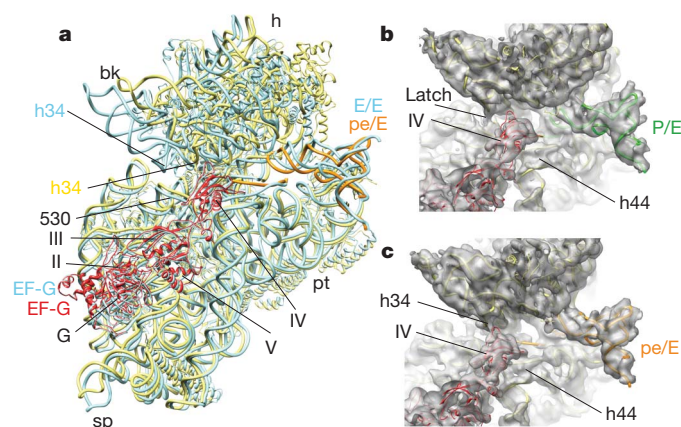


Figure 3 | EF-G stabilizes the swivelled head movement in the TI^{POST} state. **a**, Comparison of the position of FA-stalled EF-G and the 30S subunit between TI^{POST} and the POST-state 70S-EF-G-GDP-FA complex¹⁹. All shown components of the POST-state 70S-EF-G-GDP-FA complex¹⁹ are depicted as blue ribbons. The 30S, EF-G and pe/E tRNA of TI^{POST} are represented by yellow, red and orange ribbons, respectively. **b**, **c**, Close-up of the decoding region and domain IV of EF-G in the same orientation as in **a**. The surfaces of TI^{PRE} (**b**) and TI^{POST} (**c**) are transparent with molecular models in ribbon representation (30S subunit, yellow; EF-G, red; P/E tRNA, green; pe/E tRNA, orange). The arrows mark the closed latch between helix h34 and the 530 region of TI^{PRE} (**b**) and the interaction between h34 and domain IV of EF-G within TI^{POST} .

interact significantly with the ribosome (Fig. 3b), whereas a small shift in the binding position of EF-G and the large swivel of the head facilitate a more extensive interaction of domain IV of EF-G with helix h34 of the 16S rRNA in the TI^{POST} state (Fig. 3c). Together, h34 and the nucleotide 530 region of 16S rRNA form the so-called latch of the mRNA entry channel. Because of the head-swivel in the TI^{POST} state, h34 has moved about 12 Å away from the 530 region, leading to an opening of the latch (Fig. 3c) similar to that observed previously when eEF2 was trapped on the yeast 80S ribosome with sordarin¹⁵. This may facilitate the movement of the mRNA-tRNA₂ complex. Consistent

with this observation, transient protection of h34 by EF-G against chemical modification during the translocation reaction has been reported previously²³. The direct interaction of domain IV of EF-G with h34 may therefore bias the energy landscape of the ribosome towards TI^{POST} .

Until now, intermediate states of inter-subunit rotation have been considered to be intermediates on the pathway to the fully rotated state¹⁶. The present findings implicate unratcheting (in combination with the large swivel of the 30S head), rather than ratcheting, as being coupled to the translocation movement of the tRNAs and the mRNA with respect to the 30S subunit. Collectively, the insights gained from the structures of the TI^{PRE} and TI^{POST} states enable us to provide a structural explanation for the process of translocation in a model in which tRNA movements are facilitated by head-swivel, ratcheting and unratcheting motions of the ribosome (Fig. 4). These motions may be influenced by the GTPase reaction on EF-G; a network of interactions involving domain III and the ordered switch I region of EF-G and the γ -phosphate of GTP was proposed to stabilize the rotated state of the 30S subunit¹⁴. Accordingly, fast GTP hydrolysis by EF-G¹⁷ could destabilize the direct and indirect interactions of switch I of EF-G with the maximally rotated 30S subunit^{14,24}, therefore increasing the propensity of the 30S subunit to rotate backwards. The unratcheting motion produces a counter-movement of the body/platform with respect to the head, thereby reducing the distance that the tRNAs have to travel during translocation. Intra-subunit hybrid states allow the 30S subunit to maintain partial contacts with the tRNAs at any time of the translocation reaction. In the context of the ribosome's functioning during translocation as a Brownian ratchet machine²⁵, our model suggests that EF-G acts as a dynamic pawl, decoupling the unratcheting motions of the ribosome from the transition of hybrid-state tRNAs back into classical states. EF-G thereby provides directionality and accelerates translocation of the tRNAs by means of several intermediate inter-subunit and intra-subunit hybrid states into the classical P/P and E/E sites of the POST state.

METHODS SUMMARY

Tight-coupled 70S ribosomes from *Thermus thermophilus* were isolated by sucrose-gradient centrifugation and incubated with EF-G in the presence of GTP and FA. The resulting complexes were flash-frozen and imaged under low-dose conditions

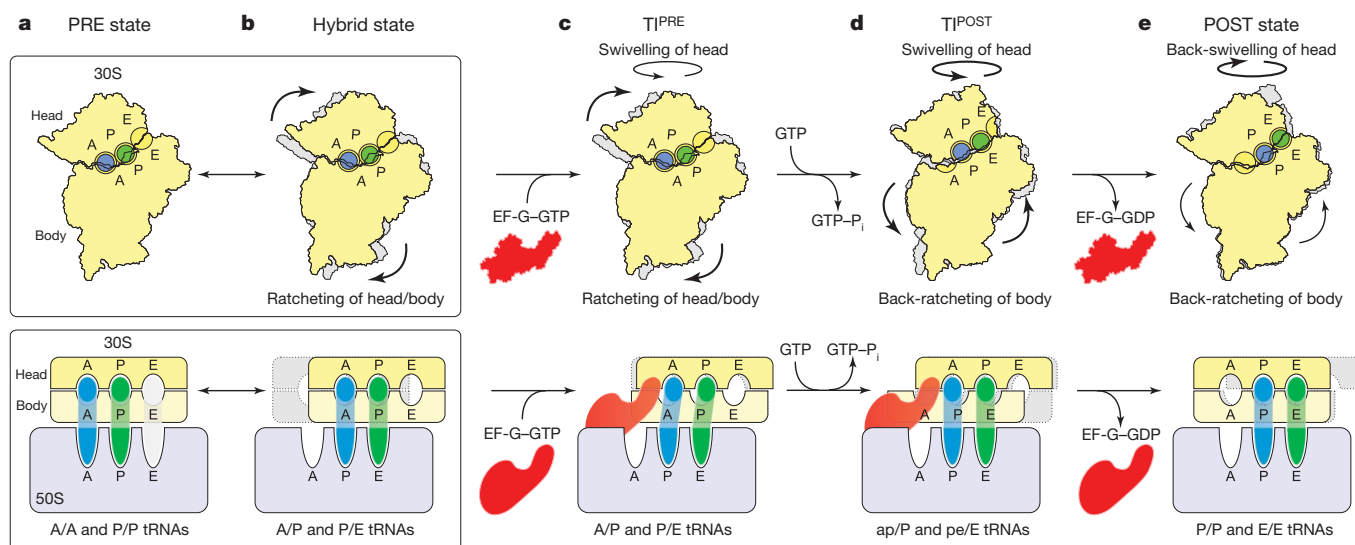


Figure 4 | Model for translocation. **a**, **b**, The PRE ribosome exists in a dynamic equilibrium between base states with classical A/A and P/P tRNAs (**a**) and rotated states with hybrid A/P and P/E tRNAs^{6,7,9–11} (**b**). **c**, Binding of EF-G-GTP to PRE state (**a**) or hybrid state (**b**) stabilizes the ratcheted state¹² as observed in TI^{PRE} . **d**, Fast GTP hydrolysis by EF-G¹⁷ accelerates translocation by means of an unlocking step on the 30S subunit¹⁸. Domain IV of EF-G uncouples unratcheting from the reverse movement of the A/P and P/E tRNAs

back into classical states; that is, a doorstop function. Through a head-swivelling and unratcheting motion, the tRNAs move from aa/P and pp/E into the 30S intra-subunit ap/P and pe/E hybrid states. **e**, Complete unratcheting of the 30S subunit leads to the POST-state 70S-EF-G complex¹⁹. Back-swivelling of the 30S head re-establishes tRNAs in the classical (pp/P) P and E (ee/E) states. Translocation is completed by the dissociation of EF-G-GDP.

with the use of an FEI Polara G2 electron microscope. The collected data were digitized and processed with multiparticle refinement protocols implemented in SPIDER²⁶. To interpret the resulting cryoelectron microscopy maps in molecular terms, a newly developed algorithm (MDFIT)²⁷ that integrates molecular simulation with experimental maps was employed.

Full Methods and any associated references are available in the online version of the paper at www.nature.com/nature.

Received 5 February; accepted 30 September 2010.

- Frank, J. & Spahn, C. M. The ribosome and the mechanism of protein synthesis. *Rep. Prog. Phys.* **69**, 1383–1417 (2006).
- Schmeing, T. M. & Ramakrishnan, V. What recent ribosome structures have revealed about the mechanism of translation. *Nature* **461**, 1234–1242 (2009).
- Shoji, S., Walker, S. E. & Fredrick, K. Ribosomal translocation: one step closer to the molecular mechanism. *ACS Chem. Biol.* **4**, 93–107 (2009).
- Ramakrishnan, V. Ribosome structure and the mechanism of translation. *Cell* **108**, 557–572 (2002).
- Moazed, D. & Noller, H. F. Intermediate states in the movement of transfer RNA in the ribosome. *Nature* **342**, 142–148 (1989).
- Munro, J. B., Altman, R. B., O'Connor, N. & Blanchard, S. C. Identification of two distinct hybrid state intermediates on the ribosome. *Mol. Cell* **25**, 505–517 (2007).
- Blanchard, S. C. *et al.* tRNA dynamics on the ribosome during translation. *Proc. Natl Acad. Sci. USA* **101**, 12893–12898 (2004).
- Munro, J. B., Sanbonmatsu, K. Y., Spahn, C. M. & Blanchard, S. C. Navigating the ribosome's metastable energy landscape. *Trends Biochem. Sci.* **34**, 390–400 (2009).
- Agirrezabala, X. *et al.* Visualization of the hybrid state of tRNA binding promoted by spontaneous ratcheting of the ribosome. *Mol. Cell* **32**, 190–197 (2008).
- Julian, P. *et al.* Structure of ratcheted ribosomes with tRNAs in hybrid states. *Proc. Natl Acad. Sci. USA* **105**, 16924–16927 (2008).
- Fischer, N. *et al.* Ribosome dynamics and tRNA movement by time-resolved electron cryomicroscopy. *Nature* **466**, 329–333 (2010).
- Valle, M. *et al.* Locking and unlocking of ribosomal motions. *Cell* **114**, 123–134 (2003).
- Frank, J. & Agrawal, R. K. A ratchet-like inter-subunit reorganization of the ribosome during translocation. *Nature* **406**, 318–322 (2000).
- Connell, S. R. *et al.* Structural basis for interaction of the ribosome with the switch regions of GTP-bound elongation factors. *Mol. Cell* **25**, 751–764 (2007).
- Spahn, C. M. *et al.* Domain movements of elongation factor eEF2 and the eukaryotic 80S ribosome facilitate tRNA translocation. *EMBO J.* **23**, 1008–1019 (2004).
- Zhang, W., Dunkle, J. A. & Cate, J. H. Structures of the ribosome in intermediate states of ratcheting. *Science* **325**, 1014–1017 (2009).
- Rodnina, M., Savelsbergh, A., Katunin, V. I. & Wintermeyer, W. Hydrolysis of GTP by elongation factor G drives tRNA movement on the ribosome. *Nature* **385**, 37–41 (1997).
- Savelsbergh, A. *et al.* An elongation factor G-induced ribosome rearrangement precedes tRNA-mRNA translocation. *Mol. Cell* **11**, 1517–1523 (2003).
- Gao, Y. G. *et al.* The structure of the ribosome with elongation factor G trapped in the posttranslocational state. *Science* **326**, 694–699 (2009).
- Penczek, P. A., Frank, J. & Spahn, C. M. A method of focused classification, based on the bootstrap 3D variance analysis, and its application to EF-G-dependent translocation. *J. Struct. Biol.* **154**, 184–194 (2006).
- Agrawal, R. K. *et al.* EF-G-dependent GTP hydrolysis induces translocation accompanied by large conformational changes in the 70S ribosome. *Nature Struct. Biol.* **6**, 643–647 (1999).
- Scheres, S. H. *et al.* Disentangling conformational states of macromolecules in 3D-EM through likelihood optimization. *Nature Methods* **4**, 27–29 (2007).
- Matassova, A. B., Rodnina, M. V. & Wintermeyer, W. Elongation factor G-induced structural change in helix 34 of 16S rRNA related to translocation on the ribosome. *RNA* **7**, 1879–1885 (2001).
- Ticu, C. *et al.* Conformational changes in switch I of EF-G drive its directional cycling on and off the ribosome. *EMBO J.* **28**, 2053–2065 (2009).
- Spirin, A. S. The ribosome as a conveying thermal ratchet machine. *J. Biol. Chem.* **284**, 21103–21119 (2009).
- Schuetz, J. C. *et al.* GTPase activation of elongation factor EF-Tu by the ribosome during decoding. *EMBO J.* **28**, 755–765 (2009).
- Whitford, P. C. *et al.* Accommodation of aminoacyl-tRNA into the ribosome involves reversible excursions along multiple pathways. *RNA* **16**, 1196–1204 (2010).

Supplementary Information is linked to the online version of the paper at www.nature.com/nature.

Acknowledgements The present work was supported by grants from the Deutsche Forschungsgemeinschaft (DFG; SFB 740 TP A3 and TP Z1, SP 1130/2-1 to C.M.T.S., FU579 1-3 to P.F., HA 1672/7-5 to R.K.H. and WI3285/1-1 to D.N.W.), the European Union 3D-EM Network of Excellence (to C.M.T.S.), the European Union and Senatsverwaltung für Wissenschaft, Forschung und Kultur Berlin (UltraStructureNetwork, Anwenderzentrum) and US National Institutes of Health (NIH; grant GM 60635 to P.A.P.), the Cluster of Excellence 'Macromolecular complexes' at the Goethe University Frankfurt (DFG Project EXC 115 to P.F. and S.C.), and the Human Frontiers of Science Program Young Investigators Award HFSP67/07 (to P.F.). We thank the New Mexico Computing Application Center for generous time on the Encanto Supercomputer. P.C.W. is currently funded by a LANL Director's Fellowship. This work was also supported by the Center for Theoretical Biological Physics sponsored by the National Science Foundation (NSF; grant PHY-0822283) with additional support from NSF-MCB-0543906, the LANL LDRD program and NIH grant R01-GM072686.

Author Contributions A.M., A.L.S. and A.D. prepared the complexes. A.H.R. and T.M. collected the cryoelectron microscopy data. A.H.R., J.L., M.B., S.R.C. and C.M.T.S. did the image processing. P.C.W., Y.Y., J.O. and K.Y.S. developed and employed the MDFIT method. P.W.H. participated in docking and analysed the FA-binding site. A.H.R., R.K.H., S.R.C., P.F., P.A.P., D.N.W. and C.M.T.S. discussed the results and wrote the paper.

Author Information The electron density maps and models of the T1^{PRE} and the T1^{POST} complexes have been deposited in the 3D-EM database with accession numbers EMD-1798 and EMD-1799, and in the Protein Data Bank database with PDB IDs 2xxy, 2xtg, 2xux and 2xuy. Reprints and permissions information is available at www.nature.com/reprints. The authors declare no competing financial interests. Readers are welcome to comment on the online version of this article at www.nature.com/nature. Correspondence and requests for materials should be addressed to C.M.T.S. (christian.spahn@charite.de) or D.N.W. (wilson@lmb.uni-muenchen.de).

METHODS

Formation of the EF-G-70S-GDP-FA complex. The *fusA* gene, encoding EF-G, was cloned from *Thermus thermophilus* HB8 genomic DNA into pET-46 Ek/LIC vector using primers (TthEFG_for, 5'-GCC CGC CCG GTG GTG ATG CAG CTC TTC CTG GGC TCC GCC CTG AAG AAC-3'; TthEFG_rev, 5'-GTT CTT CAG GGC GGA GCC CAG GAA GAG CTG CAT CAC CAC CGG GCG CGC-3') in accordance with the manufacturer's instructions (Novagen) and expressed in BL21 (DE3) cells. Recombinant EF-G protein was then purified with a Ni^{2+} -nitrilotriacetate affinity column, followed by gel filtration in a buffer containing 10 mM Tris pH 7.8, 100 mM NaCl and 10 mM 2-mercaptoethanol. Tight-coupled 70S ribosomes were purified from exponential-phase *T. thermophilus* cells by using sucrose-density-gradient centrifugation, as described previously for 30S subunits²⁸. As observed previously, the ribosomes contained a co-purified tRNA^{14,29}. Binding of EF-G to 70S ribosomes was done by incubating 20 μM purified EF-G protein for 15 min with 5 μM *T. thermophilus* 70S ribosomes, 500 μM GTP and 500 μM FA at 65 °C, in a buffer containing 10 mM HEPES-KOH pH 7.8, 30 mM MgCl_2 and 75 mM NH_4Cl . The occupancy of EF-G in the complexes was about 60–70%, as judged by centrifugal binding assay²⁸.

Cryoelectron microscopy and image processing. Ribosomal complexes were diluted to a concentration of 30 nM and subsequently frozen onto Quantifoil grids using a Vitrobot (FEI) device. Micrographs were collected on a Tecnai G2 Polara (FEI) at 300 kV and a magnification of $\times 39,000$ under low-dose conditions ($19\text{ e}^- \text{Å}^{-2}$) and scanned on a D8200 Primscan drum scanner (Heidelberger Druckmaschinen) with a step size of 4.758 μm , corresponding to 1.26 Å on the specimen scale.

The Contrast Transfer Function defocus values for the micrographs were determined with CTFind³⁰. Ribosomal projection images were automatically identified with the program Signature³¹ and were subsequently screened visually or automatically. From the selected projections, a reconstruction was generated by projection matching procedures and refined with the SPIDER software package³². The complete data set comprised 586,848 projection images collected from 677 micrographs at a defocus range of 1.3–4.8 μm . During the later refinement rounds, positivity of the reference volumes was enforced, the power spectrum of the cryoelectron microscopy map was scaled to the power spectrum of a model density derived from the atomic coordinates of the X-ray structure of the 70S ribosome³³, and the map was subsequently low-pass filtered according to the current resolution estimate.

After a first phase of multiparticle refinement^{20,26,34,35}, performed with three-times or two-times decimated pictures, we obtained a major subpopulation (52%; 303,665 particle images) that had strong EF-G density (Supplementary Fig. 1). However, as refinement progressed and the resolution reached the subnanometre range the data set was deemed heterogeneous. Parts of the 30S subunit, especially the head domain, became partly disordered. A second phase of multiparticle refinement was therefore employed, leading to the subdivision of the data into two further substates having EF-G (Supplementary Fig. 1). Both data subsets were further refined individually at full image size. The final reconstructions of substate I (113,214 particle images) and substate II (156,332 particle images) reached resolutions of 7.8 Å and 7.6 Å, respectively (Supplementary Fig. 2).

Using a similar strategy we revisited the previous data set (362,361 particle images; 371 micrographs) of the 70S-EF-G-GMPPNP complex¹⁴. In a first phase of multiparticle refinement a major population (118,991 particle images) was further sorted by a second phase of multiparticle refinement resulting in substate I (58,911 particle images) and substate II (38,055 particle images). The resolutions of the maps were 9.6 Å and 10.5 Å, respectively. As the resolution for the reconstructions of the 70S-EF-G-GMPPNP complex was significantly lower (as a result of the smaller size data set) than the resolutions obtained for the 70S-EF-G-GDP-FA complex, we restricted the comparison to a dissection of only the global conformational changes, such as ratcheting and head swivelling.

Nevertheless, this analysis suggests that the 70S-EF-G-GMPPNP complex coexists in two substates that resemble Ti^{PRE} and Ti^{POST} of the 70S-EF-G-GDP-FA complex (Supplementary Fig. 5 and Supplementary Table 1). The ratio of particles within each of the two substates of the 70S-EF-G-GMPPNP complex is inverted with respect to the 70S-EF-G-GDP-FA complex: in the 70S-EF-G-GMPPNP complex the particle ratio of Ti^{PRE} and Ti^{POST} is about 3:2 (58,911:38,055), whereas in the 70S-EF-G-GDP-FA complex the ratio is about 2:3 (113,214:156,332). This means that most of the ribosomes in the 70S-EF-G complex stalled with a non-hydrolysable GTP analogue are in Ti^{PRE} (substate I), having a fully ratcheted 30S subunit but only a modest head swivel. However, in the 70S-EF-G complex stalled with GTP and FA, Ti^{POST} dominates and here an intermediate inter-subunit rotation is coupled with a large head swivel instead (Supplementary Figs 4 and 5 and Supplementary Table 1).

Structure-based simulation fitting (MDFIT). To determine atomic models consistent with the cryoelectron microscopy densities, we employed structure-based

molecular simulation^{27,36,37} together with an energetic term developed in ref. 38, which incorporates the correlation between the simulated and experimental electron density throughout the simulation. Tama and co-workers³⁸ developed a similar method, which used a standard explicit solvent force field, as opposed to the structure-based force field. The advantage of the structure-based force field is that, because the potential energy function is defined by the X-ray structure, MDFIT retains tertiary contacts present in the X-ray structure without special constraints. Furthermore, because MDFIT explicitly includes all non-hydrogen atoms, there are no atomic clashes and proper stereochemistry is maintained in all fits.

We began the MDFIT procedure with a structure-based potential energy function defined by the classical unratcheted conformation. To induce hybrid-state formation and subunit pivoting we introduced the energetic term based on the correlation between the simulated cryoelectron microscopy map and the experimentally determined cryoelectron microscopy map. Specifically, the potential energy function is

$$V = V^{\text{SB}} + V^{\text{map}} = V^{\text{SB}} - W \sum_{ijk} \rho_{ijk}^{\text{sim}} \rho_{ijk}^{\text{exp}} \quad (1)$$

where W is the energetic weight of the map and ρ_{ijk}^{exp} and ρ_{ijk}^{sim} are the normalized experimental and simulated electron densities at voxel (i,j,k) , respectively. The quantity V^{SB} is the structure-based potential energy function. To calculate the simulated map, each atom is described by a Gaussian function of width 5 Å with the tail truncated at 1% of the peak value. Here, because the structure-based forcefield has 1 unit (all calculations were in reduced units) of stabilizing energy per atom (by construction), we set W to a comparable value of 150,000. The contributions to the force due to V^{map} were updated every 200 time steps. Fitting simulations employed Langevin dynamics. All simulations were performed with code based on Gromacs version 4.0.5 (refs 39, 40). Calculations were performed on the Encanto Supercomputer. The structure-based force field is freely available online (<http://smog.ucsd.edu>).

Structural models. The crystallographic structure of the 70S ribosome in complex with EF-G¹⁹ (PDB IDs 2WRI and 2WRJ) was used as an initial structure for MDFIT. Proteins without side chains in the X-ray structure were removed. The carboxy-terminal domain of ribosomal protein L7 from PDB entry 1RQU⁴¹ was inserted by hand, before fitting. The E-site tRNA was also removed from the initial X-ray structure in accordance with the cryoelectron microscopy map. The P-site tRNA was included in the fitting process. To facilitate fitting of the tRNA molecule into a P/E conformation, stabilizing interactions between the tRNA and the ribosome were removed. Stabilizing interactions between EF-G and the ribosome (due to their proximity in the crystal structure) were also excluded from the calculations, as were stabilizing interactions between L7 and all other components in the system. Further, crystallographic interactions found between the 3'-CCA end of the E-site tRNA with the E site of the 50S subunit were reintroduced as short-range (of the type 6-12; see refs 27, 36, 37) attractive interactions between the 3'-CCA end of the fitted tRNA and the E site of the 50S subunit. Introducing these interactions ensured that the 3'-CCA end of the P/E tRNA was in a conformation identical to that of a classically bound E-site tRNA, although because these interactions were short-range they only affected the process once the major rearrangements in the tRNA had already been achieved. Codon-anti-codon interactions were restrained by harmonic interactions with minima corresponding to the classical configuration.

The tRNA-ribosome-EF-G crystal structure was first manually aligned in VMD⁴², as a single rigid unit, to the map of Ti^{PRE} . The first round of fitting was performed with the Ti^{PRE} map after subjecting it to a 4-Å Gaussian low-pass filter. This filter decreased noise, effectively smoothing the energetic profile associated with V^{map} , which permitted more rapid fits. After 10^6 integration steps, the fit was continued for an additional 10^6 steps with V^{map} based on the Ti^{PRE} map filtered at 2 Å. The Ti^{POST} map, filtered at 2 Å, was then fitted, using the Ti^{PRE} 4-Å fitted structure as the initial structure.

28. Sharma, M. R. *et al.* Interaction of Era with the 30S ribosomal subunit implications for 30S subunit assembly. *Mol. Cell* **18**, 319–329 (2005).
29. Yusupov, M. M. *et al.* Crystal structure of the ribosome at 5.5 Å resolution. *Science* **292**, 883–896 (2001).
30. Mindell, J. A. & Grigorieff, N. Accurate determination of local defocus and specimen tilt in electron microscopy. *J. Struct. Biol.* **142**, 334–347 (2003).
31. Chen, J. Z. & Grigorieff, N. SIGNATURE: a single-particle selection system for molecular electron microscopy. *J. Struct. Biol.* **157**, 168–173 (2006).
32. Frank, J. *et al.* SPIDER and WEB: processing and visualization of images in 3D electron microscopy and related fields. *J. Struct. Biol.* **116**, 190–199 (1996).
33. Selmer, M. *et al.* Structure of the 70S ribosome complexed with mRNA and tRNA. *Science* **313**, 1935–1942 (2006).
34. Spahn, C. M. & Penczek, P. A. Exploring conformational modes of macromolecular assemblies by multiparticle cryo-EM. *Curr. Opin. Struct. Biol.* **19**, 623–631 (2009).

35. Connell, S. R. *et al.* A new tRNA intermediate revealed on the ribosome during EF4-mediated back-translocation. *Nature Struct. Mol. Biol.* **15**, 910–915 (2008).
36. Whitford, P. C. *et al.* An all-atom structure-based potential for proteins: bridging minimal models with all-atom empirical forcefields. *Proteins* **75**, 430–441 (2009).
37. Whitford, P. C. *et al.* Nonlocal helix formation is key to understanding S-adenosylmethionine-1 riboswitch function. *Biophys. J.* **96**, L7–L9 (2009).
38. Orzechowski, M. & Tama, F. Flexible fitting of high-resolution x-ray structures into cryoelectron microscopy maps using biased molecular dynamics simulations. *Biophys. J.* **95**, 5692–5705 (2008).
39. Lindahl, E., Hess, B. & van der Spoel, D. J. GROMACS 3.0: a package for molecular simulation and trajectory analysis. *J. Mol. Model.* **7**, 306–317 (2001).
40. Berendsen, H. J. C., van der Spoel, D. & van Drunen, R. GROMACS: a message-passing parallel molecular dynamics implementation. *Comput. Phys. Commun.* **91**, 43–56 (1995).
41. Bocharov, E. V. *et al.* From structure and dynamics of protein L7/L12 to molecular switching in ribosome. *J. Biol. Chem.* **279**, 17697–17706 (2004).
42. Humphrey, W., Dalke, A. & Schulten, K. VMD: visual molecular dynamics. *J. Mol. Graph.* **14**, 33–38 (1996).

Structure and mechanism of the S component of a bacterial ECF transporter

Peng Zhang¹, Jiawei Wang² & Yigong Shi³

The energy-coupling factor (ECF) transporters, responsible for vitamin uptake in prokaryotes, are a unique family of membrane transporters^{1,2}. Each ECF transporter contains a membrane-embedded, substrate-binding protein (known as the S component), an energy-coupling module that comprises two ATP-binding proteins (known as the A and A' components) and a transmembrane protein (known as the T component). The structure and transport mechanism of the ECF family remain unknown. Here we report the crystal structure of RibU, the S component of the ECF-type riboflavin transporter from *Staphylococcus aureus* at 3.6-Å resolution. RibU contains six transmembrane segments, adopts a previously unreported transporter fold and contains a riboflavin molecule bound to the L1 loop and the periplasmic portion of transmembrane segments 4–6. Structural analysis reveals the essential ligand-binding residues, identifies the putative transport path and, with sequence alignment, uncovers conserved structural features and suggests potential mechanisms of action among the ECF transporters.

The ATP-binding cassette (ABC) transporters harness the energy of ATP hydrolysis to move substrate molecules across membrane. An importer of the ABC superfamily comprises two cytosolic ABC domains, two membrane-spanning domains and a periplasmic binding protein that specifically recognizes substrate (Fig. 1a). Structural investigations on the ABC transporters have revealed major insights into their function and mechanism of action^{3–11}. Despite a similar organization (Fig. 1a), the ABC and ECF transporters have different organizational and functional properties. In contrast to the ABC importer, the S component of the ECF-type transporter is responsible for substrate binding (Fig. 1a) and there are cases where the S component alone is able to mediate high-capacity transport of substrate¹². The S component does not exhibit sequence homology with any protein of known structure. RibU^{13,14} in *Lactococcus lactis* and YpaA¹⁵ in *Bacillus subtilis* are the S components of the ECF-type transporters for riboflavin, the essential precursor for flavin mononucleotide and flavin adenine dinucleotide.

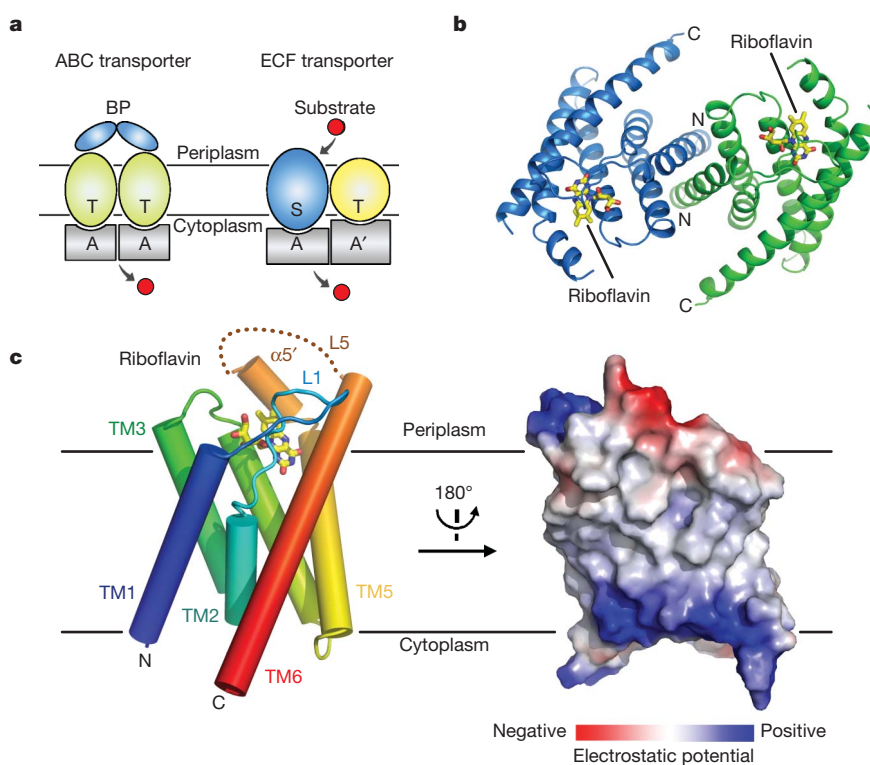


Figure 1 | The overall structure of RibU. **a**, The ECF transporter is distinct from other known ABC transporters. We show a schematic comparison between a representative ECF transporter and an ABC importer. Substrate is directly recognized by the S component of the ECF transporter, whereas substrate is bound to the binding protein in the ABC importer. **b**, Ribbon

representation of a RibU homodimer in one asymmetric unit. Each RibU molecule modelled here and elsewhere in the figures contains amino acids 10–141 and 153–188. **c**, Structure of a RibU molecule in ribbon diagram (left) and surface electrostatic potential (right). RibU is positioned roughly perpendicular to the lipid membrane. All structural figures were prepared with PyMol²⁴.

¹Department of Molecular Biology, Lewis Thomas Laboratory, Princeton University, Princeton, New Jersey 08544, USA. ²State Key Laboratory of Biomembrane and Membrane Biotechnology, Center for Structural Biology, School of Life Sciences and School of Medicine, Tsinghua University, Beijing 100084, China. ³Ministry of Education Protein Science Laboratory, Center for Structural Biology, School of Life Sciences and School of Medicine, Tsinghua University, Beijing 100084, China.

We cloned, expressed, purified and crystallized RibU from *S. aureus*. The presence of riboflavin in the recombinant RibU protein was suggested by the absorption spectrum¹⁴ (Supplementary Fig. 1a) and confirmed by mass spectrometry. The identity and function of RibU were confirmed by both *in vitro* analysis, where RibU formed a stable complex with the corresponding T, A and A' components from *S. aureus* (Supplementary Fig. 1b), and *in vivo* analysis, where all four components were required to support growth of riboflavin-auxotrophic *Escherichia coli* strains (Supplementary Fig. 1c). After numerous trials, we determined the structure by multi-wavelength anomalous dispersion at 3.6-Å resolution (Supplementary Table 1 and Supplementary Fig. 2).

There are two molecules of RibU in an asymmetric unit, arranged as a pseudo-symmetric dimer (Fig. 1b). At present, we have no evidence to support the biological relevance of the dimeric arrangement, which would result in a relatively short membrane-spanning distance of about 20 Å and burial of highly charged surface patches in the hydrophobic interior of the lipid membrane (Supplementary Fig. 3). For simplicity, we limit our discussion to one RibU molecule.

The overall structure of RibU resembles a cylinder with rugged ends (Fig. 1c). Assignment of RibU orientation in the membrane was facilitated by the observation that the carboxy (C) terminus of YpaA resides in the cytoplasm¹⁵. The outer surface of the cylinder is predominantly hydrophobic, consistent with its membrane-buried nature. By contrast, the cytoplasmic and periplasmic faces are enriched with charged amino acids (Supplementary Fig. 4). RibU comprises six transmembrane segments, not five as previously reported^{13,15}, where transmembrane segments 2 and 3 were predicted to be a single transmembrane segment. Each RibU protein contains a riboflavin molecule, which is bound on the periplasmic side about 5 Å into the predicted membrane surface (Fig. 1c).

Except transmembrane segment 2, which only contains a short, 11-residue helix, each of the other five transmembrane segments contains a continuous α -helix that probably traverses the entire lipid membrane (Fig. 1c). The intervening sequences between transmembrane segments 2 and 3, transmembrane segments 3 and 4, and transmembrane segments 4 and 5 are relatively short (Fig. 2a). An extended loop between transmembrane segments 1 and 2 (the L1 loop) contains 17 amino acids, nine of which are highly conserved among representative RibU homologues (Supplementary Fig. 5). The L1 loop hovers above the substrate-binding site, suggesting an important role (Fig. 1c).

Despite a similar reliance on the ATP-binding domains for substrate transport, the fold of RibU is markedly different from those of the ABC transporters (Supplementary Fig. 6). A search of the Protein Data Bank using DALI¹⁶ failed to identify any entry that is structurally homologous

to RibU over its entire six transmembrane segments. In particular, no structure of any membrane transporter was found to be similar to RibU. Among the proteins that exhibit limited structural similarity with RibU, five of the top seven entries are derived from particulate methane monooxygenase^{17,18}, a membrane-bound metalloenzyme. Transmembrane segments 1–5 of RibU can be superimposed with chain F of particulate methane monooxygenase¹⁸ with a root mean squared deviation of 3.3 Å over 124 aligned C α atoms (Fig. 2b and Supplementary Fig. 7).

The amino-acid sequences of RibU homologues from eight bacterial species share a high degree of pairwise sequence identity (Supplementary Fig. 5), suggesting structural conservation. We reasoned that the highly conserved amino acids among these RibU homologues may be functionally important. To examine this possibility, we mapped the conserved amino acids onto the structure of RibU (Fig. 3 and Supplementary Fig. 8). The outer surface of RibU only contains a small proportion of the conserved amino acids (Fig. 3a), whereas most of the highly conserved residues are clustered in the interior (Fig. 3b). Notably, four invariant amino acids are located around the substrate-binding pocket. In addition, the conserved amino acids also map to the interior of the cylinder-shaped RibU molecule, populating from the substrate-binding pocket to the cytoplasmic side. These amino acids appear to define the putative transport path for substrate.

The riboflavin-binding pocket measures approximately 15 Å in width and 8 Å in thickness (Fig. 4a); it is capped by the L1 loop on the periplasmic side. Despite the moderate resolution, the experimental electron density for riboflavin was clearly visible (Supplementary Fig. 9a). Nonetheless, we chose to model riboflavin after all protein atoms were in place. Riboflavin contains a ribityl side chain, with four hydroxyl groups, and an aromatic ring, which is hydrophobic on one end and polar on the other. Analysis of the structural features of RibU (Supplementary Fig. 9b) suggests only one way of orienting riboflavin into the binding pocket.

Riboflavin is recognized by relatively conserved amino acids from loop L1 and transmembrane segments 4–6, through both hydrogen bonds and van der Waals interactions (Fig. 4b, c). The non-polar portion of the riboflavin ring is nestled in a hydrophobic cage, involving 13 amino acids. These include Tyr 41/Leu 42 on the L1 loop, Val 83/Gly 84/Ala 87/Asn 88/Ala 91 on transmembrane segment 4, Leu 127/Val 134/Leu 135/Leu 138 on transmembrane segment 5 and the small helix $\alpha 5'$, and Ile 160/Phe 163 on transmembrane segment 6 (Fig. 4b and Supplementary Fig. 10). In addition, there may be eight H bonds between riboflavin and the conserved residues from RibU (Fig. 4c and Supplementary Fig. 10). In particular, Asn 131 and Asn 164, both of which are invariant among the RibU homologues, may mediate direct

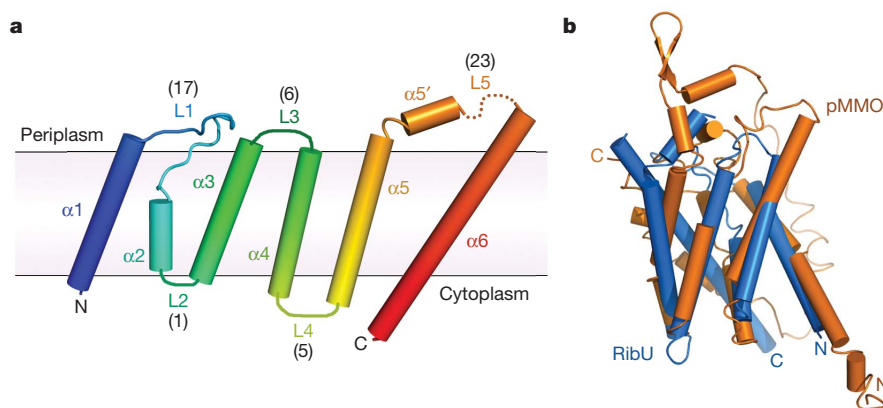


Figure 2 | Sequence alignment and structural fold of RibU. **a**, Membrane topology of RibU. The lengths of the loops connecting neighbouring transmembrane segments are indicated in parentheses. The periplasmic loop between transmembrane segments 5 and 6 (the L5 loop) has 23 amino acids, of which seven form a short α -helix ($\alpha 5'$). Eleven amino acids in this loop

(residues 142–152) have no electron density and are presumably disordered in the crystals. **b**, Structural overlay of RibU (blue) with chain F of the particulate methane monooxygenase (orange) from *Methylosinus trichosporium* OB3B (orange, Protein Data Bank accession code 3CHX¹⁸).

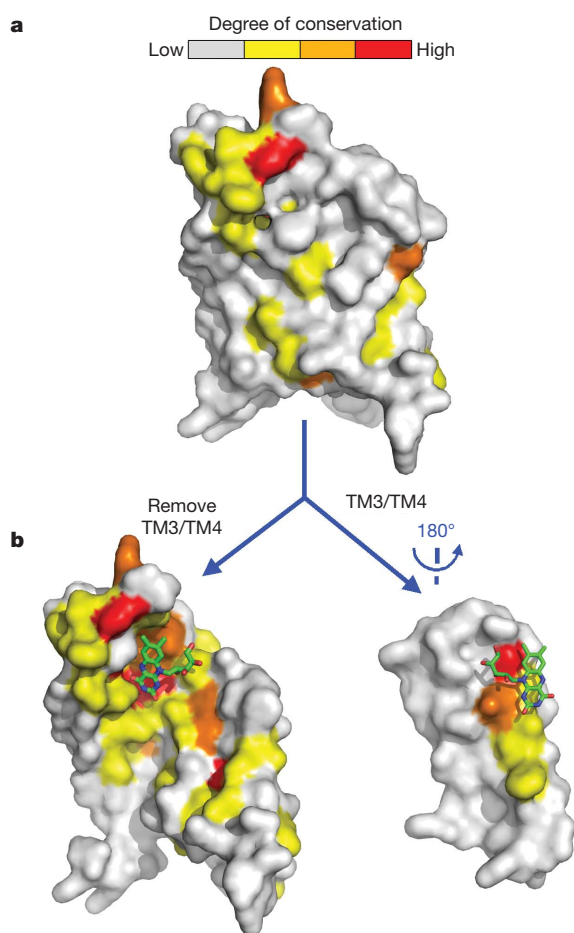


Figure 3 | Conserved amino acids map to the binding site and transport path of riboflavin. **a**, Mapping of conserved amino acids onto the structure of RibU. Based on the sequence alignment of 12 RibU homologues, residues that are conserved in seven to nine and 10 to 11 bacterial species are coloured yellow and orange, respectively. Invariant residues are highlighted in red. A surface representation is shown here. **b**, The riboflavin-binding site is enriched by highly conserved amino acids. The RibU molecule is split into two portions, transmembrane segment 3/transmembrane segment 4 and the rest, to reveal the location of the highly conserved amino acids.

H bonds to riboflavin. Similarly, Thr 43 and Lys 167, both from conserved positions in RibU homologues, are also within H-bond distances of riboflavin.

The interactions between riboflavin and RibU are extensive, consistent with the reported binding affinity of approximately 0.6 nM between riboflavin and the *L. lactis* RibU¹⁴. By contrast, flavin mononucleotide interacted with RibU with a moderate affinity of 36 nM, whereas flavin adenine dinucleotide exhibited no measurable binding¹⁴. These observations are nicely explained by our structure-based modelling analysis. Because the ribityl side chain of riboflavin is positioned towards the small periplasmic opening of the substrate-binding pocket, the phosphate group of flavin mononucleotide, but not the adenine dinucleotide of flavin adenine dinucleotide, can be tolerated by minor conformational shifts of the surrounding residues (Supplementary Fig. 11).

The relatively simple topology of RibU reveals tantalizing clues about how substrate might be imported from periplasm to the cytoplasm. RibU can be thought of having two structural modules: transmembrane segments 1–3 and 4–6 (Fig. 1c). Riboflavin is bound between these two modules, with the L1 loop coming from the transmembrane segment 1–3 module. Under this arrangement, riboflavin is probably transported through the central line of RibU surrounded by

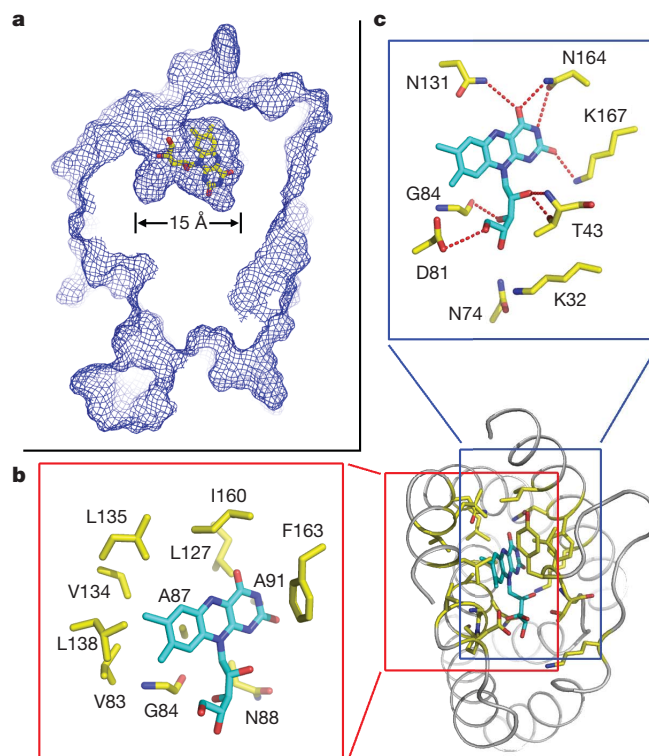


Figure 4 | Recognition of riboflavin by RibU. **a**, Riboflavin is bound at the periplasmic side of RibU. We show a slice of RibU to highlight the riboflavin-binding pocket. The surface of RibU is represented by blue mesh. **b**, Riboflavin is nestled in a hydrophobic pocket formed by 13 conserved amino acids. Except Tyr 41 and Leu 42, which are removed to present a clear view here, all other amino acids are shown. **c**, Riboflavin is recognized by multiple hydrogen bonds. Potential hydrogen bonds are represented by red dashed lines.

transmembrane segments 1–3 and 4–6. This analysis gives rise to a speculative working model (Supplementary Fig. 12). In this model, the L1 loop is thought to serve as a gate. Upon binding to riboflavin, L1 may close down to interact with the substrate molecule. Then, facilitated by the T–A–A' components as a result of ATP hydrolysis, the transmembrane segment 1–3 module may be moved away from transmembrane segments 4–6, allowing the protein to adopt a transient, inward-open conformation. Such changes may lead to disruption of interactions with riboflavin, allowing it to be released into the cytoplasm. The ADP-bound state probably resets the transport system.

Sequence alignment of RibU with representative transporters, such as those for folate, thiamine precursor and cobalamin precursor, revealed a pattern of conservation that is closely associated with the transmembrane segments of RibU (Supplementary Fig. 13). This observation suggests that the S components of at least some ECF transporters may contain six transmembrane segments, have a similar structure and adopt the same membrane topology. Notably, this conclusion may not apply to other S components such as the bipartite proteins CbiMN and NikMN². Sequence alignment of the transporters for folate and cobalamin precursor identified candidate sequences that may be responsible for binding to their respective ligands (Supplementary Fig. 14).

The ECF transporters are classified into two groups¹. Group I transporters are encoded by linked genes, which encode the S component and an S-specific A–T module. Group II transporters have a common A–T module that is shared by up to 12 different S components in the same bacterial species¹. The RibU transporter from *S. aureus* belongs to group II. Surprisingly, sequence alignment of the group II S components from the same bacterial species failed to uncover any conserved sequence feature, suggesting that interaction with the shared

A–T module may only entail short and/or degenerate motifs. This notion is consistent with the identification of two short but functionally essential Arg motifs in the T components of the ECF transporters¹⁹.

For the cytoplasmic A components to use the energy of ATP hydrolysis for substrate transport, the S component should contain a cytoplasmic motif that mediates this interaction. In addition, the candidate motif must be associated with one or more of the following cytoplasmic elements: the amino (N) and C termini, the L2 loop and the L4 loop. This analysis, and the divergent nature of the N terminus and the observation that the L2 loop contains only a single amino acid, Gly, suggests that the L4 loop and/or the C-terminal sequences are probably responsible for binding to the A components. Supporting this conjecture, the group II S components appear to have a stretch of positively charged amino acids in the L4 loop and the C terminus (Supplementary Fig. 15).

Structural elucidation of RibU represents the first of many required steps towards mechanistic understanding of the ECF transporters. At present, we have little information about how the S component interacts with the energy-coupling module or how ATP hydrolysis by the A components facilitates the transport of substrate. Answers to these questions require systematic biochemical and structural investigation.

METHODS SUMMARY

RibU was overexpressed in *E. coli*, purified to homogeneity and crystallized by the hanging-drop vapour-diffusion method. All data were collected at the X29 beamline of the Brookhaven National Laboratory and processed with HKL2000 (ref. 20). The crystals belong to the space group $P2_12_12_1$ with unit cell dimensions of $a = 50.4 \text{ \AA}$, $b = 94.2 \text{ \AA}$, $c = 115.4 \text{ \AA}$. Additional processing was performed using programs from the CCP4 suite²¹. Multiwavelength anomalous diffraction phasing was done using Phenix AutoSol. The initial model was built using the incorporated Resolve in Phenix. Additional missing residues in the auto-built model were manually added in COOT²². The final model was refined using PHENIX²³.

Full Methods and any associated references are available in the online version of the paper at www.nature.com/nature.

Received 10 March; accepted 9 September 2010.

Published online 24 October 2010.

- Rodionov, D. A. *et al.* A novel class of modular transporters for vitamins in prokaryotes. *J. Bacteriol.* **191**, 42–51 (2009).
- Rodionov, D. A., Hebbeln, P., Gelfand, M. S. & Eitinger, T. Comparative and functional genomic analysis of prokaryotic nickel and cobalt uptake transporters: evidence for a novel group of ATP-binding cassette transporters. *J. Bacteriol.* **188**, 317–327 (2006).
- Hollenstein, K., Dawson, R. J. & Locher, K. P. Structure and mechanism of ABC transporter proteins. *Curr. Opin. Struct. Biol.* **17**, 412–418 (2007).
- Rees, D. C., Johnson, E. & Lewinson, O. ABC transporters: the power to change. *Nature Rev. Mol. Cell Biol.* **10**, 218–227 (2009).
- Davidson, A. L., Dassa, E., Orelle, C. & Chen, J. Structure, function, and evolution of bacterial ATP-binding cassette systems. *Microbiol. Mol. Biol. Rev.* **72**, 317–364 (2008).
- Oldham, M. L., Davidson, A. L. & Chen, J. Structural insights into ABC transporter mechanism. *Curr. Opin. Struct. Biol.* **18**, 726–733 (2008).
- Linton, K. J. Structure and function of ABC transporters. *Physiology* **22**, 122–130 (2007).
- Dawson, R. J., Hollenstein, K. & Locher, K. P. Uptake or extrusion: crystal structures of full ABC transporters suggest a common mechanism. *Mol. Microbiol.* **65**, 250–257 (2007).
- Davidson, A. L. & Maloney, P. C. ABC transporters: how small machines do a big job. *Trends Microbiol.* **15**, 448–455 (2007).
- Locher, K. P. Review. Structure and mechanism of ATP-binding cassette transporters. *Phil. Trans. R. Soc. B* **364**, 239–245 (2009).
- Jones, P. M., O'Mara, M. L. & George, A. M. ABC transporters: a riddle wrapped in a mystery inside an enigma. *Trends Biochem. Sci.* **34**, 520–531 (2009).
- Hebbeln, P., Rodionov, D. A., Alfandega, A. & Eitinger, T. Biotin uptake in prokaryotes by solute transporters with an optional ATP-binding cassette-containing module. *Proc. Natl Acad. Sci. USA* **104**, 2909–2914 (2007).
- Burgess, C. M. *et al.* The riboflavin transporter RibU in *Lactococcus lactis*: molecular characterization of gene expression and the transport mechanism. *J. Bacteriol.* **188**, 2752–2760 (2006).
- Duurkens, R. H., Tol, M. B., Geertsma, E. R., Permentier, H. P. & Slotboom, D. J. Flavin binding to the high affinity riboflavin transporter RibU. *J. Biol. Chem.* **282**, 10380–10386 (2007).
- Vogl, C. *et al.* Characterization of riboflavin (vitamin B2) transport proteins from *Bacillus subtilis* and *Corynebacterium glutamicum*. *J. Bacteriol.* **189**, 7367–7375 (2007).
- Holm, L. & Sander, C. Protein structure comparison by alignment of distance matrices. *J. Mol. Biol.* **233**, 123–138 (1993).
- Lieberman, R. L. & Rosenzweig, A. C. Crystal structure of a membrane-bound metalloenzyme that catalyses the biological oxidation of methane. *Nature* **434**, 177–182 (2005).
- Hakemian, A. S. *et al.* The metal centers of particulate methane monooxygenase from *Methylosinus trichosporium* OB3b. *Biochemistry* **47**, 6793–6801 (2008).
- Neubauer, O. *et al.* Two essential arginine residues in the T components of energy-coupling factor transporters. *J. Bacteriol.* **191**, 6482–6488 (2009).
- Otwinski, Z. & Minor, W. Processing of X-ray diffraction data collected in oscillation mode. *Methods Enzymol.* **276**, 307–326 (1997).
- Collaborative Computational Project, N. The CCP4 suite: programs for protein crystallography. *Acta Crystallogr. D* **50**, 760–763 (1994).
- Emsley, P. & Cowtan, K. Coot: model-building tools for molecular graphics. *Acta Crystallogr. D* **60**, 2126–2132 (2004).
- Adams, P. D. *et al.* PHENIX: building new software for automated crystallographic structure determination. *Acta Crystallogr. D* **58**, 1948–1954 (2002).
- DeLano, W. L. The PyMOL molecular graphics system. <<http://www.pymol.org>> (2002).

Supplementary Information is linked to the online version of the paper at www.nature.com/nature.

Acknowledgements We thank H. Yan for technical advice, A. Schmedel for administrative assistance and *E. coli* Genetic Resources at Yale Coli Genetic Stock Center for providing mutant *E. coli* strains. This work was supported by the National Institutes of Health (R01 GM084964), funds from the Ministry of Science and Technology of China (grant number 2009CB918801) and Project 30888001 supported by National Natural Science Foundation of China.

Author Contributions P.Z. and Y.S. designed all experiments. P.Z. performed the bulk of the experiments. P.Z., J.W. and Y.S. analysed the data and contributed to manuscript preparation. Y.S. wrote the manuscript.

Author Information The atomic coordinates of RibU are deposited in Protein Data Bank under accession code 3P5N. Reprints and permissions information is available at www.nature.com/reprints. The authors declare no competing financial interests. Readers are welcome to comment on the online version of this article at www.nature.com/nature. Correspondence and requests for materials should be addressed to Y.S. (shi-lab@tsinghua.edu.cn).

METHODS

Protein preparation. We tested four different bacterial species (*S. aureus*, *Thermophilum pendens*, *Thermoanaerobacter italicus* and *B. subtilis*) by cloning, expressing and purifying the S component of the ECF transporter for riboflavin. Crystals of *B. subtilis* RibU were beautiful but failed to diffract X-rays. We focused on the RibU protein from *S. aureus*. The RibU coding sequence from *S. aureus* was chemically synthesized (Genescript), subcloned into pET15b (Novagen) and over-expressed in *E. coli* BL21(DE3) by 0.5 mM β -D-thiogalactopyranoside (IPTG) at A_{600} of about 0.8. After 14 h at 37 °C, the cells were collected, homogenized in the buffer containing 20 mM Tris-HCl, pH 8.0 and 100 mM NaCl, and lysed using a French Press with two passes at 15–20,000 p.s.i. Cell debris was removed by centrifugation. The supernatant was collected and applied to ultracentrifugation at 150,000g for 1 h. Membrane fraction was incubated with 2% (w/v) nonyl- β -D-glucopyranoside (β -NG, Anatrace) for 2 h at 4 °C. After another ultracentrifugation step at 150,000g for 30 min, the supernatant was loaded to an Ni²⁺-NTA affinity column (Qiagen). The protein was eluted from the affinity resin by 20 mM Tris, pH 8.0, 500 mM imidazole and 0.4% β -NG and concentrated to around 10 mg ml⁻¹ before further purification by gel filtration (Superdex-200, GE Healthcare). The buffer for gel filtration contained 20 mM Tris (pH 8.0), 100 mM NaCl and 0.4% β -NG. The peak fraction was collected and concentrated to approximately 8 mg ml⁻¹ for crystallization.

Formation of the RibU-T-A-A' complex. Genes encoding the four putative components of riboflavin ECF transporter in *S. aureus*, RibU, T, A and A' were subcloned into pQlink and pACYCDuet vectors to obtain two expression plasmids: pQlink-A'-A and pACYCDuet-RibU-T. The gene identity and predicted molecular masses are as follows: RibU, 161509653, 21.1 kDa; A, 15925211, 32.9 kDa; A', 15925212, 30.0 kDa; T, 15925210, 30.8 kDa. A tag of six histidine residues was added at the C terminus of the A component and the N terminus of RibU. These two plasmids were transformed separately or co-transformed into *E. coli* BL21(DE3). The A and A' components could be co-expressed in a stable complex and were co-purified by Ni²⁺-NTA affinity resin (Qiagen), followed by gel filtration chromatography (Superdex 200, GE Healthcare). By contrast, co-expression of RibU with the T component only led to expression and purification of RibU alone. The T component could only be expressed and purified in the presence of all three other components (A, A' and RibU).

Co-expression of all four components was achieved by co-transforming *E. coli* BL21(DE3) with the plasmids pQlink-A'-A and pACYCDuet-RibU-T (with 6 \times His tag at the C terminus of A and N terminus of RibU). The quaternary complex RibU-T-A-A' was purified in three sequential steps. First, the complex was co-purified by Ni²⁺-NTA affinity resin (Qiagen) and eluted with 500 mM imidazole. Second, the eluted proteins were fractionated by anion exchange chromatography (Source-15Q, GE Healthcare) using a linear gradient of 0–500 mM NaCl in 20 mM Tris buffer (pH 8.0). The quaternary complex RibU-T-A-A' stayed together on the anion exchange column and was co-eluted in the same fractions. Third, the RibU-T-A-A' complex was concentrated and further purified by gel filtration chromatography (Superdex-200, GE Healthcare). The gel filtration buffer contained 20 mM Tris, pH 8.0, 0.1 M NaCl, 0.04% DDM.

In vivo experiments. Two *E. coli* riboflavin-auxotrophic strains, ribB11 mutant BSV11 (F⁻ glnV44(AS) λ^- mcrA rfbC1 endA1 ribB11:Tn5 spoT1 thi-1 mcrB hsdR29) and ribA13 mutant BSV13 (F⁻ glnV44(AS) λ^- mcrA rfbC1 endA1 ribA13:Tn5 spoT1 thi-1 mcrB hsdR29), were obtained from the Yale Coli Genetic Stock Center (numbers 6991 and 6992). These two mutant strains were unable to synthesize riboflavin owing to disruption of the riboflavin biosynthesis pathway²⁵. The two mutants are unable to grow in regular lysogeny broth medium (which contains an unknown amount of riboflavin) but can grow after addition of

20 mg l⁻¹ riboflavin. The lysogeny broth plates were prepared in the presence of 1 mM IPTG, four concentrations of additional riboflavin (0, 0.5, 2.5 and 12.5 mg l⁻¹) and appropriate antibiotics (100 mg ml⁻¹ ampicillin, 50 mg ml⁻¹ kanamycin and 34 mg ml⁻¹ chloramphenicol). To make the strains inducible by IPTG, these two mutants were lysogenized with a λ DE3 Lysogenization Kit (Novagen). The mutant *E. coli* (DE3) strains were transformed individually with plasmids expressing RibU, T, RibU+T, A + A' and RibU + T + A + A', and cultured in lysogeny broth with additional 20 mg l⁻¹ riboflavin. The control culture was not transformed by any plasmid. The overnight culture was diluted to an A_{600} of 0.1. An equal volume of the diluted culture (10 μ l) was dispensed onto the lysogeny broth plates, occupying the upper half of each plate. The lower half of each plate was used to streak the culture from the upper half. The plates were incubated at 37 °C overnight.

Crystallization. Crystals were grown at 20 °C by the hanging-drop vapour-diffusion method. Several RibU homologues from other bacterial species were cloned, purified and attempted in crystallizations. Only RibU protein from *S. aureus* gave rise to crystals of reasonable diffraction (RibU hereafter). Large yellow-coloured crystals of RibU were obtained in many conditions containing polyethylene glycol. However, none of the crystals diffracted X-rays beyond 5 Å at the synchrotron. Polyethylene glycols with low molecular masses were found to support crystals of better diffraction. The best crystals, which diffracted X-rays to about 5 Å, were generated in 29% polyethylene glycol 550 MME, 0.1 M Tris-HCl, pH 8.4. To improve the diffraction quality further, we screened secondary detergent from a detergent screening kit (Hampton Research) and available detergents from Anatrace, each with varying ratios of protein to detergent. Addition of octyl-maltoside fluorinated to the protein with a ratio of 1:1 to 2:1 led to improvement of the diffraction limit from 5 to 4 Å. The best crystal diffracted X-rays to 3.6 Å at the X29 beamline of Brookhaven National Laboratory. The Se-Met protein crystals used for MAD phasing were obtained in a similar manner and diffracted X-rays to 3.8-Å resolution. Both native and Se-Met crystals were directly flash frozen in a cold nitrogen stream at 100 K.

Data collection and structure determination. All data sets were collected at the X29 beamline of the Brookhaven National Laboratory and processed with HKL2000 (ref. 20). The crystals belong to the space group $P2_12_12_1$ with unit cell dimensions of $a = 50.4$ Å, $b = 94.2$ Å, $c = 115.4$ Å. Additional processing was performed using programs from the CCP4 suite²¹. Data collection statistics are summarized in Supplementary Table 1. MAD phasing was done using Phenix AutoSol; six selenium sites were found, four of which were above 5 standard deviations, corresponding to Met 20 and Met 123 in the two molecules, and two of which were above 3 standard deviations, corresponding to Met 9 and Met 79 in one of the two molecules. The initial model was built using the incorporated Resolve in Phenix. Additional missing residues in the auto-built model were manually added in COOT²² with the aid of the map sharpening utility. The final model in the $P2_12_12_1$ space group was refined using PHENIX²³ with tight restraints, including non-crystallographic symmetry, experimental phases and α -helix main-chain hydrogen-bond restraints.

Mass spectrometry identification. The purified RibU protein is yellow, suggesting the presence of a bound substrate molecule. To identify the yellow-coloured 'substrate', 10 μ l purified RibU was denatured at 95 °C for 2 min, followed by addition of 40 μ l water and centrifugation at 16,000g for 5 min. The yellow-coloured supernatant (40 μ l) was then diluted with additional 360 μ l water. This sample was subjected to liquid chromatography-mass spectrometry. Riboflavin (5 μ M) was used as a positive control.

25. Bandrin, S. V., Rabinovich, P. M. & Stepanov, A. I. Three linkage groups of the genes of riboflavin biosynthesis in *Escherichia coli*. *Genetika* **19**, 1419–1925 (1983).

CAREERS

CANADA Postdocs at three universities seek union representation **p.723**

GRANTS Howard Hughes programme will fund early-career scientists **p.723**

NATUREJOBS For the latest career listings and advice www.naturejobs.com



S. MEISTER/IMAGEZOO/CORBIS

decided to give it a try. He negotiated a rate of about US\$300 and sent in the manuscript, along with further data. Several days later, he received the finished version. The methodology had been restructured, the new data were incorporated and reformatted and it read cleanly and smoothly. Petrovic and his co-author submitted it to the Belgian medical journal *Acta Clinica Belgica*, where it was promptly accepted (M. Petrovic *et al. Acta Clin. Belg.* 61, 119–126; 2006).

“What we got back was a huge improvement,” says Petrovic, a professor of geriatrics at the University of Ghent in Belgium. “It all went very smoothly.”

Scientists all over the world are increasingly turning to manuscript-editing services. Some authors hope to refine a paper before submitting it to a journal; others aim to correct problems that emerged in peer review. Most are looking for companies to provide a basic service, including correcting for grammar, spelling, punctuation, consistency, clarity, proper capitalization, accurate use of terms and logical presentation. Many services also correct for British or American usage and for adherence to particular style manuals, such as the Chicago Manual of Style, the American Medical Association or the American Psychological Association. A number of companies specialize in editing papers by authors whose first language is not English.

But polishing poor or sloppy English is not the only aim. Some authors, like Petrovic, want further scrutiny and revision, such as the incorporation of additional data. Others are looking for a more in-depth review of the science to check for valid protocols, methods and other issues. This can give rise to ethical quandaries related to authorship and fairness. As editing services become more common, potential users should consider the benefits, weigh their options and carefully review the accepted practices of the journals in which they hope to publish.

EDITING ON THE RISE

Although statistics aren't available on the expanding use of editing services, companies offering them claim that demand is steadily rising, and the number of such companies seems to be growing (see ‘Opportunities in editing’). Tightening competition for scientific publication is a big contributor to demand, say journal editors and editing-service providers alike. More papers are coming from emerging science regions such as China, India, the ►

PUBLISHING

A helping hand

Manuscript-editing services are growing. Can they turn a mediocre paper into a publishable one? And at what cost?

BY KAREN KAPLAN

Mirko Petrovic was in a jam. A paper on which he was lead author — a clinical study on the prevalence of sleeping aids among elderly patients — had been rejected for publication. Reviewers said that the article's methodology was improperly structured, its

data were scant and not in the right format, and its language needed polishing. Resolving the flaws would require at least two weeks of work, and he wanted to publish quickly.

Petrovic had heard about a company that offered copy-editing, formatting and in-depth scientific editing of manuscripts. Although he had never used such a service before, he

► Middle East and South America, swelling the overall number of manuscripts that must be reviewed — and rejected. The influx means that journal editors are recommending editing services to authors whose native language isn't English with increasing frequency.

"I deal with a lot of foreign manuscripts now, and the trend is growing — it's not going to stop," says Xiao-Fan Wang, an associate editor at the *Journal of Biological Chemistry*, who says that papers from authors in China alone represent 20% of the 500–600 submissions that the journal receives each year. "I tell them, 'You need to find an editing service — not somebody who's just going to fix your grammar but who understands your work and can highlight what's important,'" says Wang.

Among the players are Nature Publishing Group (NPG) in London, which publishes *Nature*, and Macmillan Scientific Communication, a division of Macmillan Publishers, NPG's parent company. NPG has a service called Nature Publishing Group Language Editing (NPGLE), introduced in June 2008 largely to serve non-English-speaking authors.

Macmillan Scientific Communication, meanwhile, is developing a scientific-editing service that is set for launch early next year. The venture, say project organizers, will aim to provide in-depth editorial advice on a paper's scientific content, structure and presentation.

But scientists need to be wary when hiring editors (see 'How to choose a manuscript-editing service'). Manuscript-editing companies warn that it is easy to set up a website and difficult to tell

whether the information and claims on it are valid. Authors can ask their target journal for a list of recommendations or look for them online on the journal's author resource page, says Laura Stemmler, operations director for the editing service American Journal Experts in Durham, North Carolina. She adds that an author might also ask colleagues for suggestions.

WORTH THE TROUBLE?

Can an editing service actually help an author to get published? Journal editors say that it depends. If a manuscript's principal or only problem is tortured English, neither a manuscript editor nor a peer reviewer is likely to reject it, say editors. But if the paper's writing is so mangled that it is almost impossible to read, it will be rejected regardless of its scientific quality. That is when an editing service is useful before the author even tries to submit.

"Reviewers these days are overburdened, and a properly written paper is just easier to review," says Jim Viccaro, editor of the *Journal of Applied Physics*, who routinely recommends editing services to authors.

Viccaro reads all the manuscripts received by the journal and decides whether to assign them to an associate editor for further scrutiny or to send them out for peer review at once. "Some I don't even send — I reject them out of hand. You don't want to send really bad manuscripts to reviewers. You don't want to waste their time," he says. "If you run your paper through an editing service first, you'll clear away those problems and get a fair review. Hiring an editing service doesn't guarantee publication, but it does guarantee a review with substance."

Editing services themselves are sensitive about the publication-guarantee issue. NPGLE, for example, has a large disclaimer at the bottom of its home page stating that use of its services in no way guarantees publication in *Nature* or any NPG or other journal. Most



"Reviewers these days are overburdened, and a properly written paper is just easier to review."

Jim Viccaro

for a 6,000-word paper with a 14- to 21-day turnaround to \$5,000 for a 12,000-word paper with a 48-hour turnaround. Viccaro says that it is a worthwhile investment. "This is how an author can make sure their paper is not dismissed for the wrong reason, just because no one could understand what they were talking about," he says. Wang maintains that directing non-English-speaking authors to editing companies before submission has allowed him to accept an extra 5–10% of papers that he would otherwise have rejected. "These services can offer a lot of value," he says. "Not only in English, but in highlighting what the author didn't even realize was the most important part."

Marissa Carter, president of Strategic Solutions in Cody, Wyoming, says that her editing service helps two out of three authors whose papers were rejected in peer review to get published in other journals.

Carter — whose company offers services from copy-editing and formatting for style to science editing — says that she might, for example, work with an epidemiological study on exposure to inhalable environmental agents. If the paper had been criticized because the statistical analysis wasn't adjusted for smoking, Carter says that she would request more data from the authors on subject smoking history. And she might suggest that they conduct further analysis. "But I can't rescue the paper if the study is flawed," she warns. "Sometimes authors may not have collected the data they need."

ETHICS AND AUTHORSHIP

With more in-depth, incisive editing comes the question of ethics and authorship. Companies that offer extensive science editing, addressing such issues as flawed protocols and inadequate experiment design, invite quandaries about the attribution of authorship and fairness — not every author, after all, has the extra money to secure the advantages that come with extra assistance.

Both Carter's Strategic Solutions and



"I deal with a lot of foreign manuscripts now, and the trend is growing."

Xiao-Fan Wang

THE RIGHT OPTION

How to choose a manuscript-editing service

- Select a company that specializes in academic editing and has field-specific editors with graduate-level training.
- Be suspicious of companies that post testimonials with no names or affiliations on their websites.
- Be wary of English-language editing companies based in countries where English is not the native language.
- Ask to submit a 500-word sample edit to see how the company performs.
- Look for a company with a web-based submission system (where a user logs

in, creates an account and uploads the paper). Such companies are likely to be established organizations with a high level of security.

- Don't just choose on the basis of price. Consider quality, convenience and turnaround time.
- Seek a company that offers services such as formatting, help with selecting a journal or translation from another language.
- Look for a company with a clear privacy policy that requires its editors to sign confidentiality agreements. **K.K.**

CAREER CHOICES

Opportunities in editing

Staff editors at manuscript-editing companies tend to be part-time, and are often doctoral students or postdoctoral researchers. Some companies do pay attention to the reputation of the school from which they recruit editors. Here are tips for scientists interested in working for a manuscript-editing company.

- Take a scientific editing course. The certificate may help you to get hired.
- Learn the Chicago Manual of Style and other scientific editing styles. Different journals use different styles.
- Become a journal peer reviewer to get a feel for what to look for and correct as an editor for a manuscript-editing service.
- Learn the finer details of formatting in Microsoft Word. Manuscript-editing

services are often called on to format data, tables, graphs, figures and references for a specific journal.

- Develop excellent communication and customer-relation skills. You will be working closely with the company's clients on projects that are hugely important to them and you will have to be tactful and patient, especially if a paper contains many problems or the client doesn't speak English well. In many companies you will also be working closely with other editors.
- Learn business principles. Many manuscript-editing services are start-ups and it will help them — and you — if you can market, price and advertise services, for example. **K.K.**

American Journal Experts, which has started offering what it calls 'content review' to address scientific and design flaws likely to be targets of peer review, maintain that the work they do doesn't create an ethical dilemma. Carter says she has "very strict rules" and requires that she be listed in the acknowledgements if she significantly rewrites a paper. American Journal Experts says that its content reviewers only make recommendations and identify potential problems; they are not designing the experiment or writing the paper.

"I don't believe the recommendations I make would warrant authorship status," says Anuj Kapadia, a radiologist at Duke University in Durham, North Carolina, who also acts as a content reviewer for American Journal Experts and as a peer reviewer. Journals for which he conducts peer review include *Physics in Medicine and Biology*, *IEEE Transactions on Nuclear Science*, *Analytical Chemistry* and the *Journal of Digital Imaging*.

"I'm not telling authors how to conduct the study, I'm not telling them the methods they have to follow to reach their goal," Kapadia says. "I'm telling them they said such-and-such but didn't demonstrate it — I'm not telling them how to demonstrate it."

The *New England Journal of Medicine* addresses the authorship issue by requiring authors to disclose all writing and editing assistance and to acknowledge such assistance in their paper. "Lending one's name to an article written by another party is strictly forbidden," says the journal's spokeswoman, Karen Buckley. Although Buckley would not discuss editorial policies, the journal may still

be sensitive about allegations last year, some since refuted or retracted, of ghostwriting in several top medical journals. Ghostwriting — the unacknowledged contributions of medical or other writers, often sponsored by drug companies or other corporate entities, to scientific manuscripts published under the names of academic authors — has been a thorn in the side of the medical publishing industry for a number of years.

Such touchy issues mean that authors should be careful to determine a journal's policies before submitting a manuscript. Journals in other subjects, such as physics, are unlikely to receive the scrutiny that biological and medical-science journals undergo, says Reinhardt Schuhmann, editor of *Physical Review Letters*.

Ultimately, it is impossible to police authors' use of manuscript-editing services — they have to maintain their own ethical boundaries, says Schuhmann. "We often suggest that authors whose papers are not well written consult a colleague," he says. "If the colleague were someone they paid, how would we know? We don't keep track of whether they send it to an editing service."

In general, a scientist's budget, needs and time will dictate whether to hire an editing service. But authors might also keep in mind a point on which journal editors agree — a well written paper with no glaring flaws is almost certain at least to get in the door and undergo peer review, a major step towards acceptance. "We need to be confident that we're giving the scientific community high quality at all levels," says Viccaro. "The author can help us a lot if he or she submits a manuscript that's readable." ■

Karen Kaplan is the assistant Careers editor.

CANADA

Postdoc unions

Issues such as low pay, long working hours and no holiday or sick pay have prompted postdocs at the University of Toronto and Queens University in Kingston, both in Ontario, and the University of Quebec in Montreal (UQAM) to seek union representation. Some 800 postdocs in Toronto want to affiliate with the Canadian Union of Public Employees; around 200 at Queens and 150 at UQAM want to join the Public Service Alliance of Canada (PSAC). University of Toronto administrators maintain that postdocs are not university employees and so have no right to unionize. The Ontario Labour Relations Board will decide on that right in hearings for Queens this month and Toronto in 2011. The board is reviewing an application from UQAM postdocs.

GRANTS

Awards for biomedicine

The Howard Hughes Medical Institute (HHMI) in Chevy Chase, Maryland, is to make awards to 35 early-career biomedical researchers from 18 non-US countries. The International Early Career Scientist competition will support biomedical researchers who have done a postdoc, have a research post in one of the 18 nations and trained at the doctoral, medical or postdoc level in the United States. Unlike past such HHMI competitions, it will not focus on one discipline or region. Seeking to foster collaboration and seed labs, the HHMI will give each recipient US\$650,000 over 5 years. Programme directors say that the 18 nations are small enough to benefit from the grants, but have the infrastructure to continue supporting the researchers. The competition closes on 23 February 2011.

SCOTLAND

Academic jobs safe

Despite a proposed 4% government budget cut for 2011–12, Scotland's 14,500 faculty researchers have job security this year, say officials. The £28-billion (US\$44.3-billion) Scottish draft budget for 2011–12 was announced on 17 November. It would keep the £213-million Research Excellence Grant, which supports research nationwide by paying academic salaries and grants, at the same cash level. The Scottish Funding Council hopes to keep funding to universities stable. Universities Scotland, an association that represents the country's 20 higher-education institutions, says that more cuts after 2012 might lead to layoffs.

CAREER CHOICES

Opportunities in editing

Staff editors at manuscript-editing companies tend to be part-time, and are often doctoral students or postdoctoral researchers. Some companies do pay attention to the reputation of the school from which they recruit editors. Here are tips for scientists interested in working for a manuscript-editing company.

- Take a scientific editing course. The certificate may help you to get hired.
- Learn the Chicago Manual of Style and other scientific editing styles. Different journals use different styles.
- Become a journal peer reviewer to get a feel for what to look for and correct as an editor for a manuscript-editing service.
- Learn the finer details of formatting in Microsoft Word. Manuscript-editing

services are often called on to format data, tables, graphs, figures and references for a specific journal.

- Develop excellent communication and customer-relation skills. You will be working closely with the company's clients on projects that are hugely important to them and you will have to be tactful and patient, especially if a paper contains many problems or the client doesn't speak English well. In many companies you will also be working closely with other editors.
- Learn business principles. Many manuscript-editing services are start-ups and it will help them — and you — if you can market, price and advertise services, for example. **K.K.**

American Journal Experts, which has started offering what it calls 'content review' to address scientific and design flaws likely to be targets of peer review, maintain that the work they do doesn't create an ethical dilemma. Carter says she has "very strict rules" and requires that she be listed in the acknowledgements if she significantly rewrites a paper. American Journal Experts says that its content reviewers only make recommendations and identify potential problems; they are not designing the experiment or writing the paper.

"I don't believe the recommendations I make would warrant authorship status," says Anuj Kapadia, a radiologist at Duke University in Durham, North Carolina, who also acts as a content reviewer for American Journal Experts and as a peer reviewer. Journals for which he conducts peer review include *Physics in Medicine and Biology*, *IEEE Transactions on Nuclear Science*, *Analytical Chemistry* and the *Journal of Digital Imaging*.

"I'm not telling authors how to conduct the study, I'm not telling them the methods they have to follow to reach their goal," Kapadia says. "I'm telling them they said such-and-such but didn't demonstrate it — I'm not telling them how to demonstrate it."

The *New England Journal of Medicine* addresses the authorship issue by requiring authors to disclose all writing and editing assistance and to acknowledge such assistance in their paper. "Lending one's name to an article written by another party is strictly forbidden," says the journal's spokeswoman, Karen Buckley. Although Buckley would not discuss editorial policies, the journal may still

be sensitive about allegations last year, some since refuted or retracted, of ghostwriting in several top medical journals. Ghostwriting — the unacknowledged contributions of medical or other writers, often sponsored by drug companies or other corporate entities, to scientific manuscripts published under the names of academic authors — has been a thorn in the side of the medical publishing industry for a number of years.

Such touchy issues mean that authors should be careful to determine a journal's policies before submitting a manuscript. Journals in other subjects, such as physics, are unlikely to receive the scrutiny that biological and medical-science journals undergo, says Reinhardt Schuhmann, editor of *Physical Review Letters*.

Ultimately, it is impossible to police authors' use of manuscript-editing services — they have to maintain their own ethical boundaries, says Schuhmann. "We often suggest that authors whose papers are not well written consult a colleague," he says. "If the colleague were someone they paid, how would we know? We don't keep track of whether they send it to an editing service."

In general, a scientist's budget, needs and time will dictate whether to hire an editing service. But authors might also keep in mind a point on which journal editors agree — a well written paper with no glaring flaws is almost certain at least to get in the door and undergo peer review, a major step towards acceptance. "We need to be confident that we're giving the scientific community high quality at all levels," says Viccaro. "The author can help us a lot if he or she submits a manuscript that's readable." ■

Karen Kaplan is the assistant Careers editor.

CANADA

Postdoc unions

Issues such as low pay, long working hours and no holiday or sick pay have prompted postdocs at the University of Toronto and Queens University in Kingston, both in Ontario, and the University of Quebec in Montreal (UQAM) to seek union representation. Some 800 postdocs in Toronto want to affiliate with the Canadian Union of Public Employees; around 200 at Queens and 150 at UQAM want to join the Public Service Alliance of Canada (PSAC). University of Toronto administrators maintain that postdocs are not university employees and so have no right to unionize. The Ontario Labour Relations Board will decide on that right in hearings for Queens this month and Toronto in 2011. The board is reviewing an application from UQAM postdocs.

GRANTS

Awards for biomedicine

The Howard Hughes Medical Institute (HHMI) in Chevy Chase, Maryland, is to make awards to 35 early-career biomedical researchers from 18 non-US countries. The International Early Career Scientist competition will support biomedical researchers who have done a postdoc, have a research post in one of the 18 nations and trained at the doctoral, medical or postdoc level in the United States. Unlike past such HHMI competitions, it will not focus on one discipline or region. Seeking to foster collaboration and seed labs, the HHMI will give each recipient US\$650,000 over 5 years. Programme directors say that the 18 nations are small enough to benefit from the grants, but have the infrastructure to continue supporting the researchers. The competition closes on 23 February 2011.

SCOTLAND

Academic jobs safe

Despite a proposed 4% government budget cut for 2011–12, Scotland's 14,500 faculty researchers have job security this year, say officials. The £28-billion (US\$44.3-billion) Scottish draft budget for 2011–12 was announced on 17 November. It would keep the £213-million Research Excellence Grant, which supports research nationwide by paying academic salaries and grants, at the same cash level. The Scottish Funding Council hopes to keep funding to universities stable. Universities Scotland, an association that represents the country's 20 higher-education institutions, says that more cuts after 2012 might lead to layoffs.

THE AGE OF MOMENTUM

The only way is up.

BY T. F. DAVENPORT

Over the egg-shaped stones of the dry creek bed, I led the badger by a ring in his nose. Luisa, bobbing with each step, rode atop him and squinted into the morning sun.

"There," she said. "The bend in the river is a likely spot." I followed her pointing finger to a green-topped bluff sharply eroded on its nearest face, chipped angles of grey stone exposed. Away from the river, grass sloped down to the east and north, bubbling as it went into low, misshapen hills.

With a lot of cursing and slaps to the rear flank, we got the badger up there, and pretty soon after it started digging, we knew we had chosen well. Flakes of plaster turned up right away, followed by nodes of metal and blistered, still-acrid bits of burnt plastic. Soon, human remains.

It was from the plastic, not from the frame of the building we uncovered later, that we knew this was a site of the Right-Angle Culture.

Some time between one and two thousand years ago, a short-lived society arose during a lucky climactic lull. In just a few centuries they achieved more than all previous cultures put together. They dug up and burnt the stored energy of eons. There was a brief, bizarre moment in human history when it was quite mundane to smell fossil fuels exploding in engines, to blast away mountain caps and scrape out coal, to watch ugly, angular buildings rise from the ground in days. In this moment, perhaps five generations long, it was plain to everyone that the only movement possible was upwards, ever-accelerating, into a future filled densely with light. But the Anglers, as we now call them, fell short of escape velocity.

The badger mapped out the core of the site. With two strong trunks and a dozen little fan-shaped feelers, he cleaned off the rubble and sorted it by a system at which human minds could only guess. He grunted with obscure pleasure, excavating a trumpet-shaped lamp, a twisted rebar, a shoe.

As Angler towns tended to do, this one surely extended for miles, probably on both sides of the river. What we were standing on top of, judging by the contorted, skeletal chair-frames that the badger handled with special fondness, was a private home, an



interrogation chamber, a dental clinic or a barbershop.

I got a gourd of wine from the saddlebag, brought it over to Luisa, and told her as much.

She nodded. "Interrogation chamber, I think. Look." She held them up, one after the other: sharp metal implements unadapted to dining. Hooks, barbs and spikes, electric motors with little sockets in them — we didn't want to know what fit into those. She threw down the implements and shook her head in disgust.

I offered her the wine again. This time she took it.

We had lunch under an oak tree overlooking the creek bed. Afterwards, we shared a joint. As the smoke floated, like the skeleton of the long-dry river, we told each other stories about the Anglers. I talked of how the idea of the right angle — its perfection and its wrongness — had come to obsess them. How it had manifested at every level of their culture, from their architecture and the grids of their streets right down to the microscopic etchings on the tiny, silicon flakes that constituted the great mystery of their culture.

Luisa said that was all bullshit. The Anglers had been people, just like us. They lived according to their circumstances, and the right angle, like the unsolved binary code and the written-down laws and every other 'unnatural' aberration from which philosophers made so much hay, was nothing more than a tool. The Anglers

used it because it was useful. If we didn't know how to grow our houses we would probably be Anglers, too.

"Not me." I stubbed out the joint on the oak bark. "How much of their literature have you read?"

Luisa shook her head. "I've never been good at languages." "You're not missing much," I admitted. "But they had this phrase: *going somewhere*." I translated it for her. "And its opposite: *going nowhere*. It was the worst thing that could happen to you, to be *going nowhere*."

It had nothing to do with travel, but — I gestured inadequately — progress. They never actually got anywhere, but they struggled lifelong to be going somewhere. Do you know what I mean?"

"No."

"Neither did they. But that's what it was like to be an Angler — to be trapped in this upward struggle, maybe thinking that someday you could rest, but then when you actually did rest you'd feel guilty about it. You weren't going anywhere."

Luisa stood, looking back towards the site, where the badger snored in the afternoon sun. "I've never seen what's so great about rest, myself."

I caught up with her as she started back. "You'd've fit in perfectly, then."

She smiled but said nothing. She roused the badger with a slap, squatted in its shadow, and began sifting through a pile of artefacts. I sat down to help her. We kept an eye out for plastic rectangles with rounded corners. More often than not, they proved to contain silicon flakes — potential clues to the binary code and the key to understanding, if not reproducing, the Anglers' power.

I held up a partial skull. "This," I said, "once held the confidence that someday the human race itself could rest. Up we'd go until we'd figured out everything. We'd spread through the stars, serenely conquering every obstacle, building right-angled houses on other planets, having right-angled children named Vera, Chuck and —"

"Albert, will you shut up? I'm busy!" ■

T. F. Davenport lives in California, studying for a doctorate in cognitive science. In his spare time, he would be writing more science-fiction stories, but he has no spare time, because he's studying for a doctorate in cognitive science.

► **NATURE.COM**
Discuss this story
online at:
go.nature.com/ye9b79

Crystal structure of bacterial RNA polymerase bound with a transcription inhibitor protein

Shunsuke Tagami^{1,2}, Shun-ichi Sekine^{1,2,3}, Thirumananseri Kumarevel^{4†}, Nobumasa Hino², Yuko Murayama^{1,2}, Syunsuke Kamegami^{1,2}, Masaki Yamamoto⁵, Kensaku Sakamoto² & Shigeyuki Yokoyama^{1,2,3}

The multi-subunit DNA-dependent RNA polymerase (RNAP) is the principal enzyme of transcription for gene expression. Transcription is regulated by various transcription factors. Gre factor homologue 1 (Gfh1), found in the *Thermus* genus, is a close homologue of the well-conserved bacterial transcription factor GreA, and inhibits transcription initiation and elongation by binding directly to RNAP^{1–8}. The structural basis of transcription inhibition by Gfh1 has remained elusive, although the crystal structures of RNAP and Gfh1 have been determined separately^{6–9}. Here we report the crystal structure of *Thermus thermophilus* RNAP complexed with Gfh1. The amino-terminal coiled-coil domain of Gfh1 fully occludes the channel formed between the two central modules of RNAP; this channel would normally be used for nucleotide triphosphate (NTP) entry into the catalytic site. Furthermore, the tip of the coiled-coil domain occupies the NTP β - γ phosphate-binding site. The NTP-entry channel is expanded, because the central modules are ‘ratcheted’ relative to each other by $\sim 7^\circ$, as compared with the previously reported elongation complexes. This ‘ratcheted state’ is an alternative structural state, defined by a newly acquired contact between the central modules. Therefore, the shape of Gfh1 is appropriate to maintain RNAP in the ratcheted state. Simultaneously, the ratcheting expands the nucleic-acid-binding channel, and kinks the bridge helix, which connects the central modules. Taken together, the present results reveal that Gfh1 inhibits transcription by preventing NTP binding and freezing RNAP in the alternative structural state. The ratcheted state might also be associated with other aspects of transcription, such as RNAP translocation and transcription termination.

RNAP synthesizes RNA complementary to the template DNA (Supplementary Fig. 1a). Crystallographic studies of RNAPs from thermophilic bacteria and RNAP II (Pol II) from the yeast *Saccharomyces cerevisiae* have revealed the overall structure of RNAP, which resembles a crab’s claw^{9–11} (Supplementary Fig. 1b). In the transcribing RNAP (elongation complex, EC), the nascent RNA strand remains bound to the template DNA strand, forming an 8–9 base pair DNA•RNA hybrid. The DNA•RNA hybrid and the downstream DNA duplex are tightly held in the ‘primary channel’ formed between the pincers of the crab claw, in the EC structures of the *S. cerevisiae* and *T. thermophilus* RNAPs^{12–21}. The catalytic site of nucleotide addition resides at the joint of the pincers. The substrate NTP is considered to enter the catalytic site through a pore (the ‘secondary channel’) on the back side of the crab claw (Supplementary Fig. 1b). The two pincers are connected by a long α -helix (the bridge helix), which is located at the junction of the DNA•RNA hybrid-binding site, the downstream DNA-binding site, and the secondary channel. The bridge helix is inherently flexible, adopting both the continuously-helical and kinked conformations^{9–11,22,23}.

In a previous study²⁴, we successfully crystallized *T. thermophilus* RNAP together with DNA, RNA and Gfh1, and collected X-ray

diffraction data sets for two $P2_1$ crystals (crystals 1 and 2). The nucleic-acid scaffolds employed for the crystallization included the downstream duplex DNA, the DNA•RNA hybrid, and an upstream RNA hairpin 10 or 11 nucleotides (nt) from the RNA 3′ end (Supplementary Text 1, Supplementary Fig. 2a)²⁴. In the present study, we determined the structures of the quaternary complex of RNAP•DNA•RNA•Gfh1 (EC•Gfh1) (Fig. 1a, b, Supplementary Table 1, and Methods). The structures of the three independent RNAP molecules in the asymmetric units of crystals 1 and 2 are all similar to each other (Supplementary Text 2, Supplementary Figs 3–5). RNAP and Gfh1 showed clear electron densities (Supplementary Fig. 6), and thus the inhibition mechanisms of Gfh1 were unambiguously revealed, as described below. In contrast, the electron densities of both the DNA and RNA were weak, so we only built the partial models (Supplementary Text 3, Supplementary Figs 2, 7).

The *S. cerevisiae* Pol II structure consists of four rigid modules, ‘core’, ‘shelf’, ‘clamp’ and ‘jaw-lobe’, which are mobile relative to each other¹⁰. The rigid modules of the bacterial RNAP were defined previously, on the basis of the structures of the *Thermus aquaticus* core enzyme and the *T. thermophilus* holoenzyme^{11,25,26} (Supplementary Text 4). However, the conformations of the *T. thermophilus* RNAP in the present EC•Gfh1 structures differ appreciably from those in the previously reported structures of the core enzyme, the holoenzyme and ECs^{13,14} (Fig. 1c, d). The large conformational differences enabled us to redefine the rigid-body modules of *T. thermophilus* RNAP (Fig. 1a, b, Supplementary Table 2, Supplementary Text 4, Supplementary Figs 8, 9). These rigid modules include the ‘core’, ‘shelf’, and ‘clamp’ modules, which generally correspond well to those in Pol II. The exceptions are that the active-site and dock domains belong to the ‘shelf’ module, rather than to the ‘core’ module, and the β -domain 1 (or the protrusion domain in Pol II) and the β flap domain (or the wall domain in Pol II) are not included in the ‘core’ module in *T. thermophilus* RNAP (Supplementary Text 4, Supplementary Fig. 8). The core and shelf modules are the main structural elements that form the primary, secondary and RNA-exit channels (Fig. 1a, b, Supplementary Text 4). Gfh1 is accommodated in the secondary channel and its exterior region (Fig. 1a, b, Supplementary Fig. 6). The N-terminal domain (NTD) of Gfh1 forms a coiled coil and is inserted into the secondary channel. The major relative movements among the rigid-body modules are the ‘ratcheting’ between the shelf and core modules and the ‘swinging’ of the clamp relative to the shelf module (Fig. 1c, d, Supplementary Movies 1, 2), as described below in more detail.

The clamp module is connected to the shelf module by four loops (switches 1, 2, 4 and 5, Supplementary Table 2). The protruded clamp module swings relative to the shelf module by about 15° around the centre near switch 5, and is further tilted by about 5° in EC•Gfh1 (Fig. 1a, b, Supplementary Fig. 10, Supplementary Movie 2). Consequently, the region of the primary channel outside the hybrid-binding site is

¹Department of Biophysics and Biochemistry, Graduate School of Science, University of Tokyo, 7-3-1 Hongo, Bunkyo-ku, Tokyo 113-0033, Japan. ²RIKEN Systems and Structural Biology Center, 1-7-22 Suehiro-cho, Tsurumi, Yokohama 230-0045, Japan. ³Laboratory of Structural Biology, Graduate School of Science, University of Tokyo, 7-3-1 Hongo, Bunkyo-ku, Tokyo 113-0033, Japan. ⁴Structural and Molecular Biology Laboratory, RIKEN SPring-8 Center, Harima Institute, 1-1-1 Kouto, Sayo, Hyogo 679-5148, Japan. ⁵SR Life Science Instrumentation Unit, RIKEN SPring-8 Center, Harima Institute, 1-1-1 Kouto, Sayo, Hyogo 679-5148, Japan. [†]Present address: Biometal Science Laboratory, RIKEN SPring-8 Center, Harima Institute, 1-1-1 Kouto, Sayo, Hyogo 679-5148, Japan.

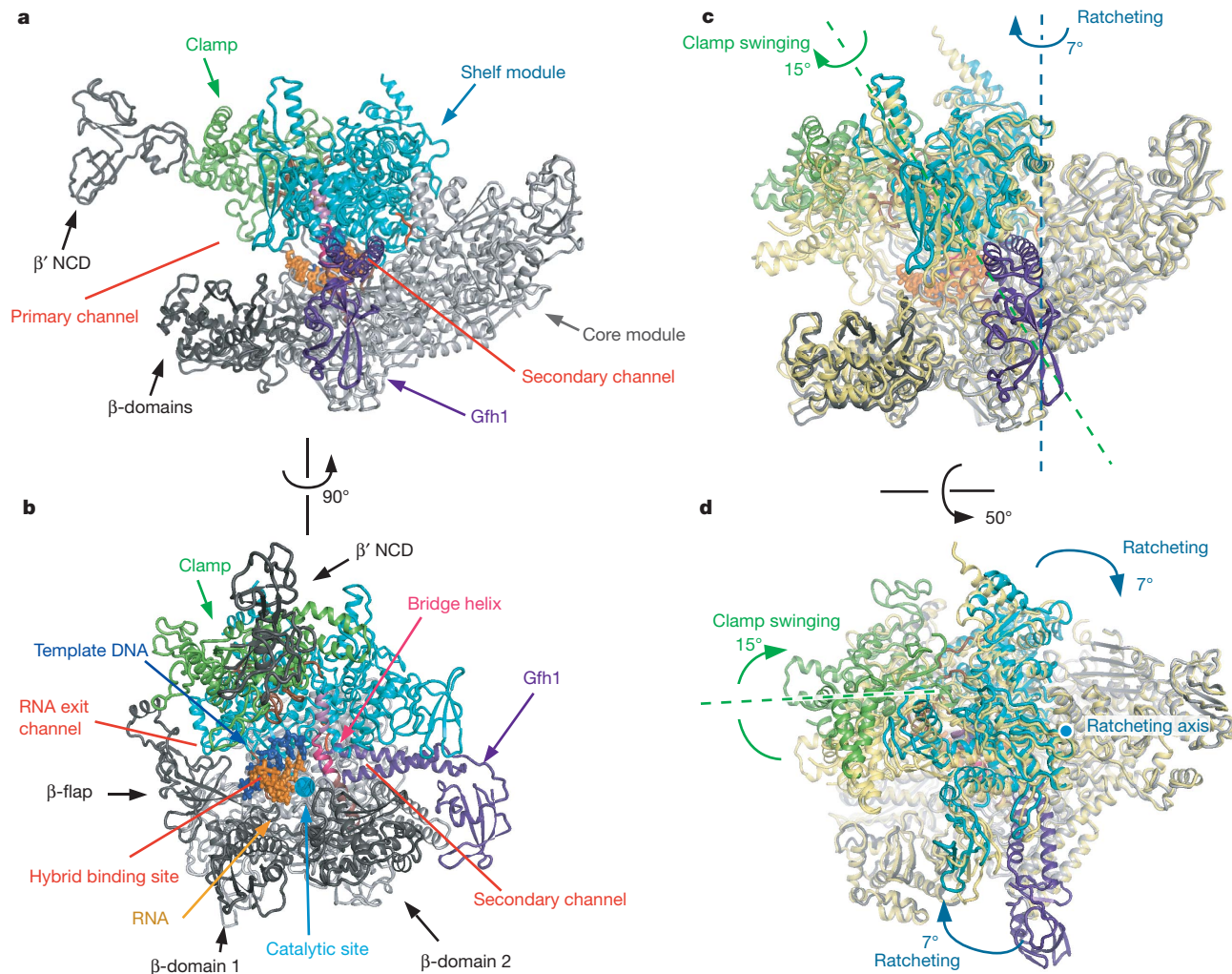


Figure 1 | Structure of EC•Gfh1. **a, b**, Overall structure of *T. thermophilus* EC•Gfh1 in two orientations. **c, d**, Superposition of EC•Gfh1 and EC (PDB 2O5I, yellow). The core modules of the two structures are superposed minimizing the root mean square deviation (RMSD) between C α atoms. Two orientations are shown. The same colour scheme is used in all figures (RNA,

orange; template DNA, blue; Gfh1, purple; shelf module, cyan; core module, grey; clamp, green; switches 1–5, brown; hinge loop, red; other domains, dark grey). The three regions of the bridge helix are coloured differently (N-terminal, dark pink; central, hot pink; C-terminal, violet).

widened (Supplementary Text 5, Supplementary Fig. 11). Considering that Gfh1 binding to RNAP occurs on the opposite side of the clamp module, and that Gfh1 does not directly contact the clamp module, the clamp swinging seems to be related to the hairpin structure in the RNA of the nucleic acid scaffolds (Supplementary Text 5).

The central body of RNAP is composed of the core and shelf modules, which are rotated by $\sim 7^\circ$ relative to each other in the present RNAP structures, as compared with the previously-reported EC state^{13,14} (Figs 1c, d, 2a, and Supplementary Movie 1). We designate this novel RNAP state as the ‘ratcheted’ state, and the previous EC state as the ‘tight’ state. The shelf module is attached to the backboard part of the core module (Fig. 1a), through interfaces of about 3,800 Å² in the ratcheted state and about 3,600 Å² in the tight state (Fig. 2b, c). The shelf–core interfaces in the two states are mostly overlapped (shown in green), but there are several contact points specific to either the ratcheted state or the tight state (shown in red and yellow, respectively). The central overlapped area of the interfaces is mainly hydrophobic, and the rotation axis of the ratcheting runs along it (Fig. 2b, c). The ratcheting axis forms an angle of about 50° to the floor of the channels on the core module (Fig. 2a). The core and shelf modules are connected by three peptide segments, the bridge helix, the loop consisting of β Tyr 998–Met 1005 (previously designated as ‘switch 3’)¹⁰, and the loop consisting of β' Ala 779–Ser 782 (designated hereafter as the ‘hinge loop’) (Fig. 2d,

Supplementary Fig. 12). As the ratcheting axis runs close to β' Pro 781 (*Escherichia coli* β' Pro 502) within the hinge loop, the conformational change due to the ratcheting is negligibly small around this loop (Fig. 2e, f, Supplementary Fig. 12). By contrast, the bridge helix is much further from the ratcheting axis, as compared with the other two peptide segments (Fig. 2b, c), and the conformational change is significant, as described below in more detail.

On the other hand, the contact points specific to the ratcheted state are also distant from the ratcheting axis (Fig. 2b, c). In particular, an α -helix of the shelf module (β' 685–696) contacts a β -hairpin from one of the α subunits (α B 184–191) (Fig. 2g). This contact probably limits the further ratcheting of the shelf module. Therefore, the ratcheted state is mostly at one extremity in the structural spectrum of bacterial RNAP, whereas the tight state observed in previous ECs^{13,14} should be the other extremity.

The shelf module ratcheting results in a composite movement that expands the hybrid-binding site and shifts the shelf module forward, relative to the core module (Fig. 2e, f, Supplementary Text 6, Supplementary Fig. 13). The bridge helix exposes its central part (β' 1084–1092), but buries its N-terminal part (β' 1070–1083) and the carboxy-terminal part (β' 1093–1102) within the core and shelf modules, respectively. As the two modules ratchet, the N- and C-terminal parts of the bridge helix shift relative to each other. Consequently, the conformation

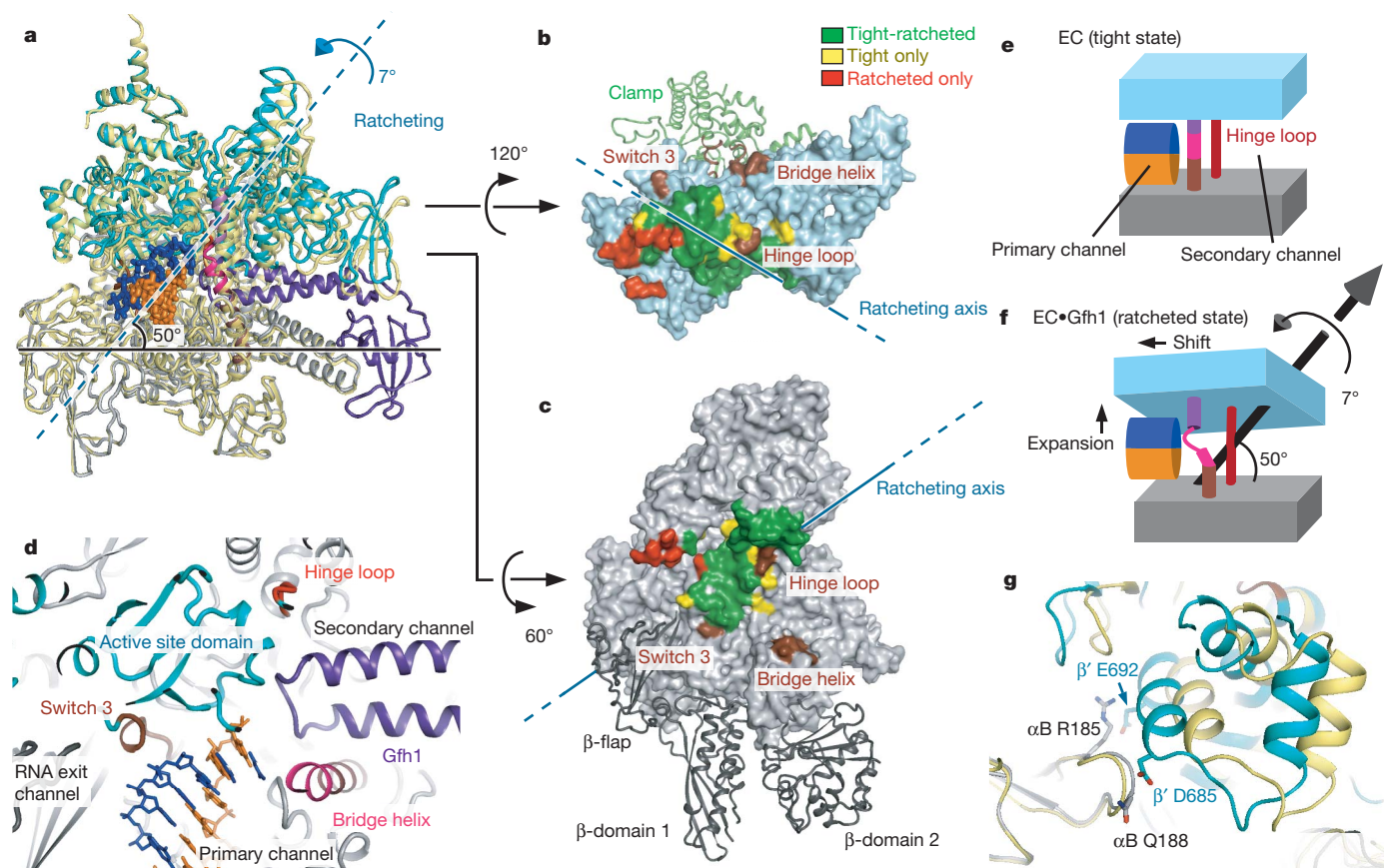


Figure 2 | Ratcheting of the shelf module. **a**, Superposition of EC-Gfh1 and EC (PDB 2O5I, yellow). The core modules of the two structures are superposed. The clamp, β' NCD, and β domains are not shown. The dashed cyan line indicates the ratcheting axis. **b**, **c**, Interaction surface between the core and the shelf modules; two orientations are shown. **d**, The structures around the active

site. The hinge loop is coloured red. **e**, **f**, A schematic drawing representing the structural differences between EC (**e**) and EC-Gfh1 (**f**). **g**, The contacts between the shelf and the core modules specific to the ratcheted state. EC-Gfh1 and EC are superposed by the core modules.

of β' Thr 1088–Gly 1092 in the central part dramatically changes from the continuous α -helix in the previous ECs, and the two discontinuous α -helices are connected by the two non-helical residues, Ser 1091–Gly 1092 (Fig. 3a). It is intriguing that mutations of these two residues reportedly affect the RNAP activity²⁷. On the other hand, the bridge helix is kinked in the RNAP structures of *T. aquaticus* core enzyme ($\alpha_2\beta\beta'\omega$) and *T. thermophilus* holoenzyme ($\alpha_2\beta\beta'\omega\sigma$) without nucleic acids^{9,11}. However, the present kinked conformation is quite different from the previous ones (Supplementary Text 7 and Supplementary Fig. 14). Here, the two α -helices that are directly connected to the trigger loop are packed against the bridge-helix C-terminal region, and are therefore shifted together with it. To avoid steric hindrance with the tips of these two helices, the residues β' Thr 1088, Ala 1089, Asp 1090 and Ser 1091 (*E. coli* β' Thr 790, Ala 791, Asn 792 and Ser 793) protrude into the DNA-RNA hybrid binding site (Fig. 3b, Supplementary Text 6, Supplementary Fig. 13). Therefore, the conformational change of the bridge helix is likely to occur synchronously with the transition to the ratcheted state (Supplementary Text 7, 8). The direct interaction between Gfh1 and RNAP may affect the fine conformation of the bridge helix, by immobilizing its N-terminal region (see below).

Within the secondary channel, the Gfh1 NTD interacts tightly with parts of the shelf module (including the trigger loop) and the core module (including the secondary-channel coiled coil (β' 958–1014) and the N-terminal part of the bridge helix), and fits particularly well with the narrowest region of the secondary channel (Fig. 3c, Supplementary Text 9, Supplementary Fig. 15, Supplementary Movie 1). The interaction between the Gfh1 NTD and the N-terminal part of the bridge helix seems to maintain the straight conformation of the N-terminal part, and to define the kinking point of the bridge helix in EC-Gfh1. It

is impossible for the Gfh1 NTD to bind to the secondary channel in the tight EC in the same manner, as the channel is too narrow (Fig. 3d). Leu 33 of the Gfh1 NTD is located in the narrowest region of the secondary channel. A Gfh1 mutant with Leu 33 replaced by Trp (L33W) lacked transcription inhibition activity, probably because of an inability to bind (Fig. 3e, Supplementary Fig. 16). The bulky side chain of Trp seems to prevent the Gfh1 NTD from penetrating into the channel. This observation also indicates that the secondary channel cannot open beyond the width of the present ratcheted state. Consequently, Gfh1 just fits into the well-defined ratcheted state. Considering that Gfh1 cannot bind to RNAP in the tight state, because of steric hindrance, it is reasonable to postulate that Gfh1 traps a dynamically occurring, ratcheted state of RNAP. To examine this possibility, we performed crosslinking experiments. The results showed that an artificial disulphide bond or photo-crosslink was formed at the ratcheted state-specific interface between the core and shelf modules, even in the absence of Gfh1 (Supplementary Text 10, Supplementary Figs 17–19). Therefore, RNAP might spontaneously and dynamically alter its conformation, from the tight state to the ratcheted state, although the result could also be explained by more localized conformational fluctuations.

Owing to the interaction of the Gfh1 NTD with the narrowest part of the secondary channel, NTP entry would be prevented. Moreover, the presence of the Gfh1 NTD is compatible with the unfolded conformation of the trigger loop, but not with the NTP-induced, folded conformation^{14,15} (Supplementary Fig. 20). The tip of the Gfh1 NTD is located near the RNAP active site (Supplementary Text 11, Supplementary Fig. 21). The end of the tip loop occupies the binding site of the β - γ phosphate groups in the NTP insertion step of the nucleotide

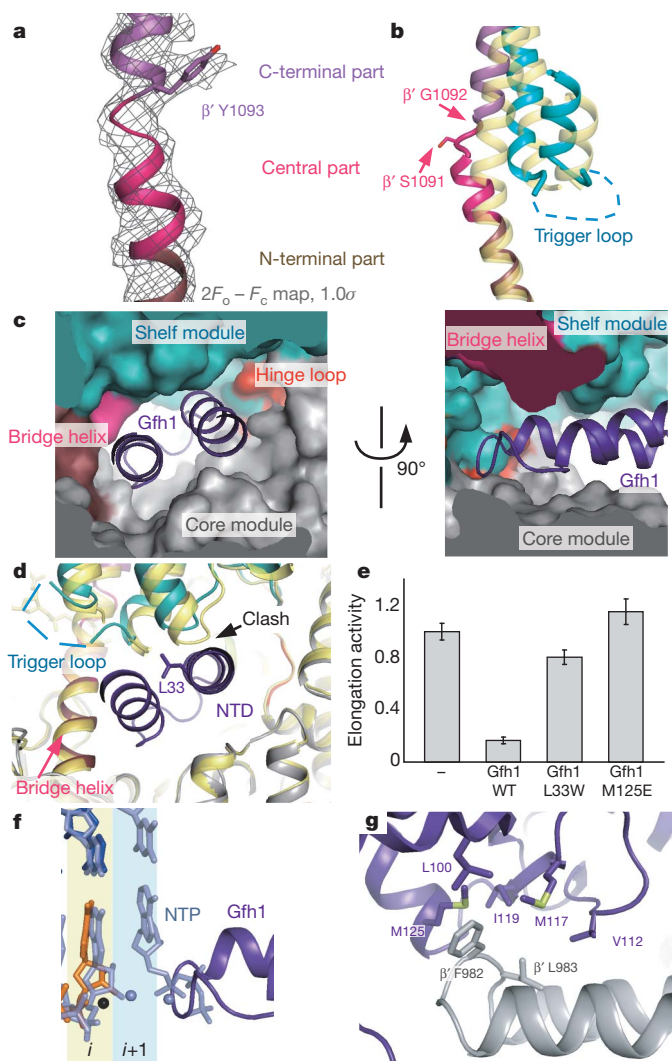


Figure 3 | The bridge helix and Gfh1. **a**, The structure and the electron density of the bridge helix in EC•Gfh1 (crystal 1, RNAP 1). **b**, The bridge helix and the helices neighbouring the trigger loop. *T. thermophilus* EC in the post-translocation state (PDB 2O5I) is superposed, and is coloured yellow. **c**, **d**, The Gfh1 NTD in the secondary channel. **d**, *T. thermophilus* EC in the post-translocation state (PDB 2O5I) is superposed. The black arrow indicates the position where Gfh1 would clash with EC in the tight state. **e**, Inhibition of the nucleotide addition reaction by Gfh1. The nucleotide addition reaction was performed by incubating the transcription elongation complex with 5 μ M Gfh1 mutants. Error bars, s.d. ($n \geq 5$). **f**, A close-up view of the active site. *T. thermophilus* EC in the NTP-bound state (PDB 2O5J) is superposed, and is coloured light blue. i and $i+1$ are the positions of the RNA 3' end and the substrate NTP, respectively, in the nucleotide addition reaction. **g**, Interaction between the tip of the Gfh1 CTD and RNAP.

addition reaction (Fig. 3f). Furthermore, Gfh1 seems to stabilize the kinked bridge helix (Fig. 3b). An antibiotic, streptolydigin, also reportedly inhibited transcription by immobilizing the bridge helix in a fixed conformation²³. Taken together, these observations provide the explanation for the inhibition of transcription elongation by Gfh1 (Supplementary Text 12, and Supplementary Figs 22, 23).

On the other hand, the C-terminal domain (CTD) of Gfh1 is bound with the edge of the secondary-channel coiled coil of the RNAP (Fig. 1a, b, Supplementary Text 13, Supplementary Fig. 24). The interaction involves the hydrophobic patch on the surface of the Gfh1 CTD (Fig. 3g). Therefore, we prepared a Gfh1 protein with the M125E mutation within the hydrophobic patch, and observed a loss of inhibition activity (Fig. 3e). Therefore, the interaction between the hydrophobic patch of the Gfh1 CTD and the secondary-channel coiled coil is

required for Gfh1 to bind to RNAP. Other Gre factors, such as GreA and GreB, share structural and sequence similarities with Gfh1 (refs 2–8). In particular, the presence of the hydrophobic patch on the CTD is well conserved. In fact, the M124E mutation of *E. coli* GreB (M125E of Gfh1) also reduces the transcript cleavage activity of GreB³. Therefore, the Gre factors seem to share a common interaction mode between the hydrophobic patch and the secondary-channel coiled coil, and probably bind to the ratcheted EC in a similar manner to Gfh1 (Supplementary Text 13, 14). Transcript cleavage stimulated by GreA and GreB would be performed in the ratcheted state. Although Pol II EC also changes its structure upon TFIIS binding^{18,28}, the observed change is much smaller than the transition to the ratcheted state of *T. thermophilus* EC upon Gfh1 binding (Supplementary Text 15).

The conformational changes of RNAP observed in the present structure, including the shelf module ratcheting and the clamp swinging, might have functional relevance to other stages of the transcription reaction, as the conformational changes should modulate the interactions of RNAP with nucleic acids. Therefore, we suggest that the conformational changes may play distinct roles in RNAP translocation and transcription termination (Supplementary Text 16, 17, Supplementary Figs 25–27). Experimental tests of these hypotheses will be required to assess the importance of these conformational changes in the absence of Gfh1.

METHODS SUMMARY

Structure determination. The structure of crystal 1 was solved by molecular replacement, using the coordinates of RNAP in *T. thermophilus* EC (PDB 2O5I)¹³ as the search model. There are three RNAP molecules in the asymmetric unit, and each RNAP is bound with Gfh1. As the relative positions of the Gfh1 NTD and CTD differ from those in free Gfh1 (PDB 2F23)⁷, they were separately placed in the electron density map. The model of the DNA•RNA hybrid was built in the extra electron density in the DNA•RNA hybrid channel. We further remodelled the coordinates of both the proteins and the nucleic acids with the program Coot²⁹. Atomic positions and grouped B-factors were refined to 4.1 Å, by using the CNS program³⁰ (Supplementary Table 1). The refinement converged to R and R_{free} values of 26.2% and 31.8%, respectively; the latter was calculated from randomly-chosen 3% of reflections excluded from the refinement. The structure of crystal 2 was solved by molecular replacement, using the coordinates of the RNAP in crystal 1 as the search model. The models of Gfh1 and the DNA•RNA hybrid were built in the extra electron density. Refinement of the coordinates was performed to 4.3 Å with CNS. The final R and R_{free} values are 31.4% and 33.8%, respectively.

Transcription inhibition analysis. We prepared two mutant Gfh1 proteins (L33W and M125E). The elongation complex was reconstituted by incubating *T. thermophilus* RNAP with a nucleic acid scaffold containing template DNA, non-template DNA, and RNA. The RNA was 5'-radiolabelled using T4 polynucleotide kinase and [γ -³²P]-ATP. The nucleotide addition reaction was performed by incubating the transcription elongation complex in the presence of Gfh1 (the wild type or one of the mutants).

Full Methods and any associated references are available in the online version of the paper at www.nature.com/nature.

Received 16 October 2009; accepted 12 October 2010.

Published online 1 December 2010.

- Borukhov, S., Polyakov, A., Nikiforov, V. & Goldfarb, A. GreA protein: a transcription elongation factor from *Escherichia coli*. *Proc. Natl Acad. Sci. USA* **89**, 8899–8902 (1992).
- Stebbins, C. E. *et al.* Crystal structure of the GreA transcript cleavage factor from *Escherichia coli*. *Nature* **373**, 636–640 (1995).
- Vassilyeva, M. N. *et al.* The carboxy-terminal coiled-coil of the RNA polymerase β' -subunit is the main binding site for Gre factors. *EMBO Rep.* **8**, 1038–1043 (2007).
- Hogan, B. P., Hartsch, T. & Erie, D. A. Transcript cleavage by *Thermus thermophilus* RNA polymerase. Effects of GreA and anti-GreA factors. *J. Biol. Chem.* **277**, 967–975 (2002).
- Laptenko, O. & Borukhov, S. Biochemical assays of Gre factors of *Thermus thermophilus*. *Methods Enzymol.* **371**, 219–232 (2003).
- Lamour, V., Hogan, B. P., Erie, D. A. & Darst, S. A. Crystal structure of *Thermus aquaticus* Gfh1, a Gre-factor paralog that inhibits rather than stimulates transcript cleavage. *J. Mol. Biol.* **356**, 179–188 (2006).
- Laptenko, O. *et al.* pH-dependent conformational switch activates the inhibitor of transcription elongation. *EMBO J.* **25**, 2131–2141 (2006).

8. Symersky, J. *et al.* Regulation through the RNA polymerase secondary channel. Structural and functional variability of the coiled-coil transcription factors. *J. Biol. Chem.* **281**, 1309–1312 (2006).
9. Zhang, G. *et al.* Crystal structure of *Thermus aquaticus* core RNA polymerase at 3.3 Å resolution. *Cell* **98**, 811–824 (1999).
10. Cramer, P., Bushnell, D. A. & Kornberg, R. D. Structural basis of transcription: RNA polymerase II at 2.8 angstrom resolution. *Science* **292**, 1863–1876 (2001).
11. Vassylyev, D. G. *et al.* Crystal structure of a bacterial RNA polymerase holoenzyme at 2.6 Å resolution. *Nature* **417**, 712–719 (2002).
12. Gnatt, A. L., Cramer, P., Fu, J., Bushnell, D. A. & Kornberg, R. D. Structural basis of transcription: an RNA polymerase II elongation complex at 3.3 Å resolution. *Science* **292**, 1876–1882 (2001).
13. Vassylyev, D. G., Vassylyeva, M. N., Perederina, A., Tahirou, T. H. & Artsimovitch, I. Structural basis for transcription elongation by bacterial RNA polymerase. *Nature* **448**, 157–162 (2007).
14. Vassylyev, D. G. *et al.* Structural basis for substrate loading in bacterial RNA polymerase. *Nature* **448**, 163–168 (2007).
15. Wang, D., Bushnell, D. A., Westover, K. D., Kaplan, C. D. & Kornberg, R. D. Structural basis of transcription: role of the trigger loop in substrate specificity and catalysis. *Cell* **127**, 941–954 (2006).
16. Westover, K. D., Bushnell, D. A. & Kornberg, R. D. Structural basis of transcription: separation of RNA from DNA by RNA polymerase II. *Science* **303**, 1014–1016 (2004).
17. Westover, K. D., Bushnell, D. A. & Kornberg, R. D. Structural basis of transcription: nucleotide selection by rotation in the RNA polymerase II active center. *Cell* **119**, 481–489 (2004).
18. Kettenberger, H., Armache, K. J. & Cramer, P. Complete RNA polymerase II elongation complex structure and its interactions with NTP and TFIIIS. *Mol. Cell* **16**, 955–965 (2004).
19. Brueckner, F. & Cramer, P. Structural basis of transcription inhibition by α -amanitin and implications for RNA polymerase II translocation. *Nature Struct. Mol. Biol.* **15**, 811–818 (2008).
20. Sydow, J. F. *et al.* Structural basis of transcription: mismatch-specific fidelity mechanisms and paused RNA polymerase II with frayed RNA. *Mol. Cell* **34**, 710–721 (2009).
21. Wang, D. *et al.* Structural basis of transcription: backtracked RNA polymerase II at 3.4 angstrom resolution. *Science* **324**, 1203–1206 (2009).
22. Temiakov, D. *et al.* Structural basis of transcription inhibition by antibiotic streptolydigin. *Mol. Cell* **19**, 655–666 (2005).
23. Tuske, S. *et al.* Inhibition of bacterial RNA polymerase by streptolydigin: stabilization of a straight-bridge-helix active-center conformation. *Cell* **122**, 541–552 (2005).
24. Tagami, S., Sekine, S., Kumarevel, T., Yamamoto, M. & Yokoyama, S. Crystallization and preliminary X-ray crystallographic analysis of *Thermus thermophilus* transcription elongation complex bound to Gfh1. *Acta Crystallogr. F* **66**, 64–68 (2010).
25. Darst, S. A. *et al.* Conformational flexibility of bacterial RNA polymerase. *Proc. Natl Acad. Sci. USA* **99**, 4296–4301 (2002).
26. Murakami, K. S., Masuda, S. & Darst, S. A. Structural basis of transcription initiation: RNA polymerase holoenzyme at 4 Å resolution. *Science* **296**, 1280–1284 (2002).
27. Tan, L., Wiesler, S., Trzaska, D., Carney, H. C. & Weinzierl, R. O. Bridge helix and trigger loop perturbations generate superactive RNA polymerases. *J. Biol.* **7**, 40 (2008).
28. Kettenberger, H., Armache, K. J. & Cramer, P. Architecture of the RNA polymerase II-TFIIIS complex and implications for mRNA cleavage. *Cell* **114**, 347–357 (2003).
29. Emsley, P. & Cowtan, K. Coot: model-building tools for molecular graphics. *Acta Crystallogr. D* **60**, 2126–2132 (2004).
30. Brunger, A. T. Version 1.2 of the Crystallography and NMR system. *Nature Protocols* **2**, 2728–2733 (2007).

Supplementary Information is linked to the online version of the paper at www.nature.com/nature.

Acknowledgements This work is based on experiments performed at SPring-8 (with the approval of the Japan Synchrotron Radiation Research Institute) and at the Swiss Light Source (SLS). We thank N. Shimizu for supporting our data collection at SPring-8 beamline BL41XU; T. Tomizaki and C. Schulze-Bries for supporting our data collection at SLS beamline X06SA; and Y. Fujii for assisting with our data collection and for comments. We thank T. Tanaka and K. Sakamoto for assistance in protein preparation. This work was supported in part by a Japan Society for the Promotion of Science (JSPS) Grant-in-Aid for Young Scientists (to S.-i.S.), a JSPS Grant-in-Aid for Scientific Research (to S.-i.S. and S.Y.), and the Targeted Proteins Research Program (TPRP), the Ministry of Education, Culture, Sports, Science and Technology (MEXT) of Japan. S.T. was supported by the JSPS Global Centers of Excellence Program (Integrative Life Science Based on the Study of Biosignaling Mechanisms).

Author Contributions S.T., S.-i.S., T. K. and S.Y. designed the research. S.T. and S.-i.S. performed the structural analysis. M.Y. supported the structural analysis. S.T., S.-i.S., N.H., S.K. and K.S. performed the disulphide-bonding and/or photo-crosslinking analyses. S.T. and Y.M. performed the biochemical analysis of Gre factors. S.-i.S. created the movies. S.T., S.-i.S. and S.Y. wrote the paper.

Author Information The structures of EC•Gfh1 have been deposited in the Protein Data Bank, under accession numbers 3AOH (crystal 1) and 3AOI (crystal 2). Reprints and permissions information is available at www.nature.com/reprints. The authors declare no competing financial interests. Readers are welcome to comment on the online version of this article at www.nature.com/nature. Correspondence and requests for materials should be addressed to S.-i.S. (sekine@biochem.s.u-tokyo.ac.jp) or S.Y. (yokoyama@biochem.s.u-tokyo.ac.jp).

METHODS

Structure determination. Crystallization and data collection were described previously²⁴. The data were reprocessed with the XDS program³¹. The structure for crystal 1 was solved by molecular replacement with the program Phaser³², using the coordinates of the core enzyme portion of *T. thermophilus* EC (PDB 2O5I)¹³ as the search model. The asymmetric unit contains three RNAP molecules. Each RNAP was divided into 25–26 rigid bodies, and their positions were refined with the program CNS version 1.2^{30,33}. Several of the rigid bodies deviated substantially from the electron density, and they were manually adjusted to the density with the program Coot²⁹. For the tip portion of the β' non-conserved domain (β' NCD, β' 132–454), the coordinates of the *T. thermophilus* holoenzyme (PDB 3DXJ)³⁴ were used. Several rounds of rigid body refinement and manual adjustment were performed. In each RNAP molecule, extra electron density, corresponding to Gfh1, was observed. The NTD and CTD coordinates of free Gfh1 (PDB 2F23)⁷ were separately placed in the $2F_o - F_c$ electron density map. One of the RNAP molecules in the asymmetric unit exhibited extra electron density corresponding to the DNA•RNA hybrid in the DNA•RNA hybrid binding site, for which we built the hybrid model. The coordinates of the DNA•RNA hybrid in *S. cerevisiae* EC (PDB 2VUM)¹⁹ were used as the starting model. The electron density for the nucleic acids in the other two RNAP complexes was weak, probably owing to low occupancy and/or high mobility, and therefore, we did not build their models.

The structures of the N- and C-terminal parts of the bridge helix in EC•Gfh1 are similar to those in the previous EC (2O5I)¹³, while the central part of the bridge helix in the present complex exhibits a conformational change, due to the ratcheting of the core and shelf modules. The region of β' 1086–1090 assumes a helical, but slightly curved conformation, and the model was built by adjusting the corresponding region in the previous EC (2O5I) to the electron density. Most parts of the bridge helix (β' 1070–1090 and β' 1093–1102) maintained the helical conformation. β' Ser 1091 and β' Gly 1092 were placed to link the two discontinuous helices, while fitting their main chains into the electron density. For this rebuilding, the position of β' Tyr 1093, which was identified by the electron density of its large side chain, was helpful (Fig. 3a). The coordinates of both the proteins and the nucleic acids were further refined with the program Coot. The atomic positions and the grouped B-factors were refined to 4.1 Å, by using CNS with strong NCS restraints among the three complexes in the asymmetric unit (Supplementary Table 1). Refinement was monitored by R_{free} , calculated from 3% of the reflections that were excluded from the refinement.

The structure for crystal 2 was solved by molecular replacement, using the coordinates of RNAP and Gfh1 in crystal 1 as the search model. A model of the DNA•RNA hybrid was placed in each RNAP in the electron density map, and positional refinement of the coordinates was performed to 4.3 Å with CNS. For the calculation of R_{free} , the same reflections as those chosen for crystal 1 were used.

The rigid bodies used in the structural refinement allowed us to define the mobile modules of *T. thermophilus* RNAP. We first superposed the RNAPs in the present EC•Gfh1 and the previous EC (2O5I)¹³ by certain rigid bodies, and then inspected the rigid bodies that superposed well concurrently. The masses of the co-relocated rigid bodies were defined as modules. Finally, we confirmed that the defined mobile modules relocated separately by the RigidFinder program³⁵.

Disulphide-bonding assay for the ratcheted RNAP. We constructed a plasmid that allows co-expression of the α , β , β' and ω subunits of *T. thermophilus* RNAP in *E. coli*, for the preparation of recombinant *T. thermophilus* RNAP (pRpoBCAZ, to be published elsewhere). The recombinant RNAPs (the wild type and the α Q188C- β' D685C mutant) were expressed using this system. They were purified by the procedure used for the natural RNAP core enzyme from *T. thermophilus* cells³⁶, except that the cell lysate was heat-treated at 70 °C for 30 min, in order to denature most of the non-thermophilic *E. coli* proteins. Then, the RNAPs were fractionated by polyethyleneimine precipitation, followed by ammonium sulphate precipitation. The recombinant RNAPs were further purified by chromatography on Q-Sepharose and Superdex pg200 columns (GE Healthcare Biosciences).

For the disulphide-bonding analysis, the recombinant RNAP (the wild type or the α Q188C- β' D685C mutant) was dissolved in 75 mM Tris-HCl buffer (pH 8.1), containing 50 mM KCl, 10 mM MgCl₂ and 1 mM DTT. Each of the RNAPs (0.2 μ M) was incubated with 0.7 μ M of the nucleic acid scaffold (DNATS/DNANT/RNA14) or 10 μ M of *T. thermophilus* Gfh1 for 30 min. Then, 2.5 mM glutathione disulphide (GSSG) was added to each RNAP solution for the mild oxidation of Cys residues. The mixtures were analysed by SDS-PAGE, using sample buffer lacking a reducing agent. The formation of a disulphide bond between α C188 and β' C685 was confirmed by the appearance of an extra band with low mobility, which corresponded to the crosslinked α and β' subunits (Supplementary Fig. 17). The sequences of the nucleic acids are as follows. The

RNA oligomer: RNA14, UUUUUGAGUCUGCGGCGAU. The DNA oligomers: DNATS, AACATACGGCTCGGACAGAGGTCTGTCTGAATCGATATCGC CGC; DNANT, CGATTACAGACAGGACCTCTGTCCGAGCCGTATGTT. The nucleic acid scaffold was designed by modifying the previously reported EC14 scaffold, which forms a stable elongation complex with *T. thermophilus* RNAP³⁷. **Photo-crosslinking assay of the ratcheted RNAP.** *p*-Benzoyl-L-phenylalanine (pBpa) is a photo-crosslinker that can be position-specifically incorporated into a recombinant protein^{38,39}. The gene encoding a pBpa-specific variant of *Methanococcus jannaschii* tyrosyl-tRNA synthetase³⁸, under the control of the *E. coli* *tyrS* promoter, was cloned in the pACYC184 vector, together with three copies of the *M. jannaschii* amber suppressor tRNA gene³⁹, to create a vector for the expression of the pBpa-specific tRNA synthetase and tRNA (ppbpaRS-3MJRI). Each tRNA gene had an *E. coli* *lpp* promoter and an *rrnC* terminator. The artificial operons for overproducing minor tRNA species, including the minor tRNA^{Pro}, were described previously⁴⁰, and were cloned in a kanamycin-resistant plasmid carrying the CloDF13-derived replication origin, to create pMINOR2.

The *rpoA* gene, C-terminally tagged with FLAG, was engineered, using a QuikChange mutagenesis kit (Stratagene), to have an amber codon in place of Arg 185, for producing the RNAP α -subunit with Arg 185 replaced with pBpa (pBpa 185) (ref. 41). The *rpoC* gene was engineered to have a methionine codon in place of Glu 692, for producing the β' subunit with the E692M substitution. The *rpoA* and *rpoC* genes in pRpoBCAZ were replaced by these mutant genes, and the vector was introduced into BL21 Star(DE3) cells (Invitrogen) harbouring the ppbpaRS-3MJRI and pMINOR2 plasmids. The cells were grown in LB medium containing 1 mM pBpa, and the gene expression was induced by the addition of 1 mM IPTG at the mid-log phase. After a further 4-h incubation, the cells were harvested and lysed by sonication in buffer A (40 mM Tris-HCl (pH 7.7), 500 mM NaCl, 10 mM EDTA, 10 mM 2-mercaptoethanol, 5% glycerol, and Complete protease inhibitor cocktail tablets (Roche)). The wild-type and engineered RNAP core enzymes were roughly purified by heat-treatment. For the photo-crosslinking, the proteins were exposed to light at 365 nm for 30 min on ice⁴¹ in a 24-well cell culture plate (BD Biosciences), followed by SDS-PAGE, Coomassie brilliant blue staining, and western blotting with an anti-FLAG antibody (Sigma) (Supplementary Fig. 19a, 19b). The RNAP core enzymes were further purified as described above. Then, 2 μ M RNAP (wild type or mutant) was incubated with the nucleic acid scaffold (2.5 μ M) or Gfh1 (10 μ M) for 30 min at room temperature in 50 mM HEPES-NaOH buffer (pH 7.5), containing 50 mM KCl, 10 mM MgCl₂ and 1 mM DTT, followed by the photo-crosslinking step (Supplementary Fig. 19c).

Transcription inhibition analysis. In the previous study, we constructed a plasmid for the expression of wild-type Gfh1 in *E. coli*²⁴. The expression plasmids for Gfh1 variants (L33W and M125E) were generated by introducing mutations to the plasmid encoding wild-type Gfh1. In addition, we constructed plasmids for the expression of wild type and mutant *T. thermophilus* GreA in *E. coli*. The wild-type and mutant Gre proteins were expressed as described previously²⁴, and were then purified by chromatography on Toyopearl Super-Q and Butyl columns (Tosoh Bioscience). The transcription elongation complex was reconstituted by incubating 0.1 μ M of *T. thermophilus* RNAP with 0.1 μ M of the nucleic acid scaffold (DNATS/DNANT/RNA14 or RNA15) for 30 min, where the sequence of RNA15 is UUUUUG AGUCUGCGGCGGAUA. The RNA was 5'-radiolabelled using T4 polynucleotide kinase and [γ -³²P]-ATP. The nucleotide addition reaction was performed by incubating the transcription elongation complex of RNA14 with 5 μ M Gfh1 (wild type or a mutant) at 20 °C in 50 mM MES-NaOH buffer (pH 6.5), containing 50 mM KCl, 10 mM MgCl₂, 1 mM DTT and 20 μ M ATP and that of RNA15 with 2.5 μ M Gfh1 (wild type or a mutant) at 55 °C in 50 mM MES-NaOH buffer (pH 6.5), containing 50 mM KCl, 1 mM MgCl₂, 1 mM DTT and 20 μ M UTP. The RNA was analysed by denaturing (8 M urea) PAGE.

- Kabsch, W. Automatic processing of rotation diffraction data from crystals of initially unknown symmetry and cell constants. *J. Appl. Crystallogr.* **26**, 795–800 (1993).
- McCoy, A. J. et al. Phaser crystallographic software. *J. Appl. Crystallogr.* **40**, 658–674 (2007).
- Brünger, A. T. et al. Crystallography & NMR system: A new software suite for macromolecular structure determination. *Acta Crystallogr. D* **54**, 905–921 (1998).
- Mukhopadhyay, J. et al. The RNA polymerase “switch region” is a target for inhibitors. *Cell* **135**, 295–307 (2008).
- Abyzov, A., Björnson, R., Felipe, M. & Gerstein, M. RigidFinder: a fast and sensitive method to detect rigid blocks in large macromolecular complexes. *Proteins* **78**, 309–324 (2010).
- Vassilyeva, M. N. et al. Purification, crystallization and initial crystallographic analysis of RNA polymerase holoenzyme from *Thermus thermophilus*. *Acta Crystallogr. D* **58**, 1497–1500 (2002).
- Kashkina, E. et al. Elongation complexes of *Thermus thermophilus* RNA polymerase that possess distinct translocation conformations. *Nucleic Acids Res.* **34**, 4036–4045 (2006).

38. Chin, J. W., Martin, A. B., King, D. S., Wang, L. & Schultz, P. G. Addition of a photocrosslinking amino acid to the genetic code of *Escherichia coli*. *Proc. Natl Acad. Sci. USA* **99**, 11020–11024 (2002).
39. Sakamoto, K. *et al.* Genetic encoding of 3-iodo-L-tyrosine in *Escherichia coli* for single-wavelength anomalous dispersion phasing in protein crystallography. *Structure* **17**, 335–344 (2009).
40. Chumpolkulwong, N. *et al.* Translation of 'rare' codons in a cell-free protein synthesis system from *Escherichia coli*. *J. Struct. Funct. Genomics* **7**, 31–36 (2006).
41. Hino, N. *et al.* Protein photo-cross-linking in mammalian cells by site-specific incorporation of a photoreactive amino acid. *Nature Methods* **2**, 201–206 (2005).

A substantial population of low-mass stars in luminous elliptical galaxies

Pieter G. van Dokkum¹ & Charlie Conroy^{2,3}

The stellar initial mass function (IMF) describes the mass distribution of stars at the time of their formation and is of fundamental importance for many areas of astrophysics. The IMF is reasonably well constrained in the disk of the Milky Way¹ but we have very little direct information on the form of the IMF in other galaxies and at earlier cosmic epochs. Here we report observations of the Na I doublet^{2,3} and the Wing–Ford molecular FeH band^{4,5} in the spectra of elliptical galaxies. These lines are strong in stars with masses less than $0.3M_{\odot}$ (where M_{\odot} is the mass of the Sun) and are weak or absent in all other types of stars^{5–7}. We unambiguously detect both signatures, consistent with previous studies⁸ that were based on data of lower signal-to-noise ratio. The direct detection of the light of low-mass stars implies that they are very abundant in elliptical galaxies, making up over 80% of the total number of stars and contributing more than 60% of the total stellar mass. We infer that the IMF in massive star-forming galaxies in the early Universe produced many more low-mass stars than the IMF in the Milky Way disk, and was probably slightly steeper than the Salpeter form⁹ in the mass range $0.1M_{\odot}$ to $1M_{\odot}$.

We obtained spectra of eight of the most luminous and massive galaxies in the nearby Universe: four of the brightest early-type galaxies in the Virgo cluster and four in the Coma cluster. The galaxies were selected to have velocity dispersions $\sigma > 250 \text{ km s}^{-1}$, and were observed with the Low-Resolution Imaging Spectrometer¹⁰ (LRIS) on the Keck I telescope. In 2009 the red arm of LRIS was outfitted with fully depleted charge-coupled devices (CCDs), which have excellent sensitivity out to wavelengths of $\lambda > 9,000 \text{ \AA}$ and almost no fringing. The individual spectra of the four galaxies in each of the two clusters were de-redshifted, averaged and binned to a resolution of 8 \AA .

In Fig. 1b and c we show the spectral region near the $\lambda = 8,183$, $\lambda = 8,195 \text{ Na I}$ doublet for the Virgo and Coma galaxies. The doublet appears as a single absorption feature due to Doppler broadening. In Fig. 1e and f we show the region around the $\lambda = 9,916 \text{ Wing–Ford}$ band for the Virgo galaxies. This region could not be observed with sufficient signal in Coma because it is redshifted to $1.015 \mu\text{m}$. The spectra are of very high quality. The median 1σ scatter of the four galaxies around the average spectrum is only about 0.3% per spectral bin. The median absolute difference between the Virgo and Coma spectra is 0.4% per spectral bin.

Both the Na I doublet and the Wing–Ford band are unambiguously detected. The central wavelength of the observed Na I line coincides with the weighted average wavelength of the doublet and the observed Wing–Ford band has the characteristic asymmetric profile reflecting the $A^4\Delta$ to $X^4\Delta$ transition of FeH (ref. 5). The Na I index is $0.058 \pm 0.006 \text{ mag}$ in the Virgo galaxies and $0.057 \pm 0.007 \text{ mag}$ in Coma. The Wing–Ford index in Virgo galaxies is 0.027 ± 0.005 . The uncertainties are determined from the scatter among the individual galaxies. We note that any residual systematic problems with the detector or atmosphere are incorporated in this scatter, as the features were originally redshifted to a different observed wavelength range for each of the galaxies.

The immediate implication is that stars with masses less than $0.3M_{\odot}$ are present in substantial numbers in the central regions of elliptical galaxies. Such low-mass stars are impossible to detect individually in external galaxies, because they are too faint: Barnard's star would have a K-band magnitude of 39 at the distance of the Virgo cluster. This in turn implies that there was a channel for forming low-mass stars in the progenitors of luminous early-type galaxies in clusters. These star-forming progenitors are thought to be relatively compact galaxies at $z = 2 - 5$ with star-formation rates of tens or hundreds of solar masses per year. Some studies have suggested truncated IMFs for such galaxies¹¹, with a cut-off below $1M_{\odot}$. Such dwarfless IMFs are effectively ruled out by the detection of the Na I lines and the Wing–Ford band.

We turn to stellar population synthesis models to quantify the number of low-mass stars in elliptical galaxies. As discussed in detail in the Supplementary Information, we use a flexible stellar population synthesis code¹² combined with an extensive empirical library of stellar near-infrared spectra¹³. In Fig. 1 we show synthetic spectra in both spectral regions for different choices of the IMF^{1,9,14}, including IMFs that are steeper than the Salpeter form. Away from the Na I doublet and the Wing–Ford band all models fit very well, with differences between data and the best-fitting model of less than 0.5% over the entire spectral range. Predicted Na I and Wing–Ford line indices are compared to the observed values in Fig. 2. The data prefer IMFs with substantial dwarf populations. The best fits are obtained for a logarithmic IMF slope of $x \approx -3$, a more dwarf-rich ('bottom-heavy') IMF than even the Salpeter form, which has $x = -2.35$. A Kroupa IMF (which is appropriate for the Milky Way) is inconsistent with the Wing–Ford data at $>2\sigma$ and inconsistent with the Na I data at $>4\sigma$, as are IMFs with even more suppressed dwarf populations^{14–16}. We note that the $x = -3$ IMF also provides a much better fit to the region around $0.845 \mu\text{m}$ than any of the other forms. Taking the Salpeter IMF as a limiting case, we find that stars with masses of $0.1M_{\odot}$ to $0.3M_{\odot}$ make up at least 80% of the total number of living stars in elliptical galaxies, and contribute at least 60% of the total stellar mass.

Although the formal uncertainty in the derived IMF slope is small we stress that some unknown systematic effect could be present in the stellar population synthesis modelling. In particular, weak features in the spectra of giant stars in elliptical galaxies may be incorrectly represented by the Milky Way giants that we use. It may also be that the Na abundance of low-mass stars in elliptical galaxies is different from that of low-mass stars in the Milky Way. The fact that all models fit the spectra of both the Virgo and Coma galaxies extremely well outside of the IMF-sensitive regions gives some confidence in our approach; as we show in the Supplementary Information, the quality of the fit constrains possible contamination of spectral features such as TiO lines.

Besides model uncertainties, the interpretation may be complicated by the fact that we are constraining the IMF some ten billion years after the stars were formed. It is now generally thought that elliptical galaxies have undergone several (or many) mergers with other galaxies after their initial collapse¹⁷, which may imply that the stellar population is

¹Astronomy Department, Yale University, New Haven, Connecticut, USA. ²Department of Astrophysical Sciences, Princeton University, Princeton, New Jersey, USA. ³Harvard-Smithsonian Center for Astrophysics, Cambridge, Massachusetts, USA.

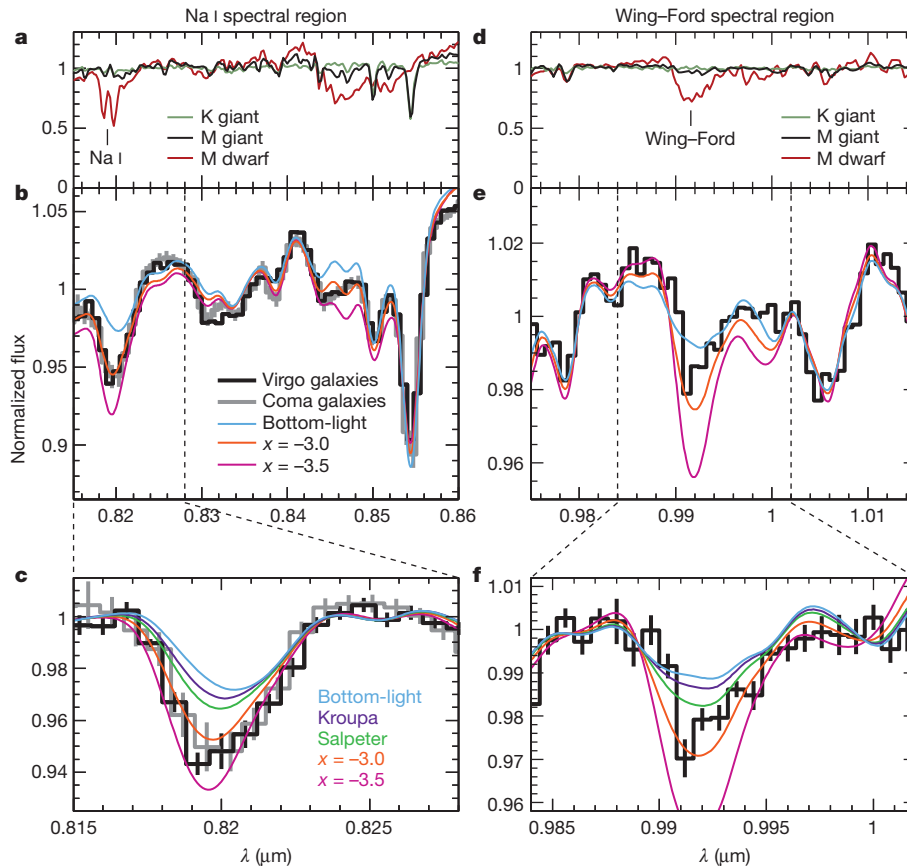


Figure 1 | Detection of the Na I doublet and the Wing-Ford band. **a**, Spectra in the vicinity of the $\lambda = 8,183$, $\lambda = 8,195$ Na I doublet for three stars from the IRTF library¹²: a K0 giant, which dominates the light of old stellar populations; an M6 dwarf, the (small) contribution of which to the integrated light is sensitive to the form of the IMF at low masses; and an M3 giant, which has potentially contaminating TiO spectral features in this wavelength range. **b**, Averaged Keck/LRIS spectra of NGC 4261, NGC 4374, NGC 4472 and NGC 4649 in the Virgo cluster (black line) and NGC 4840, NGC 4926, IC 3976 and NGC 4889 in the Coma cluster (grey line). Four exposures of 180 s were obtained for each galaxy. The one-dimensional spectra were extracted from the reduced two-dimensional data by summing the central 4'', which corresponds to about 0.4 kpc at the distance of Virgo and about 1.8 kpc at the distance of Coma. We found little or no dependence of the results on the choice of aperture.

Coloured lines show stellar population synthesis models for a dwarf-deficient 'bottom-light' IMF¹⁴, a dwarf-rich 'bottom-heavy' IMF with $x = -3$, and an even more dwarf-rich IMF. The models are for an age of 10 Gyr and were smoothed to the average velocity dispersion of the galaxies. The $x = -3$ IMF fits the spectrum remarkably well. **c**, Spectra and models around the dwarf-sensitive Na I doublet. A Kroupa IMF, which is appropriate for the Milky Way, does not produce a sufficient number of low-mass stars to explain the strength of the absorption. An IMF steeper than Salpeter appears to be needed. **d–f**, Spectra and models near the $\lambda = 9,916$ Wing-Ford band. The observed Wing-Ford band also favours an IMF that is more abundant in low-mass stars than the Salpeter IMF. All spectra and models were normalized by fitting low-order polynomials (excluding the feature of interest). The polynomials were quadratic in **a**, **b**, **d** and **e** and linear in **c** and **f**.

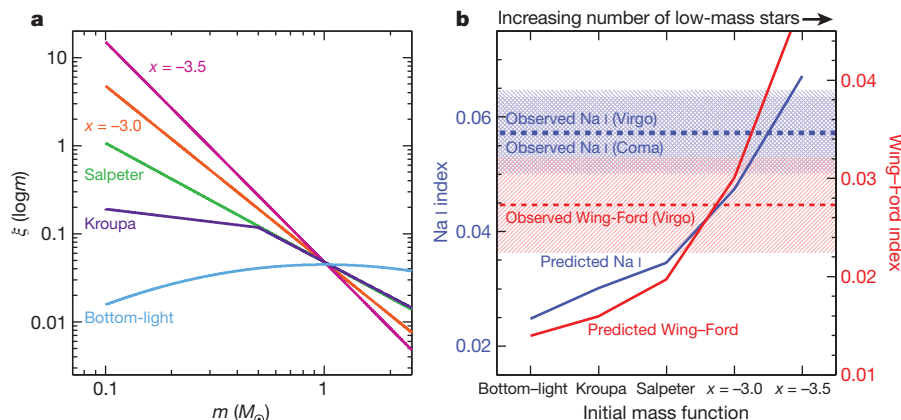


Figure 2 | Constraining the IMF. **a**, Various stellar IMFs, ranging from a 'bottom-light' IMF with strongly suppressed dwarf formation¹⁴ (light blue) to an extremely 'bottom-heavy' IMF with a slope $x = -3.5$. The IMFs are normalized at $1M_{\odot}$, because stars of approximately one solar mass dominate the light of elliptical galaxies. **b**, Comparison of predicted line Na I and Wing-Ford indices with the observed values. The indices were defined to be analogous

to those in refs 4 and 8. The Na I index has central wavelength $0.8195 \mu\text{m}$ and side bands at $0.816 \mu\text{m}$ and $0.825 \mu\text{m}$. The Wing-Ford index has central wavelength $0.992 \mu\text{m}$ and side bands at $0.985 \mu\text{m}$ and $0.998 \mu\text{m}$. The central bands and side bands are all 20 \AA wide. Both observed line indices are much stronger than expected for a Kroupa IMF. The best fits are obtained for IMFs that are slightly steeper than Salpeter.

more complex than our single-age, single-metallicity model. On the other hand, these accretion events probably mostly add stars at large radii¹⁸ and may not have affected the core regions very much. It will be interesting to search for gradients in dwarf-sensitive features with more extensive data¹⁹.

Our results are consistent with previous studies of the near-infrared spectra of elliptical galaxies^{8,20,21}. They are also consistent with recent dynamical and lensing constraints on the IMF in elliptical galaxies with large velocity dispersions²² and directly identify the stars that are responsible for their high masses: the dynamical data cannot distinguish dwarf-rich IMFs from dwarf-deficient IMFs because the latter have a large amount of mass in stellar remnants¹⁴. A steep IMF for elliptical galaxies is also qualitatively consistent with the apparently higher number of low-mass stars in the Milky Way bulge than in the disk²³. Our best-fitting IMF does not appear to be consistent with the observed colour and M/L evolution of massive cluster galaxies¹⁴, which suggest an IMF with a slope $x \approx -1$ around $1M_{\odot}$. Interpreting the evolution of the colours and luminosities of elliptical galaxies relies on the assumption that these galaxies evolve in a self-similar way, which may not be valid^{18,24}. It could also be that the form of the IMF is more complex than a power law.

Our results also seem inconsistent with theoretical arguments for dwarf-deficient IMFs at high redshift, which have centred on the idea that the characteristic mass of stars scales with the Jeans mass in molecular clouds^{25,26}. The Jeans mass has a strong temperature dependence and it has been argued that relatively high ambient temperatures in high-redshift star-forming galaxies may have set a lower boundary to the characteristic mass in the progenitors of elliptical galaxies^{14,25}. However, the Jeans mass also scales with density, and the gas densities in the star-forming progenitors of the cores of elliptical galaxies were almost certainly significantly higher than typical densities of star-forming regions in the Milky Way. Numerical simulations suggest that the formation of low-mass stars becomes inevitable if sufficiently high densities are reached on sub-parsec scales²⁷. Furthermore, recent semi-analytic models of the thermal evolution of gas clouds have emphasized the effects of dust-induced cooling²⁸, which is relatively insensitive to the ambient temperature and particularly effective at high densities. Timescale arguments suggest that the physical conditions expected in starburst galaxies at high redshift might even enhance low-mass star formation, rather than suppress it²⁹.

Taken at face value, our results imply that the form of the IMF is not universal but depends on the prevailing physical conditions: Kroupa-like in quiet, star-forming disks and dwarf-rich in the progenitors of massive elliptical galaxies. This informs models of star formation and has important implications for the interpretation of observations of galaxies in the early Universe. The stellar masses and star-formation rates of distant galaxies are usually estimated from their luminosities, assuming some form of the IMF³⁰. Our results suggest that a different form should be used for different galaxies, greatly complicating the analysis. The bottom-heavy IMF advocated here may also require a relatively low fraction of dark matter within the central regions of nearby massive galaxies²².

Received 7 July; accepted 12 October 2010.

Published online 1 December 2010.

1. Kroupa, P. On the variation of the initial mass function. *Mon. Not. R. Astron. Soc.* **322**, 231–246 (2001).
2. Faber, S. M. & French, H. B. Possible M dwarf enrichment in the semistellar nucleus of M31. *Astrophys. J.* **235**, 405–412 (1980).
3. Schiavon, R. P., Barbuy, B., Rossi, S. C. F. & Milone, A. The near-infrared Na I doublet feature in M stars. *Astrophys. J.* **479**, 902–908 (1997).
4. Wing, R. F. & Ford, W. K. The infrared spectrum of the cool dwarf Wolf 359. *Publ. Astron. Soc. Pacif.* **81**, 527–529 (1969).
5. Schiavon, R. P., Barbuy, B. & Singh, P. D. The FeH Wing-Ford band in spectra of M stars. *Astrophys. J.* **484**, 499–510 (1997).

6. Schiavon, R. P., Barbuy, B. & Bruzual, A. G. Near-infrared spectral features in single-aged stellar populations. *Astrophys. J.* **532**, 453–460 (2000).
7. Cushing, M. C., Rayner, J. T., Davis, S. P. & Vacca, W. D. FeH absorption in the near-infrared spectra of late M and L dwarfs. *Astrophys. J.* **582**, 1066–1072 (2003).
8. Couture, J. & Hardy, E. The low-mass stellar content of galaxies—constraints through hybrid population synthesis near 1 micron. *Astrophys. J.* **406**, 142–157 (1993).
9. Salpeter, E. E. The luminosity function and stellar evolution. *Astrophys. J.* **121**, 161–167 (1955).
10. Oke, J. B. *et al.* The Keck low-resolution imaging spectrometer. *Publ. Astron. Soc. Pacif.* **107**, 375–385 (1995).
11. Baugh, C. M. *et al.* Can the faint submillimetre galaxies be explained in the Λ cold dark matter model? *Mon. Not. R. Astron. Soc.* **356**, 1191–1200 (2005).
12. Conroy, C., Gunn, J. E. & White, M. The propagation of uncertainties in stellar population synthesis modeling. I. The relevance of uncertain aspects of stellar evolution and the initial mass function to the derived physical properties of galaxies. *Astrophys. J.* **699**, 486–506 (2009).
13. Rayner, J. T., Cushing, M. C. & Vacca, W. D. The Infrared Telescope Facility (IRTF) spectral library: cool stars. *Astrophys. J., Suppl.* **623**, 289–432 (2009).
14. van Dokkum, P. G. Evidence of cosmic evolution of the stellar initial mass function. *Astrophys. J.* **674**, 29–50 (2008).
15. Fardal, M. A., Katz, N., Weinberg, D. H. & Davé, R. On the evolutionary history of stars and their fossil mass and light. *Mon. Not. R. Astron. Soc.* **379**, 985–1002 (2007).
16. Davé, R. The galaxy stellar mass-star formation rate relation: evidence for an evolving stellar initial mass function? *Mon. Not. R. Astron. Soc.* **385**, 147–160 (2008).
17. Naab, T., Johansson, P. H., Ostriker, J. P. & Efsthathiou, G. Formation of early-type galaxies from cosmological initial conditions. *Astrophys. J.* **658**, 710–720 (2007).
18. van Dokkum, P. G. *et al.* The growth of massive galaxies since $z = 2$. *Astrophys. J.* **709**, 1018–1041 (2010).
19. Boroson, T. A. & Thompson, I. B. Color distributions in early type galaxies. III – Radial gradients in spectral features. *Astron. J.* **101**, 111–126 (1991).
20. Cenarro, A. J., Gorgas, J., Vazdekis, A., Cardiel, N. & Peletier, R. F. Near-infrared line-strengths in elliptical galaxies: evidence for initial mass function variations? *Mon. Not. R. Astron. Soc.* **339**, L12–L16 (2003).
21. Carter, D., Visvanathan, N. & Pickles, A. J. The dwarf star content of elliptical and lenticular galaxies. *Astrophys. J.* **311**, 637–650 (1986).
22. Treu, T. *et al.* The initial mass function of early-type galaxies. *Astrophys. J.* **709**, 1195–1202 (2010).
23. Calchi Novati, S. & de Luca, F. Jetzer, Ph. Mancini, L. & Scarpetta, G. Microlensing constraints on the Galactic bulge initial mass function. *Astron. Astrophys.* **480**, 723–733 (2008).
24. van der Wel, A. *et al.* Recent structural evolution of early-type galaxies: size growth from $z = 1$ to $z = 0$. *Astrophys. J.* **688**, 48–58 (2008).
25. Larson, R. B. Thermal physics, cloud geometry and the stellar initial mass function. *Mon. Not. R. Astron. Soc.* **359**, 211–222 (2005).
26. Bate, M. R. & Bonnell, I. A. The origin of the initial mass function and its dependence on the mean Jeans mass in molecular clouds. *Mon. Not. R. Astron. Soc.* **356**, 1201–1221 (2005).
27. Bonnell, I. A., Clark, P. & Bate, M. R. Gravitational fragmentation and the formation of brown dwarfs in stellar clusters. *Mon. Not. R. Astron. Soc.* **389**, 1556–1562 (2008).
28. Schneider, R. & Omukai, K. Metals, dust and the cosmic microwave background: fragmentation of high-redshift star-forming clouds. *Mon. Not. R. Astron. Soc.* **402**, 429–435 (2010).
29. Banerji, S., Viti, S., Williams, D. A. & Rawlings, J. M. C. Timescales for low-mass star formation in extragalactic environments: implications for the stellar initial mass function. *Astrophys. J.* **692**, 283–289 (2009).
30. Labbé, I. *et al.* Star formation rates and stellar masses of $z = 7$ –8 galaxies from IRAC observations of the WFC3/IR Early Release Science and the HUDF fields. *Astrophys. J.* **716**, L103–L108 (2010).

Supplementary Information is linked to the online version of the paper at www.nature.com/nature.

Acknowledgements We thank R. Bezanson, J. Brinchmann, R. Larson and R. Zinn for discussions. We thank R. Schiavon for comments that improved the manuscript. This study is based on observations obtained at the W. M. Keck Observatory. We recognize and acknowledge the very significant cultural role and reverence that the summit of Mauna Kea has always had within the indigenous Hawaiian community and consider ourselves fortunate to have the opportunity to conduct observations from this mountain.

Author Contributions P.G.v.D. obtained and analysed the data and contributed to the analysis and interpretation. C.C. constructed the stellar population synthesis models and contributed to the analysis and interpretation.

Author Information Reprints and permissions information is available at www.nature.com/reprints. The authors declare no competing financial interests. Readers are welcome to comment on the online version of this article at www.nature.com/nature. Correspondence and requests for materials should be addressed to P.G.v.D. (pieter.vandokkum@yale.edu).

Integrative genomics identifies *LMO1* as a neuroblastoma oncogene

Kai Wang^{1†}, Sharon J. Diskin^{2*}, Haitao Zhang^{1*}, Edward F. Attiyeh², Cynthia Winter², Cuiping Hou¹, Robert W. Schnepf², Maura Diamond², Kristopher Bosse², Patrick A. Mayes², Joseph Glessner¹, Cecilia Kim¹, Edward Frackelton¹, Maria Garriss², Qun Wang², Wendy Glaberson¹, Rosetta Chiavacci¹, Le Nguyen^{2,3,5}, Jayanti Jagannathan², Norihisa Saeki⁴, Hiroki Sasaki⁴, Struan F. A. Grant^{1,5,6}, Achille Iolascon^{7,11}, Yael P. Mosse^{2,5}, Kristina A. Cole^{2,5}, Hongzhe Li³, Marcella Devoto^{3,5,6,8}, Patrick W. McGrady⁹, Wendy B. London¹⁰, Mario Capasso^{7,11}, Nazneen Rahman¹², Hakon Hakonarson^{1,5,6} & John M. Maris^{2,5}

Neuroblastoma is a childhood cancer of the sympathetic nervous system that accounts for approximately 10% of all paediatric oncology deaths^{1,2}. To identify genetic risk factors for neuroblastoma, we performed a genome-wide association study (GWAS) on 2,251 patients and 6,097 control subjects of European ancestry from four case series. Here we report a significant association within LIM domain only 1 (*LMO1*) at 11p15.4 (rs110419, combined $P = 5.2 \times 10^{-16}$, odds ratio of risk allele = 1.34 (95% confidence interval 1.25–1.44)). The signal was enriched in the subset of patients with the most aggressive form of the disease. *LMO1* encodes a cysteine-rich transcriptional regulator, and its paralogues (*LMO2*, *LMO3* and *LMO4*) have each been previously implicated in cancer. In parallel, we analysed genome-wide DNA copy number alterations in 701 primary tumours. We found that the *LMO1* locus was aberrant in 12.4% through a duplication event, and that this event was associated with more advanced disease ($P < 0.0001$) and survival ($P = 0.041$). The germline single nucleotide polymorphism (SNP) risk alleles and somatic copy number gains were associated with increased *LMO1* expression in neuroblastoma cell lines and primary tumours, consistent with a gain-of-function role in tumorigenesis. Short hairpin RNA (shRNA)-mediated depletion of *LMO1* inhibited growth of neuroblastoma cells with high *LMO1* expression, whereas forced expression of *LMO1* in neuroblastoma cells with low *LMO1* expression enhanced proliferation. These data show that common polymorphisms at the *LMO1* locus are strongly associated with susceptibility to developing neuroblastoma, but also may influence the likelihood of further somatic alterations at this locus, leading to malignant progression.

Multiple somatically acquired chromosomal rearrangements, such as focal amplification of the *MYCN* oncogene or deletions at chromosome arms 1p or 11q, are each associated with an aggressive neuroblastoma phenotype². Although these somatically acquired genomic alterations are of clinical use as prognostic biomarkers, until recently little was known about the constitutional genetic events that initiate tumorigenesis. Highly penetrant gain-of-function mutations in the anaplastic lymphoma kinase (*ALK*) tyrosine kinase domain were recently identified as the major cause of familial neuroblastoma, and somatic mutations in this gene implicate it as a target for therapeutic intervention^{3–6}. In addition, a neuroblastoma GWAS identified common SNPs at 6p22 as being associated with susceptibility to aggressive neuroblastoma in sporadic cases⁷; follow-up association analysis on the clinically relevant group of patients with an aggressive tumour

phenotype indicated that common SNPs within *BARD1* also function as susceptibility variants⁸. Finally, our GWAS has also identified a common copy number variation at 1q21.1 being highly associated with neuroblastoma and probably playing a role in early tumorigenesis through disruption of a novel neuroblastoma breakpoint family gene (*NBPF23*)⁹. Taken together, it has become clear that the embryonal cancer neuroblastoma is genetically heterogeneous, and initiation of sporadically occurring disease requires multiple interacting genetic factors, including both sequence and copy number variants.

To identify additional genetic risk factors, we expanded our previous GWAS and analysed 1,627 neuroblastoma patients accrued through the North American-based Children's Oncology Group with 3,254 genetically matched control subjects of European ancestry (see Supplementary Methods). All subjects were genotyped using the Illumina HumanHap550 BeadChip with over 550,000 SNP markers; the genomic control inflation factor was 1.08 (Supplementary Fig. 1). Clusters of SNPs from three genomic loci reached genome-wide significance ($P < 5 \times 10^{-8}$; Fig. 1a), including two SNPs within *FLJ22536/FLJ44180* at the 6p22 locus (P values range from 2.46×10^{-14} to 3.25×10^{-13} ; Supplementary Table 1), nine SNPs within or nearby *BARD1* at the 2q35 locus (P values range from 3.05×10^{-13} to 9.69×10^{-9} ; Supplementary Table 2), each previously reported, and two SNPs within *LMO1* (LIM domain only 1), a newly identified neuroblastoma susceptibility locus at 11p15.4 (P values range from 5.12×10^{-10} to 2.83×10^{-8} ; Table 1 and Fig. 1b). Closer examination of the *LMO1* locus identified a total of four SNPs that show strong association signals ($P < 1 \times 10^{-4}$) with neuroblastoma (Table 1), which are in a moderate degree of linkage disequilibrium (Supplementary Fig. 2). We then examined each of the most significant SNPs from the 2q35, 6p22, 11p15.4 susceptibility loci and the 1q21.1 copy number variation. However, we did not find evidence for epistasis (Supplementary Tables 3 and 4), indicating that these susceptibility loci increase disease risk independently.

To replicate our findings, we examined the association results from an independent case series of 190 patients from the Children's Oncology Group and 1,507 control subjects, all of whom were genotyped on the Human610-Quad arrays. All four *LMO1* SNPs identified in the discovery effort showed the same direction of association in this replication cohort, with P values ranging from 1.01×10^{-5} to 0.058. To seek additional evidence of replication, we performed quantitative PCR-based genotyping of these four SNPs in a third independent case series

¹The Center for Applied Genomics, Children's Hospital of Philadelphia, Philadelphia, Pennsylvania 19104, USA. ²Division of Oncology and Center for Childhood Cancer Research, Children's Hospital of Philadelphia, Philadelphia, Pennsylvania 19104, USA. ³Department of Biostatistics and Epidemiology, University of Pennsylvania School of Medicine, Philadelphia, Pennsylvania, 19104, USA. ⁴Genetics Division, National Cancer Center Research Institute, Tokyo 104-0045, Japan. ⁵Department of Pediatrics, University of Pennsylvania School of Medicine, Philadelphia, Pennsylvania, 19104, USA. ⁶Division of Human Genetics, Children's Hospital of Philadelphia, Philadelphia, Pennsylvania, 19104, USA. ⁷CEINGE Biotechnologie Avanzate, Naples 80145, Italy. ⁸Department of Experimental Medicine, University La Sapienza, Rome 00185, Italy. ⁹Department of Statistics, University of Florida and Children's Oncology Group, Gainesville, Florida, 32603 USA. ¹⁰Dana-Farber Children's Hospital Cancer Center and Children's Oncology Group, Boston, Massachusetts, 02115, USA. ¹¹Department of Biochemistry and Medical Biotechnology, University of Naples Federico II, Naples 80131 Italy. ¹²Section of Cancer Genetics, Institute of Cancer Research, Sutton, Surrey SM2 5NG, UK. †Present address: Zilkha Neurogenetic Institute, Department of Psychiatry and Preventive Medicine, University of Southern California, Los Angeles, California 90089, USA.

*These authors contributed equally to this work.

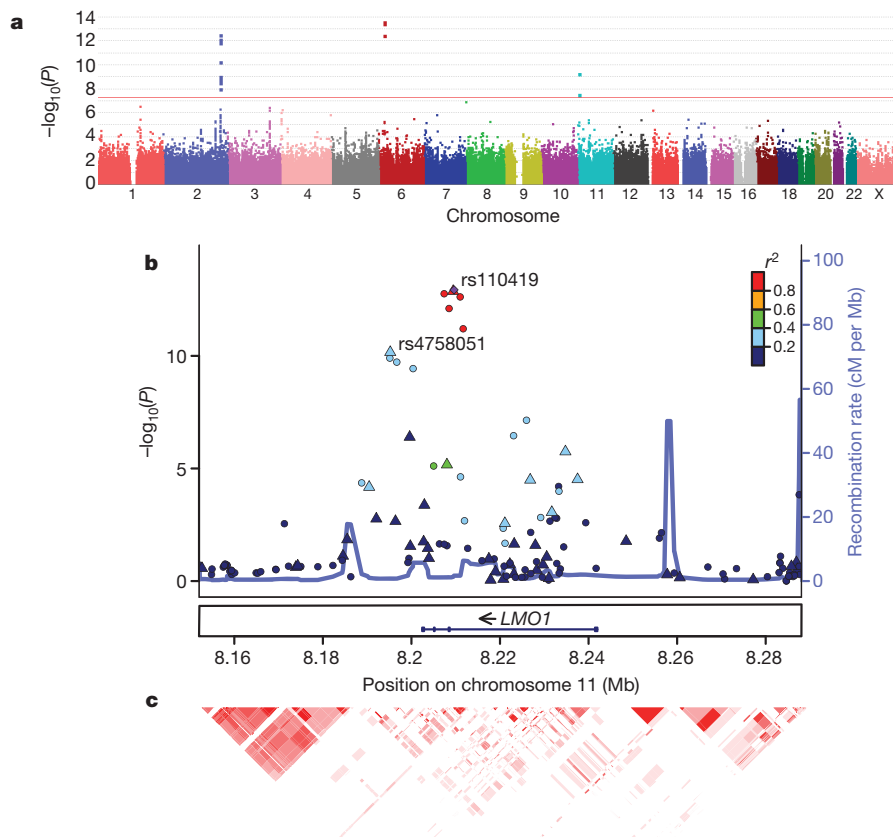


Figure 1 | Discovery of *LMO1* at 11p15.4 as a neuroblastoma susceptibility locus. **a**, Manhattan plot of GWAS results from the discovery cases series, with the red horizontal line representing genome-wide significance threshold ($P < 5 \times 10^{-8}$). **b**, Genomic position (National Center for Biotechnology Information build 36) of genotyped (triangles) and imputed (circles) SNPs. The

from UK, as well as the two most significant SNPs in a fourth independent case series from Italy. Combined analysis by the Cochran–Mantel–Haenszel method demonstrated that two of the four SNPs had P values that extend well beyond the genome-wide significance threshold (Table 1). Additionally, using the two cohorts with whole-genome genotype data (discovery cohort and US replication cohort), we performed genotype imputation at 11p15.4 and identified six additional genome-wide significant markers, the most significant being rs110420 ($P = 1.17 \times 10^{-13}$), which is in complete linkage disequilibrium ($r^2 = 1$ in HapMap CEU subjects (Utah residents with

P values are calculated by combining discovery and replication case series with whole-genome genotypes, and SNPs are coloured based on their correlations with rs110419 (purple diamond). Estimated recombination rates from the HapMap data are overlaid. **c**, Degree of linkage disequilibrium between SNPs (as r^2 values) is represented by red colour intensity in the corresponding cells.

ancestry from northern and western Europe) with the genotyped marker rs110419 (Fig. 1c and Supplementary Table 5).

We next determined if the *LMO1* genotypes were associated with a particular clinical phenotype and/or patient survival. Similar to the association pattern observed for the 6p22 and 2q35 (*BARD1*) loci^{7,8}, the risk alleles of *LMO1* were significantly associated with metastatic disease ($P = 0.0040$), advanced age (greater than 1 year, $P < 0.0001$) and a high-risk status by Children’s Oncology Group criteria for treatment stratification² ($P = 0.0010$; Supplementary Tables 6 and 7). Consistent with this observation, the rs110419 risk allele was associated

Table 1 | Significantly associated SNPs at the *LMO1* locus on 11p15.4

SNP†	Risk/non-risk allele	Discovery (HumanHap550)*			US replication (Human610)*			UK replication (TaqMan)*		
		Frequency of cases	Frequency of controls	<i>P</i> ‡	Frequency of cases	Frequency of controls	<i>P</i> ‡	Frequency of cases	Frequency of controls	<i>P</i> ‡
		(<i>n</i> = 1,627)	(<i>n</i> = 3,254)		(<i>n</i> = 190)	(<i>n</i> = 1,507)		(<i>n</i> = 253)	(<i>n</i> = 845)	
rs4758051	G/A	0.51	0.45	2.8×10^{-8}	0.55	0.45	2.1×10^{-4}	0.51	0.45	0.039
rs10840002	A/G	0.42	0.37	6.0×10^{-6}	0.44	0.38	0.019	0.37	0.36	0.61
rs110419	A/G	0.55	0.49	5.1×10^{-10}	0.61	0.49	1.0×10^{-5}	0.53	0.48	0.057
rs204938	C/T	0.49	0.44	1.2×10^{-5}	0.50	0.45	0.058	0.50	0.44	0.032
SNP†	Risk/non-risk allele	Italian replication (TaqMan)*			Combined					
		Frequency of cases	Frequency of controls	<i>P</i> ‡	CMH§ <i>P</i>	CMH OR				
		(<i>n</i> = 181)	(<i>n</i> = 491)			(95% confidence interval)¶				
rs4758051	G/A	0.45	0.42		0.45	1.4×10^{-11}	1.28 (1.19–1.37)			
rs10840002	A/G	—	—		—	8.5×10^{-7}	1.21 (1.12–1.30)			
rs110419	A/G	0.49	0.41		0.004	5.2×10^{-16}	1.34 (1.25–1.44)			
rs204938	C/T	—	—		—	1.7×10^{-7}	1.22 (1.13–1.31)			

*No deviations from Hardy–Weinberg equilibrium were observed ($P > 0.001$) in all cohorts.

†SNP: r^2 in controls between rs110419 and each of rs4758051, rs10840002 and rs204938 was 0.30, 0.17 and 0.29, respectively.

‡ P values were calculated by allelic test.

§CMH, Cochran–Mantel–Haenszel test.

¶OR, odds ratio of risk allele.

with decreased event-free survival ($P = 0.0085$; Supplementary Table 8 and Supplementary Fig. 3) and overall survival ($P = 0.0217$; Supplementary Fig. 4). Taken together, these data suggest that common germline variants at *LMO1* are associated not only with predisposition to develop neuroblastoma, but also with a predilection to develop the more aggressive form of the disease. They emphasize that *LMO1* genetic variations are associated with a particular neuroblastoma phenotype; however, this does not indicate that these variants have prognostic significance for an individual with neuroblastoma.

The *LMO1* gene encodes a cysteine-rich transcriptional regulator with two LIM zinc-binding domains that is mainly expressed in the nervous system¹⁰. *LMO1* belongs to a protein superfamily encoded by four genes, including *LMO1*, *LMO2*, *LMO3* and *LMO4*. Multiple lines of evidence, including chromosomal translocation events and mouse models, strongly implicate this gene family in the aetiology of human cancer^{11–14}. Most provocatively, retroviral insertion of the corrective gene for X-linked severe combined immunodeficiency into the *LMO2* locus resulted in T-cell leukaemias in several participants in gene therapy trials¹⁵. *LMO4* represses the transcription of *BRCA1*, and dysregulation of *LMO4* expression has been implicated in the breast carcinogenesis^{16,17}. Finally, *LMO3* has been shown to act as an oncogene in neuroblastoma through the neuronal transcription factor *HEN2*¹⁸. We therefore postulated that the common variants at the 11p15.4 locus discovered here may increase disease risk through a *cis*-acting effect on the regulation of expression or function of *LMO1*, but we cannot exclude the potential for *trans*-acting influences on loci distant from the discovered common variants.

We next examined tumour DNA genotyped on the Illumina SNP arrays for 701 neuroblastomas using a detection algorithm for copy number designed for tumour samples¹⁹. We detected relative segmental gain (copy number changes at a given locus relative to whole-genome copy number changes) at *LMO1* in 87 out of 701 tumours (12.4%); this was particularly enriched in the high-risk group where the GWAS signal was most robust (Supplementary Fig. 5a). Most tumours with 11p gain showed a duplication of the entire chromosome p arm, but four tumours (approximately 5%) showed focal gain restricted to 11p15 including the *LMO1* locus (Supplementary Fig. 5b). These data demonstrate that *LMO1* is one of many genes showing somatic copy number gain on 11p, and here we used the GWAS data to prioritize it as a potential target of this somatically acquired chromosomal rearrangement.

We next examined whether somatic *LMO1* alterations were associated with neuroblastoma clinical phenotype and survival of patients (Supplementary Table 9). Gain of *LMO1* was significantly more common in tumours from patients with metastatic disease ($P < 0.0001$), advanced age (greater than 1 year, $P < 0.0001$), unfavourable pathological grade ($P = 0.0013$) and Children's Oncology Group high-risk classification ($P < 0.0001$). Gain of 11p was rarely observed in the *MYCN* amplified cases (Supplementary Table 9). Despite the strong association of 11p gain in cases without *MYCN* amplification, a known powerful adverse prognostic factor¹, *LMO1* gain was associated with decreased overall survival of patients ($P = 0.041$) (Supplementary Table 10 and Supplementary Figs 6 and 7).

To investigate how the neuroblastoma-associated *LMO1* alleles may contribute to tumour initiation and/or clinical phenotype, we next genotyped a set of human neuroblastoma-derived cell lines with Illumina SNP arrays, and measured messenger RNA (mRNA) and protein expression levels on the subset of lines without copy number changes at 11p to avoid the influence of somatic DNA alterations on gene expression. Cell lines with diploid 11p status and harbouring homozygous risk alleles showed significantly higher *LMO1* mRNA and protein expression than those with homozygous non-risk alleles (Fig. 2a and Supplementary Table 11). This trend held in an expanded set of 25 neuroblastoma cell lines with variable 11p status (Supplementary Fig. 8). To determine if this correlation existed in diagnostic tumour tissues, we next examined mRNA expression levels on a whole-genome Affymetrix expression microarray²⁰ in a subset of 61

neuroblastoma primary tumours from patients whose blood samples and primary tumours had both been genotyped on the Illumina SNP arrays. Among these 61 tumours, 13 harboured somatic gain of 11p. Considering both somatic and germline genotypes in the same linear regression model, we detected an association between *LMO1* copy number gains and increased *LMO1* expression ($P = 0.02$; Fig. 2b and Supplementary Table 12), as well as an association between rs110419 risk alleles and increased *LMO1* expression ($P = 0.022$; Fig. 2b). To refine the genotype-expression relationships further, we subsequently used quantitative PCR to measure *LMO1* expression in an additional set of 23 tumours without *LMO1* gain. We confirmed that the rs110419 risk allele is associated with *LMO1* expression ($P = 0.01$), independent of copy number changes (Fig. 2c). To determine whether a regulatory variant exists at a narrow promoter region of *LMO1*, we performed Sanger sequencing in 20 neuroblastoma cell lines but did not detect any potential causal variant (Supplementary Table 13). Examination of the 1000 Genomes Project data identified over 300 SNPs within or surrounding *LMO1* that are in moderate to strong linkage disequilibrium ($D' > 0.5$) with rs110419 (Supplementary Table 14); however, fine mapping of this region through resequencing will be required to identify whether any are causal *cis*-regulatory variants. Subsequent experimentation will be required to determine if causal DNA variations directly impact *LMO1* expression, and if somatic copy-number gain indeed is targeting *LMO1* for further increased expression in tumour cells.

As our germline and somatic genomic analyses implicated *LMO1* as a neuroblastoma oncogene, we next sought to determine the functional

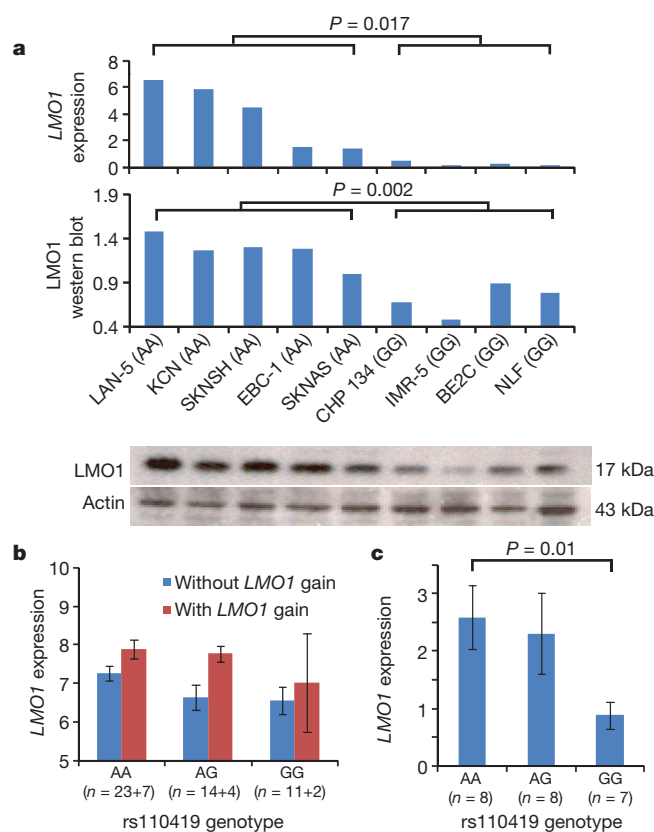


Figure 2 | *LMO1* germline genotypes and somatic copy number gains are associated with mRNA and protein expression. **a**, *LMO1* mRNA and protein expression in nine human neuroblastoma-derived cell lines are highly correlated with rs110419 genotype. **b**, Microarray-based expression profiling on 61 primary tumours confirms that *LMO1* gene expression is associated with both *LMO1* gain ($P = 0.02$, *t*-test) and risk genotypes ($P = 0.022$, linear regression). **c**, Quantitative PCR-based expression profiling of an independent set of primary neuroblastomas without *LMO1* gain confirms the same association. Error bars, s.e.m.

consequences of *LMO1* depletion or overexpression in a genotype- and expression-specific manner. First, after lentiviral-based shRNA infection of neuroblastoma cell lines, we were able to recover stable clones with 45–63% depletion of *LMO1* mRNA and protein (Fig. 3e). Cells with the homozygous neuroblastoma-associated genotype and high *LMO1* expression showed significantly decreased proliferation compared with mock-infected controls (Fig. 3a, b), whereas cells with homozygous non-risk alleles showed little phenotypic effect (Fig. 3c, d). Finally, to determine the cellular phenotypes of forced overexpression of *LMO1*, we stably overexpressed *LMO1* with approximately fourfold higher levels in the SK-N-BE2C cell line with low *de novo* *LMO1* expression, and detected significantly enhanced proliferation (Fig. 3f). Therefore it appears that inhibition of *LMO1* in cells expressing high levels of *LMO1* or activation of *LMO1* in cells with low levels of *LMO1* leads to pronounced phenotypes. Taken together, these data suggest that *LMO1* may function as an oncogene in a subset of human neuroblastomas.

In conclusion, here we have identified germline sequence variants at the *LMO1* locus that are robustly associated with neuroblastoma. We have applied an integrative genomics approach to demonstrate that common genetic polymorphisms associated with cancer predisposition may also mark regions of the genome prone to somatic alterations influencing tumour progression. Our data suggest that GWAS studies can identify previously undiscovered oncogenic drivers of a malignant

phenotype, especially when they occur in a region of the genome involved in large segmental rearrangements impacting hundreds of genes. In paediatric cancers such as neuroblastoma, the real translational potential of GWAS efforts may be in discovering therapeutic targets and predictive biomarkers of tumour aggressiveness.

METHODS SUMMARY

All genome-wide SNP genotyping for the discovery cohorts was performed using the Illumina HumanHap550 BeadChip at the Center for Applied Genomics at the Children's Hospital of Philadelphia. Multi-dimensional scaling was performed using PLINK version 1.06 on a subset of SNPs not in linkage disequilibrium to identify subjects of European ancestry, and all control subjects were genetically matched to patients. The first replication case series was genotyped by Illumina Human610 BeadChip, yet two additional replication case series were genotyped by TaqMan. Genotype imputation was performed by MACH (<http://www.sph.umich.edu/csg/abecasis/MACH/>) on discovery and replication case series with whole-genome genotypes. Alteration calls in tumour copy number were generated from data of SNP signal intensity by the OverUnder¹⁹. Survival analyses used the methods of Kaplan and Meier, with standard errors following the methods of Peto *et al.*²¹. For gene expression profiling by Affymetrix U95Av2 microarrays, the expression measures for each probe set was extracted and normalized using robust multi-array average protocols from raw CEL files. Association tests on genotype and expression were performed on log-transformed expression values by linear regression or *t*-test. For quantitative PCR on *LMO1*, TaqMan probes were purchased from Applied Biosystems with assay identity Hs00231133_m1. Relative expression of the target gene was determined by normalization to *HPRT1* using a standard curve method with ten serial dilutions according to the manufacturer's instructions. All quantitative PCR reactions were performed in triplicate with an ABI PrismTM 7900HT Sequence Detection System (Applied Biosystems). For the *LMO1* knockdown experiments, the lentiviral particles for shRNA knockdown were purchased from Santa Cruz, including copGFP Control Lentiviral Particles (catalogue number sc-108084) and *LMO1* shRNA(h) Lentiviral Particles (catalogue number sc-38025-v). Pooled clones of SK-N-BE2C cells with *LMO1* overexpression were created through stable transfection of full-length *LMO1* complementary DNA in pCDNA3.1 as previously described²².

Received 17 August 2009; accepted 22 October 2010.

Published online 1 December 2010.

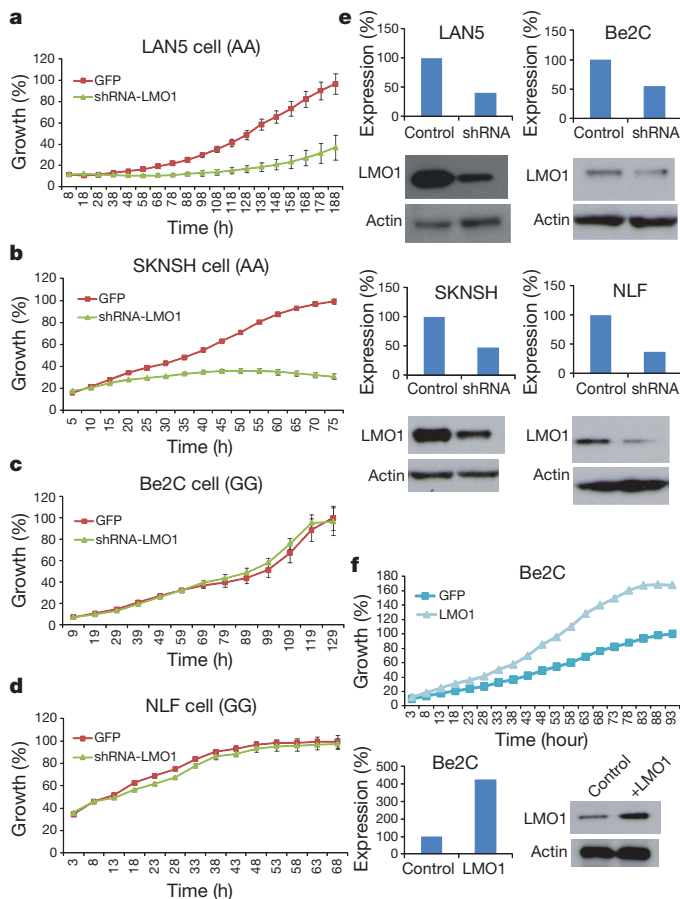


Figure 3 | Genetic manipulation of *LMO1* expression in neuroblastoma cell line models influences proliferative phenotype in an expression-specific manner. a–d, In cells with neuroblastoma risk alleles and higher *LMO1* expression levels, *LMO1* knockdown leads to inhibition of cellular proliferation. e, *LMO1* knockdown as measured by quantitative reverse-transcription PCR and western blot for experiments a–d. f, In SK-N-BE2C cells with non-risk alleles and low *LMO1* expression levels, forced overexpression of *LMO1* leads to enhanced cellular proliferation. Approximate fourfold overexpression of *LMO1* RNA and protein are shown. Error bars, s.e.m.

- Maris, J. M. Recent advances in neuroblastoma. *N. Engl. J. Med.* **362**, 2202–2211 (2010).
- Maris, J. M., Hogarty, M. D., Bagatell, R. & Cohn, S. L. Neuroblastoma. *Lancet* **369**, 2106–2120 (2007).
- Mosse, Y. P. *et al.* Identification of ALK as a major familial neuroblastoma predisposition gene. *Nature* **455**, 930–935 (2008).
- Janoueix-Lerosey, I. *et al.* Somatic and germline activating mutations of the ALK kinase receptor in neuroblastoma. *Nature* **455**, 967–970 (2008).
- Chen, Y. *et al.* Oncogenic mutations of ALK kinase in neuroblastoma. *Nature* **455**, 971–974 (2008).
- George, R. E. *et al.* Activating mutations in ALK provide a therapeutic target in neuroblastoma. *Nature* **455**, 975–978 (2008).
- Maris, J. M. *et al.* Chromosome 6p22 locus associated with clinically aggressive neuroblastoma. *N. Engl. J. Med.* **358**, 2585–2593 (2008).
- Capasso, M. *et al.* Common variations in *BARD1* influence susceptibility to high-risk neuroblastoma. *Nature Genet.* **41**, 718–723 (2009).
- Diskin, S. J. *et al.* Copy number variation at 1q21.1 associated with neuroblastoma. *Nature* **459**, 987–991 (2009).
- Su, A. I. *et al.* A gene atlas of the mouse and human protein-encoding transcriptomes. *Proc. Natl Acad. Sci. USA* **101**, 6062–6067 (2004).
- Rabbitts, T. H. *LMO* T-cell translocation oncogenes typify genes activated by chromosomal translocations that alter transcription and developmental processes. *Genes Dev.* **12**, 2651–2657 (1998).
- Rabbitts, T. H. *et al.* The effect of chromosomal translocations in acute leukemias: the *LMO2* paradigm in transcription and development. *Cancer Res.* **59**, 1794s–1798s (1999).
- Fisch, P. *et al.* T-cell acute lymphoblastic lymphoma induced in transgenic mice by the *RBTN1* and *RBTN2* LIM-domain genes. *Oncogene* **7**, 2389–2397 (1992).
- Neale, G. A., Rehg, J. E. & Goorha, R. M. Disruption of T-cell differentiation precedes T-cell tumor formation in *LMO-2* (rhombotin-2) transgenic mice. *Leukemia* **11** (suppl. 3), 289–290 (1997).
- Hacein-Bey-Abina, S. *et al.* *LMO2*-associated clonal T cell proliferation in two patients after gene therapy for SCID-X1. *Science* **302**, 415–419 (2003).
- Sum, E. Y. *et al.* The LIM domain protein *LMO4* interacts with the cofactor CtlP and the tumor suppressor *BRCA1* and inhibits *BRCA1* activity. *J. Biol. Chem.* **277**, 7849–7856 (2002).
- Visvader, J. E. *et al.* The LIM domain gene *LMO4* inhibits differentiation of mammary epithelial cells *in vitro* and is overexpressed in breast cancer. *Proc. Natl Acad. Sci. USA* **98**, 14452–14457 (2001).

18. Aoyama, M. *et al.* LMO3 interacts with neuronal transcription factor, HEN2, and acts as an oncogene in neuroblastoma. *Cancer Res.* **65**, 4587–4597 (2005).
19. Attiyeh, E. F. *et al.* Genomic copy number determination in cancer cells from single nucleotide polymorphism microarrays based on quantitative genotyping corrected for aneuploidy. *Genome Res.* **19**, 276–283 (2009).
20. Wang, Q. *et al.* Integrative genomics identifies distinct molecular classes of neuroblastoma and shows that multiple genes are targeted by regional alterations in DNA copy number. *Cancer Res.* **66**, 6050–6062 (2006).
21. Peto, R. *et al.* Design and analysis of randomized clinical trials requiring prolonged observation of each patient. II. analysis and examples. *Br. J. Cancer* **35**, 1–39 (1977).
22. Saeki, N. *et al.* GASDERMIN, suppressed frequently in gastric cancer, is a target of LMO1 in TGF-beta-dependent apoptotic signalling. *Oncogene* **26**, 6488–6498 (2007).

Supplementary Information is linked to the online version of the paper at www.nature.com/nature.

Acknowledgements We acknowledge the Children's Oncology Group for providing most blood and tumour specimens and clinical and outcome data (U10-CA98543 and U10-CA98413) from neuroblastoma patients. We thank G. P. Tonini for providing neuroblastoma DNA samples in the Italian replication cohort. This work was supported in part by National Institutes of Health grant R01-CA124709 (to J.M.M.), the Giulio D'Angio Endowed Chair (J.M.M.), the Alex's Lemonade Stand Foundation (J.M.M.), the Evan Dunbar Foundation (J.M.M.), the Rally Foundation (J.M.M.), Andrew's Army Foundation (J.M.M.), the Abramson Family Cancer Research Institute (J.M.M.), a Howard Hughes Medical Institute Research Training Fellowship (K.B.), a fellowship

from Associazione Oncologia Pediatrica e Neuroblastoma (M.C.), a Research Development Award from the Cotswold Foundation (H.H.), UL1-RR024134-03 (H.H.) and an Institutional Development Award to the Center for Applied Genomics from the Children's Hospital of Philadelphia (H.H.).

Author Contributions H.H. and J.M.M. conceived the study, guided interpretation of results and helped preparation of the manuscript. K.W., H.Z. and C.H. performed SNP association analysis. K.W., S.J.D., E.F.A. and J.J. performed gene expression and copy number analysis. C.W. and K.B. performed PCR validation of gene expression data. C.W., R.W.S., K.B., P.A.M., S.J.D. and K.A.C. performed and/or analysed shRNA transfection and *LMO1* overexpression experiments. N.S. and H.S. generated viral construct for human *LMO1* complementary DNA. M.C. and A.I. performed the replication study on the Italian case series, and N.R. performed the replication study on the UK case series. P.W.M. and W.B.L. performed outcome and clinical covariate analyses on the Children's Oncology Group samples. C.H., C.K., E.F., M.G., W.G. and R.C. generated the genotyping data. L.N. and M.D. helped with data analysis. S.F.A.G., Y.P.M., H.L. and M.D. advised on data interpretation. K.W. drafted the manuscript; H.H., J.M.M. and other authors edited it.

Author Information Microarray data are deposited in the GEO database under accession number GSE3960. The genotypic and phenotypic information from this study is deposited in dbGaP (www.ncbi.nlm.gov/gap) under accession number phs000124.v2.p1. Reprints and permissions information is available at www.nature.com/reprints. The authors declare no competing financial interests. Readers are welcome to comment on the online version of this article at www.nature.com/nature. Correspondence and requests for materials should be addressed to H.H. (hakonarson@chop.edu) or J.M.M. (maris@chop.edu).

A role for mitochondria in NLRP3 inflammasome activation

Rongbin Zhou¹, Amir S. Yazdi¹, Philippe Menu¹ & Jürg Tschopp¹

An inflammatory response initiated by the NLRP3 inflammasome is triggered by a variety of situations of host ‘danger’, including infection and metabolic dysregulation^{1,2}. Previous studies suggested that NLRP3 inflammasome activity is negatively regulated by autophagy and positively regulated by reactive oxygen species (ROS) derived from an uncharacterized organelle. Here we show that mitophagy/autophagy blockade leads to the accumulation of damaged, ROS-generating mitochondria, and this in turn activates the NLRP3 inflammasome. Resting NLRP3 localizes to endoplasmic reticulum structures, whereas on inflammasome activation both NLRP3 and its adaptor ASC redistribute to the perinuclear space where they co-localize with endoplasmic reticulum and mitochondria organelle clusters. Notably, both ROS generation and inflammasome activation are suppressed when mitochondrial activity is dysregulated by inhibition of the voltage-dependent anion channel. This indicates that NLRP3 inflammasome senses mitochondrial dysfunction and may explain the frequent association of mitochondrial damage with inflammatory diseases.

The NLRP3 inflammasome is a molecular platform activated upon signs of cellular ‘danger’ to trigger innate immune defences through the maturation of pro-inflammatory cytokines such as interleukin (IL)-1 β ¹. Strong associations of a number of human heritable and acquired diseases with dysregulated inflammasome activity highlight the importance of the NLRP inflammasome in regulating immune responses³. Key components of a functional NLRP3 inflammasome are NLRP3, the adaptor protein ASC and caspase-1 (ref. 1). Upon detecting cellular stress, NLRP3 recruits ASC and procaspase-1, which results in caspase-1 activation and processing of cytoplasmic targets, including the pro-inflammatory cytokines IL-1 β and IL-18.

A wide variety of danger signals activate the NLRP3 inflammasome. These include pathogen-associated molecular patterns⁴ and host-derived molecules that are indicative of cellular damage (danger-associated molecular patterns) such as uric-acid crystals¹. The mechanisms by which these structurally distinct molecules trigger NLRP3 inflammasome activation are currently unclear. One of the models proposes that NLRP3 is activated by a common pathway of ROS⁵. The source of ROS is currently unclear, but we previously suggested the involvement of one or several of the seven known NADPH oxidases⁵. However, macrophages deficient in subunits specific to three of the seven NADPH oxidases, that is, NOX1, NOX2 and NOX4, respond normally to inflammasome activators (C. Dostert and J.T., unpublished observations) or have even slightly increased activity⁶, which suggests a possible role of other NADPH oxidase members or functional redundancy. Alternatively, further ROS required for inflammasome activation could be generated by other cellular sources.

The main source of cellular ROS is mitochondria. Various stress conditions, including increased metabolic rates, hypoxia, or membrane damage all markedly induce mitochondrial ROS production⁷. To investigate a possible implication of mitochondria in inflammasome activation, we artificially induced ROS production in mitochondria by blocking key enzymes of the respiratory chain. Complex I is one of the main sites at which electrons can leak to oxygen and result in superoxide

production⁷. In agreement with previous reports⁸, addition of the complex I inhibitor rotenone resulted in the loss of mitochondrial membrane potential and robust ROS production (Fig. 1a, b). This was determined using three types of mitochondria-specific labels that distinguish respiring (Mitotracker deep red), total (Mitotracker green) and ROS-generating mitochondria (MitoSOX) (Fig. 1a, b). ROS-generating mitochondria were also observed when complex III was inhibited by antimycin A, whereas the complex II inhibitor thenoyltrifluoroacetone (TTFA) had only a minor effect (Fig. 1a, b).

A correlation between mitochondrial ROS activity and the presence of active IL-1 β in the supernatant of the human THP1 macrophage cell line was observed. Whereas rotenone- or antimycin-treated cells showed increased IL-1 β secretion in a dose-dependent manner, no or little cytokine was detectable if cells were treated with TTFA (Fig. 1c). In THP1 cells with knocked-down NLRP3 or caspase-1, or in bone-marrow-derived macrophages (BMDMs) from *Nlrp3*^{-/-} mice, the respiratory chain inhibitors did not induce IL-1 β or caspase-1 secretion (Fig. 1d and Supplementary Fig. 1a). In contrast, macrophages lacking the IPAF/NLRC4 inflammasome responded in a similar way to wild-type cells, indicating that activation of caspase-1 and processing and secretion of IL-1 β by inhibitors of the respiratory chain were mediated by the NLRP3 inflammasome but not the IPAF inflammasome. As previously observed for MSU, activation of the NLRP3 inflammasome by rotenone and antimycin was blocked by the ROS inhibitor APDC (Supplementary Fig. 1b). Although inhibition of complex I and III activity leads to robust ROS production, damage of the mitochondria and decrease of membrane potential appeared to be partial and did not result in cell death (Supplementary Fig. 2). Consistent with this, complete breakdown of the mitochondrial membrane potential induced by high doses of the respiratory chain uncoupler CCCP did cause only little ROS production and IL-1 β release. Nonetheless, CCCP used at a lower concentration that only partially impairs the membrane potential also spontaneously led to NLRP3 inflammasome activation (Supplementary Fig. 2). These data are compatible with the notion that ROS generated by mitochondria having reduced membrane potential can lead to NLRP3 inflammasome activation.

To avoid cellular damage, ROS-generating mitochondria are constantly removed by mitophagy, a specialized process of autophagy⁹. In agreement with this established mechanism of mitochondrial disposal, autophagy-associated LC3 puncta were found to accumulate around mitochondria after the addition of rotenone (Fig. 2a). We therefore speculated that inhibition of mitophagy/autophagy should lead to the accumulation of ROS-producing damaged mitochondria, and as a consequence, to the activation of the inflammasome. To this end, the mitophagy/autophagy inhibitor 3-methyladenine (3-MA) was added to THP1 macrophages, which, as expected, resulted in the accumulation of damaged mitochondria and increased concentrations of mitochondrial ROS (Fig. 2b and Supplementary Fig. 3a). Similar to mitochondrial respiratory chain inhibition, 3-MA-induced ROS generation was paralleled by the dose-dependent secretion of IL-1 β within 6 h of mitophagy/autophagy inhibition (Supplementary Fig. 3b), which was blocked by the antioxidant APDC (Supplementary Fig. 3c). Processing

¹Department of Biochemistry, Center of Immunity and Infection, University of Lausanne, Chemin des Boveresses 155, CH-1066 Epalinges, Switzerland.

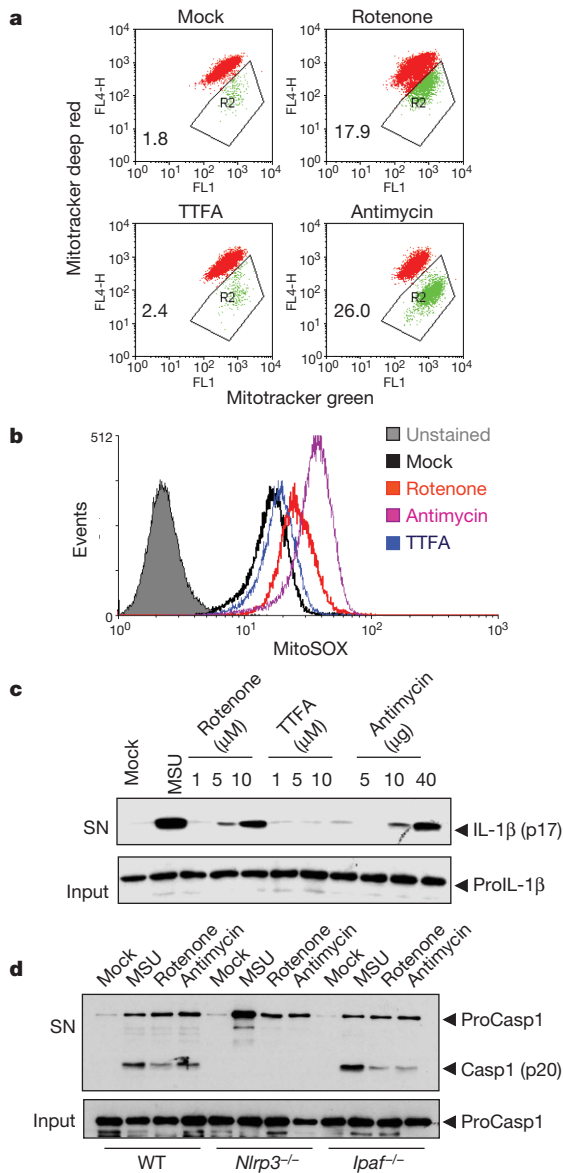


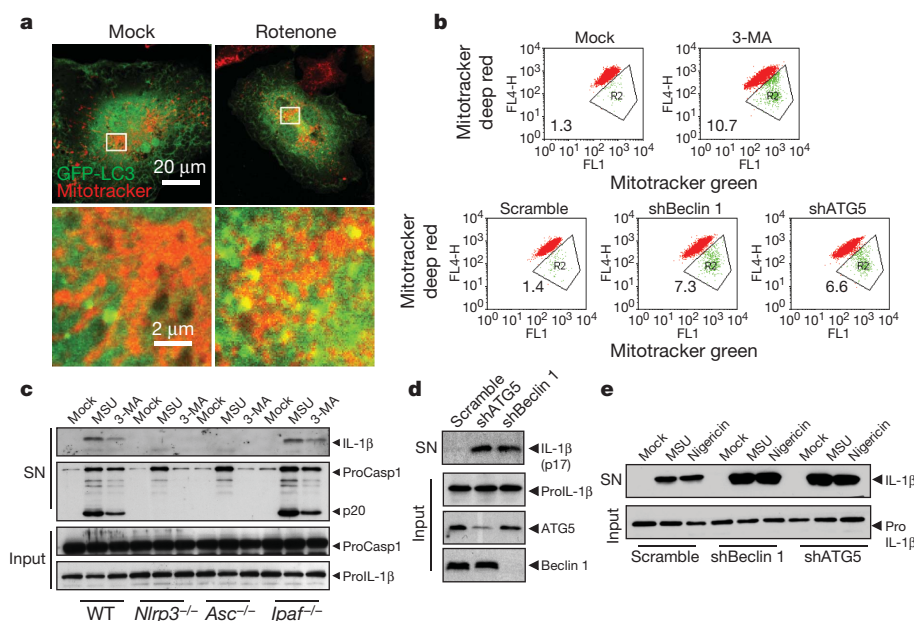
Figure 1 | Mitochondrial ROS can trigger NLRP3 inflammasome activation. **a, b**, THP1 cells were stimulated with rotenone (10 μM), TTFA (10 μM) or antimycin (40 μg ml⁻¹) for 6 h and then stained with Mitotracker green and Mitotracker deep red (**a**) or MitoSOX (**b**) for 30 min and analysed by flow cytometry. **c**, THP1 cells were stimulated for 6 h with the indicated amounts of rotenone, TTFA or antimycin. Supernatants (SN) and cell extracts (input) were analysed by western blotting as indicated. **d**, LPS-primed bone-marrow-derived macrophages (BMDMs) from wild-type (WT), *Nlrp3* or *Irf1* deficient mice were stimulated for 6 h with MSU (150 μg ml⁻¹), rotenone (10 μM for THP1 cells and 40 μM for BMDMs) or antimycin (40 μg ml⁻¹ for THP1 cells and 10 μg ml⁻¹ for BMDMs). The release of caspase-1 (western blot) was then determined. Data shown are representative of three independent experiments.

of proIL-1β caused by the blockade of mitophagy/autophagy was NLRP3- and ASC-dependent and not reliant on the IPAF inflammasome (Fig. 2d).

Because most pharmacological drugs have off-target effects, we next inhibited mitophagy/autophagy specifically through downregulation of two proteins that have crucial functions in mitophagy/autophagy, that is, beclin 1, a Bcl-2- and PI3KIII-interacting protein, and ATG5, a protein essential for autophagosome formation¹⁰. In contrast to the pharmacological inhibitors, spontaneous inflammasome activation was less efficient, as cells with knocked down beclin 1 and ATG5 had to be cultured for 24 h before we could detect active IL-1β in the culture supernatant (Fig. 2e, f). Inhibition of mitophagy/autophagy through downregulation of beclin 1 or ATG5 also sensitized macrophages for the release of IL-1β induced by MSU or nigericin (Fig. 2f). This augmented response was not associated with increased cell death (Supplementary Fig. 3d). It is therefore feasible that a functional mitophagy/autophagy system acts as a scavenger of mitochondrial ROS through removal of damaged mitochondria and thereby suppresses NLRP3 inflammasome activation.

ROS are short-lived and can act as a signalling messenger only for a short distance¹¹. Thus, NLRP3 should ideally be localized in close vicinity to mitochondria, allowing efficient sensing of the presence of damaged ROS-generating mitochondria. Of the 22 NLR members, only one, NOD5 (also called NLRX1), has a predicted mitochondrial import sequence and thus resides in the mitochondria^{12,13}. Using confocal microscopy, the localization of NLRP3 in THP1 macrophages was examined. Under non-stimulatory conditions, most NLRP3 protein was found to localize to cytoplasmic granular structures (Fig. 3). Further analysis showed a significant overlap of NLRP3 with the

Figure 2 | Inhibition of autophagy/mitophagy results in ROS generation and inflammasome activation. **a**, BMDMs expressing GFP-LC3 were stimulated with rotenone (40 μM) for 3 h and the co-localization of mitochondria and GFP-LC3 dots were analysed using confocal microscopy. **b**, THP1 cells stimulated with 3-methyladenine (3-MA, 10 mM) for 24 h or THP1 cells stably expressing shRNA against beclin 1 or ATG5 were stained with Mitotracker green and Mitotracker deep red for 30 min, and analysed by flow cytometry. **c**, LPS-primed BMDMs from wild-type, *Nlrp3*^{-/-}, *Asc*^{-/-} or *Irf1*^{-/-} knockout mice were stimulated with MSU (150 μg ml⁻¹) or 3-MA (10 mM) for 6 h and the release of active caspase-1 and IL-1β was determined. **d**, THP1 cells stably expressing shRNA against beclin 1 or ATG5 were incubated for 24 h and media supernatants (SN) and inputs were analysed by western blotting. **e**, THP1 cells stably expressing shRNA against beclin 1 or ATG5 were stimulated with MSU or nigericin for 6 h. Data shown are representative of three independent experiments.



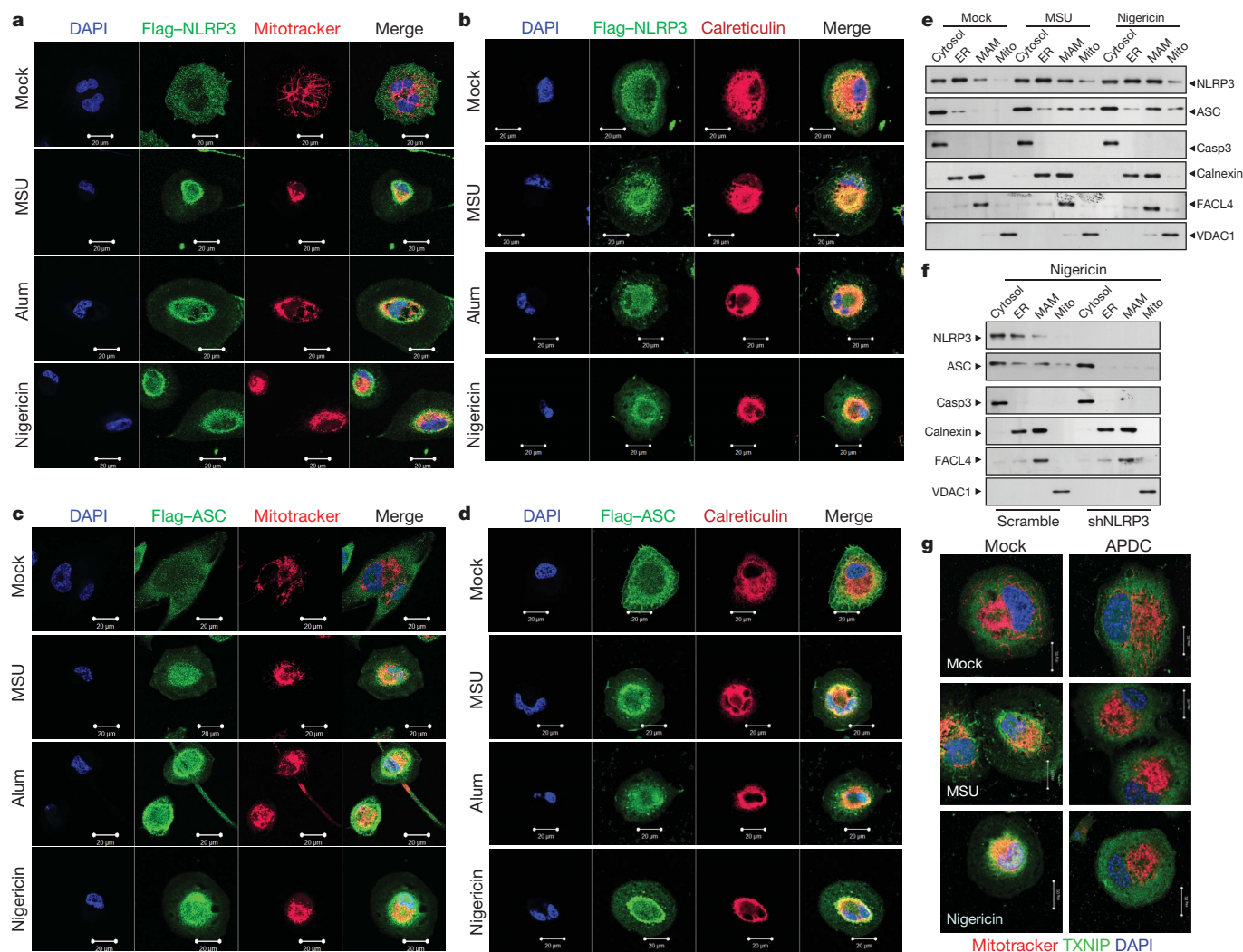


Figure 3 | Co-localization of the NLRP3 inflammasome components and endoplasmic reticulum-mitochondria. **a–d**, THP1 cells expressing Flag-NLRP3 (**a**, **b**) or Flag-ASC (**c**, **d**) were analysed for the co-localization of Flag-NLRP3 with the endoplasmic reticulum (ER) marker calreticulin or mitochondria (Mitotracker) using confocal microscopy. **e**, THP1 cells were stimulated with MSU or nigericin and then fractionated. The cytosolic, ER, MAM and mitochondrial fractions were analysed by western blotting as

indicated in the text. **f**, THP1 cells stably expressing shRNA against NLRP3 were stimulated with nigericin and subcellular fractions analysed as in **e**. **g**, TXNIP associates with mitochondria after NLRP3 inflammasome activation in a ROS-dependent manner. THP1 cells were stimulated with MSU and nigericin, and TXNIP localization was investigated in the presence or absence of the antioxidant APDC. Data shown are representative of two or three independent experiments. Scale bars: **a–g**, 20 μ m.

endoplasmic reticulum (ER) marker calreticulin, whereas no or very little co-localization was detected with Mitotracker, the Golgi marker Giantin or the lysosome/phagosome staining dye lysotracker (Fig. 3a, b and Supplementary Fig. 4). Primarily ER and not mitochondrial staining of NLRP3 was also detected when cells were analysed by electron microscopy (Supplementary Fig. 5). This localization changed significantly after inflammasome stimulation with MSU, alum or nigericin. NLRP3 relocated into the perinuclear space and co-localized with structures that stained positively for both the ER and mitochondria (Fig. 3a, b and Supplementary Fig. 6). A similar perinuclear, ER/mitochondria localization was detected for ASC after NLRP3 activation, although in contrast to NLRP3 most ASC was observed in the cytoplasm in resting cells (Fig. 3c, d and Supplementary Figs 4 and 6).

To confirm the NLRP3 association with the ER/mitochondria observed by microscopy, subcellular fractionation studies were performed. With this approach, NLRP3 was detected in both ER and cytoplasmic fractions in a roughly similar amount (Fig. 3e). ER membranes can tightly associate with mitochondria forming mitochondria-associated ER membranes (MAMs). MAMs are important, among other functions, in transferring lipids and Ca^{2+} from the ER to the mitochondria¹⁴. Addition of MSU and, in particular, nigericin induced

NLRP3 to associate partly with MAMs (Fig. 3e). In contrast to NLRP3, the majority of the ASC was found in the cytoplasmic fraction before inflammasome activation, and only a very minor portion of ASC was associated with the ER fraction. On stimulation with MSU or nigericin, however, the amount of ASC found in the mitochondrial fraction and particularly in the MAMs fraction increased considerably. ASC translocation to the MAMs and mitochondria was NLRP3 dependent, as no or little translocation was found in nigericin-activated THP1 cells in which NLRP3 was downregulated by short hairpin (sh)RNA (Fig. 3f).

We have previously reported that TXNIP, a protein implicated in type 2 diabetes, associated with NLRP3 in a ROS-dependent manner after its detachment from thioredoxin¹⁵. We therefore anticipated that TXNIP translocates to MAMs/mitochondria on NLRP3 inflammasome activation. Consistent with this idea, MSU and nigericin induced TXNIP to redistribute to mitochondria in a ROS-dependent manner (Fig. 3g), in agreement with a recently published report¹⁶.

Although the above results indicated that the prolonged presence of damaged and ROS-producing mitochondria might be implicated in inflammasome activation, the evidence was still indirect. We therefore sought to obtain more direct proof by inhibiting the activity of voltage-dependent anion channels (VDAC), which are the most abundant

proteins of the outer mitochondrial membrane and the major channels for the exchange of metabolites and ions between the mitochondria and other cellular compartments including the ER¹⁷. As such, the three VDAC isoforms are important regulators of mitochondrial metabolic activity, which is ultimately required for ROS production. We down-regulated expression of each of the three human VDAC isoforms by shRNA (Supplementary Fig. 7a) and measured inflammasome activation by MSU, R837, silica, alum and nigericin (Fig. 4a). In cells with knocked-down VDAC1, caspase-1 activation and IL-1 β secretion were considerably impaired for all inflammasome activators examined. As a consequence of VDAC1 knockdown, mitochondrial ROS was highly diminished (Supplementary Fig. 8). In contrast to the NLRP3 inflammasome, VDAC1 was not essential for the activation of the IPAF or the AIM2 inflammasome (Supplementary Fig. 7b). A significant reduction of IL-1 β secretion was also seen in cells where VDAC2 was knocked down (Fig. 4b). In all cases, impairment was seen with two distinct shRNA constructs (Supplementary Fig. 7). In contrast to VDAC1 and VDAC2, downregulation of VDAC3 had no effect on NLRP3 inflammasome activity (Supplementary Fig. 7c). The absence of VDAC1 also inhibited MSU- or nigericin-induced NLRP3 translocation to perinuclear areas (Fig. 4c).

VDAC activity is regulated by hexokinase and Bcl-2 family members¹⁷. Overexpression of Bcl-2 leads to partial VDAC closure and a concomitant decrease of mitochondrial Ca^{2+} levels and ROS production. We therefore examined whether increased Bcl-2 levels would have an impact on NLRP3 inflammasome activity and found that in supernatants of MSU-, alum- or nigericin-stimulated macrophages isolated from Bcl-2-overexpressing transgenic mice, IL-1 β levels were decreased when compared to cells from wild-type mice (Supplementary Fig. 9a). In contrast, no influence of Bcl-2 was detectable on *Salmonella*-mediated IPAF-inflammasome activity (Supplementary Fig. 9a) or LPS-mediated tumour-necrosis factor (TNF) secretion (Supplementary Fig. 9b).

It is now widely recognized that, apart from bioenergetic ATP production, mitochondria also have a crucial role in cell signalling events such as apoptotic cell death. Apoptotic signal transmission to the mitochondria results in the efflux of a number of potential apoptotic regulators such as cytochrome *c* to the cytosol that trigger caspase activation and lead to cell death. Our results now provide evidence for an unanticipated additional role of mitochondria, namely the orchestration of the inflammatory response.

Mitochondria are the major source of cellular ROS and it is therefore not completely unexpected that we found mitochondrial ROS capable

of NLRP3 inflammasome activation. This notion is based on the following observations: (1) inhibition of complex I or III of the mitochondrial respiratory chain, known to result in ROS generation, causes unprompted NLRP3 inflammasome activation; (2) inhibition of mitophagy/autophagy, resulting in the prolonged presence of damaged, ROS-generating mitochondria, leads to spontaneous inflammasome activation; (3) NLRP3 and ASC co-localize with mitochondria and MAMs in the presence of NLRP3 inflammasome activators; (4) knock down by shRNA or inhibition by Bcl-2 of VDAC ion channels that are crucial in mitochondrial activity and ROS generation significantly impair NLRP3 inflammasome activation. The dependence on VDAC is specific for the NLRP3 inflammasome and is not seen with the AIM2 or IPAF inflammasomes, indicating that the signalling pathways leading to their activation are distinct.

VDAC is essential for the uptake of Ca^{2+} into the mitochondria from MAMs to promote mitochondrial metabolic activity¹⁷. Upon NLRP3 inflammasome activation, a substantial portion of the inflammasome is associated to MAMs, indicating that NLRP3 checks and modulates mitochondrial activity.

There is a large amount of literature proposing a link between mitochondrial malfunction, ROS and chronic inflammatory diseases. Damage to mitochondria is now understood to have a role in the pathogenesis of a wide range of seemingly unrelated disorders¹⁸. For example, mutations in PINK1, PARKIN and DJ-1 are frequent causes of recessive Parkinson's disease. Both PINK1 and PARKIN are crucial in the removal of damaged mitochondria by mitophagy, whereas DJ-1 is localized to mitochondria and has a role in oxidative stress protection. Mutations in proteins involved in mitophagy/autophagy, such as ATG16 and IRGM, are also frequently found in Crohn's disease¹⁹. In line with this, increased IL-1 β production is observed in mice deficient in the autophagy gene *ATG16* (ref. 20). It is, however, unlikely that inhibition of mitophagy is generally used as a means to activate the NLRP3 inflammasome signalling pathway. In our opinion, a more direct mechanism, that is, an excessive induction of mitochondrial oxidative phosphorylation, is more likely.

Taken together, our data unravel unexpected mechanistic parallels between signalling pathways leading to apoptosis and inflammation. In both instances, signals converge at the level of mitochondria where VDAC activity seems to have a role for the activation of two seemingly unrelated downstream processes. VDAC is not only crucial for inflammasome activation, as shown here, but also has a role in apoptosis induction by Bax²¹. The mechanism that determines whether mitochondria

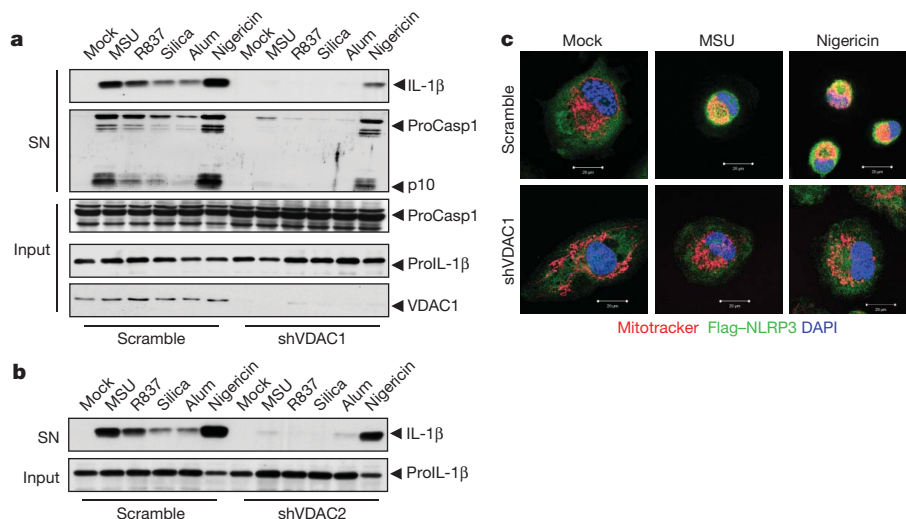


Figure 4 | VDAC is essential for NLRP3 inflammasome activation. **a**, THP1 cells stably expressing shVDAC1 were stimulated with various NLRP3 inflammasome activators and then analysed for caspase-1 activation and IL-1 β secretion. **b**, THP1 cells expressing shRNA against VDAC2 were stimulated

with MSU, R837, silica, alum or nigericin and analysed for IL-1 β secretion. **c**, THP1 cells expressing shRNA against VDAC1 were stimulated with MSU and nigericin, and NLRP3 localization was analysed by confocal microscopy. Scale bars: 20 μm .

induce inflammasome or apoptosome assembly is currently unclear. Whereas ROS is essential for the activation of both the inflammasome and apoptosome²², apoptosome formation requires in addition cytochrome *c* release from mitochondria into the cytosol. There is no evidence for cytochrome *c* being implicated in inflammasome activation, yet it cannot be ruled out that recognition of a different protein released from partially damaged mitochondria is required. The decision to induce inflammation or apoptosis must be tightly controlled to avoid pathological conditions associated with a chronic inflammatory response. Regrettably, this control mechanism seems to be easily deranged, as shown by the many diseases that are associated with mutations in genes that affect mitochondrial function.

METHODS SUMMARY

Mice. *Nlrp3*^{-/-}, *Asc*^{-/-}, *Ipa1*^{-/-} and H2K-Bcl-2 transgenic mice were described previously^{23–25}. All mice were on a C57BL/6 background except for experiments used for NLRP1b inflammasome activation (BALB/c).

Cell fractionation. MAMs, mitochondria and microsomes were isolated from PMA-differentiated THP1 cells as previously described²⁶.

Full Methods and any associated references are available in the online version of the paper at www.nature.com/nature.

Received 25 June; accepted 11 November 2010.

Published online 1 December 2010.

- Schroder, K. & Tschopp, J. The inflammasomes. *Cell* **140**, 821–832 (2010).
- Latz, E. The inflammasomes: mechanisms of activation and function. *Curr. Opin. Immunol.* **22**, 28–33 (2010).
- Kastner, D. L., Aksentijevich, I. & Goldbach-Mansky, R. Autoinflammatory disease reloaded: a clinical perspective. *Cell* **140**, 784–790 (2010).
- Franchi, L., Munoz-Planillo, R., Reimer, T., Eigenbrod, T. & Nunez, G. Inflammasomes as microbial sensors. *Eur. J. Immunol.* **40**, 611–615 (2010).
- Dostert, C. *et al.* Innate immune activation through Nalp3 inflammasome sensing of asbestos and silica. *Science* **320**, 674–677 (2008).
- Latz, E. NOX-free inflammasome activation. *Blood* **116**, 1393–1394 (2010).
- Brookes, P. S., Yoon, Y., Robotham, J. L., Anders, M. W. & Sheu, S.-S. Calcium, ATP, and ROS: a mitochondrial love-hate triangle. *Am. J. Physiol. Cell Physiol.* **287**, C817–C833 (2004).
- Li, N. *et al.* Mitochondrial complex I inhibitor rotenone induces apoptosis through enhancing mitochondrial reactive oxygen species production. *J. Biol. Chem.* **278**, 8516–8525 (2003).
- Goldman, S. J., Taylor, R., Zhang, Y. & Jin, S. Autophagy and the degradation of mitochondria. *Mitochondrion* **10**, 309–315 (2010).
- Levine, B. & Kroemer, G. Autophagy in the pathogenesis of disease. *Cell* **132**, 27–42 (2008).
- Veal, E. A., Day, A. M. & Morgan, B. A. Hydrogen peroxide sensing and signaling. *Mol. Cell* **26**, 1–14 (2007).
- Moore, C. B. *et al.* NLRX1 is a regulator of mitochondrial antiviral immunity. *Nature* **451**, 573–577 (2008).
- Tattoli, I. *et al.* NLRX1 is a mitochondrial NOD-like receptor that amplifies NF- κ B and JNK pathways by inducing reactive oxygen species production. *EMBO Rep.* **9**, 293–300 (2008).
- Hayashi, T., Rizzuto, R., Hajnoczky, G. & Su, T. P. MAM: more than just a housekeeper. *Trends Cell Biol.* **19**, 81–88 (2009).
- Zhou, R., Tardivel, A., Thorens, B., Choi, I. & Tschopp, J. Thioredoxin-interacting protein links oxidative stress to inflammasome activation. *Nature Immunol.* **11**, 136–140 (2010).
- Saxena, G., Chen, J. & Shalev, A. Intracellular shuttling and mitochondrial function of thioredoxin-interacting protein. *J. Biol. Chem.* **285**, 3997–4005 (2010).
- Colombini, M. VDAC: the channel at the interface between mitochondria and the cytosol. *Mol. Cell. Biochem.* **256**, 107–115 (2004).
- Oliveira, J. M. Nature and cause of mitochondrial dysfunction in Huntington's disease: focusing on Huntingtin and the striatum. *J. Neurochem.* **114**, 1–12 (2010).
- Restivo, N. L., Srivastava, M. D., Schafer, I. A. & Hoppel, C. L. Mitochondrial dysfunction in a patient with crohn disease: possible role in pathogenesis. *J. Pediatr. Gastroenterol. Nutr.* **38**, 534–538 (2004).
- Saitoh, T. *et al.* Loss of the autophagy protein Atg16L1 enhances endotoxin-induced IL-1 β production. *Nature* **456**, 264–268 (2008).
- Yamagata, H. *et al.* Requirement of voltage-dependent anion channel 2 for pro-apoptotic activity of Bax. *Oncogene* **28**, 3563–3572 (2009).
- Sato, T. *et al.* Fas-mediated apoptosome formation is dependent on reactive oxygen species derived from mitochondrial permeability transition in Jurkat cells. *J. Immunol.* **173**, 285–296 (2004).
- Mariathasan, S. *et al.* Differential activation of the inflammasome by caspase-1 adaptors ASC and Ipaf. *Nature* **430**, 213–218 (2004).
- Martinon, F., Petrilli, V., Mayor, A., Tardivel, A. & Tschopp, J. Gout-associated uric acid crystals activate the NALP3 inflammasome. *Nature* **440**, 237–241 (2006).
- Domen, J., Cheshier, S. H. & Weissman, I. L. The role of apoptosis in the regulation of hematopoietic stem cells: Overexpression of Bcl-2 increases both their number and repopulation potential. *J. Exp. Med.* **191**, 253–264 (2000).
- Wieckowski, M. R., Giorgi, C., Lebiedzinska, M., Duszynski, J. & Pinton, P. Isolation of mitochondria-associated membranes and mitochondria from animal tissues and cells. *Nature Protocols* **4**, 1582–1590 (2009).

Supplementary Information is linked to the online version of the paper at www.nature.com/nature.

Acknowledgements This study was supported by grants of the Swiss National Science Foundation and by the Institute for Arthritis Research. A.S.Y. is a recipient of a stipend of the DFG. We would like to thank K. Schroder, C. Thomas and J. Vince for critical reading of the manuscript and G. W. Knott, EPFL, Lausanne, for help in collecting electron micrographs.

Author Contributions R.Z., A.S.Y. and P.M. devised and performed the experiments. J.T. supervised the work.

Author Information Reprints and permissions information is available at www.nature.com/reprints. The authors declare no competing financial interests. Readers are welcome to comment on the online version of this article at www.nature.com/nature. Correspondence and requests for materials should be addressed to J.T. (jurg.tschopp@unil.ch).

METHODS

Mice. *Nlrp3*^{-/-}, *Asc*^{-/-}, *Irf1*^{-/-} and H2K-Bcl-2 transgenic mice were described previously^{23–25}. All mice were on a C57BL/6 background except for experiments used for NLRP1b inflammasome activation (BALB/c).

Cell fractionation. MAMs, mitochondria and microsomes were isolated from PMA-differentiated THP1 cells as previously described²⁶.

Reagents. Nigericin, rotenone, antimycin, thenoyltrifluoroacetone (TTFA), uric acid, (2R,4R)-4-aminopyrrolidine-2, 4-dicarboxylate (APDC), 3-methyladenine (3-MA), ATP, menadione, carbonyl cyanide 3-chlorophenylhydrazone (CCCP), poly(AT) and silica were purchased from Sigma. MitoSOX, Mitotracker green, Mitotracker deep red, JC-1 and lysotracker red were from Invitrogen. LDH release kits were from Roche. Ultrapure LPS and R837 were obtained from InvivoGen. Inject alum was from Pierce. *Salmonella typhimurium* is a gift from R. Van Bruggen. Anti-human proIL-1 β was produced in house. The anti-NLRP3 antibodies (Cryo-2) were from Adipogen. Anti-human cleaved IL-1 β (D116), anti-ATG5 (2630S), anti-beclin 1 (3738), anti-calnexin (2433S), anti-caspase-3 (9662) and anti-VDAC1 (4866) antibodies were purchased from Cell Signaling. Anti-ASC antibody (AL177) was from Adipogen. Anti-TXNIP (40-3700) antibody was from Invitrogen. Anti-VDAC3 antibody (sc-79341), anti-FACL-4 (sc-47997) and anti-human caspase-1 (sc-622) were from Santa Cruz. Anti-VDAC2 antibody (ab77160), anti-Giantin (ab24586), anti-GAPDH (ab8245) and anti-calreticulin (ab14234) were from Abcam. Anti-mouse IL-1 β antibody was a gift from R. Solari. Anti-mouse caspase-1 (p20) antibody was a gift from P. Vandenabeele. Anti-Flag (M2) antibody was from List Biological Laboratories. All tissue culture reagents were from Invitrogen.

Generation of stable THP1 cells expressing Flag-NLRP3 or Flag-ASC. Retroviral vector (LZRS-MS-IRES-ZEO/PBR-Flag-NLRP3 or Flag-ASC) was co-transfected with the helper plasmids VSV-G and Hit60 into 293T cells by calcium phosphate transfection. Culture supernatants containing recombinant viral particles were harvested and used to infect THP1 cells in the presence of polybrene (8 mg ml⁻¹). To establish stable cell lines, THP1 cells were selected with zeocin (1 mg ml⁻¹) on day 3 after infection.

Transduction of GFP-LC3 in BMDMs. Lentiviral vector (plex-GFP-LC3) was co-transfected with the helper plasmids pCMV Δ R8.91 and pMDG into 293T cells by calcium phosphate transfection. Culture supernatants containing recombinant viral particles were harvested and used to infect BMDMs on day 3 after differentiation. On day 7, the cells can be used for advanced experiments.

Cell preparation and stimulation. Human THP1 cells were cultured in RPMI 1640 media, supplemented with 10% FBS. THP1 cells were differentiated for 3 h with 100 nM phorbol-12-myristate-13-acetate (PMA). Bone marrow macrophages were derived from tibia and femoral bone marrow progenitors as described²⁷, and were primed for 4 h with 100 ng ml⁻¹ Ultra-pure LPS. For the induction of inflammasome activation, 10⁶ LPS-primed bone marrow macrophages or PMA-differentiated THP1 cells plated in 12-well plates were treated with MSU (150 μ g ml⁻¹), alum (200 μ g ml⁻¹), silica (200 μ g ml⁻¹), R837 (15 μ g ml⁻¹) for 6 h or with ATP (5 mM) or nigericin (15 μ M) for 30 min. For poly(dA:dT) transfection,

poly(dA:dT) was transfected using Lipofectamine (4 μ l ml⁻¹) as per the manufacturer's protocol (Invitrogen). Cell extracts and precipitated supernatants were analysed by immunoblot.

Generation of stable THP1 cells expressing shRNA. THP1 cells stably expressing shRNA were obtained as previously described²⁸; shRNA against NLRP3 and caspase-1 plasmids has been described¹⁵ and shRNA plasmids against beclin-1, ATG5, VDAC1, VDAC2 and VDAC3 were from Sigma.

Confocal microscopy. PMA-differentiated THP1 cells were plated on coverslips for 3 days and then used for stimulation or staining with Mitotracker red (50 nM) or Lysotracker (200 nM). After washing two times with PBST, the cells were fixed with PFA 4% in PBS for 15 min and then washed three times with PBST. After permeabilization with Triton X-100 and blocking with 10% goat serum in PBS, cells were incubated with primary antibodies (in 10% goat serum) overnight at 4 °C. After washing with PBST, cells were incubated with secondary antibodies (Invitrogen) in 10% goat serum-PBS for 60 min and rinsed in PBST. Confocal microscopy analyses were carried out using a Zeiss LSM510.

Flow cytometric analyses. Mitochondrial mass was measured by fluorescence levels upon staining with Mitotracker green and Mitotracker deep red at 50 nM for 30 min at 37 °C. Mitochondria-associated ROS levels were measured by staining cells with MitoSOX at 2.5 μ M for 30 min at 37 °C. Mitochondria membrane potential was measured using the kit from Invitrogen and performed according to the manufacturer's instructions. Cells were then washed with PBS solution and resuspended in cold PBS solution containing 1% FBS for FACS analysis.

Salmonella infection. *Salmonella typhimurium* was pre-cultured on day 1. On day 2, differentiated THP1 cells were infected for 1 h with the *S. typhimurium* culture (1:100). Cells were washed and then incubated for 3 h in OptiMEM medium with gentamycin (Invitrogen).

ELISA. Cell culture supernatants were assayed for mouse IL-1 β and TNF (R&D) according to manufacturer's instructions.

Immunoelectron microscopy. For the pre-embedding immuno-EM of cells, PMA-differentiated Flag-Nlrp3-THP1 cells were fixed with 4% PFA for 15 min and were cryoprotected in 2% glycerol and 20% DMSO in PBS. After two freeze-thaw cycles, the cells were blocked in PBS with 0.2% BSA and 0.02% Triton X-100 for 1 h. After washing, the cells were incubated with anti-Flag antibody and gold-conjugated secondary antibody. Silver enhancement was performed by incubating cells with silver enhancement reagent for 1 h in room temperature. After osmification in 0.5% osmium tetroxide for 15 min and dehydration in graded alcohol, the samples were embedded in Durcupan.

Statistical analyses. All values were expressed as the mean \pm s.e.m. of individual samples. Samples were analysed using Student's *t*-test for two groups and ANOVA for multiple groups.

27. Didierlaurent, A. *et al.* Tollip regulates proinflammatory responses to interleukin-1 and lipopolysaccharide. *Mol. Cell. Biol.* **26**, 735–742 (2006).
28. Papin, S. *et al.* The SPRY domain of Pyrin, mutated in familial Mediterranean fever patients, interacts with inflammasome components and inhibits proIL-1 β processing. *Cell Death Differ.* **14**, 1457–1466 (2007).